THE ROLE OF SARCOMERIC PROTEINS AND THEIR POST-TRANSLATIONAL MODIFICATIONS IN STRIATED MUSCLE HEALTH, DISEASE, AND AGING

By

Zachery Robert Gregorich

A dissertation submitted in partial fulfillment of the requirements for the degree of

Doctor of Philosophy

(Molecular and Cellular Pharmacology)

At the

UNIVERSITY OF WISCONSIN-MADISON

2017

Date of final oral examination: 8/22/2017

This dissertation is approved by the following members of the Final Oral Committee:

Ying Ge, PhD, Associate Professor, Cell and Regenerative Biology

Youngsook Lee, PhD, Associate Professor, Cell and Regenerative Biology

Lingjun Li, PhD, Professor, Pharmaceutical Sciences

Timothy J. Kamp, MD/PhD, Professor, Cell and Regenerative Biology

Gary Diffee, PhD, Professor and Chair, Kinesiology

© Zachery R. Gregorich 2017

All Rights Reserved

Acknowledgements

First and foremost, I would like to thank my mentor, Dr. Ying Ge. After a rough first year and a half of graduate school—during which time I switched labs and then rotated through an additional two labs without being offered a position—I was almost at the point of leaving graduate school. Fortunately for me, I decided to do one last rotation in Ying's lab. Ying's lab turned out to be a perfect fit for me, and she accepted me into her group without hesitation. She has always been incredibly supportive and it has been a genuine pleasure to work with her these past five years. Wherever I end up, I can only hope that I will have a supervisor with as much compassion, understanding, and passion for science as Ying has. Second, I would like to thank the late Dr. Patricia Keely, the former director of the Molecular and Cellular Pharmacology program. Dr. Keely truly went above and beyond the call to support me during my rocky start to graduate school, and I do not doubt that I would not be where I am today without her guidance and help. Third, I would like to thank my parents for all their love and support, not only during graduate school, but also during my undergraduate studies, and throughout my life. They have always encouraged me to pursue my passions and for that, I am extremely grateful and blessed. Lastly, I would like to thank my lab mates, both past and present. Without their training, support, and friendship my doctoral training would not have been as productive or enjoyable. Last, but certainly not least, I would like to thank my committee for their help and guidance throughout my doctoral training.

Abstract

Sarcomeric proteins, including both myofilament and Z-disc proteins, constitute the molecular machinery responsible for force production in a Ca^{2+}-dependent manner. In addition to regulation by Ca^{2+}, convincing evidence now indicates that the post-translational modification (PTM) of myofilament proteins is an essential mechanism enabling the Ca^{2+}-independent modulation of striated muscle contractility. Moreover, the view of the Z-discs as passive structures, necessary only for force transmission between adjacent sarcomeres, has undergone a paradigm shift, with the results of recent studies implicating these structures in signaling, and even in the regulation of striated muscle contractile function. In the studies detailed in this thesis, top-down mass spectrometry-based proteomics was employed in combination with functional assays to gain insights into the role of sarcomeric proteins and their PTMs in the heart under basal conditions and in response to myocardial injury, as well as in skeletal muscle during natural aging. Collectively, the key findings presented herein shed new light on the roles of myofilament protein PTMs in cardiac and skeletal muscle contractile function under basal and pathological conditions. Also noteworthy was the identification of alterations in the phosphorylation of Z-disc proteins in cardiac and skeletal muscles in response to infarction and natural aging, respectively. These findings provide the first evidence that the Z-discs may be involved in the early events in the heart after injury and in aging skeletal muscles. Moreover, evidence that enigma homolog protein isoforms, which localize to the Z-discs in striated muscles, play a role in setting the kinetics of force redevelopment, at least in mouse myocardium, is also presented. Thus, these findings not only provide new information regarding the contributions made by myofilament protein PTMs to striated muscle contractility, but also open new avenues to explore the role of Z-disc proteins in

striated muscle biology. Furthermore, these results add to a growing list of contributions made by top-down mass spectrometry to the advancement of our understanding of the functions of protein PTMs in health and disease.

Table of Contents

Acknowledgements…….. i

Abstract……ii

List of figures and Tables……..vii

CHAPTER 1 – INTRODUCTION……...1

1.1 Overview of sarcomere structure in striated muscles…….…....1

1.2 Ca^{2+}-dependent regulation of contraction in striated muscles…….……1

1.3 Ca^{2+}-independent regulation of striated muscle contractility…….....4

1.4 Emerging role of the Z-disc in striated muscle biology and signaling…….….10

1.5 Altered contractility and myofilament protein phosphorylation in heart failure (HF)..14

1.6 The role of myofilaments in sarcopenia-associated muscle dysfunction……..17

1.7 Mass spectrometry (MS)-based proteomics approaches…….. 20

1.8 Top-down proteomics in biomedical research…….…….22

CHAPTER 2 – COMPREHENSIVE ASSESSMENT OF CHAMBER-SPECIFIC AND TRANSMURAL HETEROGENEITY IN MYOFILAMENT PROTEIN PHOSPHORYLATION BY TOP-DOWN MASS SPECTROMETRY……30

2.1 Introduction……..32

2.2 Materials and methods……..33

2.3 Results……..39

2.4 Discussion……44

CHAPTER 3 – DISTINCT SEQUENCES AND POST-TRANSLATIONAL MODIFICATIONS IN CARDIAC ATRIAL AND VENTRICULAR MYOSIN LIGHT CHAINS REVEALED BY TOP-DOWN MASS SPECTROMETRY……..61

3.1 Introduction……..63

3.2 Materials and methods……..65

3.3 Results……..71

3.4 Discussion……77

CHAPTER 4 – TOP-DOWN PROTEOMICS REVEALS CONCERTED REDUCTIONS IN MYOFILAMENT AND Z-DISC PROTEIN PHOSPHORYLATION AFTER ACUTE MYOCARDIAL INFARCTION……. 121

4.1 Introduction……124

4.2 Materials and methods……126

4.3 Results……132

4.4 Discussion……..138

CHAPTER 5 – DELETION OF THE Z-DISC PROTEIN ENIGMA HOMOLOG DEPRESSES CROSS-BRIDGE CYCLING KINETICS IN MOUSE MYOCARDIUM……..179

5.1 Introduction……181

5.2 Materials and methods……183

5.3 Results……191

5.4 Discussion……..196

CHAPTER 6 – TOP-DOWN TARGETED PROTEOMICS REVEALS DECREASE IN MYOSIN REGULATORY LIGHT-CHAIN PHOSPHORYLATION THAT CONTRIBUTES TO SARCOPENIC MUSCLE DYSFUNCTION……...……220

6.1 Introduction……222

6.2 Materials and methods……224

6.3 Results……234

6.4 Discussion……..241

CHAPTER 7 – NOVEL SARCOPENIA-RELATED ALTERATIONS IN SARCOMERIC PROTEIN POST-TRANSLATIONAL MODIFICATIONS IN SKELETAL MUSCLES IDENTIFIED BY TOP-DOWN PROTEOMICS…….……265

7.1 Introduction……267

7.2 Materials and methods……270

7.3 Results……276

7.4 Discussion……..285

CHAPTER 8 – CONCLUSIONS AND FUTURE DIRECTIONS……..364

SELECTED REFERENCES……371

List of Figures and Tables

Fig. 2.1……..48

Fig. 2.2……...49

Fig. 2.3……...51

Fig. 2.4……...52

Fig. 2.5……...54

Fig. 2.6……...56

Fig. 2.7……...58

Fig. 2.8……...59

Fig. 3.1……...86

Table 3.1…….87

Fig. 3.2……...88

Fig. 3.3……...90

Fig. 3.4……...91

Fig. 3.5……...92

Fig. 3.6……...94

Fig. 3.7……...95

Fig. 3.8……...96

Fig. 3.9……...97

Table 3.2……98

Fig. 3.10……99

Fig. 3.11……...101

Fig. 3.12……...103

Fig. 3.13……..…..……104

Fig. 3.14……..…..……105

Fig. 3.15…….……..…..…107

Fig. 3.16…….……..….108

Fig. 3.17…….…..110

Fig. 3.18……..……111

Fig. 3.19……..…….112

Fig. 3.20……...……114

Fig. 3.21……..…….116

Fig. 3.22…….……..118

Fig. 3.23……..……..119

Fig. 3.24……...……120

Fig. 4.1…….……147

Fig. 4.2……..…148

Table 4.1……...……150

Fig. 4.3…….151

Fig. 4.4…….152

Table 4.2……..……153

Fig. 4.5…….155

Fig. 4.6…….158

Fig. 4.7……...……..159

Fig. 4.8……...…..161

Fig. 4.9……..…162

Fig. 4.10……163

Fig. 4.11……165

Fig. 4.12……166

Fig. 4.13……167

Fig. 4.14……168

Fig. 4.15……169

Fig. 4.16……170

Fig. 4.17……171

Fig. 4.18……172

Fig. 4.19……174

Fig. 4.20……176

Fig. 4.21……177

Fig. 4.22……178

Fig. 5.1……200

Fig. 5.2……201

Fig. 5.3……202

Fig. 5.4……203

Table 5.1……204

Fig. 5.5……206

Fig. 5.6……207

Fig. 5.7……209

Fig. 5.8……211

Fig. 5.9……212

Fig. 5.10……213

Fig. 5.11……214

Fig. 5.12……215

Fig. 5.13……216

Fig. 5.14……217

Fig. 5.15……218

Fig. 5.16……219

Fig. 6.1……248

Fig. 6.2……249

Table 6.1……251

Fig. 6.3……252

Fig. 6.4……254

Fig. 6.5……255

Fig. 6.6……256

Fig. 6.7……257

Fig. 6.8……259

Fig. 6.9……261

Fig. 6.10……262

Table 6.2……264

Fig. 7.1……298

Fig. 7.2……300

Fig. 7.3……301

Fig. 7.4……303

Fig. 7.5……..…305

Table 7.1……..…307

Fig. 7.6…….……309

Fig. 7.7…….310

Fig. 7.8…….313

Fig. 7.9…….315

Fig. 7.10……...316

Fig. 7.11……...……318

Fig. 7.12……..…….320

Fig. 7.13…….……..322

Fig. 7.14……...323

Fig. 7.15……...324

Table 7.2…….……..325

Fig. 7.16……...326

Fig. 7.17……...……328

Fig. 7.18……...330

Fig. 7.19……..…….332

Fig. 7.20…….…..334

Table 7.3……..336

Fig. 7.21……...……337

Fig. 7.22…….……..340

Fig. 7.23……...342

Fig. 7.24…….……..343

Fig. 7.25……...……345

Fig. 7.26……...…347

Fig. 7.27……...……349

Fig. 7.28……...……350

Fig. 7.29……...352

Fig. 7.30…….…..354

Fig. 7.31……..…….356

Table 7.4…….…….358

Fig. 7.32……..…….359

Fig. 7.33……...361

Fig. 7.34……..…….363

CHAPTER 1 – INTRODUCTION

1.1 Overview of sarcomere structure in striated muscles

Sarcomeres represent the most basic functional units of striated muscle, and are composed of interdigitating thin and thick filaments (the myofilaments) flanked on either side by protein dense structures known as Z-discs (alternatively Z-lines or Z-bands). While the thin filaments are predominantly composed of actin, the principal component of thick filaments is the myosin. Cyclical interactions between actin and myosin are ultimately responsible for striated muscle contraction in an ATP- and Ca^{2+}-dependent manner [1, 2]. In addition to actin and myosin are a number of proteins localizing to the thin and thick filaments that regulate actin-myosin interactions. On the thin filament, these include tropomyosin (Tpm) and troponin (Tn); a hetero-trimeric protein complex consisting of an inhibitory subunit, troponin I (TnI); a tethering subunit that anchors Tn to Tpm, troponin T (TnT); and the Ca^{2+}-binding subunit troponin C (TnC). On the other hand, thick filament regulatory proteins include the myosin essential (MLC-1) and regulatory (MLC-2) light chains, as well as myosin binding protein C (MyBP-C). Although these components are present in both cardiac and skeletal muscles, the expression of muscle-type-specific isoforms has profound implications for the Ca^{2+}-dependent and Ca^{2+}-independent regulation of contraction.

1.2 Ca^{2+}-dependent regulation of contraction in striated muscles

Despite what now seems relatively direct evidence implicating Ca^{2+} in the regulation of striated muscle contractility years earlier [3, 4], it was not until the early 1960s that Ca^{2+} was recognized as the essential physiological regulator of the contractile process [5, 6]. Nevertheless, the delayed recognition of Ca^{2+} as the trigger enabling actin-myosin interactions in striated muscle is perhaps not surprising as an understanding of Ca^{2+}-mediated regulation requires knowledge of protein constituents other than actin and myosin. In fact, given that the Ca^{2+} receptor within the myofilaments (Tn) was not identified until years later [7, 8], it is actually remarkable that an elementary mechanism for the Ca^{2+}-dependent regulation of striated muscle contraction (i.e., wherein Ca^{2+} binding to and removal from the contractile apparatus promote contraction and relaxation, respectively) was postulated in 1960 [9].

Some of the earliest evidence indicating that additional proteins participate in the regulation of actin-myosin interactions in striated muscle came in 1961 when Weber and Winicur noted that the ability of EGTA, a Ca^{2+} chelating agent, to inhibit actin-myosin interactions depended on the way in which the actin was prepared [10]. Two years later Ebashi purified an additional protein component that was necessary for chelating agent-induced relaxation in reconstituted actomyosin [11]. The protein constituent closely resembled (and was later confirmed to be) the protein Tpm, which was identified by Bailey in 1946 [12]. Subsequent experiments showed that 'native' (i.e., less pure), but not purified Tpm, was able to sensitize synthetic actomyosin to the actions of Ca^{2+}, hinting that yet another component was necessary to fully recapitulate the properties of native actomyosin [8]. This component, identified in 1964 and named Tn [8], was determined to be the Ca^{2+}-receptive element in the contractile system in 1967 [7]. The finding that Tn is localized along the thin filament at a periodicity of ~400 Å [13]—a distance that cannot be covered by Tn alone—

led to the proposal of a mechanism wherein actin-myosin interactions and, thus, muscle contraction, is prevent in resting muscle via blockage of myosin binding sites on the actin filaments by Tn and Tpm [6].

In the years that followed, this mechanism gained traction as structural studies showed that the positioning of Tpm on the thin filament was changed in activated muscle [14]. Based on these results, as well as those of previous studies, the steric blocking model of muscle regulation was put forward in the early 1970s [15]. In its simplest form, the steric blocking model posits that, at low levels of intracellular Ca^{2+}, the thin filament exists in what is referred to as the "off" state, which is characterized by steric blockage of the myosin cross-bridge binding sites on the thin filament by the Tn•Tpm complex [15]. Conversely, when the intracellular Ca^{2+} concentration rises above the threshold for binding to Tn, Ca^{2+} is bound by TnC, inducing a conformational change in Tn•Tpm that relieves inhibition of actomyosin [15]. In this state, termed the "on" state, cyclical interactions between myosin cross-bridges and actin propel the thin filaments towards the center of the sarcomere resulting in shortening and force production [15]. This model has since been refined to account for biochemical [16-18] and structural [19, 20] evidence indicating that the thin filaments in striated muscle can also exist in an third state, termed the "closed" state, which is characterized by weak binding of cross-bridges to the thin filament in a non-force-generating manner. The "closed" state, in combination with the "blocked" (analogous to the "off" state) and "open" (analogous to the "on" state) states, can explain structural changes in the thin filament that confer Ca^{2+}-dependence to striated muscle contraction.

1.3 Ca^{2+}-independent regulation of striated muscle contractility

Although the role of Ca^{2+} as the physiological trigger for muscle contraction had been appreciated since the early 1960s as detailed above, the first clues that sarcomeres are not merely slaves to the intracellular Ca^{2+} concentration did not emerge until years later. In 1970, Ashley and Ridgway utilized the Ca^{2+}-sensitive photoprotein aequorin to simultaneously monitor Ca^{2+} transients and tension in single stimulated muscle fibers isolated from the barnacle *Balanus nubilus* [21]. Strikingly, they observed that, at the time that peak tension was reached, much of the Ca^{2+} had already dissociated from the contractile apparatus and was re-sequestered within the sarcoplasmic reticulum [21]. Based on this observation, the authors concluded that, while Ca^{2+} is necessary to initiate force generation, the maintenance of tension and rate of relaxation depend on processes other than Ca^{2+} removal from the cytosol [21]. Following this study, similar findings would be reported in frog skeletal and cardiac muscles [22, 23], as well as mammalian cardiac muscle [24-28], providing strong support for the idea that, at the very least, the dynamics of relaxation depend on the intrinsic properties of the sarcomeres. Since this foundational work, the view of the sarcomeres as active determinants of striated muscle contractility has become widely accepted. Furthermore, in recent years, the post-translational modification (PTM) (e.g., phosphorylation) of contractile proteins has come to be recognized as an essential mechanism for altering force and the dynamics of force development/decay at a given level of Ca^{2+} [29-33]. Indeed, a variety of myofilament PTMs, including phosphorylation, proteolysis, nitrosylation, and O-GlcNAcylation, among others, have been reported, and many have been shown to alter contractile function in striated muscle [34-36]. However, to date, the most highly studied and best understood of these PTMs is phosphorylation.

In the heart, the phosphorylation of myofilament proteins plays a critical role in enhanced cardiac inotropy and lusitropy secondary to the activation of β-adrenergic receptors (ARs) (the so called fight or flight response). Under conditions of increased circulatory demand, stimulation of β-ARs leads to the activation of protein kinase A (PKA), which phosphorylates, among other Ca^{2+} handling proteins [37], the myofilament proteins cardiac TnI (cTnI) [38] and cardiac MyBP-C (cMyBP-C) [39]. In the case of cTnI, PKA catalyzes the phosphorylation of Ser22 and Ser23 (number is based on the human cTnI sequence, including the initiating Met, which is cleaved in the mature protein), two residues that are located within the cardiac-specific N-terminal extension of the protein [29]. Similarly, PKA phosphorylates three serine residues (i.e., Ser275, Ser284, and Ser304; number is based on the human cMyBP-C sequence, including the initiating Met, which is removed in the mature protein) in the cardiac-specific m-domain of cMyBP-C [40]. The PKA-mediated phosphorylation of cTnI and cMyBP-C has been shown to decrease the Ca^{2+} sensitivity of force and accelerates the kinetics of cross-bridge cycling in skinned myocardial preparations [29, 41, 42]. Although disentangling the respective contributions of these proteins proved difficult, the results of elegant studies conducted by the Moss lab indicate that the decrease in myofilament Ca^{2+} sensitivity secondary to β-AR stimulation is primarily mediated by phosphorylation of cTnI [42], while the increase in cross-bridge cycling kinetics can be ascribed to phosphorylation of cMyBP-C [42, 43].

Mechanistically, the decrease in the Ca^{2+} sensitivity of force precipitated by PKA-mediated phosphorylation of cTnI results from modulation of the Ca^{2+}-binding properties of TnC. Experimental evidence indicates that, in the un- or mono-phosphorylated state, the N-terminal

extension of cTnI binds the N-terminal domain of TnC, thereby stabilizing the "open" Ca^{2+}-binding conformation of TnC [44-48]. Conversely, phosphorylation of cTnI appears to reduce the affinity of the N-terminal extension for TnC, which destabilizes the TnC•Ca^{2+} complex and accelerates Ca^{2+} release [44-48].

In the case of cMyBP-C, when in the un-phosphorylated state the protein binds myosin sub-fragment 2 (S2) [49-52], stabilizing the myosin heads in a relaxed highly ordered off-state configuration about the thick filament backbone [53]. Thus, under basal conditions, cMyBP-C is thought to act as a brake, constraining movement of the myosin heads or stabilizing them in the relaxed state and depressing cross-bridge cycling kinetics as a result. The PKA-mediated phosphorylation of cMyBP-C at the aforementioned sites disrupts the interaction between the N-terminal region of cMyBP-C and myosin S2, and promoting the radial movement of myosin heads away from the thick filament backbone [54, 55]. While repositioning of cross-bridges nearer to the thin filament would increase the probability of actin-myosin interactions and, thus, can account for the increased rate of cross-bridge attachment at sub-maximal levels of activation, this mechanism alone is at odds with the fact that cMyBP-C phosphorylation does not increase cross-bridge cycling kinetics at maximal Ca^{2+} [42, 43]. If movement of cross-bridges nearer to the thin filament was indeed the sole mechanism underlying enhanced contraction kinetics, then phosphorylation of cMyBP-C would also be expected to increase cross-bridge cycling kinetics at maximal activation by increasing the probability of binding to actin [53]. Likewise, one would anticipate an increase in maximal force as well, which is not the case [55, 56]. Thus, it seems unlikely that movement of cross-bridges towards the thin filament is solely responsible for the mechanical effects of cMyBP-C phosphorylation. Other interactions, including interactions

between the N-terminal domain of phosphorylated cMyBP-C and actin [57-59] also likely play a role in the functional outcomes of cMyBP-C phosphorylation.

Therefore, alterations in mechanical activity resulting from cTnI and cMyBP-C phosphorylation act synergistically with changes in Ca^{2+} flux to simultaneously augment contractility and preserve ventricular filling at elevated heart rates. Moreover, the phosphorylation of cMyBP-C may also be important for basal cardiac function as transgenic mice expressing non-phosphorylatable cMyBP-C develop significant cardiac hypertrophy with sarcomere disarray and fibrosis in the absence of extrinsic stressors (e.g., transverse aortic contriction) [60]. It is also worth noting that the skeletal muscle isoforms of TnI and MyBP-C lack the phosphorylation sites present in their cardiac-specific counterparts and, thus, phosphorylation of these proteins is not believed to contribute to the regulation of contractile function in skeletal muscles.

In contrast to cTnI and cMyBP-C, which contain phosphorylation sites not present in their cognate isoforms in skeletal muscle, the N-terminal phosphorylation site(s) in MLC-2 are conserved in all muscle-type-specific isoforms of the protein. Functionally, the phosphorylation of serine residues near the N-terminus of MLC-2 by the Ca^{2+}/calmodulin-dependent myosin light chain kinase increases the Ca^{2+} sensitivity of force [31, 61-69], accelerates the rate of force development [31, 63], and increases force at all levels of activation [70] in skinned preparations from both skeletal and cardiac muscles. Structurally, MLC-2 phosphorylation promotes the radial movement of cross-bridges towards the thin filament [30, 55] through a mechanism involving charge repulsion between the phosphate group and negatively charged residues in the thick filament backbone [71]. Therefore, the phosphorylation of MLC-2 increases the rate of cross-bridge attachment and, thus,

the rate of force development at all levels of activation [31, 63]. However, in contrast to cMyBP-C phosphorylation, which increases both the rates of contraction and relaxation [72, 73], phosphorylation of MLC-2 increases only the rate of contraction, while simultaneously slowing the rate of relaxation [61, 70, 74]. This can be explained by the fact that the phosphorylation of MLC-2 results in a relatively high rate of cross-bridge attachment relative to the detachment rate. Under these conditions, strong cross-bridge binding favors the attachment of additional cross-bridges (as a consequence of cooperative activation of the thin filament), and results in an overall greater number of cross-bridges bound to the thin filament [74]. Thus, at a given level of Ca^{2+}, the increased number of bound cross-bridges prolongs thin filament activation and decreases the rate of decay in force even after Ca^{2+} has dissociated from the contractile apparatus [74]. Such a mechanism is supported by the observation that *N*-ethylmaleimide-modified myosin, a chemically modified strong-binding derivative of myosin that enhances thin filament activation, produces similar effects to those of MLC-2 phosphorylation [74]. The increased Ca^{2+} sensitivity of force upon MLC-2 phosphorylation can also be explained by repositioning of the myosin heads nearer to the thin filament [55]. In the heart, RLC phosphorylation is thought to set the kinetics of force development and Ca^{2+} sensitivity of force in cardiac muscle under basal conditions [65]. Studies using transgenic animals seem to indicate that phosphorylation of MLC-2 is essential not only for basal cardiac function [75], but also for adaptation of the myocardium to stress [76, 77]. Likewise, in skeletal muscle, MLC-2 phosphorylation enhances contractile function, and has been shown to underlie potentiation, the phenomenon by which successive nerve impulses trigger progressively more intense contractions [78].

The phosphorylation of Tpm isoforms in striated muscle was first demonstrated in frog skeletal muscle in 1977 [79]. Subsequent studies reported the existence of a phosphorylated form of α-Tpm in rabbit cardiac and skeletal muscles; and localized the site of phosphorylation in α-Tpm from frog and rabbit skeletal muscle, as well as rabbit cardiac muscle, to Ser283—the sole site of phosphorylation in the α and β isoforms of Tpm (the predominant isoforms expressed in striated muscles) [80]. In contrast to other sarcomeric proteins, the phosphorylation of Tpm appears to be relatively unique in that it does not appear to be subject to rapid modulation. In support of this, evidence from multiple labs has demonstrated that Tpm phosphorylation is unaltered in the failing heart despite significant changes in the phosphorylation status of other sarcomeric proteins, including cTnI [81, 82]. Moreover, the phosphorylation status of Tpm is not affected by electrically-induced tetanus in skeletal muscle [83].

Despite the fact that Tpm phosphorylation does not appear to be subject to rapid regulation, reconstituted thin filaments containing phosphorylated Tpm were found to activate myosin sub-fragment 1 Mg^{2+}-ATPase activity to a greater extent than those reconstituted with un-phosphorylated Tpm [84]. These results indicate a potential role for Tpm phosphorylation in the modulating contractile function. More recently, Nixon et al. demonstrated a role for Tpm phosphorylation in the dynamics of muscle relaxation [85]. Using exchange experiments, the authors demonstrated that reconstitution of myofibrils with pseudo-phosphorylated Tpm (i.e., wherein Ser283 was replaced with a "phospho-mimetic" Asp residue) not only increased Mg^{2+}-ATPase activity as previously demonstrated, but also prolonged the slow phase of relaxation and decreased the rate of the fast phase without altering activation kinetics [85]. Mechanistic insights were gained by examination of the kinetics of Ca^{2+} dissociation from the thin filament, which

revealed a reduction in both the on- and off-rates of Ca^{2+} from TnC in myofibrils reconstituted with pseudo-phosphorylated Tpm [85]. Collectively, these results suggest that increased Tpm phosphorylation prolongs thin filament activation and slows muscle force relaxation dynamics by modulating the kinetics of Ca^{2+} association and dissociation from TnC [85]. The molecular mechanism by which Tpm phosphorylation modulates the affinity of TnC for Ca^{2+} is unclear, but may be transmitted to Tn via TnT, which interacts with Tpm in the head-to-tail overlap region [86].

Another of the major phospho-proteins in the myofilament is TnT. Despite the fact that a number of functionally relevant phosphorylation sites have been described in cardiac TnT (cTnT) *in vitro* [87], to date, the only residue definitively confirmed to be phosphorylated *in vivo* is Ser2 (numbering based on the sequence of the human protein including the initiating Met, which is removed in the mature protein) [88-90]. Phosphorylation at this site, which is conserved across all striated muscle-type-specific isoforms of TnT, appears to be constitutive rather than dynamically regulated. In support of this, studies have shown that cTnT phosphorylation is unchanged in a variety of pathological conditions, despite marked changes in the phosphorylation of other myofilament proteins [81, 82, 91-93]. Thus, N-terminal phosphorylation of TnT may be important for the structure or stability of the protein rather than for regulating contractility.

1.4 Emerging role of the Z-disc in striated muscle biology and signaling

The anti-parallel actin filament ends from adjacent sarcomeres overlap at the Z-disc, where they are cross-linked into a highly ordered lattice structure by the actin-binding protein α-actinin—the

major protein constituent of Z-discs. In recent years, the view of the Z-disc has undergone a paradigm shift. Long thought to merely aid force transmission via the cross-linking of actin filaments of opposite polarity from adjoining sarcomeres, the importance of the Z-disc in muscle biology has come to light with the identification of a growing list of Z-disc protein mutations that have been linked to cardiac and skeletal muscle myopathies [94, 95]. Moreover, emerging evidence now indicates that these structures serve as signaling epicenters within the myocyte [96-99], and an increasing number of signaling molecules, including kinases (e.g., PKC, PAK1) and phosphatases (e.g., calcineurin), as well as proteins involved in transcription, such as the transcriptional co-regulator Ankrd2, have been found to localize to Z-discs [96, 97, 100-105].

Paramount for structural integrity and the localization of signaling factors to the Z-disc are a myriad scaffolding proteins, chief among which are those belonging to the Enigma sub-family of PDZ/LIM domain proteins [99, 100]. Proteins belonging to this family are modular proteins that contain two common domains involved in mediating protein-protein interactions—the PDZ [106] and LIM [107] domains—and participate in the organization of macromolecular signaling complexes. Enigma, the prototypical member of this sub-family, was discovered in 1994, and contains a single N-terminal PDZ domain and three C-terminal LIM domains [108]. Additional members of this protein subfamily include Enigma Homolog (ENH) [109] and Cypher (also known as ZASP or Oracle) [110-112].

The results of structural analysis of the PDZ domain of Enigma family proteins indicate that this domain interacts with the C-terminal sequence of α-actinin [113], which promotes the localization of Enigma family proteins to the Z-disc in striated muscles. This conclusion is also supported by

results from localization studies using immunofluorescence microscopy [112, 114]. More recently, it was demonstrated that the Z-disc proteins Myotilin and Calsarcin/FATZ contain class III PDZ binding motifs that bind the PDZ domains of Enigma family members [115], and, moreover, that these proteins exist in multi-protein complexes with ENH and Cypher isoforms at the Z-discs [116, 117]. There is also evidence in the literature that the PDZ domain of Enigma binds β-Tpm [118]. Conversely, the LIM domains of Enigma family proteins have been shown to interact with a variety of kinases (e.g., PKC, PKA, PKD, AMPK) [109, 112, 119-121] and other enzymes, such as phosphoglucomutase 1 (PGM1) [122]. Furthermore, evidence now suggests that, in addition to binding kinases, the LIM domains of Enigma family proteins may be capable of modulating the activity of these enzymes in the absence of activating ligands [123, 124].

Additional evidence supporting a direct and important role for Enigma family proteins in Z-disc signaling has also been published. In 2004, Arimura et al. identified a mutation (D626N) within the third LIM domain of Cypher/ZASP that was associated with familial late onset dilated cardiomyopathy (DCM) [125]. Subsequent characterization of the mutant protein revealed an increased affinity for PKC, implicating aberrant Cypher-directed PKC signaling in the pathogenesis of DCM [125]. In a second paper published in 2009, Arimura et al. provided evidence that DCM-associated mutations in Cypher are associated with reduced affinity for PGM1, an enzyme involved in glycolysis and gluconeogenesis [122]. The authors' demonstration that the Cypher-PGM1 interaction is necessary for localization of this enzyme to Z-discs under stress conditions indicates a potentially important role for the Z-disc in metabolic signaling [122]. In 2010, Yamazaki et al. showed that decreased expression of the long isoform of ENH, or overexpression of a short isoform of the protein lacking the C-terminal LIM domains, abrogates

the hypertrophic response in isolated neonatal rat cardiomyocytes treated with pro-hypertrophic stimuli, including aldosterone, phenylephrine, and endothelin [126]. In further support of a role for ENH in pro-hypertrophic signaling, a recent study by Ito et al. demonstrated that the long, but not short, isoforms of ENH mediate the hypertrophic response via regulation of the PKC/PKD1-mediated phosphorylation of the transcription factor CREB [124]. In summary, these findings support the conclusion that Enigma family proteins play a critical role in signaling processes within the Z-disc.

Evidence in the literature also suggests a role for the Z-disc in the Ca^{2+}-independent regulation of striated muscle contractility. In particular, in 2002 Pyle et al. showed that the Ca^{2+} sensitivity of force was increased in permeabilized fiber bundles isolated from transgenic mice with decreased Z-disc incorporation of CapZ, a protein that caps the barbed ends of actin filaments anchored in the Z-disc [104]. The increased Ca^{2+} sensitivity of force was found to correlate with alterations in the localization of PKC isoforms to the myofilaments [104]. Subsequent work by the same group demonstrated that CapZ is responsible for anchoring a specific sub-population of PKC-β_{II} that regulates cTnI phosphorylation and, thus, is important for altering the Ca^{2+} responsiveness of the myofilaments [127]. More recent evidence by Yang et al. indicates that CapZ may also play a role in the protein phosphatase 1α-mediated dephosphorylation of myofilament proteins as well [105]. Similarly, the regulation of protein phosphatase 2A-mediated cTnI dephosphorylation may also occur via a mechanism involving the activation of a Z-disc-associated pool of the kinase p21-activated kinase 1 [128]. Collectively, these studies provide evidence of a direct link between Z-disc signaling and control of striated muscle contractile function at the level of the myofilaments, although this crosstalk is only beginning to be understood.

1.5 Alterations in contractility and sarcomeric protein phosphorylation in heart failure (HF)

Despite advancements in the treatment of HF, the 5-year mortality rate for this devastating syndrome remains high at nearly 50% [129]. HF is also associated with substantial economic costs, with an estimated cost of $30.7 billion in the year 2012 alone, of which 68% was attributable to direct medical costs [129]. Furthermore, projections suggest that the prevalence of HF will increase by approximately 46% by the year 2030, resulting in more than 8 million people greater than 18 years of age with HF [129].

HF is a clinical syndrome that is defined by the inability of the heart to adequately supply the rest of the body with blood [130]. As such, it is important to note that HF is actually an umbrella term used to describe pump failure resulting from varying and, in some cases, uncertain, etiologies. These can include genetic causes, ischemic injury, pressure overload, inflammation, and infection, among others [130, 131]. Thus, while all of these insults can ultimately culminate in what is classified as the clinical syndrome of HF, the underlying molecular mechanisms are disparate. Therefore, to avoid potentially conflicting information stemming from differences in disease etiology, the following discussion will primarily focus on findings in ischemic and non-ischemic DCM. Moreover, as evidence indicates that distinct mechanisms may underlie cardiac pathophysiology in rodents [132], the discussion will be restricted to studies using human patient tissue or in large animal models of HF resulting from ischemic injury.

A hallmark of both ischemic and non-ischemic DCM is marked systolic (contractile) dysfunction [133]. Although alterations in Ca^{2+} homeostasis [134] and thinning of the ventricular wall

undoubtedly play a role in impaired contractility in failing hearts, evidence from mechanical analyses using reconstituted thin/thick filaments or skinned (de-membranated) muscle preparations indicates that alterations in the intrinsic properties of the contractile apparatuses also contribute to contractile dysfunction in ischemic/non-ischemic DCM. Specifically, studies have demonstrated that Mg^{2+}-ATPase activity [135] and the rates of cross-bridge cycling [136] are reduced in skinned muscle preparations from human hearts with HF resulting from ischemic and non-ischemic DCM. Additionally, an increase in the Ca^{2+} sensitivity of force has been observed in both ischemic and non-ischemic DCM in humans, as well as in swine models of HF induced by myocardial infarction [81, 82, 93, 137-140]. The maximal Ca^{2+}-activated tension may [93, 140, 141] or may not [82, 139] also be decreased.

In the end-stage failing heart, the expression of the β_1-AR is decreased and the expression of the inhibitory G-protein, G_i, is increased, which results in an overall decrease in PKA activity in the failing myocardium [142]. Diminished PKA activation, potentially in combination with an increase in phosphatase activity [143], leads to a reduced phosphorylation of cTnI [82, 144-147] and cMyBP-C [148-150] in failing hearts. Reduced phosphorylation of cTnI and cMyBP-C can largely account for impaired contractility in ischemic/non-ischemic DCM. Corroborating this are results from a number of labs demonstrating that the increased Ca^{2+} sensitivity of force in skinned muscle preparations from failing myocardium can be abolished by treatment with PKA [82, 139, 140]. Additionally, Messer et al. showed that exchange of cardiac Tn (cTn) purified from failing myocardium into reconstituted actomyosin resulted in an increased Ca^{2+} sensitivity of force compared to preparations exchanged with cTn from donor myocardium [81]. Moreover, the authors demonstrated that exchange of cTn with recombinant non-phosphorylated cTnI into the

reconstituted preparations recapitulated the HF-associated contractile defect, while exchange with cTnI phosphorylated by PKA yielded preparations with contractile function indistinguishable from those reconstituted with cTn from donor myocardium [81]. Collectively, these findings establish reduced cTnI phosphorylation as the cause of increased Ca^{2+} sensitivity of force in failing hearts. Unfortunately, definitive evidence linking decreased phosphorylation of cMyBP-C to reduced cross-bridge cycling kinetics in ischemic/non-ischemic DCM in humans and large animal models of HF has not been published. Nevertheless, given that cross-bridge cycling kinetics and cMyBP-C phosphorylation are decreased in end-stage failing hearts [136, 148-150], and the well-established link between the PKA-mediated phosphorylation of cMyBP-C by PKA and increased cross-bridge cycling kinetics (discussed above), it seems highly likely that reduced phosphorylation of cMyBP-C contributes to slowed cross-bridge cycling kinetics in the end-stage failing myocardium [53].

Reported changes in MLC-2 phosphorylation in ischemic/non-ischemic DCM in humans and large animal models of HF resulting from MI vary widely in the literature. While some studies have reported a decrease in MLC-2 phosphorylation in HF resulting from ischemic/non-ischemic DCM in humans and MI in large animals [82, 93, 137, 151], others have found no change in the phosphorylation status of this protein [140, 141]. Increased phosphorylation of MLC-2 phosphorylation in end-stage HF resulting from ischemic cardiomyopathy in humans has also been reported [152]. Therefore, there is currently no clear consensus on whether and to what extent MLC-2 phosphorylation is altered in the failing myocardium. Interestingly, although decreased MLC-2 phosphorylation would be expected to contribute to depressed cross-bridge cycling kinetics in the failing myocardium [31, 63], it would also be expected to decrease the maximal

Ca^{2+}-activated force [70] and Ca^{2+} sensitivity of force [31, 61-69] based on the established role of MLC-2 phosphorylation in striated muscle. Yet, decreased phosphorylation of MLC-2 in the failing heart has primarily been reported in the absence of changes in maximal Ca^{2+}-activated force [82, 137, 151]. Moreover, mechanical analyses indicate that, even in the context of decreased MLC-2 phosphorylation, the myofilament Ca^{2+} sensitivity in the failing myocardium is increased due to an overriding effect of decreased cTnI phosphorylation [82, 93, 137, 151]. These results seem to indicate that alterations in MLC-2 phosphorylation, in so far as they occur in HF, may be uncoupled or masked by changes in the phosphorylation of other contractile proteins.

1.6 The role of myofilaments in sarcopenia-associated skeletal muscle dysfunction

Aging is associated with a natural progressive loss of skeletal muscle mass, quality, and function, a condition that is referred to as sarcopenia [153-155]. Greater than 35% of persons over 65 years of age and 50% or more of individuals 80 years or older are estimated to be afflicted with sarcopenia [156]. The sequela of sarcopenia can directly result in frailty, physical disability, and loss of independence in the elderly [156, 157]. Not surprisingly, the economic impact of sarcopenia is staggering with an estimated cost of $18.5 billion in the United States in the year 2000 alone [158]; and costs are only expected to rise as the population ages [159].

One of the hallmarks of sarcopenia is a progressive decline in muscle function (i.e., strength) that typically becomes pronounced by the sixth decade of life and results from decreased force production by aged muscles [160-164]. Contributing to this decrease in force production is an age-related reduction in muscle mass that is attributable to both muscle fiber atrophy and a

decrease in the total number of muscle fibers [165, 166]. It should be noted, however, that age-associated atrophy and fiber loss primarily affect type II fibers (fast-twitch fibers expressing type II MHC isoforms) [166-169], while type I fibers (slow-twitch fibers expressing type I MHC isoforms) are relatively unaffected [168, 169]; at least until advanced age [170]. Nevertheless, atrophy and loss of type II muscle fibers is insufficient to fully account for impaired force production in aged muscles. Indeed, multiple studies have demonstrated that the specific force, that is, the force produced relative to muscle cross-sectional area, generated by muscles declines with age in humans and rodents [164, 171-176]. Likewise, specific force is reduced in skinned type II muscle fibers isolated from these species at advanced age [177-180], indicating that intrinsic changes in the contractile apparatuses also contribute to the decline in force production with age. In addition to specific force, studies using permeabilized muscle fibers from humans and rodents have also shown that aging is associated with a decline in the maximum unloaded shortening velocity (the velocity of shortening at zero load) [177, 179, 180].

To date, a number of studies have reported age-related changes in the expression of contractile proteins in muscles from humans and rodents. Among reported changes are alterations in the expression of myosin heavy chain [181-183], αTpm [184-187], TnT isoforms [184, 185, 188], MyBP-C [184, 187, 188], and myosin light chain isoforms [184-189]. However, results appear to vary widely in regards to age-related changes in the expression of specific contractile proteins. For example, while a decrease in the expression of MyBP-C has been reported in the gastrocnemius muscles of 30-month-old male LOU/c/jall rats [188] and 30-month-old Wistar rats (sex not indicated) [184], increased expression has also been observed in extensor digitorum longus muscles of 24-month-old male Wistar rats [187]. In this case, potential differences in age, muscle

group, and detection method (two-dimensional gel electrophoresis in the former studies and quantitative bottom-up proteomics in the latter) may underlie these disparate results. Additional confounding factors that may contribute to discrepancies in the literature include sex, activity level, and the presence of co-morbidities (e.g., cancer cachexia), among others. Unfortunately, conflicts in the literature, such as those mentioned above, make it difficult to gain a clear understanding of contractile protein expression changes in sarcopenia. Additionally, relatively few studies have determined the functional significance of age-related alterations in contractile protein expression. D'Antona et al. showed that myosin content in type I and II muscle fibers isolated from the vastus lateralis muscles of young and old men was linearly related to specific force measured in the corresponding fiber types from the same individuals [182], suggesting that decreased myosin content in aged muscles may be partly responsible for decreased force production. In a separate study, Kim et al. noted that aging was associated with changes in the relative expression of myosin light chain 1 (MLC-1F) and fast skeletal myosin light chain 3 (MLC-3F) in the semimembranosus muscles of male Fisher 344 rats [189]. The authors subsequently showed that increasing expression of MLC-3F in this muscle group via recombinant adenovirus gene transfer technology was able to partly rescue the age-induced decline in maximum unloaded shortening velocity measured in isolated fiber preparations [189]. Therefore, these findings implicate changes in the relative expression of myosin light chain isoforms in contractile dysfunction in aged skeletal muscles.

In comparison to studies examining age-related alterations in contractile protein expression, far fewer studies have assessed contractile protein PTMs in aging muscles. Using purified actin and myosin from the semimembranosus muscles of young and old Fisher 344 rats, Prochniewicz et al.

demonstrated that age was associated with a decrease in the ATPase rate of purified actomyosin [190]. Interestingly, the authors found that ATPase activity was only impaired when myosin purified from old muscles was utilized in their assay, but not when myosin purified from young muscles was paired with actin from either young or old muscles [190]. Subsequent analysis of myosin content revealed a decrease in free cysteine residues in myosin from aged muscles, indicating that the age-induced oxidative modification of cysteines in myosin may contribute to impaired contractile function [190]. In addition, evidence in the literature suggests that the phosphorylation of fast skeletal MLC-2 (MLC-2F) may be decreased in muscles from aged individuals. In 2006, Gelfi et al. reported a decrease in the phosphorylation of MLC-2F in the vastus lateralis muscles of individuals 70-76 years of age (sex not indicated). More recently, Miller et al. reported similar findings, although MLC-2F phosphorylation was found to be significantly decreased in the vastus lateralis muscles of elderly women but not elderly men [191], indicating that age-related alterations in MLC-2F phosphorylation may be sex specific.

1.7 Mass spectrometry (MS)-based proteomics approaches

Mass Spectrometry (MS) is among the most robust methods for protein analysis, as well as the only detection method that can identify protein PTMs without *a priori* knowledge, which makes it an invaluable tool for interrogation of the proteome. Two primary approaches to MS-based proteomics exist, namely, bottom-up and top-down proteomics, each with its own advantages and disadvantages for the identification of proteins and protein interacting partners, protein quantification, and the analysis of protein PTMs. In bottom-up proteomics, proteins are first digested and information obtained from MS and subsequent tandem MS (MS/MS) analyses of the

resulting peptides is used to infer the identity, quantity, and modification status of the proteins present in the sample [192-194]. In a traditional bottom-up MS workflow, proteins extracted from a cell or tissue are either subjected to in-solution proteolytic digestion using an enzyme such as trypsin or are first separated via SDS-PAGE followed by in-gel digestion. In the former case, the peptides are frequently separated by two-dimensional liquid chromatography (LC) on the basis of charge (ion exchange chromatography) and hydrophobicity (reverse phase chromatography) [195] and, in the latter case, gel bands are excised, digested, and the resulting peptides are separated using reverse phase LC. The separated peptides are then ionized, introduced into the mass spectrometer, and the number of ions at each *m/z* value is registered by the detector. After a full scan of all *m/z* values, targeted ions are isolated and fragmented using MS/MS techniques, which provide information related to protein sequence and the location of PTMs. In addition to protein identification, a number of methods are currently available that allow for both the relative and absolute quantification of proteins using bottom-up MS [192-194]. Although bottom-up proteomics is currently unparalleled in term of through-put and depth of proteome profiling, an intrinsic limitation of the method is that there can be ambiguity in terms of the specific protein isoforms present in a sample as only a handful of peptides from a given protein may be detected. Moreover, protein digestion can also result in a loss of information regarding the presence of PTMs and their inter-dependence (so called PTM crosstalk [196]).

By contrast, in top-down proteomics intact proteins are analyzed, rather than peptides, which decreases sample complexity and preserves all information related to the status of the intact protein, including PTMs and sequence variations arising from polymorphisms/mutations, truncations, and alternative splicing events [197-200]. Unfortunately, as the physiochemical

diversity of intact proteins is much greater than that of peptides, large-scale separation of intact proteins is challenging and, thus, traditional top-down studies have primarily focused on the analysis of a single or small number of proteins, typically obtained via affinity purification [201-205]. Following intact protein analysis, a specific proteoform (a term used to describe the many protein products that can be produced from a single gene as a consequence of sequence variations resulting from polymorphisms/mutations or alternative splicing, and PTMs [206]) of interest can be directly isolated and fragmented in the mass spectrometer to obtain sequence information and localize PTMs. In particular, the establishment of the electron-based MS/MS techniques, electron capture dissociation (ECD) [207] and electron transfer dissociation (ETD) [208] represents a significant advancement for top-down MS by providing a reliable method for the localization and characterization of labile PTMs such as phosphorylation [201, 204, 205, 209-213]. Top-down MS with ECD/ETD has unique advantages for the dissection of molecular complexity via the quantification of proteoforms, unambiguous localization of PTMs and polymorphisms/mutations, discovery of unexpected PTMs and sequence variations, identification and quantification of positional isomers, and the interrogation of PTM inter-dependence [201, 203-205, 209, 211-217].

1.8 Top-down proteomics in biomedical research

In recent years, the results of a growing number of studies have demonstrated that alterations in the expression of PTMs of specific proteins are causal in pathophysiology. Therefore, top-down MS, which is currently the most powerful method for the analysis of protein proteoforms, is ideally suited to contribute to our understanding of proteoform-associated disease mechanisms. Indeed, despite the fact that top-down MS is still considered an up-and-coming approach to proteomics,

the use of this methodology has already provided insights into the molecular mechanisms underlying diseases such as cardiovascular disease (CVD), cancer, and infectious disease. Moreover, several labs have developed top-down platforms enabling the detection of disease biomarkers that may have clinical utility. These applications, and the insights provided, are discussed below.

Several labs, including our own, have employed top-down proteomics to shed light on the molecular mechanisms of CVDs, including HF and coronary artery disease [202, 215, 218, 219]. In 2011, Zhang et al. systematically analyzed cTnI phosphorylation in human donor hearts, hearts with mild hypertrophy, severe hypertrophy/ventricular dilation, and congestive HF using top-down MS [218]. Group comparisons revealed a significant stage-dependent decline in cTnI phosphorylation as hearts progressed to the chronic stage, and MS/MS analysis localized the sites of cTnI phosphorylation in healthy and diseased myocardium to Ser22/23, the PKA phosphorylation sites [218]. This study represents the first clinical application of top-down MS-based quantitative proteomics for biomarker discovery from tissues, and highlights the potential usefulness of PTMs as disease biomarkers. Dong et al. quantified cTnI phosphorylation in the hearts of rats with and without hypertensive HF [202]. The authors found that cTnI phosphorylation was increased in the hearts of hypertensive rats, and localized the sites of phosphorylation in cTnI to Ser23 and Ser24, as well as Ser43/45 (corresponding to Ser22, Ser23, and Ser42/44 in humans) [202]. Notably, phosphorylation of cTnI Ser43/45 was not observed in control animals and correlated with an increase in the expression of PKC-α and –δ in myocardium from rats with hypertensive HF [202]. These results not only provided the first experimental evidence of *in vivo* phosphorylation at Ser43/45, but also provided support for the hypothesis that

PKC-mediated phosphorylation of cTnI plays a role in contractile dysfunction in pressure overload-induced HF, at least in rodents [132]. Mazur et al. analyzed apolipoproteins isolated from patients with high and low HDL-cholesterol levels using top-down MS [215]. Quantitative analysis unveiled significant changes in protein abundance for 380 different *m/z* species, one of which was an O-glycosylated form of apolipoprotein C-III—a protein previously implicated in the pathogenesis of coronary artery disease [215]. These results provided validation of the quantitative top-down MS platform developed by the authors, and indicated that this methodology may hold promise for the identification of plasma markers of coronary heart disease. In an effort to develop a panel of biomarkers enabling the monitoring of type II diabetes (T2D) and related cardiovascular complications, Borges et al. screened plasma from seven different patient subgroups representing the spectrum of conditions from healthy to T2D with congestive HF, as well as T2D with no history of HF and HF without diabetes, using top-down proteomics [219]. The authors found that the presence of increased protein oxidation, primarily presenting as methionine sulfoxidation of the apolipoproteins apoAI and apoCI, was indicative of CVD while an increase in RANTES and apoCI truncation variants (produced via enzymatic cleavage of the proteins) correlated with T2D [219]. The end result of this work was the development of a multi-dimensional biomarker panel for T2D in the context of cardiovascular co-morbidities [219]. This panel may be useful for patient screening to identify individuals at increased risk of cardiovascular complications from T2D therapies [219].

Similarly, in the field of infectious disease top-down MS-based proteomics has made substantial contributions to our understanding of the molecular mechanisms of bacterial pathogenesis [220-222]. In a seminal report by Chamot-Rooke et al., top-down MS was employed to study intact

pilin (the major component of bacterial type IV pili) from the pathogenic bacterium *N. meningitides*—the causative agent of cerebrospinal meningitis [222]. Top-down MS analysis revealed that pilin was modified with phosphoglycerol and enabled the localization of two modification sites to Ser69 and Ser93 [222]. Subsequent experiments revealed that modification of Ser93 with phosphoglycerol was responsible for the destabilization of type IV pili fiber bundles, which enhanced bacterial detachment and migration across epithelial cells [222]. Thus, in this study, top-down MS analysis played a significant role in the discovery of a potential mechanism for the spread of *N. meningitidis* during infection. Another important study by Ansong et al. revealed a unique protein S-thiolation switch in *S. typhimurium*—a Gram-negative bacterium that causes gastroenteritis—in response to infection-like conditions [220]. Utilizing top-down proteomics to profile the intact proteome of *S. typhimurium* grown under basal and infection-like conditions, the authors identified 1,665 proteoforms derived from 563 different gene products, which represents the largest bacterial top-down dataset reported to date [220]. Interestingly, the authors found that when bacteria are grown under infection-like conditions, free thiols were protected preferentially via S-cysteinylation whereas under basal conditions they were protected by S-glutathionylation [220]. Although the reason for this switch in unclear, protein S-cysteinylation may be more energetically favorable or allow for a more rapid response to changing environmental conditions [220]. The results of this study have provided the most comprehensive view of the intact proteome of the Gram-negative bacterial pathogen *S. typhimurium* to date, and revealed unique biological insights into metabolic re-wiring that may allow the bacterium to survive when under stress [220]. In a separate study, Burnaevskiy et al. employed a top-down MS-based methodology to study the molecular mechanism of *S. flexneri*-mediated regulation of the host cell secretory pathway [221]. Interestingly, top-down MS analysis of ADP-ribosylation

factor 1, a GTPase involved in the regulation of Golgi transport, revealed that the protein is N-myristoylated [221]. Moreover, the authors found that the invasion plasmid antigen (a protein produced by the bacterium) cleaved the peptide bond between Gly2 and Asp3 in the protein, and released the GTPase domain into the cytoplasm [221]. Subsequent experiments demonstrated that the invasion plasmid antigen cleaved a number of other N-myristoylated proteins in the cell, including proteins involved in cellular growth, signal transduction, and organelle function [221]. Taken together, these findings identify a previously unknown molecular mechanism by which *S. flexneri* attacks host cells [221].

Top-down MS has also provided insights into the molecular mechanisms underlying neurodegenerative diseases [223-226]. The Agar lab employed hydrogen/deuterium exchange top-down MS to determine the effects of 13 familial amyotrophic lateral sclerosis (ALS)-causing polymorphisms on superoxide dismutase 1 (SOD1) structure and dynamics [223]. Interestingly, their analysis of the familial ALS-causing SOD1 sequence variants uncovered a single structural perturbation common to all 13 variants—destabilization of the SOD1 electrostatic loop [223]. This finding sheds light on a potential mechanism by which disparate mutations in SOD1 contribute to aberrant aggregation of the protein in ALS [223]. The Agar lab has also utilized top-down MS to study cross-linking of SOD1 variants by maleimide derivatives as a potential therapeutic strategy for the treatment of familial ALS [225]. Their analysis showed that a single equivalent of the maleimide derivative was responsible for mediating the chemical cross-linking of variant SOD1 monomers, and MS/MS analysis uncovered a unique thiol-disulfide exchange reaction mechanism for SOD1 cross-linking [225]. In yet another study published by the Agar lab, Auclair et al. utilized top-down MS to assess the PTMs of SOD1 purified from post-mortem human nervous tissue [224].

The authors found cysteinylation and oxidation of specific cysteine residues to be the most common SOD1 PTMs [224]. Surprisingly, subsequent *in vitro* experiments showed that cysteinylated SOD1 was protected from peroxide-induced oxidation [224]. Therefore, in this study, top-down MS enabled the identification of a SOD1 modification that protects the protein from oxidative damage and, thus, may have therapeutic relevance for the treatment of ALS [224]. Using quantitative top-down proteomics, Cabras et al. somewhat serendipitously uncovered an increase in the levels of protein S100A7 in the saliva proteome of patients with Down syndrome [226]. This finding is particularly interesting as evidence suggests that S100A7 may be a biomarker of Alzheimer's disease, which is frequently associated with Down syndrome [226]. Moreover, the levels of S100A12, a protein that has been implicated in amyloidosis, was also found to increase in the saliva of Down syndrome patients in comparison to controls [226].

The early detection of cancer is imperative for treatment and, to date, several groups have developed platforms utilizing top-down MS for the identification of cancer biomarkers and the prediction of disease prognosis [227-229]. Zhang *et al.* developed a top-down proteomics platform to analyze global modification levels of core histones [227]. To demonstrate the utility of their platform, the authors assessed histone PTMs in $CD19^+$ B cells isolated from volunteers, patients with chronic lymphocytic leukemia, and patients with acute myeloid leukemia [227]. Interestingly, the authors identified a possible correlation between histone H2A acetylation and chronic lymphocytic leukemia [227]. Moreover, the authors demonstrated that their quantitative top-down proteomics platform was capable of detecting decreased histone acetylation in leukemia cells collected from patients treated with depsipeptide, a histone de-acetylase inhibitor [227]. Thus, this platform may have utility for the assessment of histone PTM levels in the clinical setting

for patients undergoing treatment with histone de-acetylase inhibitors [227]. Desiderio et al. utilized top-down proteomics to screen for potential biomarkers in the cerebrospinal fluid of patients with posterior cranial fossa tumors [228]. Top-down MS identified two peptides, originally believed to be contaminants from the blood, as LVV- and VV-hemorphin-7—opioid peptides produced from the enzymatic cleavage of hemoglobin [228]. Surprisingly, the absence of these peptides in the post-surgery cerebrospinal fluid of patients was strongly indicative of residual tumor mass as a result of either subtotal resection or the presence of metastases [228]. Consequently, these peptides may have potential as clinical biomarkers. In a more recent study, Hardesty et al. employed top-down proteomics with histology-directed matrix-assisted laser desorption/ionization imaging to identify protein signatures that could be used to distinguish lymph nodes harboring metastases from healthy lymph nodes in patients with melanoma [229]. Top-down proteomics analysis revealed a total of 57 different signatures displaying a 2-fold or greater change in intensity between healthy and disease lymph nodes [229]. From these data, 12 protein signals associated with survival and 3 recurrence-associated signals were combined to generate a panel of signatures enabling the grouping of patients into poor or favorable groups for recurrence and survival [229]. This method may provide clinicians with a new tool to determine prognosis in patients with melanoma.

A number of top-down MS-based methods have also been developed to aid the detection of blood disorders, including sickle cell disease and transthyretin amyloidosis [216, 217, 230]. Theberge et al. developed a novel platform integrating affinity purification and top-down MS for the detection of transthyretin and hemoglobin variants in patient blood samples [230]. Unlike previous MS-based methods for the identification of transthyretin sequence variants, the analytical platform

developed in this study utilized a combination of fragmentation methodologies (nozzle-skimmer dissociation and collision induced dissociation), in addition to high-accuracy intact mass measurement using an LTQ-Orbitrap, to identify and precisely localize amino acid variants of both transthyretin and hemoglobin [230]. More recently, Graça et al. developed a platform for the rapid on-line analysis of hemoglobin variants from patient blood samples [217]. Although the method developed in this study employed a low-resolution ion trap instrument, the fast scan speed permitted the detection and identification of hemoglobin variants resulting in at least a one Dalton shift in mass on a chromatographic timescale [217]. The Cooper lab developed a top-down MS-based methodology utilizing liquid microjunction surface sampling and high-resolution MS for the analysis of hemoglobin sequence variants from neonatal dried blood spots [216]. Following intact mass measurement, hemoglobin variants were fragmented using a combination of fragmentation methods enabling the identification hemoglobin variants from dried blood spots that were not detected using traditional assays [216]. Collectively, these studies highlight the great potential for top-down MS as a detection method for transthyretin and hemoglobin structural variants in the clinical setting.

CHAPTER 2 - COMPREHENSIVE ASSESSMENT OF CHAMBER-SPECIFIC AND TRANSMURAL HETEROGENEITY IN MYOFILAMENT PROTEIN PHOSPHORYLATION BY TOP-DOWN MASS SPECTROMETRY

Reprinted from *Journal of Molecular and Cellular Cardiology*, 87, Gregorich ZR, Peng Y, Lane NM, Wolff JJ, Wang S, Guo W, Guner H, Doop J, Hacker TA, Ge Y, Comprehensive assessment of chamber-specific and transmural heterogeneity in myofilament protein phosphorylation by top-down mass spectrometry, 102-112, Copyright 2015, with permission from Elsevier [OR APPLICABLE SOCIETY COPYRIGHT OWNER].

Abstract

The heart is characterized by a remarkable degree of heterogeneity, the basis of which is a subject of active investigation. Myofilament protein post-translational modifications (PTMs) represent a critical mechanism regulating cardiac contractility, and emerging evidence shows that pathological cardiac conditions induce contractile heterogeneity that correlates with transmural variations in the modification status of myofilament proteins. Nevertheless, whether there exists basal heterogeneity in myofilament protein PTMs in the heart remains unclear. Here we have systematically assessed chamber-specific and transmural variations in myofilament protein PTMs, specifically, the phosphorylation of cardiac troponin I (cTnI), cardiac troponin T (cTnT), tropomyosin (Tpm), and myosin light chain 2 (MLC2). We show that the phosphorylation of cTnI and αTpm vary in the different chambers of the heart, whereas the phosphorylation of MLC2 and cTnT does not. In contrast, no significant transmural differences were observed in the phosphorylation of any of the myofilament proteins analyzed. These results highlight the importance of appropriate tissue sampling—particularly for studies aimed at elucidating disease mechanisms and biomarker discovery—in order to minimize potential variations arising from basal heterogeneity in myofilament PTMs in the heart.

2.1 Introduction

The heart is characterized by a remarkable degree of heterogeneity, which underlies normal pump function and is also altered in heart failure [93, 141, 231-234]. Contractile heterogeneity, in particular, has taken on increased significance with the demonstration that transmural changes in myocardial contractility not only occur in the failing heart [93, 141, 231], but may also be predictive of adverse cardiac events [235, 236]. Myocardial contractility is governed by a number of factors, including the size and duration of Ca^{2+} transients, as well as the intrinsic properties of the contractile apparatus, which depend primarily on the expression of myofilament protein isoforms and post-translational modifications (PTMs) [34-36, 237].

Myofilament protein PTMs have emerged as a key mechanism regulating cardiac contractility in health and disease [34-36, 237]. Previous studies in humans, as well as large and small animals, have shown that aging and pathological cardiac conditions induce contractile heterogeneity across the free wall of the left ventricle (LV) that correlates with differences in the modification status of myofilament proteins [93, 141, 233]. Yet, there is conflicting evidence in the literature regarding the existence of basal heterogeneity in myofilament PTMs. Although several groups have observed transmural variations in myofilament PTMs across the LV free wall in small animals [232, 238-240], such heterogeneity does not appear to be present in humans and large animals under basal conditions [93, 141, 241]. Comparatively, very little is known regarding the existence of chamber-specific variations in myofilament protein PTMs in the heart [242]. Knowledge of basal chamber-specific or transmural variations in myofilament protein PTMs will undoubtedly be

essential for understanding cardiac physiology, elucidating PTM-associated disease mechanisms, and biomarker discovery.

Top-down mass spectrometry (MS) is a powerful tool for the comprehensive assessment of protein PTMs [197, 198, 200]. Intact proteins are analyzed in top-down MS, which allows for the detection of the entire complement of protein PTMs simultaneously without *a priori* knowledge [197, 198, 200]. Furthermore, the addition of PTMs to intact proteins has relatively little influence on their physiochemical properties, thus, allowing for the reliable quantification of modified and un-modified protein forms present within the same spectrum [197, 198, 200]. Herein, we have utilized quantitative top-down MS to systematically assess chamber-specific and transmural variations in myofilament protein PTMs in the hearts of healthy pigs, which currently represent the gold standard model system for human cardiovascular diseases [243]; with a special focus on the phosphorylation of cardiac troponin I (cTnI), cardiac troponin T (cTnT), tropomyosin (Tpm), and myosin light chain 2 (MLC2).

2.2 Materials and methods

2.2.1 Chemicals and reagents

All reagents were purchased from Sigma Chemical Co. (St. Louis, MO, USA) unless otherwise specified. Complete protease and phosphatase inhibitor cocktail tablets were purchased from Roche (Indianapolis, IN, USA). All solutions were prepared in Milli-Q water (Millipore, Billerica, MA, USA).

2.2.2 Immunoaffinity purification of cardiac troponin complex

All protein extraction procedures were performed in a cold room (4 °C) using freshly prepared buffers. Troponin complex was isolated by immunoaffinity purification as previously described [201, 202, 205, 218], with minor modifications. First, ~250 mg of tissue was homogenized in wash buffer (5 mM NaH_2PO_4, 5 mM Na_2HPO_4, 5 mM $MgCl_2$, 0.5 mM EGTA, 0.1 M NaCl, 1% Triton X-100, 5 mM DTT, 1 mM PMSF, 2 μg/mL leupeptin, and protease and phosphatase inhibitor cocktail tablets, pH 7.4) using a Polytron electric homogenizer (Model PRO200; PRO Scientific, Oxford, CT, USA) on ice. The resulting homogenate was centrifuged at 10,000 × g (Avanti J-25i; Beckman Coulter, Fullerton, CA, USA) for 10 min at 4 °C. After centrifugation, the supernatant was removed, the pellet was re-suspended in protein extraction buffer (0.7 M LiCl, 25 mM Tris, 5 mM EGTA, 0.1 mM $CaCl_2$, 5 mM DTT, 1 mM PMSF, 2 μg/mL leupeptin, and protease and phosphatase inhibitor cocktail tablets, pH 8.0), and the suspension was agitated on a nutating mixer (Thermo Scientific, Boston, MA, USA) at 4 °C for 45 min. The extract was centrifuged at 16,000 × g (Centrifuge 5415R, Eppendorf, Hamburg, Germany) for 10 min at 4 °C and the resulting supernatant was again centrifuged at 280,000 × g (Beckman L-55 ultracentrifuge; Beckman Coulter) for 50 min to remove all tissue debris prior to immunoaffinity purification of troponin complex. The supernatant was incubated with 0.3 mL of CNBr-activated Sepharose CL-4B conjugated to monoclonal anti-cTnI antibodies (MF4; HyTest, Turku, Finland) for 40 min on a nutating mixer at 4 °C. After incubating, the column was washed twice with 0.8 mL of extraction buffer to elute unbound proteins. Subsequently, antibody-bound troponin complex was eluted into six equal 0.4 mL fractions with 100 mM glycine (pH 2.0), and immediately neutralized with 40

μL of 1 M MOPS (pH 9.0). Fractions were stored at -80 ºC for later analysis using high-resolution MS.

2.2.3 Preparation of myofilament extracts

Myofilament proteins were extracted from pig myocardial tissue using a two-step extraction procedure as previously described [242, 244, 245]. Briefly, ~20 mg of cardiac tissue was homogenized in 100 μL of HEPES extraction buffer containing protease and phosphatase inhibitors (25 mM HEPES pH 7.5, 50 mM NaF, 0.25 mM Na_3VO_4, 0.25 mM PMSF, 2.5 mM EDTA) using a Teflon pestle (1.5 mL tube rounded tip; Scienceware, Pequannock, NJ, USA). The resulting homogenate was centrifuged at 16,000 × g for 15 minutes at 4 °C and the supernatant, which contains soluble cytoplasmic proteins, was discarded. The insoluble pellet was then re-homogenized in 100 μL of TFA extraction buffer (1% TFA, 1 mM TCEP) to extract myofilament proteins. After centrifugation (16,000 × g, 4 °C, 25 min), the supernatant was collected and used for MS and Western blot analyses.

2.2.4 Off-line and on-line top-down high-resolution MS and tandem MS (MS/MS)

For off-line MS analysis of immunoaffinity purified cTnI and cTnT, 100 μL from fractions E1-E4 were combined and concomitantly separated and desalted off-line using a reverse phase C4 protein microtrap (Michrom Bioresources, Auburn, CA, USA). Proteins were subsequently eluted using solutions comprised of 1% acetic acid in 30:70, 50:50, and 75:25 methanol:water. Desalted samples were introduced into a 7T linear ion trap (LTQ)/Fourier transform ion cyclotron resonance

(FT-ICR) mass spectrometer (LTQ/FT Ultra; Thermo Scientific, Bremen, Germany) using an automated nano-electrospray ionization source (Triversa NanoMate; Advion BioSciences, Ithaca, NY, USA) and a spray voltage of 1.2-1.6 kV versus the inlet of the mass spectrometer. The resolving power of the FT-ICR was set at 200,000 (at *m*/*z* 400). Typically between 800-1,000 scans were averaged to ensure the collection of high-quality spectra for data analysis and quantification. The numbers of accumulated ions for a full scan in the linear trap, FT-ICR cell, MSn FT-ICR cell, and electron capture dissociation were 3×10^4, 6×10^6, 6×10^6, and 6×10^6, respectively.

Myosin light chain 2 (MLC2) and myosin light chain 1 (MLC1) were analyzed as previously described [244], with minor modifications. Briefly, myofilament extracts from the different chambers and layers of the heart were separated using a 2D-nano-liquid chromatography (LC) system (Eksigent, Redwood City, CA, USA) equipped with a home-packed PLRP column (PLRP-S, 200 mm × 500 μm, 10 μm, 1000 Å; Varian, Lake Forest, CA, USA) and a gradient going from 20% B to 90% B over 55 min (solvent A: 0.10% formic acid in water; solvent B: 0.10% formic acid in a 50:50 mixture of acetonitrile and ethanol) at a flow rate of 12.5 μL/min. The 2D-nano-LC system was coupled on-line with an LTQ mass spectrometer (Thermo Scientific) and, after separation, a small portion of the sample was ionized and analyzed directly via LTQ/MS to track protein elution from the column. Eluting MLC2 and MLC1 were fraction collected on ice and subsequently analyzed by high-resolution MS and MS/MS using the 7T LTQ/FT Ultra. For MS/MS experiments, the molecular ions of proteins of interest from individual charge states were isolated and subsequently fragmented using electron capture dissociation with 1.5% electron energy (corresponding to 0.85 eV), a 70 ms duration, and without additional delay.

For on-line MS analysis of Tpm, myofilament extracts were diluted 1:1 (v/v) with mobile phase A (mobile phase A: 0.1% formic acid in water; mobile phase B: 0.1% formic acid in methanol) prior to LC-MS. Myofilament extracts were separated using a Dionex U3000 LC system (Thermo Scientific) equipped with a home-packed PLRP column (PLRP-S, 200 mm x 500 μm, 10 μm, 1000 Å; Varian, Lake Forest, CA, USA) and a gradient going from 20% B to 90% B over 55 min at a flow rate of 12.5 μL/min. The Dionex U3000 LC system was coupled on-line with a 12T FT-ICR (Bruker Daltonics, Billerica, MA, USA) using the Bruker electrospray ionization source. Samples were introduced into the mass spectrometer using a capillary voltage and an endcap offset of -4.5 kV and -5 kV, respectively. A resolving power of 250,000 (at *m/z* 400) and a fixed ion accumulation time of 0.02 seconds were used for spectral acquisition. Mass spectra obtained using the methods described above were highly reproducible (**Fig. 2.1**).

2.2.5 Protein identification

The raw MS/MS data files were converted to mzXML files and deconvoluted using MS-Deconv [246], an algorithm that calculates the monoisotopic masses and charges for all of the fragment ions present in a given tandem mass spectrum. Subsequently, to identify the proteins, the files containing the monoisotopic masses, intensities, and charges of each of the product ions were searched against the pig database generated from NCBI (Sscrofa10.2) using the MS-Align+ algorithm [247]. A mass accuracy cut-off of 10 ppm was utilized for MS/MS fragment ion assignments. Protein identifications were manually validated.

2.2.6 Western blot

Myofilament extracts were resolved by 12.5% SDS-PAGE and transferred to PVDF membranes (Millipore) using a Fast Semi-Dry Blotter (Thermo Scientific) as per the manufacturer's instructions. Membranes were blocked with Protein-Free Blocking Buffer (Thermo Scientific) overnight at 4 ^{o}C followed by incubation with the following primary antibodies for 3 h at room temperature: anti-cTnI (Thermo Scientific) and anti-cTnI-Ser22/23 (Cell Signaling Technology, Beverly, MA, USA). Membranes were then washed with TBST and incubated with secondary antibody for 1 hr at room temperature. After incubation with the secondary antibody, membranes were washed and protein bands were detected using ECL Western Blotting Substrate (Thermo Scientific). Western blot band densities were determined using ImageJ.

2.2.7 Quantitative analysis

All off-line mass and tandem mass spectra were analyzed using in-house developed MASH Suite software [248], with a signal-to-noise threshold of 3 and a minimum fit percentage of 60%. On-line mass spectra were analyzed using DataAnalysis software from Bruker. All program processed MS and MS/MS data were manually validated to ensure data accuracy. The most abundant relative molecular masses and monoisotopic masses are reported for intact proteins and fragment ions, respectively. For each individual protein form within a spectrum, the sum of the peak intensities for the top five isotopomers from up to three different charge states were obtained, averaged, and used to calculate the relative abundance of the protein form. The relative abundances of the mono- and bis-phosphorylated forms of each protein were defined as the summed abundances of all of

the mono- or bis-phosphorylated protein forms of a given protein over the summed abundances of the entire protein population, respectively. The total phosphorylation for each protein was calculated using the relative abundances of the mono- and bis-phosphorylated forms as previously described [202, 242, 244]. Oxidized protein forms and those associated with non-covalent adducts were included in the quantitative analysis.

2.3 Results

2.3.1 cTnI phosphorylation varies in a chamber-specific but not transmural manner in the heart

To determine whether cTnI phosphorylation varies in the different chambers of the heart, cTnI was immunoaffinity purified from the LV, RV, LA, and RA of healthy pig hearts, and analyzed by top-down MS. Three major cTnI protein forms, with relative molecular masses that matched closely with those previously reported for un-phosphorylated, mono-phosphorylated ($_{p}$cTnI), and bis-phosphorylated ($_{pp}$cTnI) cTnI from pig [205, 244], were detected in all four chambers of the heart (**Fig. 2.2A**). Several additional protein forms, including cTnI containing the V116A polymorphism reported previously [205], as well as oxidized cTnI and cTnI associated with non-covalent adducts, were also observed (**Fig. 2.2A**). MS-based quantification of the cTnI protein forms in each chamber revealed significant differences in the relative abundances of un-phosphorylated cTnI, $_{p}$cTnI, and $_{pp}$cTnI (**Fig. 2.2B**). Calculation of the total phosphorylation revealed that cTnI phosphorylation was significantly greater in the ventricles than in the atria (**Fig. 2.2C**).

Next, cTnI from the EPI, MYO, and ENDO of the LV free wall was analyzed using top-down MS to determine whether cTnI phosphorylation also varies transmurally in the heart. Un-phosphorylated cTnI, $_{p}$cTnI, and $_{pp}$cTnI were the predominant cTnI protein forms detected by top-down MS in the EPI, MYO and ENDO (**Fig. 2.2D**). Additionally, minor protein forms corresponding to cTnI associated with non-covalent adducts were also observed (**Fig. 2.2D**). Quantitative top-down MS analysis revealed no significant differences in either the relative abundances of cTnI protein forms, or total cTnI phosphorylation, across the LV free wall (**Fig. 2.2E-F**).

Western blot analysis of cTnI-Ser22/23 phosphorylation, which we have previously shown are the only sites basally phosphorylated in pig myocardium [205], was used to confirm the results of the top-down MS analysis. cTnI-Ser22/23 phosphorylation was significantly greater in the LV than in the LA and RA (**Fig. 2.3A**), which corresponds well with the significantly increased relative abundance of $_{pp}$cTnI in the LV (compared to the LA and RA) observed by MS analysis (**Fig. 2.2B**). Likewise, cTnI-Ser22/23 phosphorylation in the RV was increased relative to the LA and RA by Western blot (**Fig. 2.3A**); however, the difference between the RV and RA was not statistically significant as it was based on the MS analysis (**Fig. 2.2B**). Similarly, cTnI-Ser22/23 phosphorylation, as assessed by Western blot, was not significantly different across the layers of the LV free wall (**Fig. 2.3B**), which is also in good agreement with the results of our top-down MS analysis (**Fig. 2.2E**). Collectively, these results clearly demonstrate that basal cTnI phosphorylation varies in a chamber-specific but not transmural manner in the heart.

2.3.2 cTnT phosphorylation does not vary in the different chambers of the heart or across the LV free wall

We next sought to determine whether the phosphorylation of cTnT varies in the different chambers of the heart. Two cTnT protein forms, with relative molecular masses similar to those previously published for un-phosphorylated and mono-phosphorylated ($_p$cTnT) cTnT from pig [244], were detected by top-down MS in all four chambers of the heart (**Fig. 2.4A**). Additional protein forms corresponding to cTnT associated with non-covalent adducts were also observed in the spectra (**Fig. 2.4A**). Quantification of cTnT protein forms revealed that the relative abundances of cTnT and $_p$cTnT did not differ significantly between the LV, RV, LA, and RA (**Fig. 2.4B**). Likewise, total cTnT phosphorylation was similar across the chambers of the heart (**Fig. 2.4C**).

Similarly, top-down MS analysis of cTnT phosphorylation across the LV free wall showed no significant differences in either the relative abundances of cTnT protein forms or total cTnT phosphorylation in the EPI, MYO, or ENDO (**Fig. 2.4D–F**). These results clearly show that cTnT phosphorylation does not vary in a chamber-specific or transmural manner in the heart.

2.3.3 Tpm phosphorylation exhibits chamber-specific but not transmural heterogeneity in the heart

We next examined Tpm phosphorylation in the atria and ventricles to determine whether there is chamber-specific heterogeneity in Tpm phosphorylation in the heart. Three Tpm protein forms, with relative molecular masses similar to those previously reported for un-phosphorylated Tpm1.1 (αTpm), mono-phosphorylated Tpm1.1 ($_p$αTpm), and un-phosphorylated Tpm2.2 (βTpm) from pig

[244, 245], were detected by top-down MS analysis in the LV, RV, LA, and RA (**Fig. 2.5A**). Minor protein forms corresponding to oxidized αTpm and $_p$αTpm, respectively, were also observed in the spectra (**Fig. 2.5A**). Quantification of the Tpm protein forms in spectra from the different chambers of the heart revealed significant differences in the relative abundances of un-phosphorylated αTpm, $_p$αTpm, and un-phosphorylated βTpm (**Fig. 2.5B**). Overall, the total phosphorylation of αTpm was increased in the atria relative to the ventricles (**Fig. 2.5C**), although the difference in total phosphorylation between the RA and LV did not reach statistical significance (p = 0.050013) (**Fig. 2.5C**).

Top-down MS analysis of Tpm in the EPI, MYO, and ENDO revealed no significant differences in either the relative abundances of Tpm protein forms, or total αTpm phosphorylation, across the free wall of the LV (**Fig. 2.5D–F**). These findings confirm that αTpm phosphorylation is increased in the atria in comparison to the ventricles, but does not vary across the LV free wall.

2.3.4 The phosphorylation of MLC2 does not vary in a chamber-specific or transmural manner in the heart

We next sought to assess differences in myosin light chain protein forms in the different chambers of the heart and across the LV free wall. However, while the relative molecular masses of the ventricular isoforms of MLC1 and MLC2 (MLC1v and MLC2v, respectively) from pig have previously been determined [244], the relative molecular masses of the atrial isoforms of MLC1 and MLC2 (MLC1a and MLC2a, respectively), calculated based on sequences from the NCBI database, did not match with those experimentally determined for presumed peaks corresponding

to MLC1a and MLC2a. Thus, to confirm the identity of MLC1a and MLC2a, peaks presumably corresponding to these protein forms were isolated and fragmented by electron capture dissociation. Information from the tandem mass spectra was then searched against the pig database using MS-Align+ [247], which allowed for the high confidence identification of MLC1a (relative molecular mass: 21,502.94 Da) and MLC2a (relative molecular mass: 19,384.70 Da) from pig (**Figs. 2.6**). Thus, we have confirmed the expression of different MLC1 and MLC2 isoforms in the atria and ventricles of the pig heart (**Figs. 2.7-2.8**).

After confirming the identity of peaks corresponding to MLC1a and MLC2a, the phosphorylation of MLC2 was assessed in the different chambers of the heart. A total of four major MLC2 protein forms were detected by top-down MS analysis with forms corresponding to un-phosphorylated and mono-phosphorylated MLC2v detected in the LV and RV and forms corresponding to un-phosphorylated and mono-phosphorylated MLC2a detected in the LA and RA, respectively (**Fig. 2.8A**). Additional protein forms corresponding to oxidized MLC2 and MLC2 associated with non-covalent adducts were also observed in the spectra (**Fig. 2.8A**). Quantification of MLC2 protein forms revealed that the relative abundances of un- and mono-phosphorylated (*p*MLC2) MLC2 did not differ significantly between the LV, RV, LA, and RA (**Fig. 2.8B**). Likewise, although there was a minor increase in the total MLC2 phosphorylation in the RV (in comparison to the LV, LA, and RA), these differences were not significant (**Fig. 2.8C**).

Subsequent analysis of MLC2v phosphorylation across the EPI, MYO, and ENDO of the LV free wall revealed no significant differences in the relative abundances of MLC2v protein forms, or total MLC2v phosphorylation (**Fig. 2.8D–F**). Thus, these results demonstrate that MLC2

phosphorylation does not vary significantly across either the chambers of the heart or the LV free wall in pigs.

2.4 Discussion

Myofilament protein PTMs have emerged as a key mechanism regulating cardiac contractility, and increasing evidence has shown that the alteration of myofilament protein PTMs, particularly phosphorylation, can contribute to contractile dysfunction and heart failure [34-36, 81, 202, 218, 237, 249]. Additionally, studies in humans, as well as large and small animals, have shown that aging and pathological cardiac conditions induce transmural changes in contractile function that correlate with differences in the modification status of myofilament proteins [93, 141, 233]. Nevertheless, whether there is basal heterogeneity in myofilament protein PTMs in the heart remains an important question—particularly given the potential usefulness of myofilament PTMs as biomarkers for heart disease [218, 250].

In the present study, we have systematically assessed regional and transmural variations in myofilament protein PTMs in the hearts of healthy pigs by top-down MS, with a focus on the phosphorylation of cTnI, cTnT, αTpm, and MLC2. Here, we have demonstrated that, while the phosphorylation of certain myofilament proteins (cTnI and αTpm) varies in a chamber-specific manner within the heart, the phosphorylation of others (cTnT and MLC2) does not. Additionally, we have shown that the phosphorylation of cTnI, cTnT, αTpm, and MLC2v do not differ significantly across the LV free wall in healthy pigs. The observed differences in cTnI and αTpm

phosphorylation in the atrial and ventricular myocardium are likely due to chamber-specific variations in the expression or activity of kinases or phosphatases in the heart [251].

Previous studies have observed that there is transmural heterogeneity in the modification status of myofilament proteins across the ventricular wall in small animals [232, 238-240]. In particular, MLC2v phosphorylation has been shown to vary across the free wall of the LV in rats and mice [232, 238, 240]; however, here we found no difference in MLC2v phosphorylation (or in the phosphorylation of cTnI, cTnT, and αTpm) across the layers of the LV free wall in pigs, which is in good agreement with previous studies in pigs and humans [93, 141]. While there is the possibility that increased workload may induce transmural differences in myofilament protein phosphorylation in large animals and humans, as it does in rodents [238], this, at least, does not appear to be the case in pigs [93]. Thus, the data presented here, as well as data from other groups [93, 141, 241], suggests that transmural heterogeneity in myofilament protein phosphorylation does not exist in large animals and humans under basal conditions. Although it is possible that the phosphorylation of other myofilament proteins, such as cardiac myosin binding protein C, may vary transmurally in the heart, it seems likely that different mechanisms regulate transmural differences in mechanical function across the LV free wall in large animals and humans. Indeed, Stelzer et al. have shown that a transmural gradient in the expression of α myosin heavy chain can account for the higher rates of stretch activation and force redevelopment in the EPI in comparison to the ENDO in pig hearts [241]. It should be noted that this gradient is also present in human hearts [252]. Another similarity between pig and human hearts is that αTpm phosphorylation is increased in the atria relative to the ventricles, which we show here in pigs, and in our previous study using human donor hearts [242]. Although the significance of increased αTpm

phosphorylation in the atria remains unclear, consistency at the molecular level, as well as in the mechanisms regulating mechanical activity within the heart, highlight the benefits of using large animals, which more faithfully recapitulate human cardiac physiology and pathophysiology [132, 243], to model human cardiovascular diseases.

Furthermore, given that the phosphorylation of both cTnI and αTpm have been linked to altered Ca^{2+}-handling by the contractile apparatus [85, 237], chamber-specific differences in the phosphorylation of these proteins could underlie differences in myofilament Ca^{2+} sensitivity between the atria and ventricles. Analysis of skinned multicellular preparations from the atria and ventricles of pig by Locher et al. revealed significant differences in the rate of force redevelopment, the rate of ATP hydrolysis, the tension cost, and the calcium sensitivity between these preparations [253]. While differences in the rate of force redevelopment, rate of ATP hydrolysis, and tension cost could be explained by differences in the expression of the α and β isoforms of myosin heavy chain in the atria and ventricles, the differences in calcium sensitivity could not be explained, as no differences were found in myofilament protein phosphorylation by ProQ Diamond analysis [253]. Here, we have shown that cTnI-Ser22/23 phosphorylation, a well-known modulator of myofilament Ca^{2+} sensitivity [237], is reduced in the atria by both top-down MS analysis and Western blot, which could partly account for the differences in Ca^{2+} sensitivity between atrial and ventricular preparations observed by Locher et al. The reason that we were able to detect differences in cTnI phosphorylation in the atrial and ventricular myocardium, while they were not, may be due to the sensitivity of the ProQ Diamond stain to negatively charged amino acids within proteins [254]. Differences in myofilament Ca^{2+} sensitivity in the atria and ventricles may be

necessary for adapting mechanical activity to differences in intracellular Ca^{2+}-handling in atrial and ventricular myocytes [255].

In summary, these results demonstrate that myofilament protein PTMs vary in a chamber- and protein-specific manner in the heart. Additionally, transmural variations in myofilament protein phosphorylation do not appear to be present in pigs under basal conditions, although the possibility that there is transmural heterogeneity in the phosphorylation of myofilament proteins that were not analyzed in this study remains a possibility. Collectively, these findings highlight the importance of appropriate tissue sampling, particularly in studies aimed at elucidating PTM-associated disease mechanisms and biomarker studies, in order to minimize potential variations arising from basal heterogeneity in myofilament PTMs in the heart.

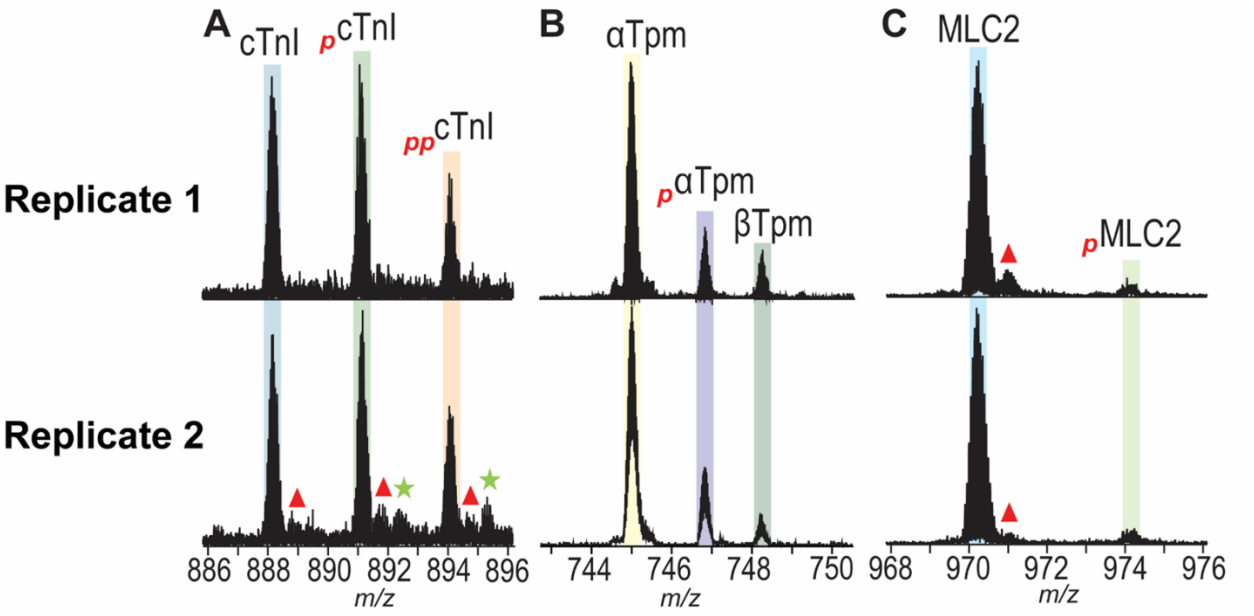

Fig. 2.1. Reproducibility of MS technical (extraction) replicates using the methods utilized here to assess myofilament protein phosphorylation in the different chambers of the heart, as well as across the LV free wall. (A) Mass spectra from extraction replicates showing a single charge state of immunoaffinity purified cTnI. (B) Mass spectra from extraction replicates showing a single charge state of Tpm analyzed using on-line top-down MS. (C) Mass spectra from extraction replicates showing a single charge state of MLC2 analyzed by high-resolution MS secondary to on-line LC-MS and fraction collection. Triangles and stars represent sodium and potassium adducts, respectively.

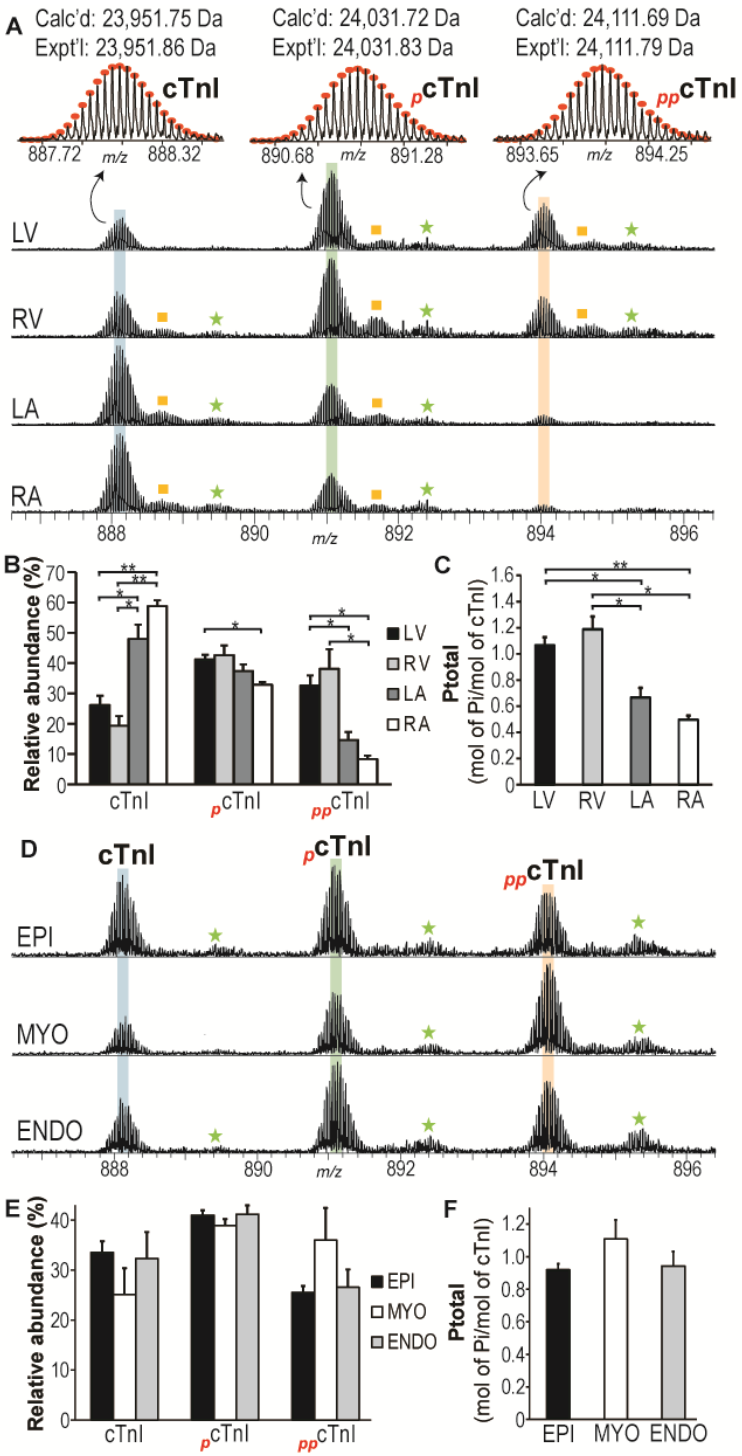

Fig. 2.2. Basal cTnI phosphorylation varies in a chamber-specific but not transmural manner in the heart. (A) Representative mass spectra for cTnI from the four chambers of the heart. Circles represent the theoretical isotopic abundance distribution of the isotopomer peaks

corresponding to the assigned mass. Squares and stars represent oxidized cTnI and potassium adducts, respectively. (B) Graph showing the relative abundances of cTnI, $_{p}$cTnI, and $_{pp}$cTnI in the four chambers of the heart. (C) Graph showing total cTnI phosphorylation in the LV, RV, LA, and RA. (D) Representative mass spectra for cTnI from the three layers of the LV free wall. Stars represent potassium adducts. (E) Graph showing the relative abundances of cTnI, $_{p}$cTnI, and $_{pp}$cTnI in the EPI, MYO, and ENDO of the LV free wall. (F) Graph showing total cTnI phosphorylation in the three layers of the LV free wall. cTnI corresponds to NCBI RefSeq accession number ABF84065. $*p < 0.05$, $**p < 0.001$.

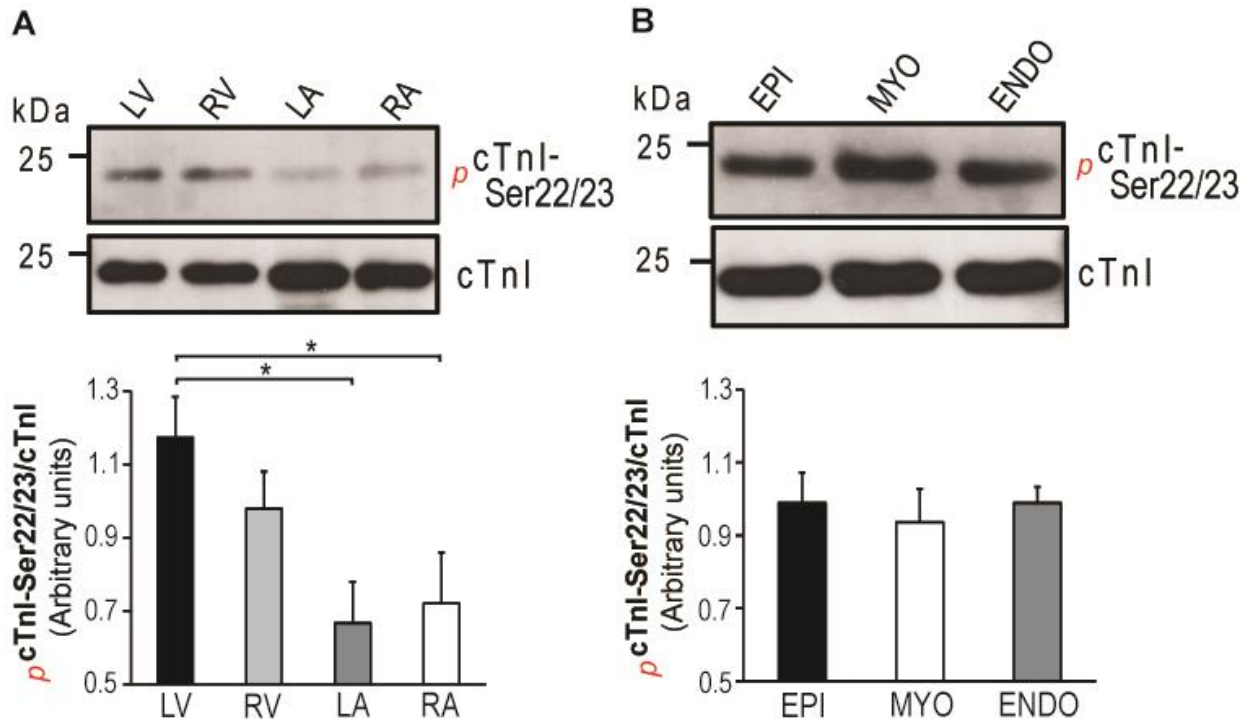

Fig. 2.3. cTnI-Ser22/23 phosphorylation is significantly increased in the LV in comparison to the LA and RA, but does not vary across the LV free wall. (A) Representative Western blots for cTnI phosphorylated at Ser22/23 and total cTnI, as well as the associated quantification results for the chamber comparison, are shown in the upper and lower panels, respectively (n=3). (B) Representative Western blots for cTnI phosphorylated at Ser22/23 and total cTnI, as well as the associated quantification results for the LV layer comparison, are shown in the upper and lower panels, respectively (n=3). $*p < 0.05$.

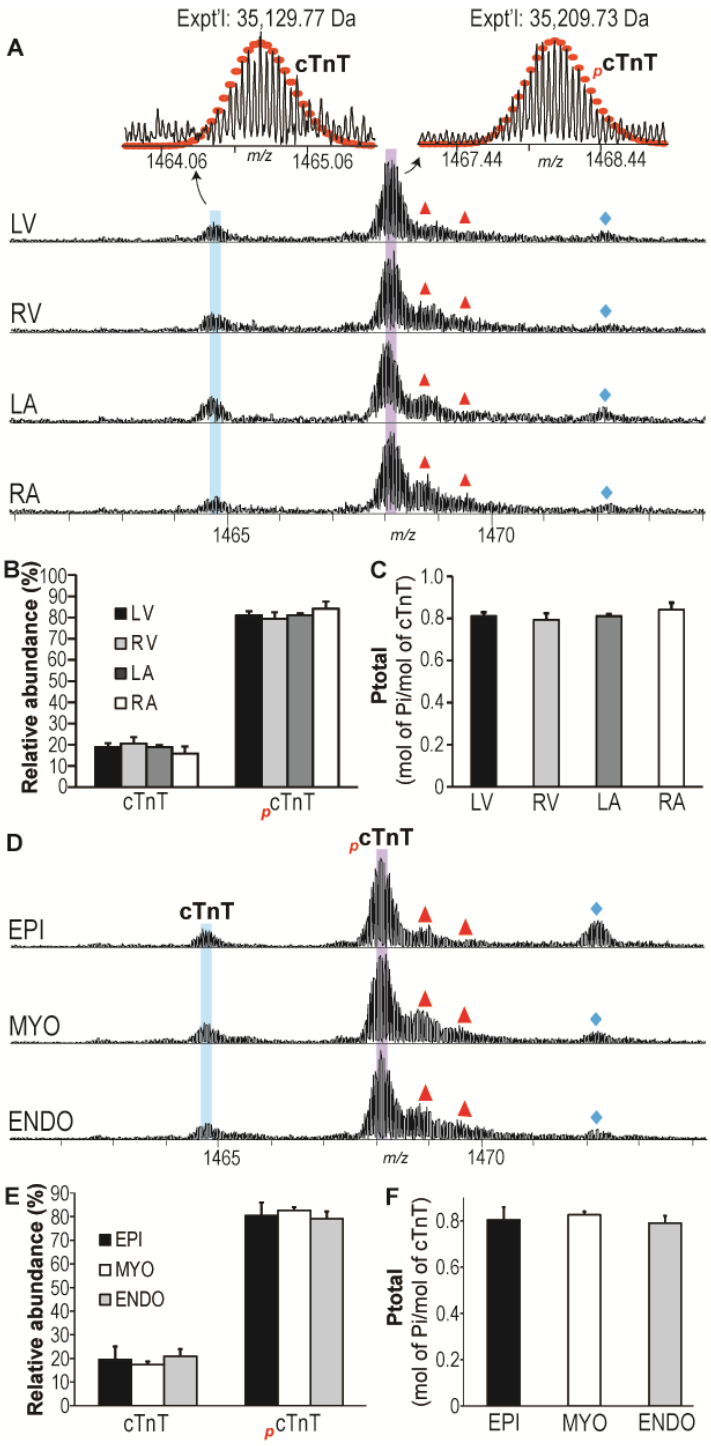

Fig. 2.4. cTnT phosphorylation does not vary in the different chambers of the heart or across the LV free wall. (A) Representative mass spectra for cTnT from the LV, RV, LA, and RA. Circles represent the theoretical isotopic abundance distribution of the isotopomer peaks

corresponding to the assigned mass. Triangles and diamonds represent sodium and phosphoric acid (+H_3PO_4) adducts, respectively. (B) Graph showing the relative abundances of cTnT and $_p$cTnT in the four chambers of the heart. (C) Graph showing total cTnT phosphorylation in the LV, RV, LA, and RA. (D) Representative mass spectra for cTnT from the EPI, MYO, and ENDO of the LV free wall. Triangles and diamonds represent sodium and phosphoric acid (+H_3PO_4) adducts, respectively. (E) Graph showing the relative abundances of cTnT and $_p$cTnT across the layers of the LV free wall. (F) Graph showing total cTnT phosphorylation in the EPI, MYO, and ENDO. cTnT corresponds to NCBI RefSeq accession number ADY80031. *$p < 0.05$, **$p < 0.001$.

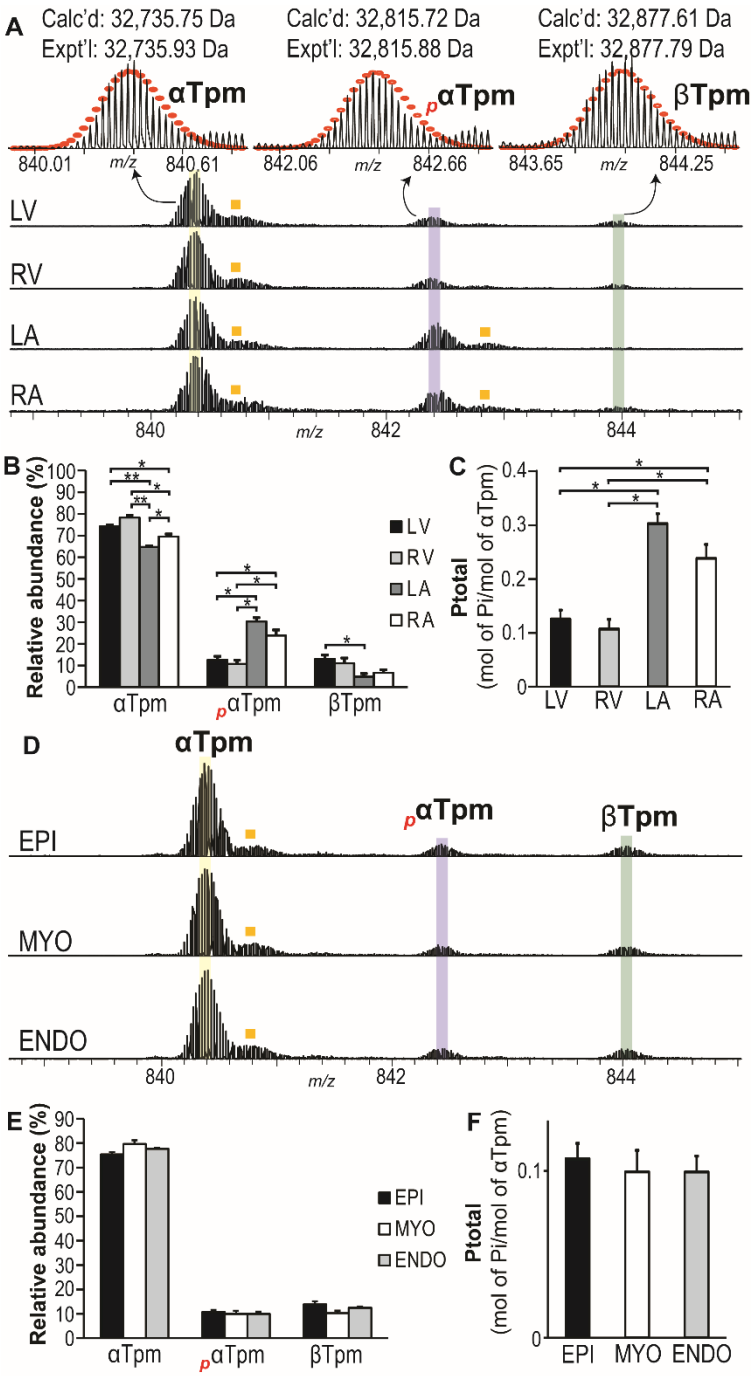

Fig. 2.5. αTpm phosphorylation exhibits chamber-specific but not transmural heterogeneity in the heart. (A) Representative mass spectra for Tpm from the LV, RV, LA, and RA. Circles represent the theoretical isotopic abundance distribution of the isotopomer peaks corresponding to the assigned mass. Squares represent oxidized Tpm. (B) Graph showing the relative abundances

of αTpm, $_p$αTpm, and βTpm in the four chambers of the heart. (C) Graph showing total αTpm phosphorylation in the LV, RV, LA, and RA. (D) Representative mass spectra for Tpm from the three layers of the LV free wall. Squares represent oxidized Tpm. (E) Graph showing the relative abundances of αTpm, $_p$αTpm, and βTpm in the EPI, MYO, and ENDO. (F) Graph showing total αTpm phosphorylation in the EPI, MYO, and ENDO. αTpm and βTpm correspond to NCBI RefSeq accession numbers NP_001090952 and XP_005660265, respectively. $*p < 0.05$, $**p < 0.001$.

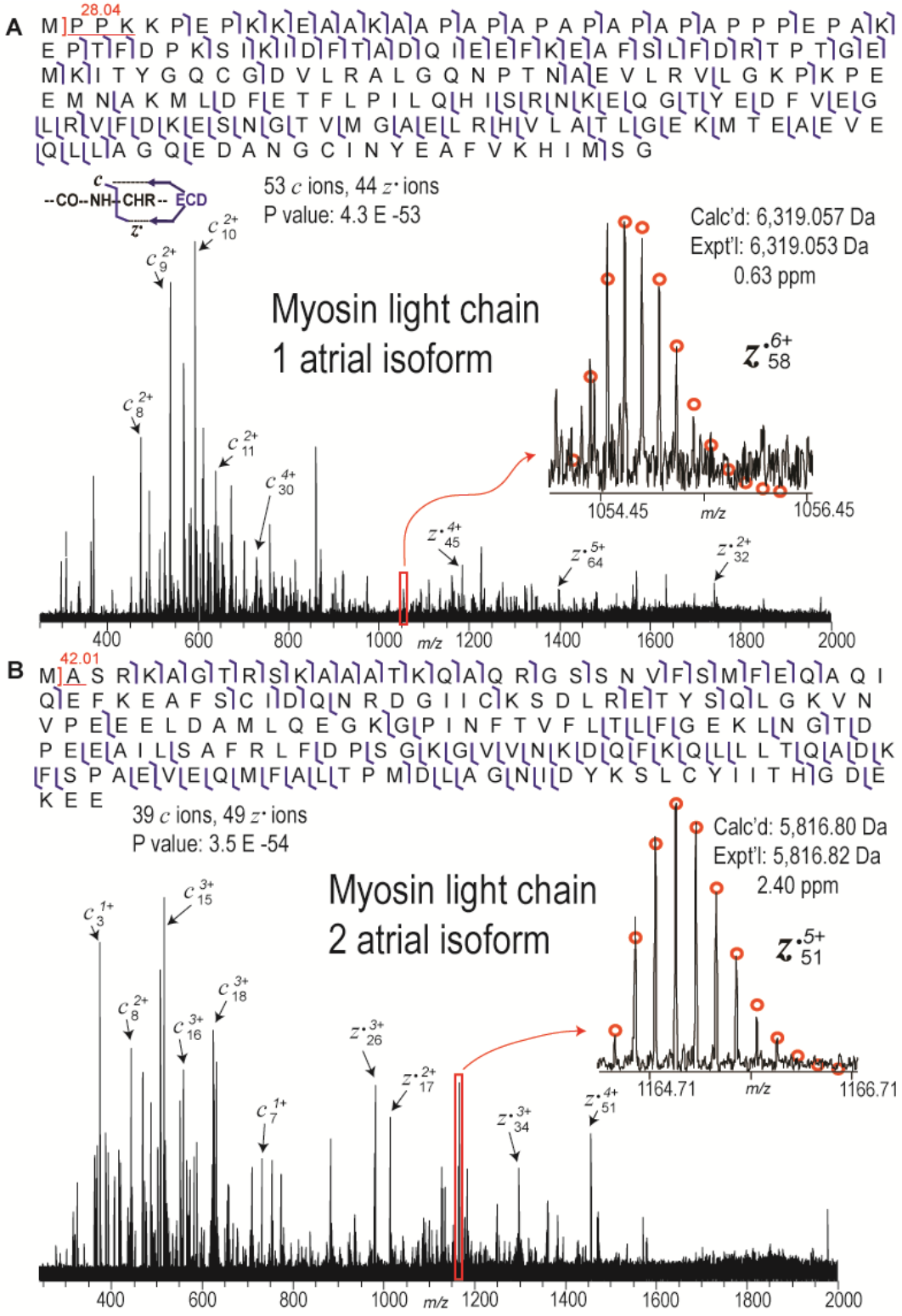

Fig. 2.6. Identification of the atrial isoforms of MLC1a and MLC2a from pig. Fragmentation maps and tandem mass spectra for (A) MLC1a and (B) MLC2a. Fragmentation maps show the

fragment ions that were matched to the sequences for MLC1a (53 *c* and 44 *z·* ions total) and MLC2a (39 *c* and 49 *z·* ions total) from *Sus scrofa* in the NCBI database. There were minor mass discrepancies of 28.04 Da and 42.01 Da localized to the N-termini of MLC1a and MLC2a, respectively. Bracket indicates removal of the N-terminal methionine. Zoomed-in spectra for representative fragment ions are shown for each protein. The P value represents the probability that the match between the spectrum and a random protein has a similarity score no less than the score for the assigned match. Thus, the low P values obtained for MLC1a and MLC2a (4.3E-53 and 3.5E-54 for MLC1a and MLC2a, respectively) translate to high confidence in the identification of these proteins. MLC1a and MLC2a correspond to NCBI RefSeq accession numbers XP_003131354 and XP_003134933, respectively.

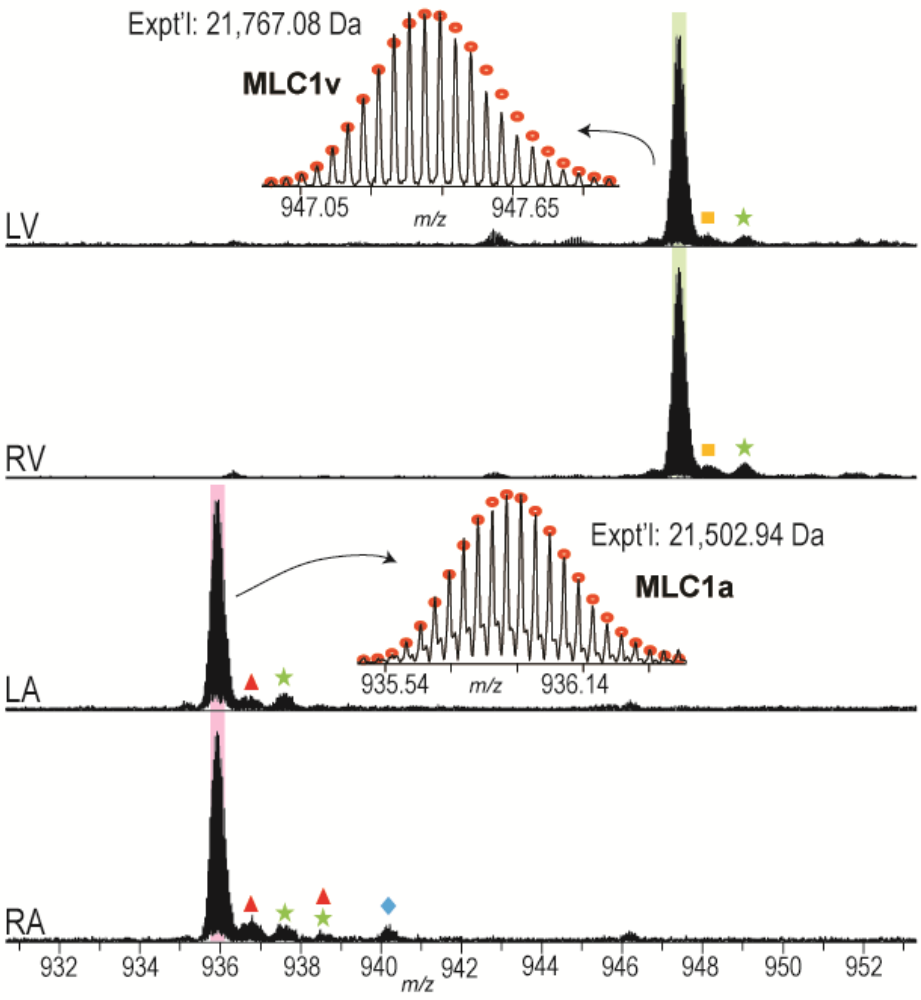

Fig. 2.7. Different MLC1 isoforms are expressed in the atria and ventricles of pig heart. Representative mass spectra for MLC1 from the LV, RV, LA, and RA. Square, star, triangle, and diamond represent oxidation, potassium adducts, sodium adducts, and phosphoric acid adducts ($+H_3PO_4$), respectively. Star and triangle combination represents MLC1 associated with both sodium and potassium. No phosphorylation was detected for MLC1. MLC1v corresponds to NCBI RefSeq accession number NP_001265702.

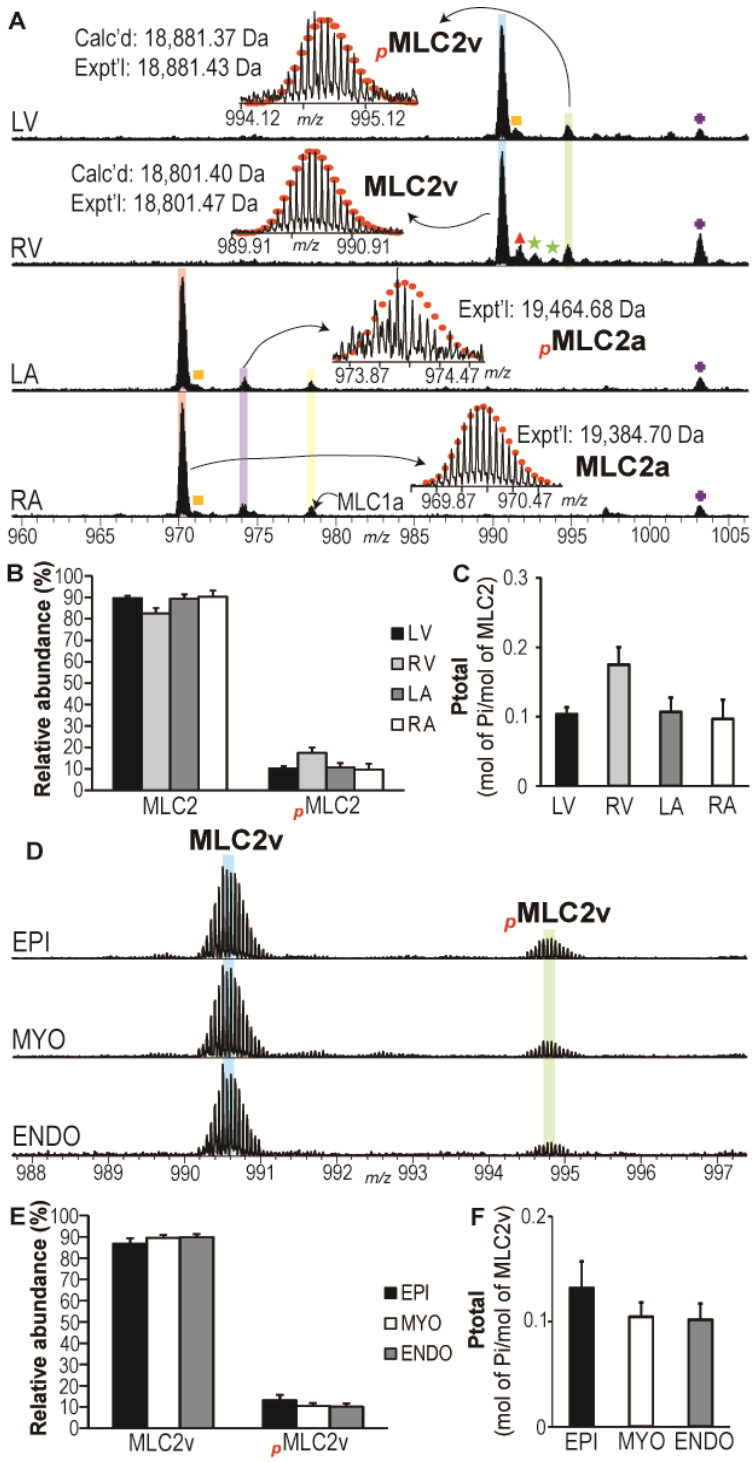

Fig. 2.8. The phosphorylation of MLC2 does not vary in a chamber-specific or transmural manner in the heart. (A) Representative mass spectra for MLC2 from the LV, RV, LA, and RA. Circles represent the theoretical isotopic abundance distribution of the isotopomer peaks

corresponding to the assigned mass. Squares, triangles, stars, and crosses represent oxidation, sodium adducts, potassium adducts, and a co-eluting protein, respectively. (B) Graph showing the relative abundances of MLC2 and $_{p}$MLC2 in the four chambers of the heart. (C) Graph showing total MLC2 phosphorylation in the LV, RV, LA, and RA. (D) Representative mass spectra for MLC2v from the EPI, MYO, and ENDO of the LV free wall. (E) Graph showing the relative abundances of MLC2v and $_{p}$MLC2v across the layers of the LV free wall. (F) Graph showing total MLC2v phosphorylation the EPI, MYO, and ENDO. MLC2v corresponds to NCBI RefSeq accession number AAM47004. *$p < 0.05$, **$p < 0.001$.

CHAPTER 3 – DISTINCT SEQUENCES AND POST-TRANSLATIONAL MODIFICATIONS IN CARDIAC ATRIAL AND VENTRICULAR MYOSIN LIGHT CHAINS REVEALED BY TOP-DOWN MASS SPECTROMETRY

Reprinted from *Journal of Molecular and Cellular Cardiology*, 107, Gregorich ZR, Cai W, Lin Z, Chen AJ, Peng Y, Kohmoto T, Ge Y, Distinct sequences and post-translational modifications in cardiac atrial and ventricular myosin light chains revealed by top-down mass spectrometry, 13-21, Copyright 2017, with permission from Elsevier [OR APPLICABLE SOCIETY COPYRIGHT OWNER].

Abstract

Myosin is the principal component of the thick filaments that, through interactions with the actin thin filaments, mediates force production during muscle contraction. Myosin is a hexamer, consisting of two heavy chains, each associated with an essential (ELC) and a regulatory (RLC) light chain, which bind the lever-arm of the heavy chain and play important modulatory roles in striated muscle contraction. Nevertheless, a comprehensive assessment of the sequences of the ELC and RLC isoforms, as well as their post-translational modifications, in the heart remains lacking. Herein, utilizing top-down high-resolution mass spectrometry (MS), we have comprehensively characterized the sequences and N-terminal modifications of the atrial and ventricular isoforms of the myosin light chains from human and swine hearts, as well as the sites of phosphorylation in the swine proteins. In addition to the correction of disparities in the database sequences of the swine proteins, we show for the first time that, whereas the ventricular isoforms of the ELC and RLC are methylated at their N-termini, which is consistent with previous studies, the atrial isoforms of the ELC and RLC from both human and swine are N^{α}-methylated and N^{α}-acetylated, respectively. Furthermore, top-down MS with electron capture dissociation enabled localization of the sites of phosphorylation in swine RLC isoforms from the ventricles and atria to Ser14 and Ser22, respectively. Collectively, these results provide new insights into the sequences and modifications of myosin light chain isoforms in the human and swine hearts, which will pave the way for a better understanding of their functional roles in cardiac physiology and pathophysiology.

3.1 Introduction

The thick filaments of muscles, including cardiac, skeletal, and smooth muscles, are predominantly composed of myosin that, through interactions with actin (the principal component of thin filaments), mediates force production during muscle contraction [2, 256]. Myosin is a hexamer consisting of two heavy chains (MHCs), each of which is associated with an essential (or alkali) light chain (ELC) and a regulatory (or phosphorylatable) light chain (RLC) [257]. In striated muscles both the ELC and RLC, which bind and stabilize the lever-arm of the MHC [258, 259], play critical roles in the modulation of contractile function [30, 32, 33, 260-262]. In support of this, mutations in both the ELC and RLC are associated with the development of cardiac and skeletal muscle myopathies [263]. Additionally, phosphorylation of the RLC by the Ca^{2+}/calmodulin-dependent myosin light chain kinase (MLCK) represents a critical mechanism regulating contractility, especially in the heart [30, 33, 65, 77, 264, 265]. In particular, recent studies have convincingly demonstrated that loss of RLC phosphorylation leads to pathological cardiac hypertrophy and heart failure [76, 77, 266, 267]. These findings have generated substantial interest in the roles played by myosin light chains and their modifications in cardiac physiology and pathophysiology; thus, a comprehensive assessment of myosin light chain isoforms and their post-translational modifications (PTMs) in the heart is apropos.

A number of different myosin light chain isoforms have been identified to date, all of which belong to the EF-hand protein super-family of Ca^{2+}-binding proteins [268]. Four of these genes are expressed in the heart, with expression patterns that vary by chamber, developmentally, and in response to pathological stimuli [32, 262, 265]. The *MYL3* and *MYL4* genes encode the ventricular

(ELC_v) and atrial (ELC_a) isoforms of the ELC, while the ventricular (RLC_v) and atrial (RLC_a) isoforms of the RLC are encoded by the *MYL2* and *MYL7* genes, respectively. Although expression of ELC_v is primarily restricted to the ventricles of the heart, ELC_a is expressed in both the atria and ventricles during normal embryonic development [32, 262]. In adulthood, however, expression of the ELC_a is restricted to the atria, although re-expression in the ventricles occurs in response to pressure overload and heart failure [32, 147, 262]. On the other hand, RLC_v expression is restricted to the ventricles both in the developing and adult heart [265]. Conversely, RLC_a, like ELC_a, is expressed throughout the heart early in development, and becomes restricted to the atria later in development [265].

Top-down mass spectrometry (MS) has gained considerable popularity as the premier approach for comprehensively characterizing proteins [197, 199, 200]. Unlike in conventional bottom-up MS, in which proteins are digested and the resulting peptides are analyzed by MS, intact proteins are analyzed in top-down MS, providing a global or "bird's eye" view of all protein species, including those containing sequence variations (due to mutations/polymorphisms or alternative splicing) and/or PTMs [90, 197, 199, 200, 213, 242, 244, 245, 269]. Following intact protein analysis, specific protein species of interest can be isolated and fragmented using a variety of tandem MS (MS/MS) techniques, including, but not limited to, electron capture dissociation (ECD) and collision induced dissociation (CID), to obtain sequence information and localize PTMs [90, 197, 199, 200, 213, 242, 244, 245, 269]. In particular, top-down MS with ECD represents a powerful method for the comprehensive characterization of proteins; especially those containing labile PTMs such as phosphorylation, which are frequently lost when proteins are fragmented using energetic dissociation methods such as CID [90]. Additionally, the use of high-

resolution mass spectrometers in top-down MS studies offers unparalleled mass accuracy, which not only increases confidence in protein identification, but also in the identification of protein PTMs [270]. Herein, utilizing top-down high-resolution MS, we have characterized the sequences and N-terminal modifications of cardiac myosin light chain isoforms from human and swine, as well as the sites of phosphorylation in the swine proteins, towards a better understanding of the functional roles of these proteins in cardiac physiology and pathophysiology. Interestingly, we found that, whereas the ventricular ELC and RLC are N^{α}-tri-methylated, the atrial ELC is methylated at its N-terminus while the atrial RLC in both swine and human is N^{α}-acetylated; making the atrial RLC unique among cardiac myosin light chain isoforms. Importantly, we have also precisely localized the sites of phosphorylation in swine RLC isoforms from the ventricles and atria to Ser14 and Ser22, respectively. Although prior studies have reported atrial RLC phosphorylation, this represents the first study to definitively localize a site of phosphorylation in this isoform.

3.2 Materials and methods

3.2.1 Chemicals and reagents

All chemicals and reagents were purchased from Sigma (St. Louis, MO, USA) unless otherwise indicated. All solutions were prepared in Milli-Q water (Millipore, Billierica, MA, USA).

3.2.2 Heart tissue

Swine heart tissue was obtained from adult Yorkshire domestic swine (*Sus scrofa*) (approximately 3 months of age) as approved by the University of Wisconsin Animal Care and Use Committee. Excised hearts were quickly sectioned into the four chambers and further sectioned into transmural sections of approximately 600-800 mg and 200 mg each for ventricular and atrial tissue, respectively. All transmural sections were flash frozen in liquid nitrogen immediately following sectioning. The left ventricular myocardium was dissected first, followed by the left atrial, right ventricular, right atrial, and septal tissue; with all tissue from the corresponding chambers being flash frozen within approximately 4, 5, 7, 8, and 12 min (total time) following excision of the heart, respectively. Following flash freezing, all tissue was stored at −80 °C for later analysis. The majority of myofilament-enriched protein extracts were prepared from the left ventricular and atrial swine myocardium, respectively; although extracts were also prepared from the right atrial and ventricular myocardium as well. No differences were observed between samples prepared from the right and left atrial and right and left ventricular swine myocardium. For MS/MS sequence characterization and the localization of phosphorylation sites, fractions are from 1-3 swine (biological replicates).

Human donor atrial and ventricular tissue samples were obtained from a single organ donor with normal cardiac function. Following excision from the body, hearts were first sectioned into the four chambers and then further sectioned into transmural segments and flash frozen in liquid nitrogen. Dissection of the donor heart was accomplished in less than one hour. Human tissue extracts were prepared from left atrial and ventricular myocardium, respectively. All procedures were approved by the University of Wisconsin-Madison Institutional Review Board.

3.2.3 Extraction of the myofilament sub-proteome

Extraction of the myofilament sub-proteome from swine or human atrial and ventricular tissue was carried out using a protocol originally developed by Van Eyk et al. [271, 272], with modifications. Approximately ~20 mg of cardiac tissue was homogenized in 100 µL of HEPES extraction buffer containing protease and phosphatase inhibitors using a Teflon pestle (1.5 mL tube rounded tip; Scienceware, Pequannock, NJ, USA). To test whether phosphatase inhibition using this protocol was sufficient, protein extracts were prepared from swine ventricular myocardium using HEPES buffer containing 25 mM HEPES pH 7.5, 5 mM Na_3VO_4, 2.5 mM EDTA, protease inhibitor cocktail (Sigma), and supplemented with: i) no Ser/Thr phosphatase inhibitors; ii) the recommended 50 mM NaF [271, 272]; or iii) 100 mM NaF, 10 mM sodium pyrophosphate, and 100 mM β-glycerophosphate. To demonstrate maximal inhibition of phosphatase activity towards RLC, HEPES buffer (25 mM HEPES pH7.5, 5 mM Na_3VO_4, 2.5 mM EDTA, protease inhibitor cocktail) supplemented with either: i) no Ser/Thr phosphatase inhibitors; ii) 500 mM NaF, 5 mM sodium pyrophosphate, and 100 mM β-glycerophosphate; or iii) 600 mM NaF, 5 mM sodium pyrophosphate, and 100 mM β-glycerophosphate, was employed. After demonstrating maximal inhibition of phosphatase activity towards RLC, HEPES buffer supplemented with 600 mM NaF, 5 mM sodium pyrophosphate, and 100 mM β-glycerophosphate was used for all subsequent experiments. After homogenization in the HEPES-based extraction buffer, the resulting homogenate was centrifuged at 16,000 × *g* for 15 minutes at 4 °C and the supernatant, which contains soluble cytoplasmic proteins, was discarded. The insoluble pellet was then re-homogenized in 100 µL of TFA extraction buffer (1% TFA, 1 mM TCEP) to solubilize the myofilament proteins. After centrifugation (16,000 × *g*, 4 °C, 25 min), the supernatant was

collected and the myofilament proteins were separated using reverse phase liquid chromatography (LC) (**Fig. 3.1**).

3.2.4 Myofilament protein separation and fraction collection

LC-based separation of the myofilament sub-proteome and fraction collection of light chain isoforms from swine was carried out as previously described [244, 269]. Briefly, myofilament extracts prepared from swine atrial or ventricular tissue were separated using a 2D-nano-LC system (Eksigent, Redwood City, CA, USA) equipped with a home-packed PLRP column (PLRP-S, 200 mm x 500 μm, 10 μm, 1000 Å; Varian, Lake Forest, CA, USA) and a gradient going from 20% B to 90% B over 55 min (solvent A: 0.10% formic acid in water; solvent B: 0.10% formic acid in a 50:50 mixture of acetonitrile and ethanol) at a flow rate of 12.5 μL/min. The 2D-nano-LC system was coupled directly on-line with a linear ion trap (LTQ) mass spectrometer (Thermo Scientific, Bremen, Germany) and, after separation, a small portion of the sample was ionized and analyzed directly via LTQ/MS to track protein elution from the column. Eluting swine ELC and RLC were fraction collected on ice and subsequently analyzed by high-resolution MS and MS/MS for comprehensive sequence characterization and PTM localization. Alternatively, for the on-line LC-MS/MS analysis of myosin light chain isoforms in the human heart, as well as the quantification of RLC phosphorylation in swine myocardium, myofilament-enriched extracts were prepared and separated using a nanoACQUITY LC system (Waters, Milford, MA, USA) equipped with a home-packed PLRP column as described above, and coupled directly on-line with a maXis II mass spectrometer (Bruker, Billerica, MA, USA). Spectra were collected using a scan rate of 1 Hz over a 500-3000 *m/z* range.

3.2.5 High-resolution MS and MS/MS analyses

Fractions containing myosin light chain isoforms from the atria and ventricles of the swine heart were introduced into either a 7T LTQ/Fourier transform ion cyclotron resonance (FT-ICR) mass spectrometer (LTQ/FT Ultra; Thermo Scientific). Samples were introduced into the mass spectrometer using an automated nano-electrospray ionization source (Triversa NanoMate; Advion BioSciences, Ithaca, NY, USA) and a spray voltage of 1.2-1.6 kV versus the inlet of the mass spectrometer, which resulted in a flow-rate of approximately 50-200 nL/min. A voltage offset of 5-25 V was used between the skimmer and the first multipole (7T LTQ/FT Ultra) to promote vibrational excitation of the ions prior to fragmentation. For the 7T LTQ/FT Ultra, the numbers of charges for a full scan in the linear trap, FT-ICR cell, MS^n FT-ICR cell, and ECD were 3×10^4, 1×10^6, 1×10^6, and 1×10^6, respectively; and a resolving power of 200,000 (at m/z 400) were employed. For MS/MS experiments, individual charge states were isolated and fragmented using either ECD or CID. The electron energy, duration, and delay for ECD, and normalized collision energy for CID, were varied on a case-by-case basis in order to optimize the fragmentation of different charge states of the myosin light chain isoforms. Between 1,000-5,000 scans were averaged for CID and ECD tandem mass spectra to ensure the collection of high quality spectra for data analysis.

For the on-line LC-MS/MS analysis of myosin light chain isoforms in the human heart, as well as the quantification of RLC phosphorylation in swine myocardium, the analysis was conducted on a high-resolution maXis II mass spectrometer (Bruker, Billerica, MA, USA). Spectra were

collected using a scan rate of 1 Hz over a 500 - 3000 *m/z* range. CID was employed for MS/MS analyses on the maXis II mass spectrometer, and the collision energy was optimized to maximize fragmentation of the specific myosin light chain isoforms.

3.2.6 Data analysis

All mass and tandem mass spectra were analyzed using in-house developed MASH Suite Pro software [273], with a signal-to-noise threshold of 2.5-3 and a minimum fit percentage of 60%. MS-based quantification of RLC phosphorylation was conducted as previously described [202, 244, 269]. Statistical analysis was carried out using unpaired two-tailed *t*-test. A *p*-value less than 0.05 was considered statistically significant. A mass accuracy cut-off of 10 ppm was utilized for MS/MS fragment ion assignments. Calculation of the mass accuracy (in parts per million or ppm) for intact proteins and fragment ions was carried out using the following equation:

$$Mass\ accuracy\ (ppm) = \left(\frac{(Experimental\ mass - Calculated\ mass)}{Calculated\ mass}\right) x\ 10^6 \quad (1)$$

As an example, at a mass accuracy of 10 ppm, the experimentally measured mass of RLC_v (calculated molecular mass of 18,801.43 Da based on the sequence in the UniProtKB/Swiss-Prot database) would be allowed to differ in mass from the calculated mass by no more than approximately ±0.19 Da. The monoisotopic masses are reported for intact proteins and fragment ions, respectively. Information pertaining to the protein sequences utilized in this study, including the UniProtKB/Swiss-Prot accession numbers, genes, and species information, are listed in **Table 3.1**. Protein sequence alignments were generated using Clustal Omega [274].

3.3 Results

3.3.1 Inhibition of phosphatase activity towards the RLC

To quantify RLC phosphorylation we employed quantitative on-line top-down LC-MS. This method provided robust and highly reproducible measurement of RLC phosphorylation in cardiac tissue extracts prepared using the two-step extraction procedure described by Van Eyk et al. [271, 272] with modifications (**Fig. 3.2**). By varying the concentration of phosphatase inhibitors used in the HEPES-based extraction buffer [271, 272], we determined that supplementation with 600 mM NaF (in combination with 5 mM sodium pyrophosphate and 100 mM β-glycerophosphate) provided maximal inhibition of phosphatase activity towards the RLC in myocardial extracts (**Figs. 3.3-3.4**). Therefore, HEPES-based buffer containing 600 mM NaF, 5 mM sodium pyrophosphate, and 100 mM β-glycerophosphate was used for all subsequent experiments to prevent de-phosphorylation of RLC during the preparation of myofilament-enriched protein extracts from atrial and ventricular myocardium.

3.3.2 Sequencing and N-terminal modification characterization of swine and human RLC_a

Top-down MS profiling of RLC_a protein species in extracts prepared from the atrial myocardium of swine revealed the presence of major and minor protein species presumably corresponding to un-phosphorylated RLC_a (M_r 19,372.59 Da), mono-phosphorylated RLC_a ($_pRLC_a$; M_r 19,452.55 Da), and bis-phosphorylated RLC_a ($_{pp}RLC_a$; 19,532.51 Da) (**Fig. 3.5A**). Top-down LC-MS-based

quantification yielded a mean value of 0.16 ± 0.03 mol of Pi/mol of RLC for swine RLC_a (n=5) (**Fig. 3.5B**).

However, the expected mass of swine RLC_a, predicted based on the current unconfirmed sequence in the UniProtKB/Swiss-Prot database (M_r 16,694.24 Da), was substantially different than the experimentally determined mass for this protein (**Fig. 3.5A**), indicating potential sequence discrepancies in the unconfirmed sequence. Therefore, to correct potential sequence discrepancies in the database sequence, we first verified the sequence of the human protein using on-line top-down LC-MS/MS (**Fig. 3.6**), and, subsequently, utilized the confirmed human RLC_a sequence as a template to characterize the swine protein. Interestingly, although previous studies have shown that ventricular myosin light chain isoforms are N^{α}-tri-methylated [275], high accuracy mass measurement revealed that human RLC_a is N-terminally acetylated (+42.010 Da) rather than tri-methylated (+42.046 Da) (**Fig. 3.6A**). Similarly, swine RLC_a was also N^{α}-acetylated rather than N-terminally methylated (**Fig. 3.5C**).

Comprehensive top-down MS analysis permitted the confirmation of 6 amino acid differences between the swine and human proteins (**Fig. 3.5D**, **Figs. 3.7-3.8**). Moreover, swine RLC_a contained a 26 amino acid N-terminal stretch not present in the unconfirmed swine sequence in the UniProtKB/Swiss-Prot database (**Fig. 3.5D**, **Fig. 3.9**). After sequencing, a total of 41 $a^{\cdot}$, 89 c, 28 y, and 87 $z^{\cdot}$ ions could be matched to the sequence of swine RLC_a (from a combined 2 ECD tandem mass spectra), representing cleavage of 144 out of 173 inter-residue bonds (~83% sequence coverage) (**Fig. 3.5D**). Note that $a^{\cdot}$, b, and c ions contain the N-terminus, while x, y, and $z^{\cdot}$ ions contain the C-terminus. Comparison of the confirmed sequences for human and swine RLC_a with

sequences in the UniProtKB/Swiss-Prot database showed that human RLC_a is more similar in sequence to swine RLC_a (approximately 97% sequence similarity) than mouse RLC_a (**Table 3.2**).

3.3.3 Localization of the phosphorylation site in swine $_pRLC_a$

Previous studies have reported the existence of mono- and bis-phosphorylated forms of RLC_a in human atrial myocardium [276]; however, the specific sites of phosphorylation in RLC_a have not been determined. To localize the site(s) of mono-phosphorylation in swine RLC_a, peaks corresponding to $_pRLC_a$ were isolated and fragmented using ECD. Analysis of the MS/MS data revealed that all *c* ions prior to and including c_{21} were observed only in their un-phosphorylated states (**Fig. 3.10A-B**), which indicates that the site(s) of phosphorylation in $_pRLC_a$ is located after Ser21. On the other hand, all *c* ions following and including c_{22} were detected only in their mono-phosphorylated state (**Fig. 3.10C-D**). This data indicates that Ser22 is a site of phosphorylation in swine RLC_a. Additionally, all $z\cdot$ ions prior to and including $z\cdot_{152}$ were detected only in their un-phosphorylated state (**Fig. 3.10E**), whereas all $z\cdot$ ions after and including $z\cdot_{154}$ were observed only in their mono-phosphorylated state (**Fig. 3.10F**). Collectively, these results indicate that Ser22 is the sole site of phosphorylation in $_pRLC_a$ from the swine heart (**Fig. 3.10G**). Unfortunately, the very low abundance of $_{pp}RLC_a$ precluded MS/MS analysis of this species and, thus, localization of the second phosphorylation site in swine RLC_a. To our knowledge this represents the first study to definitively localize a site of phosphorylation in RLC_a.

3.3.4 Sequencing and N-terminal modification characterization of ELC_a from swine and human

Top-down MS profiling of swine ELC_a protein species revealed the presence of a peak likely corresponding to un-modified ELC_a (M_r 21,489.84 Da) (**Fig. 3.11A**). Peaks corresponding to mono-phosphorylated ELC_a ($_pELC_a$) were not detected in any of the spectra and, thus, would represent less than 0.1% of the ELC_a population based on the signal intensity at the expected position of $_pELC_a$ (**Fig. 3.11A**).

As with swine RLC_a, the experimentally determined mass of swine ELC_a did not match with that calculated based on the unconfirmed sequence for this protein in the UniProtKB/Swiss-Prot database. Therefore, as above, we first verified the sequence of the human protein (**Fig. 3.12**), and utilized the confirmed human ELC_a sequence as a template to characterize the swine protein.

Comprehensive MS/MS analysis of swine ELC_a, using a combination of ECD and CID, allowed for the identification of di-methylation as the N-terminal modification in swine ELC_a (**Fig. 3.11B**), as well as the localization of 8 amino acid differences between the swine and human proteins (**Fig. 3.11C**, **Figs. 3.13-3.14**). Notably, determination of the swine ELC_a sequence revealed that the initial five N-terminal amino acids present in the unconfirmed swine sequence from the UniProtKB/Swiss-Prot database were not present in the protein (**Fig. 3.15**). Following in-depth sequencing of swine ELC_a, a total of 85 $a\cdot$, 41 *b*, 125 *c*, 66 *y*, and 126 $z\cdot$ ions could be matched to the determined ELC_a sequence (from a combined 7 ECD and 1 CID tandem mass spectra), representing cleavage of 185 out of 195 inter-residue bonds (~95% sequence coverage) (**Fig. 3.11C**). Based on the determined sequences, swine ELC_a shared the highest sequence similarity with the human protein (approximately 96% sequence similarity with human ELC_a) (**Table 3.2**).

3.3.5 Sequencing and N-terminal modification characterization of swine and human RLC_v

Analysis of myofilament-enriched protein extracts prepared from swine ventricular myocardium revealed the presence of un-modified and mono-phosphorylated forms of RLC_v in agreement with our previous findings (**Fig. 3.16**) [244]. Quantitative LC-MS analysis yielded a mean of 0.12 ± 0.01 mol of Pi/mol of RLC_v in the swine ventricular myocardium (n=6) (**Fig. 3.16C**). Sequence characterization of swine RLC_v was in good agreement with our previous analysis of this protein (**Fig. 3.16**) [244].

In addition to verifying the sequence of swine RLC_v, we have also confirmed the sequence of human RLC_v, which matched well with the UniProtKB/Swiss-Prot database sequence for this protein (accession number P10916; **Table 3.1**) after considering removal of the N-terminal Met and tri-methylation of Ala1 (**Fig. 3.17**). Surprisingly, despite high sequence similarity with human RLC_v, the sequence of swine RLC_v was most similar to the rabbit protein (**Fig. 3.18**, **Table 3.2**). Similarly, human RLC_v was most similar in sequence to rabbit RLC_v (approximately 98% sequence similarity), with swine and mouse showing identical sequence similarity to the human protein (~96% sequence similarity) (**Fig. 3.18**, **Table 3.2**).

3.3.6 Localization of the phosphorylation site in swine $_pRLC_v$

The phosphorylation site in swine RLC_v has been localized previously [244, 264]. To confirm the phosphorylation site in swine RLC_v, peaks corresponding to $_pRLC_v$ were selected for fragmentation by ECD. Comprehensive ECD MS/MS analysis revealed that swine $_pRLC_v$ is

phosphorylated at a single site (Ser14), which is in good agreement with our previous findings and those of others (**Figs. 3.19**) [244, 264].

3.3.7 Sequencing and N-terminal modification characterization of ELC_v from swine and human

Top-down MS profiling of ELC_v protein species in the swine ventricle revealed the presence of a protein species with an experimental mass (M_r 21,753.86 Da) that corresponded well with the predicted mass of swine ELC_v calculated based on the sequence in the UniProtKB/Swiss-Prot database (accession number F1SNW4; **Table 3.1**) after considering removal of the N-terminal Met and N^{α}-tri-methylation of Ala1 (**Fig. 3.20A-B**) [275]. Peaks corresponding to mono-phosphorylated ELC_v ($_pELC_v$) were not detected in any of the mass spectra analyzed and, thus, would represent less than approximately 0.5% of the entire ELC_v population based on the signal intensity at the expected position of $_pELC_v$ (**Fig. 3.20A**).

To confirm the sequence of swine ELC_v, peaks corresponding to the un-modified protein were isolated and fragmented using CID and ECD. Comprehensive sequencing allowed for confirmation of 11 amino acid differences between the swine and human proteins (**Fig. 3.20C**, **Figs. 3.21-3.22**). Following MS/MS analysis, a total of 41 $a\cdot$, 34 *b*, 102 *c*, 62 *y*, and 104 $z\cdot$ ions could be matched to the swine ELC_v sequence with high mass accuracy (from a combined 7 ECD and 3 CID tandem mass spectra) (**Fig. 3.20C**). This represents cleavage of 176 out of 195 inter-residue bonds (approximately 90% sequence coverage), providing high confidence in the sequence of swine ELC_v (**Fig. 3.20C**). In addition to verification of the swine ELC_v sequence, we also confirmed the sequence of human ELC_v, which matched well with the sequence in the

UniProtKB/Swiss-Prot database (accession number P08590; **Table 3.1**) after considering N-terminal Met removal and tri-methylation of Ala1 (**Fig. 3.23**). Comparison of the confirmed sequences for human and swine ELC_v with sequences in the UniProtKB/Swiss-Prot database showed that, while human ELC_v is closest in sequence to the swine protein (approximately 94% sequence similarity), swine ELC_v shared the highest sequence similarity with rat ELC_v (approximately 95% sequence similarity) (**Table 3.2**).

3.4 Discussion

3.4.1 Characterization of cardiac myosin light chain isoform sequences

In this study, we utilized top-down high-resolution MS/MS to characterize the sequences of cardiac myosin light chain isoforms in the human and swine hearts (**Figs. 3.5-3.6**, **3.11-3.12**, **3.16-3.17**, **3.20**, **3.23**) towards a better understanding of the functional roles of these proteins in cardiac physiology and pathophysiology.

In addition to verifying the sequence of human RLC_a, we found that swine RLC_a contained a 26 amino acid stretch not present in the UniProtKB/Swiss-Prot database sequence for this protein (**Figs. 3.5**, **3.9**). Comprehensive top-down MS/MS sequencing also enabled the confirmation of six amino acid differences between human and swine RLC_a (**Figs. 3.5**, **3.7**). These differences were distributed throughout the protein sequence, with two occurring near the N-terminus of the protein, one within the first EF-hand domain, one immediately adjacent to the first EF-hand domain, and two within the second EF-hand domain (**Fig. 3.8**). Sequence comparison using the

sequences for human and swine RLC_a confirmed herein, as well as protein sequences from other species in the UniProtKB/Swiss-Prot database, revealed that swine RLC_a was most similar in sequence to the human protein (~97% sequence similarity) (**Table 3.2**). Likewise, the sequence of human RLC_a was more similar in sequence to the swine protein than it was to the mouse protein (**Table 3.2**). Six amino acid differences were also confirmed between swine and human RLC_v isoforms (**Figs. 3.16, 3.18**). Two of these amino acid differences are located at/near the N-terminus, two are located within the second EF-hand domain, and the final two can be found in the third EF-hand domain (**Fig. 3.18**). Interestingly, although the sequences of the swine and human RLC_v isoforms were highly similar (~96% sequence similarity), the isoforms from both species shared a higher degree of sequence similarity with RLC_v from rabbit (approximately 97% and 98% sequence similarity with swine and human RLC_v, respectively) (**Table 3.2**). Nevertheless, the high degree of sequence similarity between swine and human protein isoforms in the heart highlights the usefulness of swine as a model system for modeling human cardiovascular diseases [243, 277].

In comparison, a greater number of differences were identified in the sequences of swine and human ELC isoforms. In addition to determining that the first five amino acids in the UniProtKB/Swiss-Prot database sequence for swine ELC_a are not present in the protein (**Fig. 3.15**), a total of eight and eleven amino acid differences between human and swine ELC_a and ELC_v, respectively, were localized in this study (**Figs. 3.11**, **3.14**, **3.20-3.21**). Both of the ELC isoforms expressed in the heart are long ELC isoforms (so-called A1-type ELCs), which differ from the short (A2-type) isoforms (expressed in fast skeletal and smooth muscles) in that they contain a unique N-terminal extension that is approximately 40-46 amino acids in length and is comprised

of a cluster of Lys residues at the extreme N-terminus followed by a stretch of predominantly Pro and Ala residues (**Figs. 3.15**, **3.22**) [257]. Notably, the preponderance of the amino acid differences between ELC_a and ELC_v isoforms in swine and human, as well as other species, were located within the N-terminal extensions of these isoforms (**Figs. 3.15**, **3.22**). Given that previous studies have shown that the N-terminal extensions of A1-type ELCs interact with actin [262, 278-280], differences in the N-terminal sequences of these isoforms may be, in part, responsible for differences in their actin affinities [279].

3.4.2 Identification of cardiac myosin light chain isoform N-terminal modifications

Here, we demonstrate that ELC_v and RLC_v from human and swine are N^{α}-tri-methylated (**Figs. 3.16-3.17**, **3.20**, **3.23**), which is in good agreement with the findings of previous studies in human and cow [275]. Additionally, for the first time, we show that ELC_a from human and swine is also methylated at its N-terminus, whereas RLC_a is N^{α}-acetylated (**Figs. 3.5-3.6**, **3.11-3.12**). In particular, the discovery that RLC_a is N-terminally acetylated is interesting as this modification appears to make RLC_a distinct from myosin light chain isoforms from ventricular myocardium and fast skeletal muscle as the latter isoforms contain the consensus X-Pro-Lys motif required for methylation by the N-terminal methyltransferase [281].

The N^{α}-acetylation of proteins is a common phenomenon, with predictions estimating that approximately 77% of all proteins in humans are N-terminally acetylated [282]. Nevertheless, the purpose(s) of N-terminal acetylation remains poorly understood. Traditionally, N^{α}-acetylation has been thought to protect proteins from degradation [283, 284]; however, recent studies have

suggested diverse functions for this modification, including roles in protein-protein interactions [285], intracellular targeting to specific sub-cellular compartments [286, 287], and even in protein degradation via a ubiquitin-dependent pathway [286]. Given that RLC_a N^{α}-acetylation has not been previously reported, the functional significance of this modification is unclear.

In comparison to N-terminal acetylation, methylation of the α-amino group of proteins is comparatively quite rare [288], although this modification seems to be relatively widespread in nature [275]. Furthermore, while the function(s) of protein N^{α}-acetylation remains poorly understood, even less is known about the consequences of protein N-terminal methylation. In contrast to N-terminal acetylation, tri-methylation (or di-methylation in the case of Pro) of the α-amino group of the protein dramatically alters the chemistry of the N-terminus. Specifically, quaternization of the α-amino group induces a permanent positive charge at the protein N-terminus and abrogates reactivity of the α-amino nitrogen [288]. Studies have previously suggested that charged residues at the extreme N-termini of the cardiac ELCs are important for interactions with actin [289]; therefore, it is conceivable that the permanent positive charge induced at the N-terminus by methylation of the α-amino groups of ELC_a and ELC_v may also be involved in electrostatic interactions with negatively charged amino acids on the surface of actin.

3.4.3 Regulatory light chain phosphorylation

Reported values for endogenous RLC phosphorylation vary widely in the literature. While many groups have reported relatively constant values of 0.4-0.6 mol Pi/mol of RLC across species [264, 290, 291], others have reported significantly lower values [68, 238, 292, 293], even within the

same species. Here, measurement of RLC phosphorylation using conditions under which maximal inhibition of phosphatase activity towards RLC during protein extraction was achieved (**Fig. 3.4**), we measured mean values of 0.16 ± 0.03 and 0.12 ± 0.01 mol of Pi/mol of RLC for swine RLC_a and RLC_v, respectively (**Figs. 3.5**, **3.16**). These values are higher than those reported previously by our group for swine (due to complete inhibition of phosphatase activity towards the RLC during protein extraction in this study). Nevertheless, these values are lower than those reported by others for swine [264, 291]. Given that a number of studies, including those from our own lab, have demonstrated that RLC phosphorylation does not vary transmurally in large animals (swine) and humans [93, 141, 269], as it does in rodents [240], this discrepancy is unlikely to be from differences in sampling location within the ventricular myocardium. One possibility for the differences between the values measured in this study and in other studies [264, 291], is that different methods were used for measuring RLC phosphorylation (top-down MS versus ProQ Diamond stain or SDS-PAGE PhosTag^{TM} analysis). Differences in the time taken for dissection of the heart following excision (prior to flash freezing in liquid nitrogen) [294], and swine strain differences in basal RLC phosphorylation are also possible. Regardless, we are confident that we have detected all phosphorylated forms of the atrial and ventricular RLCs as even groups reporting high levels of RLC phosphorylation (0.4-0.6 mol of Pi/mol of RLC) have observed only a singly phosphorylated form of RLC_v and both singly and doubly phosphorylated forms of RLC_a in swine and humans [264, 276, 291].

In contrast to RLC phosphorylation, which is well documented [30, 65, 264, 265], phosphorylation of the ELC has not been widely observed, with reports in only a handful of species, including rabbits, humans, and rats [141, 272, 295]. In this study, phosphorylated forms of ELC_a and ELC_v

were not detected in either human or swine myocardium (**Figs. 3.11**, **3.20**). Phosphorylation of the ELC was initially identified *in vivo* in a proteomic analysis of rabbit ventricular myocardium, and was found to increase in response to pharmacological preconditioning with adenosine [272]. It was subsequently shown that this modification was associated with increased MMP-2-mediated degradation of the ELC [295]. This modification has also been detected in the myocardium of patients with heart failure and was shown to be inversely correlated with myocardial power production, possibly as a consequence of ELC degradation by MMP-2 [141]. Consequently, given that the available evidence indicates that ELC phosphorylation is deleterious and occurs under conditions of cardiac stress, it is perhaps not surprising that phosphorylated forms of ELC_a and ELC_v were not detected by top-down high-resolution MS-based profiling of healthy swine atrial and ventricular tissue. Nevertheless, we cannot rule out the possibility that a small sub-population of phosphorylated ELC may exist in the atrial or ventricular myocardium of healthy swine but was below the detection limit (less than approximately 0.1 and 0.5% of the total ELC_a and ELC_v populations, respectively) (**Figs. 3.11**, **3.20**).

3.4.4 Localization of regulatory light chain phosphorylation sites in the swine heart

Here, we show, for the first time, that Ser22 is the sole site of basal phosphorylation in $_pRLC_a$ in the swine heart (**Fig. 3.10**). In accordance with observations from previous studies in humans [276], a bis-phosphorylated form of RLC_a was also observed in swine atrial myocardium (**Fig. 3.5**); however, the low abundance of this species did not permit MS/MS analysis and the localization of the second site of phosphorylation in swine $_{pp}RLC_a$. In addition we also definitively show that the RLC_v is basally mono-phosphorylated at a single site, Ser14, in the ventricles of the

swine heart (**Fig. 3.19**), which is in good agreement with the findings of our previous study [244]. Although $_{pp}RLC_v$ has been observed in mice [296], this species was not detected in the swine heart (**Fig. 3.16**), likely as a consequence of the replacement of Ser13 (mouse) with a non-phosphorylatable Asn residue in swine RLC_v (**Fig. 3.18**) [244]. It is noteworthy that an Asn residue is also present at position 13 in human RLC_v (**Fig. 3.18**), which suggests that RLC_v from human is also basally mono-phosphorylated and further supports the use of large animals to model human cardiovascular diseases [243, 277].

Until recently, the identity of the kinase responsible for RLC phosphorylation in the heart was unclear. While both the smooth and skeletal muscle isoforms of MLCK are expressed in the heart, previous work suggested that these isoforms do not play a significant role in RLC phosphorylation in the heart [78, 297]. In 2008, Chan *et al.* discovered a previously unidentified cardiac-specific isoform of MLCK, encoded by the *Mylk3* gene, and expressed in both the ventricles and atria of the mouse heart [298]. Subsequent work by Ding *et al.* showed that phosphorylation of RLC in the heart is predominantly mediated by cardiac MLCK [75], although the potential involvement of other kinases, such as ZIPK [299], cannot be ruled out.

3.4.5 High-resolution top-down MS/MS for myofilament protein isoform characterization.

In this study, we utilized high-resolution top-down targeted proteomics to comprehensively characterize the sequences and N-terminal modifications of cardiac ELC and RLC isoforms in the human and swine heart, as well as the phosphorylation sites in the swine proteins. In general, high-resolution MS/MS has significant advantages for protein characterization, including

increased confidence in protein and PTM identification as a consequence of enhanced mass accuracy [270]. Here, top-down high-resolution MS enabled the comprehensive sequence characterization of myosin light chain isoforms from both human and swine hearts with high sequence coverage and mass accuracy. Furthermore, high mass accuracy allowed for determination of N-terminal modifications in myosin light chain isoforms in the heart, including the assignment of N^{α}-acetylation versus N^{α}-tri-methylation—two modifications differing in mass by only ~36 mDa (**Fig. 3.24**). We show that ELC_v and RLC_v from human and swine are N^{α}-tri-methylated (**Figs. 3.16-3.17**, **3.20**, **3.23**), which is in good agreement with previous studies [275]. Additionally, for the first time, we show that human and swine ELC_a is also methylated at its N-terminus, whereas RLC_a is N^{α}-acetylated (**Figs. 3.5-3.6**, **3.11-3.12**). Although the significance of N^{α}-acetylation versus N^{α}-tri-methylation in RLC remains unclear, these results showcase the great potential of top-down high-resolution MS/MS for PTM identification.

The use of ECD allowed unambiguous localization of the basal phosphorylation sites in swine $_{p}RLC_v$ (Ser14) and $_{p}RLC_a$ (Ser22) (**Figs. 3.10**, **3.19**). It is well-known that dissociation with ECD preserves labile PTMs (e.g., phosphorylation), thereby allowing for their localization [197, 199, 200, 207]. This represents a significant advantage of electron-based dissociation methods over energetic dissociation methods, such as CID. For un-modified proteins or those with stable PTMs (e.g. acetylation), fragmentation using CID results in the cleavage of CO-NH bonds in the protein backbone, producing *b* and *y* fragment ions; however, for phosphorylated proteins, dissociation with CID leads to the preferential cleavage of the *O*-phosphoester bond, resulting in the neutral loss of phosphoric acid (H_3PO_4, 98 Da) or metaphosphoric acid (HPO_3, 80 Da), and precluding localization of the phosphorylated site [90].

Also of note is the advantage conferred by top-down MS/MS utilizing a combination of ECD and CID for comprehensive protein characterization. Studies have demonstrated that peptide/protein fragmentation by ECD is more evenly distributed along the protein backbone and, thus, tends to produce higher sequence coverage than that achieved with CID alone [207, 300]. Nevertheless, one drawback of ECD is that fragmentation N-terminal to Pro does not occur due to the cyclic structure of this amino acid and the fact that only a single bond cleavage event occurs upon electron capture [207]. Therefore, CID is a good complement to ECD as cleavage N-terminal to Pro is highly favorable for CID [301]. Here, we utilized top-down MS/MS with a combination of ECD and CID to characterize the sequences of ELC_v and ELC_a, which both contain Pro-rich N-terminal extensions that bind to actin and are important for cardiac contractile function [32, 278]. Such Pro-rich sequence extensions would traditionally pose a challenge for sequencing using either ECD or CID alone; however, as demonstrated here, top-down MS/MS employing a combination of ECD and CID enabled sequencing of ELC isoforms from the swine heart with high sequence coverage (approximately 95% and 90% sequence coverage for ELC_a and ELC_v, respectively), including extensive cleavage in the Pro-rich N-termini of these proteins. These results highlight the benefit of a top-down MS/MS strategy employing a combination of ECD and CID for comprehensive protein characterization, especially for proteins with Pro-rich stretches.

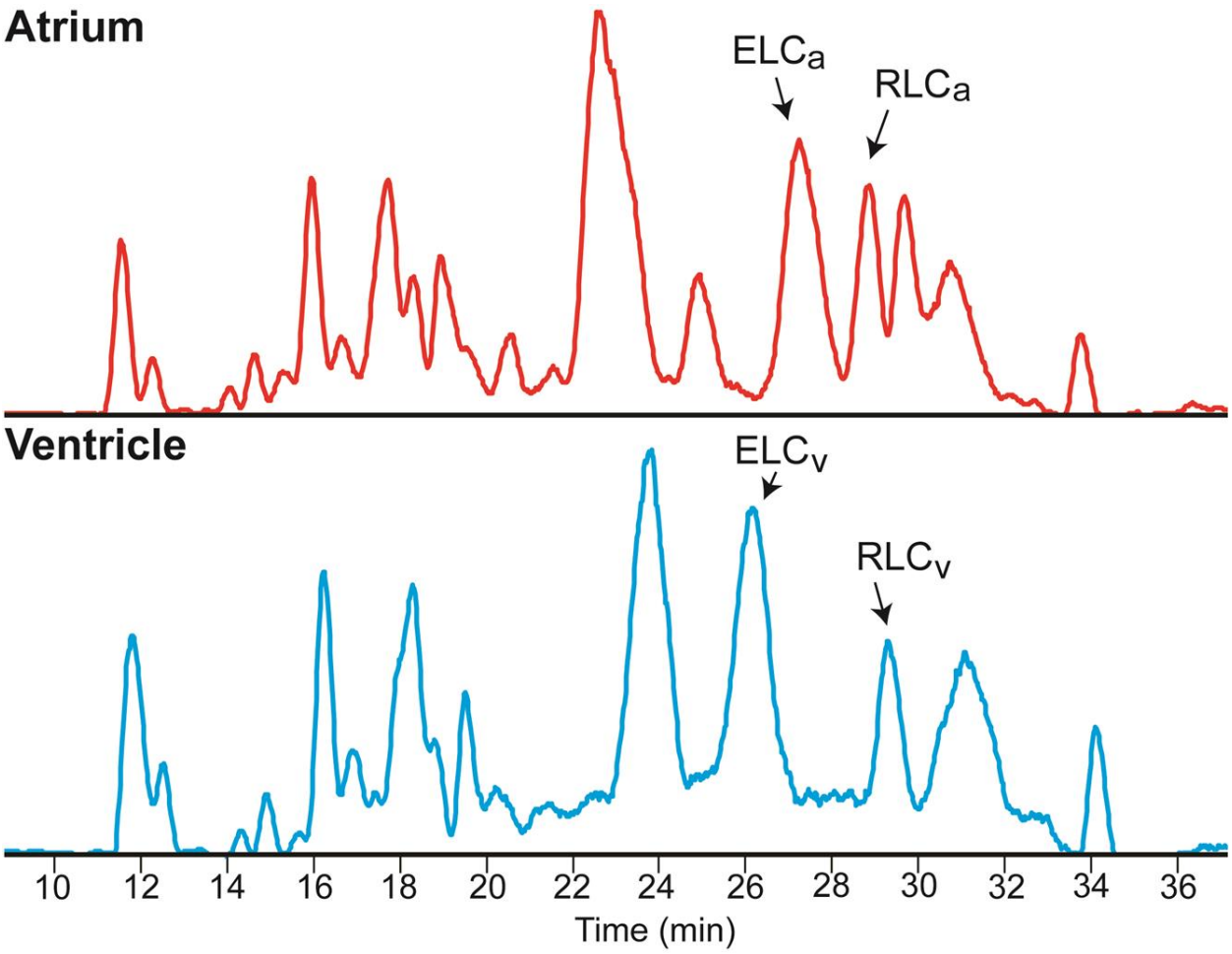

Fig. 3.1. Chromatograms showing 1D reverse phase LC separation of myofilament sub-proteomes extracted from the atrial (top) and ventricular (bottom) tissues from swine. LC peaks corresponding to myosin light chain isoforms are indicated.

Table 3.1. Information for sequences of cardiac myosin light chain isoforms utilized in this study. All sequences are from the UniProtKB/Swiss-Prot database.

Protein	Gene	Species	UniProtKB/Swiss-Prot Accession Number
RLC$_a$	*MYL7*	*Homo sapiens* (Human)	Q01449
		Sus scrofa (Swine)	F1SSF9*
		Mus musculus (Mouse)	Q9QVP4
ELC$_a$	*MYL4*	*Homo sapiens*	P12829
		Sus scrofa	F1RRT2*
		Rattus norvegicus (Rat)	P17209
		Mus musculus	P09541
RLC$_v$	*MYL2*	*Homo sapiens*	P10916
		Sus scrofa	Q8MHY0
		Rattus norvegicus	P08733
		Mus musculus	P51667
		Bos taurus (Bovine)	Q3SZE5
		Oryctolagus cuniculus (Rabbit)	Q7M2V4
ELC$_v$	*MYL3*	*Homo sapiens*	P08590
		Sus scrofa	F1SNW4
		Rattus norvegicus	P16409
		Mus musculus	P09542
		Bos taurus	P85100

*Note that the sequences corrected in this manuscript have replaced the previous incorrect sequences in the database. Direct comparison of the previous incorrect sequences and the correct sequences determined herein can be found in **Fig. 3.9** and **Fig. 3.15**.

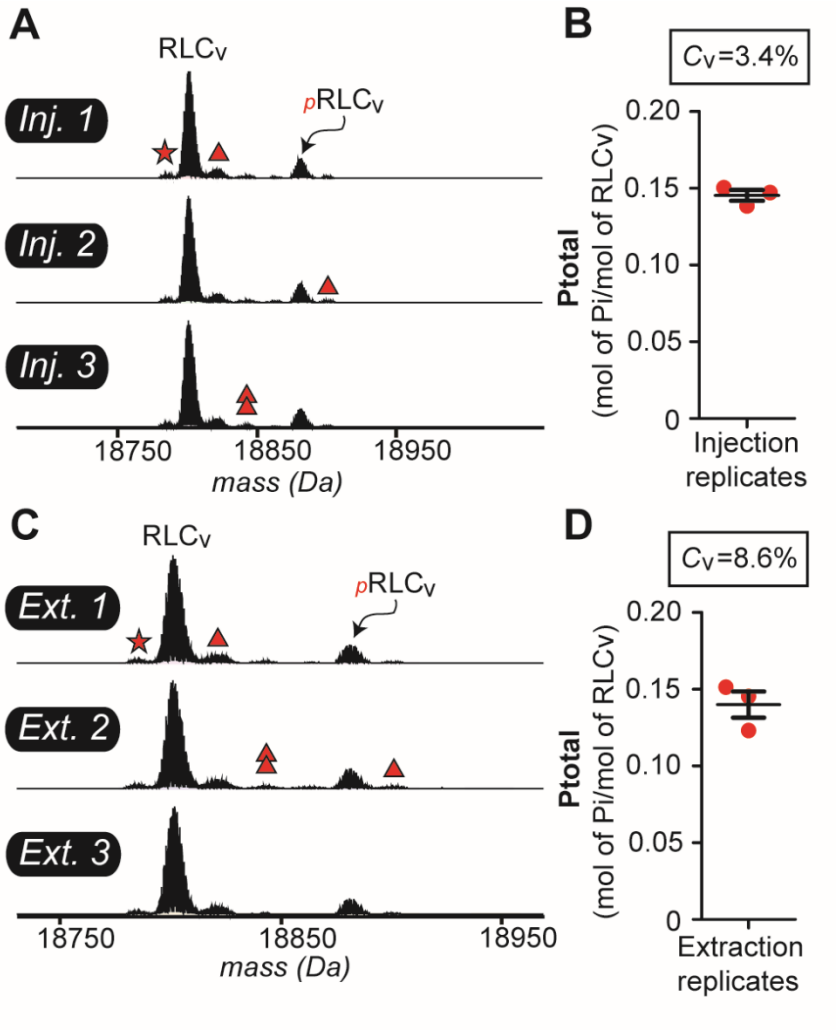

Fig. 3.2. Reproducibility of top-down high-resolution MS-based profiling of RLC phosphorylation in cardiac myocardium. (A) Alignment of mass spectra from three replicate injections of a single protein extract prepared from swine ventricular myocardium. (B) Quantification of RLC phosphorylation (mol of Pi/mol of RLC_v) across injection replicates yielded highly similar values with a coefficient of variation value of 3.4%. (C) Alignment of mass spectra from three replicate extractions from the ventricular free wall of a single swine. (D) Quantification of RLC phosphorylation (mol of Pi/mol of RLC_v) across extraction replicates yielded similar values with a coefficient of variation value of 8.6%. Star, triangle, and double triangle represent

RLC with NH_3 loss and RLC associated non-covalently with one or two sodium atoms, respectively.

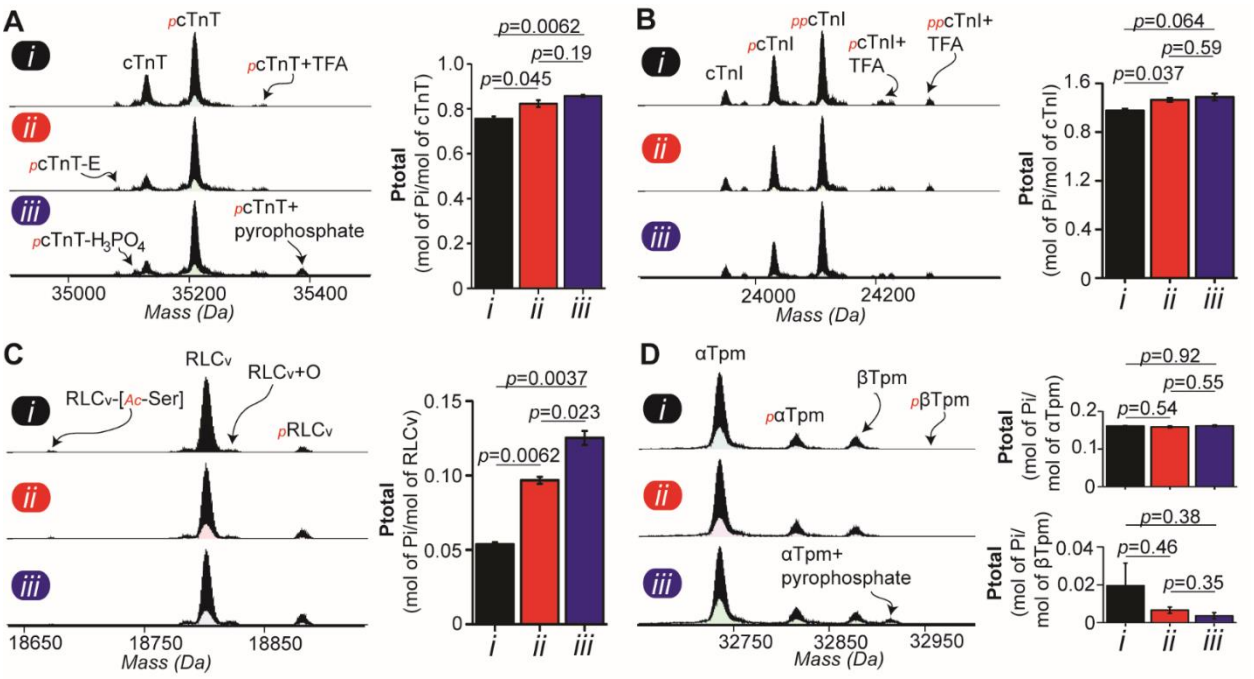

Fig. 3.3. Test of the effect of increasing phosphatase inhibitor concentrations on the phosphorylation status of different myofilament proteins. (A) Representative mass spectra and graph showing measured phosphorylation (mol of Pi/mol of protein) for cTnT from samples prepared with buffer containing: i) no Ser/Thr phosphatase inhibitors; ii) the recommended 50 mM NaF [271, 272]; or iii) 100 mM NaF, 10 mM sodium pyrophosphate, and 100 mM β-glycerophosphate. (B) Representative mass spectra and graph showing measured phosphorylation (mol of Pi/mol of protein) for cTnI. (C) Representative mass spectra and graph showing measured phosphorylation (mol of Pi/mol of protein) for RLC_v. (D) Representative mass spectra and graph showing measured phosphorylation (mol of Pi/mol of protein) for Tpm isoforms. Conditions in B, C, and D are the same as those detailed in A. Statistical analysis was performed using unpaired two-tailed *t*-test.

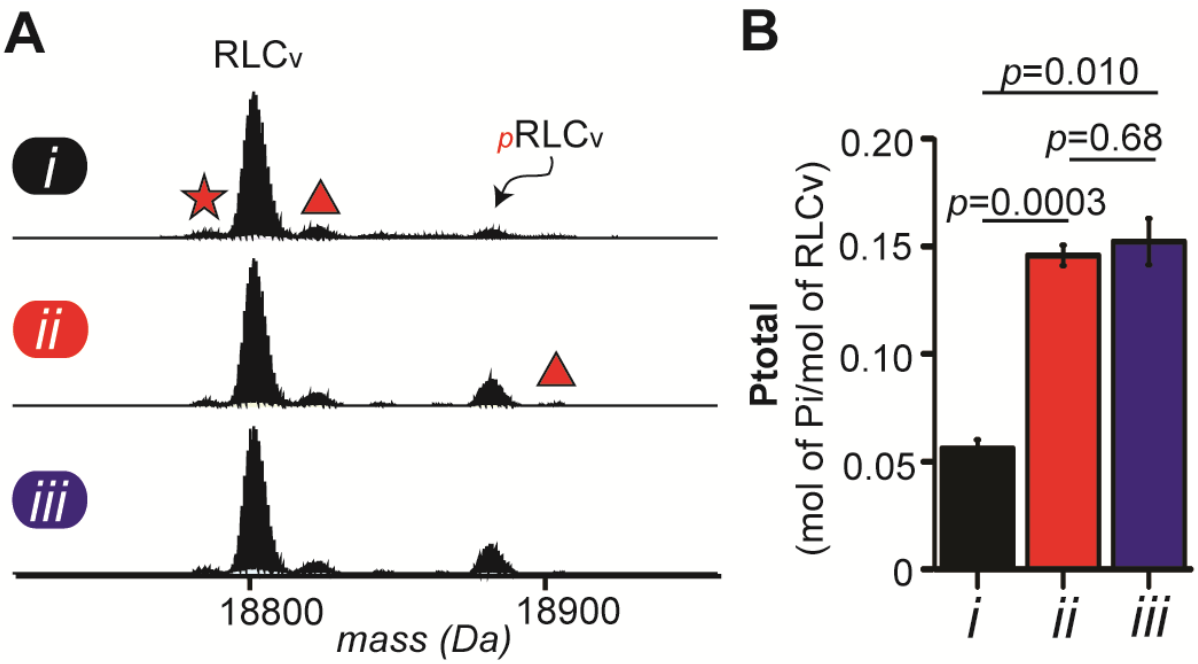

Fig. 3.4. Conditions of maximal inhibition of phosphatase activity towards the RLC. (A) Representative mass spectra for RLC_v from samples prepared with buffer containing: i) no Ser/Thr phosphatase inhibitors; ii) 500 mM NaF, 5 mM sodium pyrophosphate, and 100 mM β-glycerophosphate; or iii) 600 mM NaF, 5 mM sodium pyrophosphate, and 100 mM β-glycerophosphate. (B) Graph showing measured RLC_v phosphorylation (mol of Pi/mol of RLC_v) under different conditions (as described in A). Statistical analysis was performed using unpaired two-tailed *t*-test.

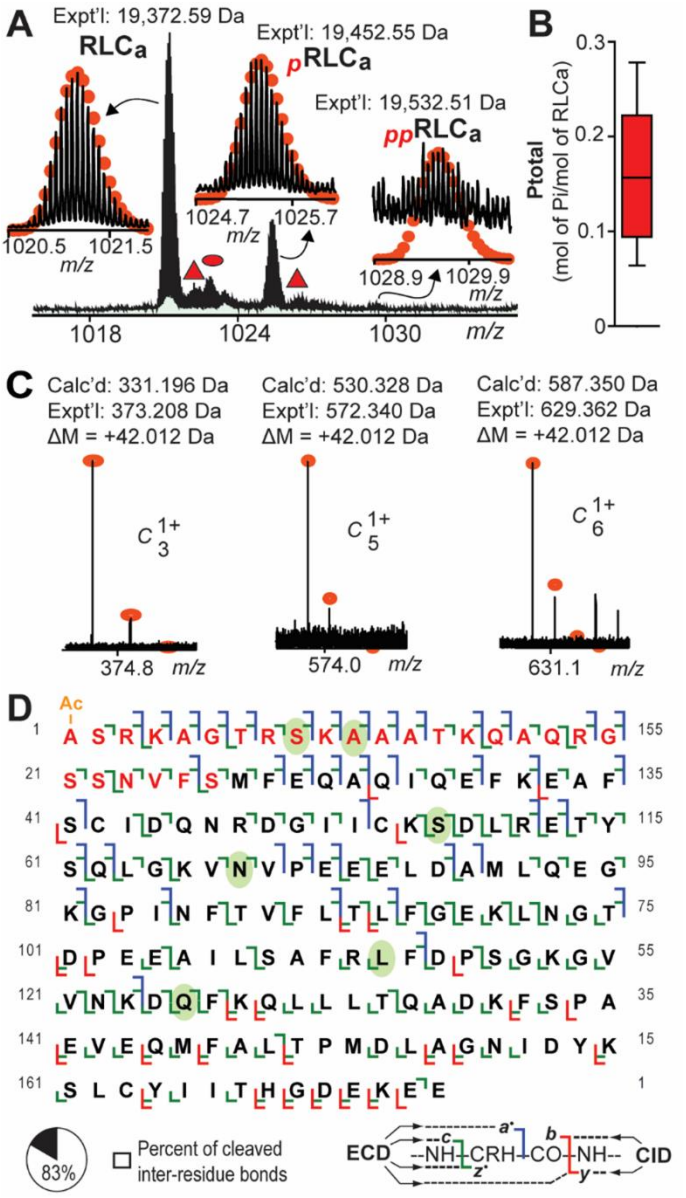

Fig. 3.5. Top-down MS analysis of swine RLC$_a$. (A) Zoomed-in mass spectrum showing detected RLC$_a$ species in extracts prepared from swine atrial myocardium. Triangle and oval represent RLC$_a$ associated non-covalently with sodium and potassium, respectively. (B) Graph showing MS-based quantification of swine RLC$_a$ phosphorylation, which had a mean value of 0.16 ± 0.03 mol of Pi/mol of RLC (n=5). (C) N-terminal fragment ions showing approximate 42.010 Da mass increase compared to the calculated masses for the corresponding un-modified fragment ions, indicating N-terminal acetylation of swine RLC$_a$. (D) Sequence table showing bond

cleavages for RLC_a (~83% of all inter-residue bonds). Residues in red are amino acids not present in the previous incorrect swine RLC_a sequence in the UniProtKB/Swiss-Prot database. Ovals indicate amino acids differing between swine and human RLC_a. "Ac-" denotes acetylation. "$_p$" and "$_{pp}$" indicate mono- and bis-phosphorylated protein forms, respectively.

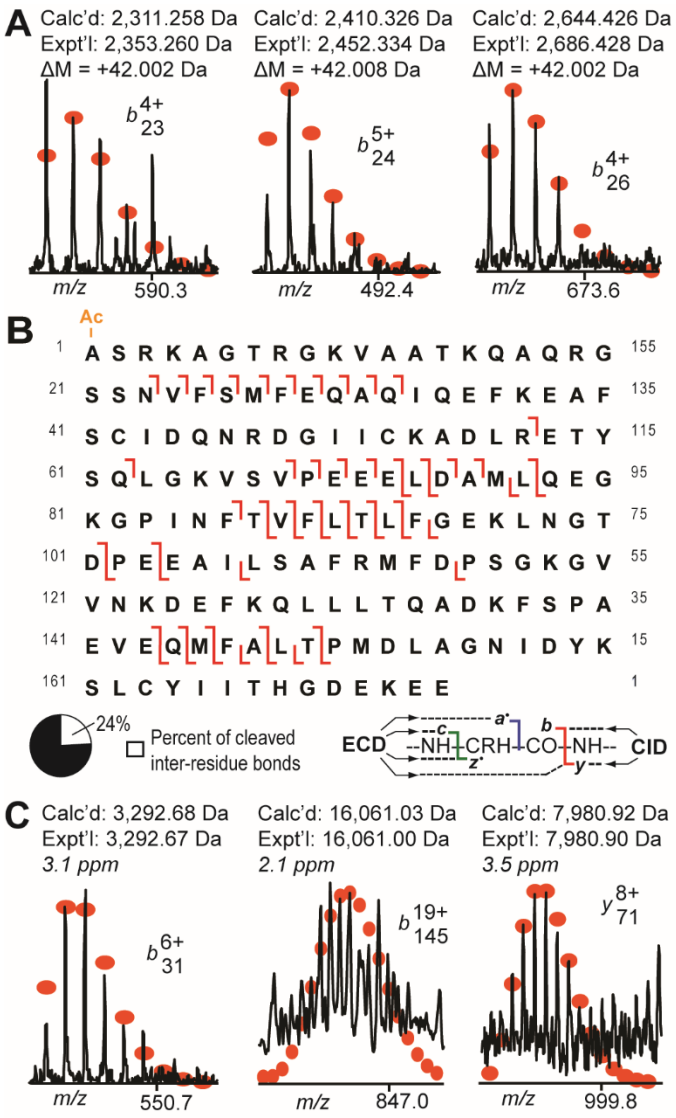

Fig. 3.6. Sequence characterization of human RLC$_a$. (A) N-terminal fragment ions showing approximate 42.010 Da mass increase compared to the calculated masses for the corresponding un-modified fragment ions, indicating N-terminal acetylation of human RLC$_a$. (B) Sequence table showing bond cleavages for RLC$_a$ (~24% of all inter-residue bonds). (C) Representative fragment ions from tandem mass spectra generated by fragmentation of human RLC$_a$.

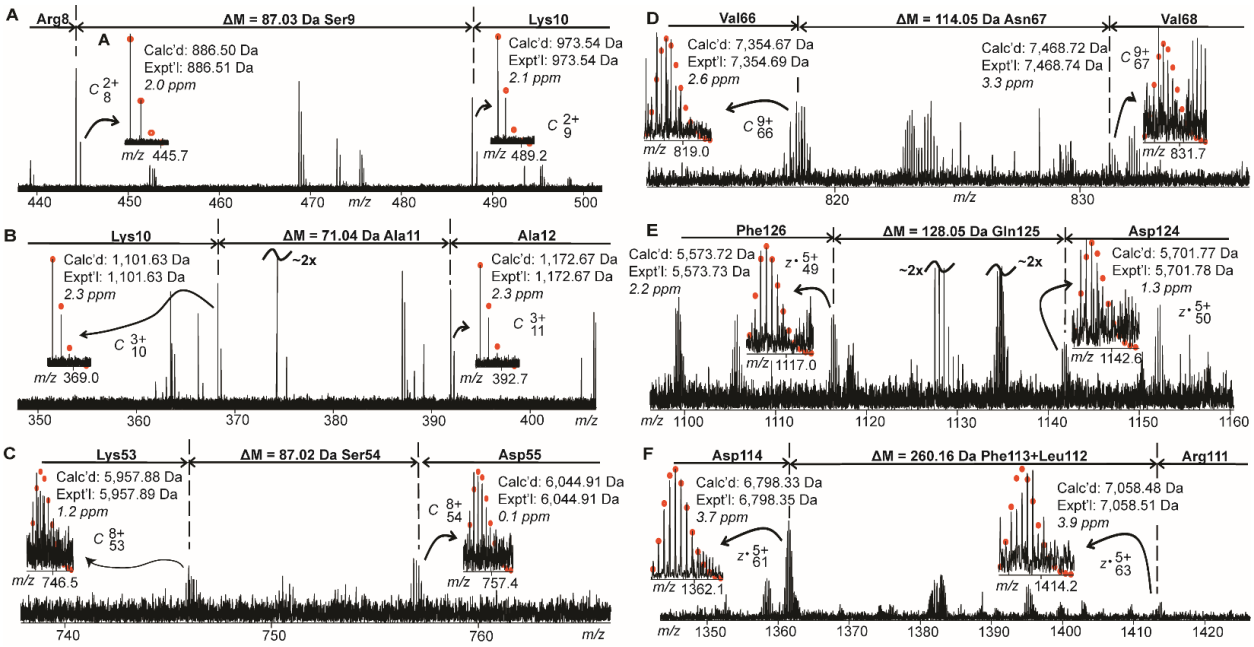

Fig. 3.7. Sequence characterization of swine RLC$_a$. (A) Zoomed-in tandem mass spectrum showing 87.03 Da mass difference between c_8 and c_9 ions, which denotes the presence of a Ser residue in position 9 of swine RLC$_a$. (B) Zoomed-in tandem mass spectrum showing 71.04 Da mass difference between c_{10} and c_{11}, which denotes the presence of an Ala residue in position 11 of swine RLC$_a$. (C) Zoomed-in tandem mass spectrum showing 87.02 Da mass difference between c_{53} and c_{54}, which indicates the presence of a Ser residue in position 54 of swine RLC$_a$. (D) Zoomed-in tandem mass spectrum showing 114.05 Da mass difference between c_{66} and c_{67}, which indicates the presence of an Asn residue in position 67 of swine RLC$_a$. (E) Zoomed-in tandem mass spectrum showing 128.05 Da mass difference between $z^{\cdot}_{49}$ and $z^{\cdot}_{50}$, which indicates the presence of a Gln residue in position 125 of swine RLC$_a$. (F) Zoomed-in tandem mass spectrum showing 260.16 Da mass difference between $z^{\cdot}_{61}$ and $z^{\cdot}_{63}$, which indicates the presence of Phe and Leu residues in positions 112 and 113 of swine RLC$_a$. Circles represent the theoretical isotopic abundance distribution of the isotopomer peaks corresponding to the assigned mass. "~" denotes peak truncation.

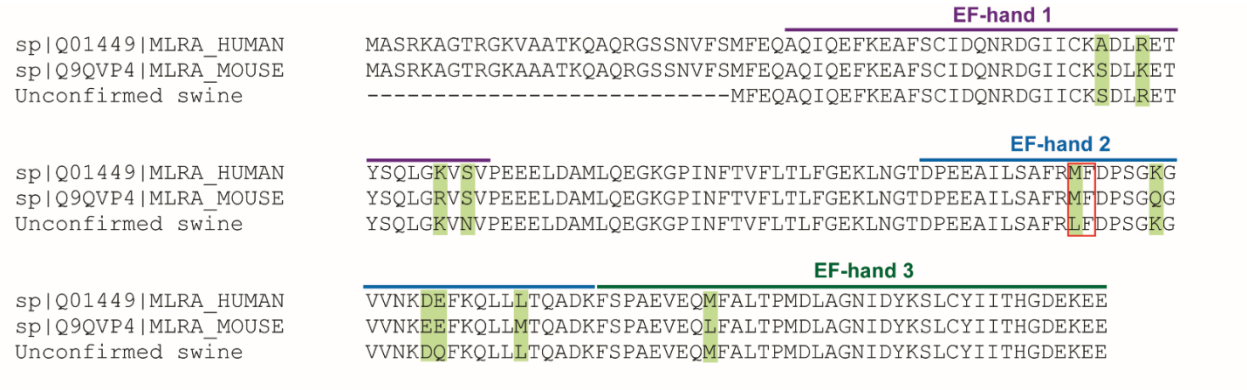

Fig. 3.8. Sequence alignment for RLC_a from different species. Sequence denoted "Unconfirmed swine" represents the previous incorrect sequence for swine RLC_a in the UniProtKB/Swiss-Prot database. Locations of EF-hand domains, amino acid differences (shaded boxes), and amino acid residues 112-113 (open box) are indicated.

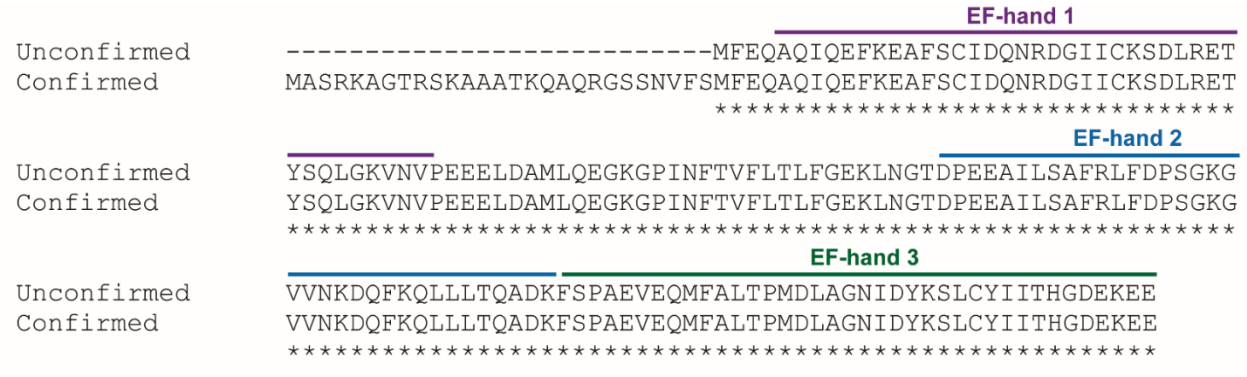

Fig. 3.9. Sequence alignment of confirmed and unconfirmed sequences for swine RLC$_a$. Unconfirmed and confirmed sequences are the previous incorrect sequence for swine RLC$_a$ in the UniProtKB/Swiss-Prot database and the sequence for swine RLC$_a$ confirmed using top-down MS/MS in this study, respectively. Locations of EF-hand domains are indicated.

Table 3.2. Comparison of myosin light chain isoform sequence similarity between species. Sequences are from **Table 3.1**.

Protein	Gene	Species	Sequence similarity (%)
RLC$_a$	***MYL7***	***Sus scrofa***	
		vs. *Homo sapiens*	96.6
		vs. *Mus musculus*	94.3
		Homo sapiens	
		vs. *Mus musculus*	95.4
ELC$_a$	***MYL4***	***Sus scrofa***	
		vs. *Homo sapiens*	95.9
		vs. *Mus musculus*	89.3
		vs. *Rattus norvegicus*	89.8
		Homo sapiens	
		vs. *Mus musculus*	89.8
		vs. *Rattus norvegicus*	89.8
RLC$_v$	***MYL2***	***Sus scrofa***	
		vs. *Homo sapiens*	96.4
		vs. *Mus musculus*	94.6
		vs. *Rattus norvegicus*	95.2
		vs. *Bos taurus*	95.8
		vs. *Oryctolagus cuniculus*	97.0
		Homo sapiens	
		vs. *Mus musculus*	96.4
		vs. *Rattus norvegicus*	95.8
		vs. *Bos taurus*	95.2
		vs. *Oryctolagus cuniculus*	97.6
ELC$_v$	***MYL3***	***Sus scrofa***	
		vs. *Homo sapiens*	94.4
		vs. *Mus musculus*	93.1
		vs. *Rattus norvegicus*	95.0
		vs. *Bos taurus*	94.9
		Homo sapiens	
		vs. *Mus musculus*	91.7
		vs. *Rattus norvegicus*	93.5
		vs. *Bos taurus*	90.4

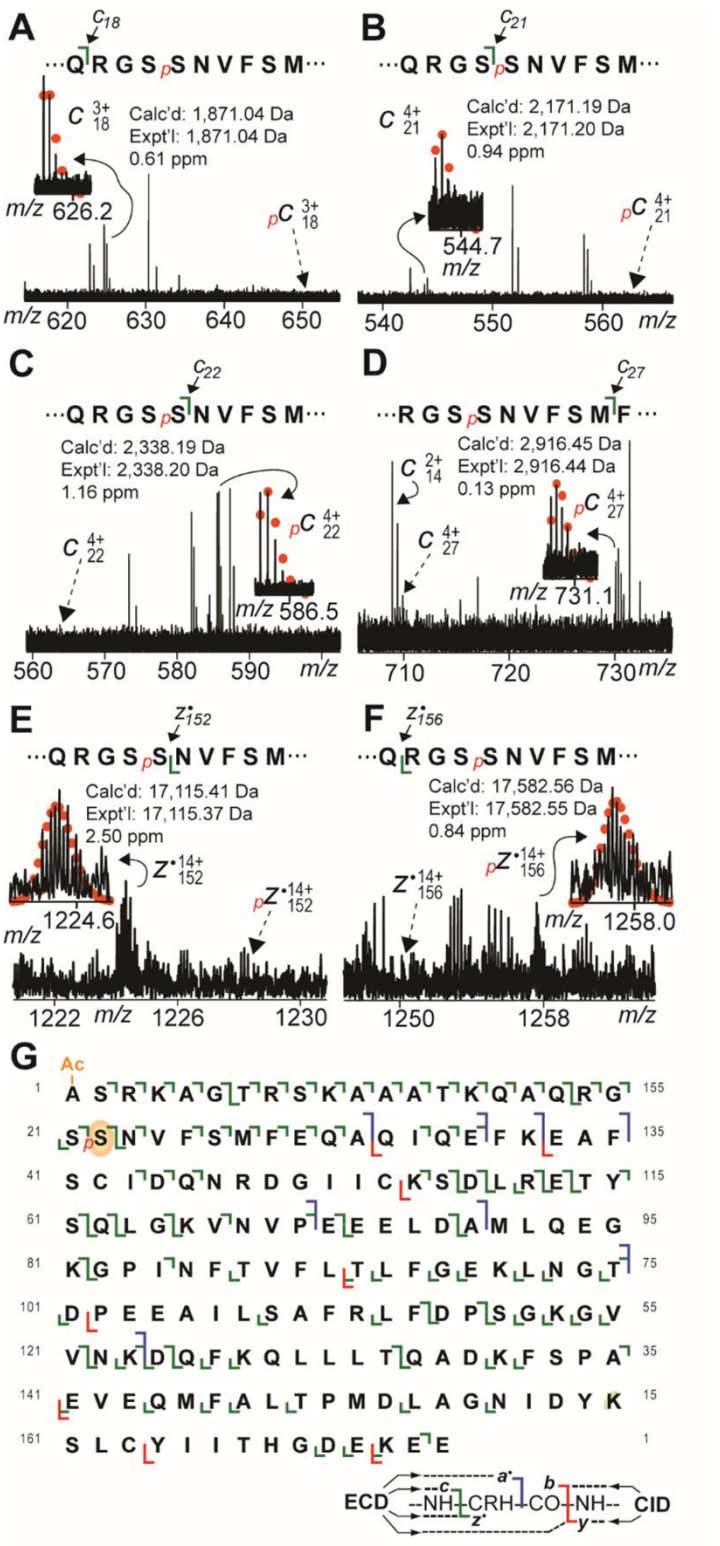

Fig. 3.10. Localization of the phosphorylation site in swine $_p$RLC$_a$ to Ser22 by top-down ECD MS/MS. (A) Zoomed-in tandem mass spectrum showing observation of un-phosphorylated c_{18}

ion without corresponding $_pc_{18}$ ion (expected position denoted by broken arrow). (B) Zoomed-in tandem mass spectrum showing observation of un-phosphorylated c_{21} ion without corresponding $_pc_{21}$ ion (expected position denoted by broken arrow). (C) Zoomed-in tandem mass spectrum showing observation of $_pc_{22}$ ion without corresponding un-phosphorylated c_{22} ion (expected position denoted by broken arrow). (D) Zoomed-in tandem mass spectrum showing observation of $_pc_{27}$ ion without corresponding un-phosphorylated c_{27} ion (expected position denoted by broken arrow). (E) Zoomed-in tandem mass spectrum showing observation of $z\cdot_{152}$ ion without corresponding $_pz\cdot_{152}$ ion (expected position denoted by broken arrow). (F) Zoomed-in tandem mass spectrum showing observation of $_pz\cdot_{156}$ without corresponding un-phosphorylated $z\cdot_{156}$ ion (expected position denoted by broken arrow). (G) Sequence table showing bond cleavages and site of phosphorylation in $_p$RLC$_a$. Oval indicates phosphorylated residue (Ser22) in swine $_p$RLC$_a$. "Ac-" denotes acetylation. "$_p$" indicates mono-phosphorylation.

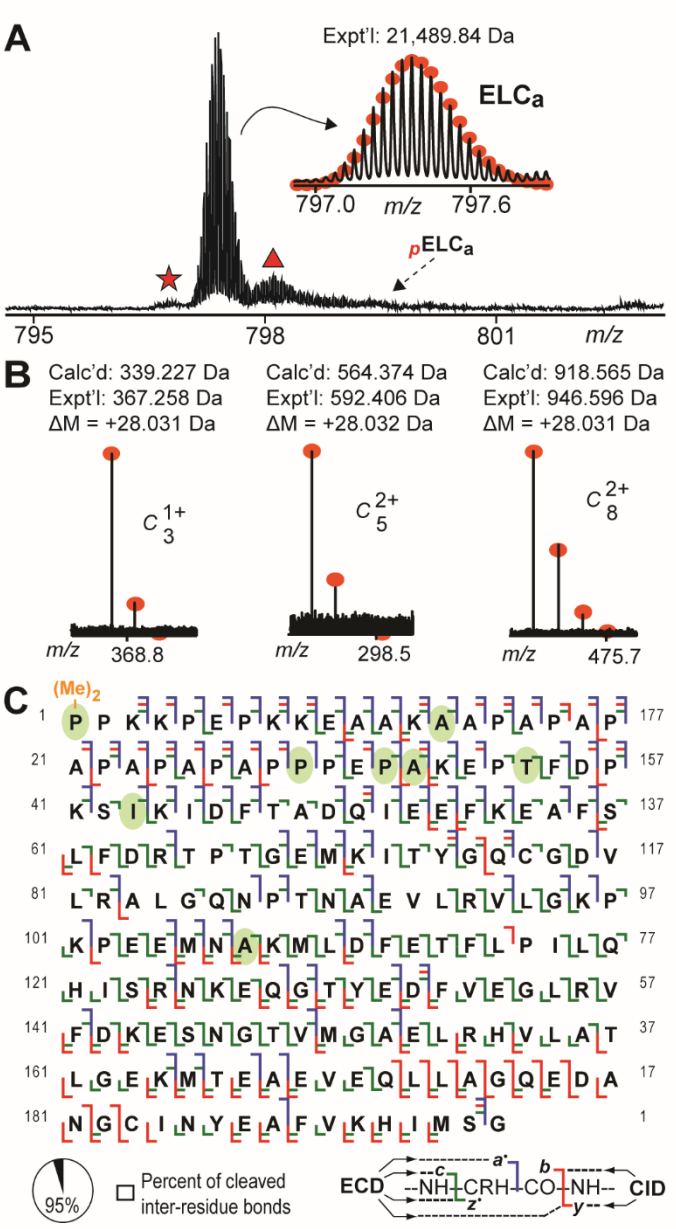

Fig. 3.11. Top-down MS and MS/MS analyses of swine ELC$_a$. (A) Zoomed-in mass spectrum showing detected ELC$_a$ protein species in extracts prepared from the atrial myocardium of swine. Broken arrow indicates expected position of un-observed $_p$ELC$_a$ species. Star and triangle mark peaks corresponding to ELC$_a$ with NH_3 loss and ELC$_a$ associated non-covalently with sodium. (B) N-terminal fragment ions showing approximate 28.031 Da mass increase compared to the calculated masses for the corresponding un-modified fragment ions, indicating N-terminal di-

methylation of swine ELC_a. (C) Sequence table for ELC_a showing bond cleavages (~95% of all inter-residue bonds). Ovals indicate amino acids differing between swine and human ELC_a. "$(Me)_2$-" denotes di-methylation. "$_p$" indicates mono-phosphorylation.

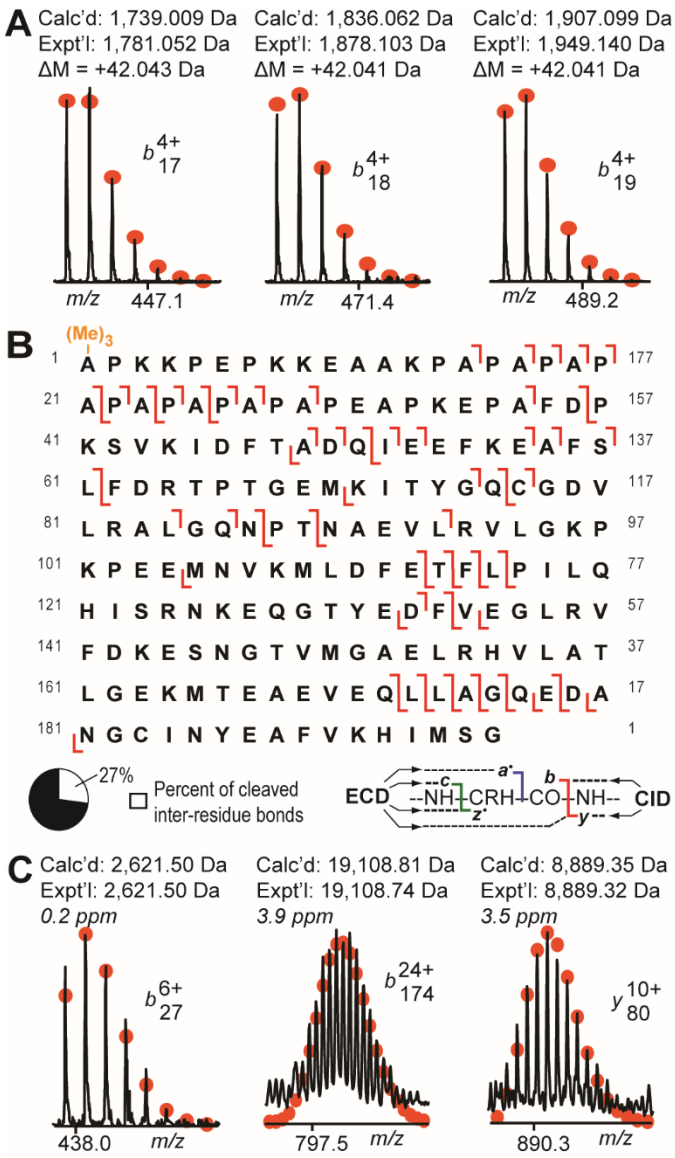

Fig. 3.12. Sequence characterization of human ELC$_a$. (A) N-terminal fragment ions showing approximate 42.046 Da mass increase compared to the calculated masses for the corresponding un-modified fragment ions, indicating N-terminal tri-methylation of human ELC$_a$. (B) Sequence table showing bond cleavages for ELC$_a$ (~27% of all inter-residue bonds). (C) Representative fragment ions from tandem mass spectra generated by fragmentation of human ELC$_a$.

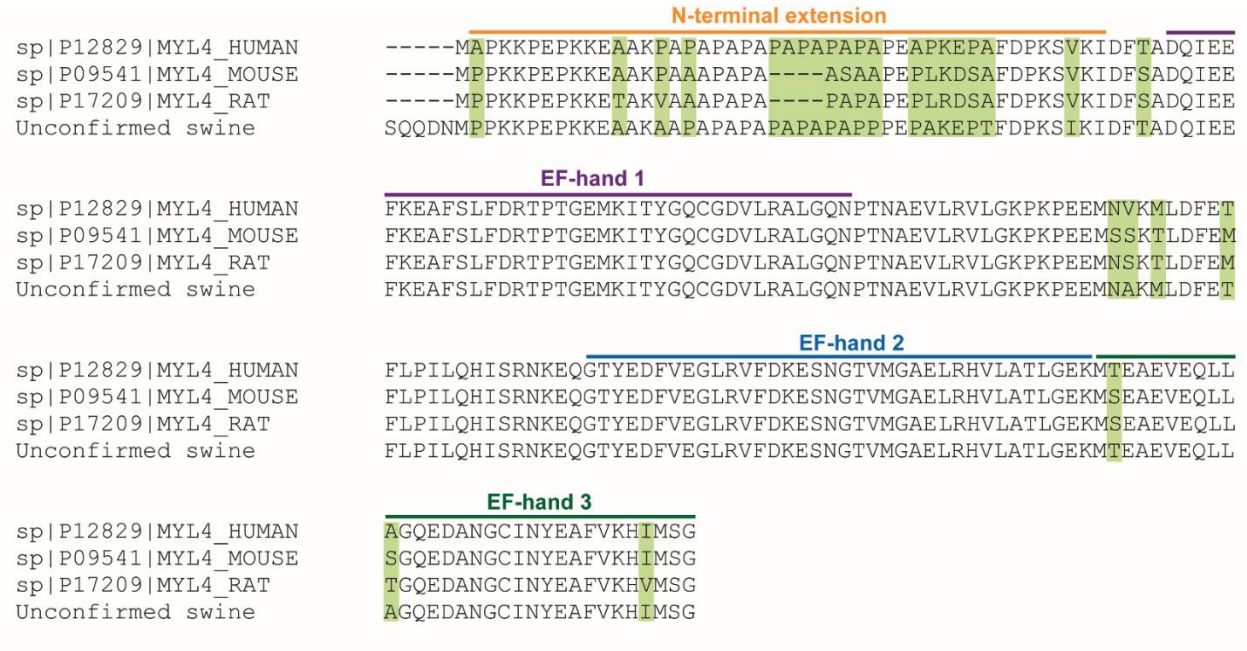

Fig. 3.13. Sequence alignment for ELC_a from different species. Sequence denoted "Unconfirmed swine" represents the previous incorrect sequence for swine ELC_a in the UniProtKB/Swiss-Prot database. Locations of N-terminal extension and EF-hand domains, as well as amino acid differences (boxes), are indicated.

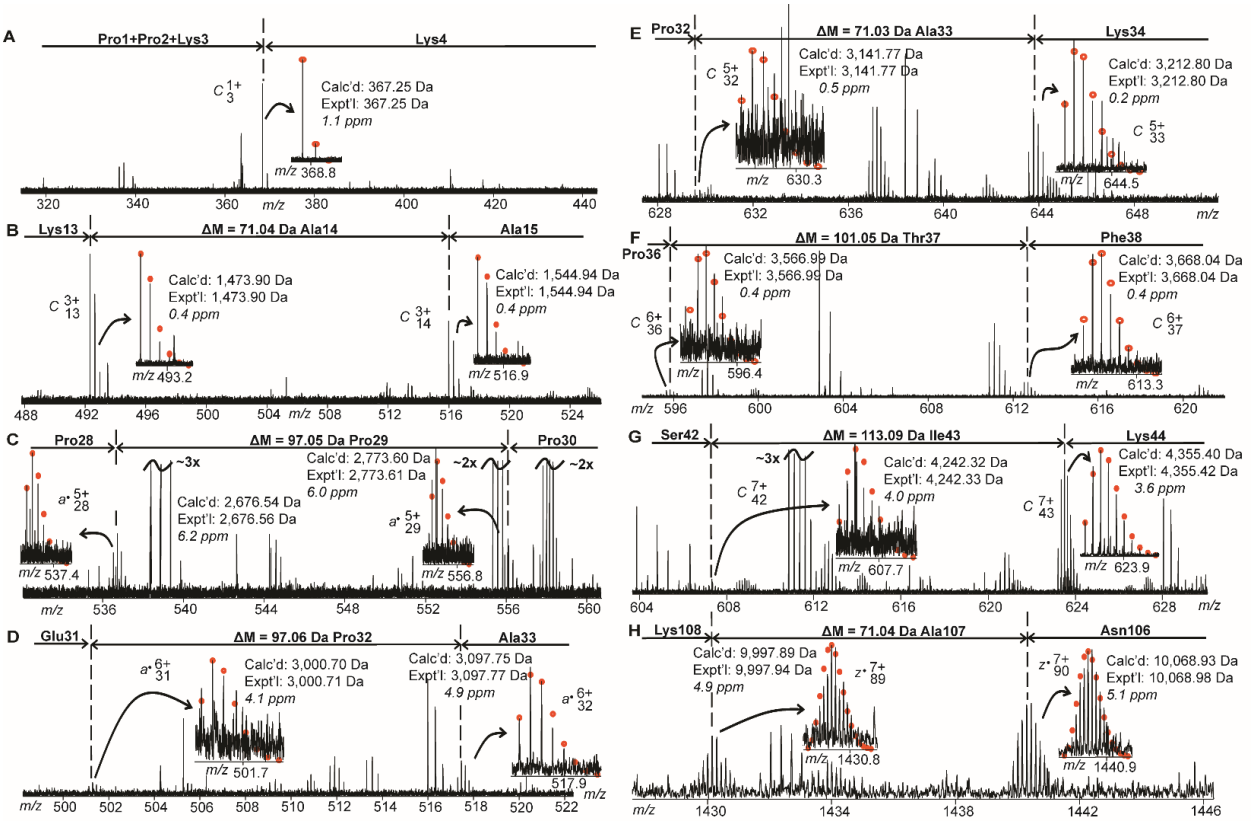

Fig. 3.14. Characterization of swine ELC$_a$. (A) Zoomed-in tandem mass spectrum showing mass of the smallest observed fragment ion (c_3), which matches well with a combination of two Pro residues and one Lys residue. (B) Zoomed-in tandem mass spectrum showing 71.04 Da mass difference between c_{13} and c_{14}, which denotes the presence of an Ala residue in position 14 of swine ELC$_a$. (C) Zoomed-in tandem mass spectrum showing 97.05 Da mass difference between $a^{\cdot}_{28}$ and $a^{\cdot}_{29}$, which indicates the presence of a Pro residue in position 29 of swine ELC$_a$. (D) Zoomed-in tandem mass spectrum showing 97.06 Da mass difference between $a^{\cdot}_{31}$ and $a^{\cdot}_{32}$, which indicates the presence of a Pro residue in position 32 of swine ELC$_a$. (E) Zoomed-in tandem mass spectrum showing 71.03 Da mass difference between c_{32} and c_{33}, which indicates the presence of an Ala residue in position 33 of swine ELC$_a$. (F) Zoomed-in tandem mass spectrum showing 101.05 Da mass difference between c_{36} and c_{37}, indicating the presence of a Thr residue in position 37 of swine ELC$_a$. (G) Zoomed-in tandem mass spectrum showing 113.09 Da mass difference

between c_{42} and c_{43}, which indicates the presence of an Ile residue in position 43 of swine ELC_a. (H) Zoomed-in tandem mass spectrum showing 71.04 Da mass difference between $z^{\cdot}_{89}$ and $z^{\cdot}_{90}$, which indicates the presence of an Ala residue in position 107 of swine ELC_a. Circles represent the theoretical isotopic abundance distribution of the isotopomer peaks corresponding to the assigned mass. "~" denotes peak truncation.

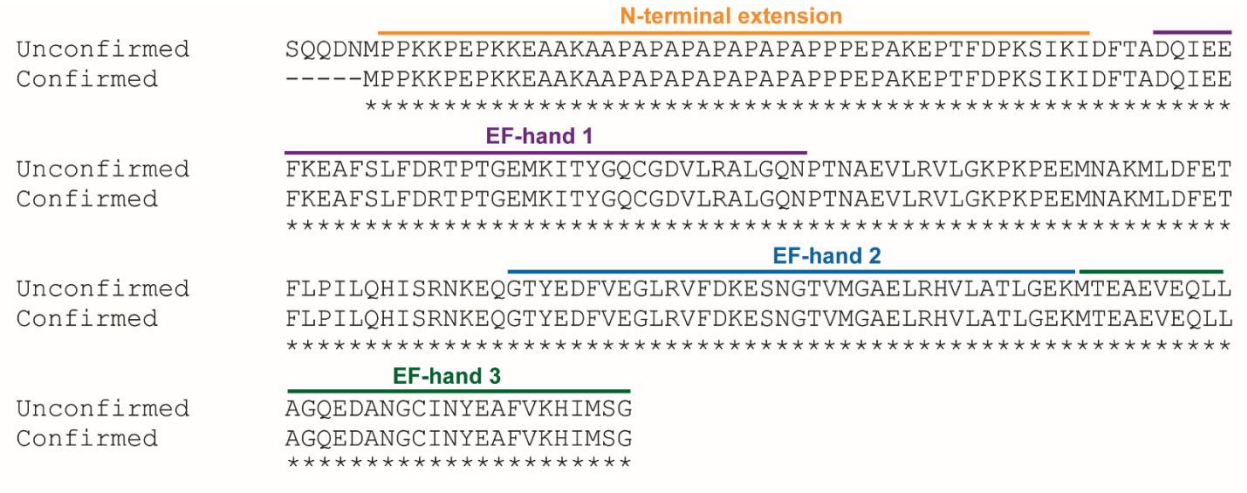

Fig. 3.15. Sequence alignment of confirmed and unconfirmed sequences for swine ELC_a. Unconfirmed and confirmed sequences are the previous incorrect sequence for swine ELC_a in the UniProtKB/Swiss-Prot database and the sequence for swine ELC_a confirmed using top-down MS/MS in this study, respectively. Locations of N-terminal extension and EF-hand domains are indicated.

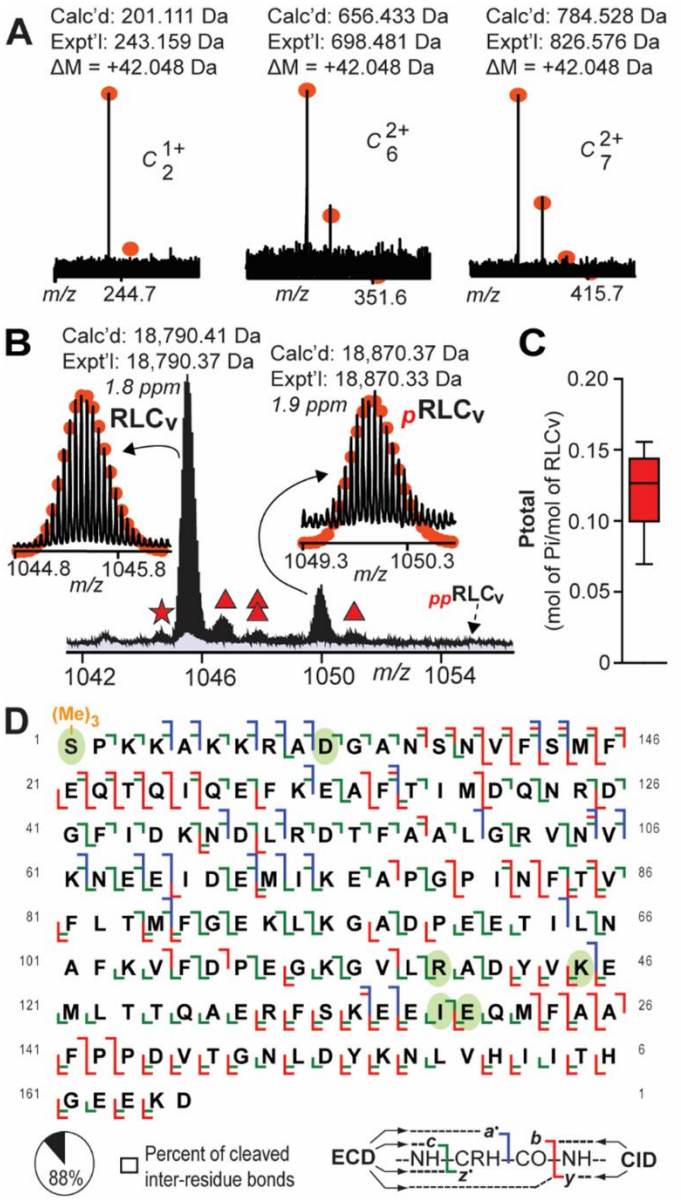

Fig. 3.16. Top-down MS and MS/MS analyses of swine RLC$_v$. (A) N-terminal fragment ions showing approximate 42.046 Da mass increase compared to the calculated masses for the corresponding un-modified fragment ions, indicating N-terminal tri-methylation of swine RLC$_v$. (B) Zoomed-in mass spectrum showing RLC$_v$ protein species in extracts prepared from swine ventricular myocardium. Broken arrow indicates expected position of un-observed $_{pp}$RLC$_v$ species. Star, triangle, and double triangle mark peaks corresponding to RLC$_v$ with NH_3 loss and RLC$_v$ associated non-covalently with one or two sodium atoms, respectively. (C) Graph showing

MS-based quantification of RLC_v phosphorylation in the swine ventricular myocardium, which had a mean value of 0.12 ± 0.01 mol of Pi/mol of RLC (n=6). (D) Sequence table for RLC_v showing bond cleavages (~88% of all inter-residue bonds). Ovals indicate amino acids differing between swine and human RLC_v. "$(Me)_3$-" denotes tri-methylation. "$_p$" and "$_{pp}$" indicate mono- and bis-phosphorylated protein forms, respectively.

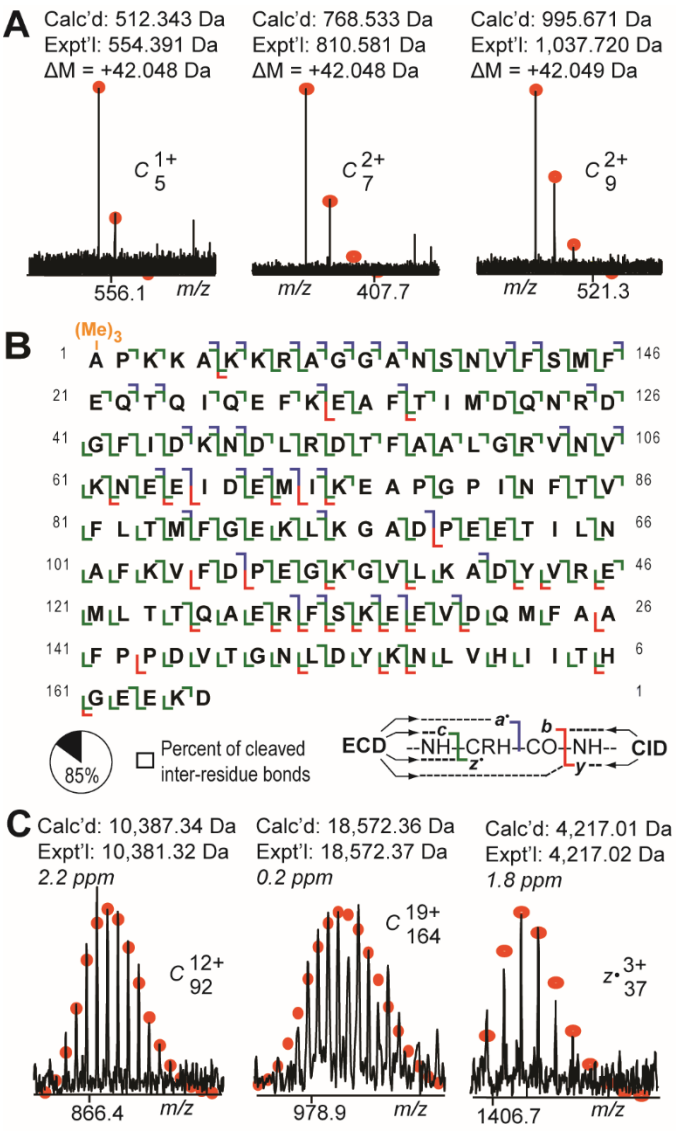

Fig. 3.17. Sequence characterization of human RLC$_v$. (A) N-terminal fragment ions showing approximate 42.046 Da mass increase compared to the calculated masses for the corresponding un-modified fragment ions, indicating N-terminal tri-methylation of human RLC$_v$. (B) Sequence table showing bond cleavages for RLC$_v$ (~85% of all inter-residue bonds). (C) Representative fragment ions from tandem mass spectra generated by fragmentation of human RLC$_v$.

Fig. 3.18. Sequence alignment for RLC$_v$ from different species. Locations of EF-hand domains, as well as amino acid differences (boxes), are indicated.

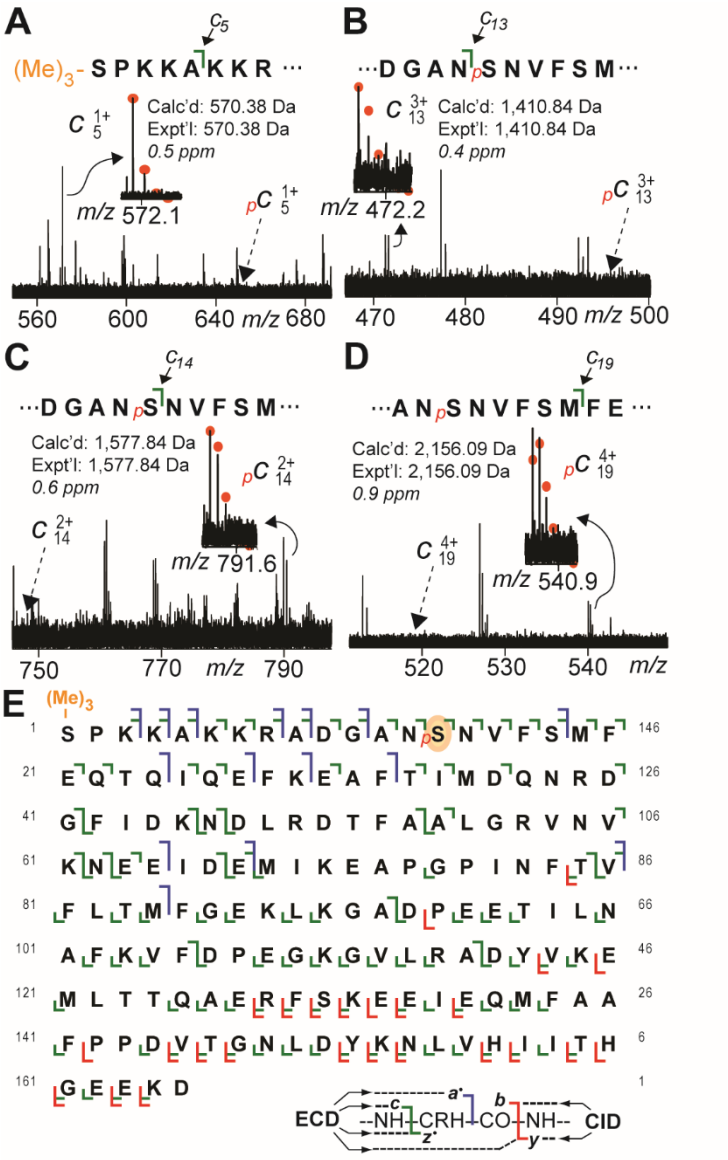

Fig. 3.19. Localization of the phosphorylation site in swine $_pRLC_v$ to Ser14 by top-down ECD MS/MS. (A) Zoomed-in tandem mass spectrum showing observation of un-phosphorylated c_5 ion without corresponding $_pc_5$ ion (expected position denoted by broken arrow). (B) Zoomed-in tandem mass spectrum showing observation of un-phosphorylated c_{13} ion without corresponding $_pc_{13}$ ion (expected position denoted by broken arrow). (C) Zoomed-in tandem mass spectrum showing observation of $_pc_{14}$ ion without corresponding un-phosphorylated c_{14} ion (expected position denoted by broken arrow). (D) Zoomed-in tandem mass spectrum showing observation

of $_{p}c_{19}$ ion without corresponding un-phosphorylated c_{19} ion (expected position denoted by broken arrow). (E) Sequence table showing bond cleavages and the site of phosphorylation in $_{p}RLC_{v}$. Oval indicates phosphorylated residue (Ser14) in swine RLC_{v}. "$(Me)_{3}$-" denotes tri-methylation. "$_{p}$" indicates mono-phosphorylation.

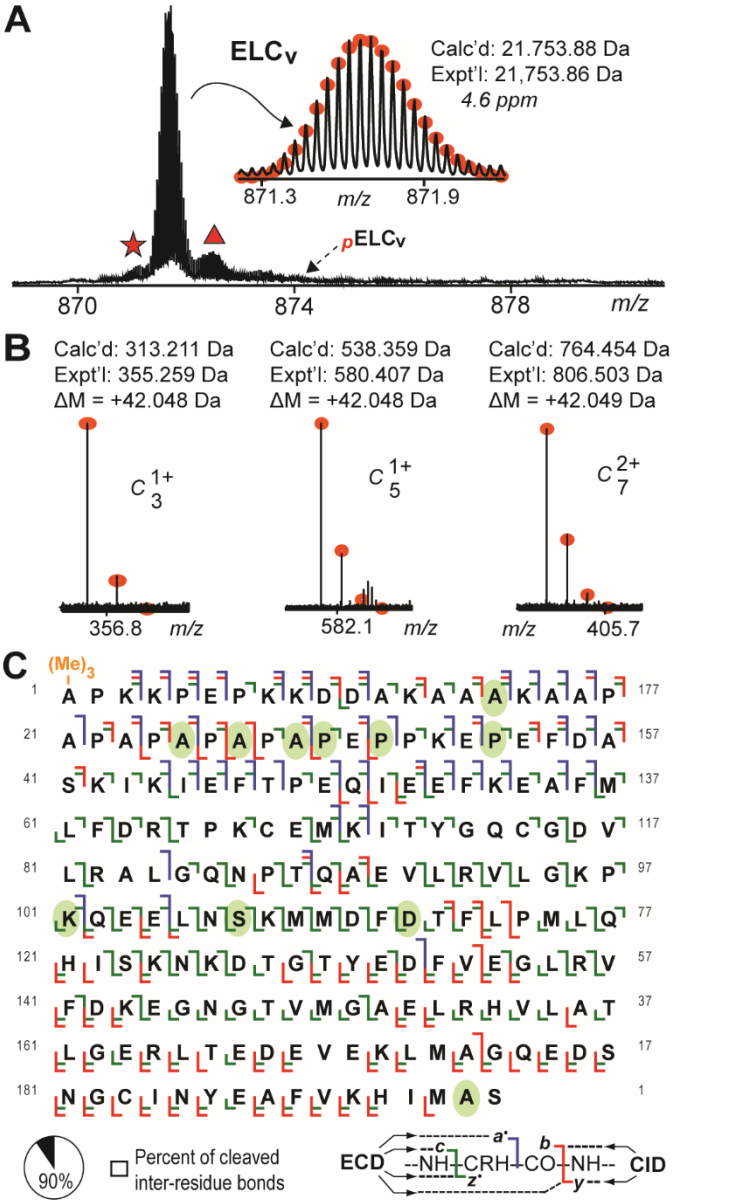

Fig. 3.20. Top-down MS and MS/MS analyses of swine ELC$_v$. (A) Zoomed-in mass spectrum showing swine ELC$_v$ protein species in extracts prepared from the ventricular myocardium of swine. Broken arrow indicates expected position of un-observed $_p$ELC$_v$ species. Star and triangle mark peaks corresponding to ELC$_v$ with NH_3 loss and ELC$_v$ associated non-covalently with sodium, respectively. (B) N-terminal fragment ions showing approximate 42.046 Da mass increase compared to the calculated masses for the corresponding un-modified fragment ions, indicating N-terminal tri-methylation of swine ELC$_v$. (C) Sequence table for ELC$_v$ showing bond

cleavages (~90% of all inter-residue bonds). Ovals indicate amino acids differing between swine and human ELC_v. "$(Me)_3$-" denotes tri-methylation. "$_p$" indicates mono-phosphorylation.

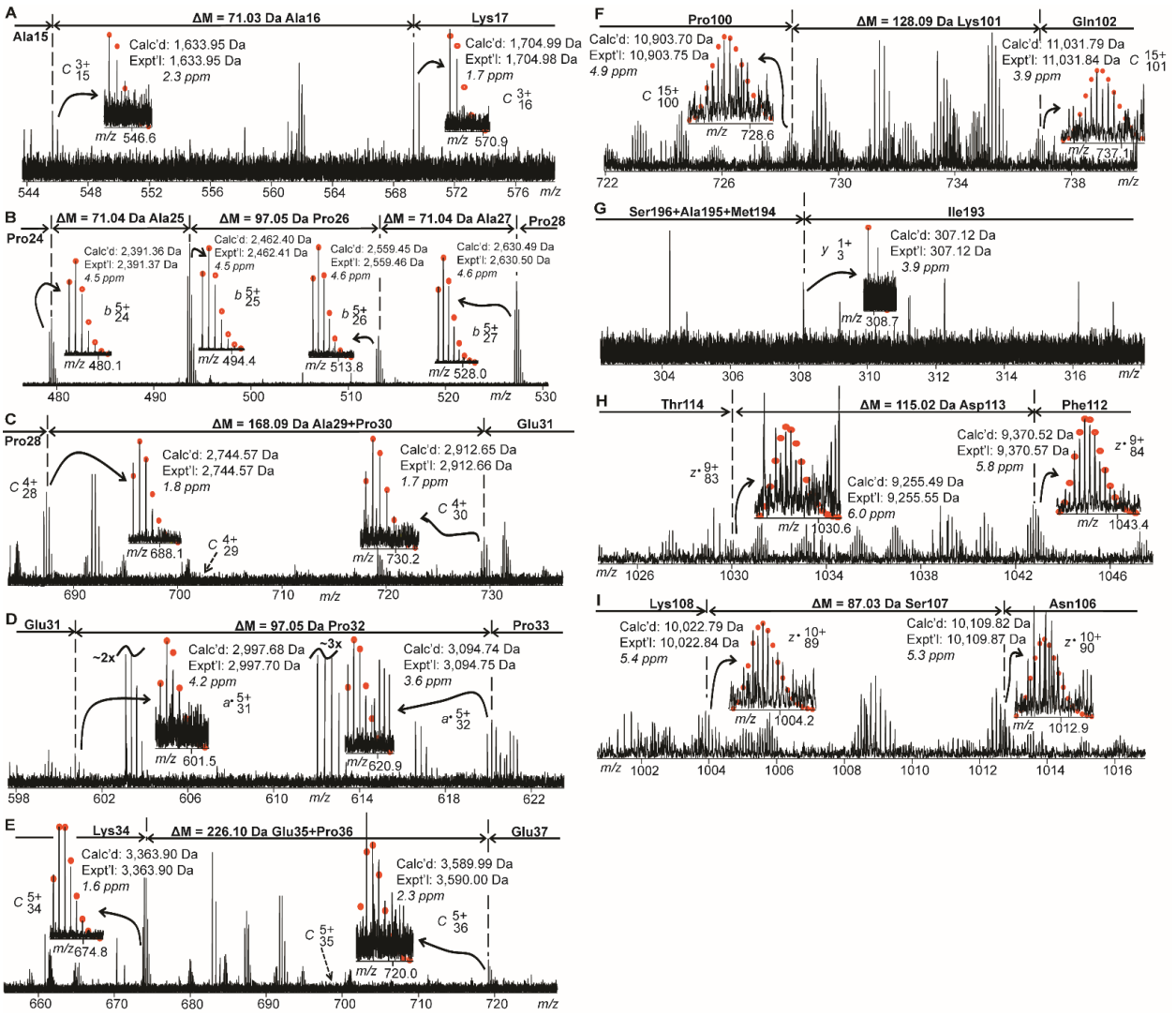

Fig. 3.21. Characterization of swine ELC$_V$. (A) Zoomed-in tandem mass spectrum showing 71.03 Da mass difference between c_{15} and c_{16}, which indicates the presence of an Ala residue in position 16 of swine ELC$_V$. (B) Zoomed-in tandem mass spectrum showing mass differences of 71.04 Da between b_{24} and b_{25}, as well as between b_{26} and b_{27}, respectively, indicating the presence of Ala residues in positions 25 and 27 of swine ELC$_V$. (C) Zoomed-in tandem mass spectrum showing 168.09 Da mass difference between c_{28} and c_{30}, which indicates the presence of Ala and Pro residues in positions 29 and 30 of swine ELC$_V$. Broken arrow denotes location of un-observed c_{29} ion. (D) Zoomed-in tandem mass spectrum showing 97.05 Da mass difference between $a^{\cdot}_{31}$

and $a_{\cdot 32}$, which indicates the presence of a Pro residue in position 32 of swine ELC_v. (E) Zoomed-in tandem mass spectrum showing 226.10 Da mass difference between c_{34} and c_{36}, indicating the presence of Glu and Pro residues in positions 35 and 36 of swine ELC_v. Broken arrow denotes location of un-observed c_{35} ion. (F) Zoomed-in tandem mass spectrum showing 128.09 Da mass difference between c_{100} and c_{101}, indicating the presence of a Lys residue in position 101 of swine ELC_v. (G) Zoomed-in tandem mass spectrum showing mass of the smallest observed C-terminal fragment ion (y_3), with matches well with a combination of Ser, Ala, and Met residues. (H) Zoomed-in tandem mass spectrum showing 115.02 Da mass difference between $z_{\cdot 83}$ and $z_{\cdot 84}$, which indicates the presence of an Asp residue in position 113 of swine ELC_v. (I) Zoomed-in tandem mass spectrum showing 87.03 Da mass difference between $z_{\cdot 89}$ and $z_{\cdot 90}$, indicating the presence of a Ser residue in position 107 of swine ELC_v. Circles represent the theoretical isotopic abundance distribution of the isotopomer peaks corresponding to the assigned mass. "~" denotes peak truncation.

Fig. 3.22. Sequence alignment for ELC_v from different species. Locations of N-terminal extension, EF-hand domains, sequence differences (shaded boxes), and conserved Pro residue in positions analogous to position 30 in swine ELC_v (open box), are indicated.

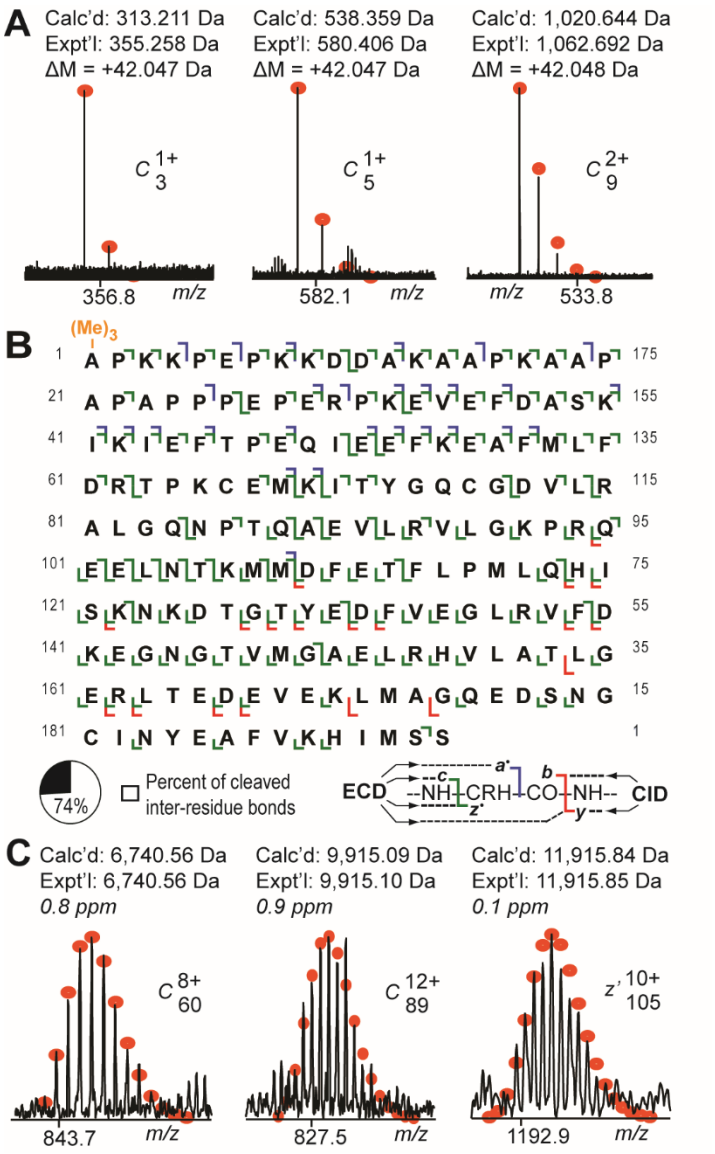

Fig. 3.23. Sequence characterization of human ELC$_v$. (A) N-terminal fragment ions showing approximate 42.046 Da mass increase compared to the calculated masses for the corresponding un-modified fragment ions, indicating N-terminal tri-methylation of human ELC$_v$. (B) Sequence table showing bond cleavages for ELC$_v$ (~74% of all inter-residue bonds). (C) Representative fragment ions from tandem mass spectra generated by fragmentation of human ELC$_v$.

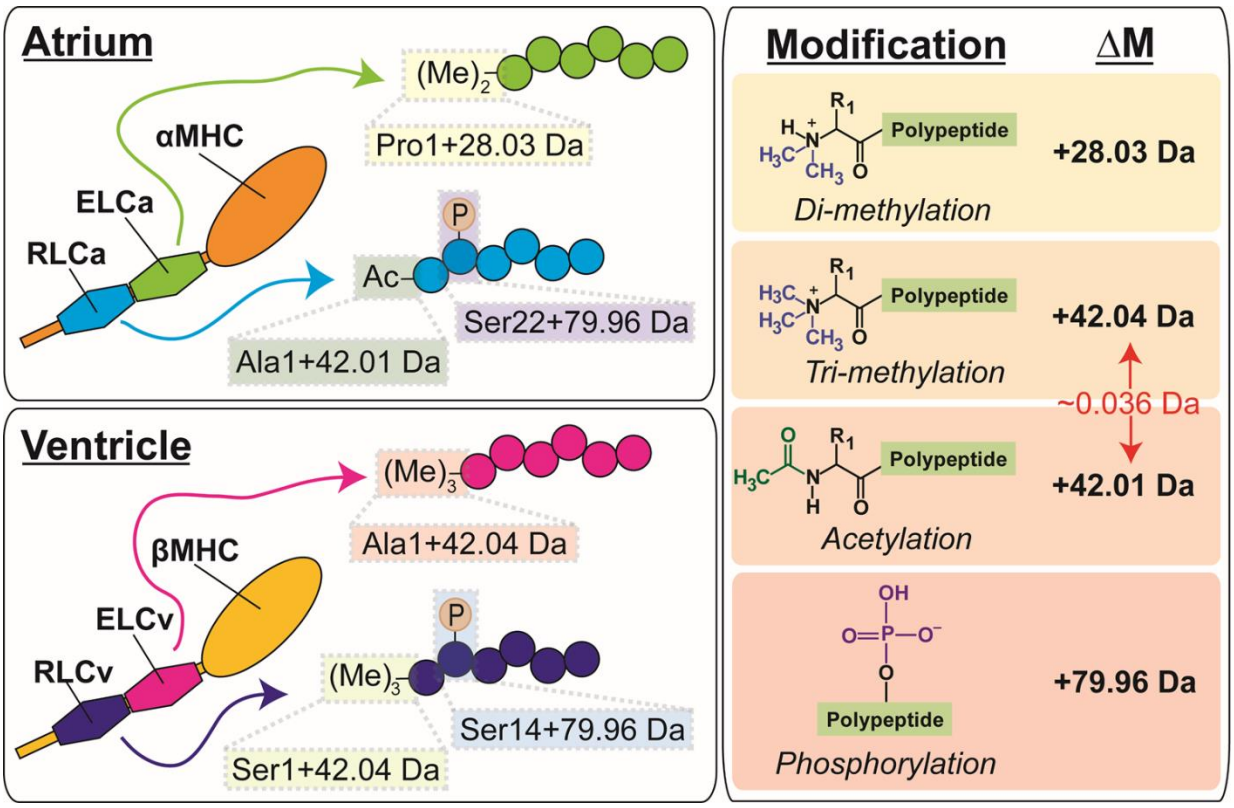

Fig. 3.24. Study overview showing localized mass differences in the atrial and ventricular isoforms of the ELC and RLC (left panels) from swine, as well as the modifications they represent (right panel). Highlighted is the approximate 36 mDa (0.036 Da) mass difference between tri-methylation and acetylation, which were distinguished using high-resolution top-down MS/MS in the present study.

CHAPTER 4 – TOP-DOWN PROTEOMICS REVEALS CONCERTED REDUCTIONS IN MYOFILAMENT AND Z-DISC PROTEIN PHOSPHORYLATION AFTER ACUTE MYOCARDIAL INFARCTION

This research was originally published in *Molecular & Cellular Proteomics*. Peng Y, Gregorich ZR, Valeja SG, Zhang H, Cai W, Chen YC, Guner H, Chen AJ, Schwahn DJ, Hacker TA, Liu X, Ge Y. Top-down proteomics reveals concerted reductions in myofilament and Z-disc protein phosphorylation after acute myocardial infarction. *Molecular & Cellular Proteomics*. 2014;13(10):2752-2764. © the American Society for Biochemistry and Molecular Biology.

Abstract

Heart failure (HF) is a leading cause of morbidity and mortality worldwide and is most often precipitated by myocardial infarction (MI). However, the molecular changes driving cardiac dysfunction immediately after MI remain poorly understood. Myofilament proteins, responsible for cardiac contraction and relaxation, play critical roles in signal reception and transduction in HF. Post-translational modifications (PTMs) of myofilament proteins afford a mechanism for the beat-to-beat regulation of cardiac function. Thus, it is of paramount importance to gain a comprehensive understanding of PTM changes of myofilament proteins in regulating early molecular events in the post-infarcted myocardium. Herein, we have developed a novel liquid chromatography-mass spectrometry (LC/MS)-based top-down proteomics strategy to comprehensively assess the modifications of key cardiac proteins in the myofilament sub-proteome extracted from a minimal amount of myocardial tissue with high reproducibility and throughput. The entire procedure that includes tissue homogenization, myofilament extraction, and on-line LC/MS takes less than three hours. Notably, enabled by this novel top-down proteomics technology, we discovered a concerted significant reduction in the phosphorylation of three crucial cardiac proteins in acutely-infarcted swine myocardium: cardiac troponin I and myosin regulatory light chain of the myofilaments and, unexpectedly, enigma homolog isoform 2 (ENH2) of the Z-disc. Furthermore, top-down MS comprehensively sequenced these proteins and pinpointed their phosphorylation sites. For the first time, we have characterized the sequence of the ENH2 and identified it as a phosphoprotein. ENH2 is localized at the Z-disc which has been increasingly recognized for its role as a nodal point in cardiac signaling. Therefore, our proteomics discovery opens up new avenues for investigation of concerted signaling between myofilament

and Z-disc in the early molecular events that contributes to cardiac dysfunction and progression to HF.

4.1 Introduction

Despite recent advances in the treatment of heart failure (HF), this devastating syndrome remains a leading cause of morbidity and mortality worldwide and imposes a significant economic burden especially on developed countries [302-304]. The most common cause of HF, myocardial infarction (MI), induces left ventricular (LV) remodeling characterized by chamber dilation and hypertrophy of the non-infarcted (remote) myocardium, which is ultimately maladaptive—leading to depressed global contractility and predisposing the heart to failure [305]. Current treatments for HF have primarily focused on symptom management after the occurrence of irreversible remodeling and functional impairment, which only delays the syndrome [303]. Understanding the molecular mechanisms driving cardiac dysfunction at the early stages could enable the development of therapeutic interventions to prevent the onset of HF. However, the molecular changes that occur immediately after MI, but prior to the maladaptive remodeling, remain poorly understood [92].

Myofilaments are responsible for cardiac contraction and relaxation, playing a central role in myocardial pathophysiology [34, 35]. Moreover, recent evidence suggests that cardiac myofilaments have a critical role in signal reception and transduction in HF [306, 307]. Myofilaments consist of the thin filament proteins that includes mainly actin, tropomyosin (Tm), and the troponin (Tn) complex (TnI, TnT and TnC) and the thick filament proteins including myosin [S-1 head domain, S-2 rod domain, essential light chain (MLC1), and regulatory light chain (MLC2)] as well as a number of accessory proteins such as myosin binding protein C (MyBP-C) [34, 213, 308, 309]. In addition to these major myofilament proteins, a significant

number of proteins have been identified in the cardiac myofilament sub-proteome [310]. Cardiac contraction requires the integrated activity of highly coordinated protein-protein interactions among myofilament proteins in the sarcomere [34, 306, 307]. Post-translational modifications (PTMs) and mutations of myofilament proteins can change these protein-protein interactions, thereby altering cardiac contractility. Thus, it is of paramount importance to gain a comprehensive understanding of the PTM changes of myofilament proteins in regulating early molecular events in contractile dysfunction immediately after acute MI (AMI).

Top-down mass spectrometry (MS) [197, 198, 209, 213, 220, 245, 311-313] has unique advantages for comprehensive assessment of protein modifications by detection and quantification of all proteoforms (a unified term to define all of the different molecular forms arising from PTMs, mutations or polymorphisms, and alternative splicing events [206]). Subsequently, the modification sites can be precisely localized by tandem MS (MS/MS) including but not limited to collisionally activated dissociation (CAD) and electron capture dissociation (ECD) [197, 198, 204, 207, 209, 213, 220, 245, 311-313]. Herein, we have successfully developed a novel liquid chromatography-mass spectrometry (LC/MS)-based top-down quantitative proteomics strategy to assess the concerted changes in myofilaments and their associated proteins in the myofilament sub-proteome. Specifically, we have rapidly separated and quantified intact proteins extracted from a minimal amount of myocardial tissue (approximately 500 μg tissue/experiment) by LC/MS with high reproducibility and throughput. Notably, we discovered a concerted significant reduction in the phosphorylation of three crucial cardiac proteins: a thin filament regulatory protein, cardiac TnI (cTnI), a thick filament regulatory protein, MLC2, and, unexpectedly, a critical Z-disc protein, enigma homolog isoform 2 (ENH2), in the acutely-infarcted myocardium

using a clinically relevant swine AMI model [314]. Subsequently, we have unambiguously localized the phosphorylation sites of these three important proteins using ECD. Particularly, for the first time, we have comprehensively sequenced swine ENH2 by top-down MS and identified it as a phosphoprotein with its phosphorylation site precisely pinpointed. ENH2 belongs to the PDZ-LIM protein family that co-localizes with α-actinin at the Z-disc [116, 315]. Although traditionally viewed as a structural component in the sarcomere, the Z-disc is increasingly recognized for its prominent role as a nodal point for cardiac signaling [96, 97, 315]. Thus, our proteomic discovery opens up new avenues for investigations of the concerted signaling between myofilament and Z-disc proteins in the early molecular events that may contribute to cardiac dysfunction and subsequent HF.

4.2 Materials and methods

4.2.1 Generation and functional characterization of swine AMI model

We induced AMI in swine via occlusion of the left anterior descending (LAD) coronary artery using an angioplasty balloon and a percutaneous femoral approach similar to that reported previously [314] (**Fig. 4.1A**). Briefly, Yorkshire swine (30-35 kg) from the University of Wisconsin-Madison colony were pre-medicated with a mixture of telazol (4–6 mg/kg IM), xylazine (2 mg/kg, IM), and propofol (2-8 mg/kg IV), intubated, anesthetized, and mechanically ventilated with isoflurane (1–5%). Baseline PV loops were obtained and the vena cava balloon was briefly inflated to alter loading conditions with the ventilator turned off. Next, a coronary balloon catheter was introduced into the proximal LAD just distal to the first diagonal arterial

branch and inflated for 90 min (AMI group, n=6). Iodinated contrast was used to confirm complete cessation of coronary blood flow distal to the balloon. After 90 min, PV loop data was again collected with the catheter in place and the LAD still occluded. PV analysis was performed in control animals (CON group; n=6). After the final PV-loop was obtained, the animal was euthanized with saturated KCl and the heart was removed and sectioned. Sections were either rapidly frozen in liquid nitrogen or placed in 10% buffered formalin for histology. 90 min occlusion of the lower one-third of the LAD created an ischemic zone comprising roughly 25% of the LV, less than 5% of the right ventricle (RV), and 5-10% of the interventricular septum (IVS). All experiments involving animals were conducted in accordance with the NIH Guide for the Care and Use of Laboratory Animals, and using protocols approved by the University of Wisconsin Institutional Animal Care and Use Committee.

4.2.2 Histopathologic analysis

Formalin-fixed heart sections were trimmed, processed, embedded in paraffin, cut 5 μm thick, and stained with hematoxylin and eosin (HE) or phosphotungstic acid-hematoxylin (PTAH). Staining with HE occurred by routine methods and PTAH staining was performed using Bouin solution as a mordant instead of Zenker fixative, followed by Gram iodine, sodium thiosulfate, potassium permanganate, and oxalic treatments before PTAH staining overnight.

4.2.3 Tissue homogenization and myofilament protein extraction

Myofilament subproteome were effectively extracted from only ~ 5 mg of pig myocardial tissue, which was sufficient for ten experiments (the equivalent of 500 μg/experiment). We chose to use ~5 mg due to the difficulty associated with handling and accurately measuring 500 μg tissue. Specifically, ~5 mg of swine cardiac tissue was homogenized in 50 μL of HEPES extraction buffer containing protease and phosphatase inhibitors (25 mM HEPES pH 7.5, 50 mM NaF, 0.25 mM Na_3VO_4, 0.25 mM PMSF, 2.5 mM EDTA) using a Teflon pestle (1.5 mL tube rounded tip, Scienceware, Pequannock, NJ, USA) to remove soluble cytoplasmic proteins. The resulting homogenate was centrifuged at 16,100 × *g* for 15 min at 4 °C (Centrifuge 5415R, Eppendorf, Hamburg, Germany) and the supernatant was discarded. The insoluble pellet was then re-homogenized in 50 μL of TFA extraction buffer (1% TFA, 1 mM TCEP) to extract the myofilament proteins [316]. After centrifugation (16,100 × *g*, 4 °C, 25 min), the supernatant, which is enriched in myofilament proteins, was collected and analyzed using LC/MS (the pellet was discarded). All tissue preparation and protein extraction procedures were performed in a cold room (4 °C) or on ice using freshly prepared buffers.

4.2.4 On-line LC/MS analysis

Rapid LC/MS profiling was performed using a 2D-nanoLC system (Eksigent®, Dublin, CA) coupled on-line with a linear ion trap (LTQ)/MS system (Thermo Scientific Inc., Bremen, Germany). Samples (equivalent to ~500 μg of tissue/injection) were loaded onto a sample loop (10 μL) before a home-packed PLRP column (200 mm ×500 μm, PLRP, 10μm, 1000Å) with a flow rate of 12.5 μL/min. The packing material (PLRP-S particles) was purchased from Varian (Lake Forest, CA). The proteins of interest were eluted with a gradient (12.5 μL/min)

of 20% B to 90% B in 55 min (Solvent A: 0.15% formic acid in water, Solvent B: 0.15% formic acid in methanol). After LC separation, a small portion of the sample (~5% of the total amount) was ionized by electrospray ionization (ESI) through a 25-30 µm i.d. tip and analyzed directly by LTQ/MS (on-line LC/MS). The remaining ~95% of the sample was simultaneously collected on ice for further high-resolution MS and MS/MS characterization (*vide infra*). 22 fractions were collected during one LC/MS experiment per injection (**Fig. 4.2**).

4.2.5 Off-line high-resolution FT-ICR MS/MS analysis

The collected fractions were analyzed using a 7T linear ion trap/ Fourier transform ion cyclotron resonance (FT-ICR) mass spectrometer (LTQ/FT Ultra, Thermo Scientific Inc., Bremen, Germany) equipped with an automated chip-based nano ESI source (Triversa NanoMate; Advion Bioscience, Ithaca, NY, USA) as described previously [202, 218, 245]. The sample was introduced into the mass spectrometer using a spray voltage of 1.3-1.5 kV, resulting in a flow rate of 50-200 nL/min. Ion transmission into the linear trap and, subsequently, the FT-ICR cell, was optimized for a maximum ion signal. The resolving power of the FT-ICR was set at 200,000 at 400 *m/z*, which resulted in an acquisition rate of 1 scan/s. The number of accumulated ions for a full scan in the linear trap, FT-ICR cell, MS^n FT-ICR cell, and electron capture dissociation (ECD) were 3×10^4, 8×10^6, 8×10^6 and 8×10^6, respectively. For MS/MS experiments, the protein molecular ions of the individual charge states were first isolated and then fragmented using 15-20% normalized collision energy for collisionally activated dissociation (CAD) or 2.5-3.5% electron energy for ECD (corresponding to 1.3-2.3 eV) with a 70 ms duration without additional delay. All MS and MS/MS spectra were analyzed by in-house developed MASH Suite software (version 1.0)

[248] using the THRASH algorithm with a signal-to-noise ratio (S/N) threshold of 3 and a minimum fit of 60%. The resulting data was then manually validated to ensure its accuracy. The most abundant mass is reported for intact proteins whereas the monoisotopic mass is reported for fragment ions.

4.2.6 Protein identification

The raw MS/MS data were converted to mzXML files and deconvoluted with MS-Deconv (release version: 0.8.0) [246], a combinatorial algorithm that determines the monoisotopic masses and charge for all of the fragment ions present in a given tandem mass spectrum. Subsequently, to identify the proteins present in the sample, the files containing the monoisotopic mass, intensity, and charge for each of the product ions were searched against the pig database generated from NCBI (Sscrofa10.2, containing 24,476 protein sequences) using the MS-Align+ search engine (release version: 0.7.1) [247]. Here, 10 ppm mass measurement accuracy was utilized as a cut-off for MS/MS fragment assignments. The maximum number of unexpected changes is 2 and the acceptance criteria is E-value less than 0.01. The use of both CAD and ECD tandem mass spectra for various charge states of the same protein resulted in unique protein identification with significantly lower statistical P values and a higher number of assigned fragments correlating directly to a higher confidence level in protein identification. All protein identifications were validated manually. Moreover, MS-Align+ is a fast algorithm for top-down protein identification based on spectral alignment that allows for the identification of sequence variations and PTMs as described previously [220, 247].

4.2.7 Quantitative analysis

We have quantitatively determined the proteoforms of major myofilament and associated proteins using both low-resolution LTQ/MS and high-resolution FT-ICR MS data. For low-resolution MS data, the areas under the MS peaks were used to quantify the relative abundances of proteoforms. For high-resolution MS data, the sum of the peak heights of the top five isotopomers for each proteoform was used to calculate the relative abundance as described previously [202, 218, 242, 245]. The relative abundances of the individual proteoforms from three separate charge states were averaged to obtain the relative percentage for each individual proteoform. To assess protein phosphorylation levels, the percentages of the mono- ($\%P_{mono}$) and/or bis- ($\%P_{bis}$) phosphorylated protein species were defined as the summed abundances of mono- and/or bis-phosphorylated species over the summed abundances of the entire protein population, respectively. Based on these percentages, the total amount of phosphorylation (P_{total}) of a single protein was calculated using the following equation (Eq. 1):

$$P_{total} = (\%P_{mono} + 2\times \%P_{bis})/100 \quad \text{(Eq. 1)}$$

Minor oxidation products and non-covalent phosphoric acid adducts ($+H_3PO_4$) were taken into consideration in the quantification.

4.2.8 Statistical analysis

Data are represented as mean ± SEM. Each biological replicate was performed in two technical replicates. Student's *t*-test was performed between group comparisons to evaluate the statistical significance of variance. Differences among means were considered to be significant at $p < 0.05$.

4.3 Results

4.3.1 A clinically relevant swine AMI model

Owing to the anatomical and physiological similarities between human and swine hearts, the swine AMI model is of high clinical relevance since it closely recapitulates human disease pathophysiology [277]. In this study, we generated a swine AMI model using a closed-chest catheter-based method [314] by inducing AMI in pigs (n=6) via occlusion of the lower one-third of the left anterior descending (LAD) coronary artery with an angioplasty balloon (**Fig. 4.1A**). Control animals (CON, n=6) were treated similarly but without LAD balloon catheterization. We chose a 90 min occlusion to mimic the typical time interval between the onset of chest pain in patients and their arrival in the emergency room for medical treatment [317]. Pressure volume (PV) analysis was performed to assess cardiac function prior to and after LAD occlusion in swine undergoing AMI, and prior to sacrifice in CON (**Fig. 4.1B**). In CON and AMI swine prior to LAD occlusion, the heart rate, end systolic pressure (ESP), stroke volume (SV), LV ejection fraction (EF), and the pre-load recruitable stroke work (PRSW) were consistent with the values previously reported for healthy swine (**Table 4.1**) [314]. After 90 min of LAD occlusion, a significant decrease in the ESP, the maximal rate of change in the pressure (dP/dt_{max}), the minimal rate of change in the pressure (dP/dt_{min}), LVEF, and PRSW (**Fig. 4.1C-E**, **Table 4.1**) was observed.

Although the histological characterization of AMI is difficult due to the fact that tissue necrosis only becomes readily apparent 4-6 hours after infarction, analysis of tissue collected from the LV and interventricular septum (IVS) was undertaken to examine for early degenerative changes. Tissue taken from the LV and IVS of infarcted swine showed signs of early stage myocardial injury and necrosis (**Fig. 4.1F**, **Fig. 4.3**). Scattered areas of sarcomere fragmentation were most common, followed by vacuolar degeneration (**Fig. 4.1F**), contraction banding (**Fig. 4.3**), and shrunken cells exhibiting cytoplasmic hypereosinophilia and pyknosis (necrosis) (**Fig. 4.1**, **Fig. 4.3**). These results are consistent with the characteristics of AMI in swine.

4.3.2 An integrated top-down quantitative proteomics strategy

We have developed a top-down LC/MS-based proteomics strategy for the separation, identification, quantification, and characterization of intact proteins from tissue extracts to reveal disease-related changes (**Fig. 4.2A**). Using this strategy, we can rapidly extract, separate, and identify intact myofilament proteins from a minimal amount of myocardial tissue (approximately 500 µg tissue per LC injection). It takes less than three hours to perform tissue homogenization, myofilament extraction and on-line LC/MS analysis. We effectively separated a number of myofilament and associated proteins (**Fig. 4.2B**). Rapid profiling by low-resolution linear ion trap (LTQ)/MS, concurrent with LC separation, allowed for the preliminary identification of myofilament proteins based on their deconvoluted molecular masses, which matched closely with the predicted sequence in the Swiss-Prot database (**Fig. 4.2B**, **Fig. 4.4**, **Table 4.2**). Meanwhile, the off-line high-resolution MS analysis of the collected fractions from LC separation enabled the

determination of the accurate relative molecular masses (M_r) of all of the detected proteoforms (**Fig. 4.4**). Subsequent high-resolution MS/MS together with the MS-Align+ algorithm [247] provided unambiguous identification of major proteins present in the myofilament sub-proteome (**Table 4.2**, **Fig. 4.5**). Both low-resolution and high-resolution MS have been used for relative quantification (*vide infra*).

4.3.3 Quantification of phosphorylation using on-line LC/MS

The high reproducibility of the LC/MS experiments (**Figs. 4.6-4.7**) allowed rapid semi-quantification of proteoform abundances based on their peak areas. To ensure an accurate comparison, we paired AMI and CON groups and performed the LC/MS back-to-back using the same experimental setup (**Fig. 4.8A-B**, **Fig. 4.9**). Despite the limited resolution of LTQ, we were able to preliminarily identify protein phosphorylation based on the mass difference of 80 Da. Quantification of the phosphorylation of myofilament and associated proteins revealed a significant reduction in the phosphorylation of cTnI (a thin filament regulatory protein), MLC2 (a thick filament regulatory protein), and ENH2 (a Z-disc protein) in the myocardium of AMI versus CON; whereas no significant changes were observed in the phosphorylation levels of cardiac TnT (cTnT) and Tm (**Fig. 4.8**). The total phosphorylation level (P_{total}, Mol Pi/Mol protein) of cTnI was significantly reduced from 1.72 ± 0.05 in CON to 0.97 ± 0.16 in AMI; the P_{total} of MLC2 decreased from 0.11 ± 0.01 to 0.09 ± 0.01, and the P_{total} of ENH2 decreased from 0.93 ± 0.02 in CON to 0.57 ± 0.09 in AMI, respectively (**Fig. 4.8C**). Collectively, these results suggest that the phosphorylation of cTnI, MLC2, and ENH2 is down-regulated in the acutely-infarcted myocardium.

4.3.4 Comprehensive proteoform assessment using high-resolution MS/MS

The amalgamation of different proteoforms into a single peak in low-resolution spectra can potentially compromise the accuracy of proteoform quantification; therefore, a more accurate quantification based on high-resolution MS is necessary. High-resolution Fourier transform ion cyclotron resonance (FT-ICR) MS analysis allowed a complete view of all types of proteoforms including those arising as a result of PTM (e.g., phosphorylation), alternative splicing events (e.g., α-Tm and β-Tm), and polymorphisms (e.g., Tm Pro64Leu) (Representative data for cTnI, MLC2, Tm, and ENH2 are shown in **Fig. 4.10**). A number of minor proteoforms, which could not be identified in the low-resolution spectra, were resolved in the high-resolution mass spectra (**Fig. 4.10A-D**). Subsequently, we quantitatively determined the relative percentages of each proteoform in the corresponding gene product group (**Fig. 4.10E**). Consistent with the low-resolution MS results (**Fig. 4.8**), we observed significantly reduced phosphorylation of cTnI, MLC2, and ENH2 from the myocardium of AMI compared to CON (**Fig. 4.10-4.12**). Additionally, dENH2 (likely a truncated form of ENH2) was up-regulated in AMI versus CON but the low abundance of this proteoform hindered further MS/MS characterization. No significant differences were observed in the relative amounts of Tm proteoforms in AMI versus CON (**Fig. 4.10E**, **Figs. 4.11-4.12**).

4.3.5 Mapping phosphorylation sites in swine cTnI to Ser22/23

cTnI is the inhibitory subunit of Tn, interacting with TnC, cTnT, and actin to inhibit muscle contraction [309]. Phosphorylation of cTnI is particularly important in modulating cardiac function [29, 306]. Since a number of kinases can phosphorylate different sites within cTnI [29, 318, 319], it is imperative to determine which sites are modified in AMI hearts. To identify the phosphorylation sites in swine cTnI, the precursor ions of mono-phosphorylated cTnI ($_{p}$cTnI) and bis-phosphorylated cTnI ($_{pp}$cTnI) were cleanly isolated and subsequently fragmented by ECD, respectively (**Figs. 4.13-4.14**). We have comprehensively sequenced $_{p}$cTnI and $_{pp}$cTnI and unambiguously mapped Ser22 as the only phosphorylation site in $_{p}$cTnI, and Ser22/23 as the two phosphorylation sites in $_{pp}$cTnI, respectively, in AMI hearts (**Figs. 4.13-4.14**). Interestingly, the fact that phosphorylation of Ser23 was only observed in the presence of Ser22 phosphorylation suggests a sequential phosphorylation mechanism, which is consistent with our previous report on human cTnI [250]. Ser22/23 are *bona fide* substrates of cAMP-dependent protein kinase A (PKA), albeit protein kinase C (PKC), protein kinase D (PKD), and cGMP-dependent protein kinase (PKG) can also cross-phosphorylate these two sites [29].

4.3.6 Comprehensive sequencing and phosphorylation site mapping in swine MLC2 to Ser14

Although thin filament proteins are well recognized as critical elements regulating force production in cardiac muscle, recent compelling evidence suggests that thick filament regulatory proteins are also important players in modulating muscle contractions [320]. MLC2 is a thick filament regulatory protein that is believed to function as a mechanical stabilizer for the neck region between the myosin head (S1) and rod (S2) during force generation and mechanical work performance [321]. Here, we showed that MLC2 is present as both un- and mono-phosphorylated

($_p$MLC2) forms, which have M_r of 18,801.45 and 18,881.41, respectively (**Fig. 4.10B**). The M_r of un-phosphorylated MLC2 matched best with the uncharacterized sequence of swine MLC2 (UnitProtKB/Swiss-Prot, F6PSL2_PIG) after considering acetylation at the N-terminus. Since this sequence is yet to be verified, we employed top-down MS/MS to comprehensively sequence both un- and mono-phosphorylated MLC2 (**Figs. 4.14-4.15**). For MLC2, a total of 51 *b* ions, 52 *y* ions, 129 *c* ions, and 131 *z·* ions were detected based on 7 ECD and 3 CAD spectra, representing 158 out of 164 bond cleavages (**Fig. 4.15**). For $_p$MLC2, 84 *c* ions and 85 *z·* ions were detected representing 134 out of 164 bond cleavages, which unambiguously revealed that Ser14 is the predominant phosphorylation site in swine $_p$MLC2 (**Fig. 4.14B**, **Fig. 4.16**).

4.3.7 Top-down MS uncovered Ser118 as a phosphorylation site in ENH2

ENH2 belongs to the PDZ-LIM protein family that co-localizes with α-actinin at the Z-disc and associates with cytoskeletal proteins through its PDZ domain [116, 126, 315]. ENH2 is a short alternatively spliced isoform of ENH that only retains the PDZ domain [116, 126, 315]. Given that ENH2 phosphorylation has not been reported previously, and that the phosphorylation of this protein is altered following AMI, we sought to identify the site of phosphorylation. Two major proteoforms of ENH2 were detected with M_r of 25,825.44 and 25,905.42 (**Fig. 4.10D**). The mass difference of 79.98 Da between these two proteoforms implies a likely phosphorylation event. However, neither of these M_r matched with the predicted M_r of 25,898.43, based on the predicted swine ENH2 sequence from the NCBI pig genomic database (Sscrofa10.2). Using the MS-Align+ algorithm we identified a modification of 15 Da between Gly60 and Lys70 (**Fig. 4.5E**). Meanwhile, a sequence homology alignment of the predicted swine, human, and mouse ENH2

sequences revealed a potential amino acid polymorphism of Ser72Cys (+15.98 Da) among these species (**Fig. 4.17**). Thus, considering a single amino acid polymorphism (+15.98 Da), removal of N-terminal Met (-131.04 Da), and acetylation of the new N-terminus (+42.01 Da), the re-calculated M_r of swine ENH2 is 25,825.38, which matches well with the observed M_r of 25,825.44 (2.3 ppm).

To further characterize the sequence and locate the phosphorylation site of swine ENH2, the precursor ion of mono-phosphorylated ENH2 ($_p$ENH2) was isolated and then fragmented by ECD. In five combined ECD spectra of $_p$ENH2, 58 *c* ions and 71 *z*· ions were detected representing 98 out of 232 bond cleavages (**Fig. 4.14C**), despite of the relatively lower quantity of ENH2 present in the myofilament extract (**Fig. 4.9**). The MS/MS data unequivocally validated the removal of the N-terminal Met, acetylation of the new N-terminus, and one amino acid polymorphism at Ser72Cys, as well as localized the mono-phosphorylation site to Ser118 (**Fig. 4.14C**, **Figs. 4.18-4.19**). Thus, our top-down MS/MS data unambiguously confirmed that the proteoform with M_r of 25,905.42 is the mono-phosphorylated form of swine ENH2 (**Fig. 4.10D**).

4.4 Discussion

4.4.1 Concerted reduction in the phosphorylation of myofilament and Z-disc proteins

The PTM of myofilament proteins is increasingly recognized as an important mechanism for the regulation of cardiac function, which requires highly coordinated protein-protein interactions among myofilament proteins in the sarcomere [34, 35]. An emerging concept is that the integrated

action of kinases and phosphatases regulates protein phosphorylation and, thus, ultimately determines the activity and function of myofilament and associated proteins [34]. Consequently, imbalance of kinase and phosphatase activities could alter contractility and lead to cardiac dysfunction. Indeed, our study presents direct evidence of early changes in protein phosphorylation occurring with cardiac dysfunction in a clinically relevant large animal AMI model. Specifically, we detected a concerted reduction in the phosphorylation of three critical proteins in the sarcomere: cTnI (a thin filament regulatory protein), MLC2 (a thick filament regulatory protein), and ENH2 (a Z-disc protein) (**Fig. 4.10, Fig. 4.20**). Using top-down high-resolution MS, we have unambiguously localized the phosphorylation sites in these three proteins (**Fig. 4.14**). Although previous studies have shown reduced phosphorylation in myofilament proteins such as cMyBP-C, MLC2, and cTnI, respectively [92, 148], this is the first report on the concerted changes in phosphorylation between myofilament proteins and Z-disc protein. Z-discs, which demarcate the ends of sarcomeres, are sophisticated structures that cross-link the myofilaments into highly ordered 3-D lattices (**Fig. 4.20**) [96, 315]. Recent compelling evidence clearly indicates that the Z-disc may serve as a nodal point for cardiac signaling and disease [315]. Importantly, our results suggest that coordinated signaling between myofilament and Z-disc may underlie contractile dysfunction in AMI.

4.4.2 The functional significance of cTnI phosphorylation at Ser22/23

Following stimulation of the β-adrenergic signaling system, activated PKA phosphorylates cTnI at residues Ser22/23, leading to decreased myofilament Ca^{2+} sensitivity and enhanced relaxation, which benefits diastolic function of the heart [29]. We and others have previously reported that

phosphorylation at Ser22/23 was significantly reduced in the human myocardium of end-stage HF compared with that of healthy donors [81, 218]. In addition to PKA, other kinases such as PKC, PKG, and PKD can also cross-phosphorylate the PKA sites of cTnI at Ser22/23 and induce similar functional effects as PKA phosphorylation [29].

Previous reports by van der Velden et al. showed reduced cTnI phosphorylation and decreased PKA levels in the myocardium remote from the infarction in swine 3 weeks after MI using the open-chest LAD surgery [140]. Avner et al. also reported the reduced phosphorylation of cTnI in the papillary muscles of mice 3-4 days after experimental MI via open-chest surgical ligation of the LAD [92]. Importantly, in this study we observed significantly decreased cTnI phosphorylation immediately following 90 min of LAD occlusion using a closed-chest catheter-based method that obviates the need for open-chest surgery. Conceivably, a precise understanding of molecular changes at this early stage before the maladaptive remodeling could aid in the development of novel therapeutic interventions to prevent remodeling and the onset of HF.

4.4.3 The functional significance of MLC2 phosphorylation

Here we have observed reduced MLC2 phosphorylation within the infarction of acutely-infarcted swine myocardium and unequivocally determined the predominant phosphorylation site to be Ser14. The decreased phosphorylation of MLC2 was also observed in human explanted end-stage failing hearts [322]. Scruggs et al. determined the phosphorylation site to be Ser13/14 (excluding the N-terminal Met) for mouse MLC2 and a single site at Ser14 for human MLC2 [296]. Ser13 in mouse MLC2 is not conserved in the human sequence, but swine and human MLC2 have the same

amino acid (Asn13) at this site; this underscores another advantage of the swine AMI model (**Fig. 4.21**). A recent study by Sheikh et al. demonstrated that knock-in mice with un-phosphorylatable (S13A/S14A) MLC2 exhibit DCM, LV torsional defects, and sudden death, underlining the importance of MLC2 phosphorylation at Ser13/Ser14 [77].

The identity (or identities) of the kinase (or kinases) that phosphorylate Ser14 of cardiac MLC2 remains unclear. Originally, MLC2 was presumed to be phosphorylated by MLC2 kinase (MLCK) and dephosphorylated by MLC2 phosphatase [264]. Although the conventional smooth and skeletal muscle MLCKs are also expressed in the heart, they do not appear to play a significant role in regulating MLC2 phosphorylation and altering cardiac function [320]. Recently, a cardiac specific MLC2 kinase (cMLCK) encoded by Mylk3 was shown to be the primary kinase phosphorylating MLC2 that modulates cardiac function in both mice and humans [298]. Besides cMLCK, other kinases such as zipper-interacting protein kinase, rho-associated kinase, and PKC may also regulate MLC2 phosphorylation [264, 320].

4.4.4 ENH2 phosphorylation and cardiac Z-disc signaling

ENH belongs to the PDZ-LIM domain protein family that co-localizes with α-actinin on the Z-disc (**Fig. 4.20**) and associates with cytoskeletal proteins through its PDZ domain [116, 126, 315]. ENH is alternatively spliced into four isoforms: isoform 1 (ENH 1) is the long isoform containing a PDZ domain and three LIM domains whereas the other three short isoforms (ENH 2-4) retain only the PDZ domain [126]. ENH2-4 are expressed mainly in cardiac and skeletal muscle whereas ENH1 is ubiquitously expressed in all tissue types. The splicing isoforms of ENH are differentially

expressed during heart development and disease [126]. ENH1 appears to be the embryonic isoform whereas the ENH2-4 isoforms are predominant in adult heart [126]. Recently, Ju Chen and co-workers found that ENH-null mice develop impaired cardiac contraction and DCM, underscoring the critical role of ENH in the heart [116]. The loss of ENH likely perturbs the integrity of the Z-disc, thus disturbing the connection between adjacent sarcomeres and the extracellular milieu [116].

Here we show that ENH2 is a phosphoprotein with a phosphorylation site at Ser118; however, the functional significance of this phosphorylation remains to be investigated. PDZ-LIM proteins typically serve as adaptor proteins in the Z-disc: the PDZ domain mediates interactions with the cytoskeleton, and the LIM domain recruits signaling proteins to the Z-disc. The perception of the cardiac Z-disc has changed considerably in the past decade [96, 97, 315]. Traditionally the Z-disc was only viewed as a structural component in the sarcomere, but, recent compelling evidence clearly indicates that the Z-disc may serve as a hub for cardiac signaling and disease [315]. An increasing number of signaling proteins, including protein kinases and phosphatases, are co-localized to the Z-disc, thereby concentrating a number of intracellular signaling molecules in this specific subcellular location [315]. Notably, for the first time, we discovered the phosphorylation of a critical Z-disc protein, ENH2, and its down-regulation after 90 min of ischemia, suggesting pivotal roles for this protein phosphorylation and the Z-disc in pathological signaling after AMI.

4.4.5 Top-down quantitative proteomics reveals concerted and unexpected proteoform changes

We have successfully developed a novel LC/MS-based top-down proteomics strategy for the highly reproducible quantification of multiple proteoforms simultaneously (**Fig. 4.2**). The major advantages of this strategy include *1) Rapid and effective separation of intact key cardiac proteins in the myofilament subproteome extracted from tissues*. Here we have shown that a majority of lower mass (<60 kDa) proteins from myofilaments and their associated proteins can be fully or partially separated on an LC time scale (**Fig. 4.2**, **Fig. 4.9**). A minimal amount of tissue (approximately 500 µg per experiment) is sufficient for both LC/MS and high-resolution MS characterization of proteins, making it suitable for the analysis of human biopsy samples. *2) Global detection of all types of modifications simultaneously without a priori knowledge*. The antibody-based methods for detecting PTMs (i.e. Western blot) require prior knowledge of the modification. In the conventional bottom-up MS approach, proteins are digested extensively with an enzyme (e.g. trypsin) resulting in many small peptides for MS and MS/MS analysis. This bottom-up approach is particularly useful for identifying proteins but suboptimal for determining modifications and alternative splice variants due to the partial recovery of digested peptides resulting in missed identification of PTMs and loss of connectivity between different modifications [323]. In contrast, a top-down MS approach analyzes whole proteins without a digestion, thus providing a comprehensive view of the protein [198, 200, 324]. Therefore, top-down MS is the only technique that can simultaneously identify all types of protein modifications universally without *a priori* knowledge. Here, we employed top-down MS to reveal a variety of proteoforms for myofilament and associated proteins arising from PTMs (i.e., phosphorylation, degradation, oxidation, acetylation), polymorphism, and alternatively spliced isoforms (**Fig. 4.10**). *3) Comprehensive sequencing and identification of (unexpected) modifications*. In the top-down MS approach, the molecular masses of the intact proteins are measured in the first step, which can

reveal any modifications occurring to the proteins, including the unexpected ones [198]. Subsequently, proteoforms of interest can be isolated and fragmented by MS/MS with ECD and CAD to locate the (unexpected) modification sites [205, 325, 326]. Here we have comprehensively sequenced cTnI, MLC2, and ENH2 (**Figs. 4.13-4.15**, **Fig. 4.18**) and mapped unexpected modifications as exemplified by an amino acid polymorphism and phosphorylation for ENH2 (**Fig. 4.14C**, **Fig. 4.18**). The use of ECD particularly allows for the localization of labile PTMs such as phosphorylation with high reliability and accuracy [198, 201, 202, 204, 213, 218]. We have localized Ser22/23 as the phosphorylation sites for cTnI, Ser14 as the phosphorylation site in MLC2, and an unexpected phosphorylation site, Ser118, in ENH2. The identification of unexpected modifications is challenging in the bottom-up approach since typically modifications need to be defined prior to database search for identification of such modifications. *4) Quantification of protein proteoforms with high reproducibility and identification of concerted changes in responding to pathophysiological stimuli*. The addition of small modifying groups to intact proteins does not change the physiochemical properties (and thus the ionization efficiency of proteins) appreciably in contrast to the dramatic impact such modifying group could have on the ionization efficiency of small peptides [204, 327, 328]. Moreover, the phosphorylation of a protein has a minimal influence on the protein charge state distribution (**Fig. 4.22**). Thus, top-down MS is the method of choice for the quantification of various protein proteoforms. We have achieved remarkable reproducibility for this top-down quantitative proteomics method (**Figs. 4.6-4.7**) and reliably quantified various proteoforms and determined the changes following AMI (**Fig. 4.10**). Appreciably, we have unambiguously identified the reduction of phosphorylation in cTnI (a thin filament regulatory protein), MLC2 (a thick filament regulatory protein), and ENH2 (a Z-disc protein) after AMI. *5) Combination of on-line low-resolution LC/MS for rapid profiling and*

off-line high-resolution MS for comprehensive proteoform characterization. Here we have employed a "LC/MS+" platform which allows fraction collection concurrent with on-line LC/MS, previously known as a "data-directed top-down" approach [329-331]. The on-line low-resolution LC/MS provides rapid screening of potential proteoform changes, which can then guide user directed data-dependent high-resolution top-down MS experiments. Meanwhile, the fractions collected simultaneously during the on-line LC/MS are used for comprehensive sequence characterization and accurate proteoform quantification. Thus, this targeted top-down proteomics approach offers the benefits of high-throughput protein profiling, high-resolution protein characterization and high-accuracy quantification of proteoforms from a sub-proteome.

The potential limitation of our 1D LC/MS-based top-down quantitative proteomics method is the failure to detect large myofilament and associated proteins such as α-actinin (~110 kDa), cMyBP-C (~140 kDa), and MHC (~220 kDa), which are known to be present in the myofilament subproteome in the cardiac sarcomere (**Fig. 4.20**). Due to the exponential decay in the signal-to-noise ratio as a function of increasing mass, it is necessary to separate the small molecules from large proteins [332]. For instance, we could use 2DLC with size exclusion chromatography as the first dimension and reverse phase chromatography as the second dimension. We have recently shown that ultra-high pressure size exclusion chromatography can be used for the rapid and high-resolution separation of intact proteins for top-down proteomics [333]. Nevertheless, 2DLC typically requires longer sample analysis time so that caution should be taken to minimize the possible artifactual modifications.

In summary, we have developed a novel LC/MS-based top-down quantitative proteomics strategy to comprehensively assess the changes in key cardiac proteins present in the myofilament sub-proteome extracted from heart tissues with high reproducibility and throughput. This entire process that includes tissue homogenization, protein extraction, and on-line LC/MS analysis only takes less than 3 hours and requires a minimal amount of myocardial tissue (~500 µg tissue/experiment), making it possible to analyze biopsy samples routinely. Enabled by this top-down quantitative proteomics strategy and a highly clinically relevant large animal (swine) model, we have unveiled the molecular changes of the critical cardiac proteins in the myofilaments and Z-disc at the early stage after AMI. Our proteomics discovery opens up new avenues for further investigation of the potential link between myofilament and Z-disc in regulating cardiac contractility at the early stage post-MI, which may lead to maladaptive remodeling and ultimately HF.

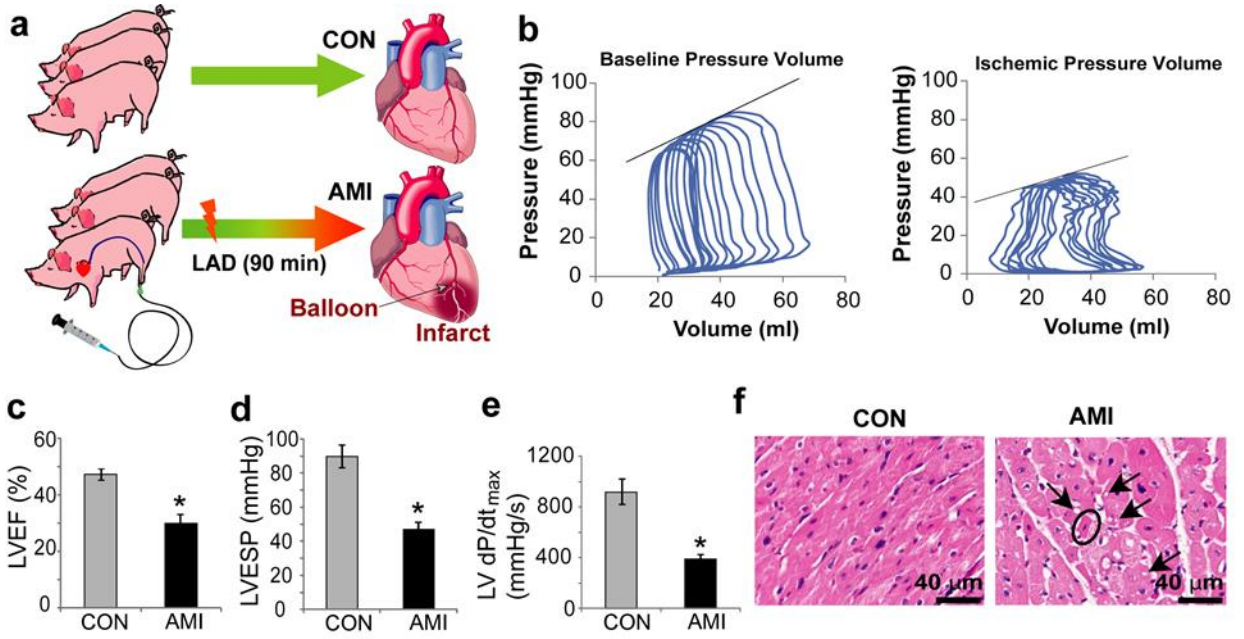

Fig. 4.1. Generation and characterization of swine AMI model. (A) Schematic of the creation of the AMI swine model versus CON. Tissue used in this study is from the area labeled infarct in AMI whereas LV tissue is used in CON. (B) PV measurements prior to (left) and after (right) 90 min of LAD coronary artery occlusion. The slope of the straight line represents the ESP-volume relation. The flatter slope in the right panel reflects a reduction in cardiac function due to ischemia. (C) LVEF is reduced in AMI compared to CON commensurate with the reduction in blood flow. (D) LVESP is lower in AMI due to the lack of blood flow. (E) LV dP/dt, a measure of systolic performance, is also significantly reduced for AMI swine compared to CON. (F) HE stained LV tissue from CON (left) and AMI (right) pigs. Arrows denote myocyte vacuolation and the circled cell displays characteristics consistent with necrosis including cellular shrinkage, cytoplasmic hypereosinophilia, and nuclear pyknosis. CON, control; AMI, acute myocardial infarction; LV, left ventricular; PV, pressure-volume; LAD, left anterior descending; ESP, end systolic pressure; EF, ejection fraction; dP/dt, the first derivative of LV pressure; HE, hematoxylin and eosin.

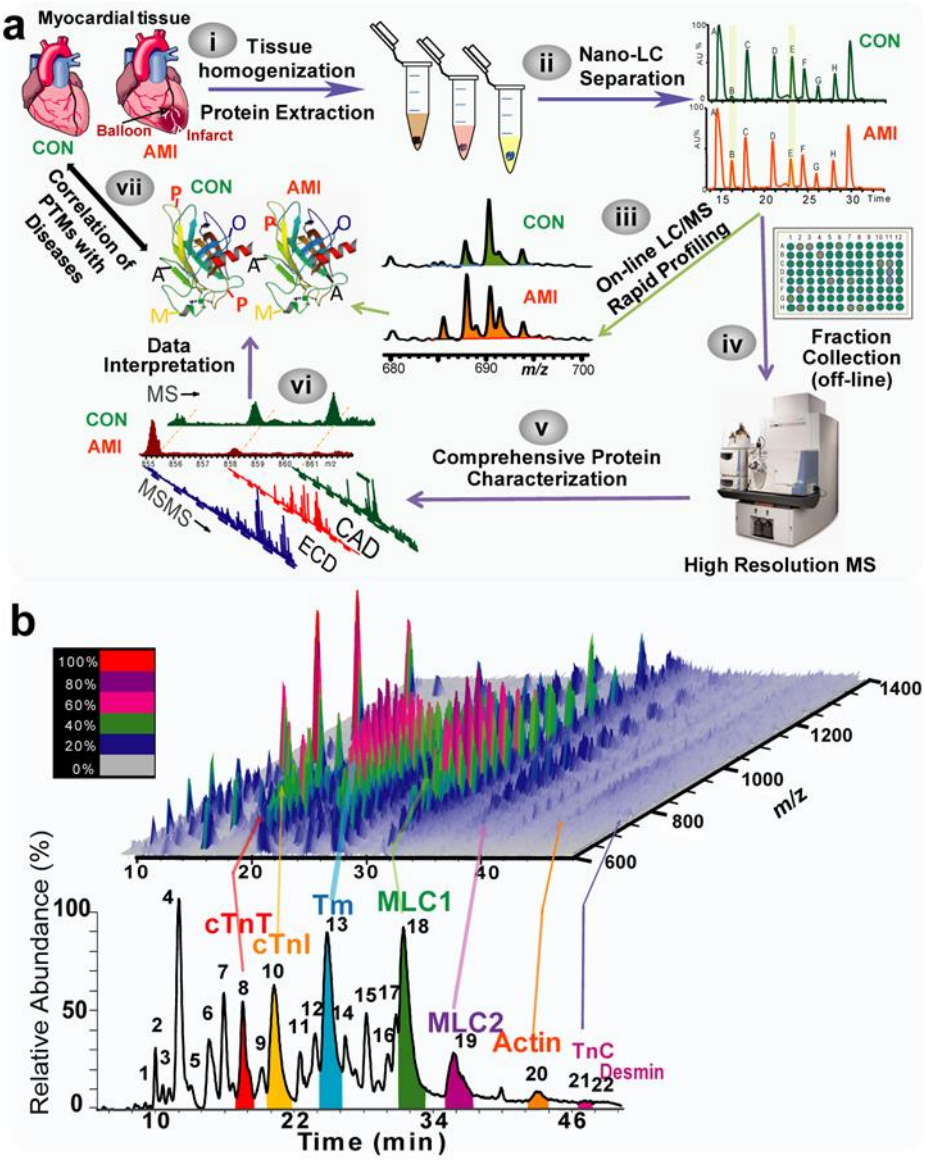

Fig. 4.2. (A) Schematic of the integrated top-down LC/MS-based quantitative proteomics strategy. This strategy consists of six steps: (i) tissue homogenization and protein extraction at low temperature (4 °C) in HEPES and TFA solutions containing protease and phosphatase inhibitors to preserve endogenous modifications and minimize artifactual degradations; (ii) on-line separation of proteins by nano-LC; (iii) rapid LC/MS profiling using low-resolution LTQ/MS (on-line); (iv) fraction collection concurrent with on-line LC/MS analysis; (v) comprehensive top-down MS analysis using high-resolution FT-ICR MS/MS (off-line); (vi) data interpretation; and

(vii) correlation of proteoform changes with disease phenotype. **(B) On-line LC/MS separation and detection of swine myofilament and associated proteins.** Bottom, LC separation of myofilament and associated proteins. The identification of each labeled peak is shown in **Table 4.2**. Top, on-line MS detection of the myofilament and associated proteins.

Table 4.1. Hemodynamic data from CON and AMI swine hearts. Values are means ± SEM. ESP, end systolic pressure; SV, stroke volume; EF%, percent ejection fraction; PRSW, preload recruitable stroke work. *$p < 0.05$ using paired student t-test. CON, control; AMI, acute myocardial infarction.

	CON (n=5)	AMI (n=5)
Heart Rate	105 ± 4	99 ± 8
ESP (mmHg)	86 ±7	62 ± 5*
dP/dt max (mmHg/sec)	853 ± 91	496 ± 25*
dP/dt min (mmHg/sec)	-1282 ± 94	-791 ± 72*
SV (ml)	29.9 ± 2.3	19.9 ± 3.0
EF%	45.7 ± 2.1	32.1 ± 3.9*
PRSW	58.5 ± 5.8	35.8 ± 6.5*

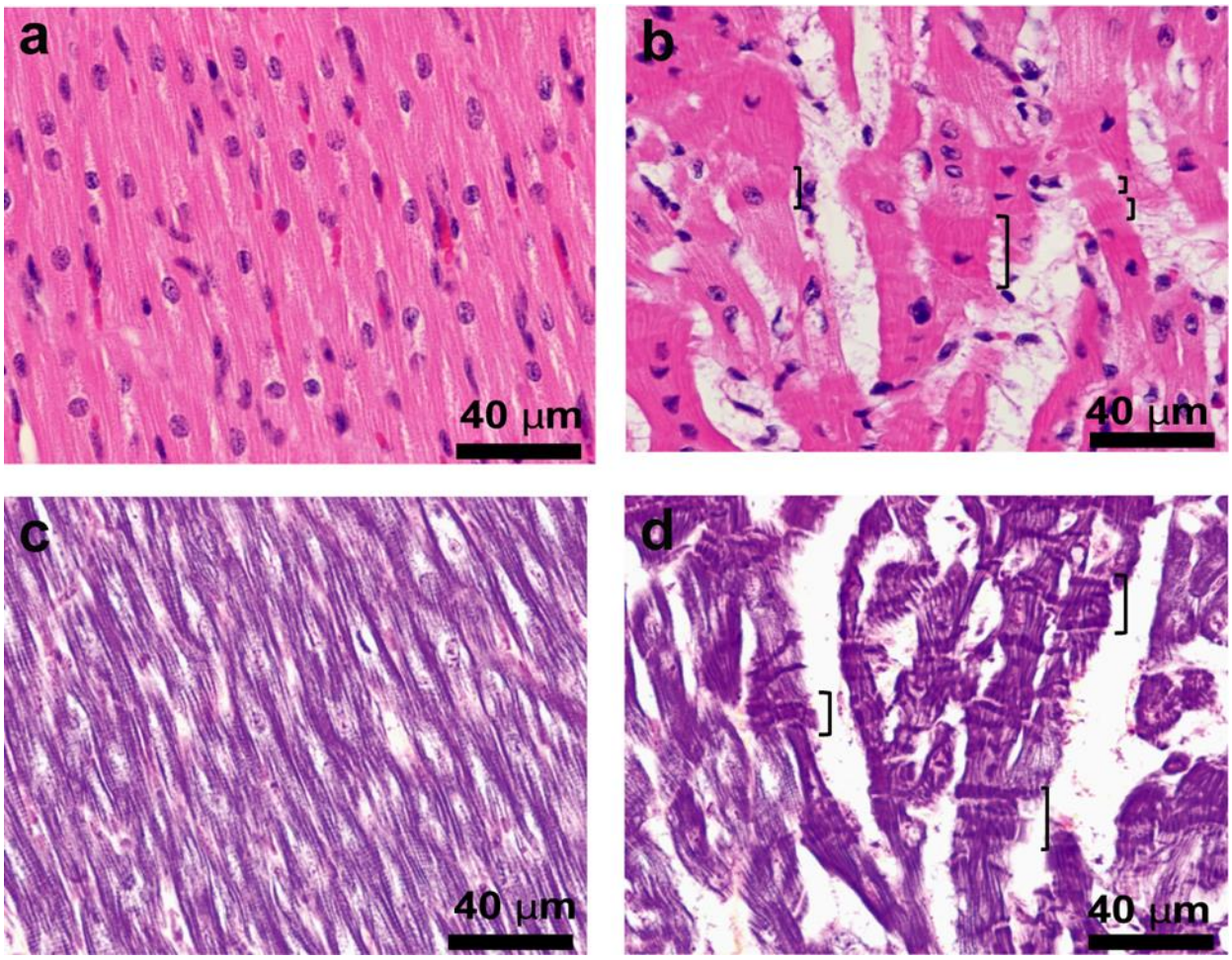

Fig. 4.3. Histological assessment of IVS. (A) HE stained IVS from control swine. (B) HE stained IVS from the ischemic zone of swine following 90 min of LAD occlusion. (C) PTAH stained IVS from control swine. (D) PTAH stained IVS from the infarct zone of swine following 90 min of LAD occlusion. Brackets denote contraction banding, a histological change associated with early necrosis. HE, hematoxylin and eosin; IVS, interventricular septum; LAD, left anterior descending; PTAH, phosphotungstic acid-hematoxylin.

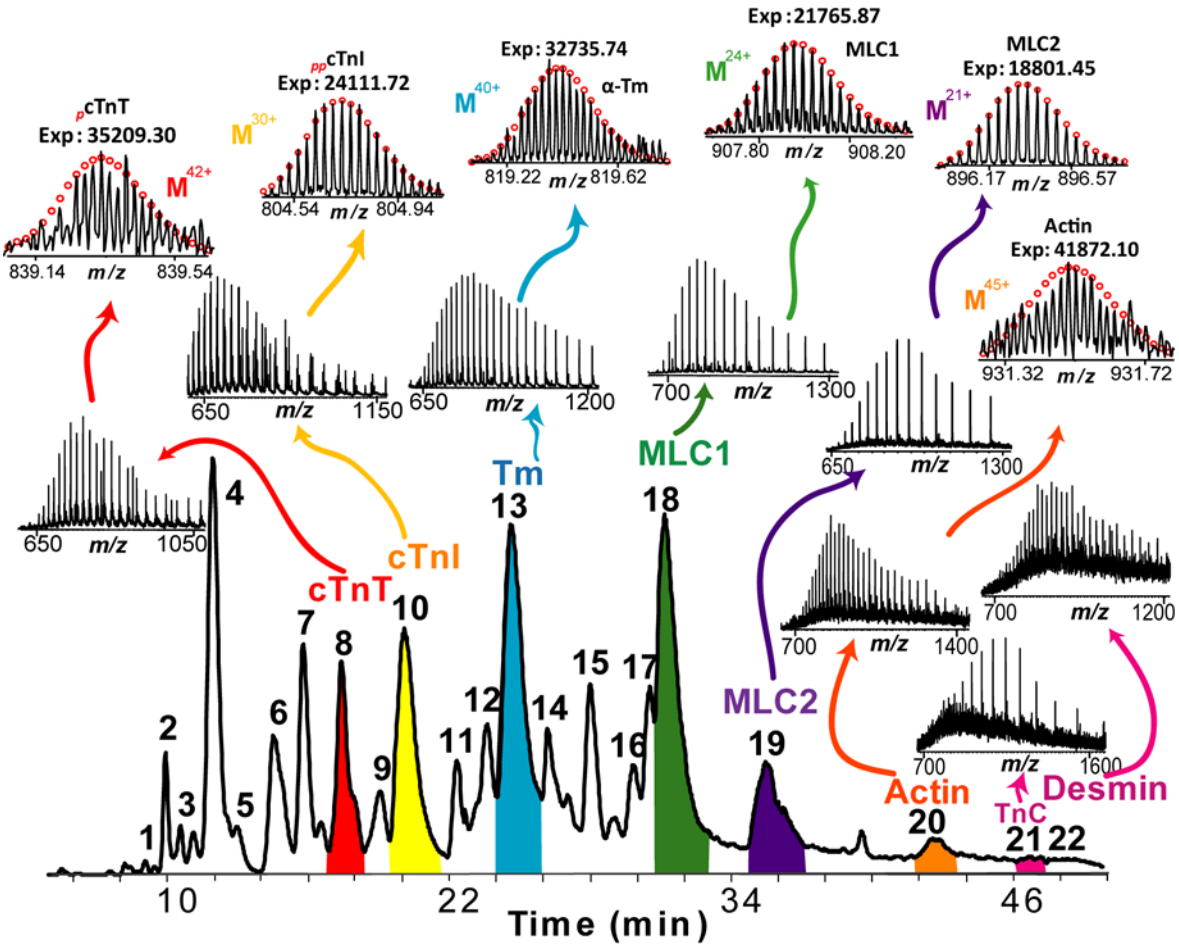

Fig. 4.4. LC/MS analysis of myofilament and associated proteins. Bottom, LC separation of myofilament and associated proteins with cTnT, cTnI, Tm, MLC1, MLC2, actin, TnC, and desmin highlighted. Top, MS detection of the myofilament proteins in both on-line low-resolution MS (shown in multiply charged ions) and off-line high-resolution MS (represented in a single charge state of un-modified ions) modes.

Table 4.2. Identification of proteins from LC/MS experiments as shown in Fig. 4.2. M_r (low res), the molecular weights of proteins derived from low-resolution LTQ/MS data. M_r (Exp) and M_r (Calc), the observed and Calc molecular weight from high-resolution MS. Key myofilament and associated proteins are highlighted in bold. cTnI, cardiac troponin I; cTnT, cardiac troponin T; TnC, cardiac troponin C; ENH2, enigma homolog isoform 2; Tm, tropomyosin; MLC1, myosin essential light chain; MLC2, myosin regulatory light chain; --, data not available.

Peak #	RT (min)	M_r (low res)	M_r (Exp)	M_r (Calc)	Error (ppm)	Protein identification
1	~8.5	4,964.5	4,962.52	4,962.49	5.4	Thymosin β-4
2	~10.0	9,392.9	9,389.83	9,389.82	0.6	ATPase inhibitor mitochondrial precursor
3	~10.7	9,258.3	9,255.93	9,255.92	1.5	Small muscular protein
4	~12.0	10,064.1	10,062.82	10,062.80	1.3	Cytochrome c oxidase subunit 6B1
5	~13.0	10,553.5	10,549.16	10,549.14	1.8	NADH dehydrogenase [ubiquinone] iron-sulfur protein 6, mitochondrial-like
6	~14.5	5,619.9	5,618.10	5,618.06	6.0	ATP synthase subunit ε, mitochondrial
7	~16.0	8,101.5	8,099.49	8,099.46	3.1	ATP synthase subunit e, mitochondrial
8	~17.5	35,139.6	35,129.75	--	0.8	**cTnT**
9	~19.0	25,830.3	25,825.44	25,825.38	2.3	**ENH2 (also known as PDZ-LIM5 isoform 2)**
10	~20.0	23,960.0	23,951.83	23,951.76	2.9	**cTnI**
11	~22.5	10,994.5	11,305.41	11,305.39	2.2	Histone H4-like
12	~23.7	7,934.6	7,933.30	7,933.27	3.0	Cytochrome b-c1 complex subunit Rieske, mitochondrial-like
13	~24.7	32,749.2	32,735.73	32,735.75	0.6	**Tm**
14	~26.3	13,793.2	13,788.60	13,788.55	3.1	Histone H2B type 2-E-like
15	~28.1	12,437.8	12,435.45	12,435.41	3.5	Cytochrome C oxidase subunit 5A, mitochondrial-like isoform 1
16	~30.0	20,922.2	20,920.43	20,920.37	2.7	ATP synthase subunit O, mitochondrial precursor
17	~30.7	15,042.0	15,037.89	15,037.83	4.4	Hemoglobin subunit α-like isoform 1
18	~31.2	21,771.9	21,765.87	--	--	**MLC1**
19	~35.5	18,804.8	18,801.45	18,801.4	2.7	**MLC2**
20	~43.1	41,876.7	41,872.09	--	--	**Actin**

21	~45.7	51,732.5	51,736.45	--	--	**Desmin**
22	~46.2	18,459.9	--	--	--	**TnC**

a

All proteins / gi|47522654|ref|NP_999080.1| ATP synthase subunit e, mitochondrial [Sus scrofa] / Peptide #1

Protein-Spectrum-Match for Spectrum #0

PrSM ID:	0	Scan(s):	1	Precursor charge:	1	Precursor m/z:	8096.477
Precursor mass:	8095.47	Adjusted precursor mass:	8095.45	Duplicate score:	73	Unique score:	46
E-value:	1.8E-22	P-value:	1.8E-21	Spectral FDR:	n/a	Protein mass:	8214.453

N-Terminal Methionine Excision(canonical)
A modification (or multiple modifications) on internal residue

M]V|P|P|V|Q|V|S|P|L|I|K|L|G R Y S|A|L|F|L|G|V|A|Y|G|A K R Y N Y L K P R A E E|E|
R|R I A A E E|K|K|K Q D|E|L K R I E R E|L A E A Q|E|D|S[12.04] T L K

b

All proteins / gi|335287018|ref|XP_003355253.1| PREDICTED: histone H2B type 2-E-like [Sus scrofa] / Peptide #1

Protein-Spectrum-Match for Spectrum #0

PrSM ID:	0	Scan(s):	1	Precursor charge:	1	Precursor m/z:	13781.507
Precursor mass:	13780.5	Adjusted precursor mass:	13780.532	Duplicate score:	86	Unique score:	48
E-value:	2.7E-21	P-value:	5.5E-22	Spectral FDR:	n/a	Protein mass:	13911.573

N-Terminal Methionine Excision(canonical)

M]P E P A K|S A|P A P K K G S K K|A V T K A Q K|K D|G K K R K R S R K E S Y S I
Y|V|Y K V L K Q V H|P D T G|I|S|S|K A M G|I|M|N|S|F|V|N|D|I|F E|R|I|A|G E|A S R
L A H|Y N K R S T I T S R E I Q T A V R L L L|P|G E|L|A K|H|A|V|S E|G T|K|A|V T
K|Y|T S S K

c

All proteins / gi|350586831|ref|XP_003482287.1| PREDICTED: cytochrome c oxidase subunit 5A, mitochondrial-like isoform 1 [Sus scrofa] / Peptide #1

Protein-Spectrum-Match for Spectrum #0

PrSM ID:	0	Scan(s):	1	Precursor charge:	1	Precursor m/z:	12429.437
Precursor mass:	12428.43	Adjusted precursor mass:	12428.39	Duplicate score:	77	Unique score:	49
E-value:	5.3E-23	P-value:	7.3E-25	Spectral FDR:	n/a	Protein mass:	16737.688

Unusual N-terminal modification

M L G A A V R R C S V A A A A V A R A S P R G L L H P T P T P G P A A A I Q S I
R C Y]S H G|S H E T D|E E F D A R W V T Y|F N K P D|I D|A W E L R K G M N T L|V|
G Y D|L V|P E|P K I I D|A A|L R A C R R L N D|F A S A V R I L|E V V K D|K A G P
H K E I|Y|P Y|V|I|Q E|L|R|P T|L|N|E|L|G|I|S|T|P E|E|L|G|L|D|K|V

d

All proteins / gi|350581842|ref|XP_003481132.1| PREDICTED: hemoglobin subunit alpha-like isoform 1 [Sus scrofa] / Peptide #1

Protein-Spectrum-Match for Spectrum #0

PrSM ID:	0	Scan(s):	1	Precursor charge:	1	Precursor m/z:	15029.807
Precursor mass:	15028.8	Adjusted precursor mass:	15028.805	Duplicate score:	110	Unique score:	72
E-value:	4.2E-35	P-value:	7.6E-35	Spectral FDR:	n/a	Protein mass:	15160.872

N-Terminal Methionine Excision(canonical)
A modification (or multiple modifications) on internal residue

M]V|L|S|A A D K A N V K A A|W G K V G G Q A G A H|G A E A L E R M F L G|F|P T T
K T Y F P H F|N|L|S H G S D|Q|V K|A H G Q K|V|A D|A|L|T|K A V G H|L D|D|L|P|G|A|
L|S|A|L|S|D|L H A H K L R V D|P V|N(-1.03) F K L L S H|C|L|L|V|T|L|A|A|H|H|P D|D F|N|P
S V|H|A|S L D|K|F|L|A N V|S T V|L|T|S|K Y R

e

All proteins / gi|350587964|ref|XP_003482524.1| PREDICTED: PDZ and LIM domain protein 5 isoform 2 [Sus scrofa] / Peptide #1

Protein-Spectrum-Match for Spectrum #2

PrSM ID:	2	Scan(s):	3	Precursor charge:	1	Precursor m/z:	25810.607
Precursor mass:	25809.6	Adjusted precursor mass:	25809.455	Duplicate score:	101	Unique score:	61
E-value:	2.6E-26	P-value:	6.5E-25	Spectral FDR:	n/a	Protein mass:	25883.396

N-Terminal Methionine Excision(canonical) and N-Terminal Acetylation
A modification (or multiple modifications) on internal residue

M]S(42.01) N Y S V S L V G P A P W G F R L Q G G K D F N M P L T I S|S L K|D G G K A S
Q|A N|V R I G D|V V L|S I D G I S A Q|G(15.09) M T H L E A Q N K I K G S T G S L N|M T
L Q R|A S A T P K P E P V P V Q|K P T V T|S V|C A E T A Q|E L A E G Q R R G S|Q
G|D|S|K Q|L|N|G K I P P K|R P P R|K H I V E R|N|T E F Y H I P T H|S D|A|S|K K R|
L M|E|D T E|D W|R P R|T G T T Q|S|R S F R|I L A Q I T G T E|H L K E S|E T|D|N T|
K|K A|K|E K I P L H V F S P K Y|T|K L|R D W H|H E V S A R A L N V Q

Fig. 4.5. Identification of proteins by high-resolution MS/MS with MS-Align+ algorithm. The peak numbers representing different fractions collected are shown in **Fig. 4.2**. The representative protein identifications are shown. The full list of identified proteins is shown in **Table 4.2**. (A) Peak #7 was identified as mitochondrial ATP synthase subunit e, with N-terminal Met loss and a potential modification (+12.04 Da) in the C-terminal 4 residues (STLK). (B) Peak#14 was identified as histone H2B type 2-E-like with N-terminal Met loss. (C) Peak #15 was identified as cytochrome *c* oxidase subunit 5A, mitochondrial-like isoform 1 with an unidentified N-terminal modification. (D) Peak #17 was identified as hemoglobin subunit α-like isoform 1 with N-terminal

Met loss and a potential modification on one of the internal residues (NFKLLSH). (E) Peak # 9 was identified as PDZ-LIM domain protein 5 isoform 2, also known as enigma homolog isoform 2 (ENH2). MS-Align+ is a fast algorithm for top-down protein identification based on spectral alignment that enables searches for PTMs. PrSM ID is the identification number of a protein-spectrum-match reported by MS-Align+. The E-value of a PrSM describes the number of hits one can "expect" to see by chance when searching the spectrum against a protein database with the same size to the target database. The P-value of a PrSM stands for the probability that the match between the spectrum and a random protein has a similarity score no less than that the score of the PrSM.

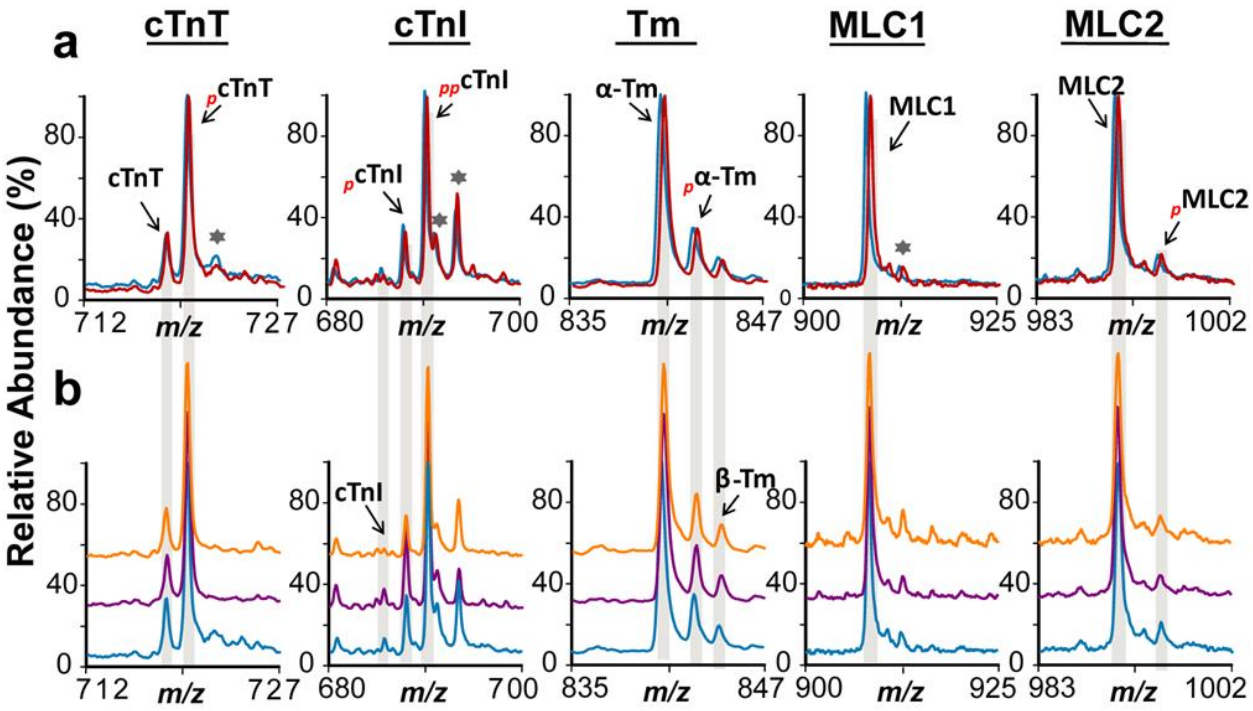

Fig. 4.6. High reproducibility of the MS method evaluated by technical replicates. Representative MS data are shown here. (A) Overlay of low-resolution mass spectra for two injection replicates from the same TFA extraction. (B) Three extraction replicates (replicates of different TFA extractions from the same tissue) were aligned vertically (note the baseline of the top two mass spectra were elevated intentionally for better visualization). Proteins were extracted from CON myocardium. Mono- and bis-phosphorylated proteins are labeled with a "$_p$" and "$_{pp}$", respectively. Stars indicate non-covalent phosphoric acid adducts.

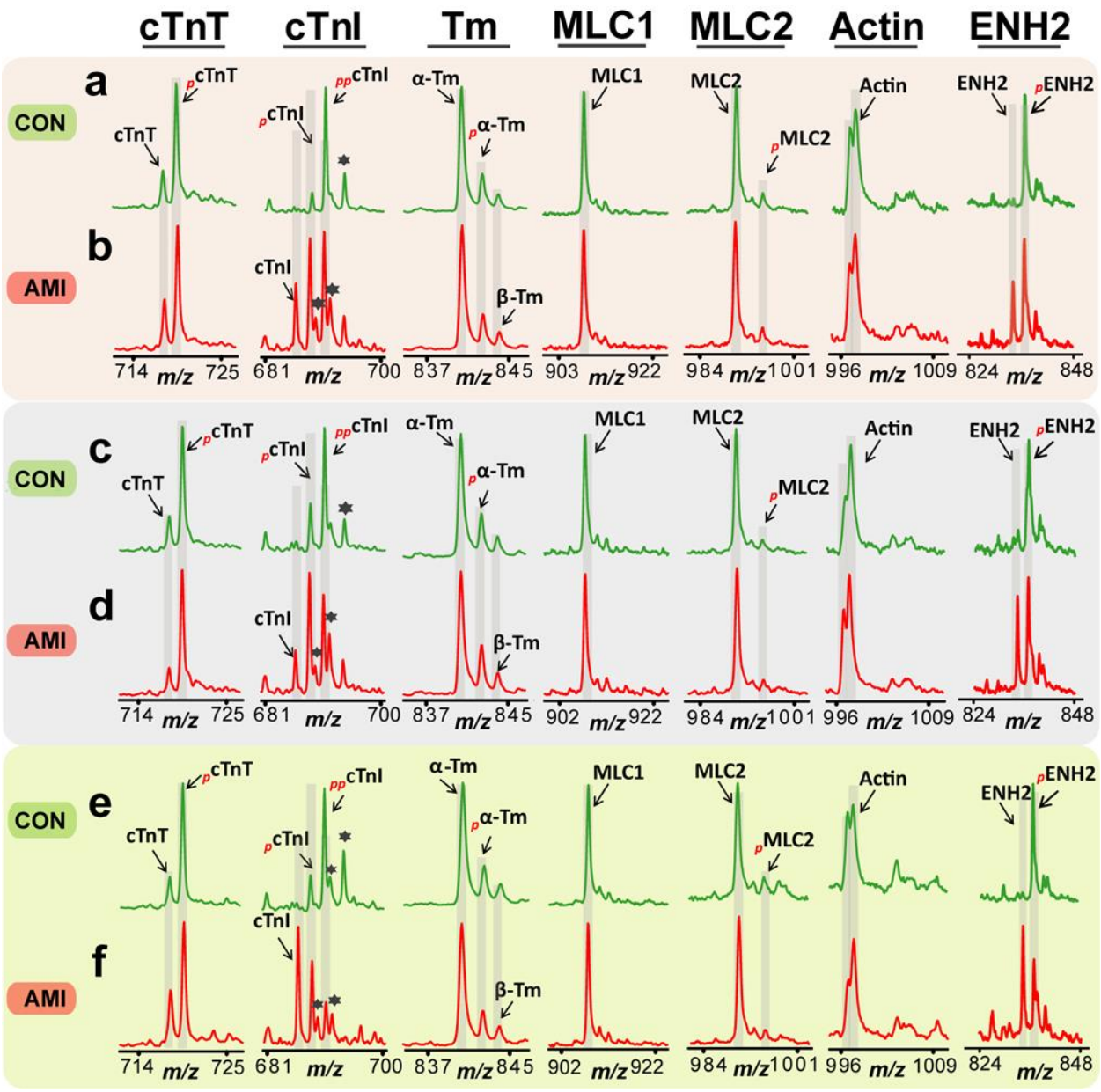

Fig. 4.7. Rapid MS profiling of key myofilament and associated proteins by on-line LC/MS analysis. Comparison of mass spectra of cTnT, cTnI, Tm, MLC1, MLC2, actin, and ENH2 from CON (A, C, E) and AMI (B, D, F) myocardium, respectively. Similar MS profiles were observed among biological replicates showcasing the high reproducibility of our method. Significant differences were detected for cTnI, MLC2, and ENH2 phosphorylation in CON and AMI hearts.

Mono- and bis-phosphorylated proteins are labeled with a "$_p$" and "$_{pp}$", respectively. Stars indicate non-covalent phosphoric acid adducts.

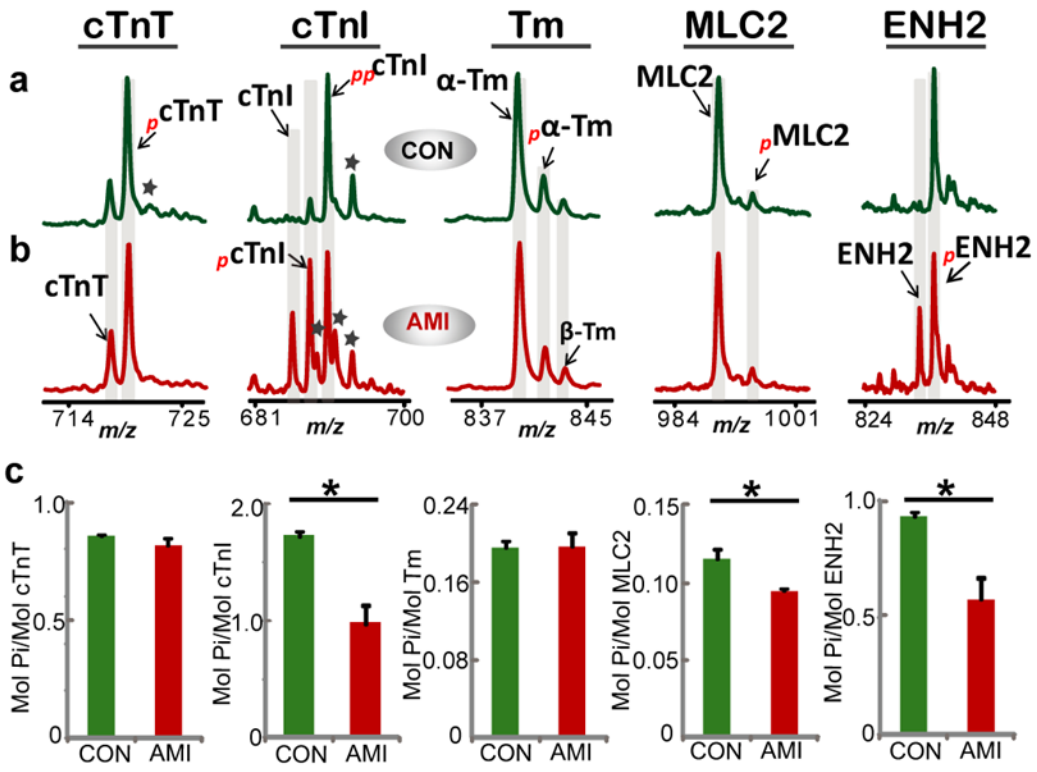

Fig. 4.8. Relative quantification of phosphorylation in myofilament and associated protein from CON and AMI swine myocardium. Representative low-resolution mass spectra showing cTnT, cTnI, Tm, MLC2, and ENH2 from CON (A) and AMI (B) myocardium, respectively. The total amount of phosphorylation of cTnT, cTnI, Tm, MLC2, and ENH2 is shown in (C). All measurements were performed with three animals per group. Two technical replicates were analyzed for each biological replicate. The data are represented as the mean peak area ± SEM. *$p < 0.05$. Mono- and bis-phosphorylated proteins are labeled with a "$_p$" and "$_{pp}$", respectively. Stars indicate non-covalent phosphoric acid adducts.

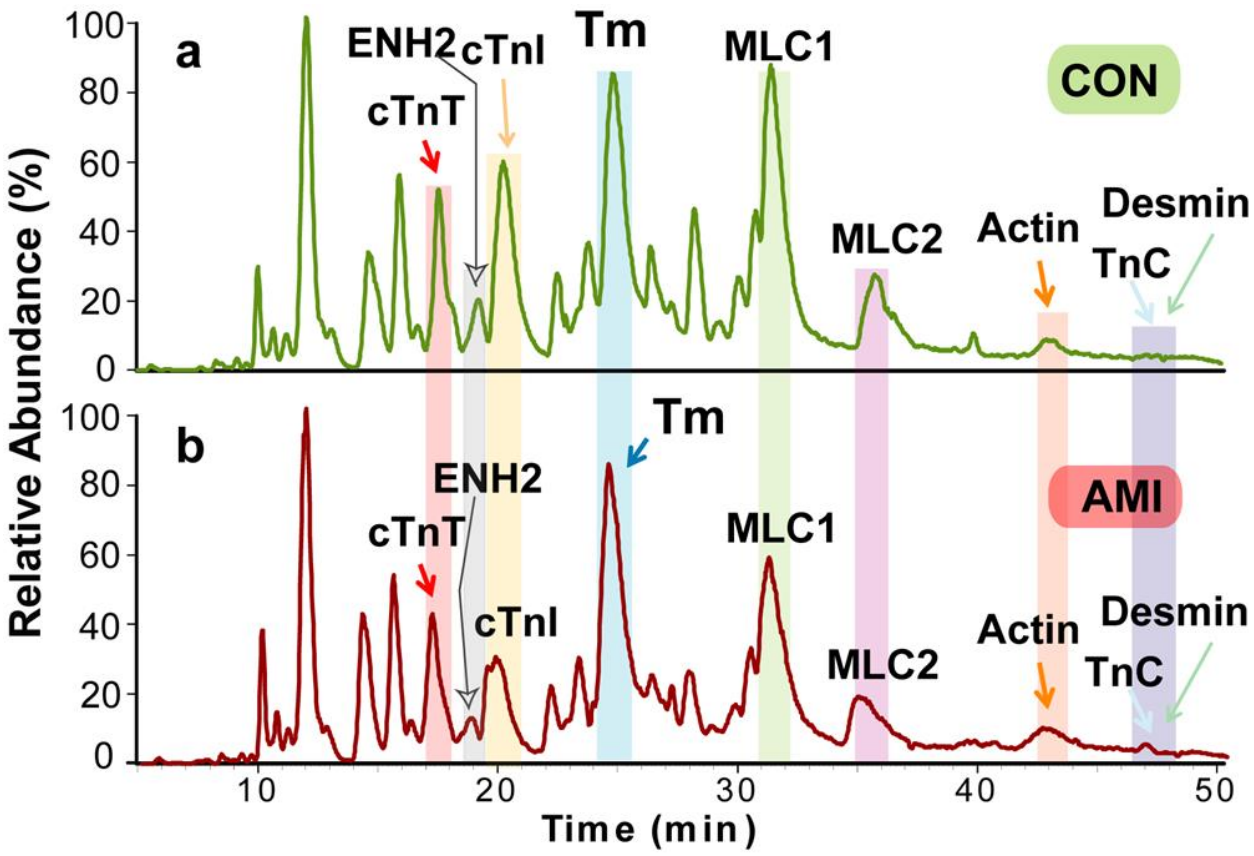

Fig. 4.9. Comparison of LC separation of myofilament and associated proteins extracted from CON (A) and AMI (B) swine hearts. Only representative cases are shown. cTnT, ENH2, cTnI, Tm, MLC1, MLC2, actin, TnC, and desmin are highlighted.

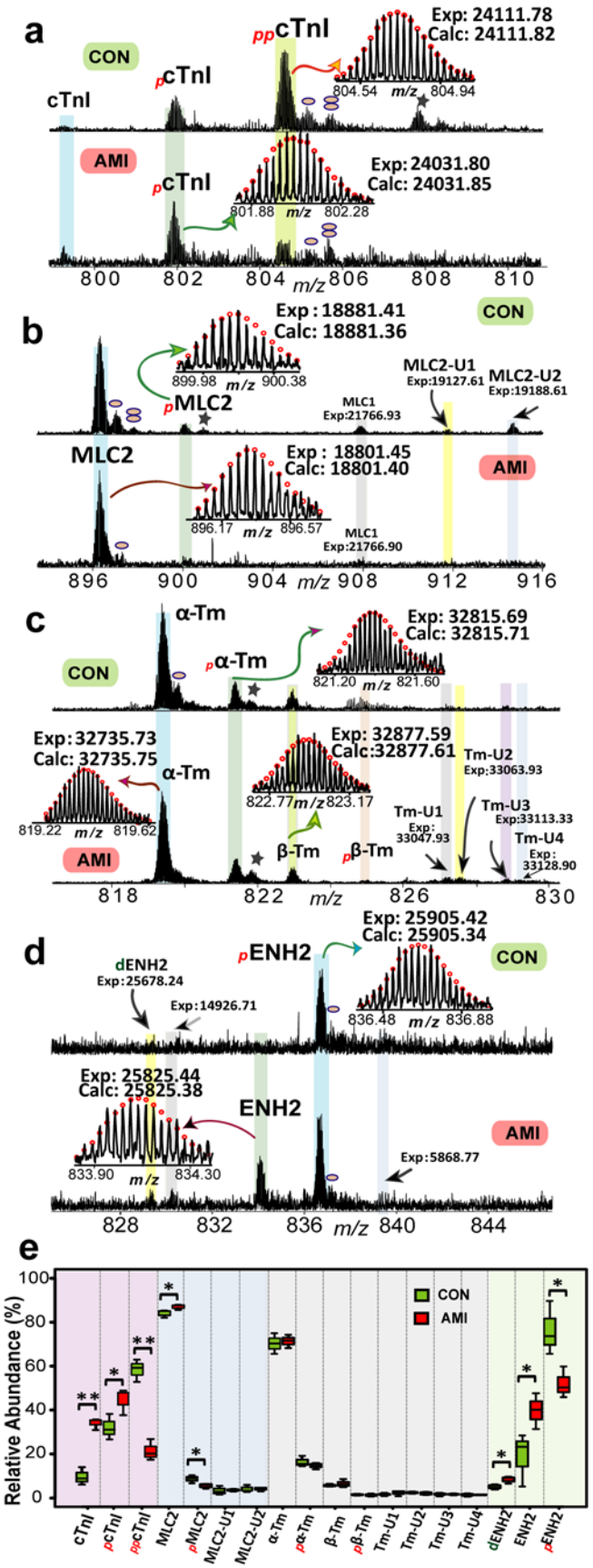
a
CON
cTnI
ppcTnI
pcTnI
Exp: 24111.78
Calc: 24111.82
804.54 m/z 804.94
AMI
pcTnI
Exp: 24031.80
Calc: 24031.85
801.88 m/z 802.28
800 802 804 m/z 806 808 810
b
CON
Exp : 18881.41
Calc: 18881.36
899.98 m/z 900.38
pMLC2
MLC2-U1
Exp:19127.61
MLC2-U2
Exp:19188.61
MLC1
Exp:21766.93
MLC2
Exp : 18801.45
Calc: 18801.40
AMI
896.17 m/z 896.57
MLC1
Exp:21766.90
896 900 904 m/z 908 912 916
c
α-Tm
pα-Tm
CON
Exp: 32815.69
Calc: 32815.71
821.20 m/z 821.60
Exp: 32735.73
Calc: 32735.75
α-Tm
819.22 m/z 819.62
AMI
Exp: 32877.59
Calc:32877.61
822.77 m/z 823.17
Tm-U2
Exp:33063.93
Tm-U1
Exp: 33047.93
Tm-U3
Exp:33113.33
Tm-U4
Exp: 33128.90
β-Tm
pβ-Tm
818 822 m/z 826 830
d
dENH2
Exp:25678.24
Exp:14926.71
pENH2
Exp: 25905.42
Calc: 25905.34
CON
836.48 m/z 836.88
Exp: 25825.44
Calc: 25825.38
ENH2
AMI
Exp:5868.77
833.90 m/z 834.30
828 832 836 m/z 840 844
e
Relative Abundance (%)
0 20 40 60 80 100
CON
AMI
cTnI
pcTnI
ppcTnI
MLC2
pMLC2
MLC2-U1
MLC2-U2
α-Tm
pα-Tm
β-Tm
pβ-Tm
Tm-U1
Tm-U2
Tm-U3
Tm-U4
dENH2
ENH2
pENH2

Fig. 4.10. High-resolution MS for qualitative and quantitative analysis of myofilament and associated protein proteoforms. (A-D) Representative high-resolution mass spectra of cTnI (A), MLC2 (B), Tm (C), and ENH2 (D) from CON (top) and AMI (bottom) myocardium, respectively. Circles represent the theoretical isotopic abundance distribution of the isotopomer peaks corresponding to the assigned mass. Single and double ellipses represent single and double oxidations, respectively. Stars represent non-covalent phosphoric acid adducts. (E) Relative quantification of cTnI, Tm, MLC2, and ENH2 protein proteoforms. All measurements were performed with three animals per group. Two technical replicates were performed per biological replicate. Box, median and interquartile range (25%, 75%). Whiskers, minimum and maximum values. $*p < 0.05$, $**p < 0.001$.

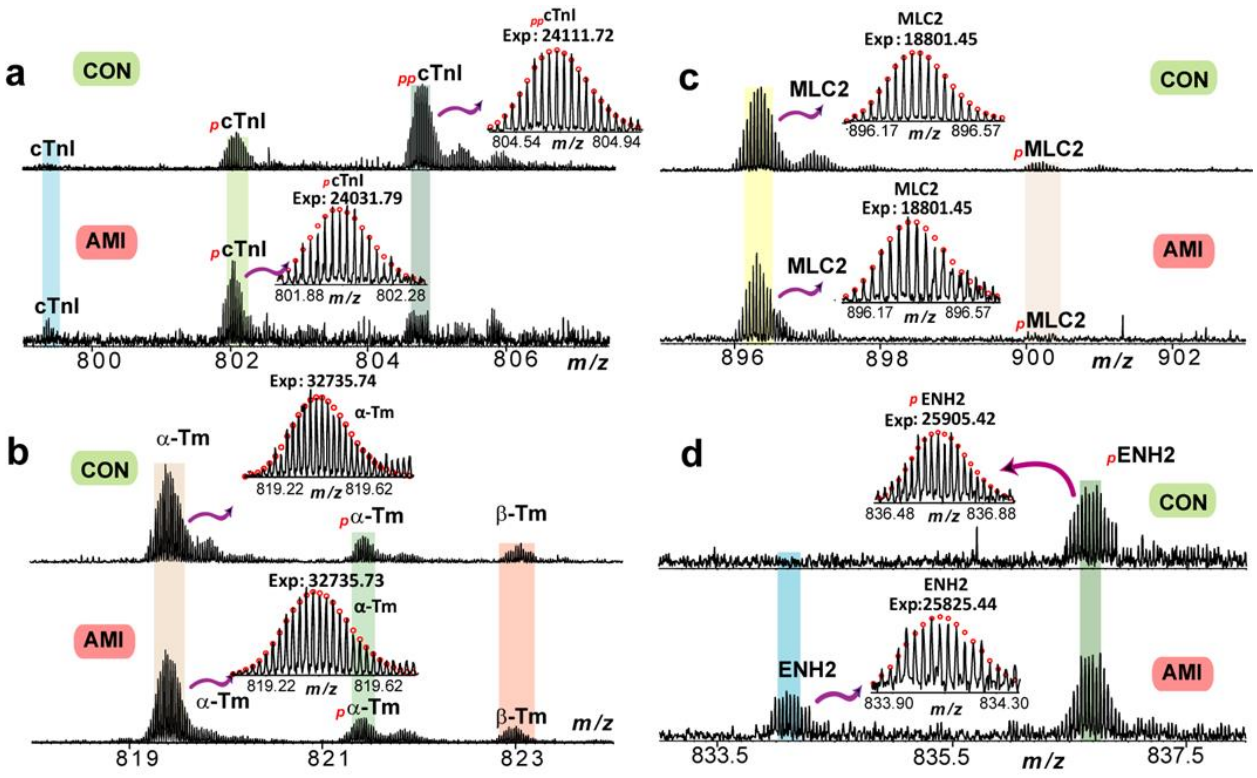

Fig. 4.11. High-resolution mass spectra of phosphorylated myofilament and associated proteins. A comparison of representative mass spectra for cTnI (A), Tm (B), MLC2 (C), and ENH2 (D) extracted from CON and AMI swine hearts. Mono- and bis-phosphorylated proteins are labeled with a "$_p$" and "$_{pp}$", respectively. Circles, the theoretical isotopic abundance distribution of the isotopomer peaks corresponding to the assigned mass. Exp, observed most abundant molecular weight.

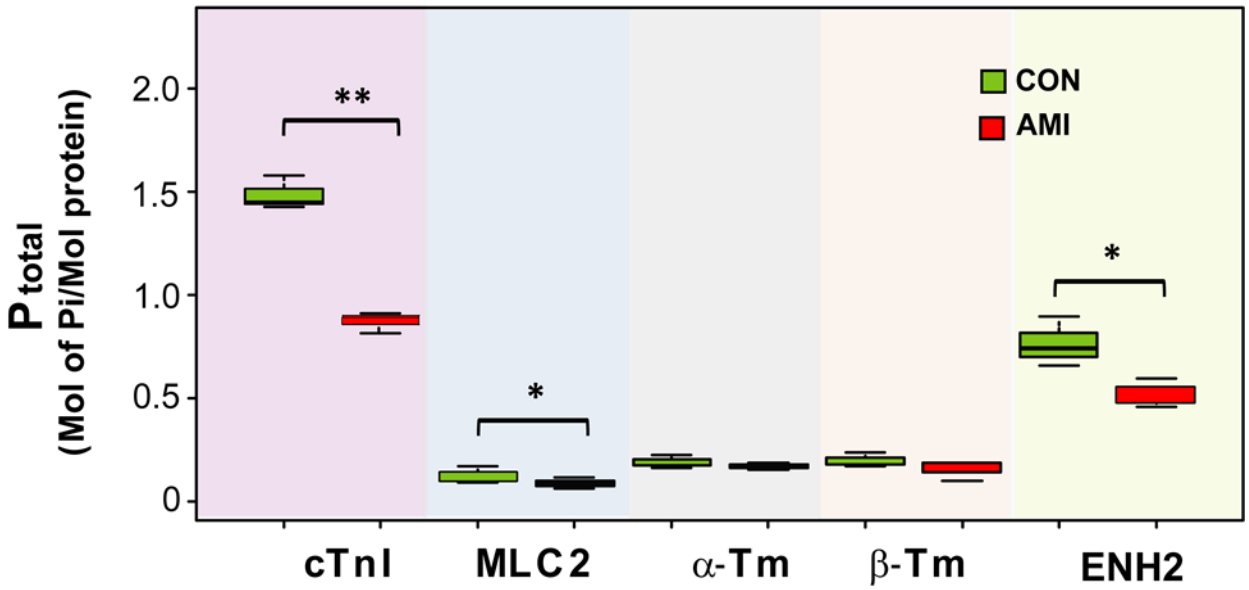

Fig. 4.12. Quantification of myofilament and associated protein phosphorylation based on high-resolution MS analysis. Quantification of the total phosphorylation level of cTnI, MLC2, α-Tm, β-Tm, and ENH2 extracted from CON and AMI hearts. All measurements are based on data from three animals per group. Two technical replicates were analyzed per biological replicate. The bar graph data are represented as the mean peak area ± SEM. Box, median and interquartile range (25%, 75%). Whiskers, minimum and maximum values. *$p < 0.05$. **$p < 0.001$.

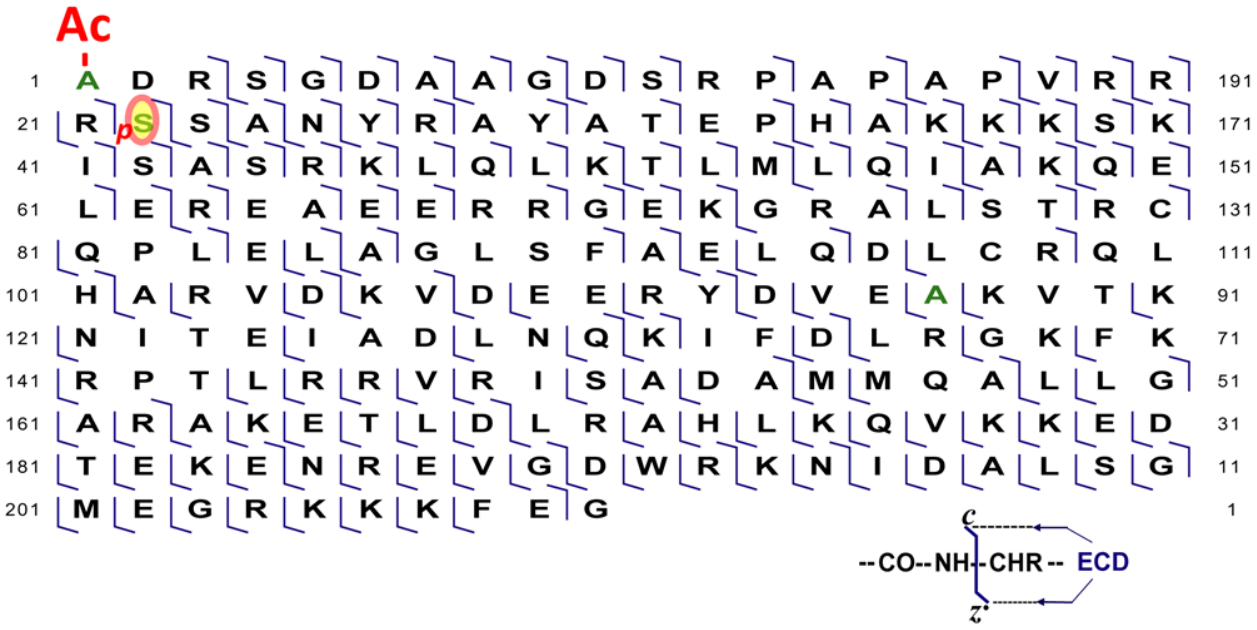

Fig. 4.13. Comprehensive characterization of $_p$cTnI by high-resolution ECD MS/MS. Fragmentation map for $_p$cTnI based on 5 ECD spectra. The phosphorylation site is labeled with "*p*". "Ac-" denotes acetylation. Both MS and MS/MS data matches best with the sequence of swine cTnI (UniProtKB/Swiss-Prot, A5X5T5, TNNI3_pig) after considering the deletion of N-terminal Met, acetylation at new N-terminus, a single amino acid polymorphism (V116A), and phosphorylation at Ser22 as we reported previously [205].

Fig. 4.14. Comprehensive sequencing by ECD pinpointed the phosphorylation sites of $_{pp}$cTnI at Ser22/23 (A), $_{p}$MLC2 at Ser14 (B), and $_{p}$ENH2 at Ser118 (C). Ac- represents acetylation and "$_p$" stands for phosphorylation. Phosphorylation sites are highlighted by circles (A-C). Amino acid polymorphism (Ser72Cys) is highlighted with a heptagon (C).

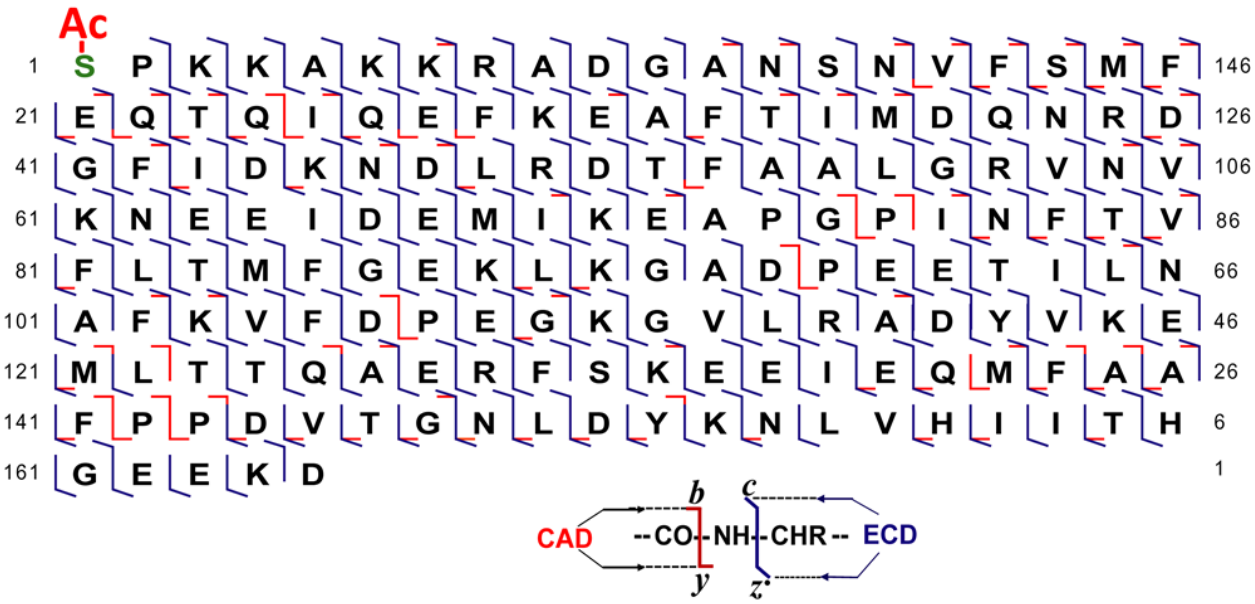

Fig. 4.15. Comprehensive sequencing of MLC2. Fragmentation maps of un-phosphorylated MLC2 based on 7 ECD and 3 CAD spectra. A total of 51 *b* ions, 52 *y* ions, 129 *c* ions and 131 *z*· ions were detected representing 158 out of 164 bond cleavages. "Ac-" denotes acetylation; MS/MS data matches best with the uncharacterized sequence of swine MLC2 (UniProtKB/Swiss-Prot, F6PSL2_PIG) after considering the acetylation at the N-terminus.

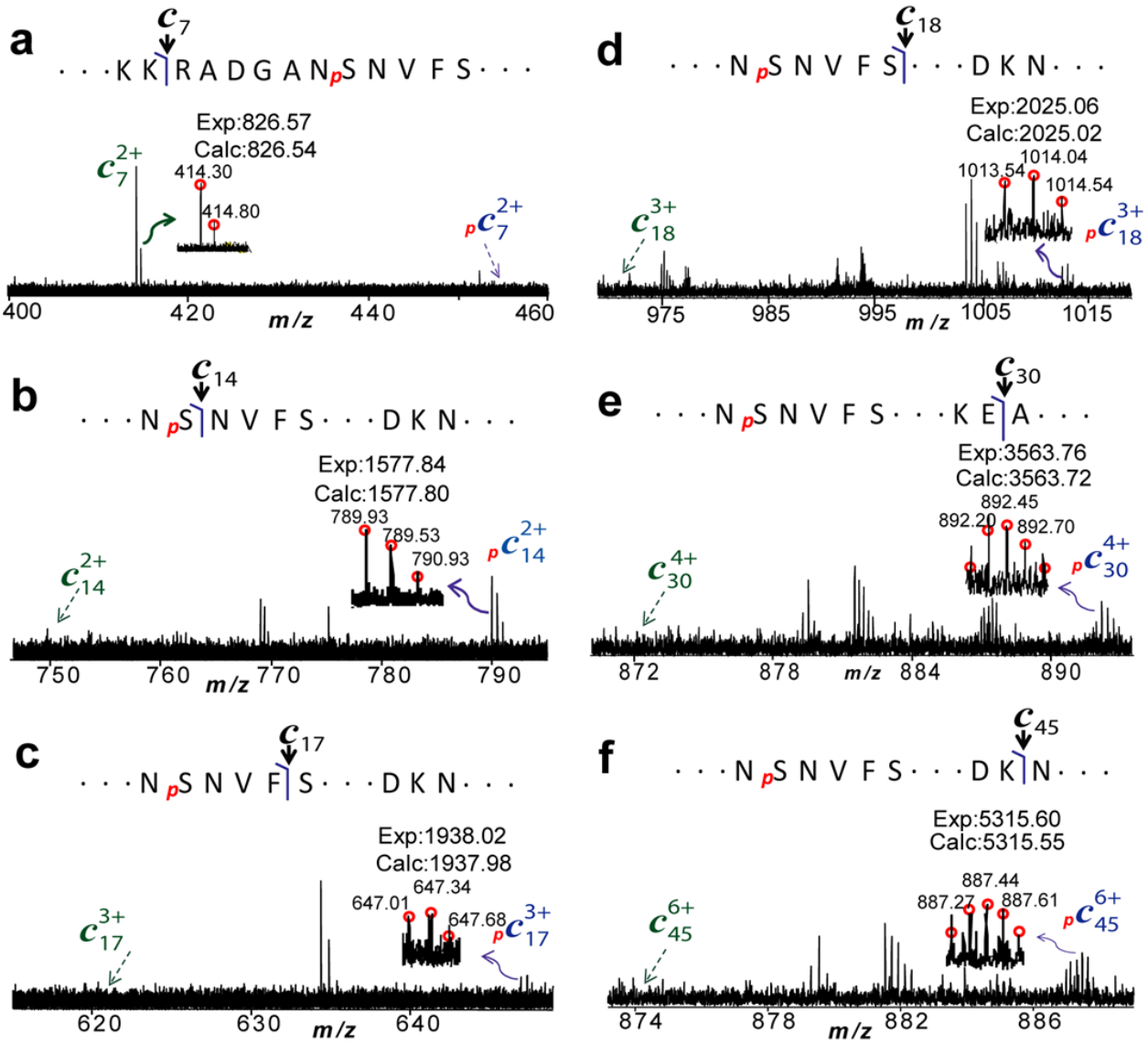

Fig. 4.16. Mapping the site of phosphorylation in MLC2 using ECD. (A-F) Representative ions from ECD spectra for determination of the phosphorylation site in mono-phosphorylated MLC2 ($_p$MLC2). "$_p$" represents the mono-phosphorylation site at Ser14, and N-terminus of $_p$MLC2 is acetylated.

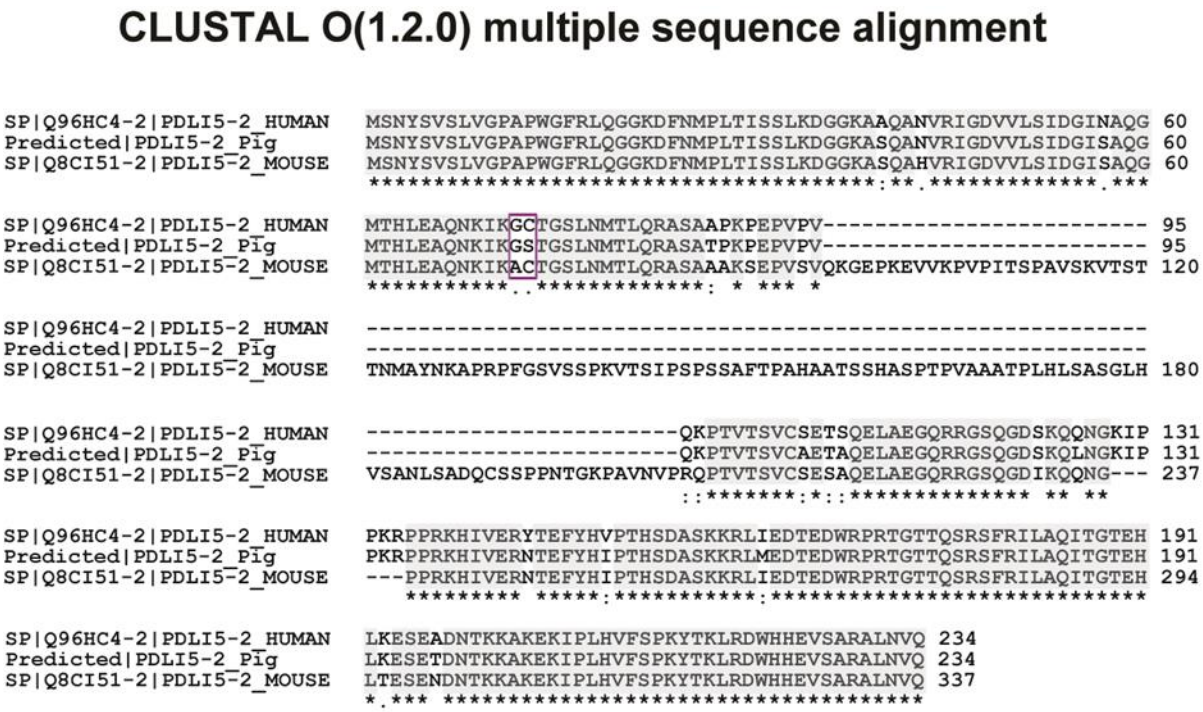

Fig. 4.17. Sequence alignment of ENH2 from different species. The region containing the potential amino acid substitutions between human, pig, and mouse based on the MS/MS data are marked in purple. Asterisks denote conserved amino acids. Human (Q96HC4-2) and mouse (Q8CI51-2) ENH2 sequences are retrieved from the Swiss-Prot database. The swine ENH2 sequence is predicted based on the genomic sequence in pig database (Sscrofa10.2) from NCBI. ENH2 is also known as PDZ-LIM domain protein 5 isoform 2—referred to as PDLI5-2_Pig in the figure.

a
1 M S N Y S V S L V G P A P W G F R L Q G 215
21 G K D F N M P L T I S S L K D G G K A S 195
41 Q A N V R I G D V V L S I D G I S A Q G 175
61 M T H L E A Q N K I K G S T G S L N M T 155
81 L Q R A S A T P K P E P V P V Q K P T V 135
101 T S V C A E T A Q E L A E G Q R R G S Q 115
121 G D S K Q L N G K I P P K R P P R K H I 95
141 V E R N T E F Y H I P T H S D A S K K R 75
161 L M E D T E D W R P R T G T T Q S R S F 55
181 R I L A Q I T G T E H L K E S E T D N T 35
201 K K A K E K I P L H V F S P K Y T K L R 15
221 D W H H E V S A R A L N V Q 1
b
Ac
1 S N Y S V S L V G P A P W G F R L Q G G 214
21 K D F N M P L T I S S L K D G G K A S Q 194
41 A N V R I G D V V L S I D G I S A Q G M 174
61 T H L E A Q N K I K G S T G S L N M T L 154
81 Q R A S A T P K P E P V P V Q K P T V T 134
101 S V C A E T A Q E L A E G Q R R G S Q G 114
121 D S K Q L N G K I P P K R P P R K H I V 94
141 E R N T E F Y H I P T H S D A S K K R L 74
161 M E D T E D W R P R T G T T Q S R S F R 54
181 I L A Q I T G T E H L K E S E T D N T K 34
201 K A K E K I P L H V F S P K Y T K L R D 14
221 W H H E V S A R A L N V Q 1
c
Ac
1 S N Y S V S L V G P A P W G F R L Q G G 214
21 K D F N M P L T I S S L K D G G K A S Q 194
41 A N V R I G D V V L S I D G I S A Q G M 174
61 T H L E A Q N K I K G C T G S L N M T L 154
81 Q R A S A T P K P E P V P V Q K P T V T 134
101 S V C A E T A Q E L A E G Q R R G S Q G 114
121 D S K Q L N G K I P P K R P P R K H I V 94
141 E R N T E F Y H I P T H S D A S K K R L 74
161 M E D T E D W R P R T G T T Q S R S F R 54
181 I L A Q I T G T E H L K E S E T D N T K 34
201 K A K E K I P L H V F S P K Y T K L R D 14
221 W H H E V S A R A L N V Q 1
d
Ac
1 S N Y S V S L V G P A P W G F R L Q G G 214
21 K D F N M P L T I S S L K D G G K A S Q 194
41 A N V R I G D V V L S I D G I S A Q G M 174
61 T H L E A Q N K I K G C T G S L N M T L 154
81 Q R A S A T P K P E P V P V Q K P T V T 134
101 S V C A E T A Q E L A E G Q R R G pS Q G 114
121 D S K Q L N G K I P P K R P P R K H I V 94
141 E R N T E F Y H I P T H S D A S K K R L 74
161 M E D T E D W R P R T G T T Q S R S F R 54
181 I L A Q I T G T E H L K E S E T D N T K 34
201 K A K E K I P L H V F S P K Y T K L R D 14
221 W H H E V S A R A L N V Q 1

Fig. 4.18. MS/MS for sequence characterization of mono-phosphorylated ENH2 ($_p$ENH2) and localization of the phosphorylation site. (A) Fragmentation assignments are made to the predicted swine ENH2 sequence (PDLI5-2) from NCBI pig database (Sscrofa10.2) without any modifications. Note that only 50 *z*· ions matched the unmodified ENH2 sequence. (B) Fragment assignments are made to predicted swine ENH2 sequence with deletion of the N-terminal Met and acetylation of the new N-terminus. 22 *c* ions were assigned in addition to 50 *z*· ions. (C) Fragment assignments are made based on the predicted swine ENH2 sequence with acetylation of the new N-teminus and one amino acid substitution (Ser72→Cys72). 30 *c* ions were assigned in addition to 50 *z*· ions. (D) Fragment assignments are made to the predicted ENH2 sequence with acetylation of the new N-teminus, one amino acid substitution and localization of the phosphorylation site at Ser118. Note that a total of 58 *c* ions and 71 *z*· ions were assigned. The amino acid substitution is highlighted in orange and "***p***" represents phosphorylation site at Ser118. Thus, we fully characterized the sequence of $_p$ENH2 with deletion of N-terminal Met, acetylation of the new N-terminus, an amino acid substitution at Ser72Cys, and phosphorylation site at Ser118. Phosphorylation sites are highlighted by circles. Amino acid polymorphism (Ser72Cys) is highlighted in heptagon.

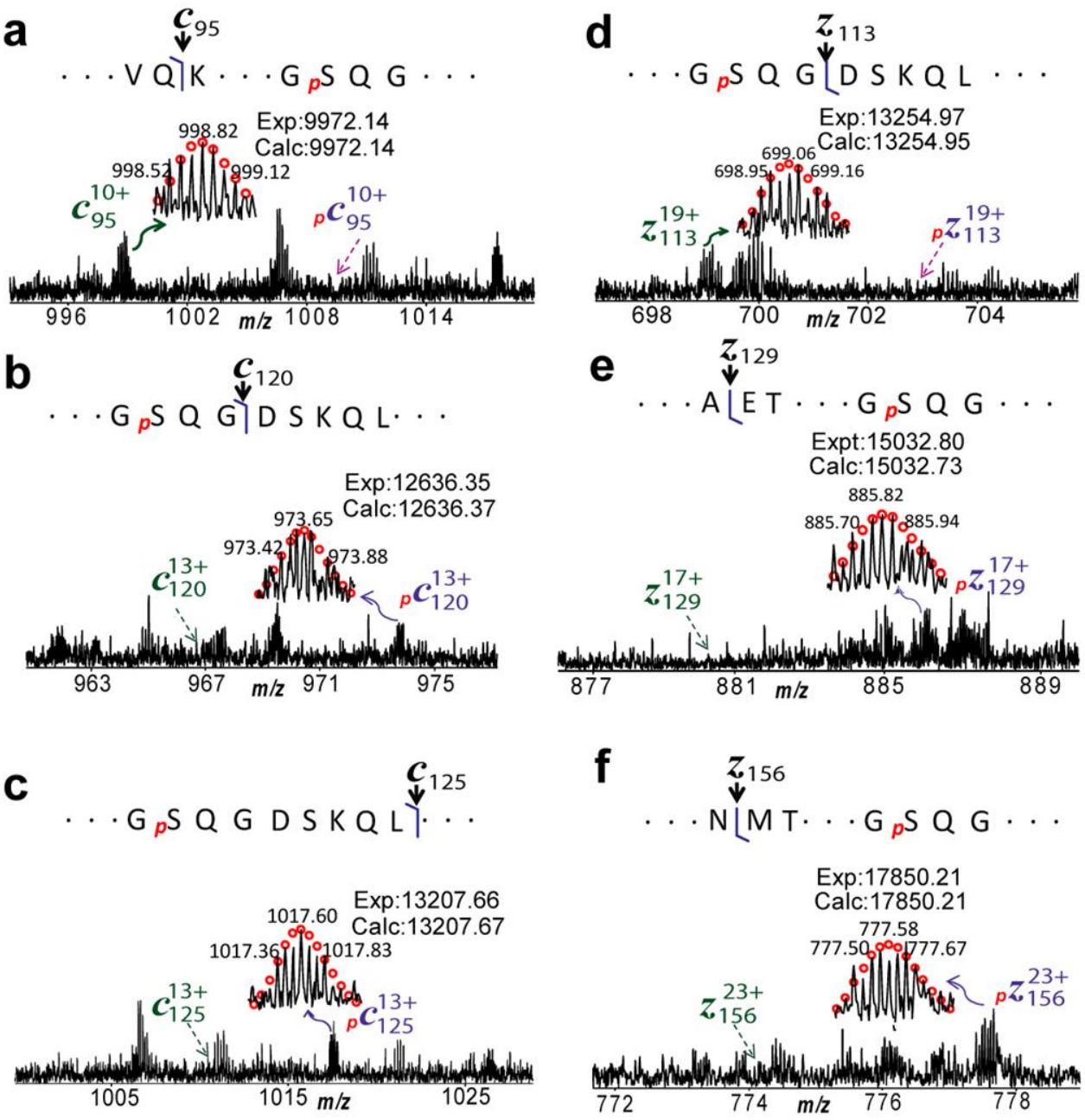

Fig. 4.19. MS/MS mapping of the phosphorylation site in swine ENH2. (A-F) Representative MS/MS spectra of *c* and *z*· ions from ECD spectra of mono-phosphorylated ENH2. The site of mono-phosphorylation was localized to Ser118. The assignment of fragment ions was made based on the predicted sequence of swine ENH2 (PDLI5-2) from NCBI pig database (Sscrofa10.2) with

deletion of the N-terminal Met, acetylation of the new N-terminus, and one amino acid substitution (Ser72→Cys72).

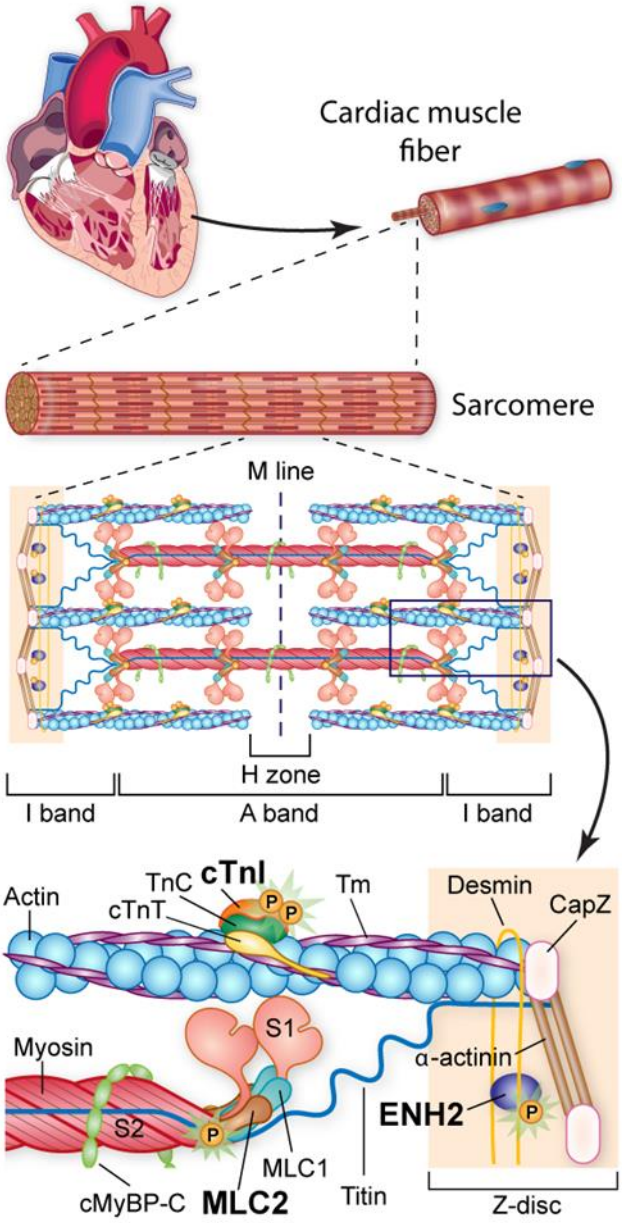

Fig. 4.20. Schematic of myofilament and Z-disc proteins in the cardiac sarcomere with the phosphorylation of cTnI, MLC2, and ENH2 highlighted. Only relevant proteins in the sarcomere, the basic contractile unit of cardiac muscle, are shown.

Fig. 4.21. Protein sequence alignment of MLC2 from different species. Clustal Omega (version 1.2.0) multiple sequence alignment among ventricles of rat (P08733), mouse (P51667), human (P10916) and pig (F6PSL2) from UniProtKB/Swiss-Prot database. Highlighted areas marked in purple for amino acid polymorphisms between human and pig, whereas those in blue for polymorphisms among the four different species.

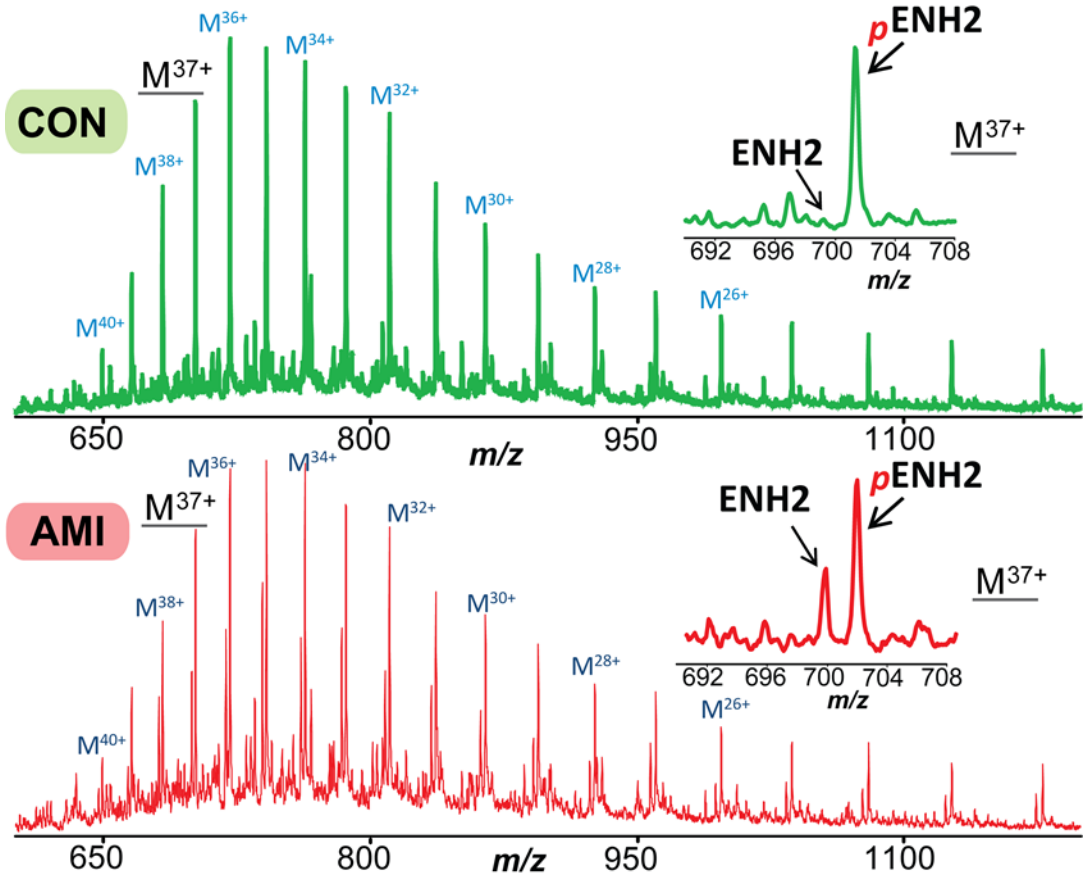

Fig. 4.22. Comparable charge state distributions of ENH2 despite different phosphorylation levels between CON and AMI. Main spectra: Representative full charge state profiles of ENH2 from on-line LC/MS analysis of myofilament sub-proteome extracted from CON and AMI hearts respectively. Insets, zoom-in spectra of a single charge state (M^{37+}) of ENH2 showing the difference in phosphorylation levels of ENH2 between AMI and CON.

CHAPTER 5 – DELETION OF THE Z-DISC PROTEIN ENIGMA HOMOLOG DEPRESSES CROSS-BRIDGE CYCLING KINETICS IN MOUSE MYOCARDIUM

Zachery R. Gregorich[a,b], Jitandra R. Patel[a,c], Wenxuan Cai[a,b], Rachel Heurer[a], Ziqing Lin[a,d], Richard L. Moss[a,c,d], Ying Ge[a,b,c,d]

[a]Department of Cell and Regenerative Biology, University of Wisconsin-Madison, 1111 Highland Ave., Madison, WI 53705, USA

[b]Molecular and Cellular Pharmacology Training Program, University of Wisconsin-Madison, 1111 Highland Ave., Madison, WI 53705, USA

[c]University of Wisconsin-Madison Cardiovascular Research Center, University of Wisconsin-Madison, 1111 Highland Ave., Madison, WI 53705, USA

[d]Human Proteomics Program, University of Wisconsin-Madison, 1111 Highland Ave., Madison, WI 53705, USA

Abstract

Enigma homolog (ENH) belongs to the PDZ/LIM protein family and localizes to the Z-discs in cardiac muscle. The results of a recent study have shown that cardiac-specific ablation of ENH isoforms results in impaired myocardial contractility and dilated cardiomyopathy; however, whether ENH is involved in the modulation of cardiac contractile function remains unclear. Here we sought to address this question using skinned trabeculae from $ENH^{+/+}$, $ENH^{+/-}$, and $ENH^{-/-}$ mice. The steady-state mechanical properties of trabeculae isolated from $ENH^{+/+}$, $ENH^{+/-}$, and $ENH^{-/-}$ mice did not differ. Conversely, a significant depression in cross-bridge cycling kinetics, indicated by a decrease in the apparent rate constant of force redevelopment (k_{tr}), was observed in $ENH^{+/-}$ and $ENH^{-/-}$ trabeculae. Alterations in the expression of β-myosin heavy chain (MHC) or in the expression/phosphorylation of thin/thick filament regulatory proteins could not account for this phenomenon, at least in $ENH^{+/-}$ mouse myocardium, indicating that changes in the expression, or potentially the phosphorylation, of ENH isoforms are likely responsible. Top-down proteomics analysis showed that neither the expression nor phosphorylation of ENH3b, a short isoform of ENH that lacks the C-terminal LIM domains, play a direct role in setting the kinetics of force redevelopment in mouse myocardium. Collectively, the results presented herein suggest that the ENH protein has a role in regulating cross-bridge cycling kinetics via a mechanism that is independent of changes in the expression or phosphorylation of contractile proteins and ENH3b. Although the specific ENH isoform(s) responsible could not be determined, these findings provide the first evidence indicating that ENH has a role in setting cross-bridge cycling kinetics in mouse myocardium.

5.1 Introduction

Sarcomeres are the most basic contractile units of striated muscle, and are composed of interdigitating actin-based thin and myosin-based thick filaments, flanked on either side by protein dense structures known as Z-discs (alternatively Z-lines or Z-bands). Although the central role of the myofilaments, which constitute the contractile apparatuses, in muscle function has been appreciated for nearly seven decades [1], the contribution of the Z-discs to muscle biology has, until recently, been largely overlooked. Long thought to merely aid force transmission via anchoring of the anti-parallel actin filaments from adjacent sarcomeres, the importance of the Z-discs in muscle biology is underscored by a growing list of identified mutations in Z-disc proteins that have been linked to cardiac and skeletal muscle myopathies [94, 95].

The Enigma Homolog (ENH) protein is a member of the Enigma subfamily of the larger PDZ/LIM family of proteins, which also contains Enigma and Cypher/ZASP/Oracle [99]. A total of nine isoforms, which arise as a consequence of alternative splicing of the ENH transcript, have been identified to date [109, 114, 116, 334]. These isoforms are sub-divided into two groups—the so-called "short" isoforms, which differ from "long" isoforms in that they contain the N-terminal PDZ domain yet lack the three C-terminal LIM domains [114, 116]. Up to seven of these isoforms (five long and two short isoforms) may be expressed in the heart [116], with expression patterns that are developmentally-regulated [126]. The N-terminal PDZ domain, which is present in all ENH isoforms, binds α-actinin and promotes localization of ENH isoforms to the Z-discs in cardiac muscle [114]. On the other hand, the LIM domains of ENH have been shown to bind a number of important signaling proteins, including several kinases [109, 120, 121]. Recently, it was shown

that the cardiac-specific loss of ENH isoform expression results in impaired cardiac function and dilated cardiomyopathy in the absence of the activation of common cardiac stress pathways [116]. Moreover, we recently identified a novel phosphorylation site in an ENH protein isoform expressed in the swine heart, and showed that the phosphorylation of this isoform is decreased following acute myocardial infarction [244]. These results indicate that the expression and/or possibly the phosphorylation of ENH protein isoforms may be important for regulating myocardial contractility.

To determine whether ENH protein isoforms play a role in modulating cardiac contractile function, we compared the steady-state and dynamic mechanical properties of trabeculae isolated from the hearts of $ENH^{+/+}$, $ENH^{+/-}$, and $ENH^{-/-}$ mice. We found that, while the steady-state mechanical properties of myocardium from all three genotypes of mice were similar, cross-bridge cycling kinetics were depressed in trabeculae isolated from $ENH^{+/-}$ and $ENH^{-/-}$ mice, with the decrease being more pronounced in $ENH^{-/-}$ mouse myocardium. Surprisingly, changes in the expression of MHC isoforms or in the expression or phosphorylation of other thin and thick filament regulatory proteins could not account for this phenomenon, at least in $ENH^{+/-}$ mouse myocardium. Moreover, top-down proteomics analysis showed that the expression and phosphorylation of ENH3b were unchanged in myocardium from $ENH^{+/+}$ and $ENH^{+/-}$ mice. Collectively, these results suggest that ENH protein isoforms, other than ENH3b, have a role in setting force redevelopment kinetics in mouse myocardium.

5.2 Materials and methods

5.2.1 Transgenic mice

Mice lacking cardiac-specific expression of ENH protein isoforms have been described previously [116]. Two pairs of male and female $ENH^{+/-}$ mice were obtained as a generous gift from Dr. Ju Chen. Mice were housed in clear plastic cages on a 12h/12h light/dark cycle with access to food and water ad libitum. Initial crossing of $ENH^{+/-}$ mice produced $ENH^{+/+}$, $ENH^{+/-}$, and $ENH^{-/-}$ animals at expected Mendalian ratios. $ENH^{-/-}$ mice were obtained by intercrossing the $ENH^{-/-}$ progeny resulting from the initial crosses. Both $ENH^{+/-}$ and $ENH^{+/+}$ mice were obtained from $ENH^{+/-}$ crosses. Genotypes were determined from toe clips by PCR with the following primer sets: P1 (5'-GCAGGAAGCACACCCAGTAT-3') versus P2 (5'-TGGTCTCCAACATTTCACCA-3') to probe for the wild-type allele, and Frtneo (5'-AATGGGCTGACCGCTTCCTCGT-3') versus P4 (5'-TCGGATGGATGCTCTCTTCT-3') to probe for the knockout allele (**Fig. 5.1**) as described previously [116]. The genotypes of animals used for mechanical analyses were reconfirmed using tail snips following removal of hearts as described below. All procedures involving animal care and handling were reviewed and approved by the University of Wisconsin School of Medicine and Public Health Animal Care and Use Committee.

5.2.2 Solutions

The composition of solutions were calculated using the computer program of Fabiato [335] and the stability constants (corrected to pH 7.0 and 22 ^{o}C) listed by Godt and Lindley [336]. Unless otherwise stated, all solutions used for mechanical measurements contained (in mmol/L) 100 BES, 15 creatine phosphate, 5 dithiothreitol, 1 free Mg^{2+}, and 4 MgATP. In addition, (a) pCa 9.0 solution contained 7 EGTA and 0.02 $CaCl_2$, (b) pCa 4.5 solution contained 7 EGTA, and 7.01 $CaCl_2$, and (c) pre-activating solution contained 0.07 EGTA. The ionic strength of all solutions was adjusted to 180 mmol/L using potassium propionate. A range of solutions containing different $[Ca^{2+}]_{free}$ were prepared by mixing pCa 9.0 and pCa 4.5 solutions.

5.2.3 Skinned right ventricular trabeculae

Right ventricular trabeculae were isolated as described previously [65, 337]. Briefly, hearts were excised from $ENH^{+/+}$, $ENH^{+/-}$, and $ENH^{-/-}$ mice of either sex (3-6 months old) previously injected (i.p.) with 5000 U heparin/kg body weight, anesthetized with isoflurane, and pinned down to the base of a dissecting dish filled with modified Ringer's solution (in mmol/L: 120 NaCl, 19 $NaHCO_3$, 1.2 Na_2HPO_4, 1.2 $MgSO_4$, 5 KCl, 1 $CaCl_2$, 10 glucose, pH 7.4, 22 ^{o}C) pre-equilibrated with 95% O_2/5% CO_2. The right ventricles were cut open and exposed to fresh Ringer's solution containing 20 mmol/L 2,3-butanedione monoxime for 30 minutes (1x solution change). The unbranched right ventricular trabeculae were then dissected free, tied to sticks to hold muscle length fixed, and transferred to relaxing solution (in mmol/L: 100 KCl, 20 imidazole, 7 $MgCl_2$, 2 EGTA, 4 ATP, pH 7.0, 4 ^{o}C) containing 1% Triton X-100 and 0.25 g/mL saponin. After skinning overnight, the trabeculae were washed in fresh relaxing solution (~1 hr) and then stored at -20 ^{o}C in relaxing solution containing glycerol (50:50 v/v). The left and right ventricles were separated

at the septum, frozen in liquid nitrogen, and stored at -80 ^{o}C for later analysis by top-down proteomics.

5.2.4 Experimental apparatus and protocols

On the day of an experiment, skinned trabeculae were washed in relaxing solution for 30 min before cutting them free from the sticks and trimming their ends. The trimmed trabeculae were then transferred to a stainless steel experimental chamber containing pCa 9.0 solution [338]. The ends of each trabecula were attached to the arms of a motor (model 312B, Aurora Scientific, Ontario, Canada) and force transducer (model 403; Aurora Scientific), as described earlier [338]. The chamber assembly was then placed on the stage of an inverted microscope (Olympus, Tokyo, Japan) fitted with a 40x objective and a CCTV camera (model WV-BL600, Panasonic, Kadoma, Japan). The light from a halogen lamp was used to illuminate the skinned preparations. Bitmap images of the preparations were acquired using an AGP 4X/2X graphics card, as well as associated software (ATI Technologies, Markham, Canada), and were used to assess mean sarcomere length (SL) during the course of each experiment. Changes in force and motor position were sampled (16-bit resolution, DAP5216a, Microstar Laboratories, Bellevue, WA, USA) at 2.0 kHz using SLControl software developed in this laboratory (http://www.slcontrol.com). Data were saved to computer files for later analysis.

Active force-pCa and rate constant of force redevelopment (k_{tr})-pCa/force relationships were established at SL 2.2 μm as described previously [337]. Briefly, the skinned trabeculae were stretched to a mean SL of ~2.2 μm in pCa 9.0 solution. After measuring length and width, the

preparations were transferred first to pre-activating solution, then to Ca^{2+} activating solution, and finally back to pCa 9.0 solution. Once in Ca^{2+} activated solution, steady-state force and k_{tr} were measured simultaneously using the modified multi-step protocol developed by Brenner and Eisenberg [339], described in detail previously [340], and illustrated in **Fig. 5.2**. Briefly, after force reached a steady level in activating solution (pCa 6.2 – 4.5), the length of the preparation was rapidly reduced by ~20%, held for ~14 ms, and then re-stretched back to its original length. As a result of re-stretch, there was an initial transient increase, followed by a decrease in force (seen as a spike in the force trace) and subsequent slow recovery of force nearing the initial steady-state level. The k_{tr} reported in the present study is the rate constant of force redevelopment after the spike. The drop in force recorded in solution of pCa 9.0 was taken as passive force and was therefore subtracted from the drop in total force at each pCa to yield the Ca^{2+}-activated force (P). The protocol was repeated to establish active force-pCa and k_{tr}-pCa/relative active force relationships. Upon completing mechanical measurements, the trabeculae were cut free at the points of attachment, placed in SDS sample buffer and stored at -80 ^{o}C until subsequent protein analysis.

To ensure that the differences in mechanical properties between $ENH^{+/+}$, $ENH^{+/-}$, and $ENH^{-/-}$ myocardium was not confounded by the differential expression of key contractile proteins, the trabeculae stored in SDS sample buffer were electrophoresed using 5% and 12.5% Tris-HCl Precast Criterion gels (BioRad, Hercules, CA, USA). The gels were silver stained using methods described previously [341] with minor modifications [70] as follows: the gels were (a) incubated for 20 min in fixing solution containing 50% methanol and 10% acetic acid, (b) washed for 20 min (4x ddH_2O changes) with ddH_2O, (c) incubated for 1.5 min in 0.01% sodium thiosulfate solution

and then rinsed 4x with ddH_2O, (d) incubated for 20 min in 0.09% silver nitrate solution and then rinsed 4x with ddH_2O, (e) incubated in developing solution containing 0.0004% sodium thiosulfate, 2% potassium carbonate, and 0.0068% formaldehyde until proteins are visible and then rinsed 4x with ddH_2O, (f) incubated for 20 min in destaining solution containing 10% methanol and 10% acetic acid, rinsed 4x in ddH_2O, and (g) finally washed for 30 min (6x ddH_2O changes) with ddH_2O. The gels were then scanned and protein bands quantified using a BioRad Chemi Doc MP Imaging System (BioRad).

5.2.5 Sample preparation

Frozen left ventricular myocardium from $ENH^{+/+}$, $ENH^{+/-}$, and $ENH^{-/-}$ mice was homogenized in approximately 25X (w/v) HEPES extraction buffer containing (in mmol/L) 25 HEPES pH 7.5, 100 sodium fluoride, 5 sodium pyrophosphate, 50 β-glycerophosphate, 5 Na_3VO_4, 2.5 EDTA, and 1x protease inhibitor cocktail (Sigma, St. Louis, MO, USA) using a Polytron electric homogenizer (Model PRO200; PRO Scientific, Oxford, CT, USA) on ice with 3-4 sec bursts. The resulting homogenates were centrifuged at 21,000 × *g* for 20 min at 4 °C, and the supernatants were discarded. The insoluble pellets were subsequently re-homogenized in 3X (w/v) TFA solution (containing 1% TFA and 10 mmol/L TCEP) to extract a protein fraction enriched in sarcomeric proteins. After centrifugation (21,000 × *g*, 4 °C, 30 min), the supernatants were transferred to new microcentrifuge tubes, taking care not to disturb the pellet, and centrifuged an additional time (21,000 × *g*, 4 °C, 90 min) to ensure complete removal of all particulate matter from the samples. Following careful collection of the supernatant, the protein concentration of individual samples was determined using the Pierce™ Coomassie Plus (Bradford) Assay Kit (Thermo Fisher

Scientific, Waltham, MA, USA) in accordance with the manufacturer's instructions. A single $ENH^{+/+}$ sample was randomly chosen and six dilutions were prepared with the following total protein concentrations (in ng): 50, 100, 250, 400, 500, and 750. These samples were used to verify that the measured protein intensities fell within the linear response range for the mass spectrometer. The remaining samples were diluted to a final total protein concentration of 400 ng. All samples were diluted in HPLC-grade water containing 0.1% formic acid and 10 mmol/L TCEP.

5.2.6 Top-down proteomics

Diluted protein extracts prepared from the left ventricular myocardium of $ENH^{+/+}$, $ENH^{+/-}$, and $ENH^{-/-}$ mice were separated using a NanoAcquity ultra-high pressure liquid chromatography system (Waters, Milford, MA, USA), equipped with a home-packed PLRP column (PLRP-S, 250 mm x 500 μm, 10 μm particle size, 1000 Å pore size; Varian, Lake Forest, CA, USA), coupled directly on-line with a high-resolution Impact II Q-TOF mass spectrometer (Bruker Daltonics, Billerica, MA, USA). Proteins were eluted using a gradient going from 5% B to 95% B over 55 min (solvent A: 0.10% formic acid in water; solvent B: 0.10% formic acid in a 50:50 mixture of acetonitrile and ethanol) at a flow rate of 8 μL/min. Spectra were collected using a scan rate of 1 Hz over a 500-3000 *m/z* range. Chromatographic separation and protein signal intensities (**Fig. 5.3**), as well as the relative intensity ratios of un-modified and modified protein forms (**Fig. 5.4**), were highly reproducible across replicates.

5.2.7 Data analysis

For mechanical measurements, $ENH^{+/+}$ (n = 15), $ENH^{+/-}$ (n = 25), and $ENH^{-/-}$ (n = 20) mice were utilized. The cross-sectional areas of skinned trabeculae were calculated by assuming that the trabeculae were cylindrical and by equating the width, measured from video images of the mounted preparations, to diameter. Each Ca^{2+}-activated force (P) at pCa between 6.2 and 5.4 was expressed as a fraction of the maximum Ca^{2+}-activated force (P_o) developed by the same preparations at pCa 4.5, i.e., P/P_o. To determine the concentration of Ca^{2+} at half-maximal activation (pCa_{50}), force-pCa data were fitted with the Hill equation:

$$\frac{P}{P_o} = [Ca^{2+}]^n/(k^n + [Ca^{2+}]^n) \quad (1)$$

where n is the slope (Hill coefficient; n_H) and k is the pCa_{50}. k_{tr} was determined by linear transformation of the half-time of force recovery using the following equation, as described previously [41, 342]:

$$k_{tr} = -\ln 0.5 \times (t_{1/2})^{-1} \quad (2)$$

Of the animals used for mechanical measurements, 9 animals from both the $ENH^{+/+}$ and $ENH^{+/-}$ groups, as well as 13 animals from the $ENH^{-/-}$ group, were selected for top-down proteomic analysis. All MS data were analyzed using DataAnalysis (Bruker Daltonics). To quantify the relative abundances of un-modified and modified protein forms, spectra were averaged across the entire width of the chromatographic peak(s) corresponding to elution of the protein of interest, deconvoluted using Maximum Entropy, and processed using the SNAP function in DataAnalysis, which yielded a mass list containing intensity values for each detected protein species in a specified

chromatographic timeframe. The total protein population intensity was determined by summing the intensity values for all un-modified and modified species corresponding to the same protein. Subsequently, the relative abundance (expressed as a percentage of the total population intensity) of each individual form of that specific protein was determined by dividing the summed intensities of all species corresponding to a specific protein form by the total population intensity for that protein and multiplying by 100%. Protein phosphorylation levels were determined using the relative abundance values calculated for all differentially phosphorylated species from the same protein using the following equation, as described previously [202, 244, 269].

$$P_{total} = (\%P_{mono} + (2\times\%P_{bis}) + (3\times\%P_{tris}) + \cdots)/100 \quad (3)$$

After calculation of the total phosphorylation, protein phosphorylation levels in $ENH^{+/-}$ and $ENH^{-/-}$ were normalized to $ENH^{+/+}$ values by dividing all of the individual protein phosphorylation values by the mean of the $ENH^{+/+}$ protein phosphorylation values.

For the MS-based quantification of sarcomeric protein expression levels in $ENH^{+/+}$, $ENH^{+/-}$, and $ENH^{-/-}$ myocardium, extracted ion chromatograms (EICs) were generated for individual sarcomeric proteins from each sample in DataAnalysis by inputting all protein forms corresponding to a specific protein of interest for the top five most abundant charge states. A line was then manually drawn under the EIC generated for a given sarcomeric protein using the Chromatogram Compounds Manually function in DataAnalysis, This procedure yielded an area value corresponding to the area under the curve (AUC), which represented the relative expression of the specific protein.

All data are presented as means ± SEM. Statistical analysis of the data was done using unpaired two-tailed *t*-tests. For all comparisons, *p* values less than 0.05 were considered statistically significant.

5.3 Results

5.3.1 Steady-state mechanical properties of $ENH^{+/+}$, $ENH^{+/-}$, and $ENH^{-/-}$ mouse myocardium

Trabeculae were isolated from the right ventricles of $ENH^{+/+}$ (n = 15), $ENH^{+/-}$ (n = 25), and $ENH^{-/-}$ (n = 20) mouse hearts, skinned, and subjected to mechanical measurements. Skinned trabeculae from $ENH^{+/+}$, $ENH^{+/-}$, and $ENH^{-/-}$ mice generated similar amounts of passive force (pCa 9.0) and maximum Ca^{2+}-activated force (pCa 4.5) (**Table 5.1**). Active force was measured over a range of Ca^{2+} concentrations (pCa 9.0 to 4.5) to determine whether the cooperativity of activation or Ca^{2+} sensitivity of force differed in $ENH^{+/+}$, $ENH^{+/-}$, and $ENH^{-/-}$ mouse myocardium. The force-pCa relationships established in all three types of trabeculae were sigmoidal and were fit to a Hill equation (as described in the Materials and methods) to yield a Hill coefficient (n_H), an index of apparent cooperativity in the activation of force, as well as pCa_{50}, an index of the Ca^{2+} sensitivity of force (**Fig. 5.5**). As reported in **Table 5.1**, the n_H values determined for $ENH^{+/-}$ and $ENH^{-/-}$ trabeculae were not significantly different from those determined for $ENH^{+/+}$ trabeculae. Likewise, the pCa_{50} values determined for $ENH^{+/-}$ and $ENH^{-/-}$ trabeculae were similar to those for $ENH^{+/+}$ trabeculae (**Table 5.1**). In summary, these results indicate that the steady-state mechanical

properties of $ENH^{+/-}$ and $ENH^{-/-}$ mouse myocardium do not differ from those of $ENH^{+/+}$ mouse myocardium.

5.3.2 Dynamic properties of $ENH^{+/+}$, $ENH^{+/-}$, and $ENH^{-/-}$ mouse myocardium

We next assessed the dynamic properties of $ENH^{+/+}$, $ENH^{+/-}$, and $ENH^{-/-}$ mouse myocardium via measurement of the apparent rate constant of force redevelopment (k_{tr}) in skinned trabeculae from these mice. All 3 types of trabeculae exhibited $[Ca^{2+}]_{free}$ (and force)-dependent changes in k_{tr}. To illustrate this, records of force redevelopment at various levels of $[Ca^{2+}]_{free}$ (and force) are shown in **Fig. 5.6** for $ENH^{+/+}$ (A), $ENH^{+/-}$ (B), and $ENH^{-/-}$ (C) trabeculae, where steady-state forces at each pCa were normalized to 1.0 to provide better visualization of changes in the kinetics of force redevelopment. The sigmoidal k_{tr}-pCa and curvilinear k_{tr}-relative force relationships established in $ENH^{+/+}$, $ENH^{+/-}$, and $ENH^{-/-}$ trabeculae are shown in **Fig. 5.7A** and **5.7B**, respectively. Compared to $ENH^{+/+}$ trabeculae, both $ENH^{+/-}$ and $ENH^{-/-}$ trabeculae redeveloped forces at a slower rate at both sub-maximal and maximal $[Ca^{2+}]_{free}$ (**Fig. 5.7A**). When k_{tr} values were re-plotted against steady-state isometric force (as a function of maximum force), the curvilinear k_{tr}-relative force relationships established in $ENH^{+/-}$ and $ENH^{-/-}$ trabeculae were to the right of those established in $ENH^{+/+}$ trabeculae (**Fig. 5.7B**). These results suggest that cross-bridge cycling kinetics are depressed in $ENH^{+/-}$ and $ENH^{-/-}$ mouse myocardium, with the decrease being greater in $ENH^{-/-}$ mouse myocardium.

Since k_{tr} corresponds to the sum of the apparent rates of attachment (f_{app}) and detachment (g_{app}) [343], the slower rates of force redevelopment in trabeculae from $ENH^{+/-}$ and $ENH^{-/-}$ mice (relative

to rates measured in $ENH^{+/+}$ trabeculae) may be due to decreased rates of cross-bridge attachment, detachment, or both. To gain insight, the natural logarithm of mean k_{tr} values were plotted against relative forces (**Fig. 5.7C**), and the value for g_{app} (y intercept) was determined by linear regression fit to the data. The resultant values of f_{app} and g_{app} for $ENH^{+/+}$ were 27.39 and 4.94 s^{-1}, $ENH^{+/-}$ were 21.08 and 4.50 s^{-1}, and $ENH^{-/-}$ were 15.54 and 3.33 s^{-1}, respectively. These results suggest that the rates of cross-bridge attachment and detachment are decreased by 23% and 9%, respectively, in $ENH^{+/-}$ mouse myocardium and 43% and 37%, respectively, in $ENH^{-/-}$ mouse myocardium.

5.3.3 Contractile protein expression in $ENH^{+/+}$, $ENH^{+/-}$, and $ENH^{-/-}$ mouse myocardium

Given that cross-bridge cycling kinetics in mammalian cardiac muscle are primarily defined by the expression pattern of myosin heavy chain (MHC) isoforms [344, 345], the relative expression of these isoforms was analyzed in the trabeculae of $ENH^{+/+}$, $ENH^{+/-}$, and $ENH^{-/-}$ mice. **Fig. 5.8** shows representative SDS-PAGE analyses of MHC isoform expression in $ENH^{+/+}$, $ENH^{+/-}$, and $ENH^{-/-}$ right ventricular trabeculae used for mechanical measurements. The relative expression of α-MHC and β-MHC did not differ in $ENH^{+/+}$ trabeculae (96.3 ± 1.1 and 3.7 ± 1.1 % for α- and β-MHC, respectively; n = 10) and $ENH^{+/-}$ trabeculae (95.0 ± 0.8 and 5.0 ± 0.8 % for α- and β-MHC, respectively; n = 20) (**Fig. 5.8A-B**). However, the relative expression of α- and β-MHC was significantly increased and decreased, respectively, in $ENH^{-/-}$ trabeculae (87.9 ± 2.3 and 12.1 ± 2.3 % for α- and β-MHC, respectively; n = 15) (**Fig. 5.8A-B**).

Next, quantitative top-down proteomics analysis was employed to determine whether the expression of other thin and/or thick filament regulatory proteins differed in ventricular myocardium from $ENH^{+/+}$, $ENH^{+/-}$, and $ENH^{-/-}$ mice. Prior to quantitative analysis, a single sarcomeric protein extract prepared from the myocardium of an $ENH^{+/+}$ mouse was analyzed by top-down proteomics at different total protein concentrations to establish the linear response range for each of the observed thin/thick filament regulatory proteins. **Fig. 5.9** shows that the instrument response between 100 ng and 750 ng total protein was highly linear ($R^2 > 0.88$) for cardiac troponin T (cTnT) isoforms, cardiac troponin I (cTnI), α-tropomyosin (αTpm), ventricular essential light chain (ELC_v), ventricular regulatory light chain (RLC_v), and troponin C (TnC), enabling the quantification of these isoforms in $ENH^{+/+}$, $ENH^{+/-}$, and $ENH^{-/-}$ mouse myocardium. Quantitative top-down proteomics analysis of sarcomeric protein extracts prepared from the myocardium of $ENH^{+/+}$ (n = 8), $ENH^{+/-}$ (n = 9), and $ENH^{-/-}$ mice (n = 12) revealed no differences in the expression of these protein isoforms (**Fig. 5.10**). The results of the quantitative top-down proteomics analysis were in agreement with those obtained from SDS-PAGE analysis of protein extracts prepared from the isolated right ventricular trabeculae used for mechanical analyses (**Fig. 5.11**). Collectively, these results indicate that, although an increase in the relative expression of β-MHC can, in part, account for depressed cross-bridge cycling kinetics in myocardium of $ENH^{-/-}$ mice, reduced force redevelopment kinetics in $ENH^{+/-}$ mouse myocardium cannot be explained by changes in the expression of MHC isoforms or thin/thick filament regulatory proteins.

5.3.4 Contractile protein phosphorylation in $ENH^{+/+}$, $ENH^{+/-}$, and $ENH^{-/-}$ mouse myocardium

As contractile protein phosphorylation can also regulate cross-bridge cycling kinetics [70, 72, 346-348], we next assessed the phosphorylation status of thin/thick filament regulatory proteins in the ventricular myocardium of $ENH^{+/+}$ (n =8), $ENH^{+/-}$ (n = 9), and $ENH^{-/-}$ (n = 12) mice using top-down proteomics. Representative zoomed-in deconvoluted mass spectra with detected cTnT (A), cTnI (B), αTpm (C), and RLC_v (D) protein species in $ENH^{+/+}$, $ENH^{+/-}$, and $ENH^{-/-}$ mouse myocardarium are shown in **Fig. 5.12**. The phosphorylation of cTnT isoforms A2 (cTnT-A2) and A1 (cTnT-A1), as well as αTpm, did not differ in the myocardium of $ENH^{+/+}$, $ENH^{+/-}$, and $ENH^{-/-}$ mice (**Fig. 5.13**). The phosphorylation of cTnT isoform A3B (cTnT-A3B) was decreased by approximately 6% in $ENH^{-/-}$ myocardium relative to that in $ENH^{+/+}$ ($p = 0.0024$) and $ENH^{+/-}$ ($p = 0.0032$) mouse myocardium (**Fig. 5.13**). Similarly, the phosphorylation of cTnI was reduced ~12% in $ENH^{-/-}$ mouse myocardium relative to that in myocardium from $ENH^{+/+}$ ($p = 0.0030$) and $ENH^{+/-}$ ($p = 0.018$) mice (**Fig. 5.13**). Although there was a trend towards decreased RLC_v phosphorylation in $ENH^{+/-}$ mouse myocardium relative to that in $ENH^{+/+}$ mouse myocardium, this trend was not statistically significant ($p = 0.082$) (**Fig. 5.13**). The phosphorylation of RLC_v was significantly decreased in $ENH^{+/-}$ mouse myocardium (~25%) relative to that in $ENH^{+/+}$ mouse myocardium ($p = 0.0014$) (**Fig. 5.13**). These results indicate that alterations in the phosphorylation status of thin/thick filament regulatory proteins may contribute to the observed depression in cross-bridge cycling kinetics in $ENH^{-/-}$ mouse myocardium, but not in myocardium from $ENH^{+/-}$ mice.

5.3.5 ENH3b isoform expression and phosphorylation in $ENH^{+/+}$, $ENH^{+/-}$, and $ENH^{-/-}$ mouse myocardium

Given that neither changes in the expression of MHC isoforms or in the expression/phosphorylation of thin/thick filament regulatory proteins can explain the observed depression in cross-bridge cycling kinetics, at least in $ENH^{+/-}$ mouse myocardium, it seems most likely that changes in the expression (or possibly phosphorylation) of ENH protein isoforms underlie this phenomenon. To gain insights into ENH protein isoform expression and phosphorylation in $ENH^{+/+}$ (n = 8), $ENH^{+/-}$ (n = 9), and $ENH^{-/-}$ (n= 12) mouse myocardium, top-down proteomics was employed. Two short isoforms, ENH3a and ENH3b [116], were detected in the myocardium of adult $ENH^{+/+}$ and $ENH^{+/-}$ mice with high mass accuracy (**Fig. 5.14**). However, ENH3a was barely detectable (either as a consequence of low expression in the myocardium or insufficient ionization of the protein), which precluded quantification of this isoform. Assessment of ENH3b expression in $ENH^{+/+}$, $ENH^{+/-}$, and $ENH^{-/-}$ mouse myocardium revealed that the expression ENH3b did not differ significantly in $ENH^{+/+}$ and $ENH^{+/-}$ mouse myocardium (p = 0.16) (**Fig. 5.15A**). Similarly, quantitative top-down proteomics analysis uncovered no differences in the phosphorylation of ENH3b in myocardium from $ENH^{+/+}$ and $ENH^{+/-}$ mice (**Figs. 5.15B, 5.16**). These results suggest that alterations in the expression or phosphorylation of ENH3b are unlikely to contribute to depressed cross-bridge cycling kinetics in $ENH^{+/-}$ and $ENH^{-/-}$ mouse myocardium.

5.4 Discussion

This is the first study to assess whether the ENH protein plays a direct role in myocardial contractility. Our results show that right ventricular trabeculae isolated from $ENH^{+/-}$ and $ENH^{-/-}$ mouse hearts had similar steady-state mechanical properties, but different dynamic mechanical

properties, than trabeculae from $ENH^{+/+}$ mice. Specifically, the passive force, maximum Ca^{2+}-activated force, apparent cooperativity in activation, and Ca^{2+} sensitivity of force measured in $ENH^{+/-}$ and $ENH^{-/-}$ trabeculae were similar to those measured in $ENH^{+/+}$ trabeculae (**Table 5.1**). The rate of force redevelopment in trabeculae from both $ENH^{+/-}$ and $ENH^{-/-}$ mouse hearts was decreased in comparison to that in trabeculae from $ENH^{+/+}$ mouse hearts at both maximal and sub-maximal levels of activation (**Figs. 5.6-5.7**), with the decrease being more pronounced in $ENH^{-/-}$ than $ENH^{+/-}$ trabeculae.

In mammalian cardiac muscle, force redevelopment kinetics are primarily defined by MHC isoform expression [344, 345] and modulated by contractile proteins such as cMyBP-C [72, 346, 347], cTnT [349], and RLC_v [70, 348]. The relative expression of β-MHC was found to be significantly increased in $ENH^{-/-}$ trabeculae relative to that in $ENH^{+/+}$ trabeculae (**Fig. 5.8**), which is in agreement with the results of prior studies showing an up-regulation of β-MHC at the mRNA level in $ENH^{-/-}$ mouse myocardium [116]. Conversely, the relative expression of MHC isoforms was similar in $ENH^{+/+}$ and $ENH^{+/-}$ trabeculae (**Fig. 5.8**), indicating that an increase in the relative expression of β-MHC cannot account for depressed cross-bridge cycling kinetics in $ENH^{+/-}$ mouse myocardium. Moreover, considering results from earlier studies in rat [345] and mouse myocardium [344], the observed increase in the expression of β-MHC would only be expected to account for approximately 8% of the roughly 40% decrease in the maximum rate of force redevelopment in $ENH^{-/-}$ mouse myocardium relative to that in myocardium from $ENH^{+/+}$ mice. Therefore, increased expression of β-MHC is insufficient to explain decreased cross-bridge cycling kinetics in $ENH^{-/-}$ mouse myocardium. Quantitiative top-down proteomics analysis also uncovered no differences in the expression of thin and thick filament regulatory proteins in the

ventricular myocardium of $ENH^{+/+}$, $ENH^{+/-}$, and $ENH^{-/-}$ mice (**Figs. 5.10**). Thus, alterations in the expression of thin/thick filament proteins also cannot explain the depressed rate of force redevelopment in $ENH^{+/-}$ and $ENH^{-/-}$ mouse myocardium.

In addition to changes in protein expression, alterations in the phosphorylation state of sarcomeric proteins, including cMyBP-C and RLC_v, have been shown to influence cross-bridge cycling kinetics in cardiac muscle [70, 347, 348]. Surprisingly, while the phosphorylation of sarcomeric proteins, including cTnT-A3B, cTnI, and RLC_v, was decreased in $ENH^{-/-}$ mouse myocardium, the phosphorylation of thin/thick filament regulatory proteins did not differ significantly in myocardium from $ENH^{+/+}$ and $ENH^{+/-}$ mice (**Figs. 5.13**). Taken together, these results indicate that neither changes in the expression of MHC isoforms or in the expression/phosphorylation of thin/thick filament regulatory proteins can account for reduced cross-bridge cycling kinetics, at least in $ENH^{+/-}$ mouse myocardium.

Based on these observations, it seems most likely that depressed cross-bridge cycling kinetics in $ENH^{+/-}$ and $ENH^{-/-}$ mouse myocardium result from changes in the expression (or possibly the phosphorylation) of ENH protein isoforms. A total of seven different isoforms (five long and two short) are expressed in the mouse heart [116], with expression patterns that are developmentally-regulated [126]. Unfortunately, isoform-specific and phospho-ENH antibodies are not available, making determination of the isoform(s) responsible challenging. However, using top-down proteomics we were able to show that changes in either the expression or phosphorylation of ENH3b, a short isoform of ENH, are unlikely to contribute to decreased cross-bridge cycling kinetics in $ENH^{+/-}$ and $ENH^{-/-}$ mouse myocardium (**Fig. 5.15**). These results indicate that changes

in the expression, or possibly phosphorylation, of ENH protein isoform (or isoforms), other than ENH3b, likely contribute to the observed decrease in force redevelopment kinetics in $ENH^{+/-}$ and $ENH^{-/-}$ mouse myocardium.

It must be noted, however, that previous studies have demonstrated that cardiac-specific ablation of ENH also decreases the expression of both Calsarcin-1 and short isoforms of Cypher, which exist in complex with ENH at the Z-disc [116]. Therefore, possible contributions from altered expression of these one or both of these proteins cannot be ruled out.

Nevertheless, in this study we provide evidence, for the first time, that the Z-disc protein ENH has a role in setting the rate of force redevelopment, although the mechanism whereby changes in the expression (or possibly phosphorylation) of ENH protein isoforms depress cross-bridge cycling kinetics remains to be determined.

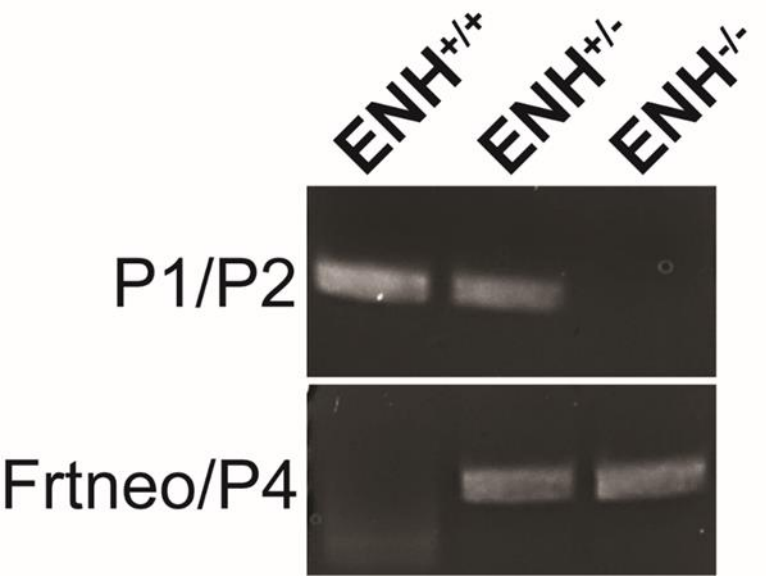

Fig. 5.1. PCR-based genotyping of $ENH^{+/+}$, $ENH^{+/-}$, and $ENH^{-/-}$ mice using toe and/or tail clips. The primer sets P1 versus P2 probes for the wild-type allele while Frtneo versus P4 probes for the presence of the knockout allele.

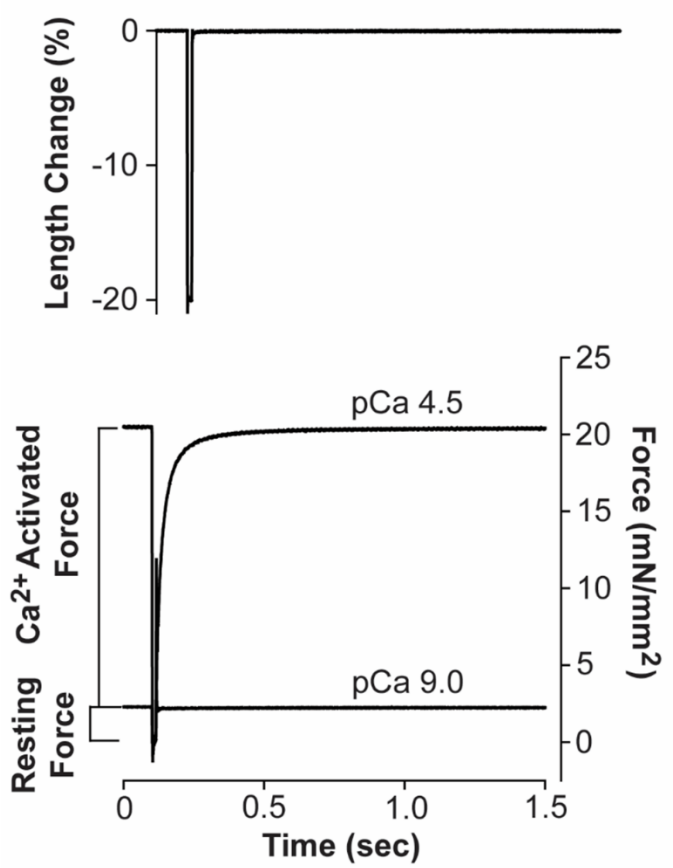

Fig. 5.2. Experimental protocol for the simultaneous determination of the Ca^{2+}-activated force and k_{tr} in skinned right ventricular trabeculae from $ENH^{+/+}$, $ENH^{+/-}$, and $ENH^{-/-}$ mice. The bottom panel shows the changes in force recorded before, during and after a step change in length (as shown in the top panel) of mice skinned right ventricular trabeculae. Once active force reached steady state in solution of pCa 4.5, muscle length was rapidly decreased by 20%. The Ca^{2+}-activated force was determined by subtracting the resting force measured at pCa 9.0 from the total force generated at pCa 4.5. Following ~14 ms of unloaded shortening, the preparation was re-stretched to its original length and the rate (k_{tr}) at which the force redeveloped was determined.

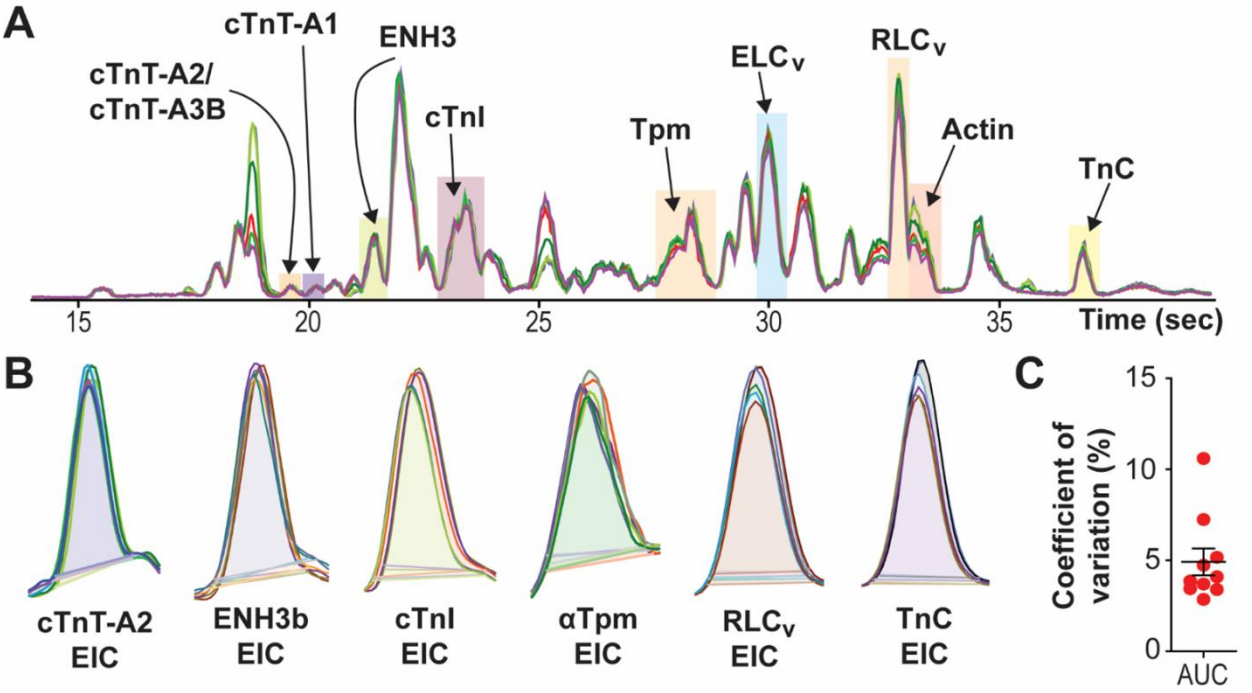

Fig. 5.3. Reproducibility of the chromatographic separation and sarcomeric protein signal intensities across multiple injections of the same sample. (A) Overlay of chromatograms from six injections of a single sample (injection replicates). Chromatographic peaks corresponding to specific sarcomeric proteins are highlighted. (B) Overlays of EICs for select sarcomeric proteins from six injection replicates. (C) Graph showing determined coefficient of variation values calculated for individual sarcomeric protein intensities (represented by the AUCs). Each dot corresponds to the coefficient of variation value computed for the intensity of a single sarcomeric protein across six injection replicates.

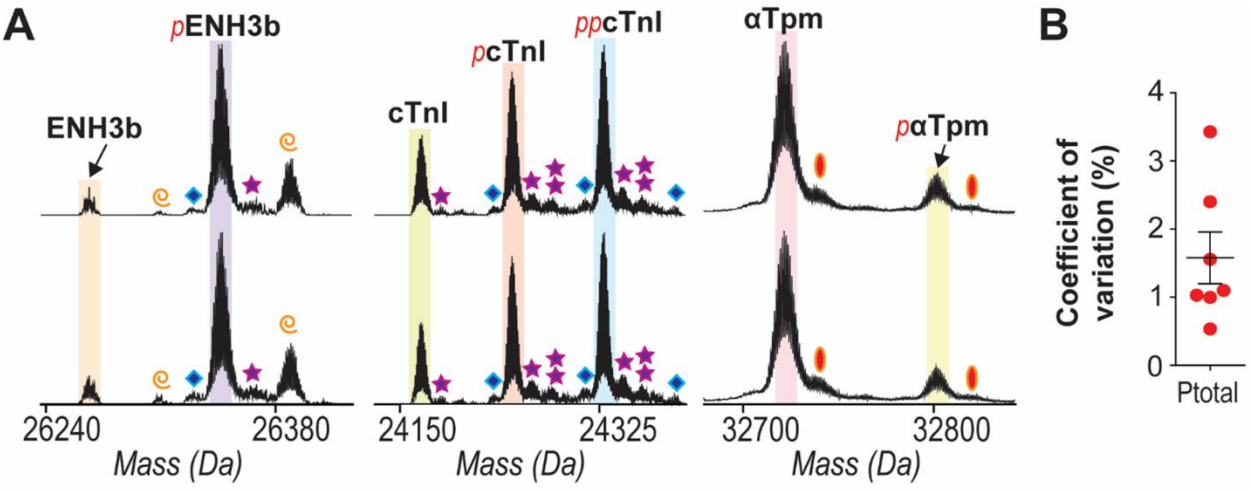

Fig. 5.4. Reproducibility of sarcomeric protein phosphorylation measured across multiple injections of the same sample. (A) Zoomed-in deconvoluted mass spectra showing the relative intensities of unmodified and modified forms of ENH3b (left), cTnI (middle), and αTpm (right) in different injections of the same sample. Swirls, diamonds, and stars denote peaks corresponding to potential acetylated forms of ENH3b and $_p$ENH3b, protein species with NH_3 loss, and oxidized protein species, respectively. (B) Calculated percent coefficient of variation values determined for the measured phosphorylation (Ptotal; in mol of Pi/mol of protein) of individual sarcomeric proteins. Each dot corresponds to the coefficient of variation value computed for the Ptotal of a single sarcomeric protein in six different injection replicates.

Table 5.1. Summary of mechanical properties of right ventricular trabeculae isolated from the hearts of $ENH^{+/+}$, $ENH^{+/-}$, and $ENH^{-/-}$ mice.

	Resting Force (mN/mm^2)	**Maximum Ca^{2+} Activated Force (mN/mm^2)**	**Hill Coefficient (n_H)**	**Ca^{2+} Sensitivity of Force (pCa_{50})**	**Maximum Rate of Force Redevelopment (s^{-1})**
$ENH^{+/+}$					
n = 15	1.83 ± 0.17	22.34 ± 1.85	2.69 ± 0.06	5.73 ± 0.01	32.33 ± 1.94
$ENH^{+/-}$					
n = 25	2.11 ± 0.20	22.78 ± 1.66	2.74 ± 0.06	5.74 ± 0.01	25.58 ± 1.65*
$ENH^{-/-}$					
n = 20	2.06 ± 0.18	17.85 ± 1.48	2.69 ± 0.04	5.75 ± 0.01	19.80 ± 1.17$^{*\#}$

The mechanical properties of skinned trabeculae isolated from the right ventricles of $ENH^{+/+}$ (n = 15), $ENH^{+/-}$ (n = 25), and $ENH^{-/-}$ (n = 20) mice were examined at sarcomere length of 2.2 µm and 22 ^{0}C. Resting force was measured at pCa 9.0. Maximum force and the apparent rate constant of force redevelopment (k_{tr}) were measured at pCa 4.5. pCa_{50} and n_H values were derived by fitting the force-pCa relationships to a Hill equation as described in the Experimental Procedures section.

* and $^{\#}$ denote that the measured values were significantly different ($p < 0.05$) from values recorded in $ENH^{+/+}$ and $ENH^{+/-}$ trabeculae, respectively, using unpaired *t*-test.

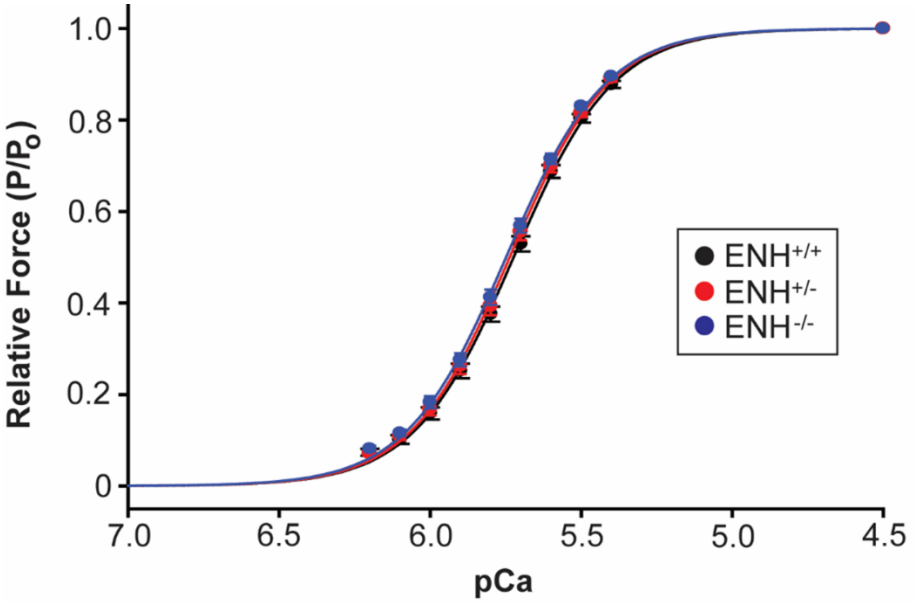

Fig. 5.5. Apparent cooperativity in activation of force and Ca^{2+} sensitivity of force of $ENH^{+/+}$, $ENH^{+/-}$, and $ENH^{-/-}$ trabeculae. Force-pCa relationships were established using skinned right ventricular trabeculae isolated from $ENH^{+/+}$ (closed black circles; n = 15), $ENH^{+/-}$ (closed red circles; n = 25), and $ENH^{-/-}$ (closed blue circles; n = 20) mice. The solid lines were generated by fitting the mean data with the Hill equation as described in the Experimental Procedures. The respective fitted values of n_H and pCa_{50} for $ENH^{+/+}$ trabeculae were 2.64 and pCa 5.72, $ENH^{+/-}$ trabeculae were 2.66 and pCa 5.74, and $ENH^{-/-}$ trabeculae were 2.63 and pCa 5.75. Each data point is the mean and error bar the SEM.

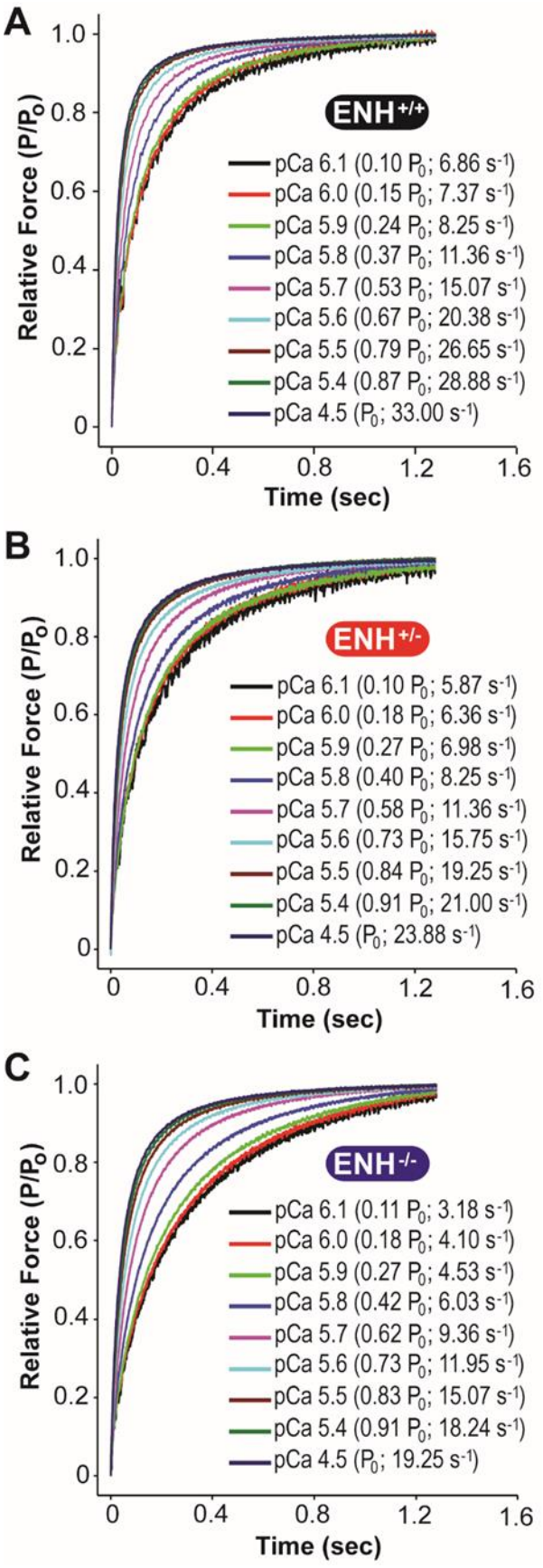
A
Relative Force (P/P0)
1.0
0.8
0.6
0.4
0.2
0
0
0.4
0.8
1.2
1.6
Time (sec)
ENH+/+
pCa 6.1 (0.10 P0; 6.86 s-1)
pCa 6.0 (0.15 P0; 7.37 s-1)
pCa 5.9 (0.24 P0; 8.25 s-1)
pCa 5.8 (0.37 P0; 11.36 s-1)
pCa 5.7 (0.53 P0; 15.07 s-1)
pCa 5.6 (0.67 P0; 20.38 s-1)
pCa 5.5 (0.79 P0; 26.65 s-1)
pCa 5.4 (0.87 P0; 28.88 s-1)
pCa 4.5 (P0; 33.00 s-1)
B
Relative Force (P/P0)
Time (sec)
ENH+/-
pCa 6.1 (0.10 P0; 5.87 s-1)
pCa 6.0 (0.18 P0; 6.36 s-1)
pCa 5.9 (0.27 P0; 6.98 s-1)
pCa 5.8 (0.40 P0; 8.25 s-1)
pCa 5.7 (0.58 P0; 11.36 s-1)
pCa 5.6 (0.73 P0; 15.75 s-1)
pCa 5.5 (0.84 P0; 19.25 s-1)
pCa 5.4 (0.91 P0; 21.00 s-1)
pCa 4.5 (P0; 23.88 s-1)
C
Relative Force (P/P0)
Time (sec)
ENH-/-
pCa 6.1 (0.11 P0; 3.18 s-1)
pCa 6.0 (0.18 P0; 4.10 s-1)
pCa 5.9 (0.27 P0; 4.53 s-1)
pCa 5.8 (0.42 P0; 6.03 s-1)
pCa 5.7 (0.62 P0; 9.36 s-1)
pCa 5.6 (0.73 P0; 11.95 s-1)
pCa 5.5 (0.83 P0; 15.07 s-1)
pCa 5.4 (0.91 P0; 18.24 s-1)
pCa 4.5 (P0; 19.25 s-1)

Fig. 5.6. Typical Ca^{2+} and force dependent changes in the apparent rate constant of force redevelopment (k_{tr}) in $ENH^{+/+}$, $ENH^{+/-}$, and $ENH^{-/-}$ skinned right ventricular trabeculae. The rate of force redevelopment was measured as described in the Materials and methods at submaximal (pCa 6.1 - 5.4) and maximal (pCa 4.5) $[Ca^{2+}]_{free}$ in skinned trabeculae isolated from the right ventricles of $ENH^{+/+}$ (A), $ENH^{+/-}$ (B), and $ENH^{-/-}$ (C) mice. The force transients were expressed relative to the peak steady state force attained after the step change in muscle length. Both, relative force and k_{tr} values for a given $[Ca^{2+}]_{free}$ are shown in parentheses.

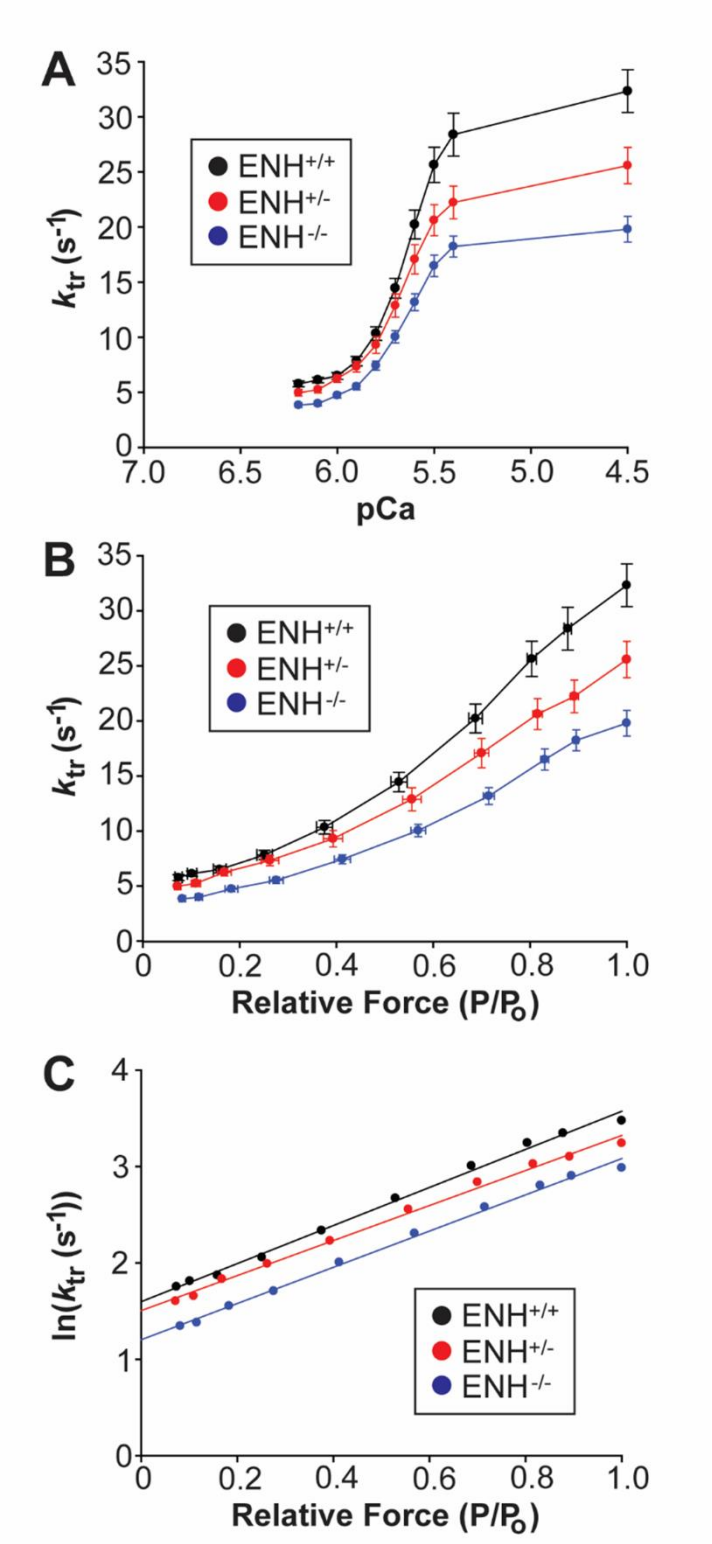

Fig. 5.7. k_{tr}-pCa, k_{tr}-relative force, and In k_{tr}-relative force relationships in ENH$^{+/+}$, ENH$^{+/-}$, and ENH$^{-/-}$ trabeculae. k_{tr}-pCa (A), k_{tr}-relative force (B), and In k_{tr}-relative force (C) relationships

were established using skinned right ventricular trabeculae isolated from the hearts of $ENH^{+/+}$ (black circles; n = 15), $ENH^{+/-}$ (red circles; n = 25), and $ENH^{-/-}$ (blue circles; n= 20) mice. In (C), logarithm of mean k_{tr} was plotted against relative force and the regression fit to the data yield y intercepts of 1.60 (g_{app} = 4.94 s^{-1}), 1.50 (g_{app} = 4.50 s^{-1}) and 1.14 (g_{app} = 3.33 s^{-1}) for $ENH^{+/+}$, $ENH^{+/-}$, and $ENH^{-/-}$ trabeculae, respectively. Each data point is the mean and error bar the SEM.

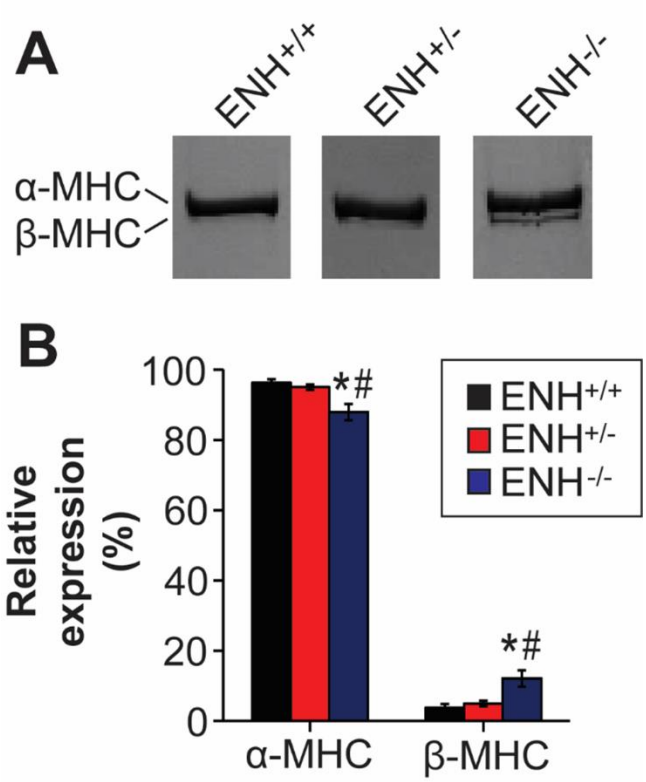

Fig. 5.8. Expression profile of MHC isoforms in right ventricular trabeculae isolated from the hearts of ENH$^{+/+}$, ENH$^{+/-}$, and ENH$^{-/-}$ mice. A. Representative sliver stained 5% Tris-HCl BioRad Precast Criterion gel showing the expression profile of myosin heavy chain isoforms in trabeculae from ENH$^{+/+}$, ENH$^{+/-}$, and ENH$^{-/-}$ mice. B. Graph showing quantification of the relative expression of α- versus β-MHC in trabeculae from ENH$^{+/+}$ (n = 10), ENH$^{+/-}$ (n = 20), and ENH$^{-/-}$ (n = 15) mice. Data are presented as mean ± SEM. * and # denote that the measured values were significantly different (p < 0.05) from values recorded in ENH$^{+/+}$ and ENH$^{+/-}$ trabeculae, respectively, using unpaired *t*-test. Abbreviations: MHC, myosin heavy chain.

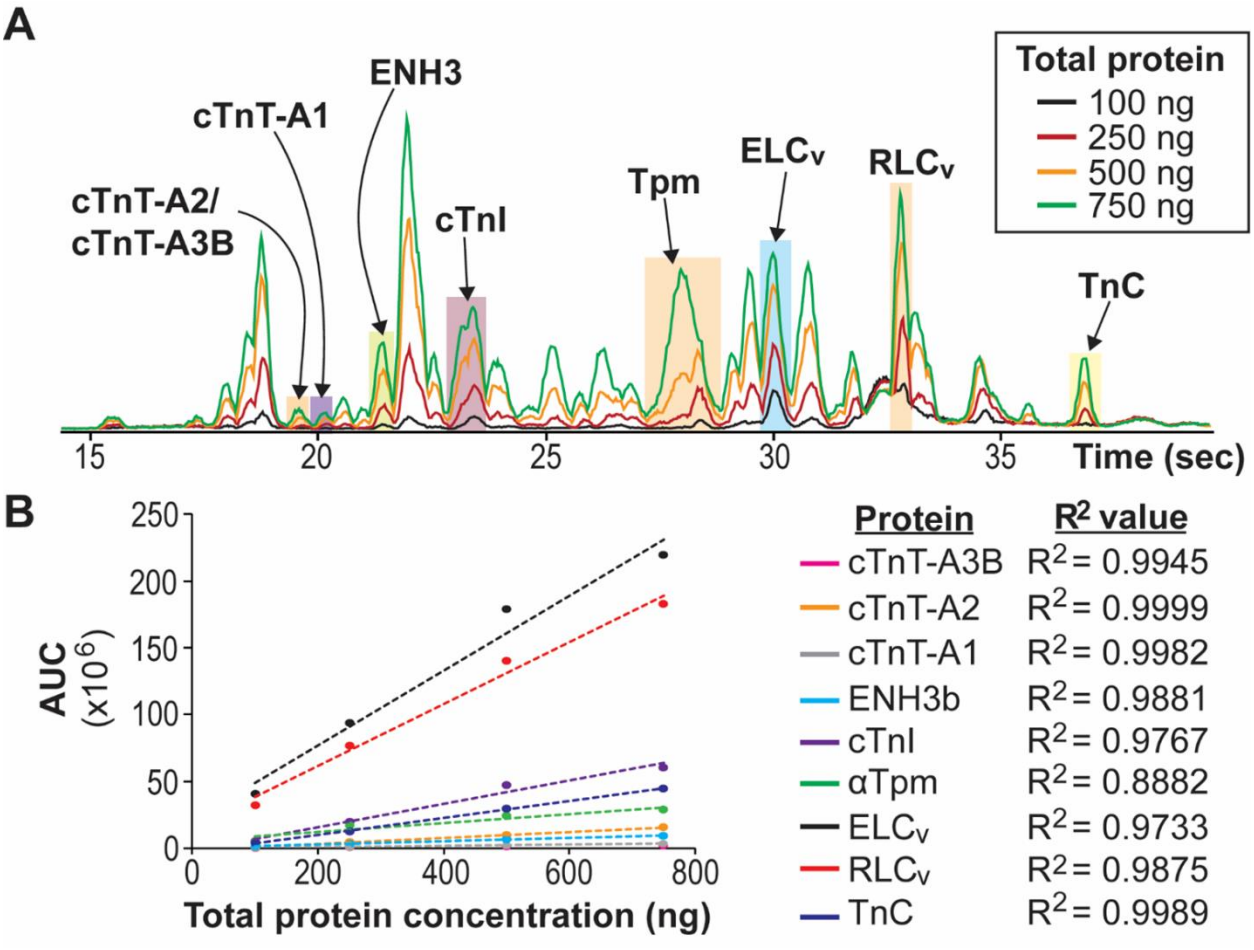

Fig. 5.9. Establishment of linear response range for individual sarcomeric proteins. (A) Overlay of base peak chromatograms obtained from injection of a single sarcomeric protein extract at four different total protein concentrations. Chromatographic peaks corresponding to specific sarcomeric proteins are highlighted. (B) Plot of the AUC versus total protein concentration for individual sarcomeric proteins. The R^2 value for the best-fit lines of individual proteins is given. Abbreviations: cTnT-A2, cardiac troponin T isoform A2; cTnT-A3, cardiac troponin T isoform A3; cTnT-A1, cardiac troponin T isoform A1; ENH3, enigma homolog isoform 3; cTnI, cardiac troponin I; Tpm, tropomyosin; ELC_v, ventricular essential light chain; RLC_v, ventricular regulatory light chain; TnC, troponin C; and AUC, area under curve.

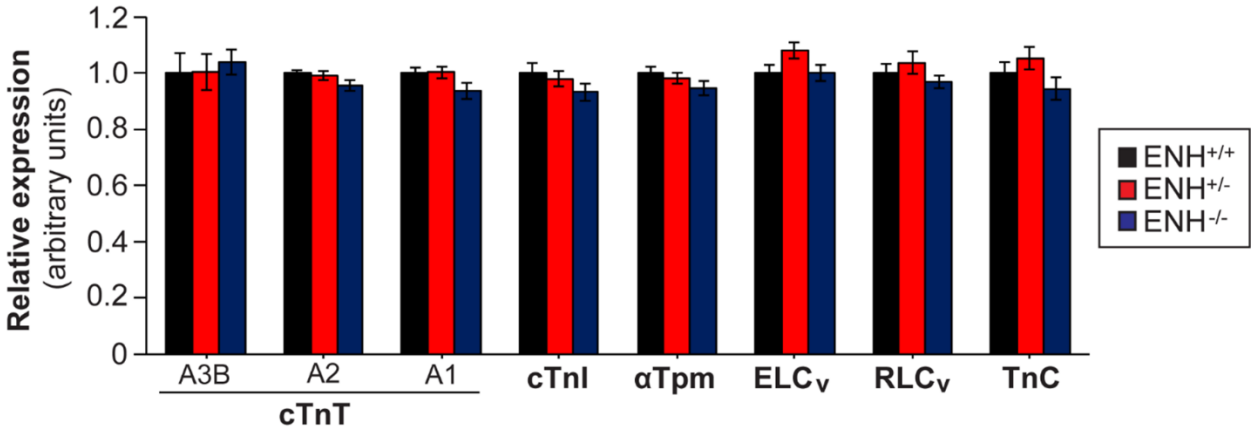

Fig. 5.10. Expression profile of sarcomeric proteins in the left ventricular myocardium of ENH$^{+/+}$, ENH$^{+/-}$, and ENH$^{-/-}$ mice. Graph showing MS-based quantification of sarcomeric protein expression in ENH$^{+/+}$ (n = 8), ENH$^{+/-}$ (n = 9), and ENH$^{-/-}$ (n = 12) mouse myocardium. Expression data are normalized to expression in ENH$^{+/+}$ mouse myocardium. All data are presented as mean ± SEM. * and # denote that the measured values were significantly different ($p < 0.05$) from values recorded in ENH$^{+/+}$ and ENH$^{+/-}$ ventricular myocardium, respectively, using unpaired two-tailed *t*-test. Abbreviations: cTnT cardiac troponin T, cTnI, cardiac troponin I; Tpm, tropomyosin; ELC$_v$, ventricular myosin essential light chain; RLC$_v$, ventricular myosin regulatory light chain; and TnC, troponin C.

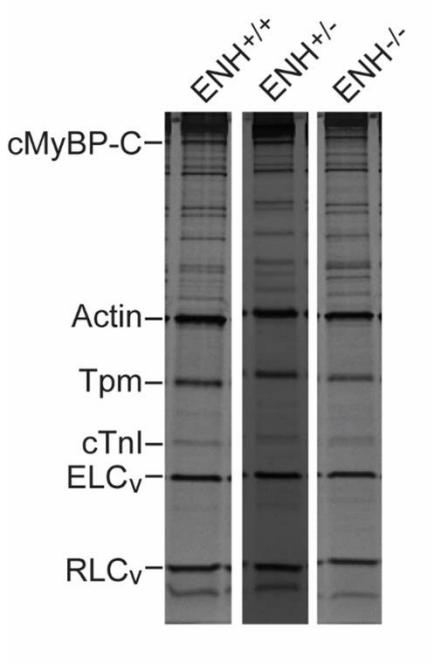

Fig. 5.11. Expression profile of contractile proteins in right ventricular trabeculae isolated from the hearts of ENH$^{+/+}$, ENH$^{+/-}$, and ENH$^{-/-}$ mice. Representative silver stained 12.5% Tris-HCl BioRad Precast Criterion gel showing the expression profile of contractile proteins in ENH$^{+/+}$, ENH$^{+/-}$, and ENH$^{-/-}$ trabeculae. Abbreviations: cMyBP-C, cardiac myosin binding protein C; Tpm, tropomyosin; cTnI, cardiac troponin I; ELC_v, ventricular essential light chain; RLC_v, ventricular regulatory light chain.

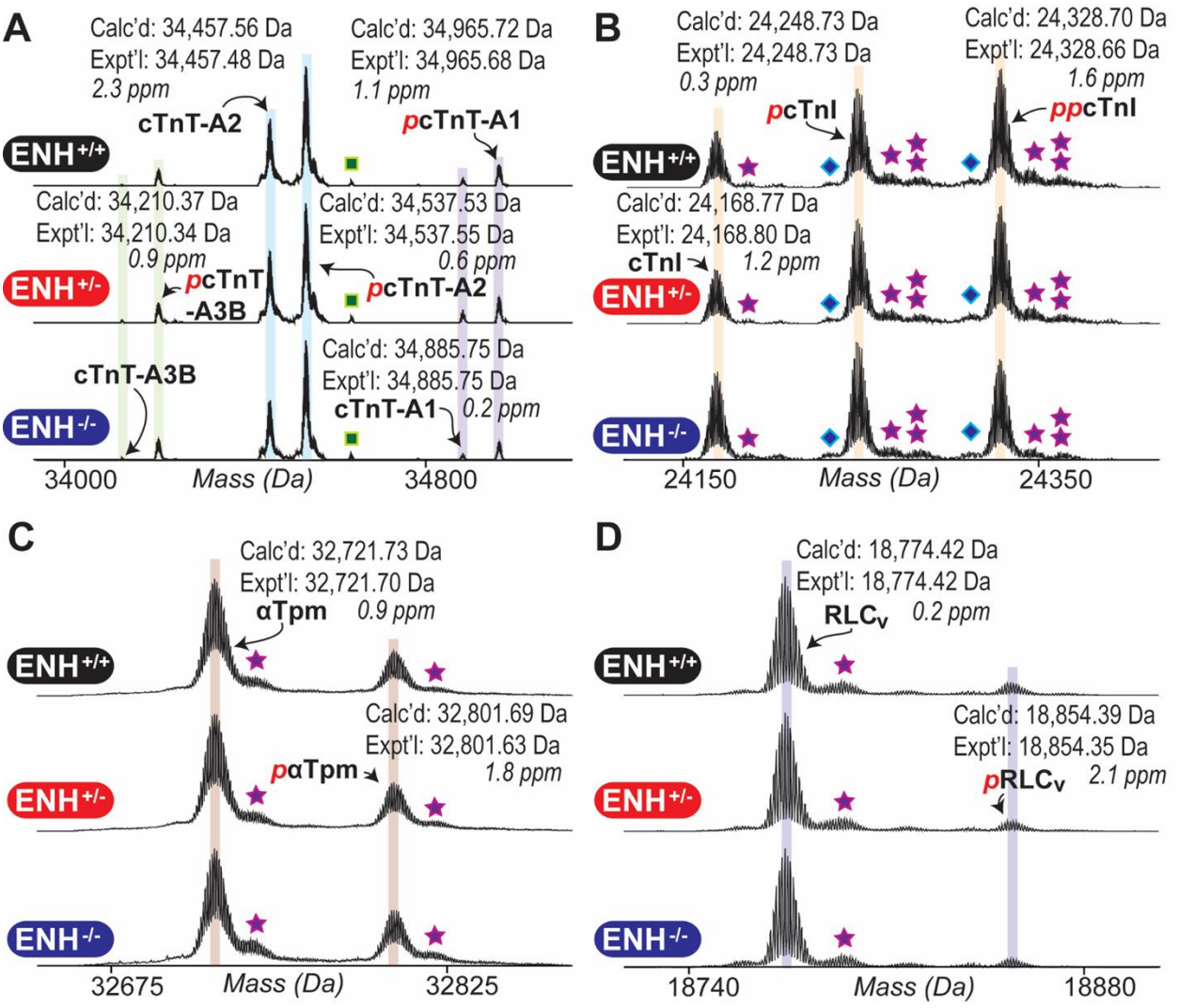

Fig. 5.12. Top-down proteomic analysis of thin/thick filament regulatory protein phosphorylation in ENH$^{+/+}$, ENH$^{+/-}$, and ENH$^{-/-}$ mouse myocardium. Representative zoomed-in deconvoluted mass spectra showing the relative intensities of unmodified and modified forms of cTnT isoforms (A), cTnI (B), αTpm (C), and RLC$_v$ (D) in ENH$^{+/+}$, ENH$^{+/-}$, and ENH$^{-/-}$ mouse myocardium. Reported masses are the most abundant masses. Squares, stars, and diamonds denote peaks corresponding to proteins associated non-covalently with phosphoric acid (+H_3PO_4), proteins associated non-covalently with sodium ions (+Na^+), and protein species with NH_3 loss, respectively. Abbreviations: cTnT cardiac troponin T; cTnI, cardiac troponin I; Tpm, tropomyosin; and RLC$_v$, ventricular myosin regulatory light chain.

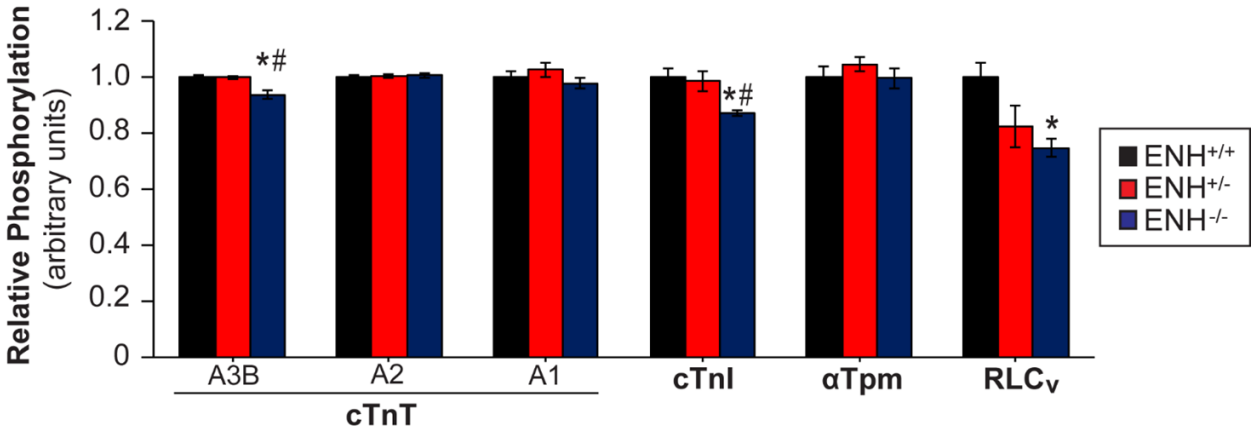

Fig. 5.13. Phosphorylation of sarcomeric proteins in ENH$^{+/+}$, ENH$^{+/-}$, and ENH$^{-/-}$ mouse myocardium. Graph showing MS-based quantification of sarcomeric protein phosphorylation in ENH$^{+/+}$ (n = 8), ENH$^{+/-}$ (n = 9), and ENH$^{-/-}$ (n = 13) mouse myocardium. Phosphorylation levels in ENH$^{+/-}$ and ENH$^{-/-}$ mouse myocardium were normalized to levels in ENH$^{+/+}$ mouse myocardium. Data are presented as mean ± SEM. * and # denote that the measured values were significantly different ($p < 0.05$) from values recorded in ENH$^{+/+}$ and ENH$^{+/-}$ ventricular myocardium, respectively, using unpaired two-tailed *t*-test. Abbreviations: cTnT cardiac troponin T; cTnI, cardiac troponin I; Tpm, tropomyosin; and RLC$_v$, ventricular myosin regulatory light chain.

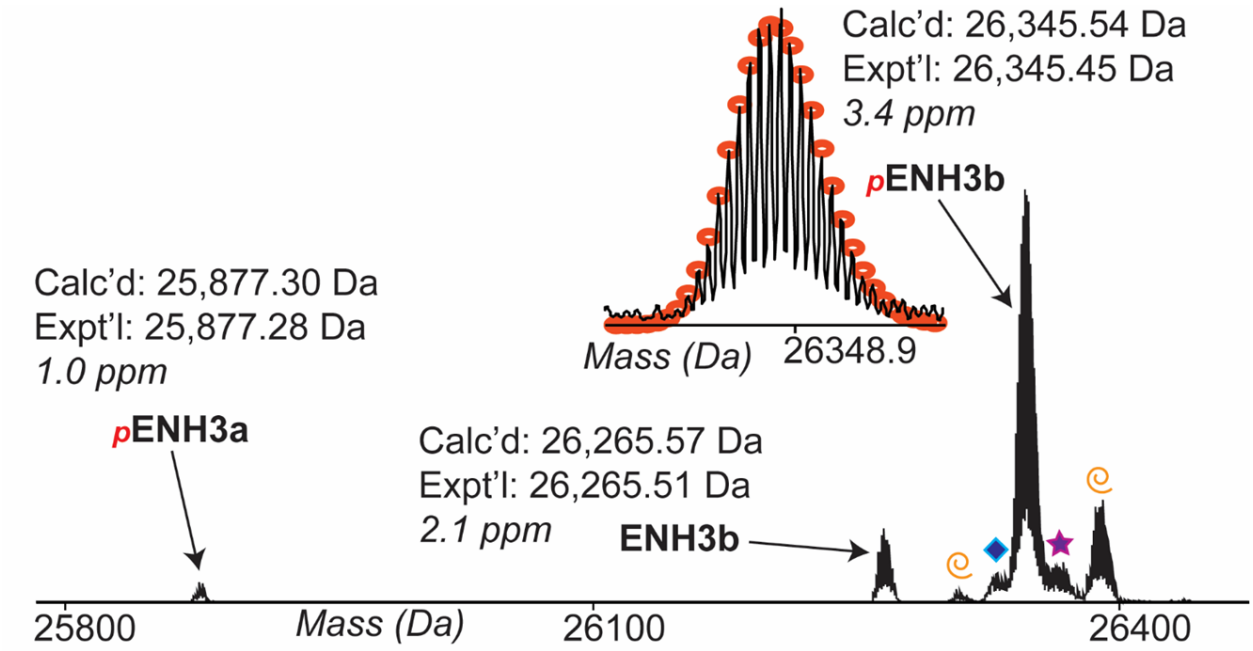

Fig. 5.14. Detection of ENH3 isoforms in mouse ventricular myocardium. Deconvoluted mass spectrum shows peaks corresponding to the phosphorylated form of ENH3a ($_p$ENH3a), as well as the non-phosphorylated and phosphorylated ($_p$ENH3b) forms of ENH3b. Swirl, diamond, and star denote potential acetylated forms of un- and phosphorylated ENH3b (ΔM = +42.00 Da versus ENH3b and $_p$ENH3b, respectively), $_p$ENH3b with NH3 loss, and oxidized $_p$ENH3b, respectively. Circles represent the theoretical isotopic abundance distribution of the isotopomer peaks corresponding to the assigned mass. Abbreviations: ENH3a, enigma homolog isoform 3a; and ENH3b, enigma homolog isoform 3b.

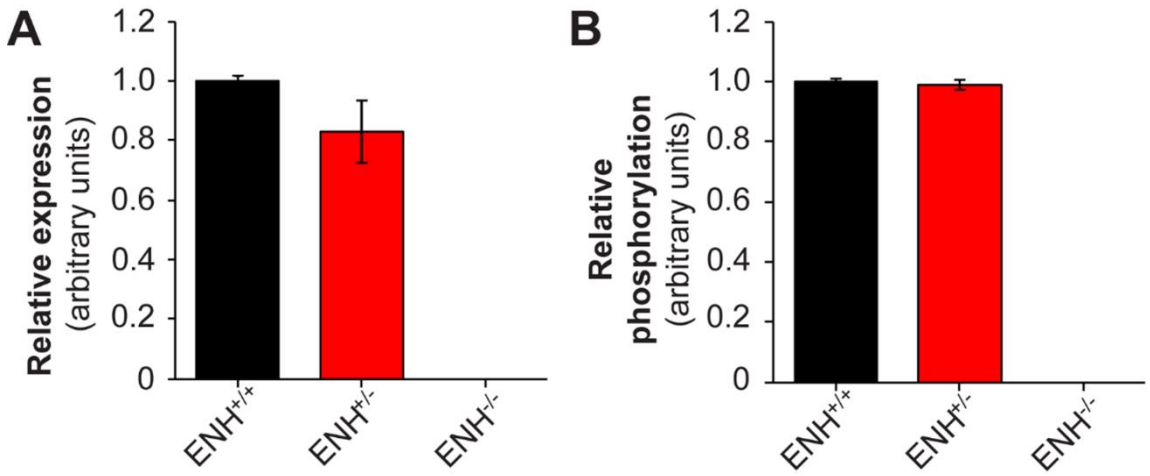

Fig. 5.15. MS-based quantification of ENH3b expression and phosphorylation in ENH$^{+/+}$, ENH$^{+/-}$, and ENH$^{-/-}$ mouse myocardium. Graphs showing MS-based quantification of ENH3b expression (A) and phosphorylation (B) in ENH$^{+/+}$ (n = 8), ENH$^{+/-}$ (n = 9), and ENH$^{-/-}$ (n = 10) mouse myocardium. Expression and phosphorylation levels in ENH$^{+/-}$ and ENH$^{-/-}$ mouse myocardium were normalized to levels in ENH$^{+/+}$ mouse myocardium. Data are presented as mean ± SEM. * and # denote that the measured values were significantly different ($p < 0.05$) from values recorded in ENH$^{+/+}$ and ENH$^{+/-}$ ventricular myocardium, respectively, using unpaired two-tailed *t*-test.

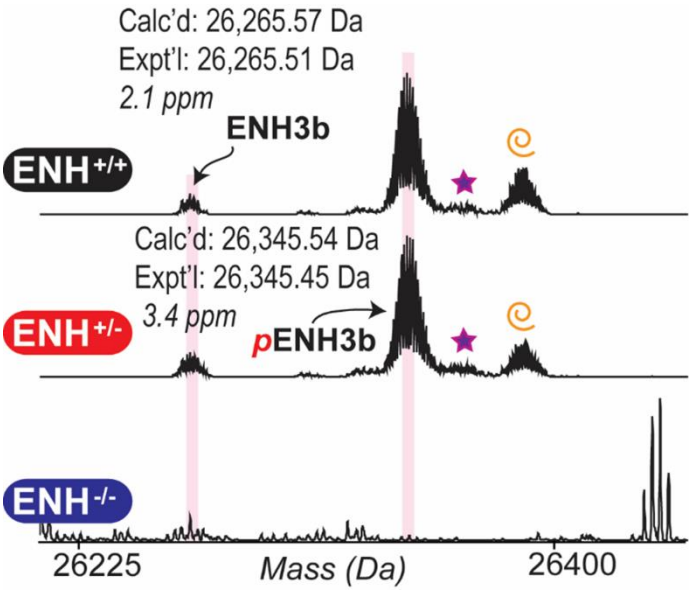

Fig. 5.16. Top-down proteomic analysis of ENH3b protein phosphorylation in ENH$^{+/+}$, ENH$^{+/-}$, and ENH$^{-/-}$ mouse myocardium. Representative zoomed-in deconvoluted mass spectra showing the relative intensities of unmodified and modified forms of ENH3b in ENH$^{+/+}$, ENH$^{+/-}$, and ENH$^{-/-}$ mouse myocardium are shown. Reported masses are the most abundant masses. Stars and swirls denote peaks corresponding to proteins associated non-covalently with sodium ions (+Na^{+}) and a protein form presumably corresponding to acetylated pENH3b (+42.00 Da relative to the $_{p}$ENH3b peak), respectively. Abbreviations: ENH3b, enigma homolog isoform 3b.

CHAPTER 6 – TOP-DOWN TARGETED PROTEOMICS REVEALS DECREASE IN MYOSIN REGULATORY LIGHT-CHAIN PHOSPHORYLATION THAT CONTRIBUTES TO SARCOPENIC MUSCLE DYSFUNCTION

Reprinted with permission from *Journal of Proteome Research*. Gregorich ZR, Peng Y, Cai W, Jin Y, Wei L, Chen AJ, McKiernan SH, Aiken JM, Moss RL, Diffee GM, Ge Y. Top-down targeted proteomics reveals decrease in myosin regulatory light chain phosphorylation that contributes to sarcopenic muscle dysfunction. *Journal of Proteome Research*. 2016;15(8):2706-2716. Copyright 2016 American Chemical Society.

Abstract

Sarcopenia, the loss of skeletal muscle mass and function with advancing age, is a significant cause of disability and loss of independence in the elderly, and, thus, represents a formidable challenge for the aging population. Nevertheless, the molecular mechanism(s) underlying sarcopenia-associated muscle dysfunction remain poorly understood. In this study, we employed an integrated approach combining top-down targeted proteomics with mechanical measurements to dissect the molecular mechanism(s) in age-related muscle dysfunction. Top-down targeted proteomic analysis uncovered a progressive age-related decline in the phosphorylation of myosin regulatory light chain (RLC), a critical protein involved in the modulation of muscle contractility, in the skeletal muscle of aging rats. Top-down tandem mass spectrometry analysis identified a previously un-reported bis-phosphorylated proteoform of fast skeletal RLC and localized the sites of decreasing phosphorylation to Ser14/15. Of these sites, Ser14 phosphorylation represents a previously unidentified site of phosphorylation in RLC from fast-twitch skeletal muscle. Subsequent mechanical analysis of single fast-twitch fibers isolated from the muscles of rats of different ages revealed that the observed decline in RLC phosphorylation can account for age-related decreases in the contractile properties of sarcopenic fast-twitch muscles. These results strongly support a role for decreasing RLC phosphorylation in sarcopenia-associated muscle dysfunction, and suggest therapeutic modulation of RLC phosphorylation may represent a new avenue for the treatment of sarcopenia.

6.1 Introduction

The worldwide increase in life expectancy has brought with it a rise in the prevalence of age-related diseases and morbid disorders in the elderly population [350]. Among age-related conditions, sarcopenia, which is the loss of skeletal muscle mass and contractile function with increasing age [153-155], represents a formidable challenge for the aging population. Sarcopenia is associated with disability, reduced quality of life, and loss of independence in the elderly [156]; and places significant demand on public health care and imposes substantial economic costs [158]. Nevertheless, the molecular mechanism(s) underlying the age-related deterioration of skeletal muscle contractile function remain incompletely understood [153, 155]. Hence, there is an urgent need for innovative approaches enabling identification of the molecular determinants of age-related muscle dysfunction to aid the development of therapeutic strategies to attenuate or prevent sarcopenia in aging individuals.

The hallmarks of sarcopenia include progressive muscle atrophy, particularly of type II (fast-twitch) skeletal muscles, which are more susceptible to age-related atrophy than type I (slow-twitch) muscles [168, 169], as well as contractile dysfunction that is, in part, due to alterations in the structure and function of myofilaments [351]. Myofilaments are composed of interdigitating thick and thin filaments that constitute the contractile apparatuses and, thus, are responsible for force production during muscle contraction [352, 353]. Myosin, the principal component of the thick filament, is a hexamer consisting of two heavy chains, two regulatory light chains (RLC), and two essential light chains [263, 352]. The dumbbell-shaped RLC stabilizes the myosin lever-arm, and plays a significant role in modulating the contractile function of skeletal muscle [30, 31,

63, 64, 74, 78, 354]. In particular, phosphorylation of RLC by Ca^{2+}/calmodulin-dependent myosin light chain kinase (MLCK) is known to potentiate both maximal force and the rate of force generation by actin-myosin cross-bridges, as well as increase the Ca^{2+}-sensitivity of the contractile apparatus [30, 31, 63, 64, 74, 78, 354]. Therefore, given that previous studies have shown that sarcopenia-associated muscle dysfunction is associated with decreased force production [178, 355], maximal shortening velocity [179, 356, 357], and Ca^{2+}-sensitivity of force [358], we hypothesized that there are age-related changes in RLC phosphorylation that contribute to sarcopenic muscle dysfunction.

Top-down mass spectrometry (MS)-based proteomics has quickly become the method of choice for the in-depth characterization of proteoforms [a term encompassing the myriad protein species arising from a single gene as a consequence of sequence variations and post-translational modifications (PTMs)] [206]. Unlike the conventional bottom-up approach, which is sub-optimal for comprehensive proteoform analysis due to protein digestion, the top-down approach analyzes whole proteins, thereby providing a "bird's eye view" of the full complement of protein proteoforms with full sequence coverage [197, 198, 200]. Following intact protein analysis, specific proteoforms of interest can be isolated and fragmented by a variety of tandem MS (MS/MS) techniques to localize PTMs and sequence variations. Although recent studies have showcased the power of large-scale top-down proteomics in discovery mode [220, 312], this approach comes at the cost of reduced sensitivity and stochastic sampling [359]. Recently, a hypothesis-driven targeted proteomics approach, which can detect and reliably quantify specific proteoforms of interest with exceptional sensitivity and reproducibility, has gained popularity [313, 329, 360-365]. We and others have shown that top-down targeted proteomics offers

unparalleled opportunities for the characterization and quantification of proteoforms towards elucidation of the underlying molecular mechanism(s) in cardiovascular and infectious diseases, among others [202, 215, 218, 221, 244, 366].

In this study, we utilized top-down targeted proteomics to assess age-related changes in RLC proteoforms in the fast-twitch skeletal muscle of rats. Our analysis uncovered a significant progressive decline in RLC phosphorylation with increasing age. Top-down MS/MS analysis identified a previously un-reported bis-phosphorylated proteoform of fast skeletal RLC and localized the sites of decreasing phosphorylation to Ser14/15. Of these sites, Ser14 phosphorylation has not previously been identified. Subsequent mechanical analysis of single skinned fast-twitch muscle fibers from rats of different ages revealed that the age-related decrease in RLC phosphorylation is responsible for altered mechanical function, including significant decreases in maximal force, the Ca^{2+}-sensitivity of force, loaded shortening velocity, and power output, in aged muscle fibers. To our knowledge, this is the first report linking a progressive decline in RLC phosphorylation to specific contractile defects in sarcopenic fast-twitch muscle fibers. Furthermore, these results suggest that therapeutic targeting of RLC phosphorylation may represent a new avenue for the treatment of sarcopenic muscle dysfunction in elderly individuals.

6.2 Materials and methods

6.2.1 Animals

Male Fisher 344 x Brown Norway F1 hybrid rats (F344BN) aged 6- (n=12), 24- (n = 12), and 36-months (n=12) were obtained from the National Institute on Aging (NIA) colony maintained by Harlan Sprague-Dawley (Indianapolis, IN, USA). Rats were individually housed in clear plastic cages on a 12h/12h light/dark cycle with access to food and water ad libitum. Handling and euthanasia were carried out under the guidelines of University of Wisconsin-Madison Animal Use and Care Committee. Rats were anesthetized by inhalation of isoflurane, and the gastrocnemius muscles were quickly excised and weighed. The gastrocnemius muscle from one leg from each rat was bisected. One-half of each muscle was prepared for histological analysis as described below, while the other half was flash frozen in liquid N_2 and stored at -80 ºC for subsequent top-down targeted proteomic analysis. The gastrocnemius muscle from the other leg was dissected in relaxing solution to prepare single fibers.

6.2.2 Histology

The gastrocnemius muscle from the left hind limb was dissected from origin to insertion and immediately weighed. Muscles were bisected at the mid-belly, embedded in optimal cutting temperature compound (Tissue-Tek; Andwin Scientific, Addison, IL, USA), frozen in liquid N_2, and stored at −80 °C for later sectioning. The contralateral gastrocnemius muscle was dissected and used to isolate fiber bundles for contractile measurements. Histological measurements were conducted as described previously [167]. Three consecutive sections (10 µm thick) were cut, starting at the mid-belly, placed on labeled ProbeOn Plus microscope slides (Fisher Scientific, Pittsburgh, PA, USA), and stored at −80 °C until use. The first section of each series was stained with hematoxylin and eosin (H&E). Sections were photographed using an Olympus BH2

microscope with an Olympus DP70 digital camera and mid-belly composites of each muscle section were reconstructed by interlacing the images using ImagePro Plus software (Media Cybernetics, Atlanta, GA, USA). For fiber counts, individual muscle fibers were annotated on the composite image of the entire muscle cross-section at the mid-belly, using Adobe Photoshop (Adobe Systems, Inc., San Jose, CA, USA), and total count was tabulated. The whole muscle cross-sectional area (CSA) at the mid-belly was measured by tracing an outline of each muscle using ImagePro Plus. To measure individual muscle fiber CSA, four images (10×) from the H&E sections were captured from gastrocnemius muscles at each age group. A grid with 25 random dots was placed over the images, and the CSA of fibers marked with the dots was measured. Six hundred fibers were measured from each muscle at each age group ([4 images per muscle] × [25 fibers per image] × [6 animals per age group] = 600 fibers). The second tissue section from each series was stained using Masson's trichrome method [367] to distinguish muscle tissue from collagen. Briefly, the tissue was incubated with Bouin's fixative for 1 hour at 56 °C, stained with Weigert's iron hematoxylin (for 10 minutes) and Biebrich scarlet-acid fuchsin (for 15 minutes), and incubated with phosphomolybdic-phosphotungstic acid (for 15 minutes) and aniline blue (for 20 minutes). Tissue sections were rinsed in double distilled H_2O after each step. With this method, muscle fibers stain red and collagen stains blue.

6.2.3 Protein extraction

Extraction of the myofilament sub-proteome from the gastrocnemius muscles of rats from different age groups was carried out as previously described [244]. Briefly, approximately 10 mg of skeletal muscle tissue was homogenized in 100 μL of HEPES extraction buffer containing protease and

phosphatase inhibitors (25 mM HEPES pH 7.5, 50 mM NaF, 0.25 mM Na_3VO_4, 0.25 mM PMSF, 2.5 mM EDTA) using a Teflon pestle (1.5 mL tube rounded tip; Scienceware, Pequannock, NJ, USA). The resulting homogenate was centrifuged at 16,000 × g for 15 min at 4 °C, and the supernatant was discarded. The insoluble pellet was then re-homogenized in 100 µL of TFA extraction buffer (1% TFA, 1 mM TCEP) to extract the myofilament proteins. After centrifugation (16,000 × g, 4 °C, 25 min), the supernatant was collected and used for MS and MS/MS analyses.

6.2.4 On-line liquid chromatography (LC)-MS

Myofilament extracts were separated using a Dionex U3000 LC system (Thermo Scientific, Bremen, Germany) equipped with a home-packed PLRP column (PLRP-S, 200 mm x 500 µm, 10 µm, 1000 Å; Varian, Lake Forest, CA, USA) and a gradient going from 20% B to 90% B (solvent A: 0.10% formic acid in water; solvent B: 0.10% formic acid in a 50:50 mixture of acetonitrile and ethanol) over 40 min at a flow rate of 12.5 µL/min. The Dionex U3000 LC system was coupled on-line with an Orbitrap Fusion Lumos Tribrid mass spectrometer (Thermo Scientific). Samples were introduced into the mass spectrometer using a spray voltage of 3.5 kV. The mass spectrometer was operated in intact protein mode with a resolution setting of 240,000 (at 200 *m/z*) and an automatic gain control target value of 200,000.

6.2.5 Fraction collection

LC-based separation of the myofilament sub-proteome and fraction collection of RLC was carried out as previously described [244], with minor modifications. Briefly, myofilament extracts

prepared from skeletal muscle tissue were separated using a 2D-nano-LC system (Eksigent, Redwood City, CA, USA) equipped with a home-packed PLRP column and a gradient going from 20% B to 90% B over 40 min (solvent A: 0.10% formic acid in water; solvent B: 0.10% formic acid in a 50:50 mixture of acetonitrile and ethanol) at a flow rate of 12.5 μL/min. The 2D-nano-LC system was coupled on-line with a linear ion trap (LTQ) mass spectrometer (Thermo Scientific). After LC separation, a small portion of the sample (~5% of the total amount) was ionized by electrospray ionization through a 25-30 μm i.d. tip and analyzed by LTQ/MS to track protein elution from the column. The remaining ~95% of the sample was collected on ice for off-line MS/MS analysis.

6.2.6 High-resolution MS/MS

The collected fractions were analyzed using a 7T linear ion trap/ Fourier transform ion cyclotron resonance (FT-ICR) mass spectrometer (LTQ/FT Ultra, Thermo Scientific) equipped with an automated chip-based nano ESI source (Triversa NanoMate; Advion Bioscience, Ithaca, NY, USA) as described previously [202, 213, 218, 244]. The sample was introduced into the mass spectrometer using a spray voltage of 1.3 kV. Ion transmission into the linear trap and, subsequently, the FT-ICR cell, was optimized to achieve maximum ion signal. The resolving power of the FT-ICR was set at 200,000 (at 400 *m/z*). The number of accumulated charges for a full scan in the linear trap, FT-ICR cell, MS^n FT-ICR cell, and electron capture dissociation (ECD) were 3×10^4, 8×10^6, 8×10^6 and 8×10^6, respectively. For MS/MS experiments, the protein molecular ions of the individual charge states were first isolated and then fragmented using ECD. The energy, delay, and duration parameters for ECD were determined on a case-by-case basis to achieve

optimal fragmentation of precursor ions. Typically between 4,000-10,000 scans were averaged for ECD experiments to ensure the collection of high quality tandem mass spectra for data analysis.

6.2.7 MS and MS/MS data analysis

All mass and tandem mass spectra were analyzed with in-house developed MASH Suite Pro software [273], which is an integrated software with MS-Align+ [247], using a signal-to-noise ratio threshold of 2.5 and a minimum fit of 60%. A 10 ppm cut-off was used for fragment ion assignments and all program-processed data was manually validated. Monoisotopic masses are reported for both intact proteins and fragment ions. At least two technical replicates were performed per biological replicate. Quantification of proteoform relative abundances based on the high-resolution MS data was carried out as described previously [202, 218, 244]. Briefly, the peak heights of the top five isotopomers from the isotopic envelopes corresponding to each RLC proteoform were summed to give the MS signal intensities of each individual RLC proteoform. Subsequently, the total RLC population intensity was determined by adding all of the individual proteoform signal intensities together, and the relative abundances of the un-phosphorylated, mono-phosphorylated, and bis-phosphorylated proteoforms of RLC were calculated by summing the intensities of all proteoforms, including oxidized and adducted proteoforms, related to the un-, mono-, and bis-phosphorylated species, and dividing by the total RLC population intensity. To assess protein phosphorylation levels, the percentages of the mono- ($\%P_{mono}$) and/or bis- ($\%P_{bis}$) phosphorylated protein species were defined as the summed abundances of mono- and/or bis-phosphorylated species over the summed abundances of the entire protein population, respectively.

Based on these percentages, the total amount of phosphorylation (P_{total}) of a single protein was calculated using the following equation:

$$P_{total} = (\%P_{mono} + 2 \times \%P_{bis})/100 \quad \text{(Eq. 1)}$$

6.2.8 Apparatus for mechanical measurements

Bundles of ~50 fibers were dissected from the gastrocnemius muscle of rats, tied to glass capillary tubes, and stored at -22 ºC for up to 4 weeks in relaxing solution containing 50% (v/v) glycerol. For each experiment an individual fiber was pulled from the end of the bundle, a control segment was saved for later protein analysis and an experimental segment 1.5-2.5 mm in length was attached to the experimental apparatus. The experimental technique for performing contractile measurements on skinned skeletal muscle fibers has been described previously [368]. Briefly, the fiber segments were attached between a capacitance-gauge transducer (Model 403, sensitivity of 20 mV/mg and resonant frequency 600 Hz; Aurora Scientific, Ontario, Canada) and a DC torque motor (Model 308; Aurora Scientific, Ontario, Canada). Fibers were attached by placing the ends of the preparation into stainless steel troughs and secured by overlaying a 0.5 mm length of 4-0 monofilament nylon suture on each end, and then tying the suture into the troughs with two loops of 10-0 monofilament suture. This preparation yields very low end compliance and highly uniform striation patterns during Ca^{2+} activations. The length of the preparation was adjusted so that sarcomere length was set to 2.5 µm in relaxing solution and sarcomere length was monitored in pCa 4.5 to determine that sarcomere length did not change significantly during activation. Length changes during contractile measurements were introduced at one end of the preparation driven by

voltage commands from a PC via a 16 bit D/A converter. Force and length signals were digitized at 1 kHz using a 16-bit A/D converter and each displayed and stored on a PC using custom software in LabView for Windows (National Instruments Corp., Austin, TX, USA). The experimental chamber contained three troughs into which the myocyte was moved to effect rapid solution changes. The apparatus was cooled to 15 ºC using peltier devices (Cambion, Cambridge, MA, USA) and a circulating water bath. The entire mechanical apparatus was mounted on a pneumatic vibration isolation table having a cut-off frequency of ~1 Hz.

6.2.9 Solutions for mechanical measurements

Relaxing and activating solutions for skinned fiber preparations have been described previously [368] and contain: 7 mM EGTA, 1 mM free Mg^{2+}, 20 mM imidazole, 4 mM ATP, 14.5 mM creatine phosphate, pH 7.0 (at 15 ºC), various free Ca^{2+} concentrations between 10^{-9} M (relaxing solution) and $10^{-4.5}$ M (maximally activating solution), and sufficient KCl to adjust ionic strength to 180 mM. The final concentrations of each metal, ligand, and metal-ligand complex were determined from the computer program of Fabiato [335].

6.2.10 Force-pCa measurement

Force (tension) was measured as a function of pCa ($-\log[Ca^{2+}]$) in the range of 9.0 to 4.5. All experiments were carried out at 15 ºC. Force was first measured in pCa 4.5, and then in randomly selected submaximal pCa solutions, with every fourth activation made in pCa 4.5 to assess any decline in fiber performance. If maximum force (in pCa 4.5) declined by more than 20% from the

first activation to the last, the cell was discarded and data from that cell were not used). For each activation steady force was allowed to develop, after which the cell was slackened and subsequently transferred to relaxing solution. Total force was measured as the difference between steady developed force and the baseline force immediately after the slack step. Active force was calculated by subtracting resting tension at pCa 9.0 from total force. Force at each pCa was expressed as a fraction of the maximum force (relative tension; measured in solution with pCa 4.5) obtained for that cell under the same conditions. A graph of the force-pCa relationship was generated by plotting, for each pCa tested, the pooled relative force data from each of the fibers from the muscles of 6-, 24-, and 36-month-old rats. As described by Hofmann et al. [260], data were analyzed by least-squares regression using the Hill equation:

$$\log[P_{rel}/(1-P_{rel})] = n(\log[Ca^{2+}] + k) \quad \text{(Eq. 2)}$$

where P_{rel} is force expressed as a fraction of maximal force, *n* is the Hill coefficient, and *k* is the intercept of the fitted line with the x axis, which corresponds to the $[Ca^{2+}]$ at half-maximal force (pCa_{50}). Using constants derived from the Hill equation, force data was fit by computer with the following equation:

$$P_{rel} = [Ca^{2+}]n/(kn + [Ca^{2+}]n) \quad \text{(Eq. 3)}$$

Confirmation of the identity of fast-twitch fibers was carried following force-pCa measurements via SDS-PAGE analysis of myosin heavy chain isoform expression [179]. Only data from fibers that were identified as expressing predominantly type IIb myosin heavy chain were used.

6.2.11 Force-velocity and power-force measurements

The solutions and protocol for force-velocity and power-load measurements were similar to those described previously for experiments on cardiac myocytes [369]. Briefly, the shortening velocity of skinned skeletal muscle fibers was determined at varied loads. All experiments were conducted with sarcomere length set to 2.3 μm. The fibers were transferred into activating solution (pCa 4.5) and steady force was allowed to develop. The computer then switched the motor from length control mode to force control mode by applying a 5 V logic pulse. The fibers were rapidly stepped to a specified force, which was maintained for 100-300 ms while changes in fiber length were monitored. Following this force clamp, the fiber was slackened to reduce the force to zero to allow measurement of the relative force during the isotonic shortening period. Several (between 8-10) different force levels were carried out on given myocytes. Force was expressed normalized to maximal force during a given activation (P/Po). Secondary to force-velocity measurements, the identity of fast-twitch fibers was confirmed by SDS-PAGE analysis of myosin heavy chain isoform expression. Only data from fibers that were identified as expressing predominantly type IIb myosin heavy chain were used. A power-load curve was constructed by multiplying, in each fiber, the velocity values times the force values for each force clamp. The resulting power output data was then summed for all trained cells and all control cells. If the maximal force declined by more than 50% during the experimental protocol that cell was discarded and the data were not used.

6.2.12 Statistical analysis

Student's *t*-test was performed between group comparisons to evaluate the statistical significance of variance. Differences among means were considered to be significant at $p < 0.05$.

6.3 Results

6.3.1 An integrated approach combining top-down targeted proteomics with functional measurements in sarcopenic fast-twitch skeletal muscle

Herein, we utilized an integrated approach combining the power of top-down targeted proteomics with functional assays to dissect the molecular mechanism(s) underlying sarcopenic fast-twitch muscle dysfunction (**Fig. 6.1**). The key features of this approach include (a) the use of a Fisher 344 x Brown Norway F1 hybrid (F344BN) rat model of sarcopenia. As recommended by the National Institute on Aging (NIA), F344BN rats were chosen for this study because they have a low incidence of age-related pathologies, which could confound the interpretation of age-associated changes in skeletal muscle mass and function [167]. Three age groups, 6- (young), 24- (middle-age) and 36-month-old (old) F344BN rats were used in this study. (b) Top-down targeted proteomic analysis enabling reliable and reproducible quantification of RLC proteoforms in the fast-twitch skeletal muscle of rats in different age groups. Here, we employed a top-down targeted liquid chromatography (LC)-MS method for the separation and quantification of fast skeletal RLC proteoforms in the muscles of rats of different ages. The entire procedure, including tissue homogenization, myofilament protein extraction, and LC-MS, can be completed in less than 3 hours. Fraction collection of fast skeletal RLC during on-line LC-MS allows for in-depth high-resolution MS/MS characterization of RLC proteoforms. Additionally, only a small amount of

muscle tissue (<5 mg) is needed [244]. (c) Mechanical measurements using single skinned muscle fibers. We assessed maximal isometric force, Ca^{2+}-sensitivity of force, and loaded shortening velocity in skinned single muscle fibers isolated from young, middle-age, and old rat skeletal muscles in parallel with proteomic analysis. Mechanical analyses conducted using single skinned fibers have advantages over analyses conducted *in vivo*, as well as those using multicellular muscle preparations. Firstly, it allows for direct analysis of contractile function at the level of actin-myosin cross-bridges and muscle regulatory proteins *in vitro*, without the confounding influence of endogenous Ca^{2+} or the nervous and endocrine systems. Secondly, the use of single fibers eliminates possible functional variations due to the presence of slow-twitch fibers, which is achieved by the selective analysis of fast-twitch muscle fibers, that are affected by sarcopenia to a greater extent that slow-twitch muscle fibers [168, 169]. (d) Correlation of the targeted proteomic data with data from mechanical assays. To our knowledge, this represents the first study combining top-down targeted proteomics with data from mechanical assays to link age-related changes in specific proteoforms to alterations in the contractile function of muscle from individuals with sarcopenia.

6.3.2 Aging is associated with a substantial loss of skeletal muscle mass and a deterioration of muscle quality

Comparison of 6-, 24-, and 36-month-old rats revealed a significant decrease in body mass occurring at advanced age (36 months of age) (**Fig. 6.2A**, **Table 6.1**). To determine if the decrease in body mass was the result of sarcopenia, gastrocnemius muscles, which are primarily composed of fast-twitch muscle fibers [370], were isolated from the hind limbs of rats in different age groups

and compared. Assessment of gastrocnemius muscles showed that muscle mass was significantly decreased at 36 months of age (**Fig. 6.2B**, **Table 6.1**). Normalization of gastrocnemius mass to body mass confirmed the age-related decrease in skeletal muscle mass (**Fig. 6.2C**, **Table 6.1**), which is consistent with the presentation of sarcopenia in aging rats [167]. In addition to decreased skeletal muscle mass, whole muscle cross sections from 36-month-old rats displayed a marked decrease in cross-sectional area (**Fig. 6.2D-G**, **Table 6.1**) in comparison to those from 6-month-old rats in accordance with the presentation of sarcopenia at advanced ages [167]. Further examination of the isolated muscles revealed a progressive decrease in both the number of muscle fibers and fiber diameter with advancing age (**Fig. 6.2H-I**, **Table 6.1**), indicating that the observed decreases in muscle mass and area are the combined result of muscle fiber loss and a concomitant decrease in the size of the remaining fibers. Histochemical analysis of gastrocnemius muscles also showed an age-related increase in fibrosis (**Fig. 6.2J-L**), which is consistent with previous reports of decreased muscle quality in aged individuals due to the deposition of fat and other non-contractile material in the skeletal muscle [153].

6.3.3 Top-down targeted proteomic analysis reveals progressive loss of RLC phosphorylation in fast-twitch skeletal muscle with increasing age

To test the hypothesis that changes in RLC proteoforms occur in sarcopenic muscle, top-down targeted proteomic analysis of RLC extracted from the gastrocnemius muscles of 6-, 24-, and 36-month-old rats was carried out. Proteomic analysis showed three RLC proteoforms with relative molecular masses of 18,868.44 Da, 18,948.40 Da, and 19,028.35 Da, respectively, present in the gastrocnemius muscles of rats in different age groups (**Fig. 6.3A**). After considering removal of

the N-terminal Met and N^{α}-tri-methylation of Ala1 [275], the peak with the relative molecular mass of 18,868.44 Da matched well with the predicted molecular mass of un-phosphorylated RLC from rat fast-twitch skeletal muscle, based on the sequence in the UniProtKB/Swiss-Prot database (accession number P04466) (**Fig. 6.3A**). The mass difference between the peak corresponding to un-phosphorylated RLC and the peak with the relative molecular mass of 18,948.40 Da was 79.96 Da, which matched well with the addition of meta-phosphoric acid (HPO_3, 79.96 Da); thus, this proteoform was assigned as mono-phosphorylated RLC ($_{p}$RLC) (**Fig. 6.3A**). Similarly, the mass difference between the peak corresponding to un-phosphorylated RLC and the peak with the relative molecular mass of 19,028.35 Da was determined to be 159.91 Da, indicating that this peak likely represents a previously un-reported bis-phosphorylated proteoform of fast-twitch skeletal RLC ($_{pp}$RLC) (**Fig. 6.3A**). Highly reproducible separation and MS analysis of biological replicates enabled MS-based quantification of the relative abundances of RLC proteoforms in the gastrocnemius muscles of rats in different age groups (**Figs. 6.4-6.5**). Quantitative top-down targeted proteomic analysis uncovered a significant increase in the relative abundance of the un-phosphorylated RLC proteoform, as well as a corresponding decrease in the relative abundances of the $_{p}$RLC and $_{pp}$RLC proteoforms, with increasing age (**Fig. 6.3B**). Consistent with this observation, total RLC phosphorylation was significantly decreased with advancing age—with reductions of approximately 18% and 26% in 24- and 36-month-old rats, respectively, compared to 6-month-old rats (**Fig. 6.3C**).

6.3.4 Ser14/15 are the sites of decreasing phosphorylation in RLC from the fast-twitch skeletal muscle of aging rats

Whereas previous studies have shown that Ser19 and Ser13/14 are the sites of phosphorylation in the smooth and cardiac muscle isoforms of RLC [296, 371], respectively, only a single site of phosphorylation has been reported in fast skeletal RLC from mouse (Ser15) [78]. Therefore, following the discovery that RLC phosphorylation in skeletal muscle declines with age (**Fig. 6.3**), we next sought to confirm the identity of the quantified MS peaks as fast skeletal RLC proteoforms, and determine the sites of decreasing phosphorylation. To accomplish this, fast skeletal RLC from the gastrocnemius muscles of rats from different age groups was fraction collected and analyzed off-line by high-resolution top-down electron capture dissociation (ECD) MS/MS. After considering removal of the N-terminal Met, all *c* ions resulting from fragmentation of un-phosphorylated RLC showed an approximately 42.046 Da mass increase compared to the predicted masses for these ions, indicating N^{α}-tri-methylation (+42.046 Da) rather than N^{α}-acetylation (+42.010 Da), based on accurate mass measurement (**Fig. 6.6A**). These results confirm those of earlier studies showing that RLC proteoforms are tri-methylated at their N-termini [275]. Note that *c* ions include the N-terminus while $z^{\cdot}$ ions contain the C-terminus (e.g., c_{21} and $z^{\cdot}_{21}$ would contain residues 1-21 and 148-168 in fast skeletal RLC, respectively). Following assignment of N-terminal tri-methylation, the sequence of RLC from fast-twitch skeletal muscle was confirmed with high sequence coverage and mass accuracy (**Fig. 6.6B**, **Fig. 6.7**). To determine the sites of phosphorylation in $_{p}$RLC and $_{pp}$RLC, MS peaks corresponding to these proteoforms were isolated and fragmented using ECD. Fragmentation of $_{p}$RLC revealed that all *c* ions prior to and including c_{14} were detected only in their un-phosphorylated state (**Fig. 6.8A**), indicating that the phosphorylation site is located after Ser14 (numbering is based on the fast skeletal RLC sequence after considering removal of the N-terminal Met). Conversely, all *c* ions after and including c_{15} were detected only in their phosphorylated state (**Fig. 6.8B**), confirming

Ser15 as a site of phosphorylation in $_{p}$RLC. Nevertheless, it is possible that the MS peak corresponding to $_{p}$RLC represents a mixed population of RLC ions phosphorylated at Ser15 and a different site (i.e., positional isomers) [198]; however, analysis of $z\cdot$ ions showed that all $z\cdot$ ions prior to $z\cdot_{154}$ were un-phosphorylated, whereas all $z\cdot$ ions after and including $z\cdot_{154}$ were mono-phosphorylated (**Fig. 6.8C-D**). Therefore, these results unambiguously confirm that Ser15 is the sole site of phosphorylation in $_{p}$RLC isolated from the fast-twitch skeletal muscle of rats of varying ages (**Fig. 6.7B**), which is consistent with previous reports in mouse fast skeletal RLC [78]. Top-down MS/MS analysis of $_{pp}$RLC revealed that all c ions prior to c_{13} were detected in their un-phosphorylated state (**Fig. 6.8E**). Conversely, all c ions after and including c_{15} were detected only in their bis-phosphorylated state (**Fig. 6.8F**), suggesting that Ser14, in addition to Ser15, are the sites of phosphorylation in $_{pp}$RLC. Analysis of $z\cdot$ ions confirmed this localization (**Fig. 6.8G-H**). Thus, we can confidently assign the sites of phosphorylation in fast skeletal $_{pp}$RLC to Ser14/15 (**Fig. 6.7C**), with phosphorylation at Ser14 not having previously been reported. The importance of Ser14/15 phosphorylation in the regulation of fast-twitch skeletal muscle contractility is underscored by the high conservation of these residues across species (**Fig. 6.9**). Collectively, these results indicate that aging is associated with decreased fast skeletal RLC phosphorylation at Ser14/15.

6.3.5 The age-related progressive loss of RLC phosphorylation is associated with impaired contractile function in fast-twitch muscle fibers from aging rats

Previous studies have shown that the contractile function of skeletal muscle is impaired in aged individuals [179, 356, 358, 372]. To determine whether the progressive age-related loss of fast

skeletal RLC phosphorylation was associated with altered contractile function in aging rats, single fast-twitch fibers from the gastrocnemius muscles of 6-, 24-, and 36-month-old rats were isolated, skinned, and subjected to mechanical measurements. Following mechanical measurements, fast-twitch fibers were identified by SDS-PAGE analysis of myosin heavy chain isoform expression. Only data from fibers that were identified as expressing predominantly type IIb myosin heavy chain (indicative of fast-twitch glycolytic fibers) were used. Force measurements made on single skinned fibers from the gastrocnemius of rats in different age groups revealed a significant decrease in maximal force (peak force) in fibers from the muscles of 36-month-old rats compared to fibers from 6-month-old rats (**Fig. 6.10A**, **Table 6.2**). Likewise, the maximal force generated by fast-twitch fibers from 36-month-old rats was significantly decreased in comparison to that from 6-month-old rats after normalization to fiber cross-sectional area (specific force; **Fig. 6.10B**, **Table 6.2**), indicating that the decrease in peak force could not be attributed solely to the observed decrease in fiber size (**Fig. 6.2I**, **Table 6.1**). At sub-maximal Ca^{2+} concentrations (i.e., concentrations of Ca^{2+} lower than those required to produce maximal force) there were significant differences in the relative force (force obtained at sub-maximal Ca^{2+} concentrations normalized to maximal force) generated by fibers in the 3 age groups; with higher levels of force being generated in fast-twitch fibers from 6- compared to 24-month-old muscles, and in 24- compared to 36-month-old muscles (**Fig. 6.10D**). As a consequence, a progressive rightward shift in the force-pCa (where pCa represents the $-\log_{10}$ of the Ca^{2+} concentration) relationship occurred as the age of the muscle fibers increased—an indication of decreased Ca^{2+}-sensitivity of force. The rightward shift in the force-pCa relationship resulted in a significant decrease ($p < 0.05$) in the pCa producing half-maximal force (pCa_{50}) as the animals aged (**Fig. 6.10C**, **Table 6.2**). Analysis of changes in the force-velocity relationship revealed that loaded shortening velocity decreased with increasing age

(**Fig. 6.10E**, **Table 6.2**), implying that the rate of cross-bridge dissociation from the thin filament also declines in aging fast-twitch muscle fibers. Derivation of the power-force relationship from the force-velocity data showed a progressive and significant decrease in normalized peak power output (where power is expressed as the product of the specific force and velocity) with advancing age (**Fig. 6.10F**, **Table 6.2**).

6.4 Discussion

Sarcopenia, which is the age-related loss of skeletal muscle mass and contractile function [153-155], represents a formidable challenge for the aging population—imposing substantial strain on health care systems and contributing to decreased quality of life in older individuals due to sarcopenia-associated disability and loss of independence [156, 158]. Nevertheless, the molecular correlates of sarcopenia-associated muscle dysfunction remain unclear. Given that previous studies have shown age-related decreases in force production [178, 355], maximal shortening velocity [179, 356, 357], and Ca^{2+}-sensitivity of force [358] in aged muscles, as well as extensive literature demonstrating that RLC phosphorylation affects these contractile parameters [30, 31, 63, 64, 74, 78, 354], we hypothesized that age-related changes in the phosphorylation of RLC can account for sarcopenic fast-twitch muscle dysfunction. Herein, top-down targeted proteomic analysis enabled the detection of a progressive age-related decrease in RLC phosphorylation at Ser14/15. Subsequent mechanical analysis of single fast-twitch muscle fibers from young (6-month-old), middle-aged (24-month-old), and old (36-month-old) rats uncovered age-related decreases in force generation, the Ca^{2+}-sensitivity of force, loaded shortening velocity, and power output; all of which can be explained by the observed decrease in RLC phosphorylation [30, 31,

63, 64, 74, 78, 354]. Therefore, our findings identify, for the first time, progressive loss of RLC phosphorylation as a critical mechanism underlying contractile dysfunction in fast-twitch muscle fibers from aged individuals, and suggest that RLC phosphorylation may represent a new target for the treatment of sarcopenic muscle dysfunction.

6.4.1 Sarcopenia and contractile dysfunction

The age-related progressive impairment in whole muscle mechanical function [179, 356, 358, 372] can, in part, be accounted for by muscle fiber atrophy, which contributes to the loss of muscle mass with age [153]. Nevertheless, changes in the contractile properties of single muscle fibers also play a role in sarcopenia-associated mechanical dysfunction as demonstrated here and by other studies [351]. In particular, we observed a decrease in the specific force (force normalized to fiber cross-sectional area) generated by fast-twitch muscle fibers from old rats (36-month-old), which is consistent with the findings of previous studies [178, 355]. Given that specific force accounts for the role played by changes in fiber size (i.e., changes in cross-sectional area due to fiber atrophy) in diminished force production, this result indicates that the age-related impairment of force generation involves alterations at the level of actin-myosin cross-bridges. Two potential mechanisms could account for this, namely, reduced storage and release of sarcoplasmic reticulum Ca^{2+} [373], or intrinsic changes in the contractile apparatuses. Although both mechanisms likely contribute to sarcopenic muscle dysfunction, the measurement of mechanical function in single skinned (permeabilized) fibers in this study removed the influence of endogenous Ca^{2+} levels and allowed the focus to be placed on the contractile apparatus as a source of age-related alterations. In addition to decreased specific force, our analysis also uncovered a progressive age-related

decrease in the Ca^{2+}-sensitivity of force, as measured by the pCa_{50}, which is consistent with the results of previous studies in rodents [358].

Age-related sarcopenia is also associated with a decline in muscle shortening velocity [179, 356]. Much of this decline in shortening velocity can be attributed to the preferential loss of type II (fast-twitch) fibers, which leaves an increased proportion of type I (slow-twitch) fibers in the muscle [355] and results in an overall slowing of muscle contractile speed with age. In order to eliminate the effect of age-associated alterations in fiber-type, we examined shortening velocity selectively in fast-twitch fibers (i.e., fibers expressing predominantly type IIb myosin heavy chain) from rats in three different age groups. Moreover, in previous studies where fiber-type specific changes in shortening velocity have been measured, aging has been associated with a decrease in maximal shortening velocity (V_{max}) [179, 356]. However, V_{max} is a measure of shortening velocity during unloaded contractions, which is an un-physiological condition because muscle always contracts under some load. A more physiologically relevant measure of contractile function is the shortening velocity when the muscle is generating force (i.e., loaded shortening velocity), as measured in this study. Force-velocity measurements in fast-twitch fibers from aging rats enabled the detection of an age-related decrease in loaded shortening velocity.

In addition to age-related changes in loaded shortening velocity, power output (work per unit time), which is the product of force and velocity, has been shown to decrease with age, and is thought to be an important indicator of physical function in older adults [374]. Since muscle fiber power output occurs only during loaded shortening, analysis of loaded shortening velocity in this study allowed for the assessment of age-related changes in power output. Not surprisingly, the observed

decrease in shortening velocity at each load resulted in a progressive decrease in the peak power output in single fibers as the muscles aged. The observed alterations in the force-velocity properties and power output in sarcopenic fast-twitch muscle fibers observed herein are consistent with the findings of previous studies [357, 375].

6.4.2 Decreased RLC phosphorylation as the underlying mechanism of sarcopenic muscle dysfunction

Our targeted proteomic analysis revealed an age-related progressive decrease in RLC phosphorylation that accounts for sarcopenic fast-twitch skeletal muscle dysfunction [30, 31, 63, 64, 74, 78, 354]. At the molecular level, RLC phosphorylation results in repositioning of the myosin heads towards the thin filament, thereby increasing the probability of weak-to-strong force-generating transitions at a given level of Ca^{2+} [30, 31]. Accordingly, based on the age-related decrease in RLC phosphorylation observed in this study, it would be expected that the proportion of myosin heads in strong-binding states would decline with advancing age, as a consequence of a decrease in the number of myosin heads positioned near the thin filament. Indeed, previous studies in aging rat muscle have shown that aging is associated with a decrease in the fraction of myosin heads that are in the strong-binding state during contraction [376]. Additionally, decreased RLC phosphorylation would be expected to decrease force potentiation and cross-bridge cycling kinetics in aged skeletal muscle fibers as a consequence of a decrease in the number of myosin heads interacting with the thin filament [30, 31, 63, 78, 377]. Consistent with this expectation, here we observed age-related decreases in the specific force and loaded shortening velocity of fast-twitch muscle fibers from aged rats, which further supports a causal role for decreased RLC

phosphorylation in sarcopenic muscle dysfunction. It is worth noting that, although the observed decreases in maximal force and shortening velocity could also be explained by age-related changes in myosin ATPase activity, previous studies have demonstrated that the ATPase activity of myosin is not altered with age [178]. In addition to positioning of the myosin head, data from *in vitro* studies has suggested that RLC phosphorylation can also regulate myosin step-size, kinetics, lever-arm stiffness, and can participate in strain-dependent myosin biochemistry [378, 379], although changes in these parameters in aging muscle have not been studied.

Szczesna et al. showed that the skeletal muscle myosin reconstituted with phosphorylated RLC produced a significantly higher Ca^{2+}-sensitivity of force in skinned muscle fibers than non-phosphorylated RLC; convincingly demonstrating that the level of endogenous RLC phosphorylation is a crucial determinant of the Ca^{2+}-sensitivity of force development [64]. In agreement with this, our analysis of sarcopenic fast-twitch fibers from young, middle-aged, and old rats revealed an age-related progressive decline in Ca^{2+}-sensitivity of force that mirrored the decline in fast skeletal RLC phosphorylation. Thus, the age-related decrease in fast skeletal RLC phosphorylation that we have shown here can account for the age-related declines in force generation, Ca^{2+}-sensitivity of force, loaded shortening velocity, and power output in sarcopenic muscle.

Therefore, the results presented herein suggest that augmentation of RLC phosphorylation may improve contractile function in sarcopenic muscle. Interestingly, a recent study also showed that the expression of pseudo-phosphorylated RLC is sufficient to abrogate or prevent the development of hypertrophic cardiomyopathy in a mouse model of hypertrophic cardiomyopathy [266], which

further underscores the significance of RLC phosphorylation as a potential drug target to correct aberrant contractile function in striated muscle. Thus, our finding that decreased RLC phosphorylation underlies age-related fast-twitch muscle dysfunction is timely, particularly given recent interest in direct therapeutic targeting of the sarcomere as a means of correcting muscle dysfunction [95].

6.4.3 Hypothesis-driven top-down targeted proteomics

While discovery-based proteomics has an advantage over targeted proteomics in terms of broad and un-biased proteome coverage, it comes at the cost of reduced sensitivity, stochastic sampling, and a bias against the detection of low abundance proteins [359]. In particular, variability in terms of proteome sampling significantly limits the usefulness of the discovery-based approach for addressing specific questions of biological relevance, especially given the extreme complexity and large dynamic range of the tissue and blood proteomes [359, 380]. On the other hand, for hypothesis-driven research, targeted proteomics provides exceptional sensitivity and reproducibility, enabling reliable quantification of specific proteoforms of interest [313, 329, 360-365]. Top-down targeted proteomics, in particular, has significant advantages for biomedical research, including the ability to detect and localize the full complement of protein PTMs and sequence variations with complete sequence coverage, as well as relative quantification of modified and un-modified proteoforms present within the same spectrum [197, 198, 200, 362, 363]. We and others have already demonstrated that the combination of top-down MS and targeted proteomics is highly promising for identifying both the molecular correlates of disease and potential diagnostic markers [202, 215, 218, 220, 221, 244, 366].

In this study, quantitative top-down targeted proteomics enabled the discovery of a progressive decline in the phosphorylation of RLC in the fast-twitch skeletal muscle of aging rats. This finding not only represents the first report linking age-related changes in the phosphorylation of fast skeletal RLC to contractile dysfunction in sarcopenic muscle, but also highlights the great potential of top-down targeted proteomics for the quantification of proteoform changes in biological samples, and the elucidation of the molecular determinants of disease pathobiology. In addition to localizing PTMs, top-down proteomics allows for the interdependence between PTMs on the same protein to be determined, which is not possible with bottom-up proteomics due to protein digestion. Herein, top-down MS/MS analysis of RLC proteoforms from the fast-twitch skeletal muscle of aging rats facilitated localization of the sites of decreasing phosphorylation to Ser14/15, with phosphorylation of Ser14 not having previously been reported. Moreover, the observation that Ser15 was the only phosphorylated residue in $_{p}$RLC, whereas Ser15 and Ser14 were phosphorylated in $_{pp}$RLC, suggests an ordered mechanism of phosphorylation wherein Ser15 is the first residue phosphorylated and Ser14 the second. As demonstrated here, top-down MS/MS with high-resolution is an especially valuable tool for proteoform analysis, enabling the confident assignment of N^{α}-tri-methylation over N^{α}-acetylation; two modifications differing by approximately 36 mDa. Collectively, the findings of this study showcase both the power of high-resolution top-down targeted proteomics for proteoform analysis, and the potential of integrated approaches combining top-down targeted proteomics with functional assays to dissect the molecular mechanisms of disease.

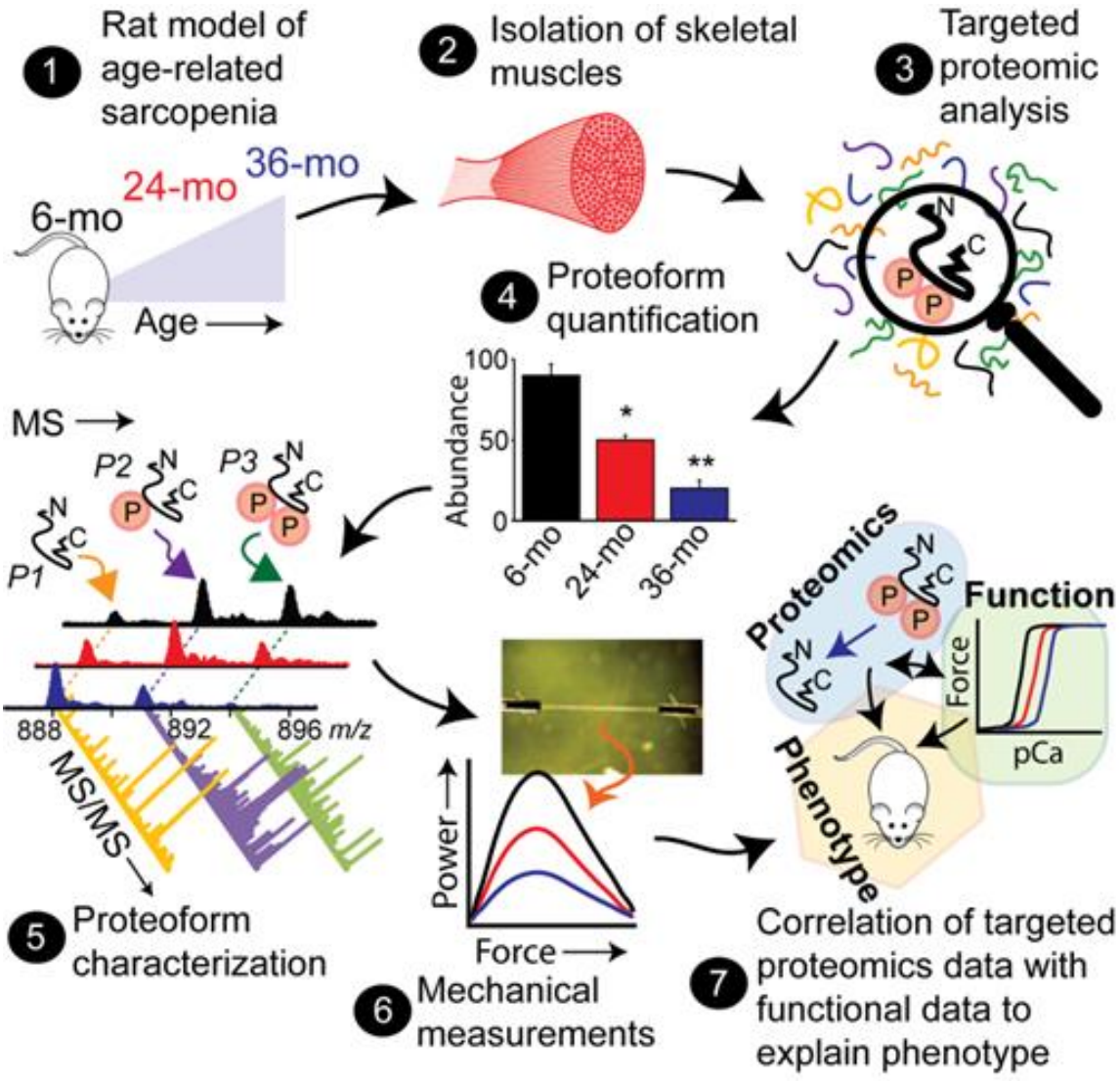

Fig. 6.1. Integrated approach combining top-down targeted proteomics with mechanical measurements to elucidate the molecular mechanism(s) underlying age-related sarcopenia. This approach includes: (1) Use of a rat model of age-related sarcopenia; (2) isolation of skeletal muscle for proteomic and mechanical analyses; (3) top-down targeted proteomics for RLC proteoform analysis; (4) MS-based proteoform quantification; (5) MS/MS analysis for the comprehensive characterization of RLC proteoform sequences and PTMs; (6) mechanical measurements on single fibers; and (7) correlation of the targeted proteomics data with functional data to explain the sarcopenic phenotype. mo, month.

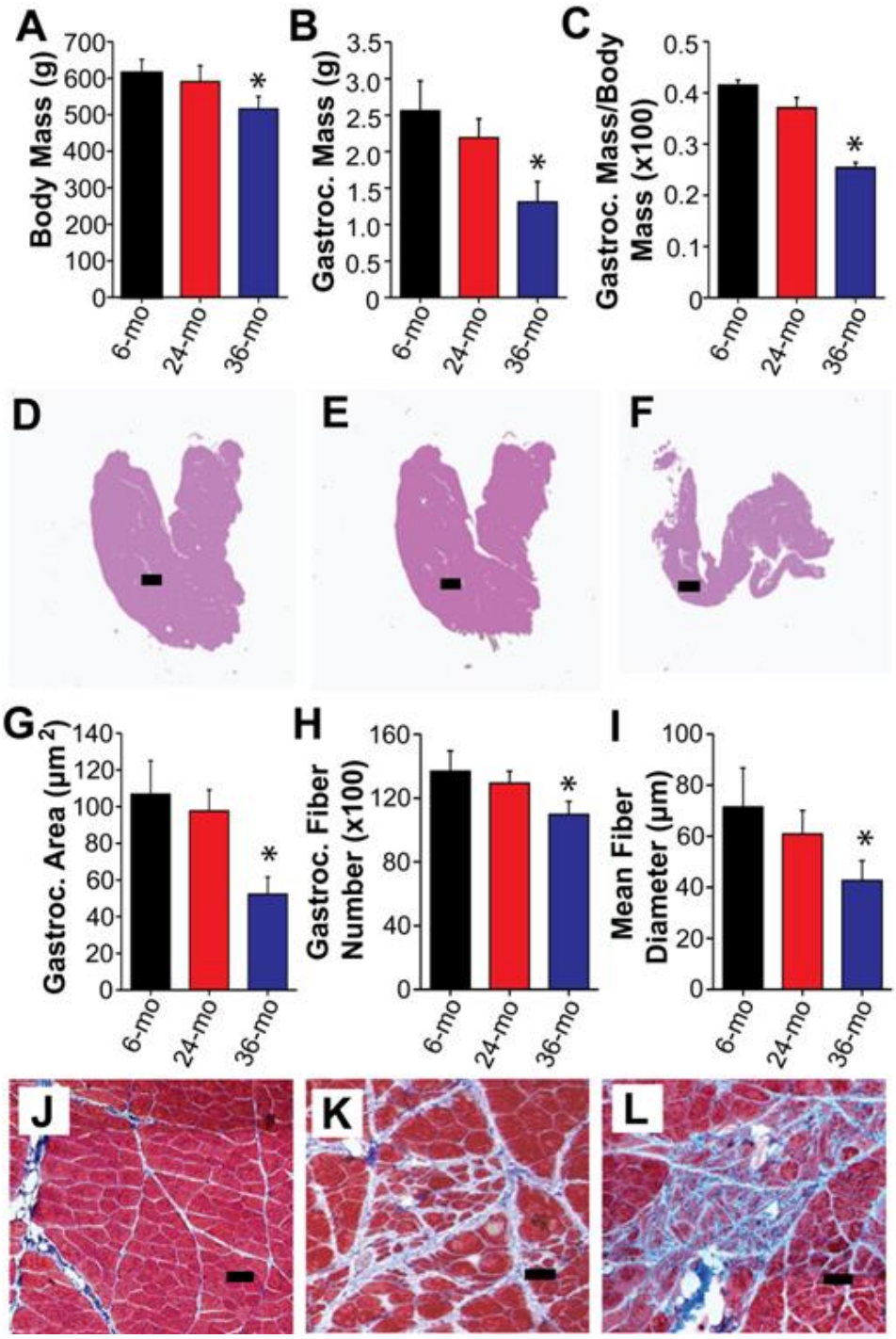

Fig. 6.2. Age-related sarcopenia is associated with loss of skeletal muscle mass and deterioration of muscle quality. (A) Body mass is decreased in 36-month-old rats compared to 6- and 24-month-old rats. The mass of the gastrocnemius muscle (B) and the gastrocnemius muscle mass-to-body mass ratio (C) decline with increasing age. Hematoxylin and eosin stained

whole muscle cross-sections from 6- (D), 24- (E), and 36-month-old rats (F). (G) Quantification of gastrocnemius muscle cross-sectional area in 6-, 24-, and 36-month-old rats. Analysis of gastrocnemius fiber number (H) and mean fiber diameter (I) in rats from different age groups. Muscle sections from 6- (J), 24- (K), and 36-month-old rats (L) stained with Masson's trichrome stain. Red and blue indicate muscle fibers and collagen, respectively. Muscle area, muscle fiber number, and mean fiber diameter were determined from histochemical analysis of muscle sections. Scale bars are 100 μm. mo, month. n = 12 for all groups. All values represent mean ± standard error of the mean (SEM). *$p < 0.05$ vs. 6 mo.

Table 6.1. Body masses and characteristics of gastrocnemius muscles from 6-, 24-, and 36-month-old rats. Muscle area, muscle fiber number, and mean fiber diameter were determined from histochemical analysis of muscle sections. mo, month. All values represent mean ± SEM. *$p < 0.05$ vs. 6 mo.

Age	n	Body Mass (g)	Muscle Mass (g)	Muscle Mass/Body Mass (x 100)	Muscle Area (μm^2)	Muscle Fiber Number	Fiber Diameter (μm)
6-mo	12	614.2 ± 37.4	2.56 ± 0.41	0.415 ± 0.01	106.81 ± 18.22	13677 ± 1284	71.49 ± 15.24
24-mo	12	591.0 ± 43.7	2.19 ± 0.26	0.371± 0.02	97.61 ± 11.47	12931 ± 747	60.88 ± 9.20
36-mo	12	516.1 ± 34.1*	1.31 ± 0.28*	0.254 ±0.01*	52.23 ± 9.32*	10976 ± 818*	42.69 ± 7.75*

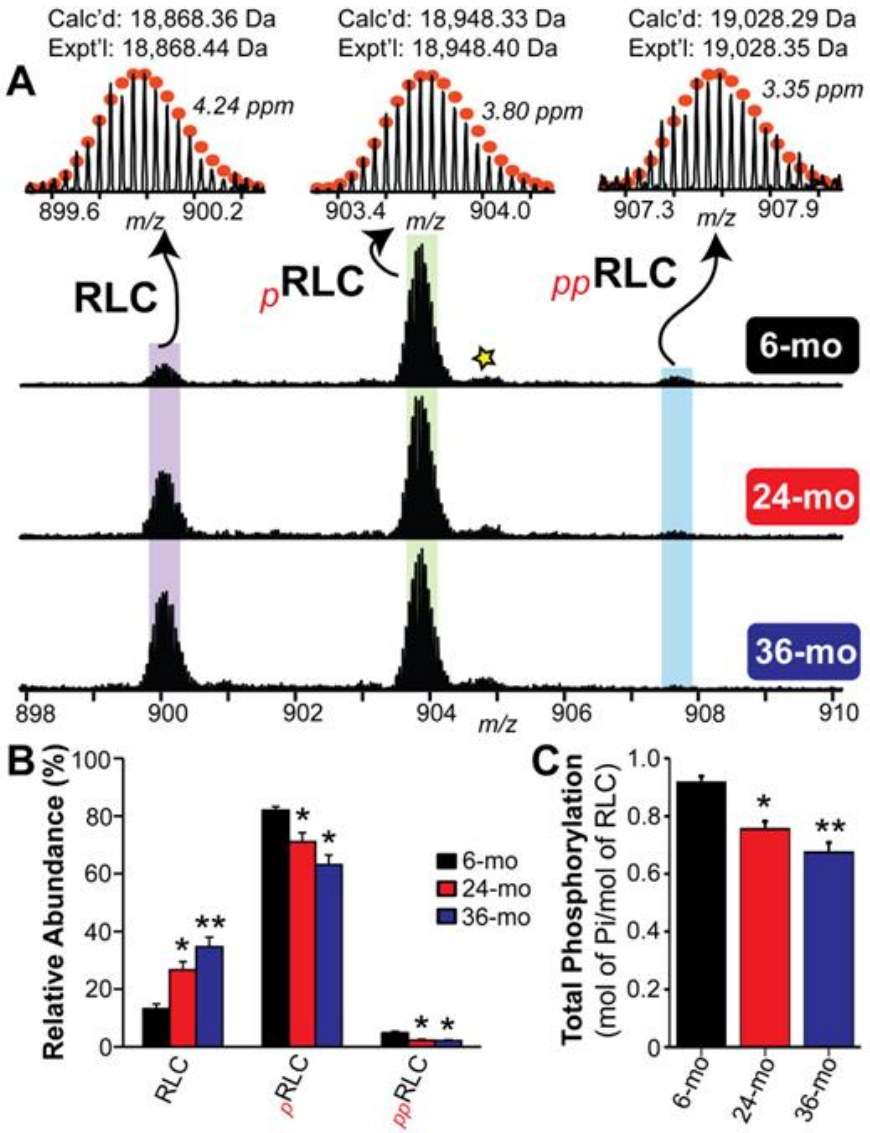

Fig. 6.3. A progressive decrease in the phosphorylation of fast skeletal RLC is observed with advancing age. (A) Representative mass spectra of RLC from 6-, 24-, and 36-month-old rats. Circles represent the theoretical isotopic abundance distribution of the isotopomer peaks corresponding to the assigned mono-isotopic mass. Star represents oxidized $_{p}$RLC. *m/z*, mass-to-charge ratio. Calc'd, calculated most abundant molecular mass based on protein sequence. Expt'l, experimentally determined molecular mass. (B) Graph showing the relative abundances of RLC, $_{p}$RLC, and $_{pp}$RLC proteoforms in the gastrocnemius muscle of rats from different age groups. (C) Graph showing decrease in total RLC phosphorylation (expressed as mol P_i/mol of RLC) with

advancing age. n = 5 for 6- and 24-month-old groups, and n = 6 for 36-month-old group. mo, month. All values represent mean ± SEM. *$p < 0.05$ vs. 6 mo, **$p < 0.001$ vs. 6 mo.

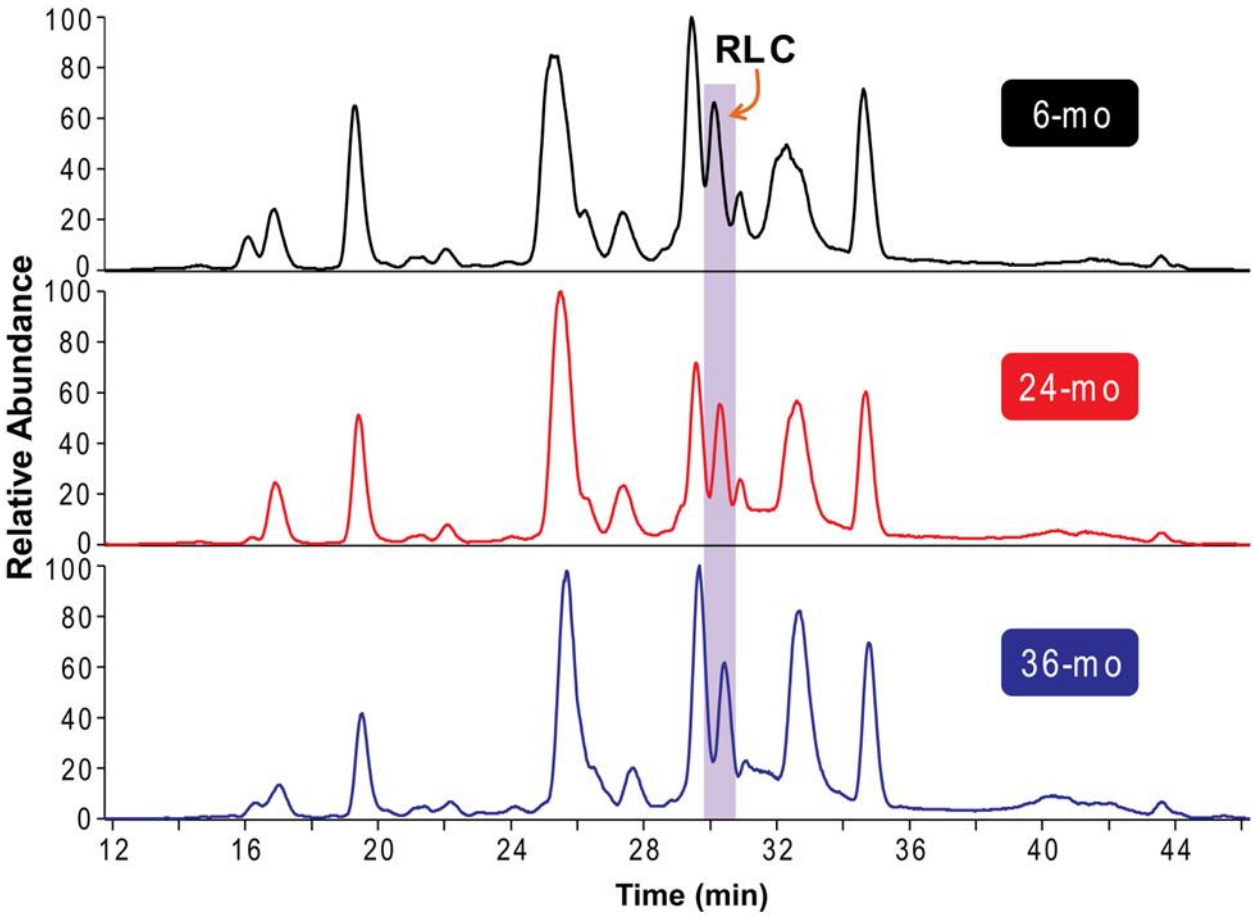

Fig. 6.4. Chromatographic separation of myofilament sub-proteome from the gastrocnemius muscles of rats in different age groups. Highlighted is the chromatographic peak corresponding to the fast-twitch skeletal muscle isoform of RLC. mo, month.

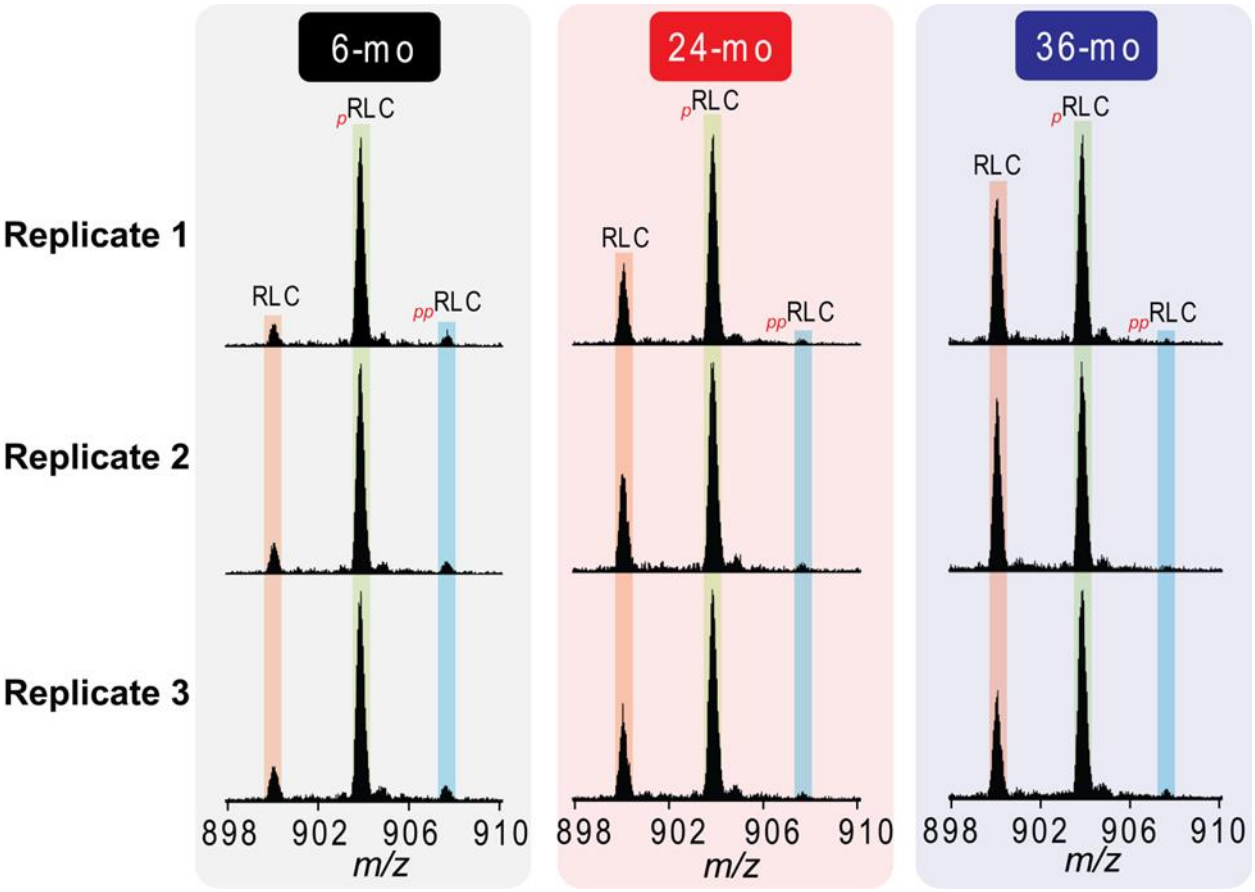

Fig. 6.5. Reproducibility of MS analysis of RLC from representative biological replicates from 6-, 24-, and 36-month-old rats. High reproducibility was observed across biological replicates in each age group. mo, month.

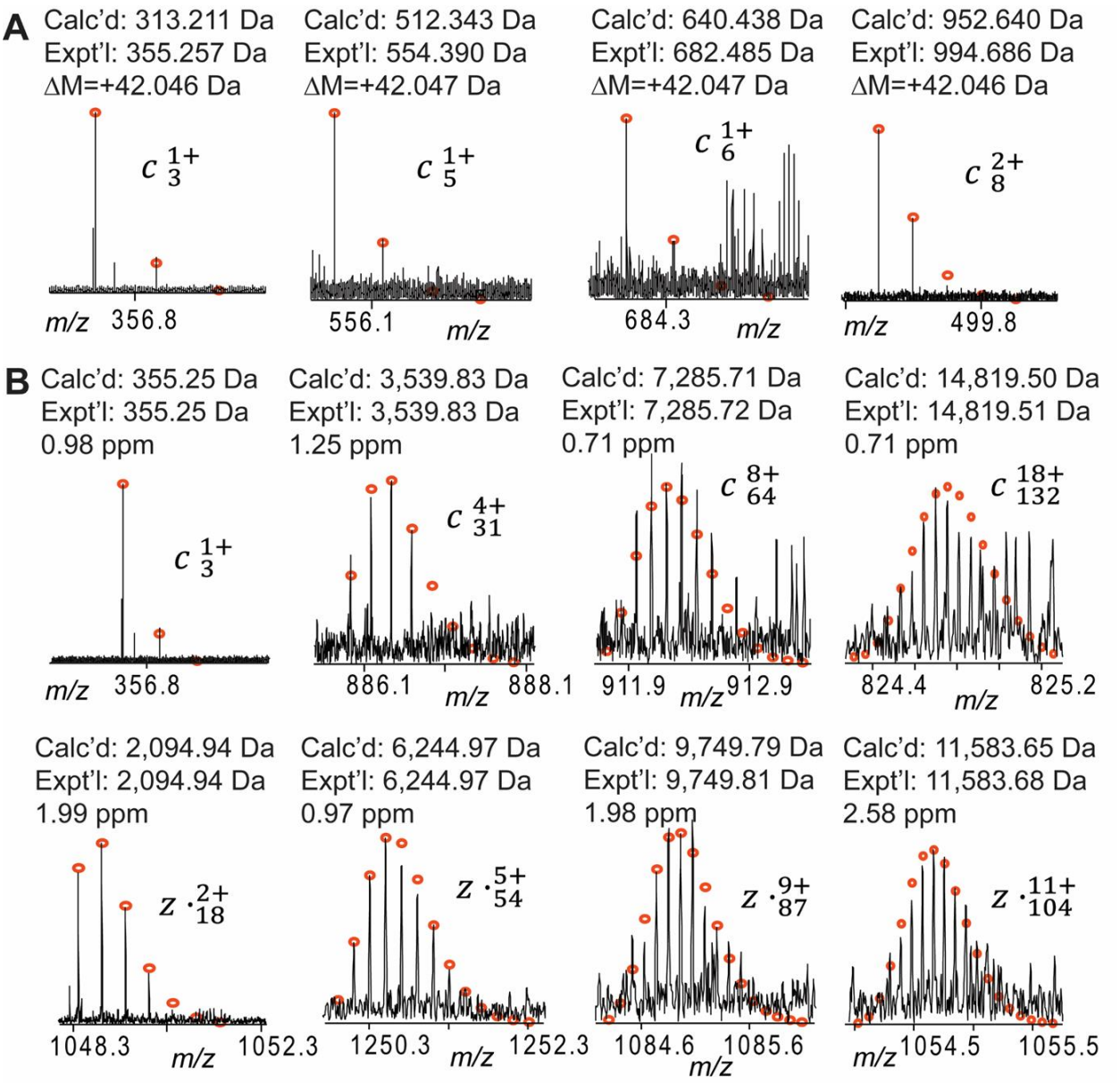

Fig. 6.6. MS/MS characterization of RLC from fast-twitch skeletal muscle. (A) Fragment ions localizing approximate 42.046 Da mass difference (tri-methylation, +42.046 Da) to the N-terminus of the fast-twitch isoform of RLC. (B) Representative *c* and *z*· fragment ions resulting from ECD MS/MS analysis of un-phosphorylated RLC isolated from rat skeletal muscle. Calc'd, calculated mono-isotopic mass based on protein sequence. Expt'l, experimentally determined mono-isotopic mass.

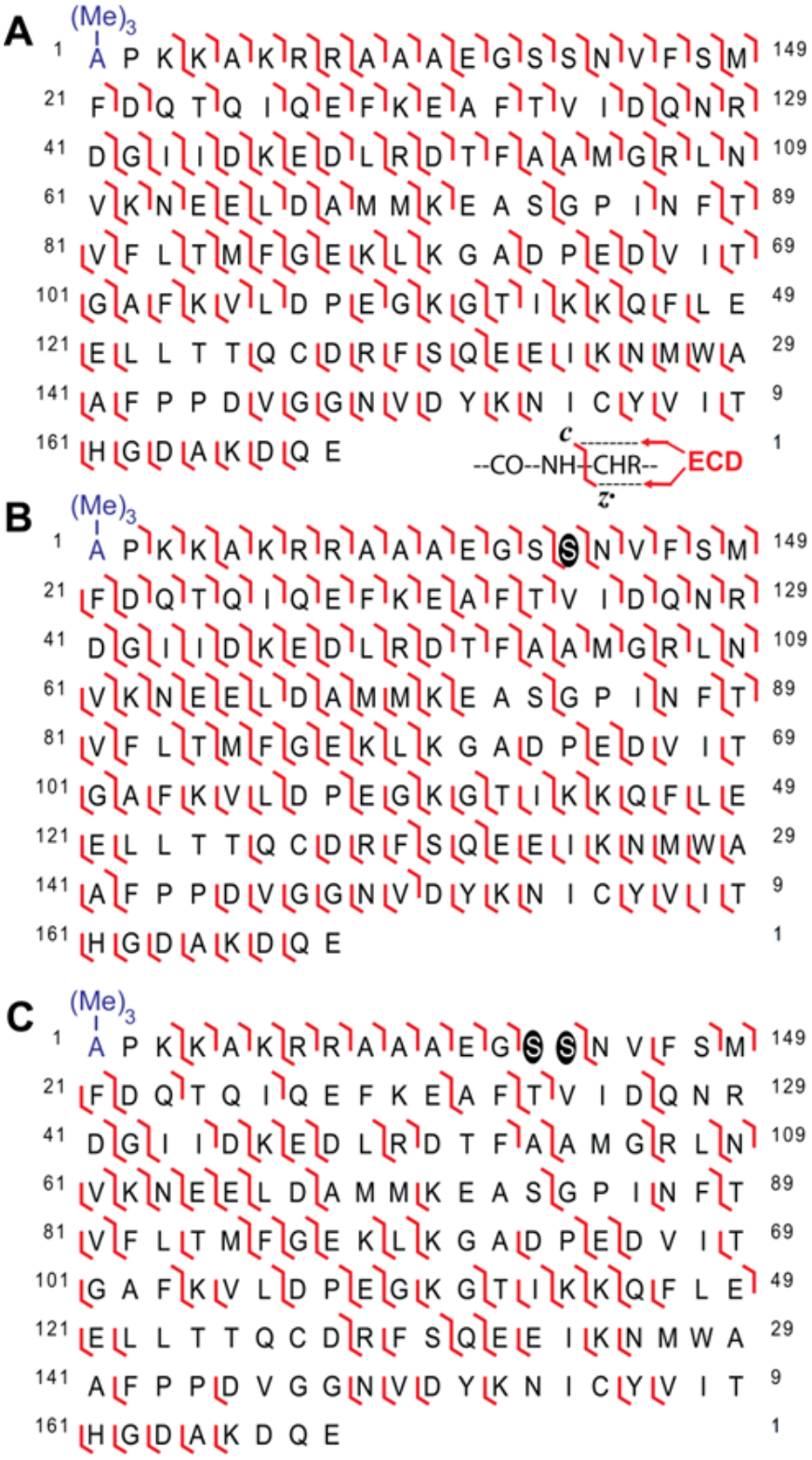

Fig. 6.7. Comprehensive top-down MS/MS analysis uncovers Ser14 and Ser15 as the sites of decreasing phosphorylation in RLC proteoforms from the fast-twitch skeletal muscle of

aging rats. (A) Fragmentation map for un-phosphorylated fast skeletal RLC. Fragmentation maps for $_{p}$RLC (B) and $_{pp}$RLC (C) proteoforms. Phosphorylation sites are highlighted by circles. $(Me)_3$- represents N^{α}-tri-methylation.

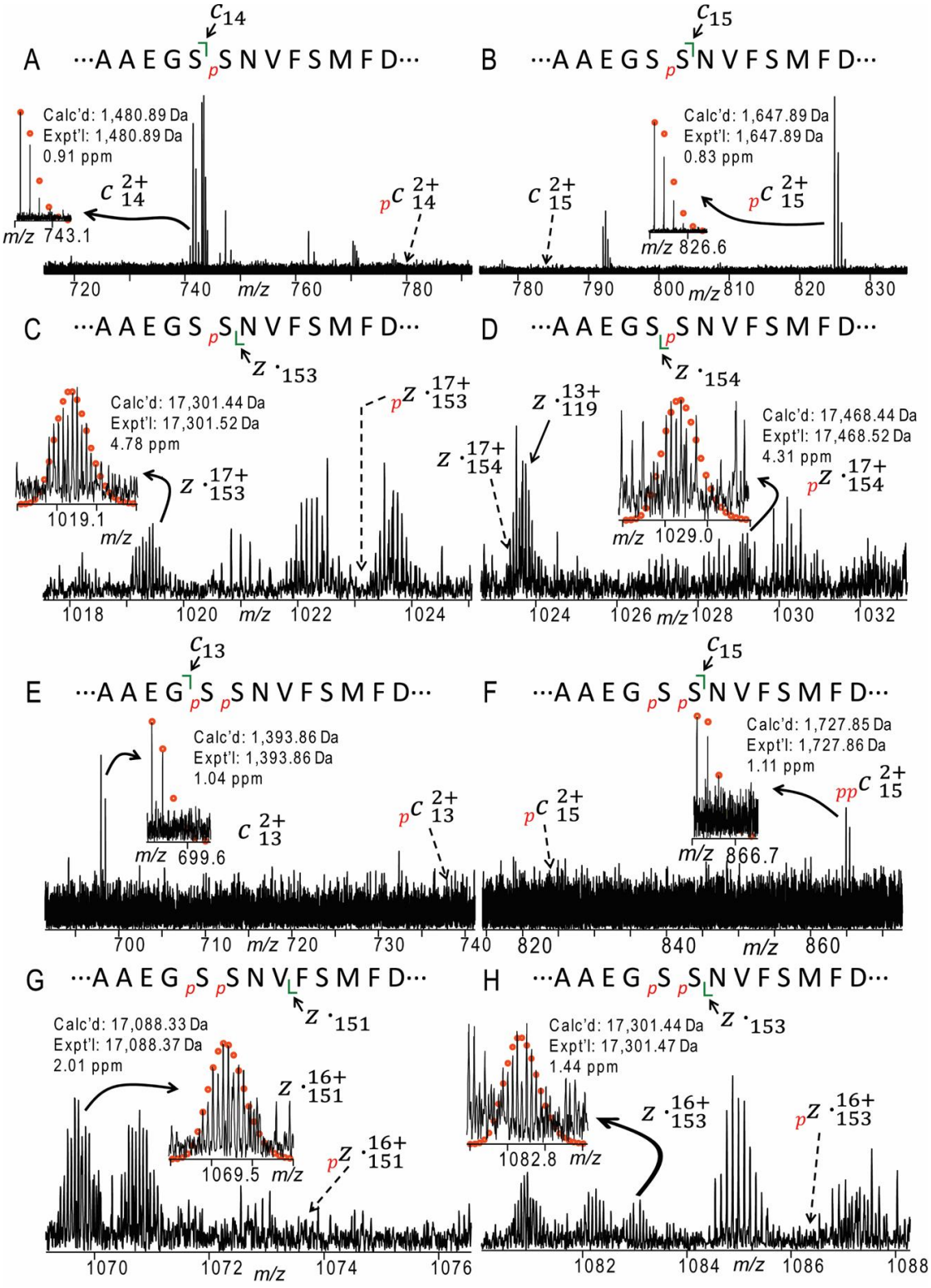

Fig. 6.8. Localization of Ser15 and Ser14/15 as the phosphorylation sites in $_{p}$RLC and $_{pp}$RLC, respectively. (A) Tandem mass spectrum showing observation of un-phosphorylated c_{14} ions

without corresponding $_{p}c_{14}$ ions. (B) Tandem mass spectrum showing observation of $_{p}c_{15}$ ions without un-phosphorylated c_{15} ions. (C) Tandem mass spectrum showing observation of un-phosphorylated $z^{\cdot}_{153}$ ions without corresponding $_{p}z^{\cdot}_{153}$ ions. (D) Tandem mass spectrum showing observation of $_{p}z^{\cdot}_{154}$ ions without the observation of un-phosphorylated $z^{\cdot}_{154}$ fragment ions. (E) Tandem mass spectrum showing observation of un-phosphorylated c_{13} ions but not $_{p}c_{13}$ ions. (F) Tandem mass spectrum showing observation of $_{pp}c_{15}$ ions without $_{p}c_{15}$ ions. (G) Tandem mass spectrum showing observation of un-phosphorylated $z^{\cdot}_{151}$ ions without corresponding $_{p}z^{\cdot}_{151}$ ions. (H) Tandem mass spectrum showing observation of $_{p}z^{\cdot}_{153}$ ions without the observation of un-phosphorylated $z^{\cdot}_{153}$ fragment ions. Broken arrow indicates expected location of unobserved ion.

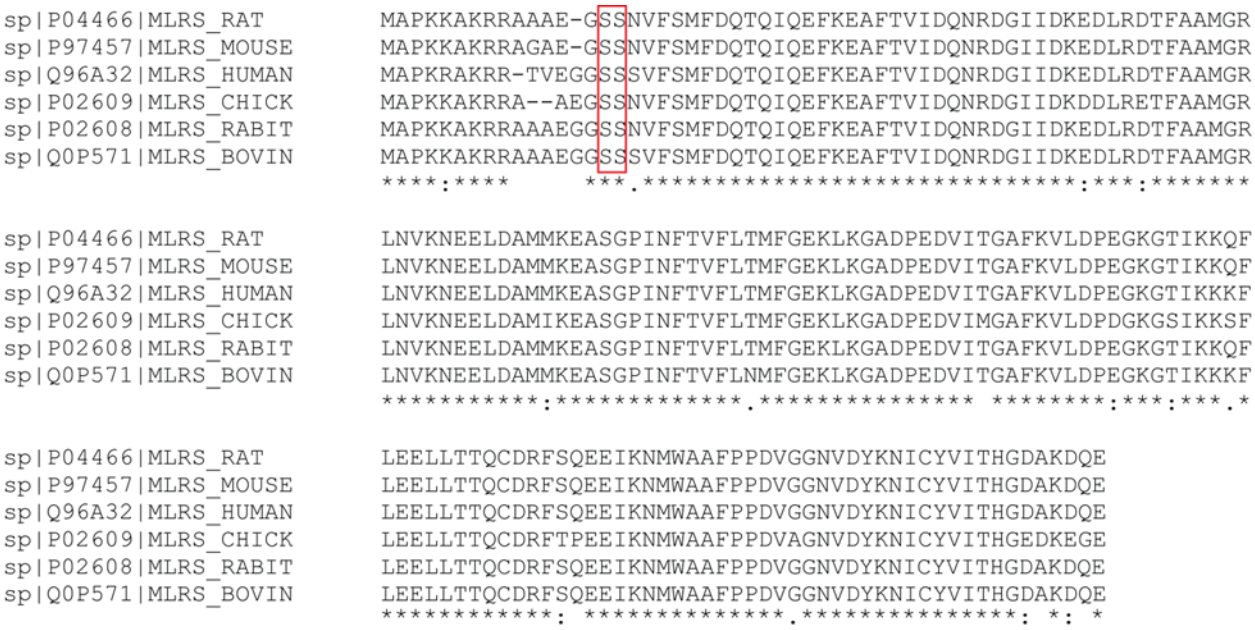

Fig. 6.9. Sequence alignment of RLC from fast-twitch skeletal muscle of different species. All sequences are from that UniProtKB/Swiss-Prot database. Box highlights highly conserved serine residues.

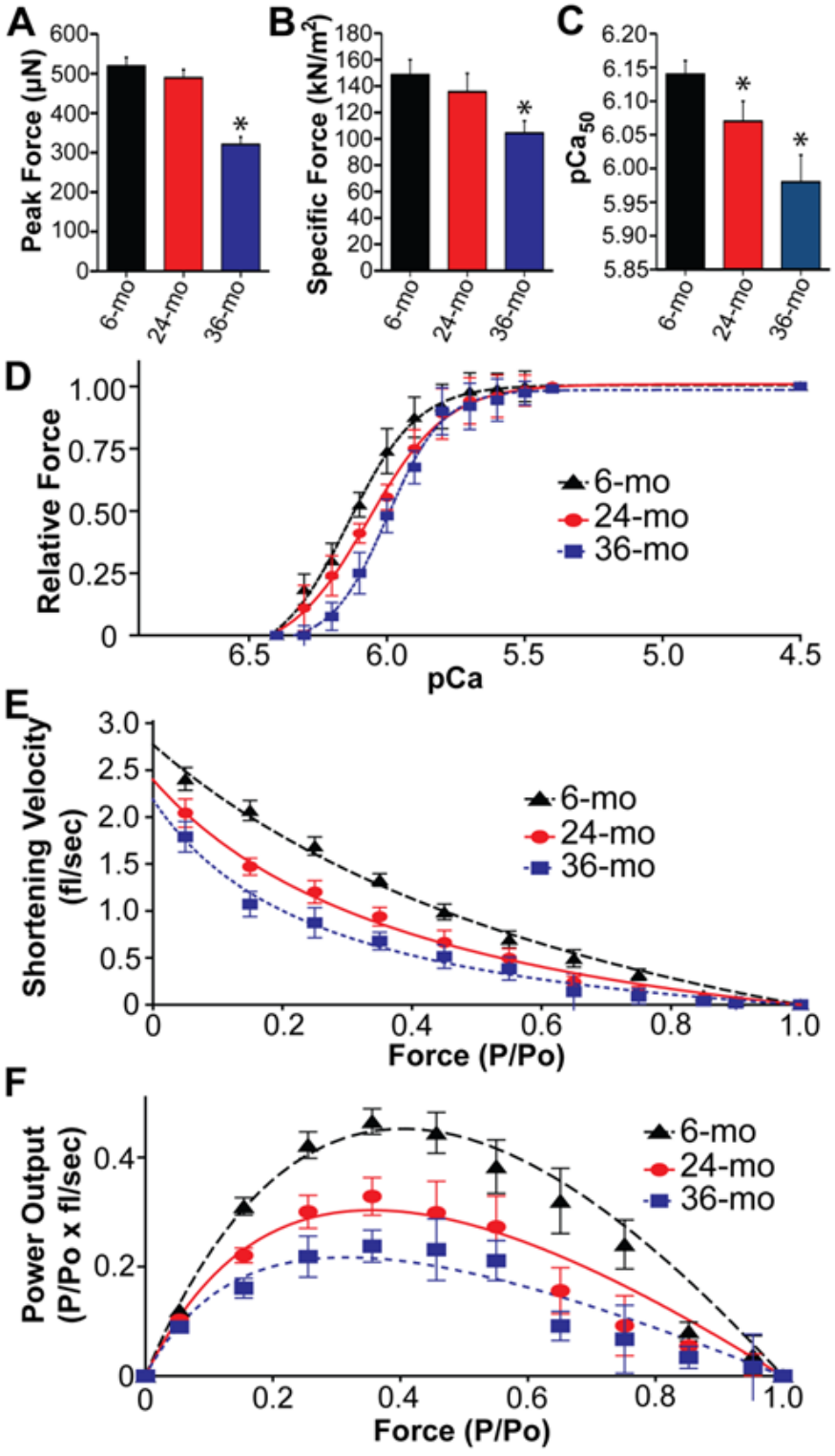

Fig. 6.10. The intrinsic contractile function of fast-twitch muscle fibers declines with age. Maximal isometric force (peak force; measured in solution with pCa 4.5) (A) and specific force

(B) of single type II (fast-twitch) fibers from 6- (n = 25), 24- (n = 33), and 36-month-old rats (n = 27). (C) Age-related decrease in pCa_{50} values from 6- (n = 25), 24- (n = 33), and 36-month-old rats (n = 27). (D) Force-pCa relationships for single skinned muscle fibers from the gastrocnemius muscles of 6-, 24-, and 36-month-old rats. n = 25 fibers (6-month), 33 fibers (24-month) and 27 fibers (36-month). Lines are best fit using the Hill equation. (E) Composite force–velocity curves from gastrocnemius fibers from 6- (n = 22), 24- (n = 26), and 36-month–old (n = 30) rats. Isotonic shortening velocity values at each load were averaged from all myocytes in each group. Lines are the best-fit regression line using the Hill equation as described in the Methods section. (F) Composite force–power curve constructed from force–velocity data. In each fiber at each load, force values (expressed as P/Po, i.e., relative force) were multiplied times mean velocity values (expressed in fl/sec), yielding a value of power output for each individual load. Lines are the best-fit regression line using the Hill equation as described in the Methods section. mo, month. All values represent mean ± SEM. $*p < 0.05$ vs. 6 mo.

Table 6.2. Single fiber contractile properties of MHC type II fibers from 6-, 24-, and 36-month-old rats. Po, maximal isometric force; Po/CSA, maximal isometric force divided by fiber cross-sectional area (specific force); pCa_{50}, concentration of Ca^{2+} producing half-maximal force. mo, month. All values represent mean ± SEM. *$p < 0.05$ vs. 6 mo.

Age	n	Fiber Diameter (μm)	P_o (μN)	P_o/CSA (kN/m^2)	pCa_{50}	Maximal Shortening Velocity ($FL \cdot s^{-1}$)	Normalized Peak Power output ($P/P_o \cdot FL \cdot s^{-1}$)
6-mo	25	74.92 ± 9.22	519.08 ± 21.6	148.66 ± 11.38	6.14 ± 0.02	2.89 ± 0.27	0.456 ± 0.011
24-mo	33	61.63 ± 6.55	489.34 ± 20.77	135.72 ± 13.95	6.07 ± 0.03*	2.58 ± 0.33	0.311± 0.026*
36-mo	27	48.98± 3.87*	320.47 ± 19.2*	104.35 ± 9.21*	5.98 ± 0.04*	2.31 ± 0.36	0.218± 0.043*

CHAPTER 7 – NOVEL SARCOPENIA-RELATED ALTERATIONS IN SARCOMERIC PROTEIN POST-TRANSLATIONAL MODIFICATIONS IN SKELETAL MUSCLES IDENTIFIED BY TOP-DOWN PROTEOMICS

Zachery R. Gregorich[a,c,#], Liming Wei[a,b,#], Ziqing Lin[a,d], Wenxuan Cai[a,c], Yutong Jin[e], Susan H. McKiernan[f], Judd M. Aiken[g], Richard L. Moss[a,d], Gary M. Diffee[f], Ying Ge[a,c,d,e]

[a]Department of Cell and Regenerative Biology, University of Wisconsin-Madison, 1111 Highland Ave., Madison, WI 53705, USA

[b]Institutes of Biomedical Sciences, Fudan University, Shanghai, 200032, P. R. China

[c]Molecular and Cellular Pharmacology Training Program, University of Wisconsin-Madison, 1111 Highland Ave., Madison, WI 53705, USA

[d]Human Proteomics Program, University of Wisconsin-Madison, 1111 Highland Ave., Madison, WI 53705, USA

[e]Department of Chemistry, University of Wisconsin-Madison, 1101 University Ave., Madison, WI 53706, USA

[f]Department of Kinesiology, University of Wisconsin-Madison, 2000 Observatory Dr., Madison, WI 53705, USA

[g]Departments of Agriculture, Food, and Nutritional Sciences, University of Alberta-Edmonton, Edmonton, AB, Canada

[#]These authors contributed equally to this work.

Abstract

Sarcopenia, the age-related loss of skeletal muscle mass and strength, is a significant cause of morbidity in the elderly and is a major burden on health care systems. Unfortunately, the underlying molecular mechanisms in sarcopenia remain poorly understood. Herein, we utilized top-down proteomics to elucidate sarcopenia-related changes in the fast- and slow-twitch skeletal muscles of aging rats with a focus on the sarcomeric proteome, which includes both myofilament and Z-disc proteins—the proteins that constitute the contractile apparatuses. Top-down quantitative proteomics identified significant changes in the post-translational modifications (PTMs) of critical myofilament proteins in the fast-twitch skeletal muscles of aging rats, in accordance with the vulnerability of fast-twitch muscles to sarcopenia. Moreover, age-related alterations in the PTMs of myofilament proteins were observed in slow-twitch skeletal muscles, supporting the emerging hypothesis that sarcopenia-associated changes also occur in slow-twitch skeletal muscles. Although many age-related protein PTM alterations were consistent in fast- and slow-twitch skeletal muscles, distinct alterations were also noted, including increased glutathionylation of slow skeletal troponin I, a novel modification that may help protect against oxidative damage in slow-twitch skeletal muscles. Furthermore, we have identified and characterized novel muscle type-specific proteoforms of myofilament proteins and Z-disc proteins, including a novel isoform of Enigma. For the first time, we provide evidence that the phosphorylation of Z-disc proteins is altered in response to aging in both fast- and slow-twitch skeletal muscles, which opens new avenues for the investigation of the role of Z-discs in age-related muscle dysfunction.

7.1 Introduction

Sarcopenia, the loss of skeletal muscle mass and function (i.e., strength) with aging, is a significant cause of morbidity and disability in the elderly population [153-155]. Greater than 35% of persons over 65 years of age and 50% or more of individuals 80 years or older are estimated to be afflicted with sarcopenia [156]. Moreover, the sarcopenia-associated burden on healthcare is substantial with an estimated cost of $18.5 billion in the United States in the year 2000 alone [158]; and costs are expected to rise due to aging of the population [159]. Nevertheless, despite the high prevalence and devastating economic impact, among types of systemic muscle loss and weakness, sarcopenia represents one of the least well understood [155].

Although muscle mass declines with age, largely as a consequence of the atrophy and loss of type II (fast-twitch) skeletal muscle fibers while type I (slow-twitch) fibers have traditionally been thought to remain relatively unaffected [168, 169], the loss of muscle strength in elderly individuals cannot be entirely explained by the age-associated loss of muscle mass [355]. Moreover, even though metabolic perturbations and cell damage resulting from age-related mitochondrial dysfunction undoubtedly contribute to muscle dysfunction with increasing age [381], it is now well-recognized that sarcopenia is associated with a loss of intrinsic contractile function that is due, in part, to alterations in myofilaments [351]. Myofilaments are components of sarcomeres, the basic contractile units of muscle; and are composed of the thin filament proteins actin, tropomyosin (Tpm), and the troponin complex, which includes troponin I (TnI), troponin T (TnT), and troponin C (TnC), as well as the thick filament proteins myosin heavy chain (MHC), regulatory light chain, essential light chain, and myosin binding protein C. The myofilaments are

flanked on either side by protein dense structures known as Z-discs that, together with the myofilaments constitute sarcomeres, which are responsible for mediating muscle contraction at high levels of intracellular Ca^{2+} [352, 353].

In addition to regulation by Ca^{2+}, which serves as the ultimate trigger for muscle contraction, myofilament protein-protein interactions (and consequently contractile function) are also regulated via the post-translational modification (PTM) of myofilaments, as well as changes in the expression of contractile protein isoforms [352, 353]. In particular, evidence in the literature has suggested that the oxidative modification of myofilaments may underlie altered contractile function in the skeletal muscles of aging individuals [382]. Specifically, the PTM of reactive cysteines in MHC has been shown to increase with age and correlates with decreased actin-activated myosin ATPase activity in aged rat skeletal muscles [190]. In agreement with findings in human skeletal muscle [191], we recently identified an age-related decrease in the phosphorylation of RLC in fast-twitch skeletal muscles of aging rats that can account for sarcopenic muscle functional impairments [383]. However, a more comprehensive assessment of changes in other contractile proteins in the fast-twitch skeletal muscles of aging individuals remains lacking. Moreover, emerging evidence indicates that slow skeletal muscles may also be vulnerable to sarcopenia at advanced age and [170], thus, the examination of changes in contractile protein PTMs during the aging process in these muscles, which may contribute to age-related alterations in contractile function, will be imperative for understanding how sarcopenia impacts muscle function in slow-twitch skeletal muscles.

Top-down mass spectrometry (MS)-based proteomics, in which intact proteins are analyzed rather than peptides as in bottom-up proteomics, has supplanted traditional methods of protein analysis as the most powerful method for the comprehensive characterization of proteoforms (a term encompassing the myriad protein forms arising from a single gene, including post-translationally modified forms and those with sequence alterations due to mutations/polymorphisms and/or alternative splicing) [206]. The analysis of intact proteoforms in top-down proteomics provides a "bird's eye" view of all protein sequence variations and PTMs, which can subsequently be localized using a variety of tandem MS (MS/MS) techniques, such as collision induced dissociation and electron capture dissociation (ECD) [197, 198, 200]. Top-down MS in combination with ECD, in particular, is useful for the localization of labile PTMs (e.g., glycosylation and phosphorylation) [90, 202, 207, 213, 218, 220, 244, 327, 384], which are preferentially lost when proteins are dissociated with slow heating methods such as collision induced dissociation [90]. Moreover, given that PTMs such as phosphorylation and minor sequence variations do not significantly impact the ionization efficiency of intact proteins as they do with peptides [385], top-down proteomics is inherently semi-quantitative with respect to the relative abundances of protein proteoforms observed within the same spectrum [197, 198, 200]. Indeed, our group and others have employed top-down MS to identify proteoform alterations towards a better understanding of the molecular mechanisms of disease [202, 218, 244, 366].

In this study, we utilized quantitative top-down proteomics to gain insights into age-related molecular changes in fast- and slow-twitch skeletal muscles, with a particular emphasis on changes occurring in the sarcomeric proteome. Interestingly, in addition to the identification of the major muscle type-specific isoforms of myofilament proteins, we detected and characterized several Z-

disc proteins, including two isoforms of Cypher, one of which has previously only been detected at the mRNA level, as well as a novel isoform of the protein Enigma. Consistent with the well-established susceptibility of fast-twitch muscle fibers to sarcopenia, top-down quantitative proteomics identified dramatic changes in the PTMs of a number of important myofilament proteins in the fast-twitch skeletal muscles of aging rats. However, surprisingly, age-related alterations in the PTMs of myofilament proteins were also observed in slow-twitch skeletal muscles, adding support to the emerging hypothesis that age-related changes also occur in slow-twitch skeletal muscles [170], which have long been thought to be relatively immune to sarcopenia [168, 169]. Interestingly, distinct alterations in sarcomeric protein proteoforms were also noted in fast and slow skeletal muscles, including increased glutathionylation of slow skeletal troponin I (*ss*TnI), a modification that may help protect against oxidative damage and contribute to differences in the presentation of sarcopenia in fast- and slow-twitch skeletal muscles. Top-down proteomics further enabled the identification of novel phosphorylated proteoforms of fast- and slow-skeletal troponin I. For the first time, we also provide evidence that the phosphorylation of Z-disc proteins is altered with age in both fast- and slow-twitch skeletal muscles.

7.2 Materials and methods

7.2.1 Animals

Male Fisher 344 × Brown Norway F1 hybrid (F344BN) rats aged 6- (n = 12), 24- (n = 12), and 36-months (n = 12) were obtained from the National Institute on Aging colony maintained by Harlan Sprague-Dawley (Indianapolis, IN, USA). Rats were individually housed in clear plastic

cages on a 12 h/12 h light/dark cycle with access to food and water ad libitum. Handling and euthanasia were carried out under the guidelines of the University of Wisconsin-Madison Animal Use and Care Committee.

7.2.2 Muscle measurements

Rats were anesthetized by inhalation of isoflurane, and the gastrocnemius (GAS) and soleus (SOL) muscles from the left hind limb were dissected from origin to insertion and immediately weighed. Muscles were bisected at the mid-belly, embedded in optimal cutting temperature compound (Tissue-Tek; Andwin Scientific, Addison, IL, USA), frozen in liquid N_2, and stored at −80 °C for later sectioning. Three consecutive sections (10 µm thick) were cut, starting at the mid-belly, placed on labeled Probe-On Plus microscope slides (Fisher Scientific, Pittsburgh, PA, USA), and stored at −80 °C until use. The first section of each series was stained with hematoxylin and eosin. Sections were photographed using an Olympus BH2 microscope (Olympus, Tokyo, Japan) with an Olympus DP70 digital camera and mid-belly composites of each muscle section were reconstructed by interlacing the images using ImagePro Plus software (Media Cybernetics, Atlanta, GA, USA). For fiber counts, individual muscle fibers were annotated on the composite image of the entire muscle cross-section at the mid-belly, using Adobe Photoshop (Adobe Systems, Inc., San Jose, CA, USA), and total count was tabulated. The whole muscle cross-sectional area (CSA) at the mid-belly was measured by tracing an outline of each muscle using ImagePro Plus. To measure individual muscle fiber CSA, four images (10×) from the H&E sections were captured from GAS and SOL muscles from rats in each age group. A grid with 25 random dots was placed over the images, and the CSA of fibers marked with the dots was measured. Six hundred fibers

were measured from each muscle at each age ([4 images per muscle] × [25 fibers per image] × [6 animals per age group] = 600 fibers). GAS and SOL muscles were dissected from the right hind limb as described above, but were immediately flash frozen in liquid N_2 and stored at -80 ^{o}C for subsequent proteomic analysis.

7.2.3 MHC isoform and ATPase staining

For ATPase staining, 10 μm-thick, transverse frozen sections of muscle were cut using a cryostat (–20 °C) and placed on Probe-On Plus slides (Fisher Scientific). Staining for myosin ATPase to determine fiber type distribution was performed according to Hintz et al. [386]. Fiber type was determined based on myosin ATPase sensitivity to pH and differences in fiber type staining intensities. Preincubation at pH 10.2 distinguishes between type I (light staining) and type II (dark staining) fibers. At acidic pH (4.5 and 4.25), type I fibers will stain dark. Type II fibers can be further classified into IIa (stain light in both pH 4.5 and 4.25), IIb (stain medium at pH 4.5 but light at pH 4.25), and IIc (stain intermediate at both pH 4.5 and 4.25) fibers. The preincubation solutions were: (1) 20 mM sodium barbital, 18 mM calcium chloride at pH 10.2 for 15 min or (2 and 3) 50 mM sodium acetate, 30 mM sodium barbital at pH 4.5 or 4.25 for 6 min. All sections were then incubated for 30 min at 37 °C in 20 mM sodium barbital, 9 mM calcium chloride, and 2.7 mM ATP at pH 9.4. Sections were subsequently rinsed in 1% calcium chloride (3 × 3 min each), immersed in 2% cobaltum chloride (3 min), rinsed in 10 changes of tap H_2O, stained in 1% ammonium sulfide (30 sec), washed in tap running H_2O (4 min), dehydrated with ethanol, cleared in xylene, and mounted in Permount (Fisher, Fair Lawn, NJ, USA).

7.2.4 Preparation of sarcomeric protein-enriched extracts

Protein extraction was carried out as previously described [244]. Briefly, approximately 10 mg of tissue from the GAS (n = 6 for each age group) or SOL (n = 6 for each age group) muscles was homogenized in 100 µL of HEPES extraction buffer containing protease and phosphatase inhibitors (25 mM HEPES pH 7.5, 50 mM NaF, 0.25 mM Na_3VO_4, 0.25 mM PMSF, 2.5 mM EDTA) using a Teflon pestle (1.5 mL tube rounded tip; Scienceware, Pequannock, NJ, USA). The resulting homogenate was centrifuged at 16,000 × *g* for 15 minutes at 4 °C, and the supernatant was discarded. The insoluble pellet was then re-homogenized in 100 µL of TFA extraction buffer (1 % trifluoroacetic acid, 1 mM tris(2-carboxyethyl)phosphine) to extract a protein sub-proteome enriched in sarcomeric proteins. After centrifugation (16,000 × *g*, 4 °C, 25 min), the supernatant was collected and used for on-line top-down proteomic analysis. At least two technical (extraction) replicates were performed per biological replicate.

7.2.5 On-line liquid chromatography (LC)-MS profiling

Protein extracts prepared from aging rat GAS and SOL muscles were separated using a nanoACQUITY LC system (Waters, Milford, MA) equipped with a home-packed PLRP column (PLRP-S, 200 mm x 500 µm, 10 µm, 1000 Å; Varian, Lake Forest, CA, USA) and a gradient going from 20% B to 90% B (solvent A: 0.10% formic acid in water; solvent B: 0.10% formic acid in a 50:50 mixture of acetonitrile and ethanol) over 40 min at a flow rate of 8 µL/min. The nanoACQUITY LC system was coupled on-line with an impact II quadrupole-time-of-flight (q-TOF) mass spectrometer (Bruker Daltonics, Billerica, MA, USA). Spectra were collected using a

scan rate of 1 Hz over a 500 - 3000 *m/z* range. Sarcomeric protein separation and the relative abundances of modified and un-modified protein proteoforms were highly reproducible across replicates (**Figs. 7.1-7.2**).

7.2.6 Fraction collection

LC separation of GAS and SOL extracts, and fraction collection of both known and unknown proteins, was carried out as previously described [244], with minor modifications. Briefly, GAS and SOL extracts containing the sarcomeric sub-proteomes were separated using a 2D-nano-LC system (Eksigent, Redwood City, CA, USA) equipped with a home-packed PLRP column and a gradient going from 20% B to 90% B over 40 min (solvent A: 0.10% formic acid in water; solvent B: 0.10% formic acid in a 50:50 mixture of acetonitrile and ethanol) at a flow rate of 12.5 µL/min. The 2D-nano-LC system was coupled on-line with a linear ion trap (LTQ) mass spectrometer (Thermo Scientific). After LC separation, a small portion of the sample (~5% of the total amount) was ionized by electrospray ionization through a 25-30 µm i.d. tip and analyzed by LTQ/MS to track protein elution from the column. The remaining ~95% of the sample was collected on ice for comprehensive protein analysis by off-line MS/MS.

7.2.7 High-resolution MS/MS protein characterization

The collected fractions were analyzed using a 7T LTQ/ Fourier transform ion cyclotron resonance (FT-ICR) mass spectrometer (LTQ/FT Ultra, Thermo Scientific, Bremen, Germany) equipped with an automated chip-based nano-electrospray ionization source (Triversa NanoMate; Advion

Bioscience, Ithaca, NY, USA) as described previously [90, 202, 218, 244]. The sample was introduced into the mass spectrometer using a spray voltage of 1.3 kV. Ion transmission into the LTQ and, subsequently, the FT-ICR cell, was optimized to achieve maximum ion signal. The resolving power of the FT-ICR was set at 200,000 (at 400 *m/z*). The number of accumulated charges for a full scan in the LTQ, FT-ICR cell, MS^n FT-ICR cell, and ECD were 3×10^4, 8×10^6, 8×10^6 and 8×10^6, respectively. For MS/MS experiments, the protein molecular ions of the individual charge states were first isolated and subsequently fragmented using ECD. The energy, delay, and duration parameters for ECD, were determined on a case-by-case basis to achieve optimal fragmentation of precursor ions. Typically between 1,000-5,000 scans were averaged for MS/MS experiments to ensure the collection of high quality tandem mass spectra for data analysis.

7.2.8 Characterization of novel Enigma isoform

The exon structure of the human *PDLIM7* gene, which encodes the Enigma protein, was obtained from Ensembl (www.ensembl.org). The amino acid sequences for Enigma coding exons were generated using the Translate Tool available at ExPASy (web.expasy.org/translate/).

7.2.9 MS and MS/MS data analysis

All mass and tandem mass spectra were analyzed with in-house developed MASH Suite Pro software [273], which is an integrated software with MS-Align+ [247], using a signal-to-noise ratio threshold of 2.5 and a minimum fit of 60%. A 15 ppm cut-off was used for fragment ion assignments and all program-processed data was manually validated. Monoisotopic masses are

reported for both intact proteins and fragment ions. For relative proteoform quantification, the intensity of individual proteoforms were obtained from deconvoluted mass spectra using the MassList function in DataAnalysis software (Bruker Daltonics), and the relative percentages of each species were calculated as described previously [202, 218, 244]. Based on these percentages, the total protein phosphorylation (P_{total}) of each phosphorylated protein was calculated using the following equation as previously published [202, 218, 244]:

$$P_{total} = (\%P_{mono} + 2 \times \%P_{bis})/100 \quad \text{(Eq. 1)}$$

Minor oxidation products and non-covalent adducts were taken into consideration in the quantification. All MS and MS/MS data have been submitted to the MassIVE data repository and are available at ftp://massive.ucsd.edu/MSV000081157.

7.2.10 Statistical analysis

Student's two-sample *t*-test (two-tailed) was performed between group comparisons to evaluate the statistical significance of variance. Differences among means were considered to be significant at $p < 0.05$.

7.3 Results

7.3.1 Both fast- and slow-twitch skeletal muscles display signs of sarcopenia

To assess potential sarcopenia-related changes in fast and slow skeletal muscles, the GAS and SOL muscles of aging F344BN rats were selected for analysis due to the reportedly high proportion of fast- and slow-twitch muscle fibers in these muscles, respectively [387]. F344BN rats were chosen as this strain is recommended by the National Institute on Aging as a model of healthy aging for age-related research [167]. The primary advantage of this model system is the very low incidence of age-related pathologies in this rat strain [388], which aids the identification of true molecular signatures of sarcopenia without the confounding influence of the other co-morbidities.

To ensure that the F344BN rat GAS and SOL muscles analyzed in this study were composed predominantly of fast- and slow-twitch muscle fibers, respectively, immunohistochemical staining for type I and type II MHC was carried out in GAS and SOL muscle serial sections. Representative serial sections from the GAS and SOL muscles of a 6-month-old rat stained for type I and type II MHC are shown (**Fig. 7.3A-B**). Quantitative analysis revealed that the vast majority (approximately 90%) of fibers within the GAS muscles of 6-month-old F344BN rats expressed type II MHC and, thus, would be classified as fast-twitch muscle fibers (**Fig. 7.3C**). There was a decrease in the relative proportion of fibers expressing type II MHC in the GAS muscles of aging F344BN rats, which is consistent with the age-associated loss of fast-twitch muscle fibers [169, 355]. However, this population still comprised approximately 70% of muscle fibers in the GAS muscles of 36-month-old animals, rendering type II fibers the dominant fiber type in GAS muscles from rats in this age group (**Fig. 7.3C**).

The relative proportion of type I MHC-expressing (slow-twitch) fibers in SOL muscles was similarly high, comprising approximately 90% of muscle fibers in this muscle group (**Fig. 7.3D**).

However, unlike the percentage of fast-twitch fibers in the GAS, immunohistochemical staining for MHC isoform expression showed that the relative proportion of slow-twitch fibers in the SOL did not change as the animals aged, although the proportion of fast-twitch fibers was increased (**Fig. 7.3D**). Since individual muscle fibers can express multiple MHC isoforms, we confirmed these results by staining muscle section from the GAS and SOL muscles for myosin ATPase activity (**Fig. 7.4**). Consistent with fiber typing by MHC isoform content, the preponderance of fibers in the GAS were type II whereas those in the SOL were type I fibers (**Fig. 7.4**). In summary, these results confirm that the GAS and SOL muscles of F344BN rats contain predominantly fast- and slow-twitch muscle fibers, respectively.

To assess the extent of sarcopenia in fast skeletal muscles from aging F344BN rats, the mass of GAS muscles isolated from 6-, 24-, and 36-month-old animals was assessed (**Fig. 7.3E**). Measurement of the mass of GAS muscles from rats in different age groups revealed a marked decrease in muscle mass in 36-month-old rats in comparison to those from 6-month-old animals (**Fig. 7.3E**). Similarly, normalization to the total body mass showed a significant decrease in the GAS mass-to-body mass ratio in the 36-month-old rats (**Fig. 7.3F**). In addition to decreased GAS muscle mass, whole muscle cross sections from the GAS muscles of 36-month-old rats displayed a marked decrease in CSA in comparison to those from 6-month-old rats (**Fig. 7.3G**). Further examination of the isolated GAS muscles revealed a significant decrease in both the number of muscle fibers and the mean fiber diameter in muscles from 36-month-old rats (**Fig. 7.3H-I**), indicating that the observed decreases in GAS mass and CSA are the combined result of muscle fiber loss and a reduction in the size of the remaining fibers.

Similar to sarcopenia-associated changes in GAS muscles, the masses of SOL muscles, as well as the SOL mass-to-body mass ratios, were also significantly decreased in 36-month-old rats in comparison to 6-month-old rats (**Fig. 7.3J-K**). SOL muscles from 36-month-old rats also had significantly reduced CSAs in comparison to muscles from 6-month-old animals (**Fig. 7.3L**). However, unlike in GAS muscles, which displayed a marked decrease in fiber number at advanced age (**Fig. 7.3H**), fiber number in SOL muscles was not significantly different between age groups (**Fig. 7.3M**). The mean fiber diameter was significantly decreased in SOL muscles from 36-month-old animals in comparison to those from 6-month-old rats (**Fig. 7.3N**), signifying that the noted decreases in the masses and CSAs of SOL muscles are almost exclusively the result of muscle fiber atrophy with little or no contributions from fiber loss. Although the observed decrease in muscle fiber CSA in SOL muscles may represent the selective age-related atrophy of the minor population of fast-twitch fibers in this muscle group, collectively, this information suggests that both fast and slow skeletal muscles are vulnerable to sarcopenia at advanced age.

7.3.2 Identification of proteins in sarcomeric protein-enriched extracts

To characterize age-related changes in the fast- and slow-twitch skeletal muscles of aging F344BN rats, we employed a top-down proteomics strategy consisting of several steps (**Fig. 7.5**). These steps include isolation of a sarcomeric-protein enriched fraction from both fast- and slow-twitch skeletal muscles; sarcomeric protein separation by 1D reverse phase LC; on-line sarcomeric proteoform profiling on a high-resolution q-TOF mass spectrometer; fraction collection of sarcomeric proteins concomitant with on-line proteoform profiling, followed by in-depth proteoform characterization off-line on a high-resolution FT-ICR mass spectrometer; and

integrated analysis of age-dependent changes in proteoform relative abundances and modifications.

As a first step, we sought to identify proteins present in sarcomeric protein-enriched extracts prepared from the fast- and slow-twitch skeletal muscles of aging F344BN rats. Following MS/MS analysis of fraction collected proteins and protein identification using MASH Suite Pro [273], we were able to identify a number of sarcomeric and non-sarcomeric proteins in extracts prepared from the GAS muscles of aging rats (**Table 7.1**, **Fig. 7.6A**). Identified fast-twitch skeletal muscle-specific sarcomeric proteins included an isoform of fast skeletal troponin T (*fs*TnT), fast skeletal troponin I (*fs*TnI), α-tropomyosin (αTpm), fast skeletal myosin essential light chain 1 (MLC-1F), fast skeletal myosin essential light chain 3 (MLC-3F), and fast skeletal troponin C (*fs*TnC) (**Table S1**, **Figs. 7.6-7.13**). The fast skeletal isoform of the myosin regulatory light chain (MLC-2F) in rat, which has previously been characterized by our group [383], was also identified in sarcomeric protein-enriched extracts prepared from rat GAS muscles (**Table 7.1, Fig. 7.6A**). We also detected a 21,153.90 Da protein (**Fig. 7.14**), which was identified as an isoform of the PDZ/LIM domain-containing protein Enigma (**Fig. 7.15**). Comprehensive sequencing of this protein revealed that it is a novel isoform of the Enigma protein (*n*Enigma) produced via alternative splicing of exons 1 (non-coding), 2-4, and 6-9 (**Table 7.2**, **Figs. 7.14-7.20**).

Similarly, a mix of sarcomeric and non-sarcomeric proteins were also identified in extracts prepared from the SOL muscles of F344BN rats (**Table 7.3**, **Fig. 7.6B**). Identified slow-twitch skeletal muscle-specific sarcomeric proteins in extracts prepared from aging rat SOL muscles included slow skeletal troponin T isoform 1 (*ss*TnT1), slow skeletal troponin I (*ss*TnI), slow

skeletal myosin essential light chain (MLC-1S), and troponin C (*ss*TnC), as well as the slow skeletal/ventricular isoforms of the myosin essential (MLC-1V) and regulatory (MLC-2S) light chains (**Table 7.3**, **Figs. 7.6B**, **7.21-7.27**).

In addition to skeletal muscle-type-specific sarcomeric protein isoforms, several sarcomeric proteins were also commonly identified in extracts prepared from both GAS and SOL muscles (**Tables 7.1**, **7.3**, **Fig. 7.6**). These included two isoforms of the PDZ/LIM domain protein Cypher and β-Tpm (βTpm) (**Tables 7.1**, **7.3**, **Figs. 7.6**, **7.28-7.31**). Not surprisingly, the α isoform of skeletal actin was also among the identified proteins (**Table 7.1**, **7.3**). Interestingly, while one of the identified Cypher isoforms corresponded to the previously observed Cypher2s isoform identified by Huang *et al.* (UniProtKB/Swiss-Prot accession number A0A0G2JXR0; **Tables 7.1**, **7.3**, **Fig. 7.30**) [389], the second isoform corresponded to an undesignated isoform of Cypher that contains exons 1-3, 5-6, and 8-10 and has, to the best of our knowledge, not previously been detected at the protein level (**Table 7.4**, **Fig. 7.29**) [390]. Therefore, the detection of this particular Cypher isoform, which we have designated Cypher4s, in the skeletal muscle of F344BN rats provides the first experimental evidence of expression of this isoform at the protein level.

7.3.3 Sarcopenic fast-twitch skeletal muscles are characterized by marked age-related changes in sarcomeric protein proteoforms

To assess age-associated molecular changes in fast-twitch skeletal muscles, sarcomeric proteome-enriched extracts were prepared from the GAS muscles of 6-, 24-, and 36-month-old rats and rapid proteoform profiling was carried out using quantitative top-down LC-MS. Consistent with

previous studies suggesting that alterations in sarcomeric proteins may underlie impaired skeletal muscle function in aged individuals [351], we observed marked differences in the relative abundances of a number of sarcomeric protein proteoforms in the GAS muscles of rats in different age groups (**Fig. 7.32**).

In particular, a significant age-related increase in the relative abundance of the phosphorylated proteoform of *fs*TnT (**Fig. 7.32A**, **7.32G**), translated to an overall increase in *fs*TnT phosphorylation in muscles from 24- and 36-month-old rats versus muscles from 6-month-old rats (**Fig. 7.34A**). A minor proteoform presumably corresponding to phosphorylated *fs*TnI ($_{p}$*fs*TnI) based on accurate mass measurement (ΔM = +79.96 Da versus un-phosphorylated *fs*TnI) was detected in sarcomeric proteome-enriched extracts prepared from the GAS muscles of rats in all three age groups (**Fig. 7.32B**, **7.32G**); however, *fs*TnI phosphorylation did not change with age (**Fig. 7.34A**). A low abundance proteoform corresponding to glutathionylated *fs*TnI (*GSS-fs*TnI; ΔM = +305.03 Da versus un-phosphorylated *fs*TnI), was also detected although, as with $_{p}$*fs*TnI, the relative abundance of this proteoform did not change as the animals aged (**Fig. 7.32B**, **7.32G**). A significant decrease in the relative abundance of phosphorylated proteoforms of Cypher (both isoforms 4s and 2s, respectively) in the GAS muscles of 24- and 36-month-old rats, relative to that in muscles from 6-month-old rats, was observed (**Fig. 7.32C-D**, **7.32G**). The decreased relative abundance of phosphorylated Cypher isoforms in muscles from 24- and 36-month-old rats corresponded to a decrease in the total phosphorylation of Cypher4s and Cypher2s as the animals aged (**Fig. 7.34A**).

A peak presumably corresponding to a phosphorylated proteoform of *n*Enigma was also detected in sarcomeric protein-enriched extracts prepared from rat GAS muscles (**Fig. 7.14**). However, this proteoform overlapped significantly with peaks corresponding to *fs*TnI, which precluded quantification of *n*Enigma phosphorylation in the GAS muscles of aging F344BN rats (**Fig. 7.14**). Conversely, the phosphorylated proteoforms of both α- and β-Tpm ($_{p}$αTpm and $_{p}$βTpm, respectively) increased in abundance at 36 months of age relative to the younger age groups (**Fig. 7.32E**, **7.32G**), which translated to an overall increase in Tpm isoform phosphorylation in the fast-twitch skeletal muscles of rats at advanced age (**Fig. 7.34A**). A significant age-dependent decrease in both the mono- ($_{p}$MLC-2F) and bis-phosphorylated ($_{pp}$MLC-2F) proteoforms of MLC-2F was also observed in the GAS muscles of aging rats (**Fig. 7.32F-G**), which is consistent with an age-related decrease in MLC-2F phosphorylation as previously described by our group and others (**Fig. 7.34A**) [191, 383].

7.3.4 Sarcomeric protein proteoform alterations occur in the slow-twitch muscles of rats with advanced sarcopenia

To determine whether molecular changes also occur in the slow-twitch skeletal muscles of aging F344BN rats, sarcomeric protein-enriched extracts were prepared from the SOL muscles of 6-, 24-, and 36-month-old rats and analyzed by top-down LC-MS. Although slow-twitch skeletal muscles are thought to be relatively unaffected by sarcopenia [168, 169], age-dependent alterations in sarcomeric protein proteoform relative abundances were observed (**Fig. 7.33**).

Similar to the increased relative abundance of the phosphorylated proteoform of *fs*TnT in GAS muscles from 36-month-old rats, the relative abundance of mono-phosphorylated *ss*TnT1 ($_p$*ss*TnT1) was likewise increased in the SOL muscles isolated from 36-month-old rats (**Fig. 7.33A**, **7.33G**). Moreover, the overall phosphorylation of *ss*TnT1 was significantly increased in muscles from aged rats in comparison to those from 6-month-old animals (**Fig. 7.34B**); although phosphorylation was not significantly increased in SOL muscles at 24 months of age (versus 6 months of age) as in the GAS (**Fig. 7.34A**). As was the case for *fs*TnI, minor proteoforms presumably corresponding to phosphorylated *ss*TnI ($_p$*ss*TnI) and glutathionylated *ss*TnI (*GSS-ss*TnI) based on accurate mass measurement (ΔM = +79.95 Da and +305.02 Da versus un-modified *ss*TnI for $_p$*ss*TnI and *GSS-ss*TnI, respectively) were observed in the SOL muscles of rats from all three age groups (**Fig. 7.33B**). However, unlike in GAS muscles, the relative abundances of both $_p$*ss*TnI and *GSS-ss*TnI were significantly increased in SOL muscles isolated from 36-month-old rats in comparison to muscles from 6-month-old rats (**Fig. 7.33G**). The increased abundance of the $_p$*ss*TnI proteoform in 36-month-old individuals corresponded with an increase in overall *ss*TnI phosphorylation in the aged animals (**Fig. 7.34B**).

The relative abundances of Cypher4s proteoforms did not change with age in SOL muscles (**Fig. 7.33C**). Conversely, the relative abundances of un-phosphorylated and phosphorylated Cypher2s ($_p$Cypher2s) were decreased and increased, respectively, in slow-twitch muscles from 36-month-old animals in comparison to muscles from 24-month-old rats (**Fig. 7.33D**, **7.33G**). The observed decrease in the relative abundance of $_p$Cypher2s translated to an overall increase in Cypher2s phosphorylation at 36 months of age (versus phosphorylation of this protein in SOL muscles from 24-month-old animals) (**Fig. 7.34B**). Neither the proteoform relative abundances nor the overall

phosphorylation of βTpm were altered in response to aging (**Figs. 7.33E**, **7.33G**, **7.34B**). As in fast-twitch skeletal muscles, there was a significant age-dependent decrease in the phosphorylation of MLC-2S in SOL muscles (**Figs. 7.33F-G**, **7.34B**). The observation that MLC-2S phosphorylation decreases in the slow-twitch skeletal muscle of aging F344BN rats is interesting given that evidence from previous studies has suggested that MLC-2S phosphorylation increases with age [391].

7.4 **Discussion**

7.4.1 Sarcopenia affects both fast- and slow-twitch skeletal muscles in aging rats

To assess sarcopenia-associated changes in sarcomeric protein proteoforms in fast- and slow-twitch skeletal muscles, we examined age-related changes in these proteins in rat GAS and SOL muscles, which previous results have demonstrated consist predominantly of fast- and slow-twitch muscle fibers, respectively [387].

In accordance with previous results, immunohistochemical analysis of MHC isoform expression revealed a preponderance of type II and type I MHC-expressing fibers in GAS and SOL muscles, respectively, from 6-month-old rats (**Fig. 7.3A-D**). Similar results were obtained when type I and type II fibers were quantified in the GAS and SOL muscles of aging F344BN rats (**Fig. 7.4**), confirming the dominance of fast- and slow-twitch muscles fibers in these muscles, respectively. Interestingly, while the relative percentage of type I and type II MHC-expressing fibers in the GAS muscles of aging rats increased and decreased, respectively, with age (**Figs. 7.3-7.4**), the

proportion of type II MHC-expressing fibers was significantly increased in the SOL muscles of 24- and 36-month-old rats in comparison to 6-month-old rats based on immunohistochemical staining for MHC isoform expression (**Fig. 7.3D**). This trend was also observed when quantification was preformed based on myosin ATPase activity, although the trend was not significant when this method was employed for muscle fiber typing (**Fig. 7.4**). Despite the fact that the observed increase in the relative proportion of fast-twitch muscle fibers in the SOL muscles of aging animals seems at odds with the results of previous reports indicating that aging is associated with the selective loss of type II muscle fibers [168, 355], it is possible that this increase instead represents an increase in fibers co-expressing multiple MHC isoforms. Indeed, evidence from other labs has indicates that the relative proportion of fibers expressing multiple MHC isoforms increases with age [392]. Therefore, the apparent age-related increase in the relative percentage of muscle fibers in the SOL expressing type II MHC can be viewed as an increase in muscle fibers expressing multiple MHC isoforms rather than as an increase in purely type II MHC-expressing fibers in this muscle group.

Consistent with previous reports of age-related fast-skeletal muscle fiber atrophy [166-169], GAS muscles from 36-month-old rats displayed characteristic signs of sarcopenia, including significant decreases in muscle mass and CSA at the muscle midbelly (**Fig. 7.3E-G**). These changes were, in part, attributable to a decrease in the mean fiber diameter (**Fig. 7.3I**), which is consistent with the well-established sarcopenia-associated atrophy of type II (fast-twitch) muscle fibers [166, 168, 169]. Interestingly, although it has traditionally been thought that sarcopenia-associated fiber atrophy affects primarily type II (fast-twitch) fibers with relatively little impact on type I (slow-twitch) fibers [168, 169], recent evidence has suggested that slow-twitch fibers are also vulnerable

to age-related atrophy, particularly at advanced age when sarcopenia becomes severe [170]. In agreement with these findings, we identified significant decreases in the masses and CSAs (at the muscle midbelly) of SOL muscles from 36-month-old rats in comparison to muscles from 6-month-old animals (**Fig. 7.3J-L**). Moreover, as in the GAS muscles (**Fig. 7.3I**), the mean fiber diameter was significantly decreased in SOL muscles from 36-month-old rats (**Fig. 7.3N**), indicating that the atrophy of slow-twitch fibers likely contributes to sarcopenic changes in slow-twitch skeletal muscles. While it is possible that these results could be due to atrophy of a small population of fast-twitch fibers in the SOL, based on the relatively small proportion of type II fibers in this muscle (**Fig. 7.3D**, **Fig. 7.4**) [387], it is unlikely that this is the reason for age-related decreases in the masses and CSAs of SOL muscles. Instead, it is more likely that slow-twitch muscle fibers, like fast-twitch muscle fibers, are in fact vulnerable to age-related atrophy.

In addition to age-related fiber atrophy, we also observed marked fiber loss in the GAS muscles of 36-month-old rats (**Fig. 7.3H**), in accordance with previous studies [165, 166]. Notably, despite the fact that fibers in the SOL muscles of 36-month-old animals showed signs of atrophy (**Fig. 7.3N**), no change in total fiber number was detected as the animals aged (**Fig. 7.3M**). These findings suggest that, while slow-twitch fibers might indeed be vulnerable to sarcopenia-associated atrophy, these fibers may also be protected from age-related fiber loss. Whether type I (slow-twitch) fibers are truly protected from age-related cell death will necessitate a better understanding of the molecular mechanisms underlying sarcopenia-associated fiber loss, which, to date, remains incompletely understood [393].

7.4.2 Age-related changes in myofilament protein proteoforms in fast- and slow-twitch skeletal muscles

The hallmarks of sarcopenia include progressive muscle fiber atrophy, as well as contractile dysfunction that is, in part, due to alterations in the structure and function of myofilaments [351]. In this study, we utilized quantitative top-down proteomics to gain insights into age-related molecular changes in fast- and slow-twitch skeletal muscles, with a particular emphasis on those occurring in sarcomeric proteins including both myofilament and Z-disc proteins.

Previous studies from our lab, as well as the labs of others, have shown that MLC-2F phosphorylation declines with age in the fast-twitch skeletal muscles [191, 383]. In agreement with these findings, in this study we observed a significant decrease in MLC-2F phosphorylation with increasing age in the fast-twitch GAS muscles of aging F344BN rats (**Figs. 7.32**, **7.34A**). Interestingly, we also observed a progressive age-related decline in the phosphorylation of MLC-2S in the slow-twitch skeletal muscles of aging rats (**Figs. 7.33**, **7.34B**). This finding is surprising given that there is evidence in the literature suggesting that the phosphorylation of MLC-2S increases in aging muscles [391]. The reason for this discrepancy may be related to the method employed for the quantification of protein phosphorylation (top-down proteomics herein versus ProQ Diamond staining in the aforementioned study). Functionally, increased phosphorylation of MLC-2 results in structural alterations within the sarcomeres that potentiate the magnitude and velocity of force production [74, 78]. Consistently, we have previously shown that the age-related decrease in the phosphorylation of MLC-2F correlates with a reduction in force production,

shortening velocity, and power output in the fast-twitch skeletal muscle fibers of aging F344BN rats [383]. Likewise, similar findings have been reported in muscles from aging humans [191].

Expanding on our previous findings, here we detected a decrease in the phosphorylation of TnT isoforms in both the fast- and slow-twitch skeletal muscles of aging F344BN rats (**Figs. 7.32-7.34**). Evidence from *in vitro* studies has suggested that at least five different phosphorylation sites exist within the cardiac isoform of TnT (sites corresponding to residues Thr204, Ser208, Thr213, Ser285, and Thr294 in human cardiac TnT) [87]. However, not all of these sites are conserved in the fast- and slow-twitch skeletal muscle isoforms of TnT and, to date, the only site of phosphorylation that has been confirmed *in vivo* is Ser2 (numbering includes the initiating Met residue that is removed in the mature protein), which is conserved across all muscle type-specific isoforms of TnT [90, 203]. Surprisingly, despite the fact that his modification was discovered nearly four decades ago [394], the functional significance of N-terminal TnT phosphorylation remains unclear. Therefore, the significance of decreased TnT isoform phosphorylation in the fast- and slow-twitch skeletal muscles of aging rats will require further investigation.

Unlike the phosphorylation of TnT isoforms, the phosphorylation of *fs*TnI was unchanged in the fast-twitch skeletal muscles of aging rats (**Figs. 7.32**, **7.34A**). Conversely, the phosphorylation of *ss*TnI was increased in the slow-twitch skeletal muscles of 36-month-old rats versus that in muscles from 6-month-old animals (**Figs. 7.33**, **7.34B**). Although phosphorylation of the cardiac isoform of TnI is well-established within the literature [29], phosphorylation of the fast- and slow-skeletal muscle-specific isoforms of TnI has not previously been reported. Thus, the functional significance of *fs*-/*ss*-TnI phosphorylation in skeletal muscle, particularly aging fast- and slow-

twitch skeletal muscle, contractile function remains to determined. Also noteworthy was the finding that the relative abundance of *GSS*-*ss*TnI, the glutathionylated proteoform of *ss*TnI, increased in the slow-skeletal muscles of aged F344BN rats (**Fig. 7.33**). This finding is particularly relevant given that oxidative protein damage is a well-established facet of the aging process [395]. Moreover, evidence in the literature suggests that the oxidative modification of contractile proteins may negatively impact contractile function [190, 382, 396]. Therefore, enhanced glutathionylation of amino acid residues vulnerable to oxidation in *ss*TnI may represent an adaptive modification that helps preserve contractile function in slow-twitch skeletal muscle.

Top-down proteomics analysis also uncovered alterations in the phosphorylation of Tpm isoforms in fast- but not slow-twitch skeletal muscles with age (**Figs. 7.32-7.34**). Specifically, the phosphorylation of αTpm in the fast-twitch skeletal muscles of aging rats was significantly increased at 36 months of age versus that in muscles from 6- and 24-month-old animals (**Fig. 7.32**, **7.34A**). The phosphorylation of βTpm was also increased in the fast-twitch skeletal muscles of aging rats at 36 months of age versus that in muscles from 24-month-old animals (but not 6-month-old rats) (**Fig. 7.32**, **7.34A**). On the other hand, βTpm phosphorylation did not vary with age in the slow-twitch skeletal muscles of F344BN rats (**Fig. 7.33**, **7.34B**). Functionally, the phosphorylation of Tpm isoforms has been shown to increase the rigidity of the Tpm head-to-tail overlap domain [397]. The increased stiffness of Tpm head-to-tail polymers enhances the responsiveness of the thin filament to intracellular Ca^{2+} concentrations [397]. Therefore, the increase in Tpm isoform phosphorylation in fast-twitch skeletal muscle may be a compensatory change in response to age-related alterations in cellular Ca^{2+} handling [398].

7.4.3 Sarcopenia is associated with changes in the phosphorylation of the Z-disc protein cypher in fast- and slow-twitch skeletal muscles

While the central role of the myofilaments, which constitute the contractile apparatuses, in muscle function has been appreciated for almost seventy years [1], the contribution of the Z-discs to muscle biology has been largely overlooked. Long considered simple structural elements necessary only for the transition of force between adjacent sarcomeres, the importance of the Z-disc in striated muscle biology has come to light in recent years as a growing list of Z-disc protein mutations have been linked to muscular dystrophies and cardiomyopathies [95]. In particular, recent studies have identified a variety of mutations in Cypher, a Z-disc protein that belongs to the Enigma subfamily of PDZ/LIM proteins, in patients with dilated cardiomyopathy, hypertrophic cardiomyopathy, and skeletal muscle myopathies, including myofibrillar myopathies [399].

Cypher contains a single N-terminal PDZ domain that binds the C-terminal domain of α-actinin, promoting the localization of Cypher to Z-discs in striated muscle, and up to three C-terminal LIM domains [399]. Alternative splicing of the Cypher pre-mRNA allows for the production of at least six different isoforms in humans and mice, all of which contain the N-terminal PDZ domain with or without the C-terminal LIM domains [389, 399]. The alternatively spliced isoforms of Cypher are divided into cardiac and skeletal muscle-specific isoforms based on the inclusions of either exon 4 (unique to cardiac variants of Cypher) or exons 5-7 (unique to skeletal muscle variants) [389]. Cardiac and skeletal muscle-specific splice isoforms of Cypher can be further classified as “long” or “short” isoforms based on whether they contain or lack the C-terminal LIM domains, respectively [399].

In this study, we were able to detect and identify two different splice isoforms of Cypher in the fast- and slow-twitch skeletal muscles of aging F344BN rats (**Figs. 7.28-7.30**). One of these isoforms is analogous to the short isoform Cypher2s, which has previously been identified in the striated muscles of mice (UniProtKB/Swiss-Prot accession number A0A0G2JXR0; **Tables 7.1**, **7.3**, **Fig. 7.30**) [389]. Interestingly, the second short isoform of Cypher that we detected and characterized using top-down proteomics was determined to be an isoform that has, to the best of our knowledge, only been detected at the transcript level (UniProtKB/Swiss-Prot accession number Q5XIG1; **Tables 7.1**, **7.3**, **Fig. 7.29**) [390]. We have designated this isoform Cypher4s, following the naming convention established by Huang et al. wherein "s" denotes Cypher isoforms containing exons 5-7, which are only found in Cypher isoforms expressed in skeletal muscle [389]. Of note, this isoform appears to be unique among skeletal muscle-specific isoforms of Cypher in that it does not contain exon 7, which is present in all other Cypher isoforms expressed in skeletal muscle (**Table 7.4**).

Surprisingly, quantitative top-down proteomics identified age-related changes in the phosphorylation of Cypher isoforms in rat fast- and slow-twitch skeletal muscles (**Figs. 7.32-7.34**). Specifically, the phosphorylation of both Cypher isoforms (Cypher4s and Cypher2s) was significantly decreased in the fast-twitch GAS muscles of rats in the 24- and 36-month-old age groups in comparison to that in muscles from 6-month-old animals (**Figs. 7.32**, **7.34A**). Conversely, while the phosphorylation of Cypher4s did not change with age in the slow-twitch SOL muscles of aging rats, Cypher2s phosphorylation was significantly increased in SOL muscles isolated from rats aged 36 months versus that in muscles from 24-month-old rats (**Fig. 7.33**,

7.34B). Although prior studies have shown that Cypher serves as an A-kinase anchoring protein and can be phosphorylated by PKA *in vitro*, as well as *in vivo* [119], the functional significance of Cypher phosphorylation remains enigmatic. Therefore, additional studies will be necessary to determine not only the functional significance of Cypher phosphorylation, but also how age-related alterations in Cypher phosphorylation affect fast- and slow-twitch skeletal muscles. Nevertheless, these results are particularly noteworthy as this represents the first demonstration of age-related changes in the phosphorylation of Z-disc proteins in the fast- and slow-twitch skeletal muscles of aging individuals. Moreover, this finding opens new avenues for the investigation of the role of the Z-disc in age-related muscle dysfunction.

7.4.4 Identification of novel isoform of the PDZ/LIM protein Enigma

Enigma is the prototypical member of the Enigma subfamily of PDZ/LIM proteins and, like all members of this protein subfamily, can produce a variety of isoforms via alternative splicing of the Enigma pre-mRNA. While only a single sequence was present in the UniProtKB/Swiss-Prot database for Enigma in rat (accession number Q9Z1Z9; corresponds to Enigma isoform 1 in human), sequences for six different isoforms of Enigma were present in the database for human (**Table 7.2**). Surprisingly, top-down MS/MS analysis revealed that the Enigma isoform identified in this study did not correspond to any known Enigma isoforms in the UniProtKB/Swiss-Prot database. Therefore, the isoform identified herein represents a novel short isoform of the Enigma protein (comprised of exons 1-4 and 6-9) that contains the N-terminal PDZ domain but lacks the three C-terminal LIM domains (**Table 7.2**, **Figs. 7.16**, **7.20**).

Originally identified in 1994 by Wu and Gill as an insulin receptor interacting protein [108], Enigma, like other members of its subfamily, is a scaffolding protein that plays a key role in the organization of macromolecular signaling complexes. In the case of insulin signaling, ensuing research showed that Enigma interacts with the adaptor protein APS [400], and plays an important regulatory role in insulin-induced cytoskeletal remodeling and glucose transporter 4 translocation [401]. A role for Enigma in mitogenic signaling was demonstrated via interactions with Ret/ptc2, a constitutively active, oncogenic form of the c-Ret receptor tyrosine kinase [402]. Specifically, Enigma was found to be required for localization of Ret/ptc2 to the plasma membrane where it induces cellular proliferation through interactions with Ras and Raf [402]. Subsequent work revealed that Enigma selectively binds short isoforms of Ret and [403], thus, may be partly responsible for critical developmental signals mediated by short, but not long, isoforms of Ret [404]. In striated muscle, the PDZ domain of Enigma was shown to interact with the C-terminus of βTpm, promoting localization of Enigma to the boundary of Z-discs and I bands [118]. Although the function(s) of Enigma isoforms in skeletal muscle have yet to be determined, the localization of Enigma to the boundary of the Z-discs in striated muscles raises the possibility that Enigma may mediate important signals generated within the Z-discs or, potentially, may influence contractility via signaling to myofilaments. Also of note, recent evidence has shown that Enigma is a target of the ubiquitin ligase Nedd4-1, which plays an important role in skeletal muscle atrophy [405].

7.4.5 High-resolution MS-based top-down proteomics for quantitative biology

In this study, we utilized powerful quantitative top-down proteomics to gain insights into age-related molecular changes in fast- and slow-twitch skeletal muscles, with a particular emphasis on those occurring in sarcomeric proteins, including both myofilament and Z-disc proteins. In general, top-down MS boasts several key advantages over the traditional method for MS-based proteomics (termed bottom-up MS) for the quantification and comprehensive characterization of protein proteoforms.

Specifically, the fact that intact proteins are analyzed in top-down proteomics, rather than peptides resulting from protein digestion as in bottom-up proteomics, greatly increases the potential for identifying and characterizing protein isoforms, particularly those containing a high degree of sequence homology. Among the sarcomeric proteins exhibiting a high degree of sequence homology are those belonging to the Enigma subfamily of PDZ/LIM domain-containing proteins. Despite the fact that individual genes are responsible for producing Enigma, Enigma Homolog, and Cypher/ZASP/Oracle, a myriad isoforms of each of these proteins can be produced via alternative splicing of the mRNA transcripts [99]. Given the significant sequence overlap between the isoforms of these proteins, as well as the fact that multiple isoforms may be present within a cell/tissue at any given time, correct identification of specific isoforms of Enigma subfamily proteins, would be expected to pose significant challenges for the peptide-based bottom-up MS. In addition to the identification of Cypher2s, which has previously been described [389], enabled by top-down proteomics, we identified an undesignated isoform of the Z-disc protein Cypher (herein named Cypher4s) that previously had not been observed at the protein level, although the specific mRNA transcript for this isoform had previously been detected (**Fig. 7.28**) [390]. Therefore, our results are the first to confirm the expression of Cypher4s at the protein level.

Moreover, top-down MS enabled the identification and characterization a novel isoform of the PDZ/LIM domain-containing protein Enigma, which is produced via alternative splicing of Enigma exons 1-4 and 6-9 (**Fig. 7.16**).

In addition, the use of high-resolution mass spectrometers in top-down proteomics studies offers unparalleled mass accuracy that not only increases confidence in protein identification, but also in the identification of protein PTMs [270]. In this study, we were able to differentiate N^{α}-acetylation and N^{α}-tri-methylation—two modifications differing in mass by only ~36 mDa (~0.0036 Da). In particular, we were able to identify N-terminal methylation of myosin light chain isoforms, including MLC-1F, MLC-1V, MLC-1S, and MLC-2S (**Figs. 7.11**, **7.24-7.26**), which verify the results of previous studies [275]. Although the significance of N^{α}-acetylation versus N^{α}-tri-methylation in proteins is not clear, these results showcase the great potential of top-down high-resolution MS/MS for PTM identification.

Another advantage of analyzing intact proteins is that PTMs such as phosphorylation and minor sequence variations do not significantly impact the ionization efficiency of intact proteins as they do with peptides [385]. Therefore, top-down MS is intrinsically semi-quantitative in regards to the relative abundances of protein isoforms and their associated proteoforms [197, 198, 200]. Herein, top-down proteomics allowed for the quantification of a variety of sarcomeric protein proteoforms from both fast- and slow-twitch skeletal muscles (**Figs. 7.32-7.33**). In addition to being the most comprehensive study of age-related changes in myofilament and Z-disc protein modifications in fast- and slow-twitch skeletal muscles to date, the observed changes in the phosphorylation of Z-discs proteins is noteworthy as this is the first report of age-related changes

in the PTMs of Z-disc proteins. Therefore, our results have opened a new avenue for the investigation of the role of the Z-disc in sarcopenia-associate skeletal muscle dysfunction.

Collectively, these results highlight the power of top-down proteomics for the identification, quantification, and comprehensive characterization of protein proteoforms, and significantly advances our understanding of age-related changes in fast- and slow-twitch skeletal muscles.

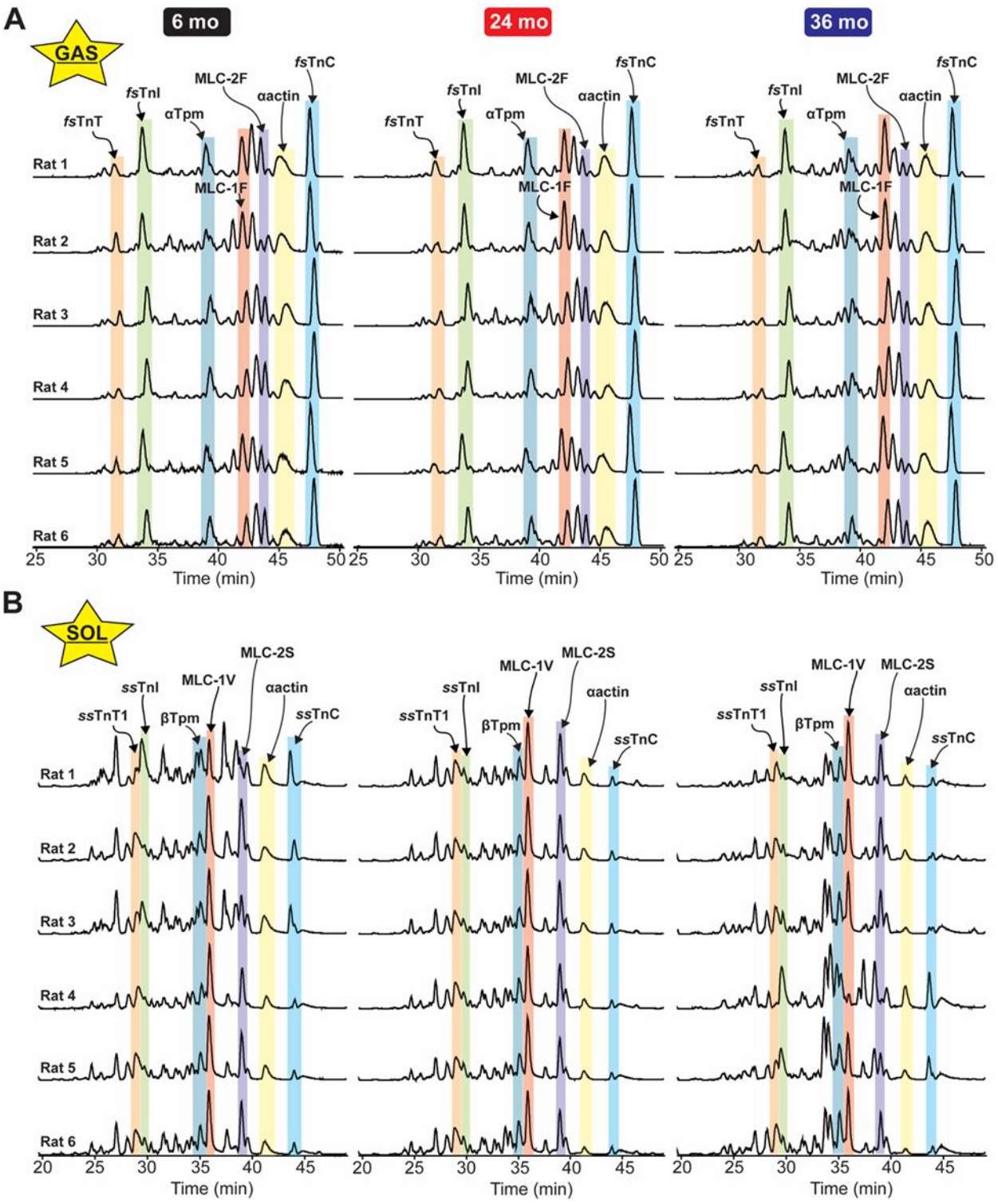

Fig. 7.1. Highly reproducible chromatographic separation of sarcomeric protein-enriched extracts prepared from the GAS and SOL muscles of rats in different age groups. (A) Chromatographic profiles of sarcomeric protein-enriched extracts prepared from the GAS muscles

of six individual rats at 6- (left), 24- (middle), and 36-months (right) of age. (B) Chromatographic profiles of sarcomeric protein-enriched extracts prepared from the SOL muscles of six individual rats at 6- (left), 24- (middle), and 36-months (right) of age. Peaks corresponding to major myofilament proteins are indicated. *fs*TnT, isoform of fast skeletal troponin T; *fs*TnI, fast skeletal troponin I; αTpm, α-tropomyosin; MLC-1F, fast skeletal myosin light chain 1; MLC-2F, fast skeletal myosin light chain 2; αactin, α skeletal actin; *fs*TnC, fast skeletal troponin C; *ss*TnT1, slow skeletal troponin T isoform 1; *ss*TnI, slow skeletal troponin I; βTpm, β-tropomyosin; MLC-1V, ventricular myosin light chain 1; MLC-2S, slow skeletal myosin light chain 2; *ss*TnC, slow skeletal troponin C.

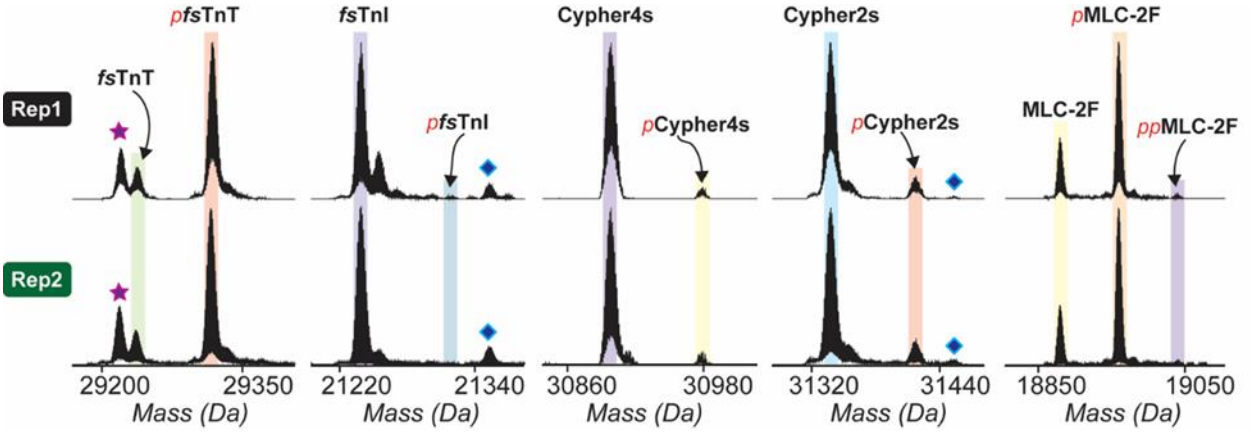

Fig. 7.2. Reproducibility of on-line high-resolution MS analysis of sarcomeric proteins from skeletal muscle protein extracts. Shown are representative zoomed-in mass spectra from two replicate protein extracts prepared from the GAS muscle of a single 24-month-old F344BN rat. Star and diamond represent H_3PO_4 loss from $_p$*fs*TnT and protein species associated non-covalently with TFA, respectively. *fs*TnT, isoform of fast skeletal troponin T; *fs*TnI, fast skeletal troponin I; Cypher4s, isoform of Cypher previously observed only at the transcript level; Cypher2s, Cypher isoform 2s; MLC-2F, fast skeletal myosin light chain 2.

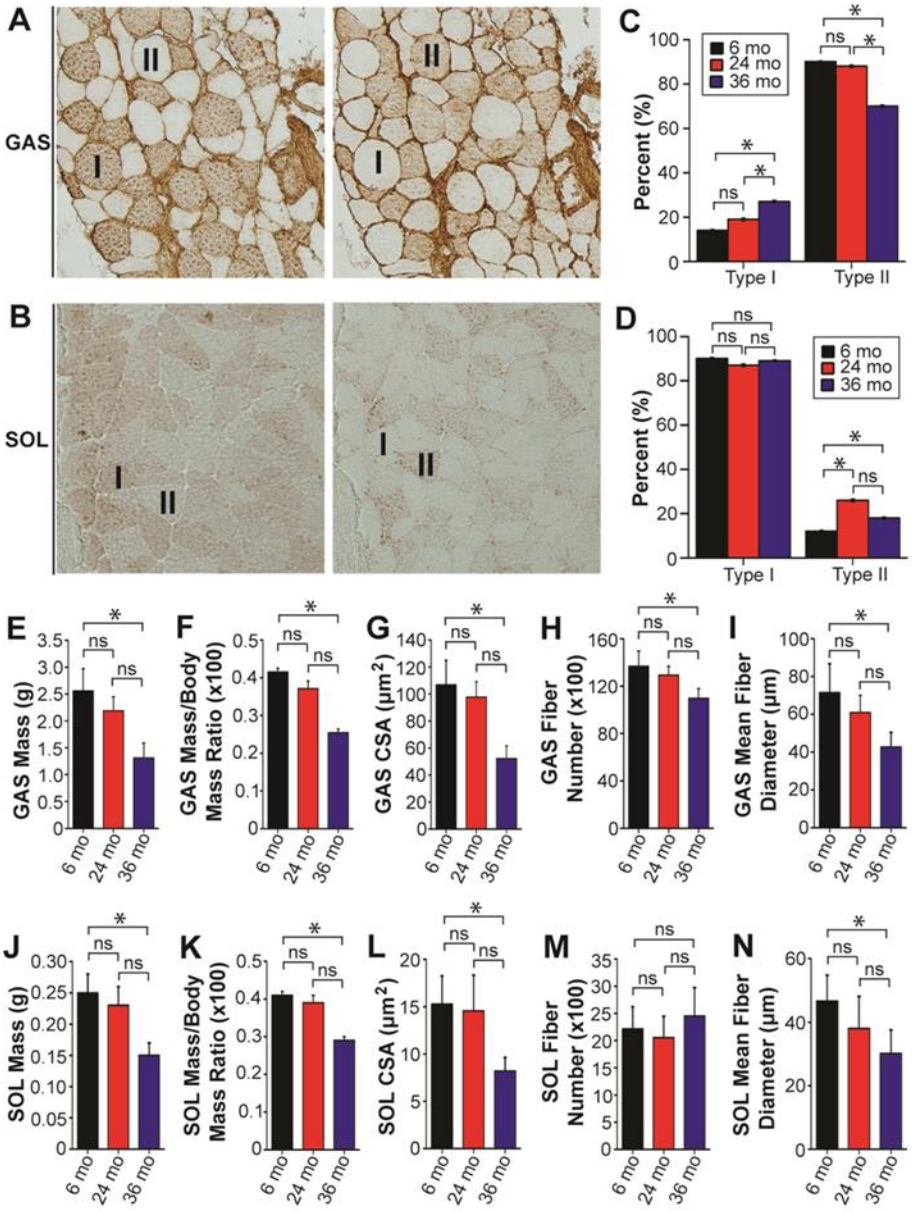

Fig. 7.3. Sarcopenia affects both fast- and slow-twitch skeletal muscles at advanced age. (A) Representative serial sections from the GAS muscle of a 6-month-old F344BN rat stained with antibodies against type I MHC (left) and type II MHC (right). "I" and "II" denote fibers expressing type I and type II MHC, respectively. (B) Representative serial sections from the SOL muscle of a 6-month-old F344BN rat stained with antibodies against type I MHC (left) and type II MHC (right). "I" and "II" denote fibers expressing type I and type II MHC, respectively. (C) Graph

showing quantification of age-dependent changes in the percentage of type I and type II MHC-expressing fibers in the GAS muscles of aging rats. (D) Graph showing quantification of age-dependent changes in the percentage of type I and type II MHC-expressing fibers in the SOL muscles of rats in different age groups. Graphs showing the muscle mass (E), muscle mass-to-body mass ratio (F), and cross-sectional area (CSA) at the muscle midbelly (G) for GAS muscles isolated from rats in different age groups. Graphs showing the quantification of fiber number (H) and mean fiber diameter (I) for GAS muscles from rats in different age groups. Graphs showing the muscle mass (J), muscle mass-to-body mass ratio (K), and CSA at the muscle mid-belly (L) for SOL muscles isolated from rats in different age groups. Graphs showing quantification of the fiber (M) and mean fiber diameter (N) for SOL muscles isolated from rats in different age groups. n = 12 for all panels. Each data point is the mean and error bar the SEM. ns, not significant. *$p < 0.05$.

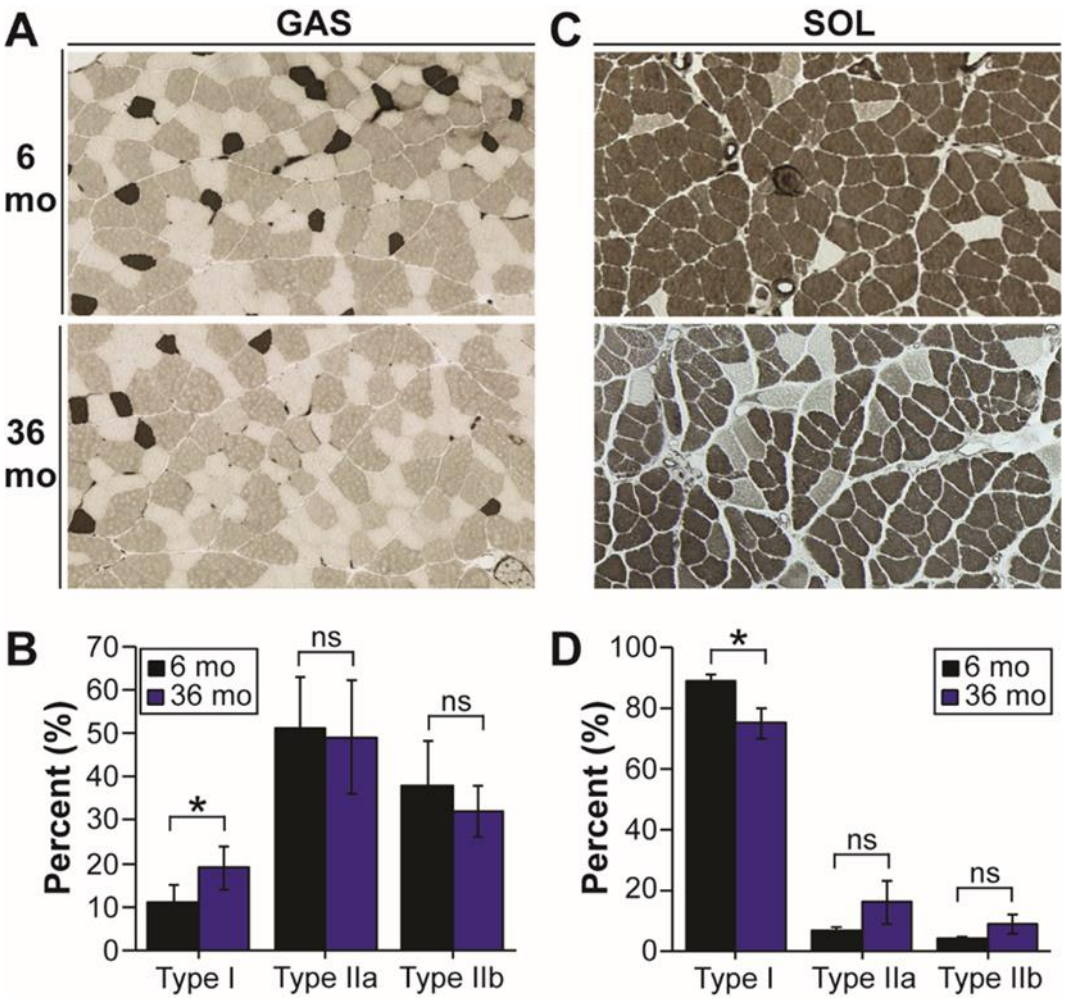

Fig. 7.4. The GAS and SOL muscles of F344BN rats are predominantly composed of type II (fast) and type I (slow) muscle fibers, respectively, as determined by myosin ATPase staining. (A) Representative sections from the GAS muscles of 6- and 36-month-old animals stained for myosin ATPase activity. (B) Quantification of type I, IIa, and IIb fibers in the GAS muscles of 6- and 36-month-old F344BN rats based on ATPase staining. (C) Representative sections from the SOL muscles of 6- and 36-month-old animals stained for myosin ATPase activity. (D) Quantification of type I, IIa, and IIb fibers in the SOL muscles of 6- and 36-month-old F344BN rats based on ATPase staining. For muscle sections, fibers with the darkest staining are type I fibers, intermediate staining fibers are type IIa fibers, and the lightest staining fibers are type IIb

fibers. Quantification was based on sections from n = 8 animals per age group. ns, not significant. *$p < 0.05$.

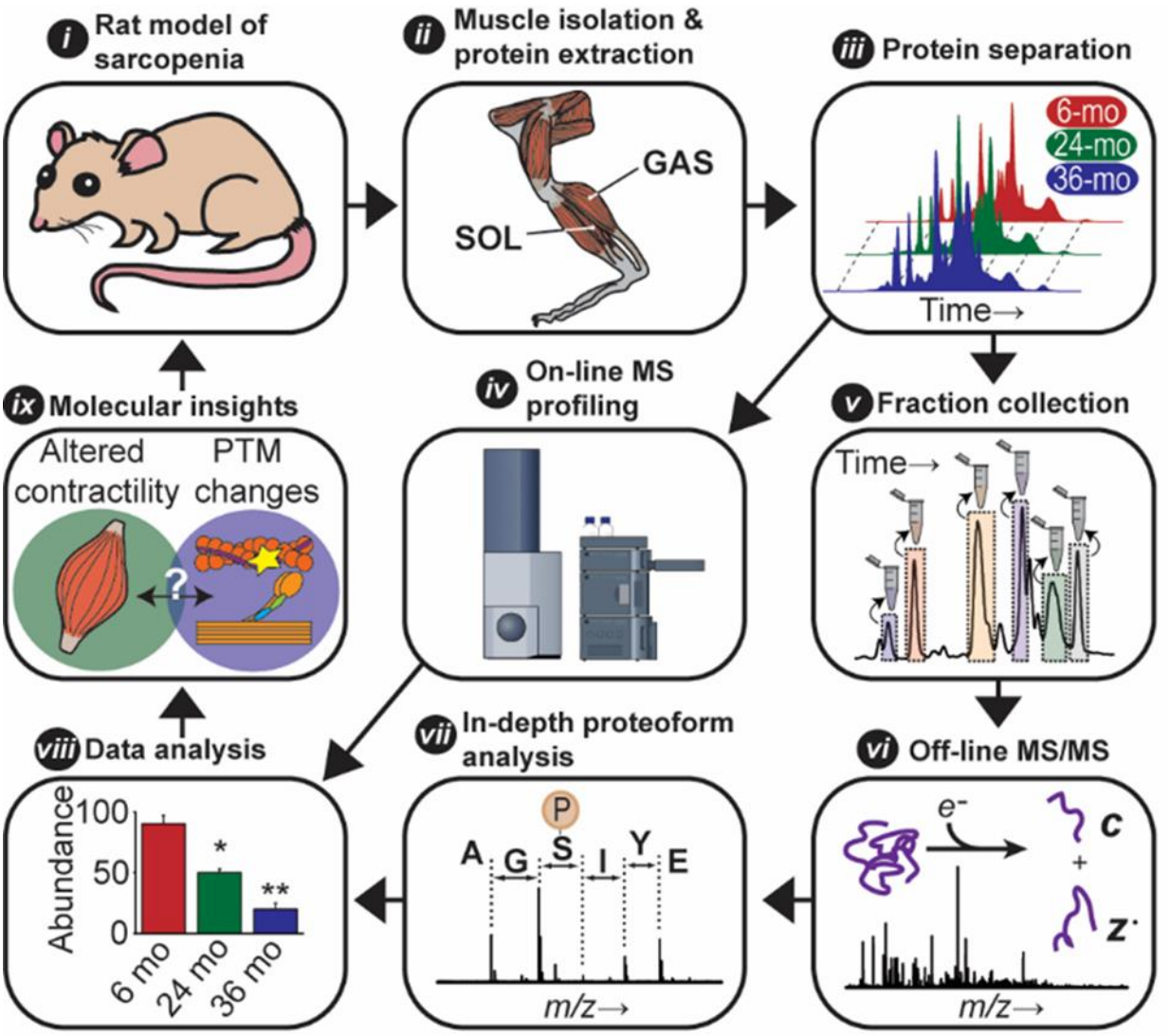

Fig. 7.5. Overview of top-down proteomics strategy employed for the quantification and in-depth characterization of sarcomeric proteins extracted from fast- (GAS) and slow-twitch (SOL) muscles isolated from 6-, 24-, and 36-month-old F344BN rats. This strategy includes: i) an NIA approved rat model of healthy aging; ii) isolation of a sarcomeric-protein enriched fraction from both fast- and slow-twitch skeletal muscles; iii) protein separation by 1D liquid chromatography (LC); iv) rapid on-line proteoform profiling on a high-resolution q-TOF mass spectrometer; v) fraction collection of sarcomeric proteins concomitant with on-line proteoform profiling; vi) off-line MS/MS on an ultra-high-resolution FT-ICR mass spectrometer; vii) in-depth

proteoform characterization; viii) integrated analysis of changes in proteoform relative abundances and modifications; and ix) correlation of age-dependent changes in fast- and slow-twitch muscles with proteomics findings to gain insights into the molecular mechanisms underlying sarcopenic phenotype.

Table 7.1 Identification of proteins in sarcomeric protein-enriched extract prepared from the fast-twitch GAS muscles of rats in different age groups.

Peak #	RT (min)	Expt'l M_r (Da)	Calc'd M_r (Da)	Error (ppm)	Protein ID	Accession #
1	~29.7	9,025.78	9,025.77	0.4	SMPX	Q925F0
2	**~30.5**	**29,219.31**	**29,219.33**	**0.7**	***fs*TnT**	**A0A0G2JSW6**
3	**~33.8**	**21,225.84**	**21,225.83**	**0.5**	***fs*TnI**	**P27768**
4	**~35.2**	**30,879.78**	**30,879.76**	**0.6**	**Cypher4s***	**Q5XIG1**
5	**~35.7**	**31,319.04**	**31,319.00**	**1.3**	**Cypher2s**	**A0A0G2JXR0**
6	**~36.0**	**21,153.90**	**21,153.90**	**0.2**	***n*Enigma**	
7	~36.5	8,318.40	8,318.41	1.2	COX6C2	P11951
8	~37.9	13,997.87	13,997.85	1.3	Histone H2A.2	P0CC09
9	~38.4	13,766.52	13,766.51	0.7	Histone H2B	G3V8B3
10	**~39.4**	**32,702.71**	**32,702.68**	**0.9**	**αTpm**	**P04692**
11	**~39.6**	**32,858.58**	**32,858.56**	**0.6**	**βTpm**	**P58775**
12	~39.8	15,187.73	15,187.72	0.7	Hemoglobin-α1/2 chain	P01946
13	~40.4	42860.80	-	-	Not identified	-
14	~41.3	17,014.93	17,014.93	0.3	Myoglobin	Q9QZ76
15	**~42.1**	**20,577.46**	**20,577.43**	**1.5**	**MLC-1F**	**P02600**
16	**~42.9**	**18,868.36**	**18,868.32**	**2.1**	**MLC-2F**	**P04466**
17	**~43.6**	**16,514.10**	**16,514.11**	**0.6**	**MLC-3F**	**P02600-2**
18	**~45.5**	**41,845.86**	**41,845.83**	**0.7**	**Actin**	**P68136**
19	**~47.6**	**17,995.28**	**17,995.30**	**1.2**	***fs*TnC**	**Q304F3**

Accession numbers correspond to UniProtKB/Swiss-Prot database accession numbers. Known sarcomeric proteins are bolded. Abbreviations are as follows: RT, retention time; Expt'l M_r, experimentally determined relative molecular mass; Calc'd M_r, calculated relative molecular mass; SMPX, small muscular protein; *fs*TnT, isoform of fast skeletal troponin T; *fs*TnI, fast skeletal troponin I; Cypher4s, isoform of Cypher previously observed only at the transcript level; Cypher2s, Cypher isoform 2s; *n*Enigma, novel isoform of Enigma; COX6C2, cytochrome *c* oxidase subunit 6C-2; MLC-1F, fast skeletal myosin light chain 1; MLC-2F, fast skeletal myosin light chain 2; MLC-3F, fast skeletal myosin light chain 3; *fs*TnC, fast skeletal troponin C. All

reported relative molecular masses correspond to the mono-isotopic molecular masses. *A previously undesignated isoform of Cypher that we have designated, here, Cypher4s.

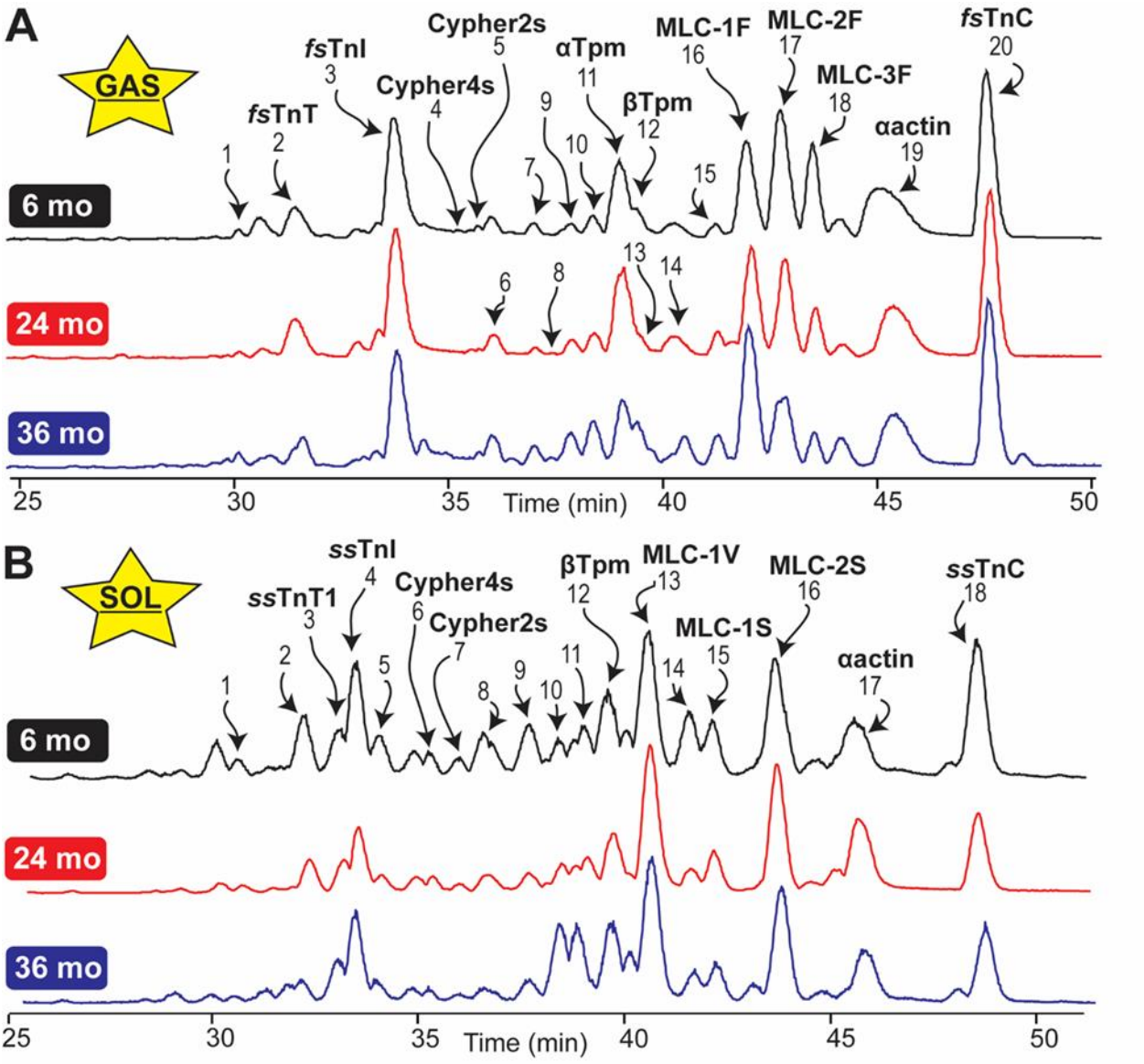

Fig. 7.6. Chromatographic separation and identification of proteins in sarcomeric protein-enriched extracts prepared from fast- and slow-twitch skeletal muscles of 6-, 24-, and 36-month-old F344BN rats. (A) Representative chromatograms of fast-twitch GAS muscle extracts from 6-, 24-, and 36-month-old F344BN rats. (B) Representative chromatograms of slow-twitch SOL muscle extracts from 6-, 24-, and 36-month-old animals. Chromatographic peaks corresponding to identified sarcomeric proteins are indicated. Numbers correspond to protein identifications listed in **Table 7.1** and **Table 7.3**.

A

All proteins / tr|A0A0G2JSW6|A0A0G2JSW6_RAT Troponin T, fast skeletal muscle OS=Rattus norvegicus GN=Tnnt3 PE=1 SV=1 / Peptide #1

Protein-Spectrum-Match for Spectrum #0

PrSM ID:	0	Scan(s):	1	Precursor charge:	36	Precursor m/z:	814.841
Precursor mass:	29298	Adjusted precursor mass:	29298.27	Duplicate score:	185	Unique score:	112
E-value:	2.8E-36	P-value:	7.6E-38	Spectral FDR:	n/a	Protein mass:	30729.906

A modification (or multiple modifications) on internal residue
N-Terminal Acetylation

42.01
M S D E E T E Q V E E Q Y E E E E E E A Q E E E V Q E E[A|P E P E E V Q E E E K P
R P K L T A P K I P E G E|K V D F|D|D I|Q K K|R|Q|N K|D L M E L Q A|L I|D S H|F|
E A|R K K|E|E E|E L I|A|L|K|E|R|I E K|R|R A E|R A E|Q|Q|R I R A E K|E R E R Q|N
R L A E|E K A R R E E E|D A K R R A E D D L|K K K K A L S S M G A N Y S|S|Y|L A|
K A D|Q|K|R G K K Q T|A|R E|M|K|K K I|L A|E|R R|K P L N I|D H|L S D|D|K|L|R|D K
A|K|E|L W D T|L|Y|Q|L|E|T|D|K|F|E|F|G|E|K|L|K|R|Q|K|Y|D|I|M|T|V|R|A|R|V|E|M|L|A|
K|F|S|K|K|A G|A|T|A|K|G|K|V|G G R W K

B

All proteins / sp|P27768|TNNI2_RAT Troponin I, fast skeletal muscle OS=Rattus norvegicus GN=Tnni2 PE=1 SV=2 / Peptide #1

Protein-Spectrum-Match for Spectrum #0

PrSM ID:	0	Scan(s):	1	Precursor charge:	29	Precursor m/z:	733.211
Precursor mass:	21233.9	Adjusted precursor mass:	21234.17	Duplicate score:	112	Unique score:	78
E-value:	6.3E-47	P-value:	6.9E-47	Spectral FDR:	n/a	Protein mass:	21314.868

N-Terminal Methionine Excision(canonical) and N-Terminal Acetylation
A modification (or multiple modifications) on internal residue

M]42.01
G D E E K R|N|R|A|I|T|A|R|R|Q H|L|K|S|V|M|L|Q|I|A A T|E|L|E|K|E|E|S|R|R|E|S|E|
K|Q|N|Y|L S E H C P P L|H I|P G S M|S E V Q E|L C K Q L|H|A|K I D A|A|E|E|E|K Y
D M E V K V Q K S S|K E L E D M|N Q K L F|D L R G K F K R P P L R R V R M S A D
A M]8.33
L K A L L G S K H K V C|M|D L|R A N L|K|Q V|K K|E|D T E|K E|R|D L R|D V|G|D
W|R|K N|I|E E|K S G|M|E|G|R|K|K M F E S E S

C

All proteins / sp|P04692|TPM1_RAT Tropomyosin alpha-1 chain OS=Rattus norvegicus GN=Tpm1 PE=1 SV=3 / Peptide #1

Protein-Spectrum-Match for Spectrum #0

PrSM ID:	0	Scan(s):	1	Precursor charge:	38	Precursor m/z:	861.605
Precursor mass:	32702.71	Adjusted precursor mass:	32702.685	Duplicate score:	101	Unique score:	68
E-value:	7.1E-28	P-value:	3.6E-28	Spectral FDR:	n/a	Protein mass:	32660.674

N-Terminal Acetylation

42.01
M D A I K|K|K|M|Q|M|L|K|L D|K|E|N|A L|D|R|A|E|Q|A|E|A|D|K K|A A|E|D R S K Q L|E|
D|E L V|S|L Q|K|K|L K G T|E|D|E L|D K Y S|E A L|K D A Q|E K L E L A|E K K A T D
A E A D V A S L N|R R I Q L V E|E E L D R A Q E R L A T A L Q K L E E A E K A A
D E S E R G M K V I E S R A Q K D E E K M E I Q E I Q L K E A|K H I A E D A D R
K Y E E V A R|K L|V I I E S D L E R A E|E R A E L S E G K C|A E L E E E L K T V
T N N|L K S L E A Q A E K Y S|Q|K E|D K Y E E E I|K V L S|D K L K|E A E|T|R A|E|
F|A E|R S V T|K|L E K S I D D L E D E|L|Y A|Q K L K Y|K A I S E E L|D H A L N D
M T S I

D

All proteins / sp|P02600|MYL1_RAT Myosin light chain 1/3, skeletal muscle isoform OS=Rattus norvegicus GN=Myl1 PE=1 SV=2 / Peptide #1

Protein-Spectrum-Match for Spectrum #0

PrSM ID:	0	Scan(s):	1	Precursor charge:	22	Precursor m/z:	936.355
Precursor mass:	20577.66	Adjusted precursor mass:	20577.432	Duplicate score:	278	Unique score:	133
E-value:	1.4E-45	P-value:	4.7E-46	Spectral FDR:	n/a	Protein mass:	20666.462

N-Terminal Methionine Excision(canonical) and N-Terminal Acetylation

M]A[42.01] P K K D V K K P A|A A A P A P|A P A P A P|A P|A|K P|K|E|E|K|I|D|L|S|A I|K|I|
E|F|S|K|E|Q|Q|E|E|F|K|E|A|F|L|L|F|D|R|T|G|E|C|K|I|T|L|S|Q|V|G|D|V|L|R|A L G T|N
P T|N|A|E V|K|K|V|L|G|N P|S|N|E|E|M|N|A|K|K I|E|F|E Q F|L P M|M|Q A I|S|N|N|K|D|
Q G|G|Y|E|D F V|E|G|L|R|V F|D|K|E|G|N|G|T|V|M G|A|E|L R H|V L A|T L G E K|M K|E
E E|V E A L L A G Q E|D S|N G C I N Y E A F V K H I M S|V

E

All proteins / sp|P02600|MYL1_RAT Myosin light chain 1/3, skeletal muscle isoform OS=Rattus norvegicus GN=Myl1 PE=1 SV=2 / Peptide #1

Protein-Spectrum-Match for Spectrum #0

PrSM ID:	0	Scan(s):	1	Precursor charge:	16	Precursor m/z:	1033.154
Precursor mass:	16514.34	Adjusted precursor mass:	16514.12	Duplicate score:	188	Unique score:	129
E-value:	1.4E-45	P-value:	2.3E-47	Spectral FDR:	n/a	Protein mass:	20666.462

A modification (or multiple modifications) on internal residue
N-Terminal Methionine Excision(canonical)

M]A[-4021.30] P K K D V K K P A A A A P A P A P A P A P A P A K P K E E K I D L S A I K I
E F S K E|Q Q E E F K E|A F|L|L|F D R|T|G|E C|K|I|T|L|S|Q V|G|D V L R|A L G T|N
P T|N|A|E V|K|K|V|L G|N P|S|N|E|E|M|N|A|K|K|I|E|F|E|Q F|L P|M|M|Q|A|I|S|N|N|K|D|
Q G|G|Y E|D|F V|E|G|L|R|V|F|D|K|E|G|N|G|T|V|M|G|A E|L R H|V L A|T L G E K|M K E
E|E V E A L L A G Q E|D S|N G C I N Y E A F V K H I M S|V

F

All proteins / tr|Q304F3|Q304F3_RAT Protein Tnnc2 OS=Rattus norvegicus GN=Tnnc2 PE=1 SV=1 / Peptide #1

Protein-Spectrum-Match for Spectrum #0

PrSM ID:	0	Scan(s):	1	Precursor charge:	16	Precursor m/z:	1125.727
Precursor mass:	17995.51	Adjusted precursor mass:	17995.309	Duplicate score:	175	Unique score:	118
E-value:	8.1E-60	P-value:	4.1E-60	Spectral FDR:	n/a	Protein mass:	18084.338

N-Terminal Methionine Excision(canonical) and N-Terminal Acetylation

M]T[42.01] D Q Q A E A R|S|Y L S|E|E|M|I|A|E F|K|A|A|F|D|M F|D|A|D|G|G|G|D|I|S|V|K|E|L
G T V M R|M|L|G|Q|T|P T|K|E|E|L|D|A I I|E|E V|D|E|D|G|S|G|T I|D F|E E F|L V M M
V R|Q M|K|E|D|A K|G|K|S|E|E|E L A|E C F|R|I|F|D|R|N|A|D|G|Y|I|D|A|E|E|L A|E I|F|
R|A S|G|E|H V T|D|E|E I E|S|L|M|K|D|G|D|K|N|N|D G R I|D|F|D E|F|L|K M M E G V Q

Fig. 7.7. Identification of contractile proteins in sarcomeric-protein enriched extracts prepared from GAS muscles by high-resolution MS/MS. The peak numbers representing different fractions collected are shown in **Fig. 7.6A**. The protein identifications are shown. The

full list of identified proteins is shown in **Table 7.1**. (A) Peak #2 was identified as fast skeletal troponin T isoform (*fs*TnT), with an N-terminal modification and a -1473.65 Da mass discrepancy in the middle of the protein, which indicates a possible sequence difference or modification. (B) Peak #3 was identified as fast skeletal troponin I (*fs*TnI), with removal of the N-terminal Met, an N-terminal modification, and a +8.33 Da mass difference in the C-terminal half of the protein. (C) Peak #10 was identified as the α isoform of tropomyosin (αTpm; Tpm1.1), with an N-terminal modification. (D) Peak #15 was identified as fast skeletal myosin light chain 1 (MLC-1F), with removal of Met1 and an N-terminal modification. (E) Peak #17 was identified as skeletal muscle myosin light chain 3 (MLC-3F), with N-terminal Met loss. (F) Peak #19 was identified as fast skeletal troponin C (*fs*TnC), with removal of Met1 and an N-terminal modification. The E-value of a Protein-Spectrum-Match (PrSM) refers to the number of hits one can "expect" to see by chance when searching the spectrum against a protein database with the same size as the database that was searched. The P-value of a PrSM represents the probability that the match between the input MS/MS spectrum and a random protein in the database has a similarity score no less than the score of the PrSM.

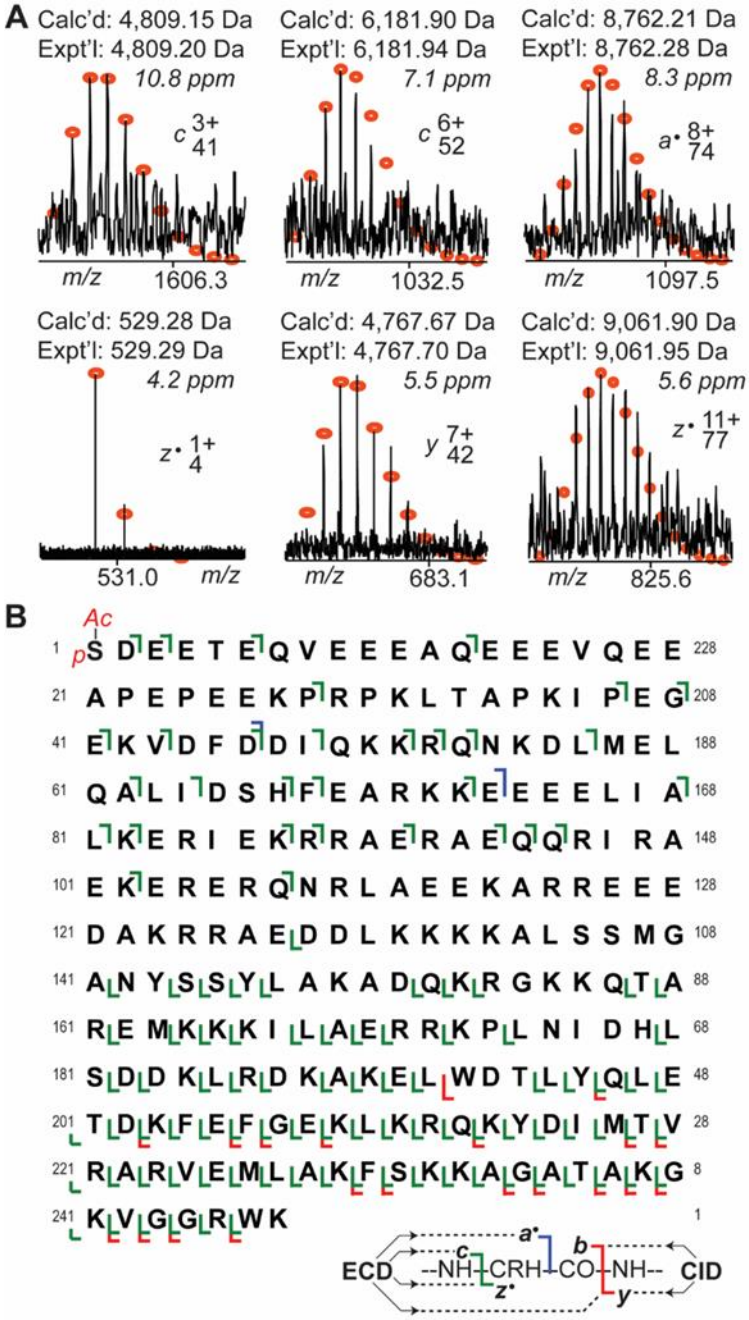

Fig. 7.8. Sequence characterization of *fs*TnT isoform by high-resolution MS/MS. (A) Representative fragment ions resulting from fragmentation of *fs*TnT by ECD. (B) Fragmentation map for *fs*TnT isoform showing bond cleavages. "*Ac*-" and "*p*" denote acetylation and phosphorylation, respectively, of Ser2 (numbering scheme includes N-terminal Met, which is

removed in the mature protein). Circles represent the theoretical isotopic abundance distribution corresponding to the assigned mass and based on averagine.

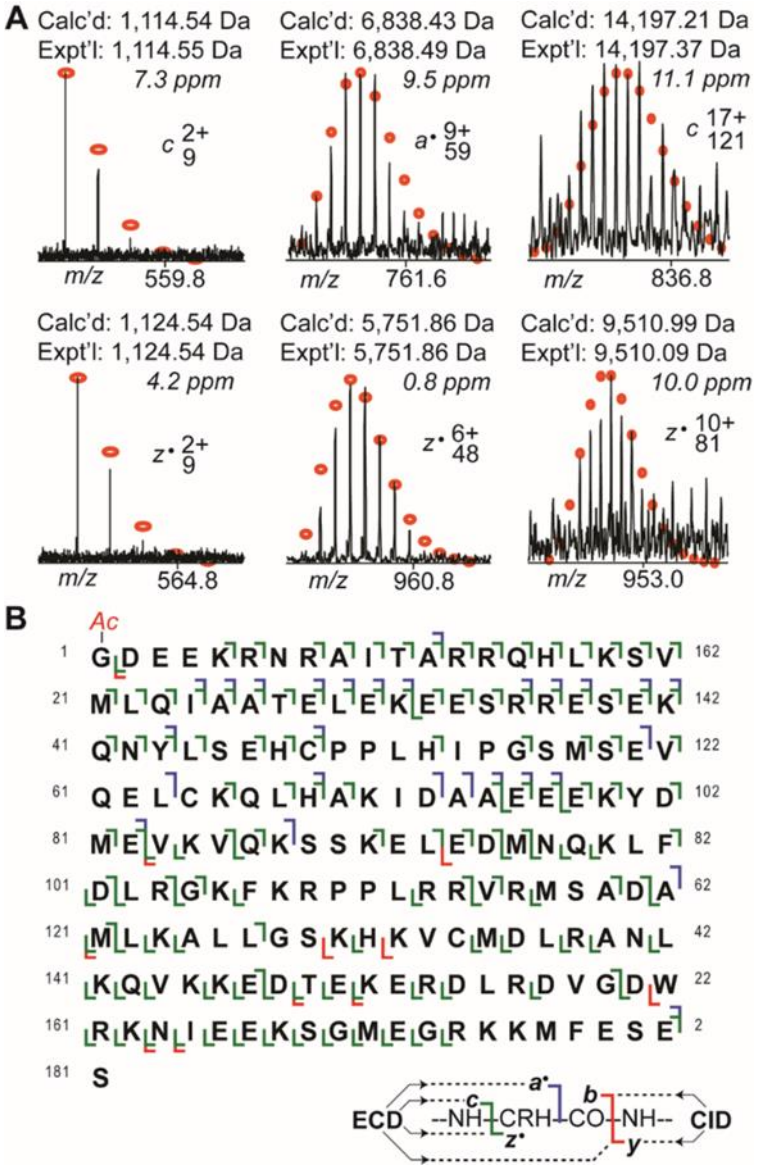

Fig. 7.9. Sequence characterization of *fs*TnI by high-resolution MS/MS. (A) Representative fragment ions resulting from fragmentation of *fs*TnI by ECD. (B) Fragmentation map for *fs*TnI showing bond cleavages. "*Ac*-" denotes acetylation of Gly2 (numbering scheme includes N-terminal Met, which is removed in the mature protein). Circles represent the theoretical isotopic abundance distribution corresponding to the assigned mass and based on averagine.

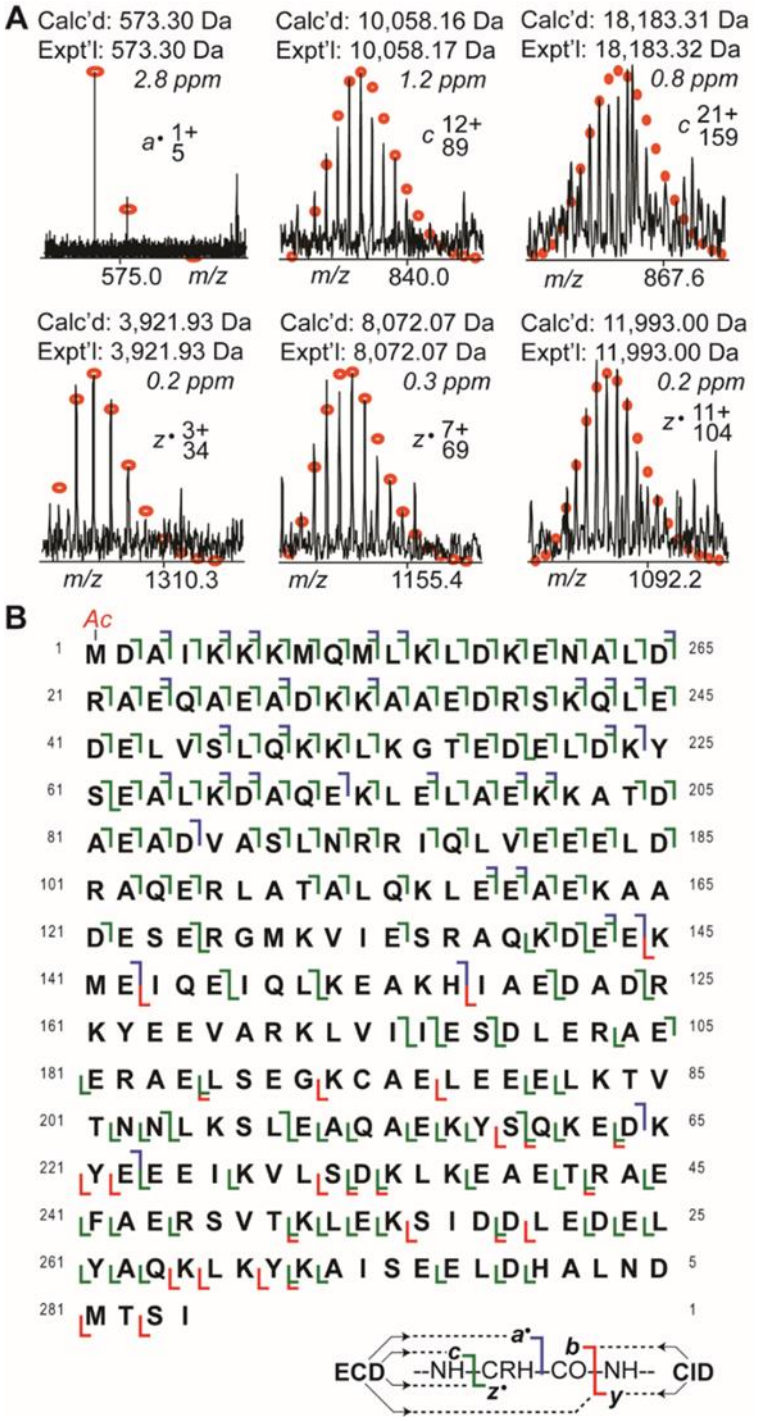

Fig. 7.10. Sequence characterization of αTpm [Tpm1.1st (a.b.b.a)] [406] by high-resolution MS/MS. (A) Representative fragment ions resulting from fragmentation of αTpm by ECD. (B) Fragmentation map for αTpm showing bond cleavages. "*Ac*-" denotes acetylation of Met1.

Circles represent the theoretical isotopic abundance distribution corresponding to the assigned mass and based on averagine.

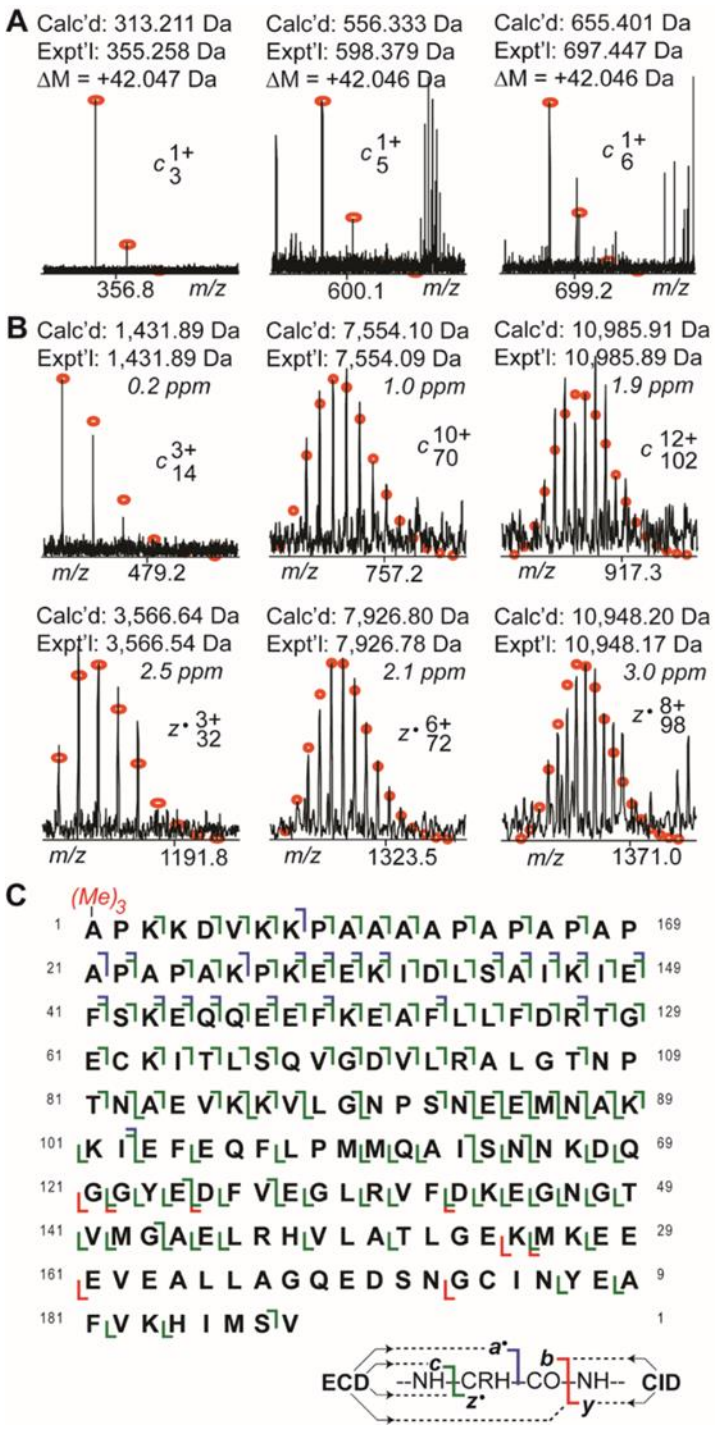

Fig. 7.11. Sequencing and N-terminal modification characterization for MLC-1F by high-resolution MS/MS. (A) N-terminal fragment ions showing approximate 42.046 Da mass increase compared to the calculated masses for the corresponding un-modified fragment ions, indicating N-terminal tri-methylation of MLC-1F. (B) Representative fragment ions resulting from

fragmentation of MLC-1F by ECD. C. Fragmentation map for MLC-1F showing bond cleavages. "*(Me)*$_3$-" denotes N$^{\alpha}$-tri-methylation of Ala2 (numbering scheme includes N-terminal Met, which is removed in the mature protein). Circles represent the theoretical isotopic abundance distribution corresponding to the assigned mass and based on averagine.

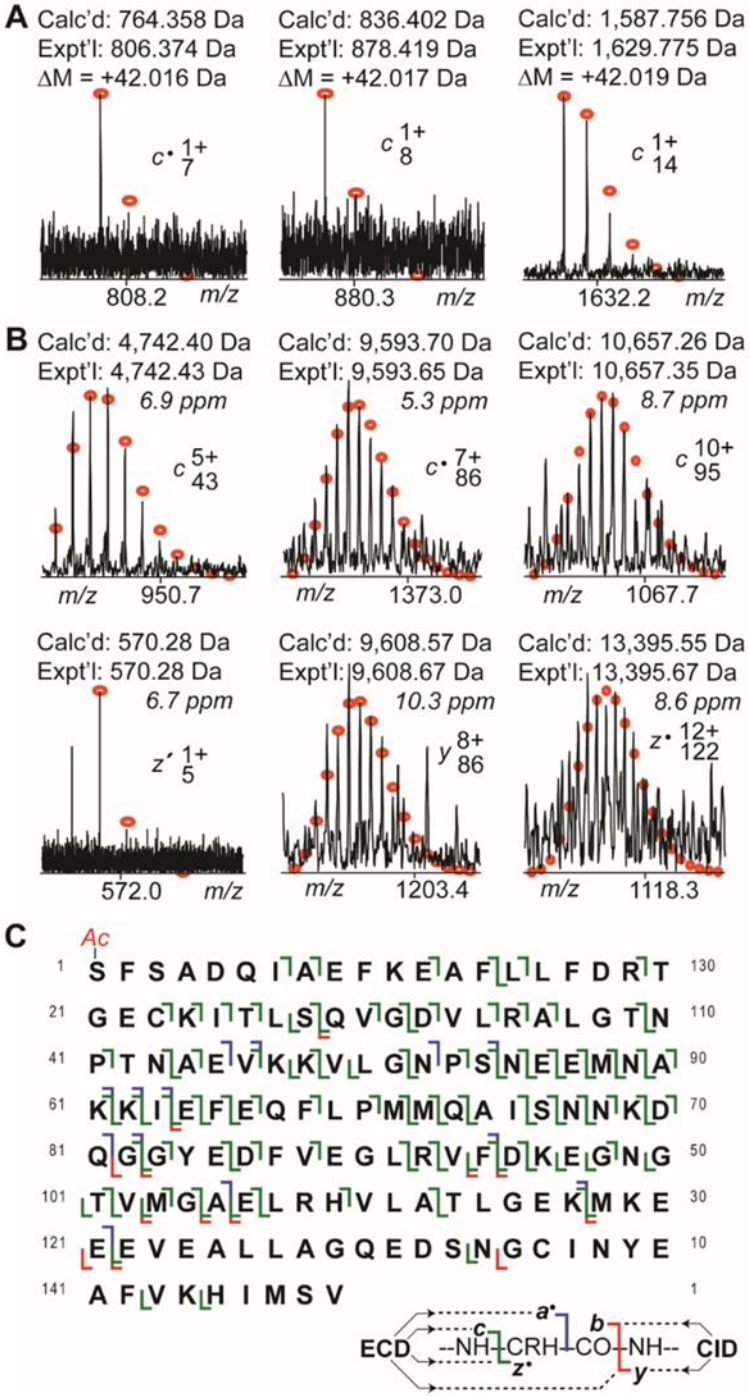

Fig. 7.12. Sequencing and N-terminal modification characterization for MLC-3F by high-resolution MS/MS. (A) N-terminal fragment ions showing approximate 42.010 Da mass increase compared to the calculated masses for the corresponding un-modified fragment ions, indicating N-terminal acetylation of MLC-3F. (B) Representative fragment ions resulting from fragmentation

of MLC-3F by ECD. (C) Fragmentation map for MLC-3F showing bond cleavages. "*Ac*-" denotes N^{α}-acetylation of Ala2 (numbering scheme includes N-terminal Met, which is removed in the mature protein). Circles represent the theoretical isotopic abundance distribution corresponding to the assigned mass and based on averagine.

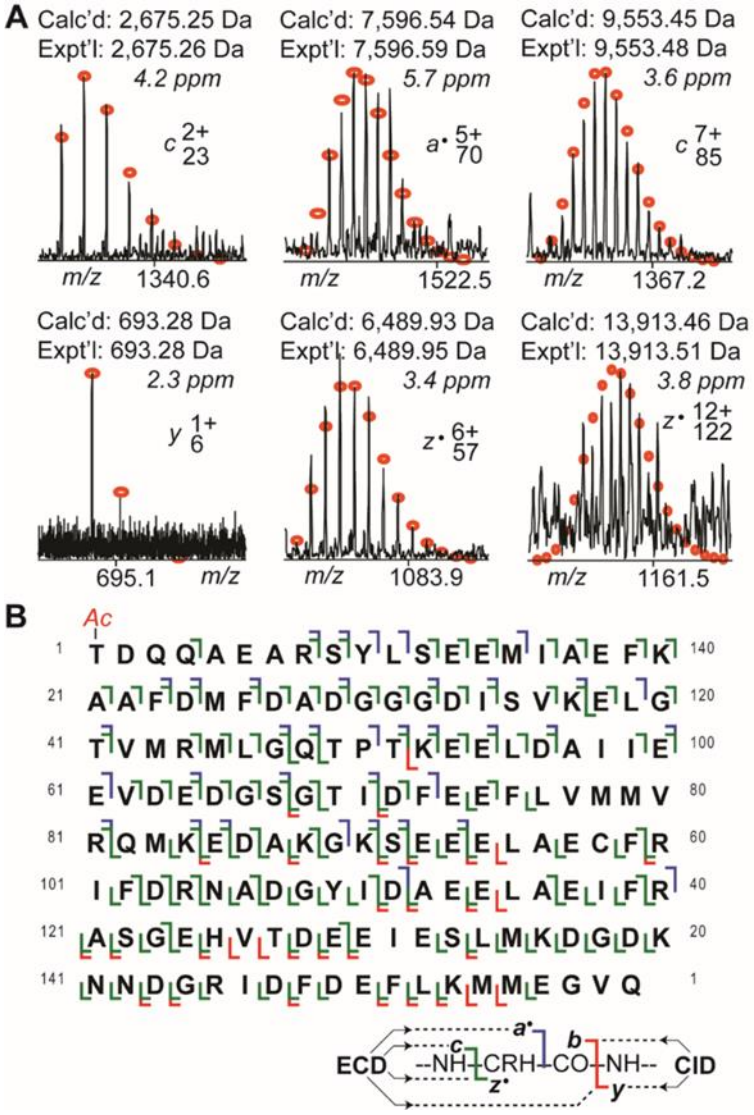

Fig. 7.13. Sequence characterization of *fs*TnC by high-resolution MS/MS. (A) Representative fragment ions resulting from fragmentation of *fs*TnC by ECD. (B) Fragmentation map for *fs*TnC showing bond cleavages. "*Ac*-" denotes acetylation of Thr2 (numbering scheme includes N-terminal Met, which is removed in the mature protein). Circles represent the theoretical isotopic abundance distribution corresponding to the assigned mass and based on averagine.

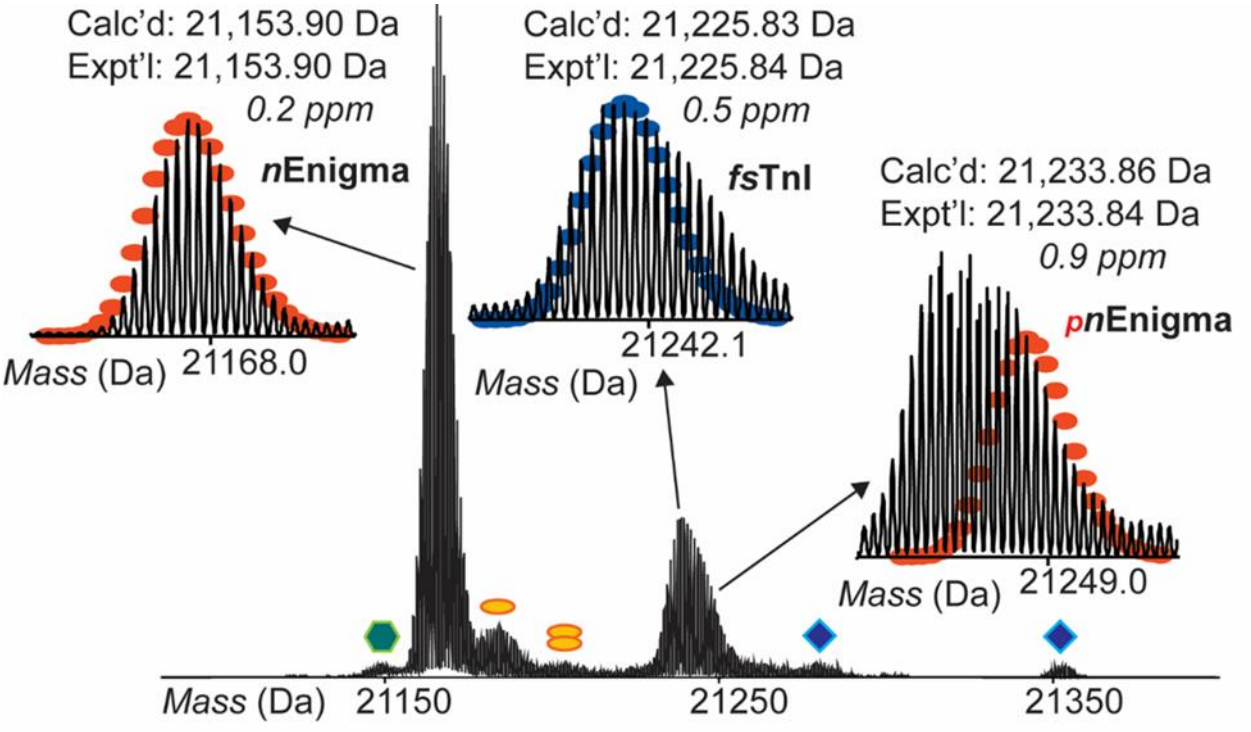

Fig. 7.14. Zoomed-in deconvoluted mass spectrum showing protein present in sarcomeric protein-enriched extracts prepared from rat GAS muscles, which was identified as a novel isoform of the PDZ/LIM domain protein Enigma (*n*Enigma). Hexagon, single oval, double oval, and diamond represent *n*Enigma with NH_3 loss, *n*Enigma with a single oxidized amino acid residue, *n*Enigma with two oxidized amino acid residues, and *n*Enigma proteoforms associated non-covalently with TFA. Peak denoted "$_p$*n*Enigma" likely represents a mono-phosphorylated proteoform of *n*Enigma that overlaps with *fs*TnI. Circles represent the theoretical isotopic abundance distribution corresponding to the assigned mass and based on averagine.

All proteins / tr|A0A091DPK3|A0A091DPK3_FUKDA PDZ and LIM domain protein 7 OS=Fukomys damarensis GN=H920_04400 PE=4 SV=1 / Peptide #1

Protein-Spectrum-Match for Spectrum #0

PrSM ID:	0	Scan(s):	1	Precursor charge:	26	Precursor m/z:	814.58
Precursor mass:	21152.878	Adjusted precursor mass:	21152.878	Duplicate score:	98	Unique score:	72
E-value:	2.6E-36	P-value:	4.9E-43	Spectral FDR:	n/a	Protein mass:	24481.623

N-Terminal Acetylation
A modification (or multiple modifications) on internal residue

42.01
M D S F K V V L|E|G P|A P|W|G|F|R|L|Q G|G|K|D|F|N|V P|L|S I S|R|L|T P|G|G|K|A|A|
Q|A|G|V|A V G|D|W|L L S I D G E N A|G S L T H I|E A Q N K I R A C G E R L S L G
L S R S Q P V Q S K P Q K A L A P A A D P P R Y T F A P S A S L N K T A R P F G
A P|L H A D S A P Q Q N G Q P L R P L V P D A S K Q R L M E N T E D W R P|R P G
T G Q S|R|S F|R I L A H|L T G T|E F M|Q|D P|D|E|E|H L K K S|R|E|K|Y|V|L|E|L|Q S
P|R Y|T|R|L|R|D|W|H H|Q|R|S|A|H V L N V Q S

-3398.80
28.04

Fig. 7.15. MS-Align+ output for novel Enigma (*n*Enigma) isoform found in sarcomeric protein-enriched extracts prepared from the fast-twitch GAS muscles of aging F344BN rats. The full list of identified proteins in GAS muscles are shown in **Table 7.1**. The peak numbers representing different fractions collected are shown in **Fig. 7.6**. Peak numbered 6 in sarcomeric protein-enriched extracts from rat GAS muscles was identified as a novel isoform of the PDZ/LIM protein Enigma, with acetylation of the N-terminal Met, a -3,398.80 Da mass discrepancy near the middle of the protein, and a +28.04 Da mass difference in the C-terminal third of the protein.

Table 7.2. Enigma isoforms listed in the UniProtKB/Swiss-Prot database, as well as novel isoform identified in this study.

Accession #	Species	Isoform	Exons	Calc'd M_r (Da)
Q9Z1Z9	*R. norvegicus* (rat)	1	1-5, 7-8, 10-15	49,922.64
Q9NR12	*H. sapiens* (human)	1	1-5, 7-8, 10-15	49,854.61
Q9NR12-2	*H. sapiens*	2	1-4, 6-8, 10-15	46,521.98
Q9NR12-3	*H. sapiens*	3	1-7	16,066.15
Q9NR12-4	*H. sapiens*	4	1-5, 7-8, 11-12	30,434.31
Q9NR12-5	*H. sapiens*	5	1-5, 7-8	20,543.50
Q9NR12-6	*H. sapiens*	6	1-5, 7-9	24,439.56
	R. norvegicus	Novel	1-4, 6-9	21,153.90

Accession numbers correspond to UniProtKB/Swiss-Prot database accession numbers. Novel isoform of Enigma is designated *n*Enigma herein. Calc'd M_r, calculated relative mono-isotopic molecular mass including N^{α}-acetylation of the N-terminal Met residue.

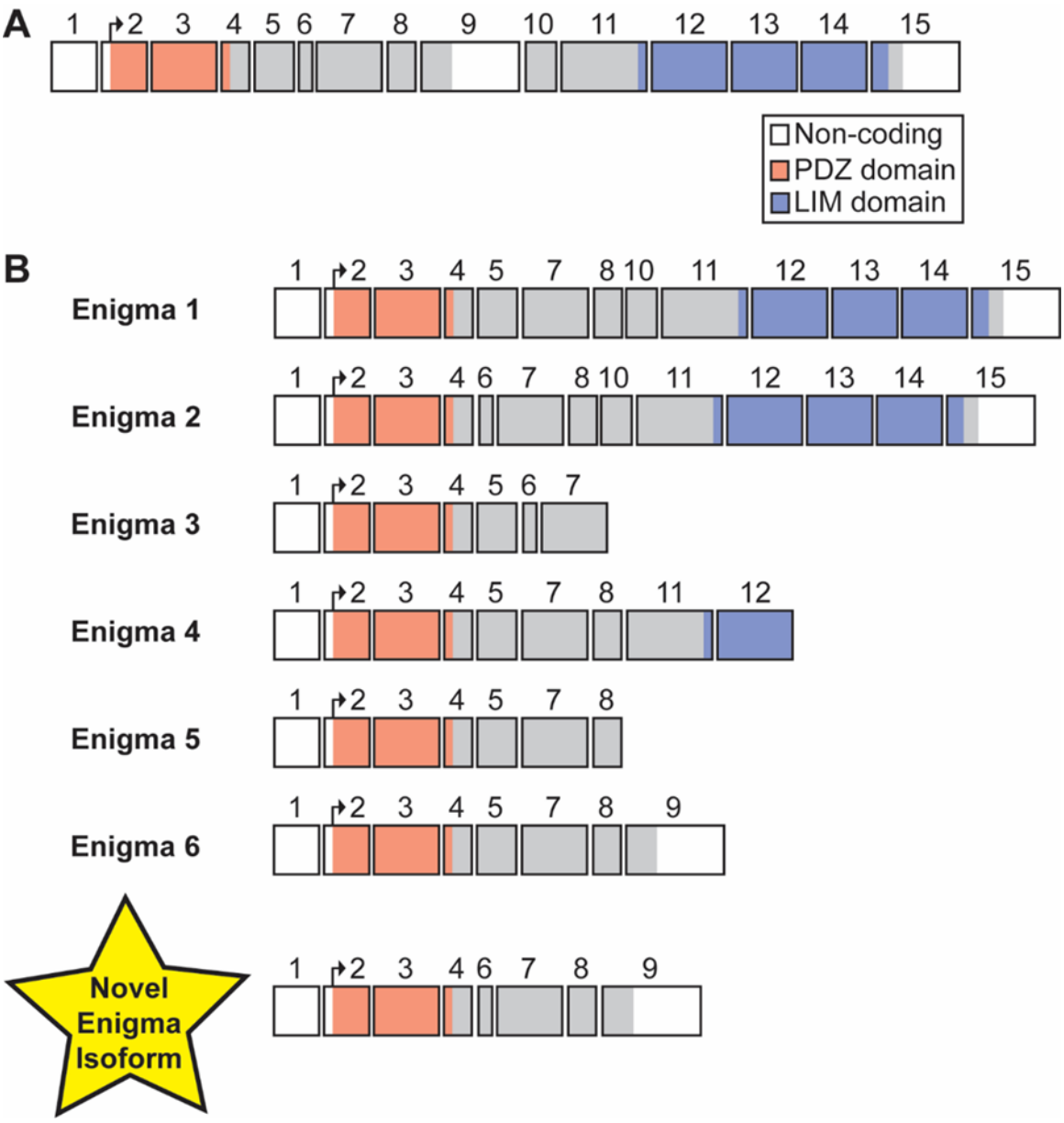

Fig. 7.16. Exon structure of *PDLIM7* gene and Enigma protein isoforms. (A) The exon structure of the Enigma gene (*PDLIM7*), which is comprised of 15 exons (14 of which are coding exons). Regions of each exon corresponding to protein coding sequence are colored and the portions encoding the PDZ and LIM domains are indicated. (B) The exon structure of human Enigma splice isoforms (Enigma 1-Enigma 6) from the UniProtKB/Swiss-Prot database are shown. The exon structure of the novel Engima (*n*Enigma) isoform identified in the GAS muscles

of F344BN rats herein is shown at the bottom of the panel. This isoform is comprised of exons 1 (non-coding), 2-4, and 6-9.

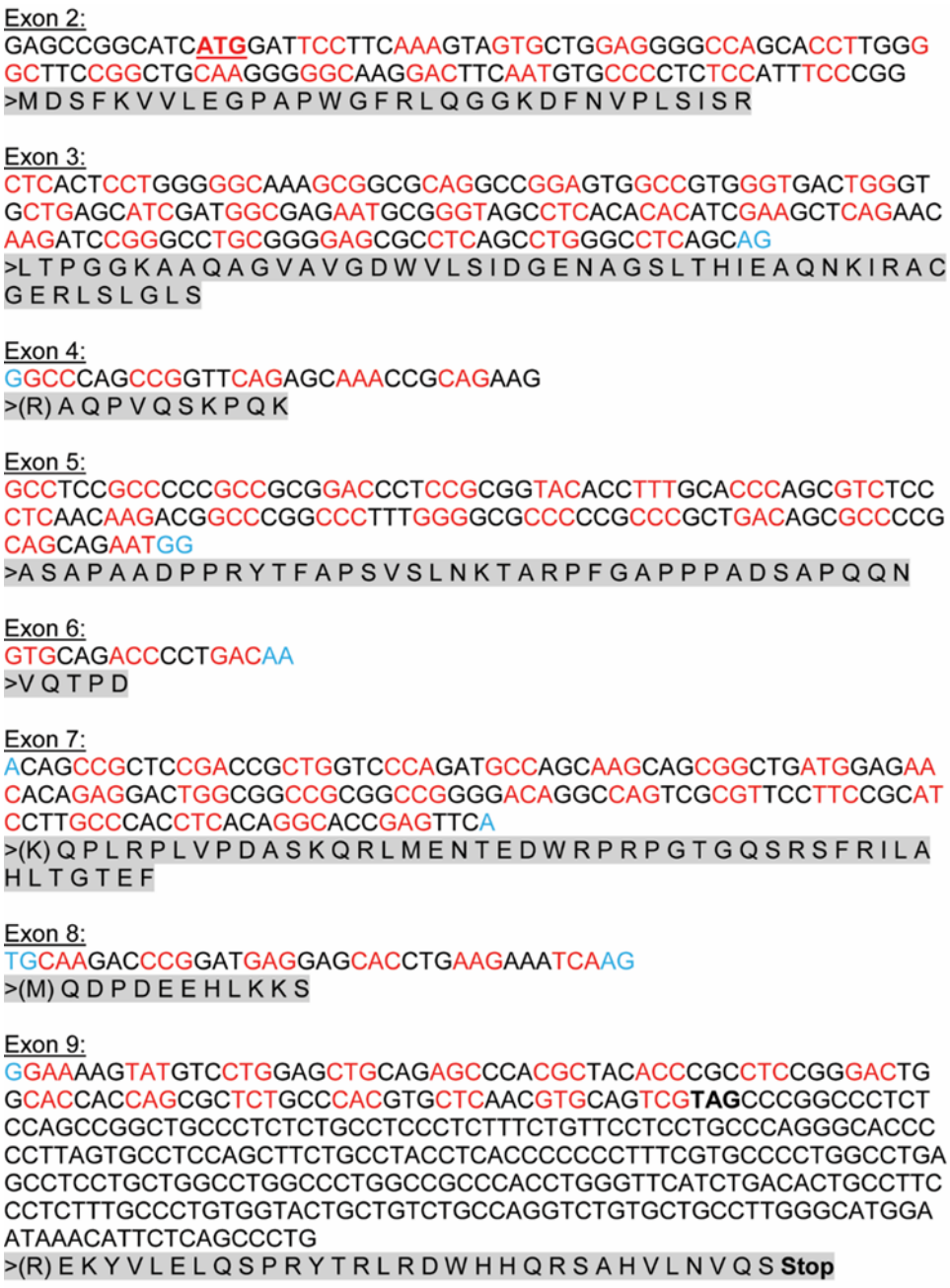

Fig. 7.17. Nucleic and corresponding amino acid sequences of coding exons 2-9 of the human *PDLIM7* gene. The nucleic acid sequences for each coding exon is shown with individual amino acid codons denoted in black or red. The codon encoding the initiating Met residue is bolded and underlined. Nucleic acids demarcated in blue are part of codons formed at exon boundaries. The

amino acid sequence for each exon follows the nucleic acid sequence, and is highlighted in grey. Amino acids denoted in parentheses are formed from codons formed at exon boundaries.

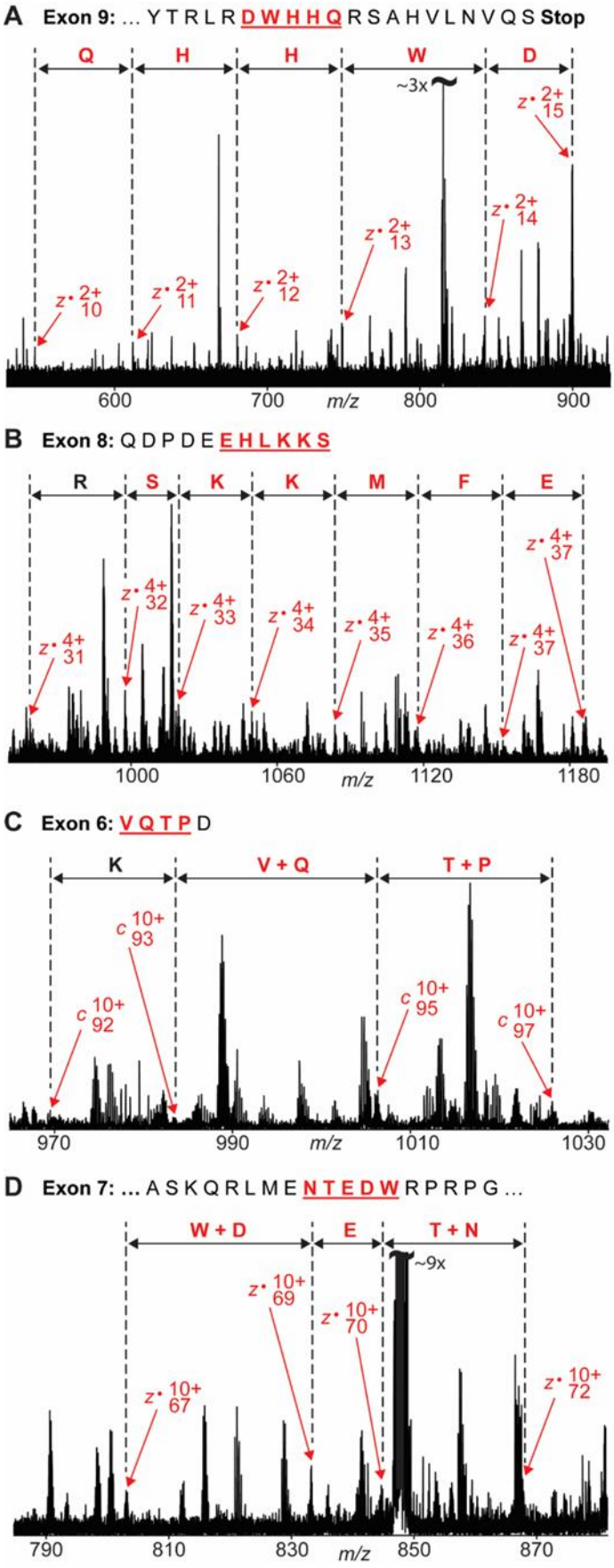
A Exon 9: ... Y T R L R D W H H Q R S A H V L N V Q S Stop
Q
H
H
W
D
~3x
z• 2+ 10
z• 2+ 11
z• 2+ 12
z• 2+ 13
z• 2+ 14
z• 2+ 15
600
700
m/z
800
900
B Exon 8: Q D P D E E H L K K S
R
S
K
K
M
F
E
z• 4+ 31
z• 4+ 32
z• 4+ 33
z• 4+ 34
z• 4+ 35
z• 4+ 36
z• 4+ 37
z• 4+ 37
1000
1060
m/z
1120
1180
C Exon 6: V Q T P D
K
V + Q
T + P
c 10+ 92
c 10+ 93
c 10+ 95
c 10+ 97
970
990
m/z
1010
1030
D Exon 7: ... A S K Q R L M E N T E D W R P R P G ...
W + D
E
T + N
~9x
z• 10+ 67
z• 10+ 69
z• 10+ 70
z• 10+ 72
790
810
830
m/z
850
870

Fig. 7.18. Exon structure of novel Enigma isoform identified in rat fast-twitch GAS skeletal muscles. (A) Zoomed-in tandem mass spectrum with labeled $z^{\cdot}$ ions and corresponding amino acid sequence. The derived amino acid sequence maps to a portion of exon 9 from the human *PDLIM7* gene. (B) Zoomed-in tandem mass spectrum with labeled $z^{\cdot}$ ions and corresponding amino acid sequence. The derived amino acid sequence maps to exon 8 from the human *PDLIM7* gene with two amino acid differences. (C) Zoomed-in tandem mass spectrum with labeled *c* ions and corresponding amino acid sequence. The derived amino acid sequence maps to exon 6 from the human *PDLIM7* gene. (D) Zoomed-in tandem mass spectrum with labeled $z^{\cdot}$ ions and corresponding amino acid sequence. The derived amino acid sequence corresponds to an amino acid segment mapping to exon 7 of the human *PDLIM7* gene.

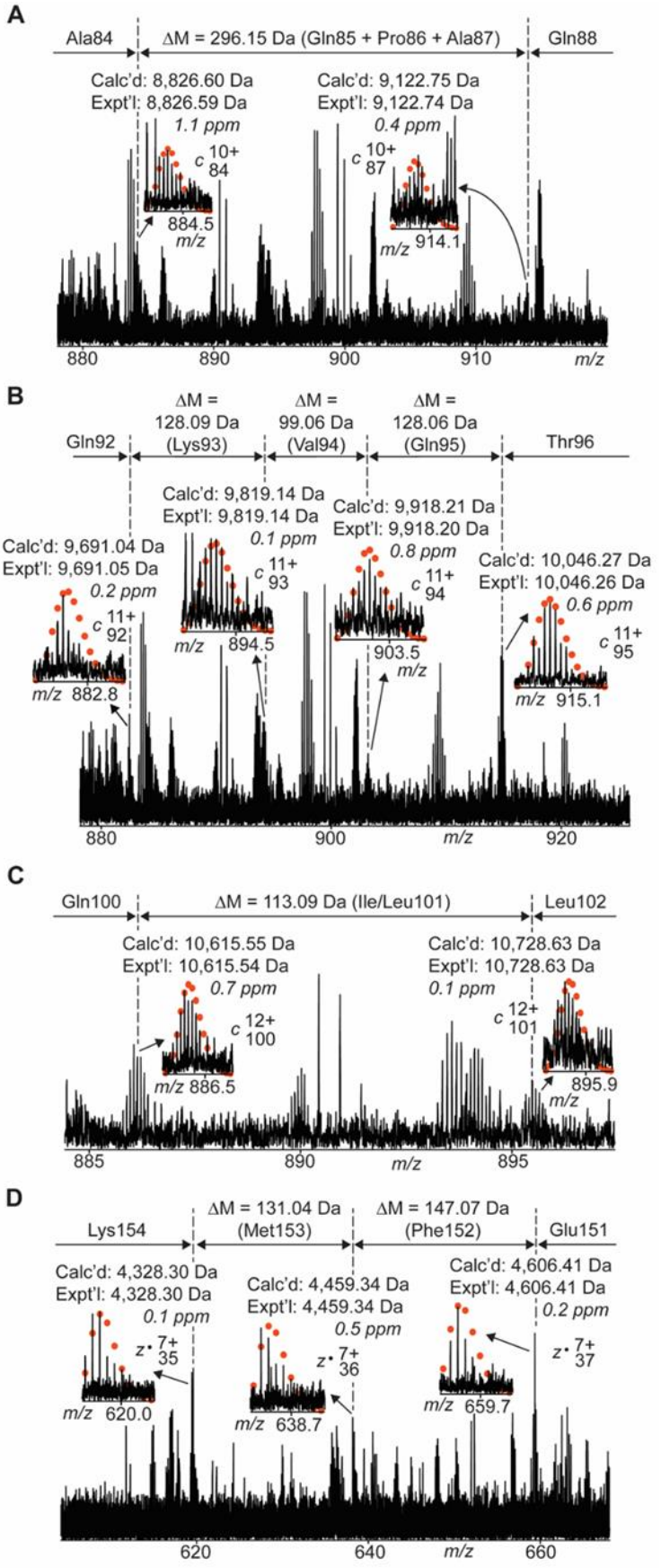
A
Ala84
ΔM = 296.15 Da (Gln85 + Pro86 + Ala87)
Gln88
Calc'd: 8,826.60 Da
Expt'l: 8,826.59 Da
1.1 ppm
c 10+ 84
884.5 m/z
Calc'd: 9,122.75 Da
Expt'l: 9,122.74 Da
0.4 ppm
c 10+ 87
914.1 m/z
880
890
900
910
m/z
B
Gln92
ΔM = 128.09 Da (Lys93)
ΔM = 99.06 Da (Val94)
ΔM = 128.06 Da (Gln95)
Thr96
Calc'd: 9,691.04 Da
Expt'l: 9,691.05 Da
0.2 ppm
c 11+ 92
882.8 m/z
Calc'd: 9,819.14 Da
Expt'l: 9,819.14 Da
0.1 ppm
c 11+ 93
894.5 m/z
Calc'd: 9,918.21 Da
Expt'l: 9,918.20 Da
0.8 ppm
c 11+ 94
903.5 m/z
Calc'd: 10,046.27 Da
Expt'l: 10,046.26 Da
0.6 ppm
c 11+ 95
915.1 m/z
880
900
m/z
920
C
Gln100
ΔM = 113.09 Da (Ile/Leu101)
Leu102
Calc'd: 10,615.55 Da
Expt'l: 10,615.54 Da
0.7 ppm
c 12+ 100
886.5 m/z
Calc'd: 10,728.63 Da
Expt'l: 10,728.63 Da
0.1 ppm
c 12+ 101
895.9 m/z
885
890
m/z
895
D
Lys154
ΔM = 131.04 Da (Met153)
ΔM = 147.07 Da (Phe152)
Glu151
Calc'd: 4,328.30 Da
Expt'l: 4,328.30 Da
0.1 ppm
z• 7+ 35
620.0 m/z
Calc'd: 4,459.34 Da
Expt'l: 4,459.34 Da
0.5 ppm
z• 7+ 36
638.7 m/z
Calc'd: 4,606.41 Da
Expt'l: 4,606.41 Da
0.2 ppm
z• 7+ 37
659.7 m/z
620
640
m/z
660

Fig. 7.19. Sequence characterization of *n*Enigma in rat. (A) Zoomed-in tandem mass spectrum showing 296.15 Da mass difference between c_{84} and the next observed *c* ion (c_{87}) ions. This mass difference corresponds well with the presence of Gln, Pro, and Ala residues. (B) Zoomed-in tandem mass spectrum showing 128.09 Da, 99.06 Da, and 128.06 Da mass differences between c_{92} and c_{93} (128.09 Da), c_{93} and c_{94} (99.06 Da), and c_{94} and c_{95} (128.06 Da). (C) Zoomed-in tandem mass spectrum showing 113.09 Da mass difference between c_{100} and c_{101}, which denotes the presence of an Ile/Leu residue in position 101 of the novel rat Enigma isoform. (D) Zoomed-in tandem mass spectrum showing 131.04 Da and 147.07 Da mass differences between $z^{\cdot}_{35}$ and $z^{\cdot}_{36}$ and $z^{\cdot}_{36}$ and $z^{\cdot}_{37}$, respectively. These mass differences indicate the presence of Met and Phe residues in positions 153 and 152, respectively, of rat *n*Enigma.

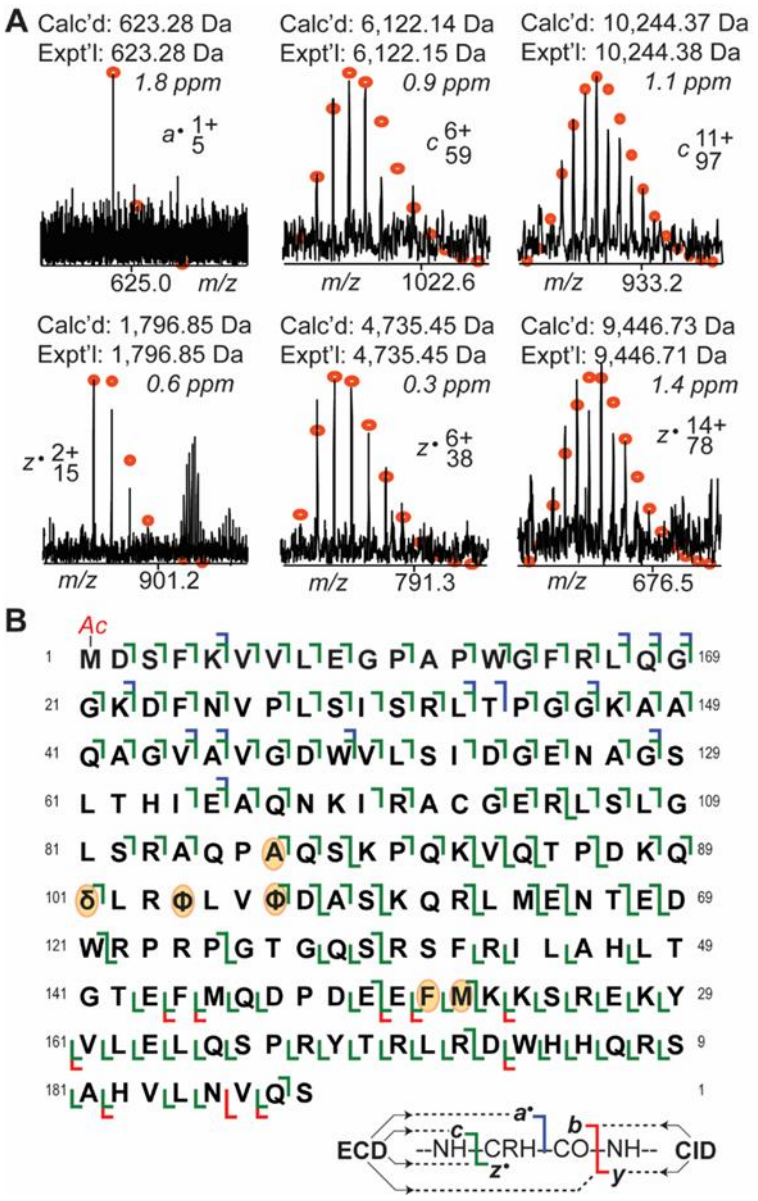

Fig. 7.20. Sequence characterization of novel isoform of Enigma (*n*Enigma) in rat by high-resolution MS/MS. (A) Representative fragment ions resulting from fragmentation of novel Enigma isoform by ECD. (B) Fragmentation map for *n*Enigma showing bond cleavages. Residues differing between rat and human confirmed in this study are highlighted (ovals). The residue marked with "δ" is either an Ile or Leu residue. One of the residues denoted "Φ" is a Gln residue and the other is a Pro residue, although the positioning of these residues could not be determined.

"*Ac*-" denotes acetylation of Met1. Circles represent the theoretical isotopic abundance distribution corresponding to the assigned mass and based on averagine.

Table 7.3. Identification of proteins in sarcomeric proteome-enriched extract prepared from the slow-twitch SOL muscles of rats in different age groups.

Peak #	RT (min)	Expt'l M_r (Da)	Calc'd M_r (Da)	Error (ppm)	Protein ID	Accession #
1	~28.5	9025.78	9025.77	0.4	SMPX	Q925F0
2	~30.6	9971.81	?		COX6B1	D3ZD09
3	**~31.5**	**31107.10**	**31107.07**	**0.96**	***ss*TnT1**	**Q7TNB2**
4	**~31.8**	**21553.53**	**21553.49**	**1.85**	***ss*TnI**	**A0A096MIZ5**
5	~32.5	23667.42	23667.11	13.0	MXD3	G3V831
6	**~33.7**	**30879.78**	**30879.76**	**0.64**	**Cypher4s***	**Q5XIG1**
7	**~34.0**	**31319.04**	**31319.00**	**1.27**	**Cypher2s**	**A0A0G2JXR0**
8	~35.0	8318.40	8318.41	1.20	COX6C2	P11951
9	~36.0	14676.53	14676.54	0.68	FABP3	P07483
10	~36.9	13977.87	13977.85	1.3	Histone H2A.2	P0CC09
11	~37.2	13766.52	13766.51	0.72	Histone H2B	G3V8B3
12	**~38.2**	**32858.58**	**32858.56**	**0.61**	**βTpm**	**P58775**
13	**~39.0**	**22053.10**	**22053.06**	**1.81**	**MLC-1V**	**P16409**
14	~40.0	17014.93	17014.93	0.3	Myoglobin	Q9QZ76
15	**~40.5**	**22689.75**	**22689.67**	**3.50**	**MLC-1S**	**D3ZHA7**
16	**~42.0**	**18779.42**	**18779.36**	**3.19**	**MLC-2S**	**P08733**
17	**~44.5**	**41845.86**	**41845.83**	**0.72**	**Actin**	**P68136**
18	**~47.0**	**18450.51**	**18450.50**	**0.54**	***ss*TnC**	**Q4PP99**

Accession numbers correspond to UniProtKB/Swiss-Prot database accession numbers. Known sarcomeric proteins are bolded. Abbreviations are as follows: RT, retention time; Expt'l M_r, experimentally determined relative molecular mass; Calc'd M_r, calculated relative molecular mass; SMPX, small muscular protein; COX6B1, cytochrome *c* oxidase subunit 6B-1; *ss*TnT1, slow skeletal troponin T isoform 1; *ss*TnI, slow skeletal troponin I; MXD3, max dimerization protein 3; Cypher4s, isoform of Cypher previously observed only at the transcript level; Cypher2s, Cypher isoform 2s; *n*Enigma, novel isoform of Enigma; COX6C2, cytochrome *c* oxidase subunit 6C-2; MLC-1V, ventricular myosin light chain 1; MLC-1S, slow skeletal specific myosin light chain 1; MLC-2S, slow skeletal myosin light chain 2; *ss*TnC, slow skeletal troponin C. All reported relative molecular masses correspond to the mono-isotopic molecular masses. *A previously undesignated isoform of Cypher that we have designated, here, Cypher4s.

A All proteins / sp|Q7TNB2|TNNT1_RAT Troponin T, slow skeletal muscle OS=Rattus norvegicus GN=Tnnt1 PE=1 SV=3 / Peptide #1

Protein-Spectrum-Match for Spectrum #0

PrSM ID:	0	Scan(s):	1	Precursor charge:	42	Precursor m/z:	743.533
Precursor mass:	31186.1	Adjusted precursor mass:	31186.1	Duplicate score:	81	Unique score:	61
E-value:	6E-21	P-value:	4E-21	Spectral FDR:	n/a	Protein mass:	31196.101

A modification (or multiple modifications) on internal residue
No N-terminal modification(non-canonical)

M S D T E E Q E Y E E E Q A E D E E A V E E E A P E E P E P V A E R E E E R P K
P|S R P V V P|P[-10.00] L I P P|K I P|E G|E|R V D|F|D|D I|H|R|K|R|M E K|D|L|L E L Q|T L
I D V H|F|E|Q|R K K E E|E E L I A|L K|D R I E R R R A E R A E Q Q R F R|T E K E
R E R Q A K L A E E K M R K E E E|E|A K K R A E D D A K K K K V L S N M G A H F
G G Y L V K A E Q K R G K R|Q T G R E|M|K L R I L S E R K K P L|N I D Y M G|E D
Q L R E K|A Q E L S E W I H|Q L|E S|E|K F|D|L|M E|K L K|Q|Q K Y|E|I|N|V L Y|N R
I|S H|A|Q|K|F|R|K|G A|G|K G|R V G|G R W K

B All proteins / tr|A0A096MIZ5|A0A096MIZ5_RAT Troponin I, slow skeletal muscle OS=Rattus norvegicus GN=Tnni1 PE=1 SV=1 / Peptide #1

Protein-Spectrum-Match for Spectrum #0

PrSM ID:	0	Scan(s):	1	Precursor charge:	28	Precursor m/z:	770.777
Precursor mass:	21553.56	Adjusted precursor mass:	21553.491	Duplicate score:	222	Unique score:	129
E-value:	1.4E-45	P-value:	1.4E-45	Spectral FDR:	n/a	Protein mass:	21684.531

N-Terminal Methionine Excision(canonical)

M]P E V E R K|S K|I|T|A|S|R|K|L|M|L|K|S|L|M|L|A|K|A|K|E C|W|E|Q E|H|E|E|R|E A|E|
K V R|Y|L|S E|R|I P T|L|Q|T|R|G|L S L|S|A L Q|D L C R|E|L H|A K V|E V V|D|E|E|R
Y|D|I E A K|C L H N T|R|E I|K|D|L|K|L K V|L|D|L R|G|K|F K R P P L|R R|V|R|V|S|A
D|A M|L|R A L|L|G|S|K|H|K V S|M D|L|R A|N|L|K|S|V K K E|D|T|E|K|E|R P V|E|V|G|D
W|R K N V|E|A|M|S G|M|E|G|R|K|K|M F D|A A K S P T S Q

C All proteins / sp|P16409|MYL3_RAT Myosin light chain 3 OS=Rattus norvegicus GN=Myl3 PE=1 SV=2 / Peptide #1

Protein-Spectrum-Match for Spectrum #0

PrSM ID:	0	Scan(s):	1	Precursor charge:	25	Precursor m/z:	883.135
Precursor mass:	22053.2	Adjusted precursor mass:	22053.057	Duplicate score:	232	Unique score:	142
E-value:	1.4E-45	P-value:	7E-46	Spectral FDR:	n/a	Protein mass:	22142.087

N-Terminal Methionine Excision(canonical) and N-Terminal Acetylation

M]A[42.01] P K K P E P K K D D A K T|A A P K A|A P|A P|A|A|A P|A|A|A P|E P|E|R P K|E|A|
E|F|D|A|S|K|I|K|I|E|F|T P|E|Q|I|E|E|F|K|E|A|F|Q|L|F|D|R|T P K|G|E|M|K|I|T|Y G Q
C G|D V|L|R A L G Q|N P T|Q|A|E V L R|V|L G|K P|K|Q|E|E|L|N|S|K M|M|D F E T F L
P M L|Q|H I|S|K|N|K|D T G|T|Y|E|D F|V|E|G|L|R|V|F|D K|E|G|N|G T|V|M|G|A E|L R|H
V L A|T L G|E R|L T|E|D E V E|K|L M|A G|Q E D S N G C I N Y E|A F|V|K H I M A|S

D

All proteins / tr|D3ZHA7|D3ZHA7_RAT Protein Myl6b OS=Rattus norvegicus GN=Myl6b PE=4 SV=1 / Peptide #1

Protein-Spectrum-Match for Spectrum #0

PrSM ID:	0	Scan(s):	1	Precursor charge:	27	Precursor m/z:	841.368
Precursor mass:	22689.75	Adjusted precursor mass:	22689.715	Duplicate score:	268	Unique score:	153
E-value:	1.4E-45	P-value:	1.3E-45	Spectral FDR:	n/a	Protein mass:	22792.72

A modification (or multiple modifications) on internal residue
Unusual N-terminal modification

M]28.04P P K|K D|A P|V|K|K P|A|G P|S|I|S|K P|A|A|K|S|T|A|G|T P|L|A|K|T|K|A|E P A|A P|
Q|T P V|K|T Q|E P P|V|D|L|S|K V V|I|E|F|N|K|D|Q|L|E|E|F|R|E A|F|E|L F|D|R V G|D
G|K|I|L Y|S Q C G|D L|M|R A L G Q|N P T|N|A|E V L|K|V|L|G|N P K S|D|E|L|K|S|R|R|
V|D|F|E T F|L P M L Q|A|V|A K|H|R|D|Q|G|T Y E|D Y|L|E|G L|R|V|F|D|K|E|G|N|G K V|
M|G|A|E L R H V L T T L G|E|K M T E E E V E T V L A G H E|D S N G C I N|Y E A F
L K H I L S L

E

All proteins / sp|P08733|MLRV_RAT Myosin regulatory light chain 2, ventricular/cardiac muscle isoform OS=Rattus norvegicus GN=Myl2 PE=1 SV=2 / Peptide #1

Protein-Spectrum-Match for Spectrum #0

PrSM ID:	0	Scan(s):	1	Precursor charge:	19	Precursor m/z:	989.407
Precursor mass:	18779.59	Adjusted precursor mass:	18779.4	Duplicate score:	102	Unique score:	76
E-value:	1E-41	P-value:	1.2E-41	Spectral FDR:	n/a	Protein mass:	18868.388

A modification (or multiple modifications) on internal residue
Unusual N-terminal modification

M]42.05S P K K A K|K|R|L|E|G G S S|N|V|F|S|M|F|E Q T|Q I Q|E F K|E|A F|T I M D|Q N|R
D|G|F I|D K|N|D L R|D|T F A A|L G R V|N V K N|E E I D E|M I|K|E A P G P I N F T
V F L T M F G|E K L K G A|D P E E|T I L|N A F K|V|F|D P E|G K|G|S|L|K A|D|Y V|R|
E|M L T|T|Q|A|E|R|F S|K|E|E|I|D|Q M|F A A|F P P D|V|T|G|N|L|D|Y|K|N|L V|H|I I T
H G E E K D

F

All proteins / tr|Q4PP99|Q4PP99_RAT Cardiac troponin C OS=Rattus norvegicus GN=Tnnc1 PE=1 SV=1 / Peptide #1

Protein-Spectrum-Match for Spectrum #0

PrSM ID:	0	Scan(s):	1	Precursor charge:	18	Precursor m/z:	1026.044
Precursor mass:	18450.66	Adjusted precursor mass:	18450.506	Duplicate score:	202	Unique score:	135
E-value:	1.4E-45	P-value:	1.4E-45	Spectral FDR:	n/a	Protein mass:	18408.495

N-Terminal Acetylation

42.01M D D I Y K|A|A V|E Q L T|E|E|Q|K|N|E|F|K|A|A|F|D|I|F|V|L G A E|D|G C|I|S T K|E|
L|G|K|V M|R|M|L|G|Q|N P|T P|E|E|L Q E|M I|D|E|V|D|E|D G|S|G|T V|D|F|D|E|F|L|V|M
M V R C M|K|D|D|S|K|G|K|S|E|E|E L|S|D|L F|R|M|F|D|K|N|A D|G|Y|I|D L|D|E L|K|M M|
L|Q|A T|G E|T I T E|D|D I E|E L M K|D|G|D|K|N|N|D G|R I D Y D E F|L|E|F M K G V
E

Fig. 7.21. Identification of contractile proteins in sarcomeric-protein enriched extracts prepared from rat SOL muscles by high-resolution MS/MS. The peak numbers representing different fractions collected are shown in **Fig. 7.6B**. The protein identifications are shown. The full list of identified proteins in SOL muscles is shown in **Table 7.3**. (A) Peak #3 was identified as slow skeletal troponin T isoform (*ss*TnT), with a -10.00 Da mass discrepancy in the N-terminal

half of the protein, suggesting a sequence difference or modification. (B) Peak #4 was identified as slow skeletal troponin I (*ss*TnI), with removal of the N-terminal Met. (C) Peak #13 was identified as the ventricular isoform of the myosin essential light chain (MLC-1V), with removal of the N-terminal Met and modification of Ala1. (D) Peak #15 was identified as slow skeletal myosin light chain 1 (MLC-1S), with removal of Met1 and an N-terminal modification. (E) Peak #16 was identified as slow skeletal muscle myosin light chain 2 (MLC-2S), with N-terminal Met removal and an N-terminal modification. (F) Peak #18 was identified as slow skeletal troponin C (*ss*TnC), with an N-terminal modification. The E-value of a Protein-Spectrum-Match (PrSM) refers to the number of hits one can "expect" to see by chance when searching the spectrum against a protein database with the same size as the database that was searched. The P-value of a PrSM represents the probability that the match between the input MS/MS spectrum and a random protein in the database has a similarity score no less than the score of the PrSM.

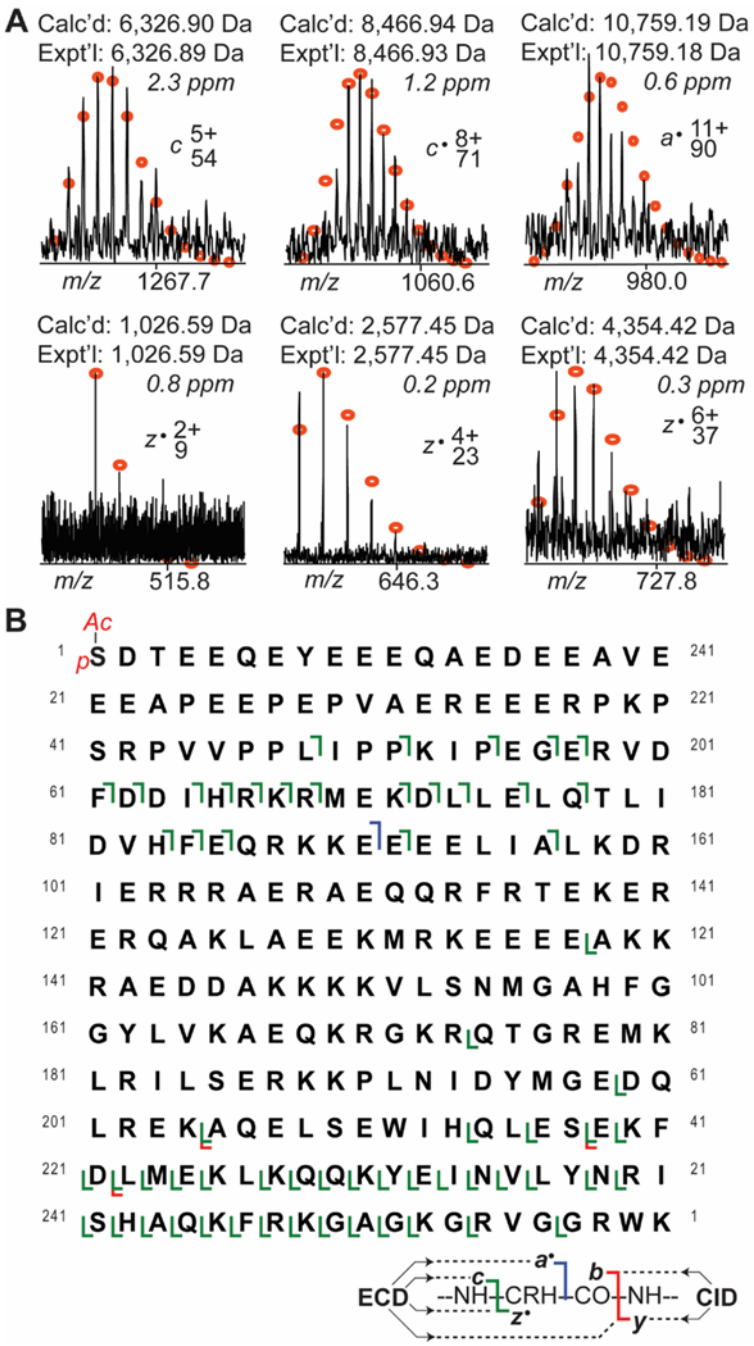

Fig. 7.22. Sequence characterization of *ss*TnT isoform 1 (*ss*TnT1) by high-resolution MS/MS. (A) Representative fragment ions resulting from fragmentation of *ss*TnT1 by ECD. (B) Fragmentation map for *ss*TnT1 showing bond cleavages. "*Ac*-" and "*p*" denote acetylation and phosphorylation, respectively, of Ser2 (numbering scheme includes N-terminal Met, which is

removed in the mature protein). Circles represent the theoretical isotopic abundance distribution corresponding to the assigned mass and based on averagine.

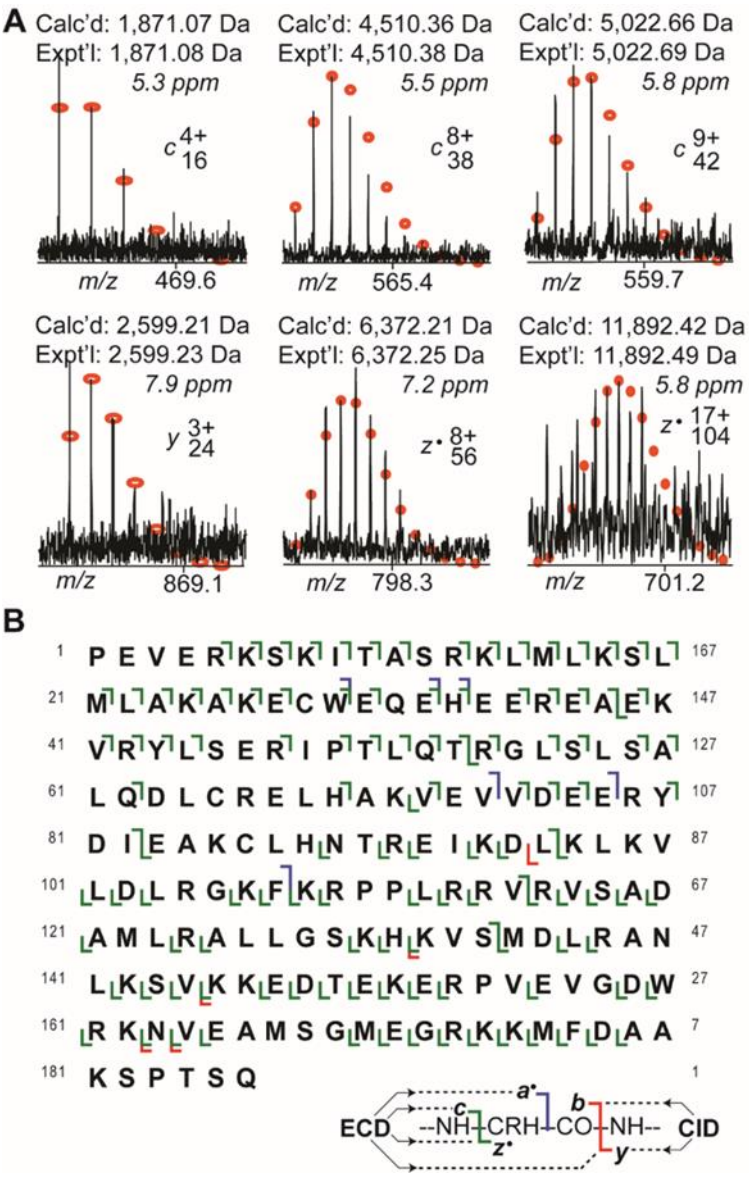

Fig. 7.23. Sequence characterization of *ss*TnI by high-resolution MS/MS. (A) Representative fragment ions resulting from fragmentation of *ss*TnI by ECD. (B) Fragmentation map for *ss*TnI showing bond cleavages. Circles represent the theoretical isotopic abundance distribution corresponding to the assigned mass and based on averagine.

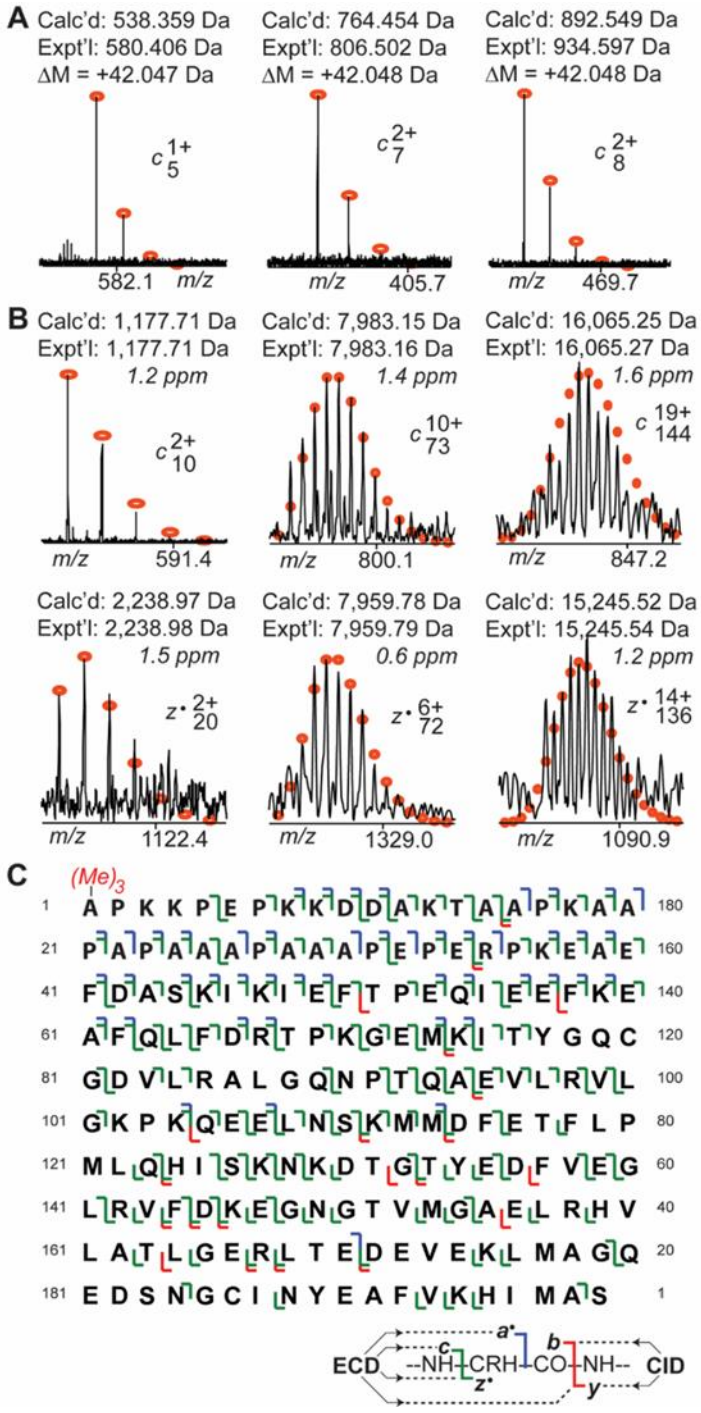

Fig. 7.24. Sequencing and N-terminal modification characterization for MLC-1V by high-resolution MS/MS. (A) N-terminal fragment ions showing approximate 42.046 Da mass increase compared to the calculated masses for the corresponding un-modified fragment ions, indicating N-terminal tri-methylation of MLC-1V. (B) Representative fragment ions resulting from

fragmentation of MLC-1V by ECD. (C) Fragmentation map for MLC-1V showing bond cleavages. "*(Me)*$_3$-" denotes N$^{\alpha}$-tri-methylation of Ala2 (numbering scheme includes N-terminal Met, which is removed in the mature protein). Circles represent the theoretical isotopic abundance distribution corresponding to the assigned mass and based on averagine.

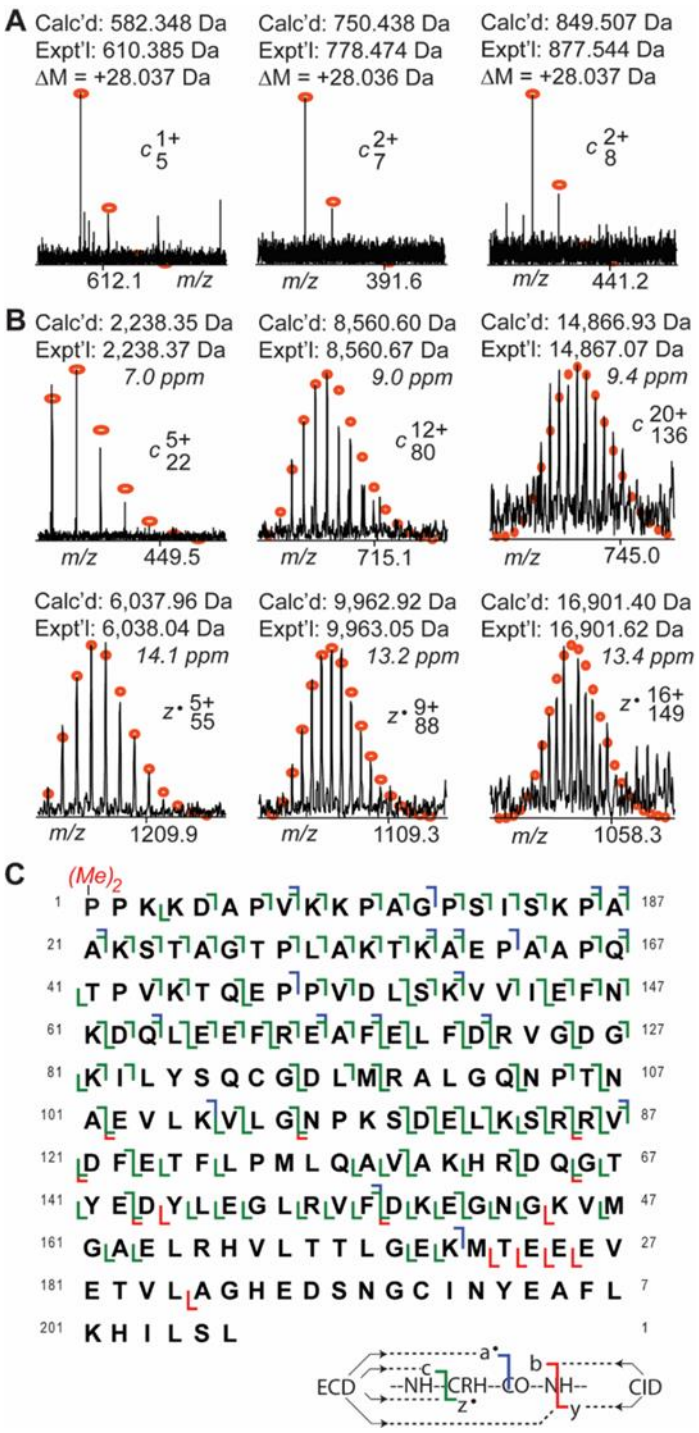

Fig. 7.25. Sequencing and N-terminal modification characterization for MLC-1S by high-resolution MS/MS. (A) N-terminal fragment ions showing approximate 28.031 Da mass increase compared to the calculated masses for the corresponding un-modified fragment ions, indicating N-terminal di-methylation of MLC-1S. (B) Representative fragment ions resulting from

fragmentation of MLC-1S by ECD. (C) Fragmentation map for MLC-1S showing bond cleavages. "*(Me)*$_2$-" denotes N^{α}-di-methylation of Pro2 (numbering scheme includes N-terminal Met removed in the mature protein). Circles represent the theoretical isotopic abundance distribution corresponding to the assigned mass and based on averagine.

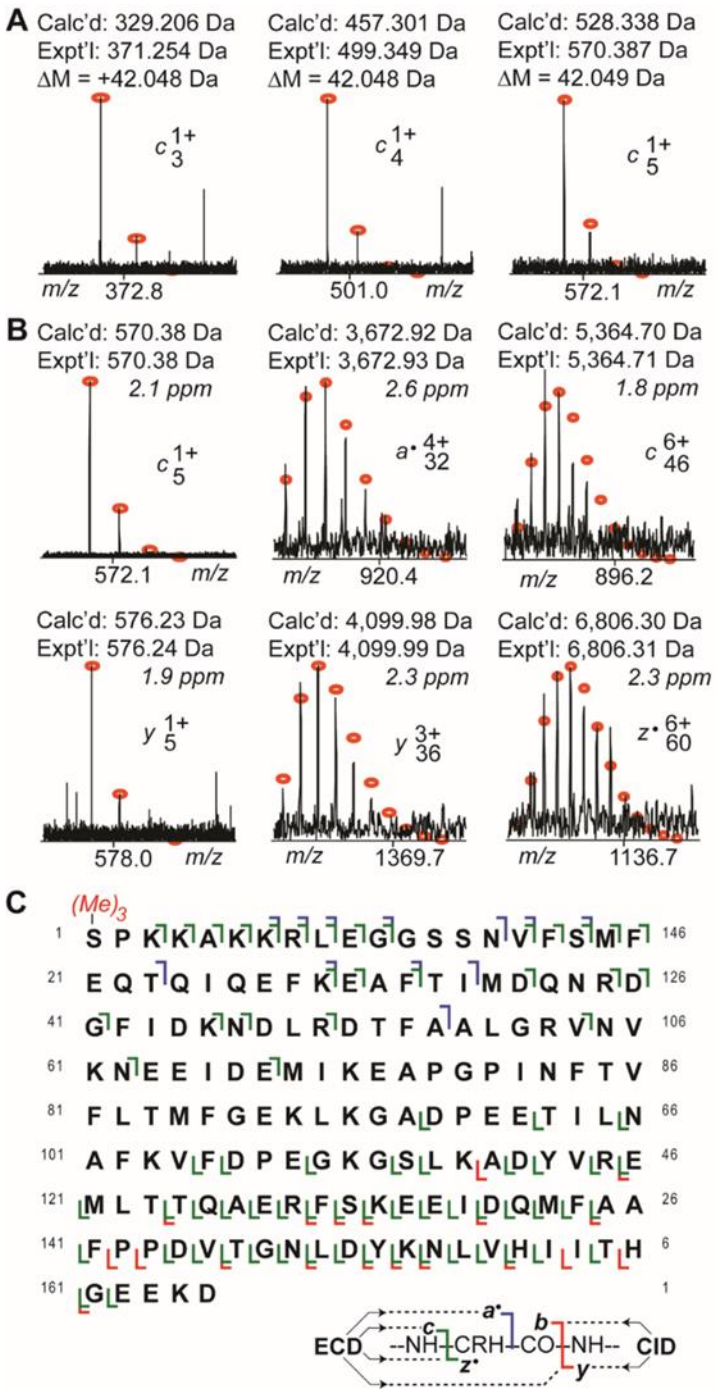

Fig. 7.26. Sequencing and N-terminal modification characterization for MLC-2S by high-resolution MS/MS. (A) N-terminal fragment ions showing approximate 42.046 Da mass increase compared to the calculated masses for the corresponding un-modified fragment ions, indicating N-terminal tri-methylation of MLC-2S. (B) Representative fragment ions resulting from

fragmentation of MLC-2S by ECD. (C) Fragmentation map for MLC-2S showing bond cleavages. "*(Me)*$_3$-" denotes N$^{\alpha}$-tri-methylation of Ser2 (numbering scheme includes N-terminal Met, which is removed in the mature protein). Circles represent the theoretical isotopic abundance distribution corresponding to the assigned mass and based on averagine.

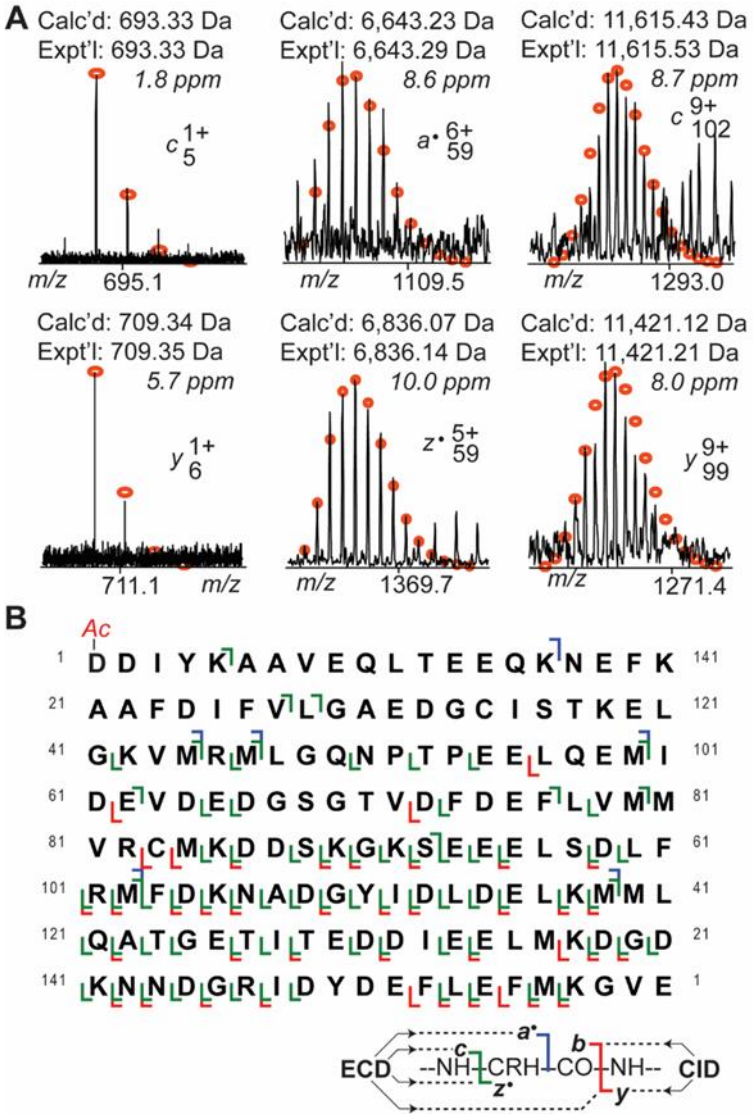

Fig. 7.27. Sequence characterization of *ss*TnC by high-resolution MS/MS. (A) Representative fragment ions resulting from fragmentation of *ss*TnC by ECD. (B) Fragmentation map for *ss*TnC showing bond cleavages. Circles represent the theoretical isotopic abundance distribution corresponding to the assigned mass and based on averagine.

A All proteins / tr|Q5XIG1|Q5XIG1_RAT Ldb3 protein OS=Rattus norvegicus GN=Ldb3 PE=2 SV=1 / Peptide #1

Protein-Spectrum-Match for Spectrum #0

PrSM ID:	0	Scan(s):	1	Precursor charge:	37	Precursor m/z:	835.596
Precursor mass:	30879.8	Adjusted precursor mass:	30879.766	Duplicate score:	230	Unique score:	148
E-value:	1.4E-45	P-value:	7E-46	Spectral FDR:	n/a	Protein mass:	30968.796

N-Terminal Methionine Excision(canonical) and N-Terminal Acetylation

M]S[42.01] Y S V T L T G P G P W G|F R L Q G G K|D F|N|M P L|T I S R I T P G S K|A A|Q|
S|Q L S|Q G D L V V A I D|G V|N T|D|T M T H L|E|A Q|N K|I|K|S|A|S Y N|L S L T|L|
Q|K|S|K|R P I P I S T T|A P P I|Q|S P L P V I P|H|Q|K|V V A N|S P A N|A|D|Y|Q|E|
R F N P|S V|L|K|D|S|A|L S|T|H|K P I|E V K G|L|G|G K A|T I I H A Q Y|N|T P I S M|
Y S Q|D A I M D A|I|A G|Q|A|Q|A|Q G S|D F S G S|L P V K D L|A V|D|S A|S P V Y Q|
A|V I|K|T|Q S|K P E|D|E A|D|E W A|R|R|S|S|N|L|Q|S|R S F|R|I L A Q|M T G|T|E|Y|M|
Q|D P D|E|E A L|R R|S|R|E|R|F|E|T|E|R|N S P|R F|A|K|L|R|N W|H|H G|L S A|Q|I L N
V K|S

B All proteins / tr|A0A0G2JXR0|A0A0G2JXR0_RAT Protein Ldb3 OS=Rattus norvegicus GN=Ldb3 PE=1 SV=1 / Peptide #1

Protein-Spectrum-Match for Spectrum #0

PrSM ID:	0	Scan(s):	1	Precursor charge:	38	Precursor m/z:	825.193
Precursor mass:	31319.06	Adjusted precursor mass:	31319.009	Duplicate score:	150	Unique score:	96
E-value:	9.3E-32	P-value:	4.7E-32	Spectral FDR:	n/a	Protein mass:	31408.039

N-Terminal Methionine Excision(canonical) and N-Terminal Acetylation

M]S[42.01] Y S|V T L T|G P G P W G F R|L Q G|G K|D F N|M P L|T I S R I|T P G S|K|A A Q|
S|Q L S|Q|G D L V V A I D|G V N T|D|T M T H L|E|A Q|N K I|K|S|A|S Y N|L S L T|L|
Q|K|S|K|R P|I P I S T T A P P I Q|S P L P V|I P|H Q|K V V A N S P A N A D|Y Q E
R F N P|S V|L K D S A L S T H K P I E V K G|L|G G K|A T I I H A Q Y N|T P I S M
Y S Q D A I M D A I|A G Q A Q A Q G S D F|S G A S P L A S|L P V K D L A V D S A
S P V Y|Q|A|V I|K|T|Q|S|K P E D|E A|D|E W A|R R|S|S|N|L Q|S|R S|F|R|I L A Q|M|T
G T|E Y|M|Q|D P D|E|E A L R|R|S|R|E|R|F|E|T|E|R|N S P|R F A K L|R N W H|H G L S
A Q|I|L N V K|S

C All proteins / sp|P58775|TPM2_RAT Tropomyosin beta chain OS=Rattus norvegicus GN=Tpm2 PE=1 SV=1 / Peptide #1

Protein-Spectrum-Match for Spectrum #0

PrSM ID:	0	Scan(s):	1	Precursor charge:	39	Precursor m/z:	843.534
Precursor mass:	32858.56	Adjusted precursor mass:	32858.561	Duplicate score:	300	Unique score:	148
E-value:	1.4E-45	P-value:	7E-46	Spectral FDR:	n/a	Protein mass:	32816.55

N-Terminal Acetylation

M[42.01] D A I K|K|K|M|Q|M L|K|L|D|K|E|N|A|I|D|R|A|E|Q|A|E|A|D|K|K|Q|A|E|D|R|C K|Q|L|E|
E E|Q Q|A|L|Q|K|K|L K|G|T|E|D|E V|E|K|Y|S|E|S|V|K|D|A|Q|E|K|L E|Q|A|E|K|K A T|D|
A E|A|D V A S|L|N|R R I Q|L V E|E E L D R A Q E R L A T|A L Q K L E E A E K A A
D E S E R G M K|V I E N R A M K D E E K M E L Q E|M Q L K E A K H I A E D S|D R
K Y E E V A R K L V I L|E G E L|E|R|S|E|E R A E V A|E S K C G D L|E E|E|L|K I V
T|N|N|L K S|L|E|A|Q|A|D|K|Y|S|T|K|E|D|K|Y|E|E|E|I|K|L|L|E|E|K|L K|E|A|E|T|R|A|E|
F|A E|R|S V|A|K|L|E|K T|I|D|D L|E|D|E|V|Y|A|Q K M|K Y|K A I S E E L D N A L N D
I T S L

Fig. 7.28. Identification of sarcomeric proteins commonly observed in extracts prepared from fast- and slow-twitch skeletal muscles by high-resolution MS/MS. The protein identifications are shown. The full list of identified proteins in GAS and SOL muscles are shown in **Tables 7.1** and **7.3**, respectively. The peak numbers representing different fractions collected are shown in **Fig. 7.6**. (A) Peaks numbered 4 (GAS) and 6 (SOL) were identified as an isoform of Cypher not previously observed at the protein level (designated herein as Cypher4s), with removal of the N-terminal Met and a +42.01 Da mass discrepancy in the N-terminal half of the protein, suggesting N-terminal acetylation of the protein. (B) Peaks numbered 5 (GAS) and 7 (SOL) were identified as the previously identified Cypher2s [389], with removal of the N-terminal Met and acetylation of Ser2. (C) Peaks numbered 11 (GAS) and 12 (SOL) were identified as the β isoform of Tpm (βTpm, Tpm2.2), with modification of Met1.

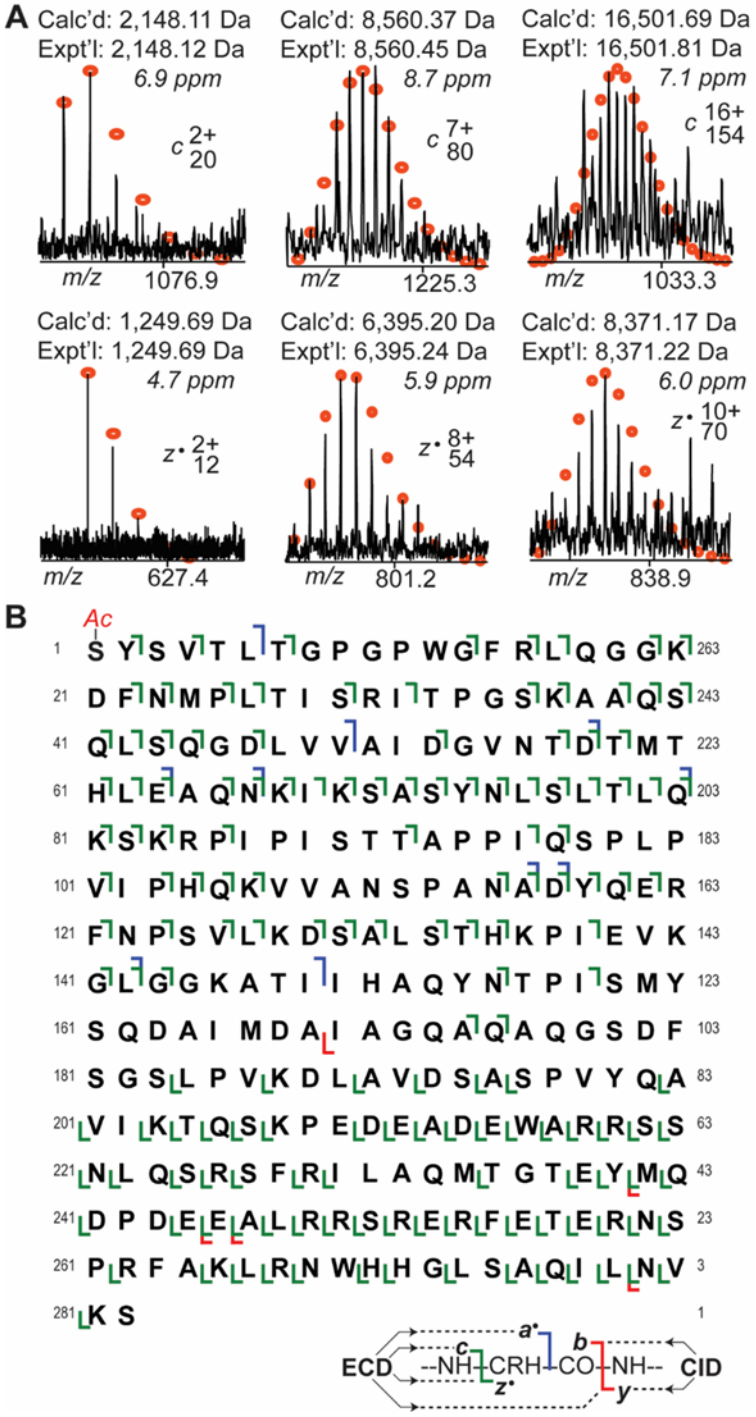

Fig. 7.29. Sequence characterization of undesignated Cypher isoform not previously observed at the protein level (referred to as Cypher4s herein) by high-resolution MS/MS. (A) Representative fragment ions resulting from fragmentation of Cypher4s by ECD. (B) Fragmentation map for Cypher4s showing bond cleavages. "*(Ac)*-" denotes N^{α}-acetylation of Ser2

(numbering scheme includes N-terminal Met, which is removed in the mature protein). Circles represent the theoretical isotopic abundance distribution corresponding to the assigned mass and based on averagine.

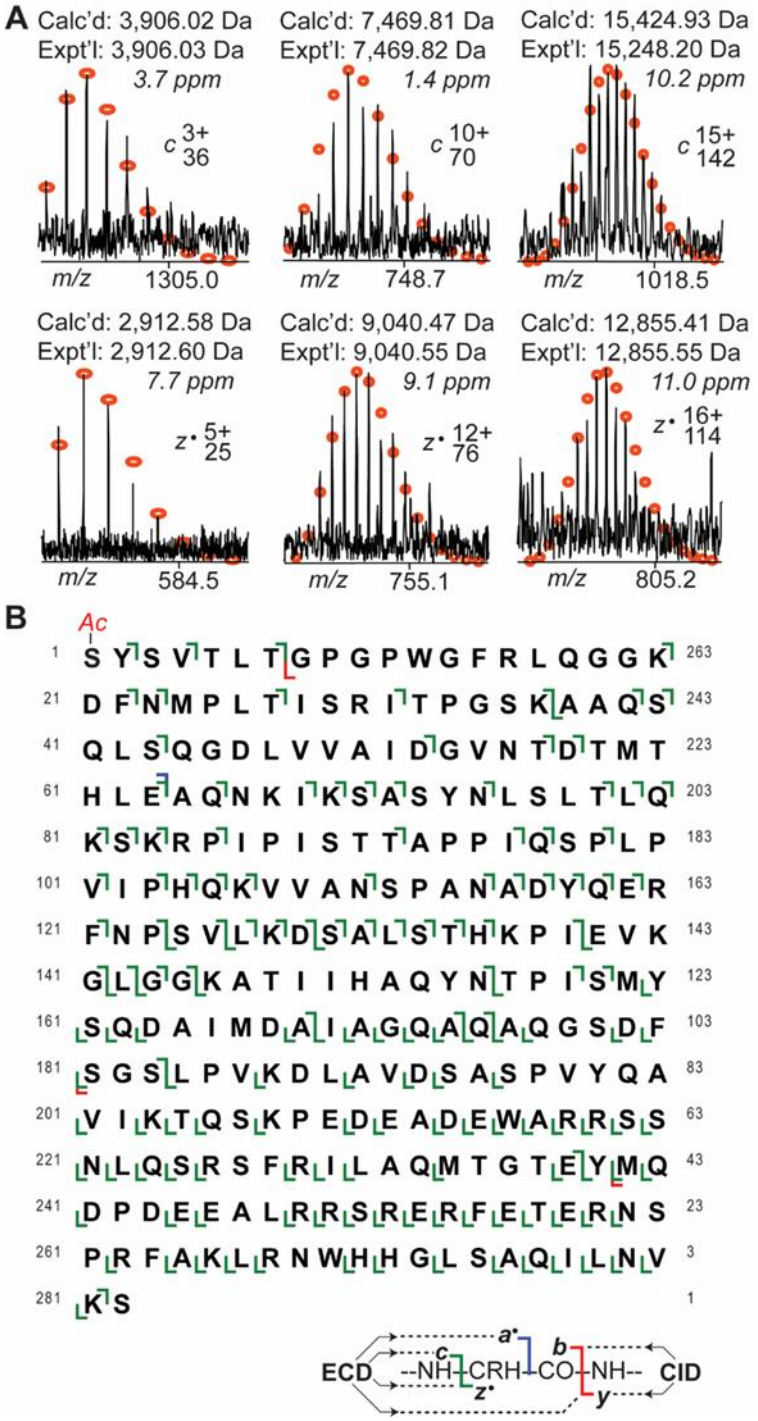

Fig. 7.30. Sequence characterization of Cypher2s by high-resolution MS/MS. (A) Representative fragment ions resulting from fragmentation of Cypher2s by ECD. (B) Fragmentation map for Cypher2s showing bond cleavages. "*(Ac)*-" denotes N^{α}-acetylation of Ser2 (numbering scheme includes N-terminal Met, which is removed in the mature protein). Circles

represent the theoretical isotopic abundance distribution corresponding to the assigned mass and based on averagine.

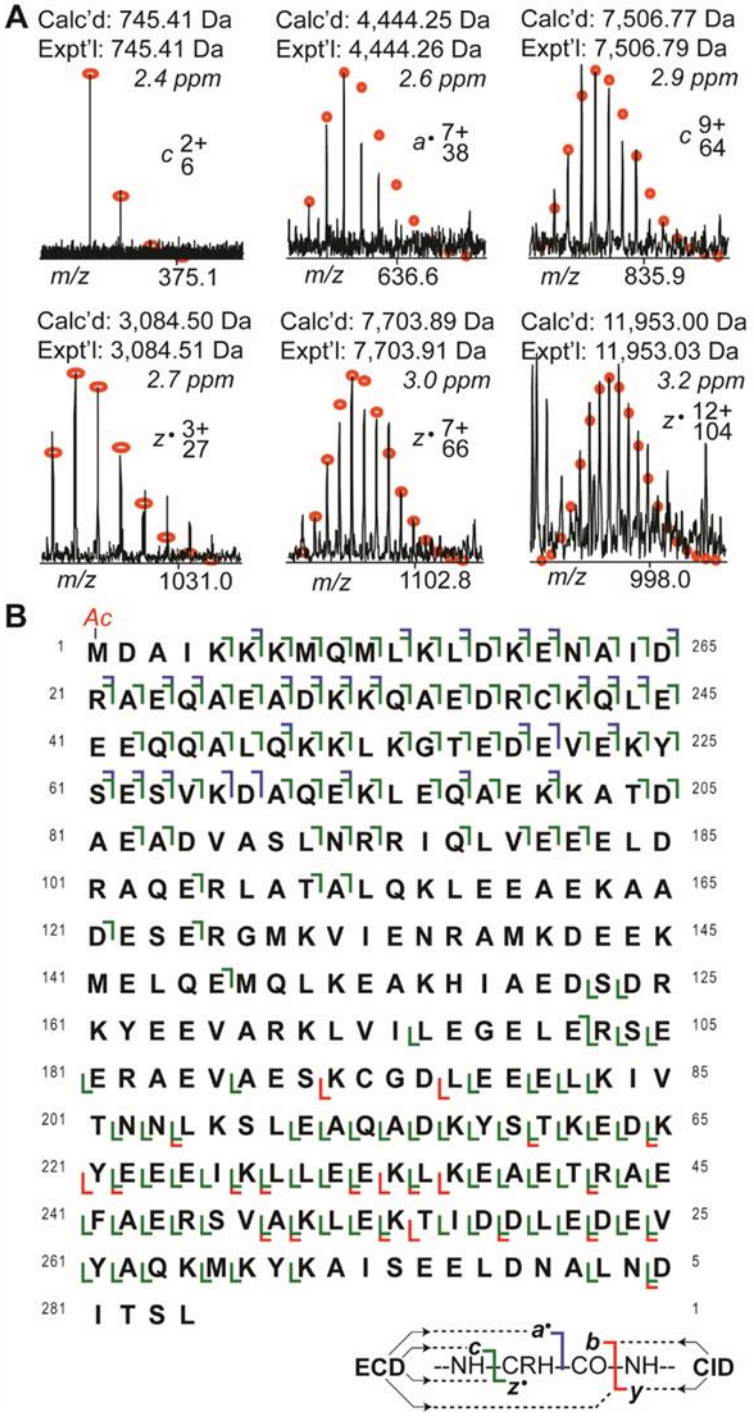

Fig. 7.31. Sequence characterization of βTpm [Tpm2.2st (a.b.b.a)] [406] by high-resolution MS/MS. (A) Representative fragment ions resulting from fragmentation of βTpm by ECD. (B) Fragmentation map for βTpm showing bond cleavages. "*(Ac)*-" denotes N^{α}-acetylation of Met1.

Circles represent the theoretical isotopic abundance distribution corresponding to the assigned mass and based on averagine.

Table 7.4. Exon structure of Cypher isoforms listed in the UniProtKB/Swiss-Prot database.

Accession #	Species	Isoform	Designation	Exons
Q9JKS4-1	*M. musculus* (mouse)	1	Cypher1c	1-4, 8-9, 11-17
Q9JKS4-2	*M. musculus*	2	Cypher1s	1-3, 5-9, 11-17
Q9JKS4-3	*M. musculus*	3	Cypher3c	1-4, 8-9, 12-17
Q9JKS4-4	*M. musculus*	4	Cypher3s	1-3, 5-9, 12-17
Q9JKS4-5	*M. musculus*	5	Cypher2c	1-4, 8-10
Q9JKS4-6	*M. musculus*	6	Cypher2s	1-3, 5-10
Q5XIG1	*R. norvegicus* (rat)		Cypher4s	1-3, 5-6, 8-10

Accession numbers correspond to UniProtKB/Swiss-Prot database accession numbers.

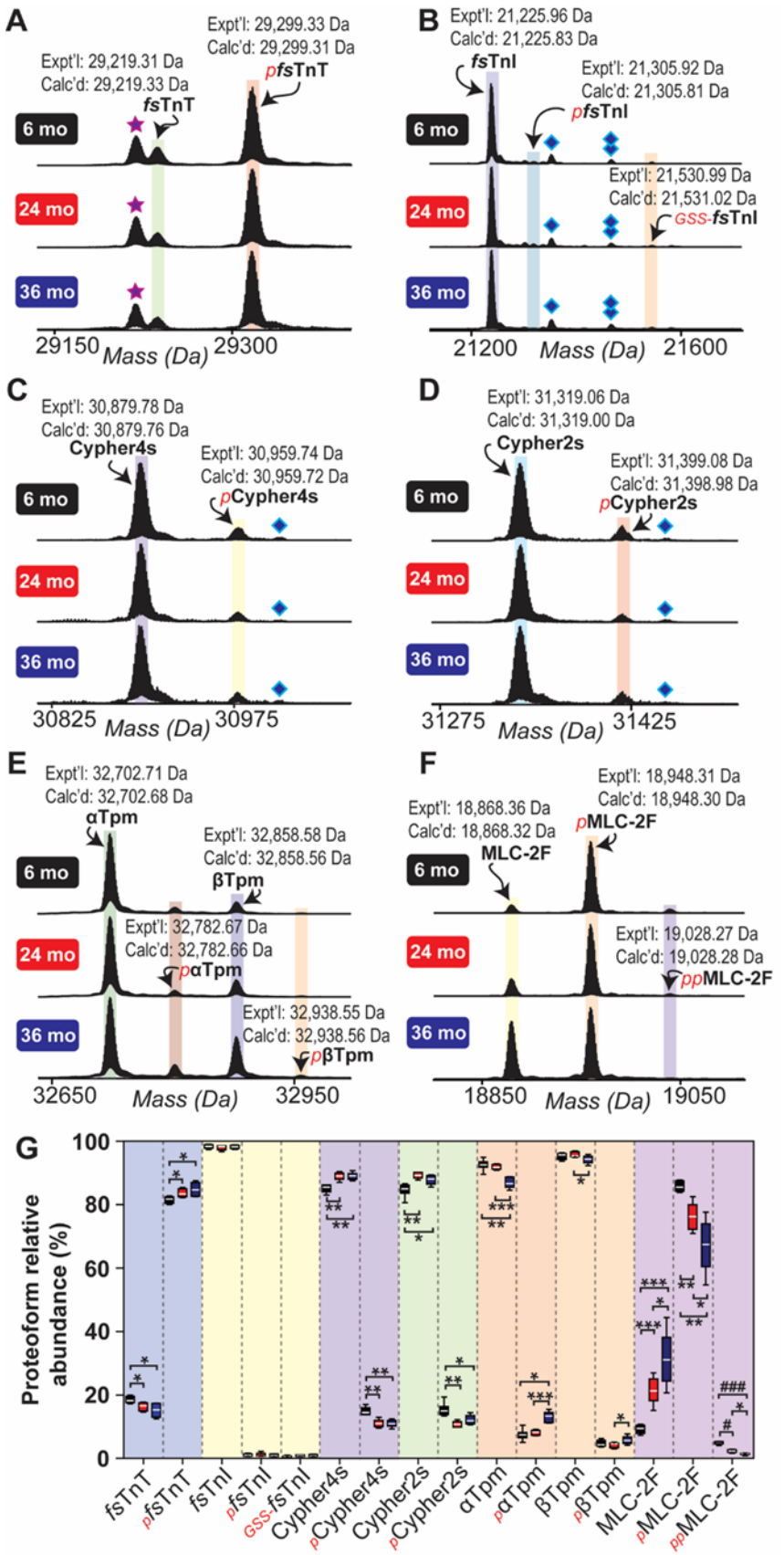
A
Expt'l: 29,219.31 Da
Calc'd: 29,219.33 Da
fsTnT
Expt'l: 29,299.33 Da
Calc'd: 29,299.31 Da
pfsTnT
6 mo
24 mo
36 mo
29150 Mass (Da) 29300
B
Expt'l: 21,225.96 Da
Calc'd: 21,225.83 Da
fsTnI
Expt'l: 21,305.92 Da
Calc'd: 21,305.81 Da
pfsTnI
Expt'l: 21,530.99 Da
Calc'd: 21,531.02 Da
GSS-fsTnI
21200 Mass (Da) 21600
C
Expt'l: 30,879.78 Da
Calc'd: 30,879.76 Da
Cypher4s
Expt'l: 30,959.74 Da
Calc'd: 30,959.72 Da
pCypher4s
30825 Mass (Da) 30975
D
Expt'l: 31,319.06 Da
Calc'd: 31,319.00 Da
Cypher2s
Expt'l: 31,399.08 Da
Calc'd: 31,398.98 Da
pCypher2s
31275 Mass (Da) 31425
E
Expt'l: 32,702.71 Da
Calc'd: 32,702.68 Da
αTpm
Expt'l: 32,858.58 Da
Calc'd: 32,858.56 Da
βTpm
Expt'l: 32,782.67 Da
Calc'd: 32,782.66 Da
pαTpm
Expt'l: 32,938.55 Da
Calc'd: 32,938.56 Da
pβTpm
32650 Mass (Da) 32950
F
Expt'l: 18,868.36 Da
Calc'd: 18,868.32 Da
MLC-2F
Expt'l: 18,948.31 Da
Calc'd: 18,948.30 Da
pMLC-2F
Expt'l: 19,028.27 Da
Calc'd: 19,028.28 Da
ppMLC-2F
18850 Mass (Da) 19050
G
Proteoform relative abundance (%)
0
20
40
60
80
100
fsTnT
pfsTnT
fsTnI
pfsTnI
GSS-fsTnI
Cypher4s
pCypher4s
Cypher2s
pCypher2s
αTpm
pαTpm
βTpm
pβTpm
MLC-2F
pMLC-2F
ppMLC-2F

Fig. 7.32. Top-down high-resolution MS-based quantification of sarcomeric protein proteoform relative abundances in fast-twitch GAS muscles isolated from 6-, 24-, and 36-month-old rats. Representative mass spectra showing *fs*TnT (A), *fs*TnI (B), Cypher4s (C), Cypher2s (D), Tpm (E), and MLC-2F (F). Star represents H_3PO_4 loss from $_p$*fs*TnT. Diamond and double diamond represent protein associated non-covalently with one and two TFA molecules, respectively. G. Graph showing the relative quantification of proteoform relative abundances in GAS muscles isolated from rats in different age groups. Quantification is based on n = 6 animals for all age groups. Expt'l, experimentally determined relative molecular mass. Calc'd, calculated relative molecular mass based on sequence in the UniProtKB/Swiss-Prot database. *$p < 0.05$; **$p < 0.001$; ***$p < 0.0001$; #$p < 0.00001$; ##$p < 0.000001$; ###$p < 0.0000001$.

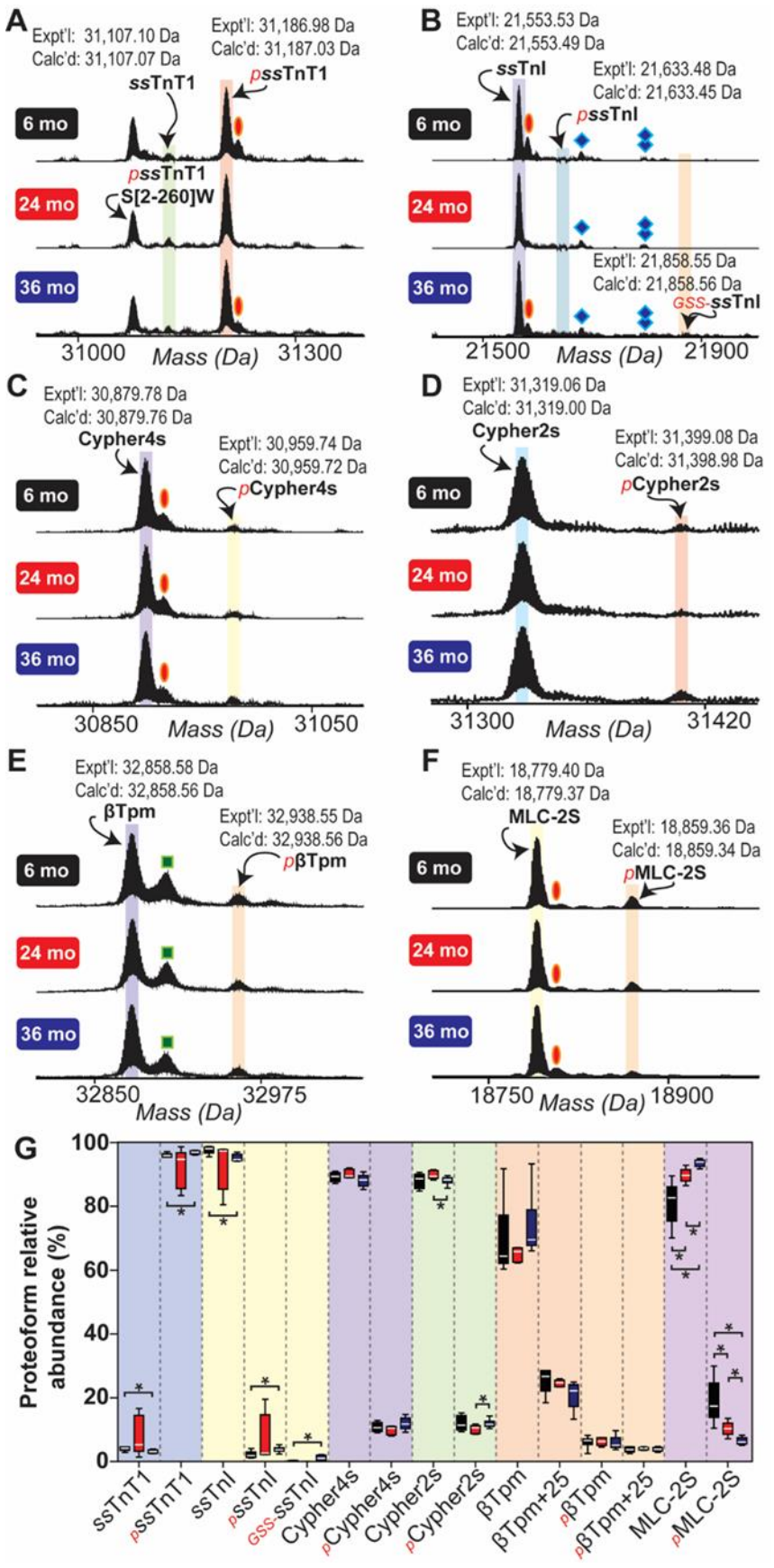
A
Expt'l: 31,107.10 Da
Calc'd: 31,107.07 Da
ssTnT1
Expt'l: 31,186.98 Da
Calc'd: 31,187.03 Da
pssTnT1
6 mo
pssTnT1
S[2-260]W
24 mo
36 mo
31000
Mass (Da)
31300
B
Expt'l: 21,553.53 Da
Calc'd: 21,553.49 Da
ssTnI
Expt'l: 21,633.48 Da
Calc'd: 21,633.45 Da
pssTnI
6 mo
24 mo
Expt'l: 21,858.55 Da
Calc'd: 21,858.56 Da
GSS-ssTnI
36 mo
21500
Mass (Da)
21900
C
Expt'l: 30,879.78 Da
Calc'd: 30,879.76 Da
Cypher4s
Expt'l: 30,959.74 Da
Calc'd: 30,959.72 Da
pCypher4s
6 mo
24 mo
36 mo
30850
Mass (Da)
31050
D
Expt'l: 31,319.06 Da
Calc'd: 31,319.00 Da
Cypher2s
Expt'l: 31,399.08 Da
Calc'd: 31,398.98 Da
pCypher2s
6 mo
24 mo
36 mo
31300
Mass (Da)
31420
E
Expt'l: 32,858.58 Da
Calc'd: 32,858.56 Da
βTpm
Expt'l: 32,938.55 Da
Calc'd: 32,938.56 Da
pβTpm
6 mo
24 mo
36 mo
32850
Mass (Da)
32975
F
Expt'l: 18,779.40 Da
Calc'd: 18,779.37 Da
MLC-2S
Expt'l: 18,859.36 Da
Calc'd: 18,859.34 Da
pMLC-2S
6 mo
24 mo
36 mo
18750
Mass (Da)
18900
G
Proteoform relative abundance (%)
100
80
60
40
20
0
ssTnT1
pssTnT1
ssTnI
pssTnI
GSS-ssTnI
Cypher4s
pCypher4s
Cypher2s
pCypher2s
βTpm
βTpm+25
pβTpm
pβTpm+25
MLC-2S
pMLC-2S

7.33. Top-down high-resolution MS-based quantification of sarcomeric protein proteoform relative abundances in slow-twitch SOL muscles isolated from 6-, 24-, and 36-month-old rats. Representative mass spectra showing *ss*TnT1 (A), *ss*TnI (B), Cypher4s (C), Cypher2s (D), βTpm (E), and MLC-2S (F). Oval, diamond, double diamond, and square represent peaks corresponding to oxidation, protein associated non-covalently with one TFA molecule, protein associated non-covalently with two TFA molecules, and a proteoform exhibiting a mass difference of +25 Da versus βTpm, respectively. G. Graph showing the relative quantification of proteoform relative abundances in SOL muscles isolated from rats in different age groups. Quantification is based on n = 6 animals for all age groups. Expt'l, experimentally determined relative molecular mass. Calc'd, calculated relative molecular mass based on sequence in the UniProtKB/Swiss-Prot database. *$p < 0.05$; **$p < 0.001$; ***$p < 0.0001$; #$p < 0.00001$; ##$p < 0.000001$; ###$p < 0.0000001$.

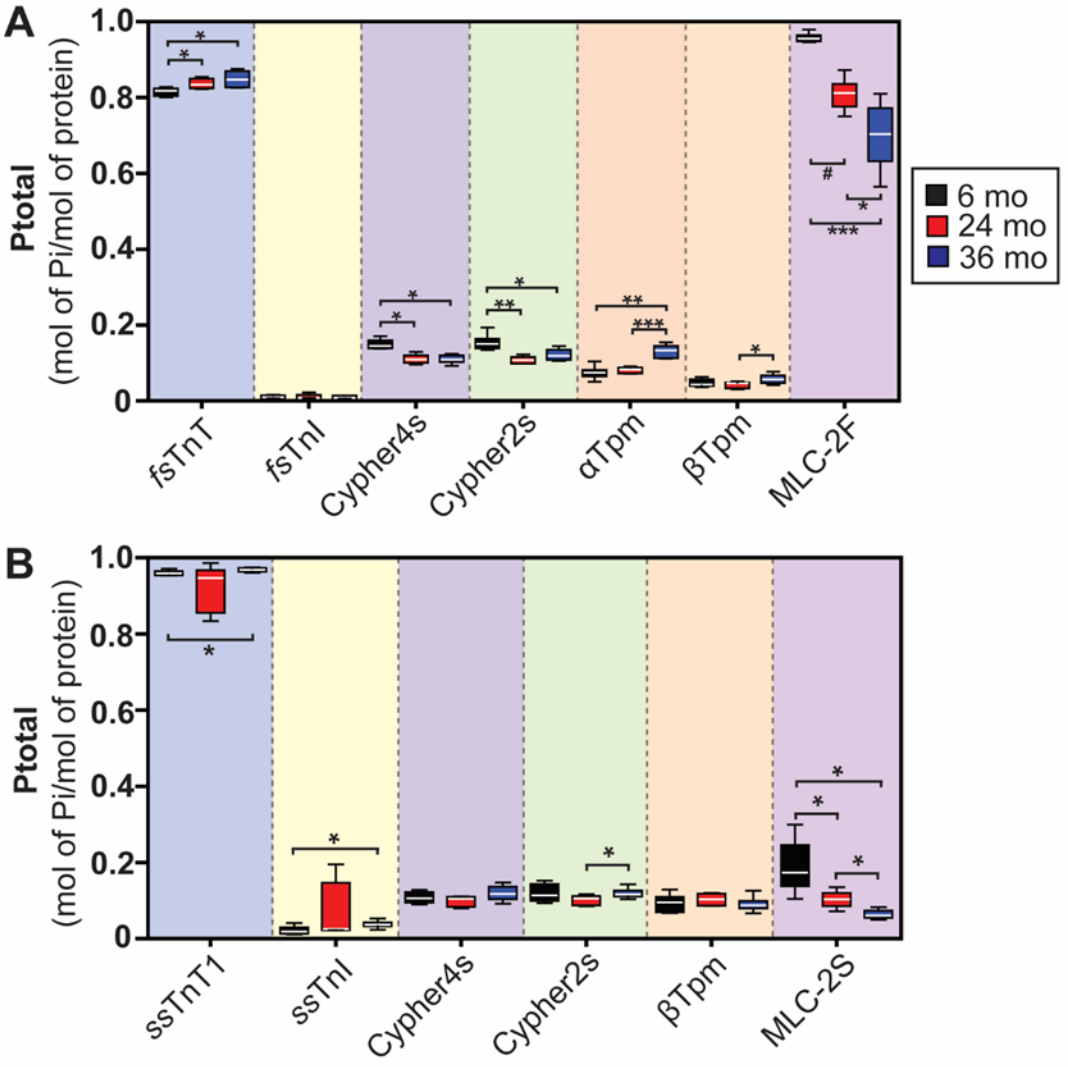

Fig. 7.34. MS-based quantification of sarcomeric protein phosphorylation in fast- and slow-twitch skeletal muscles isolated from 6-, 24-, and 36-month-old rats. (A) Quantification of sarcomeric protein phosphorylation in GAS muscles from rats in different age groups. (B) Quantification of sarcomeric protein phosphorylation in SOL muscles from aging F344BN rats. Quantification is based on n = 6 individuals for all age groups. *$p < 0.05$; **$p < 0.001$; ***$p < 0.0001$; #$p < 0.00001$.

CHAPTER 8 – CONCLUSIONS AND FUTURE DIRECTIONS

Sarcomeres are the most basic functional units of striated muscle and are composed of myofilaments, which constitute the contractile apparatuses, flanked on either side by protein-dense structures known as Z-discs. While Ca^{2+} is the ultimate trigger for muscle contraction, studies have now convincingly demonstrated that the PTM of myofilament proteins is a crucial mechanism enabling the regulation of striated muscle function in a Ca^{2+}-independent manner. Moreover, emerging evidence suggests that Z-discs represent critical signaling nodes within the myocyte and even implicates these structures in the indirect regulation of striated muscle contractile function. In the studies detailed in this thesis, top-down mass spectrometry-based proteomics was employed in combination with functional assays to gain insights into the functions of sarcomeric proteins and their PTMs in the myocardium under basal conditions and in response to injury, as well as in aged skeletal muscles.

In chapters 2 and 3, transmural and chamber-specific differences in the sequences and PTMs of myofilament proteins in the hearts of healthy adult swine were examined. A notable finding of this work is that transmural differences in the PTM of myofilament proteins, in particular, in MLC-2 phosphorylation, are not present in the swine heart under basal conditions [269]. Prior to this study, several reports had documented transmural differences in the modification status of myofilament proteins across the ventricular wall in small animals [232, 238-240]. Moreover, a gradient of increasing MLC-2 phosphorylation proceeding from the endocardium to the epicardium in the hearts of rats was shown to facilitate cardiac torsion, the twisting wringing motion of the heart, by altering tension production and the stretch activation response across the

ventricular wall [240]. However, it was not clear at the time whether such a mechanism was also responsible for cardiac torsion in large animals and humans. Thus, this data [269], as well as data from other groups [93, 141, 241], indicates that transmural differences in the phosphorylation of myofilament proteins and, specifically, in MLC-2 phosphorylation, do not underlie cardiac torsion in large animals and, likely, in humans, under basal conditions. While there is the possibility that increased workload may induce transmural differences in myofilament protein phosphorylation in humans, as it does in rodents [238], this, at least, does not appear to be the case in swine [93]. Whether a longitudinal (base to apex) gradient in MLC-2 phosphorylation, which has also been observed in the rodent heart [407], is present in the hearts of swine was not examined. As this could conceivably contribute to the counterclockwise torsional twist of the ventricle at the time of ejection, further studies to ascertain whether this gradient is present in the hearts of large animals and, samples permitting, humans are warranted.

In chapter 4, quantitative top-down proteomics was employed to study changes in the phosphorylation of myofilament proteins in the myocardium of swine after experimentally induced myocardial infarction (MI). A concerted decrease in the phosphorylation of the myofilament proteins cTnI and MLC-2, as well as the Z-disc protein, ENH2 was observed in infarcted myocardium of swine following acute MI [244]. In the context of end-stage HF resulting from ischemic or non-ischemic DCM in humans and ischemic injury in large animals, previous studies had shown that the phosphorylation of cTnI [82, 144-147] and cMyBP-C [148-150] are decreased, with or without additional alterations in MLC-2 phosphorylation [82, 93, 137, 140, 141, 151, 152]. Even though decreased phosphorylation of cTnI, cMyBP-C, and MLC-2 can largely account for contractile defects in the end-stage failing heart [81, 82, 93, 139-141], whether alterations in

myofilament protein phosphorylation occur prior to the onset of post-MI ventricular remodeling was an under-explored area of investigation [92]. Thus, the findings presented in chapter 4 demonstrate that myofilament protein phosphorylation is indeed altered prior to ventricular remodeling in swine with acute MI [244], and potentially implicates these alteration in impaired contractile function in the post-MI myocardium.

Nevertheless, it must be noted that myofilament protein PTMs were examined in myocardium that will ultimately die and be replaced by a fibrous scar (i.e., the ischemic zone myocardium). This was because one concern was that changes, insofar as they occurred, would be too minor to be detected in myocardium distal to the infarct, as hearts were harvested directly following occlusion of the left anterior coronary artery for 60 minutes without reperfusion. Now that we have established that alterations occur in the infarcted myocardium, an essential next step will be to determine whether similar changes contribute to contractile dysfunction in the tissue bordering the infarct (the infarct border zone) early after MI. An answer to this question is likely to be clinically relevant as evidence in the literature indicates that even partial recovery of contractile function in this region can benefit global cardiac function following MI [408].

In chapter 5, the results of mechanical and proteomics analyses of $ENH^{+/+}$, $ENH^{+/-}$, and $ENH^{-/-}$ mouse myocardium are reported. The purpose of these experiments was to determine whether the ENH protein, which was identified as a novel phospho-protein in chapter 4, plays a role in cardiac contractile function. Surprisingly, the findings of these experiments suggest that ENH protein isoforms may have a part in setting cross-bridge cycling kinetics, at least in the mouse myocardium. Based on the results detailed in chapter 5, changes in the expression of MHC

isoforms or in the expression or phosphorylation of other thin and thick filament regulatory proteins cannot account for this phenomenon, at least in $ENH^{+/-}$ mouse myocardium. Therefore, in the absence of changes in the expression/phosphorylation of these proteins, it seems most likely that alterations in the expression, or possibly the phosphorylation, of ENH isoforms are responsible.

At least seven isoforms of ENH are expressed in the mouse heart—five long isoforms containing three C-terminal LIM domains and two short isoforms lacking them [116]. Unfortunately, isoform-specific and phospho-ENH antibodies are not available, making it difficult to link the depression in force redevelopment kinetics to changes in the expression/phosphorylation of one or more of these isoforms. In our study, using top-down proteomics two short isoforms, ENH3a and ENH3b, were detected in the myocardium of $ENH^{+/+}$ and $ENH^{+/-}$ mice, although quantification was only possible for the latter. Our results show that neither the expression nor phosphorylation of ENH3b differed significantly in the myocardium of $ENH^{+/+}$ and $ENH^{+/-}$ mice. These results suggest that alterations in the expression (or potentially the phosphorylation) of ENH isoforms other than ENH3b contribute to reduced cross-bridge cycling kinetics in $ENH^{+/-}$ and $ENH^{-/-}$ mouse myocardium. Methodological advancements enabling the detection and quantification of additional ENH isoforms (or the generation of isoform-specific and phospho-ENH antibodies) will be necessary to determine the contributions of other isoforms.

Previous studies have demonstrated that cardiac-specific ablation of ENH isoform expression also decreases the expression of both Calsarcin-1 and short isoforms of Cypher, which exist in complex with ENH at the Z-disc [116]. Thus, a second possibility is that alterations in the expression of

Calsarcin-1 and/or Cypher isoform expression may underlie or contribute to the depression in cross-bridge cycling kinetics in $ENH^{+/-}$ and $ENH^{-/-}$ mouse myocardium. As antibodies to these proteins are commercially available, an immediate next step will be to determine whether the expression of Calsarcin-1 or Cypher isoforms is altered in the myocardium of $ENH^{+/-}$ mice, and whether these changes correlate with cross-bridge cycling kinetics.

Another important question remaining to be answered is how changes in the expression of proteins in the Z-discs affect actin-myosin interactions occurring in the A band? To date, the only Z-disc protein with a known role in regulating striated muscle contractility is the giant protein nebulin [409]. A previous study by Chandra et al. demonstrated that nebulin has a role in setting cross-bridge cycling kinetics, as well as the Ca^{2+} sensitivity and cooperativity of activation, in skeletal muscle [409]. However, while nebulin is anchored in the Z-disc, the protein spans the length of the thin filament. Therefore, it seems most likely that the portion of the protein that extends into the A band is directly responsible for the modulation of actin-myosin interactions [409]. The fact that ablation of nebulette, the short cardiac-specific isoform of nebulin, which is also anchored in the Z-disc but does not span the thin filament, does not alter the steady-state or dynamic mechanical properties of the myocardium supports this conclusion [410]. Therefore, a separate mechanism is likely at work in $ENH^{+/-}$ and $ENH^{-/-}$ mouse myocardium as ENH protein isoforms, like nebulette, are confined within the Z-disc [114].

One potential explaination is that changes in the expression of ENH isoforms reduces the integrity of the Z-disc and, in so doing, introduces compliance in the sarcomeres. Alterations in Z-disc structure in $ENH^{-/-}$ mouse myocardium would seem to be in agreement with such a mechanism

[116]. Our data show that the rate of force redevelopment (k_{tr}), which is defined as the sum of the apparent rate constants of cross-bridge attachment (f_{app}) and detachment (g_{app}) [343], is decreased in the myocardium of $ENH^{+/-}$ and $ENH^{-/-}$ mice. Based on estimation of g_{app} (the y-intercept in the plot of the natural logarithm of the k_{tr} versus relative force), it is be predicted that the rates of cross-bridge attachment and detachment are both decreased in $ENH^{+/-}$ and $ENH^{-/-}$ mouse myocardium, with the decreases in these rates being more pronounced in the latter. However, a more direct approximation of g_{app} is to measure the tension cost (the ratio of myosin Mg^{2+}-ATPase activity to tension). Thus, if changes in ENH expression do indeed alter cross-bridge cycling kinetics, we would expect g_{app} to be decreased in the myocardium of $ENH^{+/-}$ mice. In this case, g_{app} in $ENH^{-/-}$ mouse myocardium would likewise be decreased, but to a greater extent that in $ENH^{+/-}$ mouse myocardium as β-MHC expression is increased in the hearts of $ENH^{-/-}$ mice. Conversely, if our hypotheis is correct, and alterations in ENH isoform expression introduce sarcomeric compliance that underlies the decrease in k_{tr} measured in $ENH^{+/-}$ and $ENH^{-/-}$ mice, then we would expect g_{app} to be unchanged in $ENH^{+/-}$ mouse myocardium. This would imply that the decrease in k_{tr} is due solely to a decrease in the rate of cross-bridge attachment, which is suggestive of an increase in the compliance of the system. In this scenario, a decrease in g_{app} would still be observed in $ENH^{-/-}$ mouse myocardium as increased expression of β-MHC in these mice will slow cross-bridge cycling kinetics.

In chapters 6 and 7, age-related changes in sarcomeric protein PTMs were assessed in the fast- and slow-twitch skeletal muscles of aging rats. Notably, a variety of age-associated changes in myofilament, as well as Z-disc, protein PTMs were observed in both fast- and slow-twitch skeletal muscles from aging rats. One of these changes, an age-related progressive decline in fast skeletal

MLC-2 phosphorylation at Ser14 and Ser15, can account for contractile defects observed fast-twitch skeletal muscles [383]. However, whether changes in the PTMs of other myofilament proteins with age also contribute to contractile dysfunction in fast- and slow-twitch skeletal muscles will require further investigation. An important first step will be to determine the specific sites of modification that are changing with age. Another noteworthy finding was the identification of alterations in the phosphorylation of Cypher isoforms in both fast- and slow-twitch skeletal muscles of aging animals. This finding is significant as it represents the first report of changes in the phosphorylation of Z-disc in aging skeletal muscles. Prior studies have shown that Cypher serves as an A-kinase anchoring protein and can be phosphorylated by PKA *in vitro,* as well as *in vivo* [119]; however, the specific site(s) of modification and its functional significance remain enigmatic. Thus, future studies should also seek to address these knowledge gaps.

In summary, the results presented in this dissertation not only provide new insights into the roles of myofilament protein PTMs in cardiac and skeletal muscle contractile function under basal and pathological conditions, but also provides the first evidence that Z-discs protein PTMs are altered in the heart after injury and in aging skeletal muscles. Moreover, findings implicating ENH isoform expression in the kinetics of force redevelopment suggests a new role for Z-disc structural integrity in contractile function. Thus, these findings not only provide new information regarding the contributions made by myofilament protein PTMs to striated muscle contractility, but also open new avenues to explore the role of Z-disc proteins in striated muscle biology. Furthermore, the results presented herein add to a growing list of contributions made by top-down mass spectrometry to the advancement of our understanding of the functions of protein PTMs in health and disease.

SELECTED REFERENCES

[1] H. HUXLEY, J. HANSON, Changes in the cross-striations of muscle during contraction and stretch and their structural interpretation, Nature 173(4412) (1954) 973-6.

[2] H.E. Huxley, The mechanism of muscular contraction, Science 164(3886) (1969) 1356-65.

[3] L.V. HEILBRUNN, F.J. WIERCINSKI, The action of various cations on muscle protoplasm, J Cell Comp Physiol 29(1) (1947) 15-32.

[4] R. Niedergerke, Local muscular shortening by intracellularly applied calcium, The Journal of Physiology 128 (1955) 12-13.

[5] A. WEBER, On the role of calcium in the activity of adenosine 5'-triphosphate hydrolysis by actomyosin, J Biol Chem 234 (1959) 2764-9.

[6] S. Ebashi, M. Endo, Calcium ion and muscle contraction, Prog Biophys Mol Biol 18 (1968) 123-83.

[7] S. Ebashi, F. Ebashi, A. Kodama, Troponin as the Ca++-receptive protein in the contractile system, J Biochem 62(1) (1967) 137-8.

[8] S. EBASHI, F. EBASHI, A NEW PROTEIN COMPONENT PARTICIPATING IN THE SUPERPRECIPITATION OF MYOSIN B, J Biochem 55 (1964) 604-13.

[9] S. Ebashi, Calcium binding and relaxation in the actomyosin system, The Journal of Biochemistry 48(1) (1960) 150-151.

[10] A. WEBER, S. WINICUR, The role of calcium in the superprecipitation of actomyosin, J Biol Chem 236 (1961) 3198-202.

[11] S. EBASHI, THIRD COMPONENT PARTICIPATING IN THE SUPERPRECIPITATION OF 'NATURAL ACTOMYOSIN', Nature 200 (1963) 1010.

[12] K. BAILEY, Tropomyosin: a new asymmetric protein component of muscle, Nature 157 (1946) 368.

[13] I. Otsuki, T. Masaki, Y. Nonomura, S. Ebashi, Periodic distribution of troponin along the thin filament, J Biochem 61(6) (1967) 817-9.

[14] D.A. Parry, J.M. Squire, Structural role of tropomyosin in muscle regulation: analysis of the x-ray diffraction patterns from relaxed and contracting muscles, J Mol Biol 75(1) (1973) 33-55.

[15] J. Squire, Muscle regulation: a decade of the steric blocking model, Nature 291(5817) (1981) 614-5.

[16] D.F. McKillop, M.A. Geeves, Regulation of the interaction between actin and myosin subfragment 1: evidence for three states of the thin filament, Biophys J 65(2) (1993) 693-701.

[17] R. Maytum, S.S. Lehrer, M.A. Geeves, Cooperativity and switching within the three-state model of muscle regulation, Biochemistry 38(3) (1999) 1102-10.

[18] R. Maytum, B. Westerdorf, K. Jaquet, M.A. Geeves, Differential regulation of the actomyosin interaction by skeletal and cardiac troponin isoforms, J Biol Chem 278(9) (2003) 6696-701.

[19] P. Vibert, R. Craig, W. Lehman, Steric-model for activation of muscle thin filaments, J Mol Biol 266(1) (1997) 8-14.

[20] R. Craig, W. Lehman, Crossbridge and tropomyosin positions observed in native, interacting thick and thin filaments, J Mol Biol 311(5) (2001) 1027-36.

[21] C.C. Ashley, E.B. Ridgway, On the relationships between membrane potential, calcium transient and tension in single barnacle muscle fibres, J Physiol 209(1) (1970) 105-30.

[22] J.R. Blinks, R. Rüdel, S.R. Taylor, Calcium transients in isolated amphibian skeletal muscle fibres: detection with aequorin, J Physiol 277 (1978) 291-323.

[23] D.G. Allen, J.R. Blinks, Calcium transients in aequorin-injected frog cardiac muscle, Nature 273(5663) (1978) 509-13.

[24] D.G. Allen, S. Kurihara, Calcium transients in mammalian ventricular muscle, Eur Heart J Suppl A (1980) 5-15.

[25] J.N. Peterson, W.C. Hunter, M.R. Berman, Estimated time course of Ca2+ bound to troponin C during relaxation in isolated cardiac muscle, Am J Physiol 260(3 Pt 2) (1991) H1013-24.

[26] P.M. Janssen, L.B. Stull, E. Marbán, Myofilament properties comprise the rate-limiting step for cardiac relaxation at body temperature in the rat, Am J Physiol Heart Circ Physiol 282(2) (2002) H499-507.

[27] T. Ishikawa, J. O-Uchi, S. Mochizuki, S. Kurihara, Evaluation of the cross-bridge-dependent change in the Ca2+ affinity of troponin C in aequorin-injected ferret ventricular muscles, Cell Calcium 37(2) (2005) 153-62.

[28] P.H. Backx, W.D. Gao, M.D. Azan-Backx, E. Marban, The relationship between contractile force and intracellular [Ca2+] in intact rat cardiac trabeculae, J Gen Physiol 105(1) (1995) 1-19.

[29] J. Layland, R.J. Solaro, A.M. Shah, Regulation of cardiac contractile function by troponin I phosphorylation, Cardiovasc Res 66(1) (2005) 12-21.

[30] H.L. Sweeney, B.F. Bowman, J.T. Stull, Myosin light chain phosphorylation in vertebrate striated muscle: regulation and function, Am J Physiol 264(5 Pt 1) (1993) C1085-95.

[31] J.M. Metzger, M.L. Greaser, R.L. Moss, Variations in cross-bridge attachment rate and tension with phosphorylation of myosin in mammalian skinned skeletal muscle fibers. Implications for twitch potentiation in intact muscle, J Gen Physiol 93(5) (1989) 855-83.

[32] I. Morano, Tuning the human heart molecular motors by myosin light chains, J Mol Med (Berl) 77(7) (1999) 544-55.

[33] D. Szczesna, Regulatory light chains of striated muscle myosin. Structure, function and malfunction, Curr Drug Targets Cardiovasc Haematol Disord 3(2) (2003) 187-97.

[34] C. Yuan, R.J. Solaro, Myofilament proteins: From cardiac disorders to proteomic changes, Proteomics Clin Appl 2(6) (2008) 788-99.

[35] W. Jin, A.T. Brown, A.M. Murphy, Cardiac myofilaments: from proteome to pathophysiology, Proteomics Clin Appl 2(6) (2008) 800-10.

[36] N. Hamdani, V. Kooij, S. van Dijk, D. Merkus, W.J. Paulus, C.D. Remedios, D.J. Duncker, G.J. Stienen, J. van der Velden, Sarcomeric dysfunction in heart failure, Cardiovasc Res 77(4) (2008) 649-58.

[37] D.M. Bers, Cardiac excitation-contraction coupling, Nature 415(6868) (2002) 198-205.

[38] R.J. Solaro, A.J. Moir, S.V. Perry, Phosphorylation of troponin I and the inotropic effect of adrenaline in the perfused rabbit heart, Nature 262(5569) (1976) 615-7.

[39] S.A. Jeacocke, P.J. England, Phosphorylation of a myofibrillar protein of Mr 150 000 in perfused rat heart, and the tentative indentification of this as C-protein, FEBS Lett 122(1) (1980) 129-32.

[40] M. Gautel, O. Zuffardi, A. Freiburg, S. Labeit, Phosphorylation switches specific for the cardiac isoform of myosin binding protein-C: a modulator of cardiac contraction?, EMBO J 14(9) (1995) 1952-60.

[41] J.R. Patel, D.P. Fitzsimons, S.H. Buck, M. Muthuchamy, D.F. Wieczorek, R.L. Moss, PKA accelerates rate of force development in murine skinned myocardium expressing alpha- or beta-tropomyosin, Am J Physiol Heart Circ Physiol 280(6) (2001) H2732-9.

[42] J.E. Stelzer, J.R. Patel, J.W. Walker, R.L. Moss, Differential roles of cardiac myosin-binding protein C and cardiac troponin I in the myofibrillar force responses to protein kinase A phosphorylation, Circ Res 101(5) (2007) 503-11.

[43] C.W. Tong, J.E. Stelzer, M.L. Greaser, P.A. Powers, R.L. Moss, Acceleration of crossbridge kinetics by protein kinase A phosphorylation of cardiac myosin binding protein C modulates cardiac function, Circ Res 103(9) (2008) 974-82.

[44] D.G. Ward, M.P. Cornes, I.P. Trayer, Structural consequences of cardiac troponin I phosphorylation, J Biol Chem 277(44) (2002) 41795-801.

[45] N.E. Keane, P.G. Quirk, Y. Gao, V.B. Patchell, S.V. Perry, B.A. Levine, The ordered phosphorylation of cardiac troponin I by the cAMP-dependent protein kinase--structural consequences and functional implications, Eur J Biochem 248(2) (1997) 329-37.

[46] V. Gaponenko, E. Abusamhadneh, M.B. Abbott, N. Finley, G. Gasmi-Seabrook, R.J. Solaro, M. Rance, P.R. Rosevear, Effects of troponin I phosphorylation on conformational exchange in the regulatory domain of cardiac troponin C, J Biol Chem 274(24) (1999) 16681-4.

[47] G. Ferrières, M. Pugnière, J.C. Mani, S. Villard, M. Laprade, P. Doutre, B. Pau, C. Granier, Systematic mapping of regions of human cardiac troponin I involved in binding to cardiac troponin C: N- and C-terminal low affinity contributing regions, FEBS Lett 479(3) (2000) 99-105.

[48] D.G. Ward, S.M. Brewer, M.P. Cornes, I.P. Trayer, A cross-linking study of the N-terminal extension of human cardiac troponin I, Biochemistry 42(34) (2003) 10324-32.

[49] A. Ababou, M. Gautel, M. Pfuhl, Dissecting the N-terminal myosin binding site of human cardiac myosin-binding protein C. Structure and myosin binding of domain C2, J Biol Chem 282(12) (2007) 9204-15.

[50] A. Ababou, E. Rostkova, S. Mistry, C. Le Masurier, M. Gautel, M. Pfuhl, Myosin binding protein C positioned to play a key role in regulation of muscle contraction: structure and interactions of domain C1, J Mol Biol 384(3) (2008) 615-30.

[51] G. Kunst, K.R. Kress, M. Gruen, D. Uttenweiler, M. Gautel, R.H. Fink, Myosin binding protein C, a phosphorylation-dependent force regulator in muscle that controls the attachment of myosin heads by its interaction with myosin S2, Circ Res 86(1) (2000) 51-8.

[52] M. Gruen, M. Gautel, Mutations in beta-myosin S2 that cause familial hypertrophic cardiomyopathy (FHC) abolish the interaction with the regulatory domain of myosin-binding protein-C, J Mol Biol 286(3) (1999) 933-49.

[53] R.L. Moss, D.P. Fitzsimons, J.C. Ralphe, Cardiac MyBP-C regulates the rate and force of contraction in mammalian myocardium, Circ Res 116(1) (2015) 183-92.

[54] R.W. Kensler, R. Craig, R.L. Moss, Phosphorylation of cardiac myosin binding protein C releases myosin heads from the surface of cardiac thick filaments, Proc Natl Acad Sci U S A 114(8) (2017) E1355-E1364.

[55] B.A. Colson, M.R. Locher, T. Bekyarova, J.R. Patel, D.P. Fitzsimons, T.C. Irving, R.L. Moss, Differential roles of regulatory light chain and myosin binding protein-C phosphorylations in the modulation of cardiac force development, J Physiol 588(Pt 6) (2010) 981-93.

[56] P.P. Chen, J.R. Patel, I.N. Rybakova, J.W. Walker, R.L. Moss, Protein kinase A-induced myofilament desensitization to Ca(2+) as a result of phosphorylation of cardiac myosin-binding protein C, J Gen Physiol 136(6) (2010) 615-27.

[57] J.Y. Mun, M.J. Previs, H.Y. Yu, J. Gulick, L.S. Tobacman, S. Beck Previs, J. Robbins, D.M. Warshaw, R. Craig, Myosin-binding protein C displaces tropomyosin to activate cardiac thin filaments and governs their speed by an independent mechanism, Proc Natl Acad Sci U S A 111(6) (2014) 2170-5.

[58] S.J. van Dijk, K.L. Bezold, S.P. Harris, Earning stripes: myosin binding protein-C interactions with actin, Pflugers Arch 466(3) (2014) 445-50.

[59] M.S. Bhuiyan, J. Gulick, H. Osinska, M. Gupta, J. Robbins, Determination of the critical residues responsible for cardiac myosin binding protein C's interactions, J Mol Cell Cardiol 53(6) (2012) 838-47.

[60] S. Sadayappan, J. Gulick, H. Osinska, L.A. Martin, H.S. Hahn, G.W. Dorn, R. Klevitsky, C.E. Seidman, J.G. Seidman, J. Robbins, Cardiac myosin-binding protein-C phosphorylation and cardiac function, Circ Res 97(11) (2005) 1156-63.

[61] J.S. Davis, C.L. Satorius, N.D. Epstein, Kinetic effects of myosin regulatory light chain phosphorylation on skeletal muscle contraction, Biophys J 83(1) (2002) 359-70.

[62] A. Persechini, J.T. Stull, R. Cooke, The effect of myosin phosphorylation on the contractile properties of skinned rabbit skeletal muscle fibers, J Biol Chem 260(13) (1985) 7951-4.

[63] H.L. Sweeney, J.T. Stull, Alteration of cross-bridge kinetics by myosin light chain phosphorylation in rabbit skeletal muscle: implications for regulation of actin-myosin interaction, Proc Natl Acad Sci U S A 87(1) (1990) 414-8.

[64] D. Szczesna, J. Zhao, M. Jones, G. Zhi, J. Stull, J.D. Potter, Phosphorylation of the regulatory light chains of myosin affects Ca2+ sensitivity of skeletal muscle contraction, J Appl Physiol (1985) 92(4) (2002) 1661-70.

[65] M.C. Olsson, J.R. Patel, D.P. Fitzsimons, J.W. Walker, R.L. Moss, Basal myosin light chain phosphorylation is a determinant of Ca2+ sensitivity of force and activation dependence of the kinetics of myocardial force development, Am J Physiol Heart Circ Physiol 287(6) (2004) H2712-8.

[66] I. Morano, F. Hofmann, M. Zimmer, J.C. Rüegg, The influence of P-light chain phosphorylation by myosin light chain kinase on the calcium sensitivity of chemically skinned heart fibres, FEBS Lett 189(2) (1985) 221-4.

[67] Y. Pi, D. Zhang, K.R. Kemnitz, H. Wang, J.W. Walker, Protein kinase C and A sites on troponin I regulate myofilament Ca2+ sensitivity and ATPase activity in the mouse myocardium, J Physiol 552(Pt 3) (2003) 845-57.

[68] A. Sanbe, J.G. Fewell, J. Gulick, H. Osinska, J. Lorenz, D.G. Hall, L.A. Murray, T.R. Kimball, S.A. Witt, J. Robbins, Abnormal cardiac structure and function in mice expressing nonphosphorylatable cardiac regulatory myosin light chain 2, J Biol Chem 274(30) (1999) 21085-94.

[69] H.L. Sweeney, J.T. Stull, Phosphorylation of myosin in permeabilized mammalian cardiac and skeletal muscle cells, Am J Physiol 250(4 Pt 1) (1986) C657-60.

[70] J.E. Stelzer, J.R. Patel, R.L. Moss, Acceleration of stretch activation in murine myocardium due to phosphorylation of myosin regulatory light chain, J Gen Physiol 128(3) (2006) 261-72.

[71] H.L. Sweeney, Z. Yang, G. Zhi, J.T. Stull, K.M. Trybus, Charge replacement near the phosphorylatable serine of the myosin regulatory light chain mimics aspects of phosphorylation, Proc Natl Acad Sci U S A 91(4) (1994) 1490-4.

[72] J.E. Stelzer, D.P. Fitzsimons, R.L. Moss, Ablation of myosin-binding protein-C accelerates force development in mouse myocardium, Biophys J 90(11) (2006) 4119-27.

[73] J.E. Stelzer, J.R. Patel, R.L. Moss, Protein kinase A-mediated acceleration of the stretch activation response in murine skinned myocardium is eliminated by ablation of cMyBP-C, Circ Res 99(8) (2006) 884-90.

[74] J.R. Patel, G.M. Diffee, X.P. Huang, R.L. Moss, Phosphorylation of myosin regulatory light chain eliminates force-dependent changes in relaxation rates in skeletal muscle, Biophys J 74(1) (1998) 360-8.

[75] P. Ding, J. Huang, P.K. Battiprolu, J.A. Hill, K.E. Kamm, J.T. Stull, Cardiac myosin light chain kinase is necessary for myosin regulatory light chain phosphorylation and cardiac performance in vivo, J Biol Chem 285(52) (2010) 40819-29.

[76] S.A. Warren, L.E. Briggs, H. Zeng, J. Chuang, E.I. Chang, R. Terada, M. Li, M.S. Swanson, S.H. Lecker, M.S. Willis, F.G. Spinale, J. Maupin-Furlowe, J.R. McMullen, R.L. Moss, H. Kasahara, Myosin light chain phosphorylation is critical for adaptation to cardiac stress, Circulation 126(22) (2012) 2575-88.

[77] F. Sheikh, K. Ouyang, S.G. Campbell, R.C. Lyon, J. Chuang, D. Fitzsimons, J. Tangney, C.G. Hidalgo, C.S. Chung, H. Cheng, N.D. Dalton, Y. Gu, H. Kasahara, M. Ghassemian, J.H. Omens, K.L. Peterson, H.L. Granzier, R.L. Moss, A.D. McCulloch, J. Chen, Mouse and computational models link Mlc2v dephosphorylation to altered myosin kinetics in early cardiac disease, J Clin Invest 122(4) (2012) 1209-21.

[78] G. Zhi, J.W. Ryder, J. Huang, P. Ding, Y. Chen, Y. Zhao, K.E. Kamm, J.T. Stull, Myosin light chain kinase and myosin phosphorylation effect frequency-dependent potentiation of skeletal muscle contraction, Proc Natl Acad Sci U S A 102(48) (2005) 17519-24.

[79] H. Ribolow, M. BARANY, Phosphorylation of tropomyosin in live frog muscle, Arch Biochem Biophys 179(2) (1977) 718-20.

[80] A. Mak, L.B. Smillie, M. Bárány, Specific phosphorylation at serine-283 of alpha tropomyosin from frog skeletal and rabbit skeletal and cardiac muscle, Proc Natl Acad Sci U S A 75(8) (1978) 3588-92.

[81] A.E. Messer, A.M. Jacques, S.B. Marston, Troponin phosphorylation and regulatory function in human heart muscle: dephosphorylation of Ser23/24 on troponin I could account for the contractile defect in end-stage heart failure, J Mol Cell Cardiol 42(1) (2007) 247-59.

[82] J. van der Velden, Z. Papp, R. Zaremba, N.M. Boontje, J.W. de Jong, V.J. Owen, P.B. Burton, P. Goldmann, K. Jaquet, G.J. Stienen, Increased Ca2+-sensitivity of the contractile apparatus in end-stage human heart failure results from altered phosphorylation of contractile proteins, Cardiovasc Res 57(1) (2003) 37-47.

[83] K. Bárány, M. Bárány, J.M. Gillis, M.J. Kushmerick, Myosin light chain phosphorylation during the contraction cycle of frog muscle, Fed Proc 39(5) (1980) 1547-51.

[84] D.H. Heeley, M.H. Watson, A.S. Mak, P. Dubord, L.B. Smillie, Effect of phosphorylation on the interaction and functional properties of rabbit striated muscle alpha alpha-tropomyosin, J Biol Chem 264(5) (1989) 2424-30.

[85] B.R. Nixon, B. Liu, B. Scellini, C. Tesi, N. Piroddi, O. Ogut, R.J. Solaro, M.T. Ziolo, P.M. Janssen, J.P. Davis, C. Poggesi, B.J. Biesiadecki, Tropomyosin Ser-283 pseudo-phosphorylation slows myofibril relaxation, Arch Biochem Biophys 535(1) (2013) 30-8.

[86] S.P. White, C. Cohen, G.N. Phillips, Structure of co-crystals of tropomyosin and troponin, Nature 325(6107) (1987) 826-8.

[87] A.S. Streng, D. de Boer, J. van der Velden, M.P. van Dieijen-Visser, W.K. Wodzig, Posttranslational modifications of cardiac troponin T: an overview, J Mol Cell Cardiol 63 (2013) 47-56.

[88] N.B. Gusev, A.B. Dobrovolskii, S.E. Severin, Isolation and some properties of troponin T kinase from rabbit skeletal muscle, Biochem J 189(2) (1980) 219-26.

[89] N.B. Gusev, N.V. Barskaya, A.D. Verin, I.V. Duzhenkova, Z.A. Khuchua, A.O. Zheltova, Some properties of cardiac troponin T structure, Biochem J 213(1) (1983) 123-9.

[90] J. Zhang, H. Zhang, S. Ayaz-Guner, Y.C. Chen, X. Dong, Q. Xu, Y. Ge, Phosphorylation, but not alternative splicing or proteolytic degradation, is conserved in human and mouse cardiac troponin T, Biochemistry 50(27) (2011) 6081-92.

[91] L.A. Walker, J.S. Walker, S.K. Ambler, P.M. Buttrick, Stage-specific changes in myofilament protein phosphorylation following myocardial infarction in mice, J Mol Cell Cardiol 48(6) (2010) 1180-6.

[92] B.S. Avner, K.M. Shioura, S.B. Scruggs, M. Grachoff, D.L. Geenen, D.L. Helseth, M. Farjah, P.H. Goldspink, R.J. Solaro, Myocardial infarction in mice alters sarcomeric function via post-translational protein modification, Mol Cell Biochem 363(1-2) (2012) 203-15.

[93] J. van der Velden, D. Merkus, V. de Beer, N. Hamdani, W.A. Linke, N.M. Boontje, G.J. Stienen, D.J. Duncker, Transmural heterogeneity of myofilament function and sarcomeric protein phosphorylation in remodeled myocardium of pigs with a recent myocardial infarction, Front Physiol 2 (2011) 83.

[94] R. Knöll, B. Buyandelger, M. Lab, The sarcomeric Z-disc and Z-discopathies, J Biomed Biotechnol 2011 (2011) 569628.

[95] P.M. Hwang, B.D. Sykes, Targeting the sarcomere to correct muscle function, Nat Rev Drug Discov 14(5) (2015) 313-28.

[96] W.G. Pyle, R.J. Solaro, At the crossroads of myocardial signaling: the role of Z-discs in intracellular signaling and cardiac function, Circ Res 94(3) (2004) 296-305.

[97] D. Frank, N. Frey, Cardiac Z-disc signaling network, J Biol Chem 286(12) (2011) 9897-904.

[98] P.K. Luther, The vertebrate muscle Z-disc: sarcomere anchor for structure and signalling, J Muscle Res Cell Motil 30(5-6) (2009) 171-85.

[99] M. Zheng, H. Cheng, I. Banerjee, J. Chen, ALP/Enigma PDZ-LIM domain proteins in the heart, J Mol Cell Biol 2(2) (2010) 96-102.

[100] D. Frank, C. Kuhn, H.A. Katus, N. Frey, The sarcomeric Z-disc: a nodal point in signalling and disease, J Mol Med (Berl) 84(6) (2006) 446-68.

[101] S. Lange, E. Ehler, M. Gautel, From A to Z and back? Multicompartment proteins in the sarcomere, Trends Cell Biol 16(1) (2006) 11-8.

[102] S. Kojic, E. Medeot, E. Guccione, H. Krmac, I. Zara, V. Martinelli, G. Valle, G. Faulkner, The Ankrd2 protein, a link between the sarcomere and the nucleus in skeletal muscle, J Mol Biol 339(2) (2004) 313-25.

[103] J. Heineke, H. Ruetten, C. Willenbockel, S.C. Gross, M. Naguib, A. Schaefer, T. Kempf, D. Hilfiker-Kleiner, P. Caroni, T. Kraft, R.A. Kaiser, J.D. Molkentin, H. Drexler, K.C. Wollert, Attenuation of cardiac remodeling after myocardial infarction by muscle LIM protein-calcineurin signaling at the sarcomeric Z-disc, Proc Natl Acad Sci U S A 102(5) (2005) 1655-60.

[104] W.G. Pyle, M.C. Hart, J.A. Cooper, M.P. Sumandea, P.P. de Tombe, R.J. Solaro, Actin capping protein: an essential element in protein kinase signaling to the myofilaments, Circ Res 90(12) (2002) 1299-306.

[105] F. Yang, D.L. Aiello, W.G. Pyle, Cardiac myofilament regulation by protein phosphatase type 1alpha and CapZ, Biochem Cell Biol 86(1) (2008) 70-8.

[106] Y. Ivarsson, Plasticity of PDZ domains in ligand recognition and signaling, FEBS Lett 586(17) (2012) 2638-47.

[107] J.L. Kadrmas, M.C. Beckerle, The LIM domain: from the cytoskeleton to the nucleus, Nat Rev Mol Cell Biol 5(11) (2004) 920-31.

[108] R.Y. Wu, G.N. Gill, LIM domain recognition of a tyrosine-containing tight turn, J Biol Chem 269(40) (1994) 25085-90.

[109] S. Kuroda, C. Tokunaga, Y. Kiyohara, O. Higuchi, H. Konishi, K. Mizuno, G.N. Gill, U. Kikkawa, Protein-protein interaction of zinc finger LIM domains with protein kinase C, J Biol Chem 271(49) (1996) 31029-32.

[110] G. Faulkner, A. Pallavicini, E. Formentin, A. Comelli, C. Ievolella, S. Trevisan, G. Bortoletto, P. Scannapieco, M. Salamon, V. Mouly, G. Valle, G. Lanfranchi, ZASP: a new Z-band alternatively spliced PDZ-motif protein, J Cell Biol 146(2) (1999) 465-75.

[111] R. Passier, J.A. Richardson, E.N. Olson, Oracle, a novel PDZ-LIM domain protein expressed in heart and skeletal muscle, Mech Dev 92(2) (2000) 277-84.

[112] Q. Zhou, P. Ruiz-Lozano, M.E. Martone, J. Chen, Cypher, a striated muscle-restricted PDZ and LIM domain-containing protein, binds to alpha-actinin-2 and protein kinase C, J Biol Chem 274(28) (1999) 19807-13.

[113] Y. Au, R.A. Atkinson, R. Guerrini, G. Kelly, C. Joseph, S.R. Martin, F.W. Muskett, A. Pallavicini, G. Faulkner, A. Pastore, Solution structure of ZASP PDZ domain; implications for sarcomere ultrastructure and enigma family redundancy, Structure 12(4) (2004) 611-22.

[114] N. Nakagawa, M. Hoshijima, M. Oyasu, N. Saito, K. Tanizawa, S. Kuroda, ENH, containing PDZ and LIM domains, heart/skeletal muscle-specific protein, associates with cytoskeletal proteins through the PDZ domain, Biochem Biophys Res Commun 272(2) (2000) 505-12.

[115] P. von Nandelstadh, M. Ismail, C. Gardin, H. Suila, I. Zara, A. Belgrano, G. Valle, O. Carpen, G. Faulkner, A class III PDZ binding motif in the myotilin and FATZ families binds enigma family proteins: a common link for Z-disc myopathies, Mol Cell Biol 29(3) (2009) 822-34.

[116] H. Cheng, K. Kimura, A.K. Peter, L. Cui, K. Ouyang, T. Shen, Y. Liu, Y. Gu, N.D. Dalton, S.M. Evans, K.U. Knowlton, K.L. Peterson, J. Chen, Loss of enigma homolog protein results in dilated cardiomyopathy, Circ Res 107(3) (2010) 348-56.

[117] M. Zheng, H. Cheng, X. Li, J. Zhang, L. Cui, K. Ouyang, L. Han, T. Zhao, Y. Gu, N.D. Dalton, M.L. Bang, K.L. Peterson, J. Chen, Cardiac-specific ablation of Cypher leads to a severe form of dilated cardiomyopathy with premature death, Hum Mol Genet 18(4) (2009) 701-13.

[118] P.M. Guy, D.A. Kenny, G.N. Gill, The PDZ domain of the LIM protein enigma binds to beta-tropomyosin, Mol Biol Cell 10(6) (1999) 1973-84.

[119] C. Lin, X. Guo, S. Lange, J. Liu, K. Ouyang, X. Yin, L. Jiang, Y. Cai, Y. Mu, F. Sheikh, S. Ye, J. Chen, Y. Ke, H. Cheng, Cypher/ZASP is a novel A-kinase anchoring protein, J Biol Chem 288(41) (2013) 29403-13.

[120] A.D. Maturana, S. Wälchli, M. Iwata, S. Ryser, J. Van Lint, M. Hoshijima, W. Schlegel, Y. Ikeda, K. Tanizawa, S. Kuroda, Enigma homolog 1 scaffolds protein kinase D1 to regulate the activity of the cardiac L-type voltage-gated calcium channel, Cardiovasc Res 78(3) (2008) 458-65.

[121] Y. Yan, O. Tsukamoto, A. Nakano, H. Kato, H. Kioka, N. Ito, S. Higo, S. Yamazaki, Y. Shintani, K. Matsuoka, Y. Liao, H. Asanuma, M. Asakura, K. Takafuji, T. Minamino, Y. Asano, M. Kitakaze, S. Takashima, Augmented AMPK activity inhibits cell migration by phosphorylating the novel substrate Pdlim5, Nat Commun 6 (2015) 6137.

[122] T. Arimura, N. Inagaki, T. Hayashi, D. Shichi, A. Sato, K. Hinohara, M. Vatta, J.A. Towbin, T. Chikamori, A. Yamashina, A. Kimura, Impaired binding of ZASP/Cypher with phosphoglucomutase 1 is associated with dilated cardiomyopathy, Cardiovasc Res 83(1) (2009) 80-8.

[123] A.D. Maturana, N. Nakagawa, N. Yoshimoto, K. Tatematsu, M. Hoshijima, K. Tanizawa, S. Kuroda, LIM domains regulate protein kinase C activity: a novel molecular function, Cell Signal 23(5) (2011) 928-34.

[124] J. Ito, M. Iijima, N. Yoshimoto, T. Niimi, S. Kuroda, A.D. Maturana, Scaffold protein enigma homolog activates CREB whereas a short splice variant prevents CREB activation in cardiomyocytes, Cell Signal 27(12) (2015) 2425-33.

[125] T. Arimura, T. Hayashi, H. Terada, S.Y. Lee, Q. Zhou, M. Takahashi, K. Ueda, T. Nouchi, S. Hohda, M. Shibutani, M. Hirose, J. Chen, J.E. Park, M. Yasunami, H. Hayashi, A. Kimura, A Cypher/ZASP mutation associated with dilated cardiomyopathy alters the binding affinity to protein kinase C, J Biol Chem 279(8) (2004) 6746-52.

[126] T. Yamazaki, S. Wälchli, T. Fujita, S. Ryser, M. Hoshijima, W. Schlegel, S. Kuroda, A.D. Maturana, Splice variants of enigma homolog, differentially expressed during heart development, promote or prevent hypertrophy, Cardiovasc Res 86(3) (2010) 374-82.

[127] W.G. Pyle, G. La Rotta, P.P. de Tombe, M.P. Sumandea, R.J. Solaro, Control of cardiac myofilament activation and PKC-betaII signaling through the actin capping protein, CapZ, J Mol Cell Cardiol 41(3) (2006) 537-43.

[128] Y. Ke, L. Wang, W.G. Pyle, P.P. de Tombe, R.J. Solaro, Intracellular localization and functional effects of P21-activated kinase-1 (Pak1) in cardiac myocytes, Circ Res 94(2) (2004) 194-200.

[129] E.J. Benjamin, M.J. Blaha, S.E. Chiuve, M. Cushman, S.R. Das, R. Deo, S.D. de Ferranti, J. Floyd, M. Fornage, C. Gillespie, C.R. Isasi, M.C. Jiménez, L.C. Jordan, S.E. Judd, D. Lackland, J.H. Lichtman, L. Lisabeth, S. Liu, C.T. Longenecker, R.H. Mackey, K. Matsushita, D. Mozaffarian, M.E. Mussolino, K. Nasir, R.W. Neumar, L. Palaniappan, D.K. Pandey, R.R. Thiagarajan, M.J. Reeves, M. Ritchey, C.J. Rodriguez, G.A. Roth, W.D. Rosamond, C. Sasson, A. Towfighi, C.W. Tsao, M.B. Turner, S.S. Virani, J.H. Voeks, J.Z. Willey, J.T. Wilkins, J.H. Wu, H.M. Alger, S.S. Wong, P. Muntner, A.H.A.S.C.a.S.S. Subcommittee, Heart Disease and Stroke Statistics-2017 Update: A Report From the American Heart Association, Circulation 135(10) (2017) e146-e603.

[130] B. Ziaeian, G.C. Fonarow, Epidemiology and aetiology of heart failure, Nat Rev Cardiol 13(6) (2016) 368-78.

[131] A.L. Bui, T.B. Horwich, G.C. Fonarow, Epidemiology and risk profile of heart failure, Nat Rev Cardiol 8(1) (2011) 30-41.

[132] S.B. Marston, P.P. de Tombe, Troponin phosphorylation and myofilament Ca2+-sensitivity in heart failure: increased or decreased?, J Mol Cell Cardiol 45(5) (2008) 603-7.

[133] R.E. Hershberger, D.J. Hedges, A. Morales, Dilated cardiomyopathy: the complexity of a diverse genetic architecture, Nat Rev Cardiol 10(9) (2013) 531-47.

[134] M. Luo, M.E. Anderson, Mechanisms of altered Ca^{2+} handling in heart failure, Circ Res 113(6) (2013) 690-708.

[135] E.D. Pagani, A.A. Alousi, A.M. Grant, T.M. Older, S.W. Dziuban, P.D. Allen, Changes in myofibrillar content and Mg-ATPase activity in ventricular tissues from patients with heart failure caused by coronary artery disease, cardiomyopathy, or mitral valve insufficiency, Circ Res 63(2) (1988) 380-5.

[136] R.J. Hajjar, J.K. Gwathmey, Cross-bridge dynamics in human ventricular myocardium. Regulation of contractility in the failing heart, Circulation 86(6) (1992) 1819-26.

[137] J. van Der Velden, L.J. Klein, R. Zaremba, N.M. Boontje, M.A. Huybregts, W. Stooker, L. Eijsman, J.W. de Jong, C.A. Visser, F.C. Visser, G.J. Stienen, Effects of calcium, inorganic phosphate, and pH on isometric force in single skinned cardiomyocytes from donor and failing human hearts, Circulation 104(10) (2001) 1140-6.

[138] R.J. Hajjar, R.H. Schwinger, U. Schmidt, C.S. Kim, D. Lebeche, A.A. Doye, J.K. Gwathmey, Myofilament calcium regulation in human myocardium, Circulation 101(14) (2000) 1679-85.

[139] M.R. Wolff, S.H. Buck, S.W. Stoker, M.L. Greaser, R.M. Mentzer, Myofibrillar calcium sensitivity of isometric tension is increased in human dilated cardiomyopathies: role of altered beta-adrenergically mediated protein phosphorylation, J Clin Invest 98(1) (1996) 167-76.

[140] J. van der Velden, D. Merkus, B.R. Klarenbeek, A.T. James, N.M. Boontje, D.H. Dekkers, G.J. Stienen, J.M. Lamers, D.J. Duncker, Alterations in myofilament function contribute to left ventricular dysfunction in pigs early after myocardial infarction, Circ Res 95(11) (2004) e85-95.

[141] P. Haynes, K.E. Nava, B.A. Lawson, C.S. Chung, M.I. Mitov, S.G. Campbell, A.J. Stromberg, S. Sadayappan, M.R. Bonnell, C.W. Hoopes, K.S. Campbell, Transmural heterogeneity of cellular level power output is reduced in human heart failure, J Mol Cell Cardiol 72 (2014) 1-8.

[142] M.J. Lohse, S. Engelhardt, T. Eschenhagen, What is the role of beta-adrenergic signaling in heart failure?, Circ Res 93(10) (2003) 896-906.

[143] J. Heijman, M. Dewenter, A. El-Armouche, D. Dobrev, Function and regulation of serine/threonine phosphatases in the healthy and diseased heart, J Mol Cell Cardiol 64 (2013) 90-8.

[144] G.S. Bodor, A.E. Oakeley, P.D. Allen, D.L. Crimmins, J.H. Ladenson, P.A. Anderson, Troponin I phosphorylation in the normal and failing adult human heart, Circulation 96(5) (1997) 1495-500.

[145] A. Knott, I. Purcell, S. Marston, In vitro motility analysis of thin filaments from failing and non-failing human heart: troponin from failing human hearts induces slower filament sliding and higher Ca(2+) sensitivity, J Mol Cell Cardiol 34(4) (2002) 469-82.

[146] D.R. Zakhary, C.S. Moravec, R.W. Stewart, M. Bond, Protein kinase A (PKA)-dependent troponin-I phosphorylation and PKA regulatory subunits are decreased in human dilated cardiomyopathy, Circulation 99(4) (1999) 505-10.

[147] I. Morano, K. Hädicke, H. Haase, M. Böhm, E. Erdmann, M.C. Schaub, Changes in essential myosin light chain isoform expression provide a molecular basis for isometric force regulation in the failing human heart, J Mol Cell Cardiol 29(4) (1997) 1177-87.

[148] A. El-Armouche, L. Pohlmann, S. Schlossarek, J. Starbatty, Y.H. Yeh, S. Nattel, D. Dobrev, T. Eschenhagen, L. Carrier, Decreased phosphorylation levels of cardiac myosin-binding protein-C in human and experimental heart failure, J Mol Cell Cardiol 43(2) (2007) 223-9.

[149] R. Zaremba, D. Merkus, N. Hamdani, J.M. Lamers, W.J. Paulus, C. Dos Remedios, D.J. Duncker, G.J. Stienen, J. van der Velden, Quantitative analysis of myofilament protein phosphorylation in small cardiac biopsies, Proteomics Clin Appl 1(10) (2007) 1285-90.

[150] A.M. Jacques, O. Copeland, A.E. Messer, C.E. Gallon, K. King, W.J. McKenna, V.T. Tsang, S.B. Marston, Myosin binding protein C phosphorylation in normal, hypertrophic and failing human heart muscle, J Mol Cell Cardiol 45(2) (2008) 209-16.

[151] J. van der Velden, Z. Papp, N.M. Boontje, R. Zaremba, J.W. de Jong, P.M. Janssen, G. Hasenfuss, G.J. Stienen, Myosin light chain composition in non-failing donor and end-stage failing human ventricular myocardium, Adv Exp Med Biol 538 (2003) 3-15.

[152] N. Hamdani, M. de Waard, A.E. Messer, N.M. Boontje, V. Kooij, S. van Dijk, A. Versteilen, R. Lamberts, D. Merkus, C. Dos Remedios, D.J. Duncker, A. Borbely, Z. Papp, W. Paulus, G.J. Stienen, S.B. Marston, J. van der Velden, Myofilament dysfunction in cardiac disease from mice to men, J Muscle Res Cell Motil 29(6-8) (2008) 189-201.

[153] J.G. Ryall, J.D. Schertzer, G.S. Lynch, Cellular and molecular mechanisms underlying age-related skeletal muscle wasting and weakness, Biogerontology 9(4) (2008) 213-28.

[154] Y. Rolland, S. Czerwinski, G. Abellan Van Kan, J.E. Morley, M. Cesari, G. Onder, J. Woo, R. Baumgartner, F. Pillard, Y. Boirie, W.M. Chumlea, B. Vellas, Sarcopenia: its assessment, etiology, pathogenesis, consequences and future perspectives, J Nutr Health Aging 12(7) (2008) 433-50.

[155] S. Cohen, J.A. Nathan, A.L. Goldberg, Muscle wasting in disease: molecular mechanisms and promising therapies, Nat Rev Drug Discov 14(1) (2015) 58-74.

[156] I. Janssen, S.B. Heymsfield, R. Ross, Low relative skeletal muscle mass (sarcopenia) in older persons is associated with functional impairment and physical disability, J Am Geriatr Soc 50(5) (2002) 889-96.

[157] R. Roubenoff, Sarcopenia and its implications for the elderly, Eur J Clin Nutr 54 Suppl 3 (2000) S40-7.

[158] I. Janssen, D.S. Shepard, P.T. Katzmarzyk, R. Roubenoff, The healthcare costs of sarcopenia in the United States, J Am Geriatr Soc 52(1) (2004) 80-5.

[159] J.M. Wiener, J. Tilly, Population ageing in the United States of America: implications for public programmes, Int J Epidemiol 31(4) (2002) 776-81.

[160] M.G. Bemben, B.H. Massey, D.A. Bemben, J.E. Misner, R.A. Boileau, Isometric muscle force production as a function of age in healthy 20- to 74-yr-old men, Med Sci Sports Exerc 23(11) (1991) 1302-10.

[161] S.V. Brooks, J.A. Faulkner, Skeletal muscle weakness in old age: underlying mechanisms, Med Sci Sports Exerc 26(4) (1994) 432-9.

[162] L. Larsson, G. Grimby, J. Karlsson, Muscle strength and speed of movement in relation to age and muscle morphology, J Appl Physiol Respir Environ Exerc Physiol 46(3) (1979) 451-6.

[163] M.V. Narici, M. Bordini, P. Cerretelli, Effect of aging on human adductor pollicis muscle function, J Appl Physiol (1985) 71(4) (1991) 1277-81.

[164] A.A. Vandervoort, A.J. McComas, Contractile changes in opposing muscles of the human ankle joint with aging, J Appl Physiol (1985) 61(1) (1986) 361-7.

[165] J. Lexell, Human aging, muscle mass, and fiber type composition, J Gerontol A Biol Sci Med Sci 50 Spec No (1995) 11-6.

[166] J. Lexell, C.C. Taylor, M. Sjöström, What is the cause of the ageing atrophy? Total number, size and proportion of different fiber types studied in whole vastus lateralis muscle from 15- to 83-year-old men, J Neurol Sci 84(2-3) (1988) 275-94.

[167] E.B. Lushaj, J.K. Johnson, D. McKenzie, J.M. Aiken, Sarcopenia accelerates at advanced ages in Fisher 344xBrown Norway rats, J Gerontol A Biol Sci Med Sci 63(9) (2008) 921-7.

[168] S. Ciciliot, A.C. Rossi, K.A. Dyar, B. Blaauw, S. Schiaffino, Muscle type and fiber type specificity in muscle wasting, Int J Biochem Cell Biol 45(10) (2013) 2191-9.

[169] L.V. Thompson, Effects of age and training on skeletal muscle physiology and performance, Phys Ther 74(1) (1994) 71-81.

[170] F.M. Purves-Smith, N. Sgarioto, R.T. Hepple, Fiber typing in aging muscle, Exerc Sport Sci Rev 42(2) (2014) 45-52.

[171] S.A. Jubrias, I.R. Odderson, P.C. Esselman, K.E. Conley, Decline in isokinetic force with age: muscle cross-sectional area and specific force, Pflugers Arch 434(3) (1997) 246-53.

[172] S.A. Bruce, D. Newton, R.C. Woledge, Effect of age on voluntary force and cross-sectional area of human adductor pollicis muscle, Q J Exp Physiol 74(3) (1989) 359-62.

[173] H. Klitgaard, M. Mantoni, S. Schiaffino, S. Ausoni, L. Gorza, C. Laurent-Winter, P. Schnohr, B. Saltin, Function, morphology and protein expression of ageing skeletal muscle: a cross-sectional study of elderly men with different training backgrounds, Acta Physiol Scand 140(1) (1990) 41-54.

[174] T.J. Overend, D.A. Cunningham, J.F. Kramer, M.S. Lefcoe, D.H. Paterson, Knee extensor and knee flexor strength: cross-sectional area ratios in young and elderly men, J Gerontol 47(6) (1992) M204-10.

[175] A.M. Payne, S.L. Dodd, C. Leeuwenburgh, Life-long calorie restriction in Fischer 344 rats attenuates age-related loss in skeletal muscle-specific force and reduces extracellular space, J Appl Physiol (1985) 95(6) (2003) 2554-62.

[176] M.G. Urbanchek, E.B. Picken, L.K. Kalliainen, W.M. Kuzon, Specific force deficit in skeletal muscles of old rats is partially explained by the existence of denervated muscle fibers, J Gerontol A Biol Sci Med Sci 56(5) (2001) B191-7.

[177] L.V. Thompson, M. Brown, Age-related changes in contractile properties of single skeletal fibers from the soleus muscle, J Appl Physiol (1985) 86(3) (1999) 881-6.

[178] D.A. Lowe, D.D. Thomas, L.V. Thompson, Force generation, but not myosin ATPase activity, declines with age in rat muscle fibers, Am J Physiol Cell Physiol 283(1) (2002) C187-92.

[179] L. Larsson, X. Li, W.R. Frontera, Effects of aging on shortening velocity and myosin isoform composition in single human skeletal muscle cells, Am J Physiol 272(2 Pt 1) (1997) C638-49.

[180] F. Yu, M. Hedström, A. Cristea, N. Dalén, L. Larsson, Effects of ageing and gender on contractile properties in human skeletal muscle and single fibres, Acta Physiol (Oxf) 190(3) (2007) 229-41.

[181] P. Balagopal, O.E. Rooyackers, D.B. Adey, P.A. Ades, K.S. Nair, Effects of aging on in vivo synthesis of skeletal muscle myosin heavy-chain and sarcoplasmic protein in humans, Am J Physiol 273(4 Pt 1) (1997) E790-800.

[182] G. D'Antona, M.A. Pellegrino, R. Adami, R. Rossi, C.N. Carlizzi, M. Canepari, B. Saltin, R. Bottinelli, The effect of ageing and immobilization on structure and function of human skeletal muscle fibres, J Physiol 552(Pt 2) (2003) 499-511.

[183] J.O. Marx, W.J. Kraemer, B.C. Nindl, L. Larsson, Effects of aging on human skeletal muscle myosin heavy-chain mRNA content and protein isoform expression, J Gerontol A Biol Sci Med Sci 57(6) (2002) B232-8.

[184] P. Doran, K. O'Connell, J. Gannon, M. Kavanagh, K. Ohlendieck, Opposite pathobiochemical fate of pyruvate kinase and adenylate kinase in aged rat skeletal muscle as revealed by proteomic DIGE analysis, Proteomics 8(2) (2008) 364-77.

[185] C. Gelfi, A. Vigano, M. Ripamonti, A. Pontoglio, S. Begum, M.A. Pellegrino, B. Grassi, R. Bottinelli, R. Wait, P. Cerretelli, The human muscle proteome in aging, J Proteome Res 5(6) (2006) 1344-53.

[186] K. O'Connell, J. Gannon, P. Doran, K. Ohlendieck, Proteomic profiling reveals a severely perturbed protein expression pattern in aged skeletal muscle, Int J Mol Med 20(2) (2007) 145-53.

[187] D.F. Chaves, P.C. Carvalho, D.B. Lima, H. Nicastro, F.M. Lorenzeti, M. Siqueira-Filho, S.M. Hirabara, P.H. Alves, J.J. Moresco, J.R. Yates, A.H. Lancha, Comparative proteomic analysis

of the aging soleus and extensor digitorum longus rat muscles using TMT labeling and mass spectrometry, J Proteome Res 12(10) (2013) 4532-46.

[188] I. Piec, A. Listrat, J. Alliot, C. Chambon, R.G. Taylor, D. Bechet, Differential proteome analysis of aging in rat skeletal muscle, FASEB J 19(9) (2005) 1143-5.

[189] J.H. Kim, W.S. Torgerud, K.H. Mosser, H. Hirai, S. Watanabe, A. Asakura, L.V. Thompson, Myosin light chain 3f attenuates age-induced decline in contractile velocity in MHC type II single muscle fibers, Aging Cell 11(2) (2012) 203-12.

[190] E. Prochniewicz, D.D. Thomas, L.V. Thompson, Age-related decline in actomyosin function, J Gerontol A Biol Sci Med Sci 60(4) (2005) 425-31.

[191] M.S. Miller, N.G. Bedrin, D.M. Callahan, M.J. Previs, M.E. Jennings, P.A. Ades, D.W. Maughan, B.M. Palmer, M.J. Toth, Age-related slowing of myosin actin cross-bridge kinetics is sex specific and predicts decrements in whole skeletal muscle performance in humans, J Appl Physiol (1985) 115(7) (2013) 1004-14.

[192] R. Aebersold, M. Mann, Mass spectrometry-based proteomics, Nature 422(6928) (2003) 198-207.

[193] Y. Zhang, B.R. Fonslow, B. Shan, M.C. Baek, J.R. Yates, Protein analysis by shotgun/bottom-up proteomics, Chem Rev 113(4) (2013) 2343-94.

[194] J.R. Yates, C.I. Ruse, A. Nakorchevsky, Proteomics by mass spectrometry: approaches, advances, and applications, Annu Rev Biomed Eng 11 (2009) 49-79.

[195] M.P. Washburn, D. Wolters, J.R. Yates, Large-scale analysis of the yeast proteome by multidimensional protein identification technology, Nat Biotechnol 19(3) (2001) 242-7.

[196] T. Hunter, The age of crosstalk: phosphorylation, ubiquitination, and beyond, Mol Cell 28(5) (2007) 730-8.

[197] N. Siuti, N.L. Kelleher, Decoding protein modifications using top-down mass spectrometry, Nat Methods 4(10) (2007) 817-21.

[198] H. Zhang, Y. Ge, Comprehensive analysis of protein modifications by top-down mass spectrometry, Circ Cardiovasc Genet 4(6) (2011) 711.

[199] Z.R. Gregorich, Y.H. Chang, Y. Ge, Proteomics in heart failure: top-down or bottom-up?, Pflugers Arch 466(6) (2014) 1199-209.

[200] Z.R. Gregorich, Y. Ge, Top-down proteomics in health and disease: challenges and opportunities, Proteomics 14(10) (2014) 1195-210.

[201] S. Ayaz-Guner, J. Zhang, L. Li, J.W. Walker, Y. Ge, In vivo phosphorylation site mapping in mouse cardiac troponin I by high resolution top-down electron capture dissociation mass spectrometry: Ser22/23 are the only sites basally phosphorylated, Biochemistry 48(34) (2009) 8161-70.

[202] X. Dong, C.A. Sumandea, Y.C. Chen, M.L. Garcia-Cazarin, J. Zhang, C.W. Balke, M.P. Sumandea, Y. Ge, Augmented phosphorylation of cardiac troponin I in hypertensive heart failure, J Biol Chem 287(2) (2012) 848-57.

[203] R. Sancho Solis, Y. Ge, J.W. Walker, Single amino acid sequence polymorphisms in rat cardiac troponin revealed by top-down tandem mass spectrometry, J Muscle Res Cell Motil 29(6-8) (2008) 203-12.

[204] V. Zabrouskov, Y. Ge, J. Schwartz, J.W. Walker, Unraveling molecular complexity of phosphorylated human cardiac troponin I by top down electron capture dissociation/electron transfer dissociation mass spectrometry, Mol Cell Proteomics 7(10) (2008) 1838-49.

[205] J. Zhang, X. Dong, T.A. Hacker, Y. Ge, Deciphering modifications in swine cardiac troponin I by top-down high-resolution tandem mass spectrometry, J Am Soc Mass Spectrom 21(6) (2010) 940-8.

[206] L.M. Smith, N.L. Kelleher, C.f.T.D. Proteomics, Proteoform: a single term describing protein complexity, Nat Methods 10(3) (2013) 186-7.

[207] R.A. Zubarev, D.M. Horn, E.K. Fridriksson, N.L. Kelleher, N.A. Kruger, M.A. Lewis, B.K. Carpenter, F.W. McLafferty, Electron capture dissociation for structural characterization of multiply charged protein cations, Anal Chem 72(3) (2000) 563-73.

[208] J.E. Syka, J.J. Coon, M.J. Schroeder, J. Shabanowitz, D.F. Hunt, Peptide and protein sequence analysis by electron transfer dissociation mass spectrometry, Proc Natl Acad Sci U S A 101(26) (2004) 9528-33.

[209] Y. Ge, B.G. Lawhorn, M. ElNaggar, E. Strauss, J.H. Park, T.P. Begley, F.W. McLafferty, Top down characterization of larger proteins (45 kDa) by electron capture dissociation mass spectrometry, J Am Chem Soc 124(4) (2002) 672-8.

[210] H.J. Cooper, K. Håkansson, A.G. Marshall, The role of electron capture dissociation in biomolecular analysis, Mass Spectrom Rev 24(2) (2005) 201-22.

[211] S.M. Eliuk, D. Maltby, B. Panning, A.L. Burlingame, High resolution electron transfer dissociation studies of unfractionated intact histones from murine embryonic stem cells using on-line capillary LC separation: determination of abundant histone isoforms and post-translational modifications, Mol Cell Proteomics 9(5) (2010) 824-37.

[212] Z. Tian, N. Tolić, R. Zhao, R.J. Moore, S.M. Hengel, E.W. Robinson, D.L. Stenoien, S. Wu, R.D. Smith, L. Paša-Tolić, Enhanced top-down characterization of histone post-translational modifications, Genome Biol 13(10) (2012) R86.

[213] Y. Ge, I.N. Rybakova, Q. Xu, R.L. Moss, Top-down high-resolution mass spectrometry of cardiac myosin binding protein C revealed that truncation alters protein phosphorylation state, Proc Natl Acad Sci U S A 106(31) (2009) 12658-63.

[214] V. Zabrouskov, X. Han, E. Welker, H. Zhai, C. Lin, K.J. van Wijk, H.A. Scheraga, F.W. McLafferty, Stepwise deamidation of ribonuclease A at five sites determined by top down mass spectrometry, Biochemistry 45(3) (2006) 987-92.

[215] M.T. Mazur, H.L. Cardasis, D.S. Spellman, A. Liaw, N.A. Yates, R.C. Hendrickson, Quantitative analysis of intact apolipoproteins in human HDL by top-down differential mass spectrometry, Proc Natl Acad Sci U S A 107(17) (2010) 7728-33.

[216] R.L. Edwards, P. Griffiths, J. Bunch, H.J. Cooper, Top-down proteomics and direct surface sampling of neonatal dried blood spots: diagnosis of unknown hemoglobin variants, J Am Soc Mass Spectrom 23(11) (2012) 1921-30.

[217] D. Coelho Graca, P. Lescuyer, L. Clerici, Y.O. Tsybin, R. Hartmer, M. Meyer, K. Samii, D.F. Hochstrasser, A. Scherl, Electron transfer dissociation mass spectrometry of hemoglobin on clinical samples, J Am Soc Mass Spectrom 23(10) (2012) 1750-6.

[218] J. Zhang, M.J. Guy, H.S. Norman, Y.C. Chen, Q. Xu, X. Dong, H. Guner, S. Wang, T. Kohmoto, K.H. Young, R.L. Moss, Y. Ge, Top-down quantitative proteomics identified phosphorylation of cardiac troponin I as a candidate biomarker for chronic heart failure, J Proteome Res 10(9) (2011) 4054-65.

[219] C.R. Borges, P.E. Oran, S. Buddi, J.W. Jarvis, M.R. Schaab, D.S. Rehder, S.P. Rogers, T. Taylor, R.W. Nelson, Building multidimensional biomarker views of type 2 diabetes on the basis of protein microheterogeneity, Clin Chem 57(5) (2011) 719-28.

[220] C. Ansong, S. Wu, D. Meng, X. Liu, H.M. Brewer, B.L. Deatherage Kaiser, E.S. Nakayasu, J.R. Cort, P. Pevzner, R.D. Smith, F. Heffron, J.N. Adkins, L. Pasa-Tolic, Top-down proteomics reveals a unique protein S-thiolation switch in Salmonella Typhimurium in response to infection-like conditions, Proc Natl Acad Sci U S A 110(25) (2013) 10153-8.

[221] N. Burnaevskiy, T.G. Fox, D.A. Plymire, J.M. Ertelt, B.A. Weigele, A.S. Selyunin, S.S. Way, S.M. Patrie, N.M. Alto, Proteolytic elimination of N-myristoyl modifications by the Shigella virulence factor IpaJ, Nature 496(7443) (2013) 106-9.

[222] J. Chamot-Rooke, G. Mikaty, C. Malosse, M. Soyer, A. Dumont, J. Gault, A.F. Imhaus, P. Martin, M. Trellet, G. Clary, P. Chafey, L. Camoin, M. Nilges, X. Nassif, G. Dumenil, Posttranslational modification of pili upon cell contact triggers N. meningitidis dissemination, Science 331(6018) (2011) 778-82.

[223] K.S. Molnar, N.M. Karabacak, J.L. Johnson, Q. Wang, A. Tiwari, L.J. Hayward, S.J. Coales, Y. Hamuro, J.N. Agar, A common property of amyotrophic lateral sclerosis-associated variants: destabilization of the copper/zinc superoxide dismutase electrostatic loop, J Biol Chem 284(45) (2009) 30965-73.

[224] J.R. Auclair, J.L. Johnson, Q. Liu, J.P. Salisbury, M.S. Rotunno, G.A. Petsko, D. Ringe, R.H. Brown, Jr., D.A. Bosco, J.N. Agar, Post-translational modification by cysteine protects Cu/Zn-superoxide dismutase from oxidative damage, Biochemistry 52(36) (2013) 6137-44.

[225] J.R. Auclair, K.J. Boggio, G.A. Petsko, D. Ringe, J.N. Agar, Strategies for stabilizing superoxide dismutase (SOD1), the protein destabilized in the most common form of familial amyotrophic lateral sclerosis, Proc Natl Acad Sci U S A 107(50) (2010) 21394-9.

[226] T. Cabras, E. Pisano, C. Montaldo, M.R. Giuca, F. Iavarone, G. Zampino, M. Castagnola, I. Messana, Significant modifications of the salivary proteome potentially associated with complications of Down syndrome revealed by top-down proteomics, Mol Cell Proteomics 12(7) (2013) 1844-52.

[227] L. Zhang, M.A. Freitas, J. Wickham, M.R. Parthun, M.I. Klisovic, G. Marcucci, J.C. Byrd, Differential expression of histone post-translational modifications in acute myeloid and chronic lymphocytic leukemia determined by high-pressure liquid chromatography and mass spectrometry, J Am Soc Mass Spectrom 15(1) (2004) 77-86.

[228] C. Desiderio, L. D'Angelo, D.V. Rossetti, F. Iavarone, B. Giardina, M. Castagnola, L. Massimi, G. Tamburrini, C. Di Rocco, Cerebrospinal fluid top-down proteomics evidenced the potential biomarker role of LVV- and VV-hemorphin-7 in posterior cranial fossa pediatric brain tumors, Proteomics 12(13) (2012) 2158-66.

[229] W.M. Hardesty, M.C. Kelley, D. Mi, R.L. Low, R.M. Caprioli, Protein signatures for survival and recurrence in metastatic melanoma, J Proteomics 74(7) (2011) 1002-14.

[230] R. Theberge, G. Infusini, W. Tong, M.E. McComb, C.E. Costello, Top-Down Analysis of Small Plasma Proteins Using an LTQ-Orbitrap. Potential for Mass Spectrometry-Based Clinical Assays for Transthyretin and Hemoglobin, Int J Mass Spectrom 300(2-3) (2011) 130-142.

[231] Z.A. McCrossan, R. Billeter, E. White, Transmural changes in size, contractile and electrical properties of SHR left ventricular myocytes during compensated hypertrophy, Cardiovasc Res 63(2) (2004) 283-92.

[232] O. Cazorla, S. Szilagyi, J.Y. Le Guennec, G. Vassort, A. Lacampagne, Transmural stretch-dependent regulation of contractile properties in rat heart and its alteration after myocardial infarction, FASEB J 19(1) (2005) 88-90.

[233] S.G. Campbell, P. Haynes, W. Kelsey Snapp, K.E. Nava, K.S. Campbell, Altered ventricular torsion and transmural patterns of myocyte relaxation precede heart failure in aging F344 rats, Am J Physiol Heart Circ Physiol 305(5) (2013) H676-86.

[234] Q. Lou, V.V. Fedorov, A.V. Glukhov, N. Moazami, V.G. Fast, I.R. Efimov, Transmural heterogeneity and remodeling of ventricular excitation-contraction coupling in human heart failure, Circulation 123(17) (2011) 1881-90.

[235] G. de Simone, R.B. Devereux, M.J. Koren, G.A. Mensah, P.N. Casale, J.H. Laragh, Midwall left ventricular mechanics. An independent predictor of cardiovascular risk in arterial hypertension, Circulation 93(2) (1996) 259-65.

[236] K. Wachtell, E. Gerdts, V. Palmieri, M.H. Olsen, M.S. Nieminen, V. Papademetriou, K. Boman, B. Dahlöf, G.P. Aurigemma, J.E. Rokkedal, R.B. Devereux, In-treatment midwall and endocardial fractional shortening predict cardiovascular outcome in hypertensive patients with preserved baseline systolic ventricular function: the Losartan Intervention For Endpoint reduction study, J Hypertens 28(7) (2010) 1541-6.

[237] P.P. de Tombe, R.J. Solaro, Integration of cardiac myofilament activity and regulation with pathways signaling hypertrophy and failure, Ann Biomed Eng 28(8) (2000) 991-1001.

[238] C. Hidalgo, Y. Wu, J. Peng, W.F. Siems, K.B. Campbell, H. Granzier, Effect of diastolic pressure on MLC2v phosphorylation in the rat left ventricle, Arch Biochem Biophys 456(2) (2006) 216-23.

[239] Y. Ait Mou, J.Y. le Guennec, E. Mosca, P.P. de Tombe, O. Cazorla, Differential contribution of cardiac sarcomeric proteins in the myofibrillar force response to stretch, Pflugers Arch 457(1) (2008) 25-36.

[240] J.S. Davis, S. Hassanzadeh, S. Winitsky, H. Lin, C. Satorius, R. Vemuri, A.H. Aletras, H. Wen, N.D. Epstein, The overall pattern of cardiac contraction depends on a spatial gradient of myosin regulatory light chain phosphorylation, Cell 107(5) (2001) 631-41.

[241] J.E. Stelzer, H.S. Norman, P.P. Chen, J.R. Patel, R.L. Moss, Transmural variation in myosin heavy chain isoform expression modulates the timing of myocardial force generation in porcine left ventricle, J Physiol 586(21) (2008) 5203-14.

[242] Y. Peng, D. Yu, Z. Gregorich, X. Chen, A.M. Beyer, D.D. Gutterman, Y. Ge, In-depth proteomic analysis of human tropomyosin by top-down mass spectrometry, J Muscle Res Cell Motil 34(3-4) (2013) 199-210.

[243] V. Kooij, V. Venkatraman, J. Tra, J.A. Kirk, J. Rowell, A. Blice-Baum, A. Cammarato, J.E. Van Eyk, Sizing up models of heart failure: Proteomics from flies to humans, Proteomics Clin Appl 8(9-10) (2014) 653-64.

[244] Y. Peng, Z.R. Gregorich, S.G. Valeja, H. Zhang, W. Cai, Y.C. Chen, H. Guner, A.J. Chen, D.J. Schwahn, T.A. Hacker, X. Liu, Y. Ge, Top-down proteomics reveals concerted reductions in myofilament and Z-disc protein phosphorylation after acute myocardial infarction, Mol Cell Proteomics 13(10) (2014) 2752-64.

[245] Y. Peng, X. Chen, H. Zhang, Q. Xu, T.A. Hacker, Y. Ge, Top-down targeted proteomics for deep sequencing of tropomyosin isoforms, J Proteome Res 12(1) (2013) 187-98.

[246] X. Liu, Y. Inbar, P.C. Dorrestein, C. Wynne, N. Edwards, P. Souda, J.P. Whitelegge, V. Bafna, P.A. Pevzner, Deconvolution and database search of complex tandem mass spectra of intact proteins: a combinatorial approach, Mol Cell Proteomics 9(12) (2010) 2772-82.

[247] X. Liu, Y. Sirotkin, Y. Shen, G. Anderson, Y.S. Tsai, Y.S. Ting, D.R. Goodlett, R.D. Smith, V. Bafna, P.A. Pevzner, Protein identification using top-down, Mol Cell Proteomics 11(6) (2012) M111.008524.

[248] H. Guner, P.L. Close, W. Cai, H. Zhang, Y. Peng, Z.R. Gregorich, Y. Ge, MASH Suite: a user-friendly and versatile software interface for high-resolution mass spectrometry data interpretation and visualization, J Am Soc Mass Spectrom 25(3) (2014) 464-70.

[249] V. Kooij, R.J. Holewinski, A.M. Murphy, J.E. Van Eyk, Characterization of the cardiac myosin binding protein-C phosphoproteome in healthy and failing human hearts, J Mol Cell Cardiol 60 (2013) 116-20.

[250] P. Zhang, J.A. Kirk, W. Ji, C.G. dos Remedios, D.A. Kass, J.E. Van Eyk, A.M. Murphy, Multiple reaction monitoring to identify site-specific troponin I phosphorylated residues in the failing human heart, Circulation 126(15) (2012) 1828-37.

[251] S.T. DeGrande, S.C. Little, D.J. Nixon, P. Wright, J. Snyder, W. Dun, N. Murphy, A. Kilic, R. Higgins, P.F. Binkley, P.A. Boyden, C.A. Carnes, M.E. Anderson, T.J. Hund, P.J. Mohler, Molecular mechanisms underlying cardiac protein phosphatase 2A regulation in heart, J Biol Chem 288(2) (2013) 1032-46.

[252] P. Bouvagnet, H. Mairhofer, J.O. Leger, P. Puech, J.J. Leger, Distribution pattern of alpha and beta myosin in normal and diseased human ventricular myocardium, Basic Res Cardiol 84(1) (1989) 91-102.

[253] M.R. Locher, M.V. Razumova, J.E. Stelzer, H.S. Norman, R.L. Moss, Effects of low-level α-myosin heavy chain expression on contractile kinetics in porcine myocardium, Am J Physiol Heart Circ Physiol 300(3) (2011) H869-78.

[254] G. Agnetti, L.A. Kane, C. Guarnieri, C.M. Caldarera, J.E. Van Eyk, Proteomic technologies in the study of kinases: novel tools for the investigation of PKC in the heart, Pharmacol Res 55(6) (2007) 511-22.

[255] A.P. Walden, K.M. Dibb, A.W. Trafford, Differences in intracellular calcium homeostasis between atrial and ventricular myocytes, J Mol Cell Cardiol 46(4) (2009) 463-73.

[256] A.F. Huxley, R.M. Simmons, Proposed mechanism of force generation in striated muscle, Nature 233(5321) (1971) 533-8.

[257] A.G. Weeds, S. Lowey, Substructure of the myosin molecule. II. The light chains of myosin, J Mol Biol 61(3) (1971) 701-25.

[258] I. Rayment, H.M. Holden, M. Whittaker, C.B. Yohn, M. Lorenz, K.C. Holmes, R.A. Milligan, Structure of the actin-myosin complex and its implications for muscle contraction, Science 261(5117) (1993) 58-65.

[259] I. Rayment, W.R. Rypniewski, K. Schmidt-Bäse, R. Smith, D.R. Tomchick, M.M. Benning, D.A. Winkelmann, G. Wesenberg, H.M. Holden, Three-dimensional structure of myosin subfragment-1: a molecular motor, Science 261(5117) (1993) 50-8.

[260] P.A. Hofmann, J.M. Metzger, M.L. Greaser, R.L. Moss, Effects of partial extraction of light chain 2 on the Ca2+ sensitivities of isometric tension, stiffness, and velocity of shortening in skinned skeletal muscle fibers, J Gen Physiol 95(3) (1990) 477-98.

[261] S. Lowey, K.M. Trybus, Role of skeletal and smooth muscle myosin light chains, Biophys J 68(4 Suppl) (1995) 120S-126S; discussion 126S-127S.

[262] O.M. Hernandez, M. Jones, G. Guzman, D. Szczesna-Cordary, Myosin essential light chain in health and disease, Am J Physiol Heart Circ Physiol 292(4) (2007) H1643-54.

[263] K. Poetter, H. Jiang, S. Hassanzadeh, S.R. Master, A. Chang, M.C. Dalakas, I. Rayment, J.R. Sellers, L. Fananapazir, N.D. Epstein, Mutations in either the essential or regulatory light chains of myosin are associated with a rare myopathy in human heart and skeletal muscle, Nat Genet 13(1) (1996) 63-9.

[264] S.B. Scruggs, R.J. Solaro, The significance of regulatory light chain phosphorylation in cardiac physiology, Arch Biochem Biophys 510(2) (2011) 129-34.

[265] F. Sheikh, R.C. Lyon, J. Chen, Functions of myosin light chain-2 (MYL2) in cardiac muscle and disease, Gene 569(1) (2015) 14-20.

[266] C.C. Yuan, P. Muthu, K. Kazmierczak, J. Liang, W. Huang, T.C. Irving, R.M. Kanashiro-Takeuchi, J.M. Hare, D. Szczesna-Cordary, Constitutive phosphorylation of cardiac myosin regulatory light chain prevents development of hypertrophic cardiomyopathy in mice, Proc Natl Acad Sci U S A 112(30) (2015) E4138-46.

[267] D. Szczesna, D. Ghosh, Q. Li, A.V. Gomes, G. Guzman, C. Arana, G. Zhi, J.T. Stull, J.D. Potter, Familial hypertrophic cardiomyopathy mutations in the regulatory light chains of myosin affect their structure, Ca2+ binding, and phosphorylation, J Biol Chem 276(10) (2001) 7086-92.

[268] Z. Grabarek, Structural basis for diversity of the EF-hand calcium-binding proteins, J Mol Biol 359(3) (2006) 509-25.

[269] Z.R. Gregorich, Y. Peng, N.M. Lane, J.J. Wolff, S. Wang, W. Guo, H. Guner, J. Doop, T.A. Hacker, Y. Ge, Comprehensive assessment of chamber-specific and transmural heterogeneity in

myofilament protein phosphorylation by top-down mass spectrometry, J Mol Cell Cardiol 87 (2015) 102-12.

[270] M. Mann, N.L. Kelleher, Precision proteomics: the case for high resolution and high mass accuracy, Proc Natl Acad Sci U S A 105(47) (2008) 18132-8.

[271] L.A. Kane, I. Neverova, J.E. Van Eyk, Subfractionation of heart tissue: the "in sequence" myofilament protein extraction of myocardial tissue, Methods Mol Biol 357 (2007) 87-90.

[272] D.K. Arrell, I. Neverova, H. Fraser, E. Marbán, J.E. Van Eyk, Proteomic analysis of pharmacologically preconditioned cardiomyocytes reveals novel phosphorylation of myosin light chain 1, Circ Res 89(6) (2001) 480-7.

[273] W. Cai, H. Guner, Z.R. Gregorich, A.J. Chen, S. Ayaz-Guner, Y. Peng, S.G. Valeja, X. Liu, Y. Ge, MASH Suite Pro: A Comprehensive Software Tool for Top-down Proteomics, Mol Cell Proteomics (2015).

[274] F. Sievers, A. Wilm, D. Dineen, T.J. Gibson, K. Karplus, W. Li, R. Lopez, H. McWilliam, M. Remmert, J. Söding, J.D. Thompson, D.G. Higgins, Fast, scalable generation of high-quality protein multiple sequence alignments using Clustal Omega, Mol Syst Biol 7 (2011) 539.

[275] G.D. Henry, I.P. Trayer, S. Brewer, B.A. Levine, The widespread distribution of alpha-N-trimethylalanine as the N-terminal amino acid of light chains from vertebrate striated muscle myosins, Eur J Biochem 148(1) (1985) 75-82.

[276] I. Morano, M. Wankerl, M. Böhm, E. Erdmann, J.C. Rüegg, Myosin P-light chain isoenzymes in the human heart: evidence for diphosphorylation of the atrial P-LC form, Basic Res Cardiol 84(3) (1989) 298-305.

[277] J.A. Dixon, F.G. Spinale, Large animal models of heart failure: a critical link in the translation of basic science to clinical practice, Circ Heart Fail 2(3) (2009) 262-71.

[278] I. Morano, O. Ritter, A. Bonz, T. Timek, C.F. Vahl, G. Michel, Myosin light chain-actin interaction regulates cardiac contractility, Circ Res 76(5) (1995) 720-5.

[279] I. Morano, H. Haase, Different actin affinities of human cardiac essential myosin light chain isoforms, FEBS Lett 408(1) (1997) 71-4.

[280] P. Muthu, L. Wang, C.C. Yuan, K. Kazmierczak, W. Huang, O.M. Hernandez, M. Kawai, T.C. Irving, D. Szczesna-Cordary, Structural and functional aspects of the myosin essential light chain in cardiac muscle contraction, FASEB J 25(12) (2011) 4394-405.

[281] K.J. Webb, R.S. Lipson, Q. Al-Hadid, J.P. Whitelegge, S.G. Clarke, Identification of protein N-terminal methyltransferases in yeast and humans, Biochemistry 49(25) (2010) 5225-35.

[282] T. Arnesen, P. Van Damme, B. Polevoda, K. Helsens, R. Evjenth, N. Colaert, J.E. Varhaug, J. Vandekerckhove, J.R. Lillehaug, F. Sherman, K. Gevaert, Proteomics analyses reveal the evolutionary conservation and divergence of N-terminal acetyltransferases from yeast and humans, Proc Natl Acad Sci U S A 106(20) (2009) 8157-62.

[283] B. Persson, C. Flinta, G. von Heijne, H. Jörnvall, Structures of N-terminally acetylated proteins, Eur J Biochem 152(3) (1985) 523-7.

[284] A. Hershko, H. Heller, E. Eytan, G. Kaklij, I.A. Rose, Role of the alpha-amino group of protein in ubiquitin-mediated protein breakdown, Proc Natl Acad Sci U S A 81(22) (1984) 7021-5.

[285] A.T. Coulton, D.A. East, A. Galinska-Rakoczy, W. Lehman, D.P. Mulvihill, The recruitment of acetylated and unacetylated tropomyosin to distinct actin polymers permits the discrete regulation of specific myosins in fission yeast, J Cell Sci 123(Pt 19) (2010) 3235-43.

[286] C.S. Hwang, A. Shemorry, A. Varshavsky, N-terminal acetylation of cellular proteins creates specific degradation signals, Science 327(5968) (2010) 973-7.

[287] R. Behnia, B. Panic, J.R. Whyte, S. Munro, Targeting of the Arf-like GTPase Arl3p to the Golgi requires N-terminal acetylation and the membrane protein Sys1p, Nat Cell Biol 6(5) (2004) 405-13.

[288] A. Stock, S. Clarke, C. Clarke, J. Stock, N-terminal methylation of proteins: structure, function and specificity, FEBS Lett 220(1) (1987) 8-14.

[289] H.L. Sweeney, Function of the N terminus of the myosin essential light chain of vertebrate striated muscle, Biophys J 68(4 Suppl) (1995) 112S-118S; discussion 118S-119S.

[290] S.A. Jeacocke, P.J. England, Phosphorylation of myosin light chains in perfused rat heart. Effect of adrenaline and increased cytoplasmic calcium ions, Biochem J 188(3) (1980) 763-8.

[291] C. Toepfer, V. Caorsi, T. Kampourakis, M.B. Sikkel, T.G. West, M.C. Leung, S.A. Al-Saud, K.T. MacLeod, A.R. Lyon, S.B. Marston, J.R. Sellers, M.A. Ferenczi, Myosin regulatory light chain (RLC) phosphorylation change as a modulator of cardiac muscle contraction in disease, J Biol Chem 288(19) (2013) 13446-54.

[292] P.J. Silver, L.M. Buja, J.T. Stull, Frequency-dependent myosin light chain phosphorylation in isolated myocardium, J Mol Cell Cardiol 18(1) (1986) 31-7.

[293] T. Kampourakis, M. Irving, Phosphorylation of myosin regulatory light chain controls myosin head conformation in cardiac muscle, J Mol Cell Cardiol 85 (2015) 199-206.

[294] L.A. Walker, A.M. Medway, J.S. Walker, J.C. Cleveland, P.M. Buttrick, Tissue procurement strategies affect the protein biochemistry of human heart samples, J Muscle Res Cell Motil 31(5-6) (2011) 309-14.

[295] V.J. Cadete, J. Sawicka, J.S. Jaswal, G.D. Lopaschuk, R. Schulz, D. Szczesna-Cordary, G. Sawicki, Ischemia/reperfusion-induced myosin light chain 1 phosphorylation increases its degradation by matrix metalloproteinase 2, FEBS J 279(13) (2012) 2444-54.

[296] S.B. Scruggs, R. Reisdorph, M.L. Armstrong, C.M. Warren, N. Reisdorph, R.J. Solaro, P.M. Buttrick, A novel, in-solution separation of endogenous cardiac sarcomeric proteins and identification of distinct charged variants of regulatory light chain, Mol Cell Proteomics 9(9) (2010) 1804-18.

[297] P. Ohlmann, A. Tesse, C. Loichot, H. Ralay Ranaivo, G. Roul, C. Philippe, D.M. Watterson, J. Haiech, R. Andriantsitohaina, Deletion of MLCK210 induces subtle changes in vascular reactivity but does not affect cardiac function, Am J Physiol Heart Circ Physiol 289(6) (2005) H2342-9.

[298] J.Y. Chan, M. Takeda, L.E. Briggs, M.L. Graham, J.T. Lu, N. Horikoshi, E.O. Weinberg, H. Aoki, N. Sato, K.R. Chien, H. Kasahara, Identification of cardiac-specific myosin light chain kinase, Circ Res 102(5) (2008) 571-80.

[299] A.N. Chang, G. Chen, R.D. Gerard, K.E. Kamm, J.T. Stull, Cardiac myosin is a substrate for zipper-interacting protein kinase (ZIPK), J Biol Chem 285(8) (2010) 5122-6.

[300] J. Axelsson, M. Palmblad, K. Håkansson, P. Håkansson, Electron capture dissociation of substance P using a commercially available Fourier transform ion cyclotron resonance mass spectrometer, Rapid Commun Mass Spectrom 13(6) (1999) 474-7.

[301] T.G. Schaaff, B.J. Cargile, J.L. Stephenson, S.A. McLuckey, Ion trap collisional activation of the (M + 2H)2+ - (M + 17H)17+ ions of human hemoglobin beta-chain, Anal Chem 72(5) (2000) 899-907.

[302] J.O. Mudd, D.A. Kass, Tackling heart failure in the twenty-first century, Nature 451(7181) (2008) 919-28.

[303] G. de Couto, M. Ouzounian, P.P. Liu, Early detection of myocardial dysfunction and heart failure, Nat Rev Cardiol 7(6) (2010) 334-44.

[304] V.L. Roger, A.S. Go, D.M. Lloyd-Jones, E.J. Benjamin, J.D. Berry, W.B. Borden, D.M. Bravata, S. Dai, E.S. Ford, C.S. Fox, H.J. Fullerton, C. Gillespie, S.M. Hailpern, J.A. Heit, V.J. Howard, B.M. Kissela, S.J. Kittner, D.T. Lackland, J.H. Lichtman, L.D. Lisabeth, D.M. Makuc, G.M. Marcus, A. Marelli, D.B. Matchar, C.S. Moy, D. Mozaffarian, M.E. Mussolino, G. Nichol, N.P. Paynter, E.Z. Soliman, P.D. Sorlie, N. Sotoodehnia, T.N. Turan, S.S. Virani, N.D. Wong, D. Woo, M.B. Turner, A.H.A.S.C.a.S.S. Subcommittee, Executive summary: heart disease and stroke statistics--2012 update: a report from the American Heart Association, Circulation 125(1) (2012) 188-97.

[305] M.A. Pfeffer, E. Braunwald, Ventricular remodeling after myocardial infarction. Experimental observations and clinical implications, Circulation 81(4) (1990) 1161-72.

[306] R.J. Solaro, Multiplex kinase signaling modifies cardiac function at the level of sarcomeric proteins, J Biol Chem 283(40) (2008) 26829-33.

[307] R.J. Solaro, C.M. Warren, S.B. Scruggs, Why is it important to analyze the cardiac sarcomere subproteome?, Expert Rev Proteomics 7(3) (2010) 311-4.

[308] R.L. Moss, M. Razumova, D.P. Fitzsimons, Myosin crossbridge activation of cardiac thin filaments: implications for myocardial function in health and disease, Circ Res 94(10) (2004) 1290-300.

[309] S. Takeda, A. Yamashita, K. Maeda, Y. Maéda, Structure of the core domain of human cardiac troponin in the Ca(2+)-saturated form, Nature 424(6944) (2003) 35-41.

[310] X. Yin, F. Cuello, U. Mayr, Z. Hao, M. Hornshaw, E. Ehler, M. Avkiran, M. Mayr, Proteomics analysis of the cardiac myofilament subproteome reveals dynamic alterations in phosphatase subunit distribution, Mol Cell Proteomics 9(3) (2010) 497-509.

[311] X. Han, M. Jin, K. Breuker, F.W. McLafferty, Extending top-down mass spectrometry to proteins with masses greater than 200 kilodaltons, Science 314(5796) (2006) 109-12.

[312] J.C. Tran, L. Zamdborg, D.R. Ahlf, J.E. Lee, A.D. Catherman, K.R. Durbin, J.D. Tipton, A. Vellaichamy, J.F. Kellie, M. Li, C. Wu, S.M. Sweet, B.P. Early, N. Siuti, R.D. LeDuc, P.D. Compton, P.M. Thomas, N.L. Kelleher, Mapping intact protein isoforms in discovery mode using top-down proteomics, Nature 480(7376) (2011) 254-8.

[313] C.M. Ryan, P. Souda, S. Bassilian, R. Ujwal, J. Zhang, J. Abramson, P. Ping, A. Durazo, J.U. Bowie, S.S. Hasan, D. Baniulis, W.A. Cramer, K.F. Faull, J.P. Whitelegge, Post-translational modifications of integral membrane proteins resolved by top-down Fourier transform mass spectrometry with collisionally activated dissociation, Mol Cell Proteomics 9(5) (2010) 791-803.

[314] M.T. Tomkowiak, A.J. Klein, K.K. Vigen, T.A. Hacker, M.A. Speidel, M.S. VanLysel, A.N. Raval, Targeted transendocardial therapeutic delivery guided by MRI-x-ray image fusion, Catheter Cardiovasc Interv 78(3) (2011) 468-78.

[315] X. Wang, H. Su, Unraveling enigma in the z-disks, Circ Res 107(3) (2010) 321-3.

[316] I. Neverova, J.E. Van Eyk, Application of reversed phase high performance liquid chromatography for subproteomic analysis of cardiac muscle, Proteomics 2(1) (2002) 22-31.

[317] G. Vilahur, O. Juan-Babot, E. Peña, B. Oñate, L. Casaní, L. Badimon, Molecular and cellular mechanisms involved in cardiac remodeling after acute myocardial infarction, J Mol Cell Cardiol 50(3) (2011) 522-33.

[318] R.J. Solaro, J. van der Velden, Why does troponin I have so many phosphorylation sites? Fact and fancy, J Mol Cell Cardiol 48(5) (2010) 810-6.

[319] R.J. Solaro, M. Henze, T. Kobayashi, Integration of troponin I phosphorylation with cardiac regulatory networks, Circ Res 112(2) (2013) 355-66.

[320] F. Sheikh, R.C. Lyon, J. Chen, Getting the skinny on thick filament regulation in cardiac muscle biology and disease, Trends Cardiovasc Med 24(4) (2014) 133-41.

[321] R.L. Moss, D.P. Fitzsimons, Myosin light chain 2 into the mainstream of cardiac development and contractility, Circ Res 99(3) (2006) 225-7.

[322] J. van der Velden, Z. Papp, N.M. Boontje, R. Zaremba, J.W. de Jong, P.M. Janssen, G. Hasenfuss, G.J. Stienen, The effect of myosin light chain 2 dephosphorylation on Ca2+ -sensitivity of force is enhanced in failing human hearts, Cardiovasc Res 57(2) (2003) 505-14.

[323] B.T. Chait, Chemistry. Mass spectrometry: bottom-up or top-down?, Science 314(5796) (2006) 65-6.

[324] J.D. Tipton, J.C. Tran, A.D. Catherman, D.R. Ahlf, K.R. Durbin, N.L. Kelleher, Analysis of intact protein isoforms by mass spectrometry, J Biol Chem 286(29) (2011) 25451-8.

[325] P. Kuhn, Q. Xu, E. Cline, D. Zhang, Y. Ge, W. Xu, Delineating Anopheles gambiae coactivator associated arginine methyltransferase 1 automethylation using top-down high resolution tandem mass spectrometry, Protein Sci 18(6) (2009) 1272-80.

[326] S.K. Sze, Y. Ge, H. Oh, F.W. McLafferty, Top-down mass spectrometry of a 29-kDa protein for characterization of any posttranslational modification to within one residue, Proc Natl Acad Sci U S A 99(4) (2002) 1774-9.

[327] J.J. Pesavento, C.A. Mizzen, N.L. Kelleher, Quantitative analysis of modified proteins and their positional isomers by tandem mass spectrometry: human histone H4, Anal Chem 78(13) (2006) 4271-80.

[328] J.J. Pesavento, C.R. Bullock, R.D. LeDuc, C.A. Mizzen, N.L. Kelleher, Combinatorial modification of human histone H4 quantitated by two-dimensional liquid chromatography coupled with top down mass spectrometry, J Biol Chem 283(22) (2008) 14927-37.

[329] B. Thangaraj, C.M. Ryan, P. Souda, K. Krause, K.F. Faull, A.P. Weber, P. Fromme, J.P. Whitelegge, Data-directed top-down Fourier-transform mass spectrometry of a large integral membrane protein complex: photosystem II from Galdieria sulphuraria, Proteomics 10(20) (2010) 3644-56.

[330] J. Whitelegge, F. Halgand, P. Souda, V. Zabrouskov, Top-down mass spectrometry of integral membrane proteins, Expert Rev Proteomics 3(6) (2006) 585-96.

[331] P. Souda, C.M. Ryan, W.A. Cramer, J. Whitelegge, Profiling of integral membrane proteins and their post translational modifications using high-resolution mass spectrometry, Methods 55(4) (2011) 330-6.

[332] P.D. Compton, L. Zamdborg, P.M. Thomas, N.L. Kelleher, On the scalability and requirements of whole protein mass spectrometry, Anal Chem 83(17) (2011) 6868-74.

[333] X. Chen, Y. Ge, Ultrahigh pressure fast size exclusion chromatography for top-down proteomics, Proteomics 13(17) (2013) 2563-6.

[334] N. Niederländer, N.A. Fayein, C. Auffray, P. Pomiès, Characterization of a new human isoform of the enigma homolog family specifically expressed in skeletal muscle, Biochem Biophys Res Commun 325(4) (2004) 1304-11.

[335] A. Fabiato, Computer programs for calculating total from specified free or free from specified total ionic concentrations in aqueous solutions containing multiple metals and ligands, Methods Enzymol 157 (1988) 378-417.

[336] R.E. Godt, B.D. Lindley, Influence of temperature upon contractile activation and isometric force production in mechanically skinned muscle fibers of the frog, J Gen Physiol 80(2) (1982) 279-97.

[337] J.R. Patel, J.M. Pleitner, R.L. Moss, M.L. Greaser, Magnitude of length-dependent changes in contractile properties varies with titin isoform in rat ventricles, Am J Physiol Heart Circ Physiol 302(3) (2012) H697-708.

[338] R.L. Moss, A.E. Swinford, M.L. Greaser, Alterations in the Ca2+ sensitivity of tension development by single skeletal muscle fibers at stretched lengths, Biophys J 43(1) (1983) 115-9.

[339] B. Brenner, E. Eisenberg, Rate of force generation in muscle: correlation with actomyosin ATPase activity in solution, Proc Natl Acad Sci U S A 83(10) (1986) 3542-6.

[340] J.R. Patel, D.P. Fitzsimons, S.H. Buck, M. Muthuchamy, D.F. Wieczorek, R.L. Moss, PKA accelerates rate of force development in murine skinned myocardium expressing α- or β-tropomyosin, Am. J. Physiol. 280 (2001) H2732-H2739.

[341] A. Shevchenko, M. Wilm, O. Vorm, M. Mann, Mass spectrometric sequencing of proteins silver-stained polyacrylamide gels, Anal Chem 68(5) (1996) 850-8.

[342] P.B. Chase, D.A. Martyn, J.D. Hannon, Isometric force redevelopment of skinned muscle fibers from rabbit activated with and without Ca2+, Biophys J 67(5) (1994) 1994-2001.

[343] B. Brenner, Effect of Ca2+ on cross-bridge turnover kinetics in skinned single rabbit psoas fibers: implications for regulation of muscle contraction, Proc Natl Acad Sci U S A 85(9) (1988) 3265-9.

[344] S.J. Ford, M. Chandra, The effects of slow skeletal troponin I expression in the murine myocardium are influenced by development-related shifts in myosin heavy chain isoform, J Physiol 590(23) (2012) 6047-63.

[345] M.R. Locher, M.V. Razumova, J.E. Stelzer, H.S. Norman, J.R. Patel, R.L. Moss, Determination of rate constants for turnover of myosin isoforms in rat myocardium: implications for in vivo contractile kinetics, Am J Physiol Heart Circ Physiol 297(1) (2009) H247-56.

[346] F.S. Korte, K.S. McDonald, S.P. Harris, R.L. Moss, Loaded shortening, power output, and rate of force redevelopment are increased with knockout of cardiac myosin binding protein-C, Circ Res 93(8) (2003) 752-8.

[347] R. Mamidi, K.S. Gresham, S. Verma, J.E. Stelzer, Cardiac Myosin Binding Protein-C Phosphorylation Modulates Myofilament Length-Dependent Activation, Front Physiol 7 (2016) 38.

[348] C.N. Toepfer, T.G. West, M.A. Ferenczi, Revisiting Frank-Starling: regulatory light chain phosphorylation alters the rate of force redevelopment (ktr) in a length-dependent fashion, J Physiol 594(18) (2016) 5237-54.

[349] S.K. Gollapudi, R. Mamidi, S.L. Mallampalli, M. Chandra, The N-terminal extension of cardiac troponin T stabilizes the blocked state of cardiac thin filament, Biophys J 103(5) (2012) 940-8.

[350] K. Christensen, G. Doblhammer, R. Rau, J.W. Vaupel, Ageing populations: the challenges ahead, Lancet 374(9696) (2009) 1196-208.

[351] M.S. Miller, D.M. Callahan, M.J. Toth, Skeletal muscle myofilament adaptations to aging, disease, and disuse and their effects on whole muscle performance in older adult humans, Front Physiol 5 (2014) 369.

[352] R.L. Moss, G.M. Diffee, M.L. Greaser, Contractile properties of skeletal muscle fibers in relation to myofibrillar protein isoforms, Rev Physiol Biochem Pharmacol 126 (1995) 1-63.

[353] S. Schiaffino, C. Reggiani, Molecular diversity of myofibrillar proteins: gene regulation and functional significance, Physiol Rev 76(2) (1996) 371-423.

[354] J.T. Stull, K.E. Kamm, R. Vandenboom, Myosin light chain kinase and the role of myosin light chain phosphorylation in skeletal muscle, Arch Biochem Biophys 510(2) (2011) 120-8.

[355] L.V. Thompson, Age-related muscle dysfunction, Exp Gerontol 44(1-2) (2009) 106-11.

[356] H. Degens, F. Yu, X. Li, L. Larsson, Effects of age and gender on shortening velocity and myosin isoforms in single rat muscle fibres, Acta Physiol Scand 163(1) (1998) 33-40.

[357] T.J. Eddinger, R.G. Cassens, R.L. Moss, Mechanical and histochemical characterization of skeletal muscles from senescent rats, Am J Physiol 251(3 Pt 1) (1986) C421-30.

[358] G.S. Lynch, B.J. Rodgers, D.A. Williams, The effects of age and low-intensity endurance exercise on the contractile properties of single skinned fast- and slow-twitch skeletal muscle fibres, Growth Dev Aging 57(3) (1993) 147-61.

[359] B. Domon, R. Aebersold, Options and considerations when selecting a quantitative proteomics strategy, Nat Biotechnol 28(7) (2010) 710-21.

[360] R. Schiess, B. Wollscheid, R. Aebersold, Targeted proteomic strategy for clinical biomarker discovery, Mol Oncol 3(1) (2009) 33-44.

[361] J.P. Whitelegge, H. Zhang, R. Aguilera, R.M. Taylor, W.A. Cramer, Full subunit coverage liquid chromatography electrospray ionization mass spectrometry (LCMS+) of an oligomeric membrane protein: cytochrome b(6)f complex from spinach and the cyanobacterium Mastigocladus laminosus, Mol Cell Proteomics 1(10) (2002) 816-27.

[362] J.P. Whitelegge, V. Zabrouskov, F. Halgand, P. Souda, S. Bassilian, W. Yan, L. Wolinsky, J.A. Loo, D.T. Wong, K.F. Faull, Protein-Sequence Polymorphisms and Post-translational Modifications in Proteins from Human Saliva using Top-Down Fourier-transform Ion Cyclotron Resonance Mass Spectrometry, Int J Mass Spectrom 268(2-3) (2007) 190-197.

[363] K.J. Webb, A. Laganowsky, J.P. Whitelegge, S.G. Clarke, Identification of two SET domain proteins required for methylation of lysine residues in yeast ribosomal protein Rpl42ab, J Biol Chem 283(51) (2008) 35561-8.

[364] F. Halgand, V. Zabrouskov, S. Bassilian, P. Souda, J.A. Loo, K.F. Faull, D.T. Wong, J.P. Whitelegge, Defining intact protein primary structures from saliva: a step toward the human proteome project, Anal Chem 84(10) (2012) 4383-95.

[365] D.L. Puppione, C.M. Ryan, S. Bassilian, P. Souda, X. Xiao, O.A. Ryder, J.P. Whitelegge, Detection of two distinct forms of apoC-I in great apes, Comp Biochem Physiol Part D Genomics Proteomics 5(1) (2010) 73-9.

[366] J. Chamot-Rooke, G. Mikaty, C. Malosse, M. Soyer, A. Dumont, J. Gault, A.F. Imhaus, P. Martin, M. Trellet, G. Clary, P. Chafey, L. Camoin, M. Nilges, X. Nassif, G. Duménil, Posttranslational modification of pili upon cell contact triggers N. meningitidis dissemination, Science 331(6018) (2011) 778-82.

[367] D. Sheehan, B. Hrapchak, Theory and practice of histotechnology, 2nd ed., Mosby, St. Louis, 1980.

[368] G.M. Diffee, M.L. Greaser, F.C. Reinach, R.L. Moss, Effects of a non-divalent cation binding mutant of myosin regulatory light chain on tension generation in skinned skeletal muscle fibers, Biophys J 68(4) (1995) 1443-52.

[369] G.M. Diffee, E. Chung, Altered single cell force-velocity and power properties in exercise-trained rat myocardium, J Appl Physiol (1985) 94(5) (2003) 1941-8.

[370] A.S. Cornachione, P.C. Benedini-Elias, J.C. Polizello, L.C. Carvalho, A.C. Mattiello-Sverzut, Characterization of fiber types in different muscles of the hindlimb in female weanling and adult Wistar rats, Acta Histochem Cytochem 44(2) (2011) 43-50.

[371] R. Jakes, F. Northrop, J. Kendrick-Jones, Calcium binding regions of myosin 'regulatory' light chains, FEBS Lett 70(1) (1976) 229-34.

[372] A. Macaluso, G. De Vito, Muscle strength, power and adaptations to resistance training in older people, Eur J Appl Physiol 91(4) (2004) 450-72.

[373] E. Gonzalez, M.L. Messi, Z. Zheng, O. Delbono, Insulin-like growth factor-1 prevents age-related decrease in specific force and intracellular Ca2+ in single intact muscle fibres from transgenic mice, J Physiol 552(Pt 3) (2003) 833-44.

[374] K.F. Reid, R.A. Fielding, Skeletal muscle power: a critical determinant of physical functioning in older adults, Exerc Sport Sci Rev 40(1) (2012) 4-12.

[375] T.G. Graber, J.H. Kim, R.W. Grange, L.K. McLoon, L.V. Thompson, C57BL/6 life span study: age-related declines in muscle power production and contractile velocity, Age (Dordr) 37(3) (2015) 9773.

[376] D.A. Lowe, J.T. Surek, D.D. Thomas, L.V. Thompson, Electron paramagnetic resonance reveals age-related myosin structural changes in rat skeletal muscle fibers, Am J Physiol Cell Physiol 280(3) (2001) C540-7.

[377] R.W. Grange, C.R. Cory, R. Vandenboom, M.E. Houston, Myosin phosphorylation augments force-displacement and force-velocity relationships of mouse fast muscle, Am J Physiol 269(3 Pt 1) (1995) C713-24.

[378] Y. Wang, K. Ajtai, T.P. Burghardt, Ventricular myosin modifies in vitro step-size when phosphorylated, J Mol Cell Cardiol 72 (2014) 231-7.

[379] M.J. Greenberg, T.R. Mealy, J.D. Watt, M. Jones, D. Szczesna-Cordary, J.R. Moore, The molecular effects of skeletal muscle myosin regulatory light chain phosphorylation, Am J Physiol Regul Integr Comp Physiol 297(2) (2009) R265-74.

[380] M.A. Gillette, S.A. Carr, Quantitative analysis of peptides and proteins in biomedicine by targeted mass spectrometry, Nat Methods 10(1) (2013) 28-34.

[381] M.L. Johnson, M.M. Robinson, K.S. Nair, Skeletal muscle aging and the mitochondrion, Trends Endocrinol Metab 24(5) (2013) 247-56.

[382] D.M. Callahan, M.S. Miller, A.P. Sweeny, T.W. Tourville, J.R. Slauterbeck, P.D. Savage, D.W. Maugan, P.A. Ades, B.D. Beynnon, M.J. Toth, Muscle disuse alters skeletal muscle contractile function at the molecular and cellular levels in older adult humans in a sex-specific manner, J Physiol 592(20) (2014) 4555-73.

[383] Z.R. Gregorich, Y. Peng, W. Cai, Y. Jin, L. Wei, A.J. Chen, S.H. McKiernan, J.M. Aiken, R.L. Moss, G.M. Diffee, Y. Ge, Top-Down Targeted Proteomics Reveals Decrease in Myosin Regulatory Light-Chain Phosphorylation That Contributes to Sarcopenic Muscle Dysfunction, J Proteome Res 15(8) (2016) 2706-16.

[384] K.F. Medzihradszky, X. Zhang, R.J. Chalkley, S. Guan, M.A. McFarland, M.J. Chalmers, A.G. Marshall, R.L. Diaz, C.D. Allis, A.L. Burlingame, Characterization of Tetrahymena histone H2B variants and posttranslational populations by electron capture dissociation (ECD) Fourier transform ion cyclotron mass spectrometry (FT-ICR MS), Mol Cell Proteomics 3(9) (2004) 872-86.

[385] H. Steen, J.A. Jebanathirajah, J. Rush, N. Morrice, M.W. Kirschner, Phosphorylation analysis by mass spectrometry: myths, facts, and the consequences for qualitative and quantitative measurements, Mol Cell Proteomics 5(1) (2006) 172-81.

[386] C.S. Hintz, E.F. Coyle, K.K. Kaiser, M.M. Chi, O.H. Lowry, Comparison of muscle fiber typing by quantitative enzyme assays and by myosin ATPase staining, J Histochem Cytochem 32(6) (1984) 655-60.

[387] R.S. Staron, W.J. Kraemer, R.S. Hikida, A.C. Fry, J.D. Murray, G.E. Campos, Fiber type composition of four hindlimb muscles of adult Fisher 344 rats, Histochem Cell Biol 111(2) (1999) 117-23.

[388] R.D. Lipman, C.E. Chrisp, D.G. Hazzard, R.T. Bronson, Pathologic characterization of brown Norway, brown Norway x Fischer 344, and Fischer 344 x brown Norway rats with relation to age, J Gerontol A Biol Sci Med Sci 51(1) (1996) B54-9.

[389] C. Huang, Q. Zhou, P. Liang, M.S. Hollander, F. Sheikh, X. Li, M. Greaser, G.D. Shelton, S. Evans, J. Chen, Characterization and in vivo functional analysis of splice variants of cypher, J Biol Chem 278(9) (2003) 7360-5.

[390] R.L. Strausberg, E.A. Feingold, L.H. Grouse, J.G. Derge, R.D. Klausner, F.S. Collins, L. Wagner, C.M. Shenmen, G.D. Schuler, S.F. Altschul, B. Zeeberg, K.H. Buetow, C.F. Schaefer, N.K. Bhat, R.F. Hopkins, H. Jordan, T. Moore, S.I. Max, J. Wang, F. Hsieh, L. Diatchenko, K. Marusina, A.A. Farmer, G.M. Rubin, L. Hong, M. Stapleton, M.B. Soares, M.F. Bonaldo, T.L. Casavant, T.E. Scheetz, M.J. Brownstein, T.B. Usdin, S. Toshiyuki, P. Carninci, C. Prange, S.S. Raha, N.A. Loquellano, G.J. Peters, R.D. Abramson, S.J. Mullahy, S.A. Bosak, P.J. McEwan, K.J. McKernan, J.A. Malek, P.H. Gunaratne, S. Richards, K.C. Worley, S. Hale, A.M. Garcia, L.J. Gay, S.W. Hulyk, D.K. Villalon, D.M. Muzny, E.J. Sodergren, X. Lu, R.A. Gibbs, J. Fahey, E. Helton, M. Ketteman, A. Madan, S. Rodrigues, A. Sanchez, M. Whiting, A.C. Young, Y. Shevchenko, G.G. Bouffard, R.W. Blakesley, J.W. Touchman, E.D. Green, M.C. Dickson, A.C. Rodriguez, J. Grimwood, J. Schmutz, R.M. Myers, Y.S. Butterfield, M.I. Krzywinski, U. Skalska, D.E. Smailus, A. Schnerch, J.E. Schein, S.J. Jones, M.A. Marra, M.G.C.P. Team, Generation and initial analysis of more than 15,000 full-length human and mouse cDNA sequences, Proc Natl Acad Sci U S A 99(26) (2002) 16899-903.

[391] J. Gannon, P. Doran, A. Kirwan, K. Ohlendieck, Drastic increase of myosin light chain MLC-2 in senescent skeletal muscle indicates fast-to-slow fibre transition in sarcopenia of old age, Eur J Cell Biol 88(11) (2009) 685-700.

[392] L.M. Snow, L.K. McLoon, L.V. Thompson, Adult and developmental myosin heavy chain isoforms in soleus muscle of aging Fischer Brown Norway rat, Anat Rec A Discov Mol Cell Evol Biol 286(1) (2005) 866-73.

[393] S.E. Alway, P.M. Siu, Nuclear apoptosis contributes to sarcopenia, Exerc Sport Sci Rev 36(2) (2008) 51-7.

[394] A.J. Moir, H.A. Cole, S.V. Perry, The phosphorylation sites of troponin T from white skeletal muscle and the effects of interaction with troponin C on their phosphorylation by phosphorylase kinase, Biochem J 161(2) (1977) 371-82.

[395] T. Finkel, N.J. Holbrook, Oxidants, oxidative stress and the biology of ageing, Nature 408(6809) (2000) 239-47.

[396] R.J. Moen, J.C. Klein, D.D. Thomas, Electron paramagnetic resonance resolves effects of oxidative stress on muscle proteins, Exerc Sport Sci Rev 42(1) (2014) 30-6.

[397] W. Lehman, G. Medlock, X.E. Li, W. Suphamungmee, A.Y. Tu, A. Schmidtmann, Z. Ujfalusi, S. Fischer, J.R. Moore, M.A. Geeves, M. Regnier, Phosphorylation of Ser283 enhances the stiffness of the tropomyosin head-to-tail overlap domain, Arch Biochem Biophys 571 (2015) 10-5.

[398] O. Delbono, K.S. O'Rourke, W.H. Ettinger, Excitation-calcium release uncoupling in aged single human skeletal muscle fibers, J Membr Biol 148(3) (1995) 211-22.

[399] F. Sheikh, M.L. Bang, S. Lange, J. Chen, "Z"eroing in on the role of Cypher in striated muscle function, signaling, and human disease, Trends Cardiovasc Med 17(8) (2007) 258-62.

[400] R. Barrès, T. Gonzalez, Y. Le Marchand-Brustel, J.F. Tanti, The interaction between the adaptor protein APS and Enigma is involved in actin organisation, Exp Cell Res 308(2) (2005) 334-44.

[401] R. Barrès, T. Grémeaux, P. Gual, T. Gonzalez, J. Gugenheim, A. Tran, Y. Le Marchand-Brustel, J.F. Tanti, Enigma interacts with adaptor protein with PH and SH2 domains to control insulin-induced actin cytoskeleton remodeling and glucose transporter 4 translocation, Mol Endocrinol 20(11) (2006) 2864-75.

[402] K. Durick, G.N. Gill, S.S. Taylor, Shc and Enigma are both required for mitogenic signaling by Ret/ptc2, Mol Cell Biol 18(4) (1998) 2298-308.

[403] M.G. Borrello, E. Mercalli, C. Perego, D. Degl'Innocenti, S. Ghizzoni, E. Arighi, B. Eroini, M.G. Rizzetti, M.A. Pierotti, Differential interaction of Enigma protein with the two RET isoforms, Biochem Biophys Res Commun 296(3) (2002) 515-22.

[404] E. de Graaff, S. Srinivas, C. Kilkenny, V. D'Agati, B.S. Mankoo, F. Costantini, V. Pachnis, Differential activities of the RET tyrosine kinase receptor isoforms during mammalian embryogenesis, Genes Dev 15(18) (2001) 2433-44.

[405] R. D'Cruz, P.J. Plant, L.A. Pablo, S. Lin, J. Chackowicz, J. Correa, J. Bain, J. Batt, PDLIM7 is a novel target of the ubiquitin ligase Nedd4-1 in skeletal muscle, Biochem J 473(3) (2016) 267-76.

[406] M.A. Geeves, S.E. Hitchcock-DeGregori, P.W. Gunning, A systematic nomenclature for mammalian tropomyosin isoforms, J Muscle Res Cell Motil 36(2) (2015) 147-53.

[407] R. Rajashree, B.C. Blunt, P.A. Hofmann, Modulation of myosin phosphatase targeting subunit and protein phosphatase 1 in the heart, Am J Physiol Heart Circ Physiol 289(4) (2005) H1736-43.

[408] Z. Zhang, K. Sun, D.A. Saloner, A.W. Wallace, L. Ge, A.J. Baker, J.M. Guccione, M.B. Ratcliffe, The benefit of enhanced contractility in the infarct borderzone: a virtual experiment, Front Physiol 3 (2012) 86.

[409] M. Chandra, R. Mamidi, S. Ford, C. Hidalgo, C. Witt, C. Ottenheijm, S. Labeit, H. Granzier, Nebulin alters cross-bridge cycling kinetics and increases thin filament activation: a novel mechanism for increasing tension and reducing tension cost, J Biol Chem 284(45) (2009) 30889-96.

[410] G. Mastrototaro, X. Liang, X. Li, P. Carullo, N. Piroddi, C. Tesi, Y. Gu, N.D. Dalton, K.L. Peterson, C. Poggesi, F. Sheikh, J. Chen, M.L. Bang, Nebulette knockout mice have normal cardiac function, but show Z-line widening and up-regulation of cardiac stress markers, Cardiovasc Res 107(2) (2015) 216-25.